THEORETICAL AND EXPERIMENTAL STUDIES OF THE CONFORMATIONS AND VIBRATIONS OF SMALL MOLECULES

by

PETER ROLAND FRANKE

(Under the Direction of Gary E. Douberly)

ABSTRACT

The vibrational spectra of small, organic radicals are measured and interpreted. A major focus is the effective use of *ab initio* quantum chemistry to describe anharmonic resonance polyads in the CH stretching fundamental region (about 2800 – 3150 cm^{-1}). An accurate, cost-effective protocol is employed that uses vibrational perturbation theory, based on hybrid quartic force fields, with large effective Hamiltonian treatments of resonances. The Second-Order Vibrational Perturbation Theory with Resonances (VPT2+K) approach is shown to be very successful at modeling the CH stretch regions of isoprene and is notably much more successful at predicting relative intensities than approaches with less extensive resonance treatments. Clear vibrational signatures of the higher energy *gauche* isoprene isomer are reported for the first time, and improved thermochemical predictions are made with the aid of coupled-cluster theory. Vibrationally resolved CH stretching spectra of the propyl radicals and ethylperoxy radical are measured in helium droplets. These represent the highest quality vibrational spectra of these species to date, revealing numerous overtone and combination band transitions. VPT2+K describes these radicals with varying levels of success, depending on the severity of their large amplitude motion. New theoretical predictions are presented for the *tert*-butylperoxy and HO_4^+ systems. The structure, energetics, and vibrational spectroscopy of both the ground and lowest electronically excited state of *tert*-butylperoxy radical are modeled with high-level coupled cluster theory. Theoretical studies of the HO_4^+ system are focused on understanding its argon-tagged infrared

photodissociation spectrum, also reported here. Various new isomers are located with a combination of multiconfigurational methods and single-reference coupled-cluster theory. The spectra of HO_4^+ and DO_4^+ are understood as arising from these new isomers, which are not traditional proton-bound dimers.

INDEX WORDS: INFRARED SPECTROSCOPY, VIBRATIONAL ANHARMONICITY, HELIUM NANODROPLET ISOLATION, THEORETICAL CHEMISTRY, PEROXY RADICALS

THEORETICAL AND EXPERIMENTAL STUDIES OF THE CONFORMATIONS AND VIBRATIONS OF SMALL MOLECULES

by

PETER ROLAND FRANKE

B.S., Virginia Commonwealth University, 2014

A Dissertation Submitted to the Graduate Faculty of The University of Georgia in Partial Fulfillment of the Requirements for the Degree

DOCTOR OF PHILOSHOPY

ATHENS, GEORGIA

2020

THEORETICAL AND EXPERIMENTAL STUDIES OF THE CONFORMATIONS AND VIBRATIONS OF SMALL MOLECULES

by

PETER ROLAND FRANKE

Major Professor:	Gary E. Douberly
Committee:	Michael A. Duncan
	Henning H. Meyer

Electronic Version Approved:

Ron Walcott
Interim Dean of the Graduate School
The University of Georgia
August 2020

DEDICATION

I dedicate this dissertation to Joe Pesci.

TABLE OF CONTENTS

Page

CHAPTER

INTRODUCTION AND LITERATURE REVIEW

1.1. History of Droplets and Matrix Isolation

The essential history of helium droplets begins with the experiments of Becker, Klingelhofer, and Lohse in 1961, in which they reported the production of liquid helium droplets, for the first time, via expansion of gas into vacuum from a cryogenic nozzle.[1-2] A later experiment by Stephens and King formed helium clusters via supersonic expansion and studied them with mass spectrometry.[3] This study was primarily concerned with determination of magic numbers (i.e. cluster sizes of notably high stability) for clusters of fewer than 50 atoms. The first example of a doped helium droplet was provided in 1990 with the pick-up of a neon atom.[4] This was achieved in a crossed molecular beam configuration and detected via mass spectrometry of electron-ionized droplets.

The first molecular spectroscopy in a helium droplet was conducted on sulfur hexafluoride.[5,6] SF_6 was interrogated with laser-induced beam depletion spectroscopy, using N_2O and CO_2 lasers, which limited the spectral resolution that could be achieved. An infrared absorption feature was measured; it was found to be only minimally shifted from the gas-phase value; indeed, helium perturbations to band origins are seldom more than 1-2 cm^{-1}. The feature also had a doublet appearance, which was interpreted as SF_6 residing near/on the surface of the droplet. However, theoretical works[7-8] and a follow-up experiment[9] with improved resolution, thanks to the use of a diode laser, established that SF_6 was solvated closer to the center of the droplet. The high-resolution rovibrational antisymmetric stretch band could be straightforwardly fit using a spherical top Hamiltonian, implying preservation of molecular symmetry; however, the rotational constant needed to be reduced by a factor of three compared to its gas phase value.[10-11]

The factor of three reduction could be rationalized by modeling a system of SF_6 surrounded by eight helium atoms, symmetrically distributed into its tetrahedral binding sites. Moreover, the relative intensities of rovibrational lines allowed for a rotational temperature of 0.37 K to be determined.[11]

Neutral molecules are preferentially solvated inside helium droplets, trapped by a potential which arises from the stronger attractive interaction between the molecule and a helium atom than between two helium atoms.[12] Various particle-in-a-box states (i.e. states of the dopant in the helium "box") are predicted to be thermally populated at the droplet temperature, which contributes somewhat to broadening of spectral lines.[12] In contrast to the behavior of most molecules, some open-shell atoms (most notably alkali and alkaline earth metal atoms) sit on the surface of the droplet, and the interaction between a helium droplet and a hydrogen atom is known to be repulsive.[13]

Another important study was published shortly thereafter involving droplets doped with OCS.[14] Excellent rotational resolution was achieved in a droplet of ^{4}He; however, the same rovibrational band appeared as a single, broad feature in droplets of ^{3}He. This was taken as evidence for the superfluidity of ^{4}He droplets. Droplets of ^{3}He are not superfluid even at their colder equilibrium temperature of 0.15 K. Moreover, ^{3}He droplets doped with ^{4}He atoms were studied. With about sixty ^{4}He atoms present, the rotational resolution of OCS was observed to return, and by one hundred ^{4}He atoms, the rotational resolution of the pure ^{4}He droplet is almost completely recovered. This was interpreted as the formation of a cavity of superfluid ^{4}He within the larger ^{3}He droplet. Similar results were later found for SF_6.[15]

Some early electronic and vibronic spectroscopy was also conducted on doped helium droplets. The spectrum of glyoxal showed an electronic transition that was minimally shifted with respect to the gas-phase value.[16] Laser-induced fluorescence spectra were measured for sodium

atoms bound to the surface of helium droplets.[17] Vibrationally resolved bands were assigned to transitions of both singlet and triplet state sodium dimers. Additionally, an unresolved feature was observed, thought to arise from sodium trimer. Transitions were broadened by tens of cm^{-1}, but centers were only minimally shifted from gas-phase values.[18]

It is worthwhile to also describe older matrix isolation techniques. Matrix isolation involves the codeposition of analyte(s) and non-reactive material (most commonly rare gasses) onto a cryogenically-cooled window, freezing the chemical species of interest in a solid matrix. The technique originates from the work of George Pimentel in 1954.[19-20] Matrix isolation provided an opportunity to study the spectroscopy of many unstable species for the first time. As an example, triplet methylene, a classic unstable molecule of great interest to theoreticians and experimentalists alike, was studied in both argon and nitrogen matrices—within only a few years.[21-23] Long residence times and high concentrations of analytes in a matrix allow for a high degree of averaging and for direct absorption measurements to be performed (now often via commercial FTIR instruments). Because mass selection is not possible in direct-absorption matrix isolation spectroscopy, signals from contaminants and products of undesired chemical reactions can be of concern. Both secondary photolysis and annealing can be used to identify spectral carriers, helping to disentangle rich matrix spectra.

Although matrix isolation with liquid helium has been explored, the technique is not well-developed, owing to issues with condensation of the analyte molecules.[24-27] This was alleviated by various techniques to continuously introduce analytes into the matrix. However, only spectra of atomic and diatomic systems have been measured in helium matrices.[25] The most esteemed modern matrix environment is probably *para* hydrogen (p-H_2), which has been described as a "quantum solid" due to the long de Broglie wavelength and large-amplitude zero-point motion of hydrogen.[28] Typical perturbations to vibrational band origins are redshifts of around 5-10 cm^{-1}, which is similar to neon and generally superior to argon and nitrogen matrices.

For some systems, it is even possible to observe rotational structure in *p*-H_2; although, the structure is complicated by matrix site-effects.[29] Site-effects arise from inhomogeneity of the analyte local chemical environments and can unfortunately also lead to splittings of vibrational bands, as seen with *n*-propyl radical's high frequency CH_2 stretches.[30] In addition to introducing splittings, site effects, which are operative in all matrix environments, are also responsible for broadening and symmetry-breaking.

1.2. Advantages and Characteristics of Droplets

Helium droplets offer a compromise between matrix isolation and molecular beam experiments.[31] They offer a cold, highly dissipative environment in which to interrogate molecular systems—colder than nitrogen, argon, neon, and *p*-H_2, matrices. Rather than site effects, helium droplet spectra instead may reveal effects due to variations in droplet size; however, these are substantially less significant than matrix site effects and can usually be ignored. Moreover, the droplet environment also preserves the fundamental symmetry of the dopant molecule(s). From molecular beams, droplet beams inherit their high degree of control. Multiple dopants may be introduced at various points along the droplet beam path; the only requirement is adequate vapor pressure. Droplets contain isolated chemical systems, of dopant monomers, dimers, etc. With careful control of dopant pressures and use of mass selection, the spectra of specific chemical systems are far easier to disentangle and study compared to matrix isolation. Reactions may be conducted in droplets, or weakly-bound clusters may be assembled from the bottom-up. This affords the ability to study non-equilibrium clusters that might otherwise by inaccessible to experiment.

The de Broglie wavelength of ^{4}He atoms exceeds the average interparticle separation below about 2.2 K, implying significant delocalization of the bosonic ^{4}He particles.[32] This is the foundation for superfluidity in finite droplets of helium. In the bulk phase, this temperature is

known as the lambda point, and it represents the onset of superfluid behavior (or the phase transition from Helium I to Helium II). The rotational constant reductions that occur in helium droplets, discussed in the previous section, can be envisioned as due to a small number of helium atoms adiabatically following the rotation of a molecule.[33] For heavy rotors, a reduction factor of around three is typical, as with SF_6; however, the rotational constants of small molecules (~ 1 cm^{-1} and greater) are reduced by much less (~ 10%). This has been interpreted as the rotational motion being too fast for the helium to follow.[34-35]

The rapid rate of cooling of the superfluid helium environment, which is estimated from spectral linewidths, allows for stabilization of metastable clusters and conformers.[33, 36-40] If a bimolecular reaction can be shown to occur in a helium droplet, then this can usually be taken as evidence that the process is barrierless (unless it proceeds via a quantum tunneling mechanism faster than the experiment timescale). Even when a reaction does not occur, a weakly-bound entrance-channel complex will be trapped; helium droplets provide an ideal environment for the assembly and investigation of these.[41-42] Ability to trap gas-phase thermal populations of isomers allows for experimental determination of thermochemical quantities via van't Hoff analysis.[43-44] The enhancement of the population of higher energy isomers at higher temperatures is exploited in Chapter 5 to distinguish vibrational transitions of different rotamers. This helps to simplify a complicated spectrum.

In addition to vibrational and electronic band-origins, perturbations to dipole moments are also small; dipole moments for helium solvated molecules are generally slightly smaller than gas-phase values.[45] This effect can be accounted for with a simple model that is based on the formation of a cavity of polarized helium. Fitting of Stark spectra of molecules solvated in helium droplets offers an experimental route to determination of the vibrationally-averaged dipole moments of unstable molecules and weakly-bound complexes.

Although the experiments discussed in this dissertation have used helium droplets as a tool to study molecules, where the contribution of the droplet to the spectrum is mostly ignored, there is still much that is not known about droplet effects and therefore much reason to design further helium droplet experiments to specifically investigate them. Some examples of further droplet effects include modification of the Lambda doublet splitting in hydroxyl radical[46-47] and modification of the tunneling splitting in vinyl radical.[48]

1.3. Computation of Infrared Spectra

Most simulations of vibrational spectra begin with determination of the normal modes of vibration and application of the harmonic oscillator approximation.[49-50] This approximation entails that the Potential Energy Surface (PES) is a quadratic function of 3N-6 (or 3N-5 if linear) uncoupled normal coordinates. A similar approximation is made to the Dipole Moment Surface (DMS), which governs the intensity of infrared absorption. It is taken to be a linear function of the normal coordinates. Together these assumptions comprise the "double harmonic" approximation. This approach is most successful for molecules with well-defined equilibrium structures, lacking low frequency vibrations, and having low degrees of vibrational excitation, such that their vibrational motions do not carry them far from the equilibrium structure. The necessary terms in the PES and DMS can respectively be expressed as second derivatives of the electronic energy and first derivatives of the dipole moment, with respect to normal coordinate displacements. A version of the harmonic analysis is implemented in all major quantum chemistry programs; although, the electronic structure methods which support it usually depend on the availability of analytic energy derivatives.

In order to achieve quantitative accuracy, descriptions of molecular vibration beyond the harmonic approximation are necessary. Methods of treating this "anharmonicity," in a harmonic oscillator basis, include Vibrational Perturbation Theory (VPT) and variational approaches, both

based on Taylor series expansions of the potential.[51] The Vibrational Self-Consistent Field (VSCF) method[52] is an alternative, which variationally improves the zeroth-order wavefunctions. Further corrections are then typically made to the VSCF wavefunctions, which are analogous to the MP2, CI, and CC treatments of electron correlation.

1.4. Challenges Associated with Non-Rigid Molecules

All of the systems discussed in Chapters 4-8 possess some degree of non-rigidity (or floppiness). This is the condition in which a system may explore large amounts of its nuclear configuration space in the vibrational ground state. Such a thing is also referred to as Large Amplitude Motion (LAM), contrasting with the small amplitude motion of (mostly) harmonic oscillators vibrating about a well-defined equilibrium structure.[49] One consequence of LAM is that it often gives rise to multiple conformers, complicating (or perhaps enriching) interpretation of spectral patterns.

In theoretical chemistry, a small to moderate amount of LAM leads to increased errors in the harmonic oscillator model and in anharmonic models which build upon it, such as VPT. Although much of the error is often found to be isolated in the low-frequency normal coordinates, predictions of reasonable but diminished quality may still be made for high-frequency vibrations, as seen with floppy alkyl radicals in Chapter 4. The *n*- and *i*-propyl radicals have low barriers to torsional and wagging motions, respectively, localized on their radical sites. They also feature one and two methyl tops, respectively, which are notorious for undergoing weakly hindered rotation. In the case of severe LAM, the errors become catastrophic, and the normal-mode harmonic oscillator starting point should be abandoned in favor of descriptions based on curvilinear internal coordinates and more expansive potential energy surfaces, such as discrete variable representation approaches[53] or extensions of VSCF.[54] A case of severe LAM is exhibited by the proton-bound dimers of Chapter 8.

In certain cases of LAM, a situation arises in which the electronic PES has multiple minima separated by a sufficiently shallow barrier, such that the ground state wavefunction is highly delocalized, with largest amplitude above the barrier.[55] Similarly, it can sometimes be shown that zero-point correction merges the shallow multiple-well features into a single well.[56] In these cases, although the PES holds several wells, these likely do not correspond to conformers. The equilibrium structures cease to be meaningful, and although one might be tempted to carry out an anharmonic analysis at the transition state structure (i.e. at the top of the barrier), this is not a straightforward procedure for most methods (e.g. VPT).[56]

1.5. Dissertation Structure

In the remainder of this document, methods are reviewed in Chapters 2 and 3, published works are described in detail in Chapters 4-8, and conclusions are given in Chapter 9. Chapter 2 briefly covers the features of the helium nanodroplet isolation instrument and experimental design aspects relevant to the later chapters. Chapter 3 primarily discusses vibrational perturbation theory and the specific variant, Second-Order Vibrational Perturbation Theory with Resonances (VPT2+K), for the prediction of X-H stretching vibrations. It is written as a tutorial, reprinting most important formulas and providing numerous simple examples. It discusses the philosophy and practical considerations behind vibrational simulations, including but not limited to: computational method selection, cost-saving approximations, approaches to evaluating intensity, resonance identification, and effective Hamiltonian structure.

Chapter 4 discusses infrared spectroscopy of the propyl radicals, presenting clean spectra of cold *n*- and *i*-propyl and comparing the abilities of *ab initio* VPT2+K and a semi-empirical local mode Hamiltonian model to describe the extensive stretch-bend Fermi couplings in these systems. Chapter 5 gives a theoretical thermochemical analysis of the isomerization between *trans* and *gauche* isoprene, reports a new infrared spectrum, models it with VPT2+K, and assigns

a few features to the elusive *gauche* conformer. In Chapter 6, ethylperoxy radical is formed by the barrierless reaction of ethyl radical and molecular oxygen. Based on comparisons to VPT2+K simulations, significant populations of both *trans* and *gauche* ethylperoxy are formed. A force field transformation procedure is also described, which improves the accuracy of the cubic and quartic force constants. Chapter 7 reports an entirely theoretical study of the *tert*-butyl peroxy radical with high-level coupled-cluster theory. Previous experimental assignments are confirmed, and predictions for unobserved vibrational fundamentals are made. In Chapter 8, experimental infrared spectra are reported, for the first time, for the obscure HO_4^+ and DO_4^+ ions, with the aid of argon-tagging and infrared photodissociation spectroscopy. An extensive theoretical study of the potential energy surface is discussed, revealing isomers having multiconfigurational character and non-rigidity that are, in many cases, extreme. The experimental spectra arise from previously unidentified covalent-like isomers.

References

(1) Becker, E. W.; Klingelhofer, R.; Lohse, P. Strahlen aus Kondensiertem Helium im Hochvakuum. *Z. Naturforsch., A: Astrophys., Phys. Phys. Chem.* **1961**, *16*, 1259-1259.

(2) Becker, E. W. On the History of Cluster Beams. *Z. Phys. D: At., Mol. Clusters* **1986**, *3*, 101-107.

(3) Stephens, P. W.; King, J. G. Experimental Investigation of Small Helium Clusters - Magic Numbers and the Onset of Condensation. *Phys. Rev. Lett.* **1983**, *51*, 1538-1541.

(4) Scheidemann, A.; Toennies, J. P.; Northby, J. A. Capture of Neon Atoms by ^{4}He Clusters. *Phys. Rev. Lett.* **1990**, *64*, 1899-1902.

(5) Goyal, S.; Schutt, D. L.; Scoles, G. Vibrational Spectroscopy of Sulfur-Hexafluoride Attached to Helium Clusters. *Phys. Rev. Lett.* **1992**, *69*, 933-936.

(6) Goyal, S.; Schutt, D. L.; Scoles, G. Vibrational Spectroscopy of Sulfur-Hexafluoride Attached to Helium Clusters (vol 69, pg 933, 1992). *Phys. Rev. Lett.* **1994**, *73*, 2512-2512.

(7) Krotscheck, E.; Chin, S. A. The Delocalization of SF_6 in Helium Clusters. *Chem. Phys. Lett.* **1994**, *227*, 143-148.

(8) Barnett, R. N.; Whaley, K. B. Molecules in Helium Clusters - SF_6He_N. *J. Chem. Phys.* **1993**, *99*, 9730-9744.

(9) Frochtenicht, R.; Toennies, J. P.; Vilesov, A. High-Resolution Infrared-Spectroscopy of SF_6 Embedded in He Clusters. *Chem. Phys. Lett.* **1994**, *229*, 1-7.

(10) Hartmann, M.; Miller, R. E.; Toennies, J. P.; Vilesov, A. F. High-Resolution Molecular Spectroscopy of van der Waals Clusters in Liquid Helium Droplets. *Science* **1996**, *272*, 1631-1634.

(11) Hartmann, M.; Miller, R. E.; Toennies, J. P.; Vilesov, A. Rotationally Resolved Spectroscopy of SF_6 in Liquid-Helium Clusters - A Molecular Probe of Cluster Temperature. *Phys. Rev. Lett.* **1995**, *75*, 1566-1569.

(12) Lehmann, K. K. Potential of a Neutral Impurity in a Large ^{4}He Cluster. *Mol. Phys.* **1999**, *97*, 645-666.

(13) Ancilotto, F.; Lerner, P. B.; Cole, M. W. Physics of Solvation. *J. Low Temp. Phys.* **1995**, *101*, 1123-1146.

(14) Grebenev, S.; Toennies, J. P.; Vilesov, A. F. Superfluidity Within a Small Helium-4 Cluster: The Microscopic Andronikashvili Experiment. *Science* **1998**, *279*, 2083-2086.

(15) Harms, J.; Hartmann, M.; Sartakov, B.; Toennies, J. P.; Vilesov, A. F. High Resolution Infrared Spectroscopy of Single SF_6 Molecules in Helium Droplets. II. The Effect of Small Amounts of ^{4}He in Large ^{3}He Droplets. *J. Chem. Phys.* **1999**, *110*, 5124-5136.

(16) Hartmann, M.; Mielke, F.; Toennies, J. P.; Vilesov, A. F.; Benedek, G. Direct Spectroscopic Observation of Elementary Excitations in Superfluid He Droplets. *Phys. Rev. Lett.* **1996**, *76*, 4560-4563.

(17) Stienkemeier, F.; Higgins, J.; Ernst, W. E.; Scoles, G. Spectroscopy of Alkali Atoms and Molecules Attached to Liquid He Clusters. *Z. Phys. B: Condens. Matter* **1995**, *98*, 413-416.

(18) Stienkemeier, F.; Higgins, J.; Ernst, W. E.; Scoles, G. Laser Spectroscopy of Alkali-Doped Helium Clusters. *Phys. Rev. Lett.* **1995**, *74*, 3592-3595.

(19) Whittle, E.; Dows, D. A.; Pimentel, G. C. Matrix Isolation Method for the Experimental Study of Unstable Species. *J. Chem. Phys.* **1954**, *22*, 1943-1943.

(20) Norman, I.; Porter, G. Trapped Atoms and Radicals in a Glass Cage. *Nature* **1954**, *174*, 508-509.

(21) Milligan, D. E.; Pimentel, G. C. Matrix Isolation Studies - Possible Infrared Spectra of Isomeric forms of Diazomethane and of Methylene, CH_2. *J. Chem. Phys.* **1958**, *29*, 1405-1412.

(22) Demore, W. B.; Pritchard, H. O.; Davidson, N. Photochemical Experiments in Rigid Media at Low Temperatures .II. The Reactions of Methylene, Cyclopentadienylene and Diphenylmethylene. *J. Am. Chem. Soc.* **1959**, *81*, 5874-5879.

(23) Schaefer, H. F. Methylene - A Paradigm for Computational Quantum-Chemistry. *Science* **1986**, *231*, 1100-1107.

(24) Boltnev, R. E.; Gordon, E. B.; Khmelenko, V. V.; Krushinskaya, I. N.; Martynenko, M. V.; Pelmenev, A. A.; Popov, E. A.; Shestakov, A. F. Luminescence of Nitrogen and Neon Atoms Isolated in Solid Helium. *Chem. Phys.* **1994**, *189*, 367-382.

(25) Takahashi, Y.; Sano, K.; Kinoshita, T.; Yabuzaki, T. Spectroscopy of Alkali Atoms and Molecules in Superfluid-Helium. *Phys. Rev. Lett.* **1993**, *71*, 1035-1038.

(26) Fujisaki, A.; Sano, K.; Kinoshita, T.; Takahashi, Y.; Yabuzaki, T. Implantation of Neutral Atoms into Liquid-Helium by Laser Sputtering. *Phys. Rev. Lett.* **1993**, *71*, 1039-1042.

(27) Gordon, E. B.; Khmelenko, V. V.; Pelmenev, A. A.; Popov, E. A.; Pugachev, O. F. Impurity-Helium van der Waals Crystals. *Chem. Phys. Lett.* **1989**, *155*, 301-304.

(28) Okumura, M.; Chan, M. C.; Oka, T. High-Resolution Infrared-Spectroscopy of Solid Hydrogen - The Tetrahexacontapole-Induced $\Delta J=6$ Transitions. *Phys. Rev. Lett.* **1989**, *62*, 32-35.

(29) Momose, T.; Shida, T. Matrix-Isolation Spectroscopy Using Solid Parahydrogen as the Matrix: Application to High-Resolution Spectroscopy, Photochemistry, and Cryochemistry. *Bull. Chem. Soc. Jpn.* **1998**, *71*, 1-15.

(30) Pullen, G. T.; Franke, P. R.; Haupa, K. A.; Lee, Y. P.; Douberly, G. E. Infrared Spectroscopy of the *n*-Propyl and *i*-Propyl Radicals in Solid *para*-Hydrogen. *J. Mol. Spectrosc.* **2019**, *363*, 111170.

(31) Callegari, C.; Lehmann, K. K.; Schmied, R.; Scoles, G. Helium Nanodroplet Isolation Rovibrational Spectroscopy: Methods and Recent Results. *J. Chem. Phys.* **2001**, *115*, 10090-10110.

(32) Kwon, Y. K.; Whaley, K. B. Atomic-Scale Quantum Solvation Structure in Superfluid Helium-4 Clusters. *Phys. Rev. Lett.* **1999**, *83*, 4108-4111.

(33) Choi, M. Y.; Douberly, G. E.; Falconer, T. M.; Lewis, W. K.; Lindsay, C. M.; Merritt, J. M.; Stiles, P. L.; Miller, R. E. Infrared Spectroscopy of Helium Nanodroplets: Novel Methods for Physics and Chemistry. *Int. Rev. Phys. Chem.* **2006**, *25*, 15-75.

(34) Miller, I.; Faulkner, T.; Raston, P. L. Laser Spectroscopy of Methanol Isotopologues in ^{4}He Nanodroplets: Probing the Inertial Response Around a Moderately Light Rotor. *J. Phys. Chem. A* **2019**, *123*, 1630-1636.

(35) Faulkner, T.; Miller, I.; Raston, P. L. Quantum Cascade Laser Spectroscopy of OCS Isotopologues in ^{4}He Nanodroplets: A Test of Adiabatic Following for a Heavy Rotor. *J. Chem. Phys.* **2018**, *148*, 044308.

(36) Scheidemann, A.; Schilling, B.; Toennies, J. P. Anomalies in the Reactions of He^{+} with SF_6 Embedded in Large ^{4}He Clusters. *J. Phys. Chem.* **1993**, *97*, 2128-2138.

(37) Douberly, G. E.; Miller, R. E.; Xantheas, S. S. Formation of Exotic Networks of Water Clusters in Helium Droplets Facilitated by the Presence of Neon Atoms. *J. Am. Chem. Soc.* **2017**, *139*, 4152-4156.

(38) Douberly, G. E.; Miller, R. E. The Growth of HF Polymers in Helium Nanodroplets: Probing the Barriers to Ring Insertion. *J. Phys. Chem. B* **2003**, *107*, 4500-4507.

(39) Toennies, J. P.; Vilesov, A. F. Superfluid Helium Droplets: A Uniquely Cold Nanomatrix for Molecules and Molecular Complexes. *Angew. Chem., Int. Ed.* **2004**, *43*, 2622-2648.

(40) Nauta, K.; Miller, R. E. Nonequilibrium Self-Assembly of Long Chains of Polar Molecules in Superfluid Helium. *Science* **1999**, *283*, 1895-1897.

(41) Skouteris, D.; Manolopoulos, D. E.; Bian, W. S.; Werner, H. J.; Lai, L. H.; Liu, K. P. van der Waals Interactions in the Cl+HD Reaction. *Science* **1999**, *286*, 1713-1716.

(42) Nguyen, T. L.; Xue, B. C.; Weston, R. E.; Barker, J. R.; Stanton, J. F. Reaction of HO with CO: Tunneling Is Indeed Important. *J. Phys. Chem. Lett.* **2012**, *3*, 1549-1553.

(43) Leavitt, C. M.; Moore, K. B.; Raston, P. L.; Agarwal, J.; Moody, G. H.; Shirley, C. C.; Schaefer, H. F.; Douberly, G. E. Liquid Hot NAGMA Cooled to 0.4 K: Benchmark Thermochemistry of a Gas-Phase Peptide. *J. Phys. Chem. A* **2014**, *118*, 9692-9700.

(44) Skvortsov, D. S.; Vilesov, A. F. Using He Droplets for Measurements of Interconversion Enthalpy of Conformers in 2-Chloroethanol. *J. Chem. Phys.* **2009**, *130*, 151101.

(45) Stiles, P. L.; Nauta, K.; Miller, R. E. Dipole Moments of Molecules Solvated in Helium Nanodroplets. *Phys. Rev. Lett.* **2003**, *90*, 135301.

(46) Raston, P. L.; Liang, T.; Douberly, G. E. Observation of the *Q*(3/2) Lambda-Doublet Transitions for $X^2\Pi_{3/2}$ OD in Helium Nanodroplets. *Mol. Phys.* **2014**, *112*, 301-303.

(47) Raston, P. L.; Liang, T.; Douberly, G. E. Anomalous Lambda-Doubling in the Infrared Spectrum of the Hydroxyl Radical in Helium Nanodroplets. *J. Phys. Chem. A* **2013**, *117*, 8103-8110.

(48) Raston, P. L.; Liang, T.; Douberly, G. E. Infrared Spectroscopy and Tunneling Dynamics of the Vinyl Radical in ^{4}He Nanodroplets. *J. Chem. Phys.* **2013**, *138*, 174302.

(49) Wilson, E. B., Jr.; Decius, J. C.; Cross, P. C. *Molecular Vibrations: The Theory of Infrared and Raman Vibrational Spectra*; McGraw-Hill, 1955, p 388.

(50) Califano, S. *Vibrational States*; John Wiley & Sons, Ltd., 1976, p 335.

(51) Mills, I. M. *Vibration-Rotation Structure in Asymmetric and Symmetric Top Molecules*. Academic Press: 1972; p 115-140.

(52) Bowman, J. M. The Self-Consistent-Field Approach to Polyatomic Vibrations. *Acc. Chem. Res.* **1986**, *19*, 202-208.

(53) Colbert, D. T.; Miller, W. H. A Novel Discrete Variable Representation for Quantum-Mechanical Reactive Scattering via the S-Matrix Kohn Method. *J. Chem. Phys.* **1992**, *96*, 1982-1991.

(54) Changala, P. B.; Baraban, J. H. Ab Initio Effective Rotational and Rovibrational Hamiltonians for Non-Rigid Systems via Curvilinear Second Order Vibrational Møller-Plesset Perturbation Theory. *J. Chem. Phys.* **2016**, *145*, 174106.

(55) Brown, A. R.; Franke, P. R.; Douberly, G. E. Helium Nanodroplet Isolation of the Cyclobutyl, 1-Methylallyl, and Allylcarbinyl Radicals: Infrared Spectroscopy and Ab Initio Computations. *J. Phys. Chem. A* **2017**, *121*, 7576-7587.

(56) Li, C. Y.; Agarwal, J.; Wu, C. H.; Allen, W. D.; Schaefer, H. F. Intricate Internal Rotation Surface and Fundamental Infrared Transitions of the *n*-Propyl Radical. *J. Phys. Chem. B* **2015**, *119*, 728-735.

CHAPTER 2

EXPERIMENTAL METHODS

2.1. Overview

The majority of research reported herein utilizes the Helium Nanodroplet Isolation (HENDI) technique.[1] The experimental and instrumental design is described in this chapter; whereas, historical information and capabilities of the technique are discussed in Chapter 1. The HENDI apparatus combines mass spectrometry and laser spectroscopy in an infrared action spectroscopy scheme. A schematic of the instrument is shown in Figure 2.1.

2.2. Droplet Formation

Ultra-high purity helium gas (variously 99.9995% or 99.9999% purity), at 35 bar backing pressure, is expanded into vacuum from a 5 micron diameter nozzle. The nozzle is cryogenically cooled via a closed-cycle helium refrigerator, typically to 17 K, and the temperature is stabilized to better than ± 0.01 K. As it expands into vacuum, the helium cools further and forms droplets. The droplets contain about five thousand helium atoms on average, stabilize to a temperature of 0.4 K, and travel through the instrument at 300-500 m/s, implying an experiment timescale on the order of milliseconds.[2-4]

The distribution of produced droplet sizes is a function of nozzle temperature, backing pressure, and nozzle diameter. Lower nozzle temperature, smaller nozzle diameter, and higher backing pressure are all associated with larger helium droplets. As the nozzle is a precisely machined metal aperture, its diameter is not an adjustable parameter. The extent to which droplet

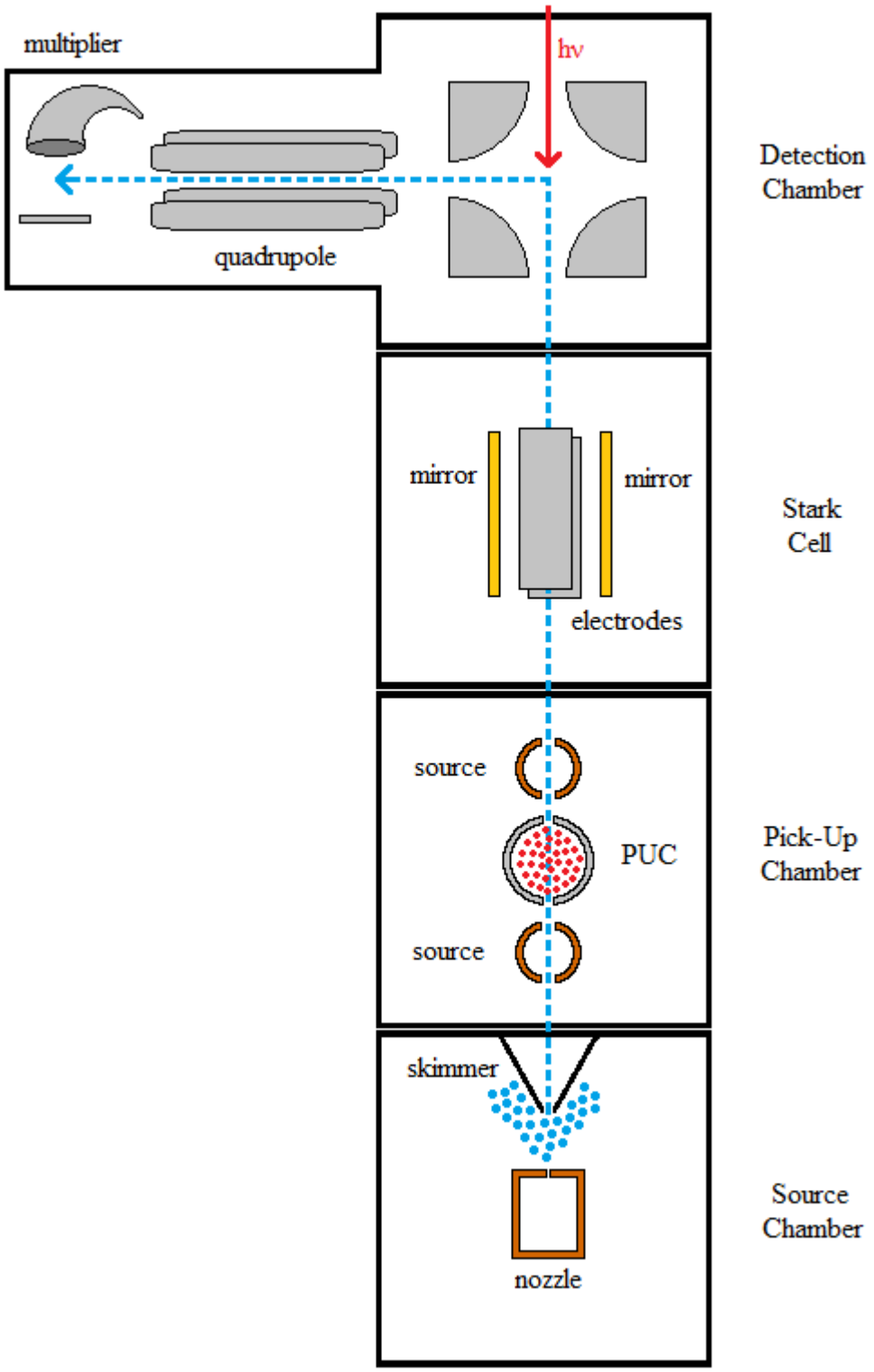

Figure 2.1. Schematic of HENDI Instrument. Dotted line shows the path of the helium beam. A counterpropagating laser/droplet beam alignment is shown, as was used for all experiments.

size can be controlled by backing pressure is also limited—by the pumping speed of the source chamber diffusion pump. Thus, in practice, droplet size is usually tuned by adjusting the nozzle temperature. Infrared spectra have been successfully measured for nozzle temperatures ranging from about 12 K up to 21 K. At the lower limit, colder nozzle temperatures simply cannot be achieved with the present apparatus; at the upper limit, the quality of measured spectra starts to rapidly decline. Nevertheless, typical operating temperature is 17 K for single pick-up experiments, as it is found to maximize signal/noise. When bond-forming reactions are studied, the optimal nozzle temperature is somewhat lower. The experiment discussed in Chapter 6 uses a 15 K nozzle temperature to offset large depletion of the droplets by an ~ 33 kcal/mol C-O bond formation (corresponding to loss of 2300 helium atoms).[5]

The droplets described above are produced by a gas-phase nucleation mechanism. If much larger droplets (~ 10^6 - 10^9 atoms) are desired, this has been achieved by other research groups by a fragmentation of liquid jet mechanism, operative at lower nozzle temperatures.[6-8] These large droplets are less suitable for infrared action spectroscopy, as vibrational excitation cannot induce significant depletion; however, they have been used in studies of droplet physics, including quantum vortices, which do not manifest in small droplets.[9-12]

2.3. Droplet Doping

The helium droplet expansion is skimmed into a beam by a conical skimmer with 0.4 mm diameter, as the droplets enter into a second "pick-up" chamber, where relevant molecules are introduced. In this region, droplets may collide with gas phase radicals, produced via pyrolysis of organic precursors, as they effuse from the orthogonally-oriented, resistively-heated ends of load-lockable pyrolysis sources.[13-14] The position of the pyrolysis source is optimized to maximize spectroscopy signal; its rotation angle and the degree of penetration into the chamber can be readily changed. Vertical position can be tuned somewhat by applying external pressure to the top

or bottom of the source. Also, the outputs of the sources may optionally be enclosed in metal shields, as drawn in Figure 2.1.

Alternatively the droplets may pick up gas phase molecules from a differentially-pumped Pick-Up Cell (PUC), as the beam passes through the small holes on either side. As with pyrolysis sources, molecules are introduced into this cell from sample bulbs or gas bottles via a fine metering valve. This cell has a base pressure on the order of 10^{-7} Torr and typically operates at pressures between $2x10^{-6}$ and $4x10^{-6}$ Torr, when pick-up of single molecules is desired. Upon gas phase collision with a helium droplet, dopants are rapidly solvated and cooled down to the droplet temperature of 0.4 K; helium atoms are evaporated to dissipate the internal energy of the dopants (~ 1 helium atom per 5 cm^{-1}).[15]

The pick-up process obeys Poisson statistics.[1] Pick-up events are independent of one-another, and the probability for a droplet to pick up *n* dopants is given by Equation 2.1,

$$P(n) = \frac{(\rho\sigma L)^n}{n!} e^{-\rho\sigma L} \tag{2.1}$$

where ρ is the number density of dopants, σ is the cross-sectional area of the droplet, and L is the length of the pick-up region. Similar experimental considerations apply here as for droplet production. The length of the pick-up region is not adjustable during an experiment; thus, holding the average droplet size constant, pick-up conditions are optimized by adjusting the pressure of dopants. The PUC pressure at which the probability of picking up one dopant molecule is maximal is half the pressure that optimizes for the pick-up of two molecules, and one third the pressure that optimizes for three molecules, and so on. In order to minimize the population of droplets which pick up multiple dopants, experiments are often performed at pressures somewhat *lower* than the pressure optimizing for single pick-up. Plots of depletion signal vs. PUC pressure can be useful for determining the carriers of spectral bands (monomer, dimer, trimer, etc.).

2.4. Radical Generation

Radicals are generated via pyrolysis of organic precursors.[16] Several types of precursors are available, compatible with different types of sources: quartz-tantalum, silicon carbide, and crucible-style solid sources.[13] The quartz-tantalum source is composed of a quartz tube, wrapped at the end with tantalum wire. The coil of tantalum wire is resistively heated by water-cooled copper electrodes. Precursor molecules are introduced from a glass sample bulb, though a fine metering valve. The precursor molecules collide with the hot walls of the quartz tube and break apart, and the decomposition products are promptly solvated by a droplet. Precursor pressures are kept sufficiently low to suppress bimolecular reactions. The second type of source design exchanges the tantalum-wrapped quartz for a silicon carbide tube, heated by graphite electrodes.[17] Its primary advantage over the quartz-tantalum source is its ability to achieve higher temperatures, which can be helpful or even necessary to pyrolyze certain types of precursors (e.g. chlorine).

The experiments discussed in Chapters 4 and 6 involve the generation of alkyl radicals (propyl and ethyl, respectively). These are produced in the quartz-tantalum pyrolysis source from organic nitrite precursors. The nitrites are synthesized from commercially obtained alcohols.[18] Organic alkylnitrites (ethyl and larger) thermally decompose into one formaldehyde, one nitric oxide, and one hydrocarbon radical, which ranks them low in terms of their radical production efficiency (33%). However this is balanced by their straightforward synthesis and their ease of handling. Organic peroxides represent a second class of precursors. They are generally less accessible, owing to their low stability and lack of a simple one-step synthesis from a stable precursor. The hydroxyl radical has been successfully generated via pyrolysis of *tert*-butyl hydroperoxide.[14] This pyrolysis yields one hydroxyl, one methyl, and one acetone (33% efficiency). In Chapter 6, di-*tert*-amylperoxide was also used. It offers a higher doping efficiency

(50%), yielding two acetones and two ethyl radicals. Both peroxides are compatible with the quartz-tantalum source.

Organic iodide precursors decompose homolytically into one hydrocarbon radical and one iodine atom (50% doping efficiency). Iodoethane was considered as an ethyl radical source; however, it proved a less effective source than di-*tert*-amylperoxide. Sulfones ($R\text{-}SO_2\text{-}R$) are highly optimal precursors, offering 66% doping efficiency when both R groups correspond to the desired radical. These are typically solids at room temperature, which are only compatible with a crucible-style source.[19-20] Commercial availability can also be a concern for sulfone precursors. Divinylsulfone has been used to produce vinyl radical in helium droplets; although, it is a liquid and used the quartz-tantalum source.[21]

2.5. Mass Spectrometry

In the final chamber of the apparatus, the droplet beam is ionized by electron-impact, and the cationic fragments are subsequently detected with quadrupole mass spectrometry. The majority of the fragments are $(He^+)He_n$ ions, which appear in increments of 4 u; however, in doped droplets, there is also a chance for charge-transfer ionization of the dopant to occur.[22] This confers a large amount of energy to the dopant, equal to the difference between its Ionization Potential (IP), typically 7-12 eV, and the IP of helium, 24.6 eV. The energized ion is then ejected from the droplet. Its excess internal energy is often sufficient to induce fragmentation, analogous to but "softer" than electron-impact ionization in the gas phase. The dopant parent ion and/or its fragments are then detected in the mass spectrometer with a Channeltron electron multiplier.

2.6. Infrared Spectroscopy

The density of dopants is not high enough for direct absorption spectroscopy to be viable, as it is in matrix isolation; instead, infrared spectra are obtained with action spectroscopy. A continuous-wave infrared Optical Parametric Oscillator (OPO) is directed into the chamber

through CaF_2 windows; it counterpropagates the droplet beam and is continuously tunable over the CH stretching region.[23] The Aculight C-Module is used, which has quoted spectral coverage of 2600-3150 cm^{-1}. The pump laser is a fiber laser, which is both thermally and piezoelectrically tunable around 1064 nm, and it is amplified to 12-15 W before it enters the OPO cavity. By tuning the pump laser frequency, the frequency of the idler output from the OPO is tuned proportionately. For the experiments described in this dissertation, the laser is piezo-scanned in 2-3 cm^{-1} sweeps, corresponding to application of 0-200 V. Temperature-tuning of the fiber laser is used only as a supplemental technique to access problematic spectral regions. Typical laser powers of the idler beam are 1-2 Watts over its mid-infrared tuning range.

Upon resonant vibrational excitation of a dopant within a helium droplet, nonradiative relaxation processes dissipate the energy to the droplet, leading to helium atom evaporation. This causes a frequency-dependent reduction in the ionization cross sections of doped droplets, which is observed as a depletion of the ion current on the dopant fragment mass channels. The laser is mechanically chopped at 80 Hz, and the laser-on/laser-off difference signal is converted into a voltage and processed with a lock-in amplifier. By scanning the laser through the CH stretch region, an infrared spectrum is acquired.

The infrared laser may alternatively be directed into the third chamber of the experimental apparatus (Fig. 2.1), in which it is made to intersect the droplet beam between gold-coated mirrors, in a multipass orientation. Although the multipass cell serves to extend the length of the laser interaction region, the overlap with the droplet beam is inferior to that of the standard counterpropagating orientation. However its advantage is that it confines the laser interaction to a small region, to which an external electric or magnetic field may be applied, allowing for Stark or Zeeman spectroscopy, respectively.[14, 24-25]

A primary challenge in the early stages of a HENDI experiment is the selection of a mass channel (m/z) at which to measure the depletion signal. Although, the quadrupole may be

operated in an "rf-only" mode, in which depletion signal is collected from all mass channels simultaneously, this is not always desirable. Mass selectivity is valuable for reducing the number of contaminant absorptions, and this is particularly important when using pyrolytic precursors that generate unwanted decomposition products. For the HENDI experiments described in Chapters 4, 5, and 6, depletion signals were measured on individual mass channels. The technique known as Optically Selective Mass Spectrometry (OSMS) was used to help select the mass channels for these experiments.[26] It is performed by tuning the infrared laser to an absorption band, suspected to belong to a desired chemical species, scanning the quadrupole mass filter, and recording the depletion signal. This is very nearly the opposite of the infrared action spectroscopy scheme. OSMS typically reveals several candidate mass channels, and infrared spectra are then recorded on each to assess the signal-to-noise ratios and presence or absence of contaminant features.

References

(1) Choi, M. Y.; Douberly, G. E.; Falconer, T. M.; Lewis, W. K.; Lindsay, C. M.; Merritt, J. M.; Stiles, P. L.; Miller, R. E. Infrared Spectroscopy of Helium Nanodroplets: Novel Methods for Physics and Chemistry. *Int. Rev. Phys. Chem.* **2006**, *25*, 15-75.

(2) Toennies, J. P.; Vilesov, A. F. Superfluid Helium Droplets: A Uniquely Cold Nanomatrix for Molecules and Molecular Complexes. *Angew. Chem., Int. Ed.* **2004**, *43*, 2622-2648.

(3) Lewerenz, M.; Schilling, B.; Toennies, J. P. A New Scattering Deflection Method for Determining and Selecting the Sizes of Large Liquid Clusters of ^{4}He. *Chem. Phys. Lett.* **1993**, *206*, 381-387.

(4) Buchenau, H.; Knuth, E. L.; Northby, J.; Toennies, J. P.; Winkler, C. Mass-Spectra and Time-of-Flight Distributions of Helium Cluster Beams. *J. Chem. Phys.* **1990**, *92*, 6875-6889.

(5) Wilke, J. J.; Allen, W. D.; Schaefer, H. F. Establishment of the C_2H_5+O_2 Reaction Mechanism: A Combustion Archetype. *J. Chem. Phys.* **2008**, *128*, 074308.

(6) Jiang, T.; Northby, J. A. Fragmentation Clusters Formed in Supercritical Expansions of ^{4}He. *Phys. Rev. Lett.* **1992**, *68*, 2620-2623.

(7) Knuth, E. L.; Henne, U. Average Size and Size Distribution of Large Droplets Produced in a Free-Jet Expansion of a Liquid. *J. Chem. Phys.* **1999**, *110*, 2664-2668.

(8) Grisenti, R. E.; Toennies, J. P. Cryogenic Microjet Source for Orthotropic Beams of Ultralarge Superfluid Helium Droplets. *Phys. Rev. Lett.* **2003**, *90*, 234501.

(9) Henne, U.; Toennies, J. P. Electron Capture by Large Helium Droplets. *J. Chem. Phys.* **1998**, *108*, 9327-9338.

(10) Frochtenicht, R.; Henne, U.; Toennies, J. P.; Ding, A.; FieberErdmann, M.; Drewello, T. The Photoionization of Large Pure and Doped Helium Droplets. *J. Chem. Phys.* **1996**, *104*, 2548-2556.

(11) Bernando, C.; Vilesov, A. F. Kinematics of the Doped Quantum Vortices in Superfluid Helium Droplets. *J. Low Temp. Phys.* **2018**, *191*, 242-256.

(12) Jones, C. F.; Bernando, C.; Tanyag, R. M. P.; Bacellar, C.; Ferguson, K. R.; Gomez, L. F.; Anielski, D.; Belkacem, A.; Boll, R.; Bozek, J., et al. Coupled Motion of Xe Clusters and Quantum Vortices in He Nanodroplets. *Phys. Rev. B* **2016**, *93*, 180510.

(13) Kupper, J.; Merritt, J. M.; Miller, R. E. Free Radicals in Superfluid Liquid Helium Nanodroplets: A Pyrolysis Source for the Production of Propargyl Radical. *J. Chem. Phys.* **2002**, *117*, 647-652.

(14) Raston, P. L.; Liang, T.; Douberly, G. E. Anomalous Lambda-Doubling in the Infrared Spectrum of the Hydroxyl Radical in Helium Nanodroplets. *J. Phys. Chem. A* **2013**, *117*, 8103-8110.

(15) Chin, S. A.; Krotscheck, E. Systematics of Pure and Doped ^{4}He Clusters. *Phys. Rev. B* **1995**, *52*, 10405-10428.

(16) Zhang, X.; Friderichsen, A. V.; Nandi, S.; Ellison, G. B.; David, D. E.; McKinnon, J. T.; Lindeman, T. G.; Dayton, D. C.; Nimlos, M. R. Intense, Hyperthermal Source of Organic Radicals for Matrix-Isolation Spectroscopy. *Rev. Sci. Instrum.* **2003**, *74*, 3077-3086.

(17) Moradi, C. P.; Douberly, G. E. Infrared Laser Spectroscopy of the L-Shaped Cl-HCl Complex Formed in Superfluid ^{4}He Nanodroplets. *J. Phys. Chem. A* **2015**, *119*, 12028-12035.

(18) Noyes, W. A. *n*-Butyl Nitrite. *Org. Synth.* **1936**, *16*, 7.

(19) Liang, T.; Flynn, S. D.; Morrison, A. M.; Douberly, G. E. Quantum Cascade Laser Spectroscopy and Photoinduced Chemistry of Al-$(CO)_n$ Clusters in Helium Nanodroplets. *J. Phys. Chem. A* **2011**, *115*, 7437-7447.

(20) Leavitt, C. M.; Moore, K. B.; Raston, P. L.; Agarwal, J.; Moody, G. H.; Shirley, C. C.; Schaefer, H. F.; Douberly, G. E. Liquid Hot NAGMA Cooled to 0.4 K: Benchmark Thermochemistry of a Gas-Phase Peptide. *J. Phys. Chem. A* **2014**, *118*, 9692-9700.

(21) Raston, P. L.; Liang, T.; Douberly, G. E. Infrared Spectroscopy and Tunneling Dynamics of the Vinyl Radical in ^{4}He Nanodroplets. *J. Chem. Phys.* **2013**, *138*, 174302.

(22) Mauracher, A.; Echt, O.; Ellis, A. M.; Yang, S.; Bohme, D. K.; Postler, J.; Kaiser, A.; Denifl, S.; Scheier, P. Cold Physics and Chemistry: Collisions, Ionization and Reactions Inside Helium Nanodroplets Close to Zero K. *Phys. Rep.* **2018**, *751*, 1-90.

(23) Morrison, A. M.; Liang, T.; Douberly, G. E. Automation of an "Aculight" Continuous-Wave Optical Parametric Oscillator. *Rev. Sci. Instrum.* **2013**, *84*, 013102.

(24) Brice, J. T. Infrared Stark and Zeeman Spectroscopy of Complexes Formed from Sequential Capture in Helium Nanodroplets. Doctoral Dissertation, University of Georgia, Athens, GA, 2019.

(25) Moradi, C. P.; Douberly, G. E. On the Stark effect in Open Shell Complexes Exhibiting Partially Quenched Electronic Angular Momentum: Infrared Laser Stark Spectroscopy of OH-C_2H_2, OH-C_2H_4, and OH-H_2O. *J. Mol. Spectrosc.* **2015**, *314*, 54-62.

(26) Lewis, W. K.; Lindsay, C. M.; Bemish, R. J.; Miller, R. E. Probing Charge-Transfer Processes in Helium Nanodroplets by Optically Selected Mass Spectrometry (OSMS): Charge Steering by Long-Range Interactions. *J. Am. Chem. Soc.* **2005**, *127*, 7235-7242.

CHAPTER 3

THEORETICAL METHODS

3.1. Introduction to Vibrational Perturbation Theory

Second-Order Vibrational Perturbation Theory (VPT2) is an old and widely used method for dealing with anharmonicity in molecular vibrations.[1-2] Anharmonicity is defined as the deviation of vibrations from the harmonic model. In standard applications of perturbation theory, the Hamiltonian is separated into a zeroth-order part, the exact eigenfunctions of which are known, and a perturbation which is assumed to be small. The common, analytic formulation of VPT is based on the Watson Hamiltonian; accordingly, it uses a rectilinear normal coordinate system.[3-5] This means that the vibrational displacement coordinates are linear combinations of Cartesian coordinates, and atoms move in straight (as opposed to curved) paths. The implications of this fact are far-reaching; however, that is beyond the scope of this discussion.[6] The zeroth order part of the vibrational Hamiltonian corresponds to the harmonic oscillator Hamiltonian, which is based on a quadratic expansion of the potential energy surface, and the perturbation is the anharmonic potential. The rotation-vibration (Coriolis) interaction is also normally included, again as a perturbation. It is common to subdivide the perturbation into numbered Hamiltonians, and this will soon make it more clear what kinds of terms can contribute to each part of the energy expression.[7]

$$\hat{H} = \hat{H}_0 + \hat{H}' = \hat{H}_{HO} + \hat{V}_{anh} + \hat{H}_{cor} = \hat{H}_{HO} + \hat{H}_1 + \hat{H}_2 \tag{3.1}$$

For convenience, the normal coordinates are additionally made dimensionless, and most of the involved parameters (harmonic frequencies, anharmonic force constants, and rotational

constants) are expressed in wavenumbers. The anharmonic potential energy is represented by a Taylor series expansion in the normal coordinates,

$$\hat{V}_{anh} = \frac{1}{3!}\sum_{rst} \phi_{rst}\hat{q}_r\hat{q}_s\hat{q}_t + \frac{1}{4!}\sum_{rstu} \phi_{rstu}\hat{q}_r\hat{q}_s\hat{q}_t\hat{q}_u + \frac{1}{5!}\sum_{rstuv} \phi_{rstuv}\hat{q}_r\hat{q}_s\hat{q}_t\hat{q}_u\hat{q}_v + \cdots \quad (3.2)$$

where the factors of 1/n! are Taylor series coefficients; *r,s,t,u,v* are normal coordinates; $\hat{q}_r$, $\hat{q}_s$, $\hat{q}_t$, $\hat{q}_u$, $\hat{q}_v$ are the associated position operators; and ϕ_{rst} is a cubic force constant,

$$\phi_{rst} = \left(\frac{\partial^3 E}{\partial q_r \partial q_s \partial q_t}\right) \quad (3.3)$$

a third derivative of the electronic energy with respect to displacement along coordinates *r,s,t*. Note the summation is unrestricted, so force constants where *r*, *s*, and/or *t* refer to the same coordinate will appear. Also, there are six equivalent permutations of *r,s,t*; three equivalent permutations of *r,s,s*; and only one permutation of *r,r,r*. This redundancy is accounted for by introducing degeneracy factors. Analogously, ϕ_{rstu} is a quartic force constant, and ϕ_{rstuv} is a quintic force constant. The quartic force constants (and all higher force constants) have similar definitions.

$$\phi_{rstu} = \left(\frac{\partial^4 E}{\partial q_r \partial q_s \partial q_t \partial q_u}\right) \quad (3.4)$$

3.2. Harmonic Oscillator Integrals

The harmonic oscillator Hamiltonian, $\hat{H}_{HO}$, is of course diagonal in the harmonic oscillator basis set, and its eigenvalues are simply linear combinations of the 3N-6 (or 3N-5) harmonic frequencies of the system. A great advantage of anharmonic approaches that use the traditional rectilinear normal coordinate system and harmonic oscillator basis set is the ease of integral evaluation. The matrix elements of the normal coordinate position, $\hat{q}$, and momentum, $\hat{p}$, operators, which appear in the anharmonic terms, have simple analytic formulas, which are published in various texts.[8-9] In order to determine the VPT2 energy, matrix elements are required

in which the exponent of the $\hat{q}$ operator ranges from 0 to 4. Integrals involving products of position and momentum operators also appear in the rotation-vibration terms. Many of these are not required in VPT2, as only the diagonal rotation-vibration matrix elements are included. Furthermore, these integrals can all be rewritten in terms of position integrals.[10] The harmonic oscillator position integrals up to the fourth power are provided below.

$$\langle i'|i\rangle = \delta_{i',i} \tag{3.5}$$

$$\langle i'|\hat{q}|i\rangle = \frac{1}{\sqrt{2}}\left[\delta_{i',i-1}\sqrt{i} + \delta_{i',i+1}\sqrt{i+1}\right] \tag{3.6}$$

$$\langle i'|\hat{q}^2|i\rangle = \frac{1}{2}\left[\delta_{i',i-2}\sqrt{i(i-1)} + \delta_{i',i}(2i+1) + \delta_{i',i+2}\sqrt{(i+1)(i+2)}\right] \tag{3.7}$$

$$\langle i'|\hat{q}^3|i\rangle = \frac{1}{2\sqrt{2}}\begin{bmatrix} \delta_{i',i-3}\sqrt{i(i-1)(i-2)} + \delta_{i',i-1}\left(3i^{3/2}\right) + \\ \delta_{i',i+1}\left(3(i+1)^{3/2}\right) + \delta_{i',i+3}\sqrt{(i+1)(i+2)(i+3)} \end{bmatrix} \tag{3.8}$$

$$\langle i'|\hat{q}^4|i\rangle = \frac{1}{4}\begin{bmatrix} \delta_{i',i-4}\sqrt{i(i-1)(i-2)(i-3)} + \\ \delta_{i',i-2}(4i-2)\sqrt{i(i-1)} + \delta_{i',i}(6i^2+6i+3) + \\ \delta_{i',i+2}(4i+6)\sqrt{(i+1)(i+2)} + \\ \delta_{i',i+4}\sqrt{(i+1)(i+2)(i+3)(i+4)} \end{bmatrix} \tag{3.9}$$

In these expressions, $\hat{q}$ is the position operator associated with a particular normal coordinate, and the indices *i* and i' are the number of quanta of excitation in that coordinate. The harmonic oscillator integrals are straightforwardly solved for within the raising/lowering operator formalism where,

$$\hat{a}^\dagger|i\rangle = \sqrt{i+1}|i+1\rangle \tag{3.10}$$

$$\hat{a}|i\rangle = \sqrt{i}|i-1\rangle \tag{3.11}$$

shows the result of operating on an arbitrary vibrational state, $|i\rangle$, with the raising and lowering operators, respectively. In this formalism, the position and momentum operators respectively adopt the following forms:

$$\hat{q} = \frac{1}{\sqrt{2}}\left(\hat{a} + \hat{a}^\dagger\right) \tag{3.12}$$

$$\hat{p} = -\frac{i}{\sqrt{2}}\left(\hat{a} - \hat{a}^{\dagger}\right) \tag{3.13}$$

The harmonic oscillator integrals can be solved by successive application of raising and lowering operators to an arbitrary vibrational state. Returning to the vibrational Hamiltonian, $\widehat{H}_1$ is the cubic potential operator which can be expressed as follows:

$$\widehat{H}_1 = \frac{1}{3!}\sum_{rst} \phi_{rst}\hat{q}_r\hat{q}_s\hat{q}_t \tag{3.14}$$

Similarly, $\widehat{H}_2$ contains the quartic potential and also the rotation-vibration Hamiltonian,

$$\widehat{H}_2 = \frac{1}{4!}\sum_{rstu} \phi_{rstu}\hat{q}_r\hat{q}_s\hat{q}_t\hat{q}_u + \widehat{H}_{cor} \tag{3.15}$$

The relevant (diagonal) part of the Coriolis Hamiltonian can be written as,

$$\widehat{H}_{cor} = \sum_{r,s>r}\left[\left(\frac{\omega_r^2+\omega_s^2}{\omega_r\omega_s}\right)\left(A_e(\zeta_{rs}^a)^2 + B_e\left(\zeta_{rs}^b\right)^2 + C_e(\zeta_{rs}^c)^2\right)\right]\hat{q}_r^2\hat{q}_s^2 \tag{3.16}$$

where ω_r represents the harmonic frequency of normal coordinate *r*, A_e, B_e, and C_e are the equilibrium rotational constants, and ζ is a Coriolis constant. Coriolis constants are unitless and are interpreted as follows: ζ_{rs}^a couples normal coordinates *r* and *s* via a rotation about the *a* inertial axis.

3.3. Sum-over-States VPT2

The standard expression for the energy of state a, to second-order in perturbation theory, is given below.

$$E_a = \langle a|\widehat{H}_0|a\rangle + \langle a|\widehat{H}'|a\rangle + \sum_{b\neq a}\left(\frac{\langle a|\widehat{H}'|b\rangle\langle b|\widehat{H}'|a\rangle}{\langle a|\widehat{H}_0|a\rangle - \langle b|\widehat{H}_0|b\rangle}\right) \tag{3.17}$$

This formulation of VPT2 is referred to as Sum-over-States (SoS) VPT2. The sum runs over all zeroth-order states, of which there are an infinite number. This can be simplified first by introducing,

$$\epsilon_a = \langle a|\hat{H}_{HO}|a\rangle \tag{3.18}$$

$$E_a = \epsilon_a + \langle a|\hat{H}'|a\rangle + \sum_{b\neq a} \frac{\langle a|\hat{H}'|b\rangle\langle b|\hat{H}'|a\rangle}{\epsilon_a - \epsilon_b} \tag{3.19}$$

choosing ϵ instead of ω to represent the energy of any arbitrary harmonic state. The definition of "orders" of vibrational perturbation theory is somewhat unconventional. Ordinarily, only the terms in the perturbation expansion are considered to have "orders." From left to right, the terms in the VPT2 energy expression are zeroth-, first-, and second-order. However in VPT, also the order of an operator is considered; this is given by the total number of position and momentum operators contained in it minus two. Accordingly, $\hat{H}_1$ contains first-order terms, and $\hat{H}_2$ contains second-order terms. The overall order of the operator and perturbation theory correction determines what terms contribute to each order of VPT.[7, 11]

The motivation for these definitions of perturbation orders is probably the fact that all odd-order potential terms could make contributions to the second-order perturbation theory term; likewise, all even-order potential terms could contribute to the first-order perturbation theory term. In principle, one might have access to force constants of an arbitrarily high order. Only by requiring a truncation of the potential operator is it possible to create a clear definition of what VPT2 includes.

The harmonic approximation can be considered VPT0. Only the zeroth-order term involving the zeroth-order Hamiltonian operator appears. VPT1 introduces the first-order perturbation theory term, which is a diagonal correction; however, only first-order operators may contribute to this. Upon inspection of the terms in the first-order Hamiltonian, $\hat{H}_1$, three sets of rules become apparent.

For $\phi_{rrr}\hat{q}_r^3 = \phi_{iii}\langle r|\hat{q}_r^3|r'\rangle$,
$\Delta n_r = \pm 1, \pm 3$ can be nonzero.

For terms $\phi_{rrs}\hat{q}_r^2\hat{q}_s = \phi_{rrs}\langle r|\hat{q}_r^2|r'\rangle\,\langle s|\hat{q}_s|s'\rangle$,
$\Delta n_r = 0, \pm 2, \Delta n_s = \pm 1$ can be nonzero.

For terms $\phi_{rst}\hat{q}_r\hat{q}_s\hat{q}_t = \phi_{rst}\langle r|\hat{q}_r|r'\rangle\,\langle s|\hat{q}_s|s'\rangle\,\langle t|\hat{q}_t|t'\rangle$,
$\Delta n_r = \pm 1, \Delta n_s = \pm 1, \Delta n_t = \pm 1$ can be nonzero.

In these cases, Δn_r represents the number of quanta that is allowed to change in normal coordinate *r*. All of the diagonal matrix elements of the $\hat{H}_1$ operator must be zero; therefore, there is no first-order contribution to the VPT energy, and VPT1 would be no different from the harmonic approximation. It is important to note that when a $\hat{q}_r^n$ operator is absent from a term in $\hat{H}$, it corresponds to $\hat{q}_r^0$, which is the overlap integral/Kronecker delta. This means that the excitation level in other normal coordinates is not permitted to change.

Moving now to VPT2, the second-order perturbation theory term, involving off-diagonal coupling matrix elements, is introduced, but only the first-order Hamiltonian matrix elements are retained in it. In addition to this, now the second-order Hamiltonian is allowed to contribute to the first-order energy correction. The second-order perturbation theory terms including $\hat{H}_1$ involve off-diagonal matrix elements between arbitrary pairs of vibrational states, and there are many opportunities for these to be nonzero. For example, the terms of the form $\phi_{rrr}\hat{q}_r^3$ will allow $|r\rangle$ to couple to $|r+1\rangle$ and $|r+3\rangle$ but not to $|r+2\rangle$. More generally, the matrix elements will permit coupling between harmonic oscillator states that differ by either 1 or 3 net quanta. Can any of the first-order terms involving $\hat{H}_2$ be nonzero? Numerous types of quartic terms are contained in $\hat{H}_2$, and they obey the following five sets of rules.

For $\phi_{rrrr}\hat{q}_r^4 = \phi_{rrrr}\langle r|\hat{q}_r^4|r'\rangle$,
$\Delta n_r = 0, \pm 2, \pm 4$ can be nonzero.

For $\phi_{rrss}\hat{q}_r^2\hat{q}_s^2 = \phi_{rrss}\langle r|\hat{q}_r^2|r'\rangle\langle s|\hat{q}_s^2|s'\rangle$,
$\Delta n_r = 0, \pm 2, \Delta n_s = 0, \pm 2$ can be nonzero.

For $\phi_{rrrs}\hat{q}_r^3\hat{q}_s = \phi_{rrrs}\langle r|\hat{q}_r^3|r'\rangle\langle s|\hat{q}_s|s'\rangle$,
$\Delta n_r = \pm 1, \pm 3, \Delta n_s = \pm 1$ can be nonzero.

For $\phi_{rrst}\hat{q}_r^2\hat{q}_s\hat{q}_t = \phi_{rrst}\langle r|\hat{q}_r^2|r'\rangle\langle s|\hat{q}_s|s'\rangle\langle t|\hat{q}_t|t'\rangle$,
$\Delta n_r = 0, \pm 2, \Delta n_s = \pm 1, \Delta n_t = \pm 1$ can be nonzero.

For $\phi_{rstu}\hat{q}_r\hat{q}_s\hat{q}_t\hat{q}_u = \phi_{rstu}\langle r|\hat{q}_r|r'\rangle\langle s|\hat{q}_s|s'\rangle\langle t|\hat{q}_t|t'\rangle\langle u|\hat{q}_u|u'\rangle$,
$\Delta n_r = \pm 1, \Delta n_s = \pm 1, \Delta n_t = \pm 1, \Delta n_u = \pm 1$ can be nonzero.

The first two types of quartic terms can be nonzero when the number of quanta does not change. The rotation-vibration terms are analogous to the second type of quartic potential term, containing $\hat{q}_r^2\hat{q}_s^2$ operators, so they may also contribute to the VPT2 energy. None of the other quartic terms may contribute to the VPT2 energy. This fact is greatly advantageous. Although all cubic force constants are necessary to evaluate the VPT2 energy, no quartic force constants with three or four unique indices need to be known. Thanks to the restrictive definition of VPT2 and the properties of the harmonic oscillator integrals, the energy expression simplifies further.

$$E_a = \epsilon_a + \langle a|\hat{H}_2|a\rangle + \sum_{b\neq a}\frac{\langle a|\hat{H}_1|b\rangle\langle b|\hat{H}_1|a\rangle}{\epsilon_a - \epsilon_b} \tag{3.20}$$

It was previously stated that only vibrational states differing by one or three net quanta can be coupled by $\hat{H}_1$. From this, it is clear that the sum over states can be truncated without any loss of accuracy. To determine the VPT2 energy of any vibrational state, it is sufficient to sum over only those vibrational states that are singly or triply excited or de-excited with respect to it. (Point group symmetry can impose further restrictions, as only states of the same symmetry may couple.) With these considerations, along with extensive algebra, the sum over vibrational states and all of the integrals can be eliminated from the VPT2 energy expression, rendering it down to an algebraic form with finite sums over the normal coordinates. It can then be arranged into a familiar, spectroscopic form.

3.4. The VPT2 Equations for Asymmetric Tops

Efficient VPT2 implementations are based on "anharmonicity constants." These are multidimensional analogs of the $\omega_e x_e$ term that appears in the Dunham expansion for the

rovibrational energy of a diatomic molecule.[1] Given below is the Dunham expansion truncated at the first three pure vibrational terms.

$$E(\mathrm{v}) = \omega_e\left(\mathrm{v}+\frac{1}{2}\right) - \omega_e x_e\left(\mathrm{v}+\frac{1}{2}\right)^2 + \omega_e y_e\left(\mathrm{v}+\frac{1}{2}\right)^3 \tag{3.21}$$

The diagonal and off-diagonal anharmonicity constants are defined as follows.

$$\chi_{rr} = \frac{1}{16}\phi_{rrrr} - \frac{1}{32}\sum_s \phi_{rrs}^2\left(\frac{1}{2\omega_r+\omega_s} + \frac{4}{\omega_s} - \frac{1}{2\omega_r-\omega_s}\right) \tag{3.22}$$

$$\begin{aligned}\chi_{rs} = \frac{1}{4}\phi_{rrss} - \frac{1}{4}\sum_t \frac{\phi_{rrt}\phi_{sst}}{\omega_t} \\ -\frac{1}{8}\sum_t \phi_{rst}^2\left(\frac{1}{\omega_r+\omega_s+\omega_t} + \frac{1}{-\omega_r+\omega_s+\omega_t} + \frac{1}{\omega_r-\omega_s+\omega_t} - \frac{1}{\omega_r+\omega_s-\omega_t}\right) \\ + \left(A_e(\zeta_{rs}^a)^2 + B_e\left(\zeta_{rs}^b\right)^2 + C_e(\zeta_{rs}^c)^2\right)\left(\frac{\omega_r}{\omega_s} + \frac{\omega_s}{\omega_r}\right)\end{aligned} \tag{3.23}$$

The VPT2 energy can be defined in terms of the anharmonicity constants,

$$E(\mathrm{v}) = \sum_r \omega_r\left(\mathrm{v}_r+\frac{1}{2}\right) + \sum_r\sum_s \chi_{rs}\left(\mathrm{v}_r+\frac{1}{2}\right)\left(\mathrm{v}_s+\frac{1}{2}\right) \tag{3.24}$$

where v_r and v_s are the number of quanta in normal coordinates *r* and *s*, respectively. Additionally, the double sum has the condition that $s \geq r$. This results in equivalent anharmonicity constants χ_{rs} and χ_{sr} only being counted once. Calculating the energy of a vibrational state using this summation over anharmonicity constants is exactly equivalent to (but far more compact than) performing the sum-over-states with the second-order perturbation theory expression.

In principle, VPT2 can be applied to any molecule; however, linear molecules, symmetric tops, and spherical tops all have special (i.e. annoying) formulas to correctly handle excitation in degenerate normal coordinates and the vibrational angular momentum that results.[9, 12] While it is not rigorously correct to use the asymmetric top expressions for these systems of higher symmetry, other sources of error in the treatment (e.g. perturbation theory and quality of the potential surface) will usually dominate. Some of the structure of degenerate overtone bands is

not recovered unless the proper equations are used, and this may be of concern to high-resolution spectroscopists. But because of the relative simplicity and ubiquity of the asymmetric top expressions, this discussion concerns only them.

Setting all $\mathrm{v} = 0$ and allowing *r* to run over all 3N-6 normal coordinates would give the full anharmonic Zero-Point Vibrational Energy (ZPVE). Instead, ignore the sums over *r* and compute the ZPVE associated only with normal coordinate *a*.

ia.) Vibrational ground state (ZPVE) of normal coordinate *a*:

$$E_0 = \omega_a\left(\mathrm{v}_a + \tfrac{1}{2}\right) + \textstyle\sum_s \chi_{as}\left(\mathrm{v}_a + \tfrac{1}{2}\right)\left(\mathrm{v}_s + \tfrac{1}{2}\right) \tag{3.25}$$

It will be helpful to distinguish terms involving diagonal and off-diagonal anharmonicity constants. Do this by imposing a restriction on the sum and withdrawing the term where $s = a$.

$$\begin{aligned} E_0 &= \omega_a\left(\mathrm{v}_a + \tfrac{1}{2}\right) + \chi_{aa}\left(\mathrm{v}_a + \tfrac{1}{2}\right)\left(\mathrm{v}_a + \tfrac{1}{2}\right) + \textstyle\sum_{s\neq a} \chi_{as}\left(\mathrm{v}_a + \tfrac{1}{2}\right)\left(\mathrm{v}_s + \tfrac{1}{2}\right) \\ &= \omega_a\left(0 + \tfrac{1}{2}\right) + \chi_{aa}\left(0 + \tfrac{1}{2}\right)\left(0 + \tfrac{1}{2}\right) + \textstyle\sum_{s\neq a} \chi_{as}\left(0 + \tfrac{1}{2}\right)\left(0 + \tfrac{1}{2}\right) \\ &= \tfrac{1}{2}\omega_a + \tfrac{1}{4}\chi_{aa} + \tfrac{1}{4}\textstyle\sum_{s\neq a}\chi_{as} \end{aligned} \tag{3.26}$$

ib.) First excited state of normal coordinate *a*:

$$\begin{aligned} E_1 &= \omega_a\left(\mathrm{v}_a + \tfrac{1}{2}\right) + \chi_{aa}\left(\mathrm{v}_a + \tfrac{1}{2}\right)\left(\mathrm{v}_a + \tfrac{1}{2}\right) + \textstyle\sum_{s\neq a} \chi_{as}\left(\mathrm{v}_a + \tfrac{1}{2}\right)\left(\mathrm{v}_s + \tfrac{1}{2}\right) \\ &= \omega_a\left(1 + \tfrac{1}{2}\right) + \chi_{aa}\left(1 + \tfrac{1}{2}\right)\left(1 + \tfrac{1}{2}\right) + \textstyle\sum_{s\neq a} \chi_{as}\left(1 + \tfrac{1}{2}\right)\left(0 + \tfrac{1}{2}\right) \\ &= \tfrac{3}{2}\omega_a + \tfrac{9}{4}\chi_{aa} + \tfrac{3}{4}\textstyle\sum_{s\neq a}\chi_{as} \end{aligned} \tag{3.27}$$

ic.) Fundamental frequency of normal coordinate *a*:

$$\nu_a = E_1 - E_0 = \left(\tfrac{3}{2}\omega_a + \tfrac{9}{4}\chi_{aa} + \tfrac{3}{4}\textstyle\sum_{s\neq a}\chi_{as}\right) - \left(\tfrac{1}{2}\omega_a + \tfrac{1}{4}\chi_{aa} + \tfrac{1}{4}\textstyle\sum_{s\neq a}\chi_{as}\right)$$

$$\boxed{\nu_a = \omega_a + 2\chi_{aa} + \tfrac{1}{2}\textstyle\sum_{s\neq a}\chi_{as}} \tag{3.28}$$

iia.) Vibrational ground state of normal coordinates *b* and *c*:

$$E_0 = \omega_b\left(\mathrm{v}_b + \tfrac{1}{2}\right) + \omega_c\left(\mathrm{v}_c + \tfrac{1}{2}\right) + \sum_s \chi_{bs}\left(\mathrm{v}_b + \tfrac{1}{2}\right)\left(\mathrm{v}_s + \tfrac{1}{2}\right) + \sum_s \chi_{cs}\left(\mathrm{v}_c + \tfrac{1}{2}\right)\left(\mathrm{v}_s + \tfrac{1}{2}\right) \quad (3.29)$$

Now the outer sum runs over both normal coordinates. The sums can be restricted such that $s \neq b$ and $s \neq c$. Note that χ_{cb} does not appear in the original summations; however, the equivalent constant χ_{bc} does.

$$\begin{aligned}
E_0 &= \omega_b\left(\mathrm{v}_b + \tfrac{1}{2}\right) + \omega_c\left(\mathrm{v}_c + \tfrac{1}{2}\right) + \chi_{bb}\left(\mathrm{v}_b + \tfrac{1}{2}\right)\left(\mathrm{v}_b + \tfrac{1}{2}\right) + \textstyle\sum_{s\neq\{b,c\}} \chi_{bs}\left(\mathrm{v}_b + \tfrac{1}{2}\right)\left(\mathrm{v}_s + \tfrac{1}{2}\right) + \\
&\quad \chi_{bc}\left(\mathrm{v}_c + \tfrac{1}{2}\right)\left(\mathrm{v}_b + \tfrac{1}{2}\right) + \chi_{cc}\left(\mathrm{v}_c + \tfrac{1}{2}\right)\left(\mathrm{v}_c + \tfrac{1}{2}\right) + \textstyle\sum_{s\neq\{b,c\}} \chi_{cs}\left(\mathrm{v}_c + \tfrac{1}{2}\right)\left(\mathrm{v}_s + \tfrac{1}{2}\right) \\
&= \omega_b\left(\mathrm{v}_b + \tfrac{1}{2}\right) + \omega_c\left(\mathrm{v}_c + \tfrac{1}{2}\right) + \chi_{bb}\left(\mathrm{v}_b + \tfrac{1}{2}\right)\left(\mathrm{v}_b + \tfrac{1}{2}\right) + \chi_{cc}\left(\mathrm{v}_c + \tfrac{1}{2}\right)\left(\mathrm{v}_c + \tfrac{1}{2}\right) + \\
&\quad \chi_{bc}\left(\mathrm{v}_b + \tfrac{1}{2}\right)\left(\mathrm{v}_c + \tfrac{1}{2}\right) + \textstyle\sum_{s\neq\{b,c\}} \chi_{bs}\left(\mathrm{v}_b + \tfrac{1}{2}\right)\left(\mathrm{v}_s + \tfrac{1}{2}\right) + \sum_{s\neq\{b,c\}} \chi_{cs}\left(\mathrm{v}_c + \tfrac{1}{2}\right)\left(\mathrm{v}_s + \tfrac{1}{2}\right) \\
&= \omega_b\left(0 + \tfrac{1}{2}\right) + \omega_c\left(0 + \tfrac{1}{2}\right) + \chi_{bb}\left(0 + \tfrac{1}{2}\right)^2 + \chi_{cc}\left(0 + \tfrac{1}{2}\right)^2 + \chi_{bc}\left(0 + \tfrac{1}{2}\right)^2 + \\
&\quad \textstyle\sum_{s\neq\{b,c\}} \chi_{bs}\left(0 + \tfrac{1}{2}\right)^2 + \sum_{s\neq\{b,c\}} \chi_{cs}\left(0 + \tfrac{1}{2}\right)^2 \\
&= \tfrac{1}{2}\omega_b + \tfrac{1}{2}\omega_c + \tfrac{1}{4}\chi_{bb} + \tfrac{1}{4}\chi_{cc} + \tfrac{1}{4}\chi_{bc} + \tfrac{1}{4}\textstyle\sum_{s\neq\{b,c\}}(\chi_{bs} + \chi_{cs})
\end{aligned} \quad (3.30)$$

iib.) Doubly-excited state in normal coordinates *b* and *c* (one quantum in each):

$$\begin{aligned}
E_1 &= \omega_b\left(\mathrm{v}_b + \tfrac{1}{2}\right) + \omega_c\left(\mathrm{v}_c + \tfrac{1}{2}\right) + \chi_{bb}\left(\mathrm{v}_b + \tfrac{1}{2}\right)\left(\mathrm{v}_b + \tfrac{1}{2}\right) + \chi_{cc}\left(\mathrm{v}_c + \tfrac{1}{2}\right)\left(\mathrm{v}_c + \tfrac{1}{2}\right) + \\
&\quad \chi_{bc}\left(\mathrm{v}_b + \tfrac{1}{2}\right)\left(\mathrm{v}_c + \tfrac{1}{2}\right) + \textstyle\sum_{s\neq\{b,c\}} \chi_{bs}\left(\mathrm{v}_b + \tfrac{1}{2}\right)\left(\mathrm{v}_s + \tfrac{1}{2}\right) + \sum_{s\neq\{b,c\}} \chi_{cs}\left(\mathrm{v}_c + \tfrac{1}{2}\right)\left(\mathrm{v}_s + \tfrac{1}{2}\right) \\
&= \omega_b\left(1 + \tfrac{1}{2}\right) + \omega_c\left(1 + \tfrac{1}{2}\right) + \chi_{bb}\left(1 + \tfrac{1}{2}\right)\left(1 + \tfrac{1}{2}\right) + \chi_{cc}\left(1 + \tfrac{1}{2}\right)\left(1 + \tfrac{1}{2}\right) + \\
&\quad \chi_{bc}\left(1 + \tfrac{1}{2}\right)\left(1 + \tfrac{1}{2}\right) + \textstyle\sum_{s\neq\{b,c\}} \chi_{bs}\left(1 + \tfrac{1}{2}\right)\left(0 + \tfrac{1}{2}\right) + \sum_{s\neq\{b,c\}} \chi_{cs}\left(1 + \tfrac{1}{2}\right)\left(0 + \tfrac{1}{2}\right) \\
&= \tfrac{3}{2}\omega_b + \tfrac{3}{2}\omega_c + \tfrac{9}{4}\chi_{bb} + \tfrac{9}{4}\chi_{cc} + \tfrac{9}{4}\chi_{bc} + \tfrac{3}{4}\textstyle\sum_{s\neq\{b,c\}}(\chi_{bs} + \chi_{cs})
\end{aligned} \quad (3.31)$$

iic.) Binary combination transition of normal coordinates *b* and *c*:

$$\begin{aligned}
(\nu_b + \nu_c) = E_1 - E_0 &= \left(\tfrac{3}{2}\omega_b + \tfrac{3}{2}\omega_c + \tfrac{9}{4}\chi_{bb} + \tfrac{9}{4}\chi_{cc} + \tfrac{9}{4}\chi_{bc} + \tfrac{3}{4}\textstyle\sum_{s\neq\{b,c\}}(\chi_{bs} + \chi_{cs})\right) - \\
&\quad \left(\tfrac{1}{2}\omega_b + \tfrac{1}{2}\omega_c + \tfrac{1}{4}\chi_{bb} + \tfrac{1}{4}\chi_{cc} + \tfrac{1}{4}\chi_{bc} + \tfrac{1}{4}\textstyle\sum_{s\neq\{b,c\}}(\chi_{bs} + \chi_{cs})\right)
\end{aligned}$$

$$\boxed{(\nu_b + \nu_c) = \omega_b + \omega_c + 2\chi_{bb} + 2\chi_{cc} + 2\chi_{bc} + \tfrac{1}{2}\textstyle\sum_{s\neq\{b,c\}}(\chi_{bs} + \chi_{cs})} \quad (3.32)$$

This can also be written in terms of one-quantum transitions of the normal modes:

$$\boxed{(\nu_b + \nu_c) = \nu_b + \nu_c + \chi_{bc}} \tag{3.33}$$

Likewise, for the first overtone of normal coordinate a. The frequency is given by:

$$\boxed{2\nu_a = 2\omega_a + 6\chi_{aa} + \sum_{s \neq a} \chi_{as}} \tag{3.34}$$

Or expressed in terms of one-quantum transitions:

$$\boxed{2\nu_a = \nu_a + \nu_a + 2\chi_{aa}} \tag{3.35}$$

A simple formula for the VPT2 energy of any arbitrarily excited vibrational state can be determined in this manner. In the absence of anharmonic resonances, this is all that is required to obtain predictions of vibrational frequencies with VPT2.

3.5. Anharmonic Resonance

The anharmonicity constants contain "resonance denominators." These are terms in the summations that have differences of harmonic frequencies in their denominators. The resonance denominators shown below are those present in χ_{rr} and χ_{rs}, respectively.

$$\frac{1}{2\omega_r - \omega_s} \tag{3.36}$$

$$\frac{1}{-\omega_r + \omega_s + \omega_t}, \ \frac{1}{\omega_r - \omega_s + \omega_t}, \ \frac{1}{\omega_r + \omega_s - \omega_t} \tag{3.37}$$

For certain cases, it is clear that these terms will "blow up." This signifies a breakdown in the perturbation theory approximation. These terms can be selectively removed from the anharmonicity constant expressions. This is referred to as deperturbation. Deperturbation is as simple as subtracting the offending terms, undoing the damage caused by including them in the sums in the first place. The most commonly encountered cases are the Fermi-Dennison (shortened to Fermi) resonances types I and II:

Fermi Type I: $\omega_a \approx 2\omega_b$

Fermi Type II: $\omega_a \approx \omega_b + \omega_c$

From this point on, these same indices (a, b, and c) will be used whenever these resonance cases are referenced by name. Identification of resonances is somewhat arbitrary in nature, and many different resonance diagnostics have been used. The more successful ones typically weigh both the harmonic frequency difference and the magnitude of the associated cubic force constant. A Fermi resonance requires that vibrational states are sufficiently close in energy and also coupled sufficiently strongly by the cubic terms in the potential expansion. A simple yet reliable resonance diagnostic is the eponymous Martin Test.[13] This is the difference between the variational and second-order perturbation corrections to the energies of a pair of states. The mathematical expressions are given below (Eqn. 3.38-3.41).

Perturbation Theory Correction (Type I):

$$\frac{\left(\frac{1}{4}\phi_{abb}\right)^2}{\omega_a - 2\omega_b} \tag{3.38}$$

Variational Correction (Type I) (obtained from eigenvalues of this matrix):

$$\begin{pmatrix} \omega_a & \frac{1}{4}\phi_{abb} \\ \frac{1}{4}\phi_{abb} & 2\omega_b \end{pmatrix} \rightarrow \lambda = \frac{\omega_a + 2\omega_b \pm \sqrt{(\omega_a - 2\omega_b)^2 + \frac{1}{4}\phi_{abb}^2}}{2} \tag{3.39}$$

Perturbation Theory Correction (Type II):

$$\frac{\left(\frac{1}{2\sqrt{2}}\phi_{abc}\right)^2}{\omega_a - \omega_b - \omega_c} \tag{3.40}$$

Variational Correction (Type II) (obtained from eigenvalues of this matrix):

$$\begin{pmatrix} \omega_a & \frac{1}{2\sqrt{2}}\phi_{abc} \\ \frac{1}{2\sqrt{2}}\phi_{abc} & \omega_b + \omega_c \end{pmatrix} \rightarrow \lambda = \frac{\omega_a + \omega_b + \omega_c \pm \sqrt{(\omega_a - \omega_b - \omega_c)^2 + \frac{1}{2}\phi_{abc}^2}}{2} \tag{3.41}$$

The difference can be evaluated for every two-state interaction, and a list of resonances can be populated by choosing an arbitrary cut-off value. A cut-off of 1 cm^{-1} is commonly used. The "harmonic derivatives" are an alternative resonance diagnostic, proposed by Matthews and Stanton, and implemented in the GUINEA module of CFOUR 2.1.[14-15]

After resonant terms are removed from an anharmonicity constant, it is customary to give the modified constant an asterisk and refer to it as "deperturbed." Moreover, any vibrational state calculated with deperturbed anharmonicity constants is also said to be deperturbed. To deperturb the anharmonicity constants for a Fermi Type I resonance, remove one term from χ_{bb} (Eqn. 3.42) and one term from χ_{ab} (Eqn. 3.43).

$$-\frac{1}{32}\left(\frac{\phi_{abb}^2}{\omega_a-2\omega_b}\right) \tag{3.42}$$

$$\frac{1}{8}\left(\frac{\phi_{abb}^2}{\omega_a-2\omega_b}\right) \tag{3.43}$$

To deperturb the anharmonicity constants for a Fermi Type II resonance, remove one term from both χ_{ac} and χ_{ab} (Eqn. 3.44) and one term from χ_{bc} (Eqn. 3.45).

$$\frac{1}{8}\left(\frac{\phi_{abc}^2}{\omega_a-\omega_b-\omega_c}\right) \tag{3.44}$$

$$-\frac{1}{8}\left(\frac{\phi_{abc}^2}{\omega_a-\omega_b-\omega_c}\right) \tag{3.45}$$

Quitting now and calculating vibrational energies with the deperturbed constants is sometimes called Deperturbed Second-Order Vibrational Perturbation Theory (DVPT2).[16] It provides an incomplete solution to the vibrational problem where the strongest couplings are not treated at all. This is not ideal. Instead, the strong couplings can be reintroduced within a variational framework. A small "effective Hamiltonian" matrix can be constructed of the vibrational states that are in resonance with each other. The diagonal elements of the matrix are taken to be the deperturbed VPT2 frequencies of each state. The off-diagonal elements are

(typically) the same as what would be used for a standard variational calculation. The eigenvalues of such a matrix are the corrected vibrational energy levels, and the eigenvectors reflect the character/composition of the new vibrational states.

It is best to think about anharmonic coupling in terms of interacting *states* rather than interacting *transitions*; however, because all excited vibrational states share a common ground state, this choice has no bearing on the predicted transition frequencies. Choosing the diagonal elements of the matrix to be the energies of vibrational *states* and then subtracting from the ZPVE gives equivalent predictions to using the frequencies of *transitions* as the diagonal elements and defining the ZPVE as zero.

3.6. Anharmonic Intensity

3.6.1. Overview

In order to understand transition intensity, it is useful to first introduce the language of mechanical anharmonicity and electrical anharmonicity.[17] Mechanical anharmonicity is sometimes also called intensity borrowing or intensity stealing. It describes the deviation from harmonicity (i.e. anharmonicity) of the vibrational wavefunctions. In contrast, electrical anharmonicity describes the deviation of the dipole moment function from linearity (in the normal coordinates). The approximation that the dipole moment is a linear function of the normal coordinates is referred to as the electrical harmonicity approximation. It is a special case of property anharmonicity, distinct from wavefunction anharmonicity. Various ways of evaluating intensity can be mechanically anharmonic, electrically anharmonic, both, or neither.[18]

Infrared intensity is proportional to the square of the transition dipole moment. It is most commonly expressed in units of kilometers per mole (km/mol) and less commonly as absorption cross-section (cm^2/molecule) or oscillator strength (unitless). The conversion factor to km/mol includes the frequency; the infrared intensity is therefore higher for higher frequency transitions.[19]

In this sense, one of the consequences of mechanical anharmonicity, which usually lowers frequencies, is a small reduction to intensities. For many applications, it is sufficient to determine only transitions from the vibrational ground state. However, in cases where low energy states are thermally populated, transitions from excited states can be weighted by their Boltzmann populations. This can lead to issues if using VPT2 transition moments, as the available analytic expressions describe only transitions from the ground vibrational state.

After the transition dipole moment is determined, evaluation of infrared intensity is straightforward for full VPT2. For variationally-corrected VPT2, detailed in Section 3.8, the transition moments must first be transformed into the basis of the effective Hamiltonian eigenvectors. This allows transitions that are initially "dark" to obtain intensity via mechanical anharmonicity. This also means that variationally-corrected VPT2 intensities are always at least partially mechanically anharmonic. The sum of the final intensities is usually close to, but not identical to, the intensity of the initial "bright" transition in the absence of the effective Hamiltonian treatment.

3.6.2. Evaluation of the Transition Dipole Moment

The dipole moment function may be expanded in the normal coordinates analogously to the potential energy (Eqn. 3.2),

$$\hat{\mu} = \mu_{eq} + \sum_r \mu_r \hat{q}_r + \frac{1}{2}\sum_{rs} \mu_{rs} \hat{q}_r \hat{q}_s + \frac{1}{6}\sum_{rst} \mu_{rst} \hat{q}_r \hat{q}_s \hat{q}_t + \cdots \tag{3.46}$$

where μ_{eq} is the equilibrium dipole moment, and μ_r, μ_{rs}, and μ_{rst} are first, second, and third dipole derivatives, respectively. In practice, this expansion is usually also "semi-diagonal," such that the highest-order terms with no shared indices are absent. Unlike the electronic potential energy, the first derivatives of the dipole moment are not, in general, zero; in fact, they are responsible for the majority of spectral intensity. Integrals of the dipole moment function, in the harmonic oscillator basis, can be evaluated with Equations 3.5-3.9. In this way, truncating Eqn.

3.46 at the linear terms, harmonic intensities can be determined for transitions between arbitrary harmonic oscillator states.

It would appear that the easiest way to move beyond harmonic intensity would be to expand the dipole moment function further. For harmonic oscillators, contributions to the intensity follow an alternating pattern: 1-quantum transition moments arise from the first, third, fifth, … derivatives; 2-quanta from second, fourth, sixth, … derivatives; 3-quanta from third, fifth, seventh, … derivatives; etc. So expanding the dipole moment function to the cubic terms provides the leading terms in the transition moments of 1, 2, and 3-quanta transitions and the second term for 1-quantum transitions. Determining transition moments using this expansion, in the harmonic oscillator basis, provides intensities that are electrically anharmonic but not necessarily mechanically anharmonic. Such a scheme is quite unusual, as it is uncommon to possess high-order dipole derivatives but not high-order potential derivatives, or it is uncommon to possess high-order potential derivatives and not use them in a treatment of mechanical anharmonicity. Moreover, the mechanical anharmonicity contribution to intensities is usually much more substantial than the electrical anharmonicity contribution.

As stated in Section 3.6.1, intensities in variationally-corrected VPT2 incorporate some mechanical anharmonicity effects (the most important ones, when the simulation is intelligently designed). For this reason, it is often adequate to use harmonic oscillator transition moments. These are simple to evaluate, resonance-free, and only require the first derivatives of the dipole moment. Yet it is important to appreciate that the original basis functions for an effective Hamiltonian are not harmonic oscillator states; rather, they are partial VPT2 states. Therefore, the use of harmonic oscillator transition moments is not rigorously correct.

Transition moments may alternatively be evaluated in the framework of vibrational perturbation theory.[19-20] Transition moments at this level of approximation are both mechanically and electrically anharmonic. Transition moment integrals can be determined between any two

VPT2 or VPT4 states, using a sum-over-states expression.[14, 19] Analytic expressions for VPT2 transition moments also exist for 1-, 2-, and 3-quanta transitions from the vibrational ground state.[16, 19, 21] The VPT2 transition moment for transitions of four quanta or greater are exactly zero. VPT2 transition moments are typically the highest quality source of intensity for a VPT2 simulation. For variationally-corrected VPT2, even the VPT2 transition moments are not fully rigorous, and it has been recognized that they require a form of deperturbation in order to correspond to the partial VPT2 effective Hamiltonian basis states.[22] Formulas for deperturbed transition moments of 1 and 2-quanta transitions (from the vibrational ground state) have been published by Vazquez and Stanton,[22] and GUINEA is capable of computing intensities for variationally-corrected VPT2 for even more general cases.[14]

3.6.3. Manifestation of Resonances in VPT2 Transition Moments

In addition to being much more complicated than the corresponding energy expressions, VPT2 transition moments are susceptible to several kinds of anharmonic resonances.[22] The effect of resonances on transition moments can be profound, and because intensity is proportional to the square, the errors are magnified. Careless use of VPT2 transition moments cannot therefore be recommended. Consider the cases of 1-, 2-, and 3-quanta transitions from the vibrational ground state. The transition moment for 2-quanta transitions is more compact than for the other two cases, and it contains only 1:2 resonance denominators (i.e. Fermi resonances). Identification of Fermi resonances via the Martin Test and subsequent deperturbation can be successful; however, a loose Martin Test threshold (perhaps 0.1 cm^{-1}) often performs better. The 1- and 3-quanta transition moments contain not only 1:2 resonance denominators but 1:1 and 1:3 Darling-Dennison resonances, respectively. While these types of resonances are seldom as severe as Fermi resonances, they should not be ignored, and they must be identified using a different type of diagnostic. Similar to the way Fermi resonances are handled in Darling-Dennison constants (Section 3.9), these 1:1 and 1:3 resonance terms are left deperturbed.

3.7. Computation of Anharmonic Force Fields

3.7.1. Overview and Electronic Structure Considerations

When simulating a vibrational spectrum via VPT2, the most time-consuming step is the computation of the anharmonic force field. This requires many derivatives of the electronic potential energy with respect to the normal coordinates. Anharmonicity constants require cubic force constants of the form: $\phi_{rrr},\ \phi_{rrs},\ \phi_{rst}$ (i.e. all of them); however, they only require the ϕ_{rrrr} and ϕ_{rrss} quartic force constants. Therefore, in order to perform vibrational perturbation theory to second order, the complete sets of quadratic and cubic force constants and only a small part of the quartic force constants are required. The cubic and quartic force constants are commonly determined by numerically differentiating lower derivatives calculated at geometries displaced in the normal coordinates. The displacement algorithms provide enough derivative information to also compute the ϕ_{rrrs} and ϕ_{rrst} quartic force constants. Such a truncation is referred to as a semi-diagonal quartic force field, and its calculation is implemented in CFOUR, Gaussian, ORCA, and other packages.[14, 23-25] It differs from a full quartic force field in that it lacks force constants with four distinct indices, ϕ_{rstu}. These would require many more displacements and derivative calculations. In VPT2+K (Section 3.9), the lack of ϕ_{rstu} force constants means that certain resonance constants cannot be determined.

In choosing a level of theory at which to compute force constants, it is most important to consider the reference wavefunction, the basis set, and the level of electron correlation. With regard to the reference wavefunction, the first question that must be answered is whether a single-configurational description is a reasonable starting point or if the wavefunction is intrinsically multi-configurational in nature. When this is in doubt, the multiconfigurational character of a system is judged by performing Complete Active Space Self Consistent Field (CASSCF) computations.[26-27] When affordable, the active space is chosen as the valence space, but this can be truncated to remove strongly doubly-occupied orbitals or nearly unoccupied orbitals. At least a

polarized double zeta basis set should be used. If more than one of the squared CASCI coefficients adopts a large value, then this is indicative of a multi-configurational system. The cut-off value is arbitrary; however, a value of 0.05 or higher for the second most dominant configuration is considered to be notable, and a value of 0.10 or higher is considered to be severe. Single-reference Coupled Cluster (CC) computations also have diagnostic value, as the T_1 and T_2 amplitudes reflect the importance of mixing with excited configurations. A large T_2 amplitude can indicate that the wavefunction has biradical character.[28] Large T_1 amplitudes are more difficult to interpret. In some open-shell systems, large T_1 amplitudes are not a cause for concern; instead, they are reflective of orbital relaxation effects.[29]

Once it is established that a system is single-configurational, the starting point for describing the electronic wavefunction is the Hartree-Fock Self-Consistent Field (HF-SCF) method. Closed shell systems are described from a Restricted Hartree-Fock (RHF) starting point, which usually does not warrant any special discussion. Unrestricted Hartree-Fock (UHF) and Restricted Open shell Hartree-Fock (ROHF) are the two most commonly encountered references for open shell systems, and post-HF electron correlation methods and analytic derivatives are well-developed based upon both types. The correct choice is not at all obvious.[30-31] A UHF reference is susceptible to a phenomenon known as spin contamination; wherein, the wavefunction is artificially stabilized by mixing with wavefunctions of different multiplicities. As a consequence of this, the UHF wavefunction is not an eigenfunction of the total spin squared operator; although, the true wavefunction must be. Electron correlation repairs this; particularly, iterative coupled cluster methods are very effective at reducing the spin contamination of the wavefunction. ROHF does not suffer from spin contamination, and on this basis it would seem to be the superior choice to UHF. Though, it is interesting to note that typical electron correlation treatments based on an ROHF reference can actually introduce small amounts of spin contamination.[32-33]

There is a further problem called artefactual symmetry breaking. This can affect both types of reference; although, it has been stated that ROHF is more susceptible.[30] Artefactual symmetry-breaking can occur when an alternative, lower-energy SCF solution exists which has lower symmetry than the point group of the system. Such a thing is also not physical, as the wavefunction symmetry must match the molecular symmetry. Stated differently, the molecular orbitals must transform as irreducible representations of the point group of the molecule. At higher symmetry structures, it is sometimes possible to constrain the wavefunction to conform to the molecular symmetry. However, it is much more difficult to prevent the SCF procedure from converging to a broken symmetry solution at a displaced, lower symmetry geometry, where the real and artefactual solutions have the same symmetry. Numerically differentiating points which have converged to different SCF solutions will lead to nothing but garbage. In this way, symmetry-breaking can be a serious concern whenever numerical differentiation is employed, such as in the determination of quartic force fields. Symmetry breaking is not totally unrelated to spin contamination; oftentimes, the alternative SCF solutions can be identified by their expectation values of the total spin squared operator. Finally, it is important to understand that symmetry breaking does not actually require there to be any symmetry elements. The essence of artefactual symmetry breaking is the incorrect localization of electron density; this can happen even in the absence of symmetry, and spurious SCF solutions will arise.

There is a third, even less obvious source of error that can affect both UHF and ROHF references. In certain regions of nuclear displacement space, different SCF solutions may become exactly degenerate; although, the true wavefunctions are unlikely to be. The different SCF solutions may correspond to real, excited electronic states, or they may be spurious, localized solutions, like those discussed above. These are referred to as orbital instabilities.[34-35] The electronic energy and all energy-derivative properties will tend toward positive or negative infinity as they approach these points. Such behavior would be reasonable if these were the true

wavefunctions of two electronic states in the vicinity of an intersection. Unfortunately, the degeneracies between SCF solutions are still meaningful, even in highly-correlated wavefunctions. When the equilibrium geometry determined with a correlated level of theory is near the location of an SCF degeneracy, the accuracy of force constant predictions is degraded. More complete electron correlation reduces the size of these problematic "near instability" regions, in nuclear configuration space, and iterative methods are more effective. In fact, perturbative methods can actually worsen the problem.[34] Orbital instabilities are only completely eliminated in the full CI limit. It is effectively a matter of luck as to what extent vibrational frequencies are affected by near-instabilities. A useful diagnostic for problem is the "stability analysis" implemented in most software packages, which evaluates the second derivatives of the HF-SCF energy with respect to rotations (i.e. optimizations) of the orbitals. Small second derivatives (either positive or negative valued) may be a cause for concern.[36]

It is for these reasons that it is advisable to perform computations on open-shell systems with both types of reference and to compare the frequencies. If they match closely, it is unlikely that any of these reference problems are an issue. If they disagree, then more detailed investigations should be carried out, potentially involving EOM-CC, CCSDT, Brückner CC, or multireference methods.[37-39]

The most affordable treatment of dynamical electron correlation is by Møller-Plesset second-order perturbation theory (MP2), and it is fairly accurate for making force constant predictions. In order to achieve a superior description of harmonic frequencies than MP2, CCSD(T) should typically be chosen next. Frequencies from CCSD are often worse than MP2, except in cases where the electronic structure is particularly challenging or pathological.[40] Other electronic structure methods, such as EOM-CC, are normally reserved for troublesome systems. However, when extreme accuracy is the goal, it may be desirable to extend electron correlation to CCSDT(Q) for a well-behaved system. Usually this should also be balanced with various

auxiliary corrections such as core-correlation, scalar relativity, the diagonal Born-Oppenheimer correction, and spin-orbit coupling, as in various high accuracy thermochemistry methodologies.[41-42] These methodologies often utilize explicit correlation or extrapolation techniques to approach a Complete Basis Set (CBS) quality description.[43-45]

Refocusing the discussion away from composite model chemistries and back to single "levels of theory," the basis sets of choice for computing vibrational frequencies of small organic molecules are often derived from the Atomic Natural Orbital (ANO) basis set of Almlöf and Taylor.[46] Two benchmarking studies have found that the ANO basis sets generally perform well for harmonic frequencies, and they often perform better than the similar sized Dunning basis sets.[47-48] Their superior performance is more pronounced for smaller basis sets (double and triple zeta) quality. The full ANO basis set is quadruple zeta, denoted ANO2, and its triple and double zeta truncations are denoted ANO1 and ANO0, respectively. Section 3.7.2 delves into more detail about effective use of these basis sets.

A final consideration in choosing an electronic structure method is the availability of analytic energy derivatives. Analytic formulations of third and fourth derivatives are only available for Hartree-Fock[49-51] and DFT[52] and are not commonly implemented in quantum chemistry software packages. A quartic force field contains up to fourth geometrical derivatives of the electronic energy; thus, quartic force fields are usually determined numerically. Differentiation of lower analytic derivatives (i.e. first or second) helps to reduce the number of normal coordinate displacements and reduce the numerical differentiation error. Electronic structure methods with at least analytic first derivatives available are very desirable for computation of quartic force fields. The CFOUR package has analytic derivatives implemented for numerous *ab initio* methods.[53] A few important methods are listed below. Hartree-Fock (RHF, UHF, and ROHF) has up to second derivatives. Most correlated methods based on ROHF [MP2, CCSD, CCSD(T)] have first derivatives, and most correlated methods based on RHF and UHF

[MP2, CCSD, CCSD(T)] have up to second derivatives.[54-55] For higher levels of theory, CCSDT, CCSDT(Q), and CCSDTQ first derivatives are available with RHF. First derivatives are also available with various EOM-CC models. Access to analytic second derivatives for higher-order standard coupled cluster methods is possible with the MRCC program.[56-57]

3.7.2. Hybrid Force Field Approximations

The motivation behind making a "hybrid approximation" to a quartic force field will be introduced first, and then it will actually be explained what is meant by the term. The use of hybrid approximations is motivated by three points. First, harmonic frequencies are more sensitive to level of theory than higher-order force constants. A primary reason for this is the increased importance of the nuclear repulsion energy for higher order derivatives, which is always treated exactly.[58] Second, it is intuitively obvious that it requires less computational expense to compute harmonic frequencies than to compute an entire quartic force field at the same level of theory. Third, anharmonic predictions are more sensitive to the quality of the harmonic frequencies, as these constitute the zeroth-order picture, than they are to the quality of the higher-order force constants.

A hybrid approximation entails the combination of force constants from different levels of theory, ideally forming a force field that is both accurate and economical. For the work discussed herein, harmonic (i.e. quadratic) force constants are evaluated at a "higher-level" of theory, and the cubic/quartic force constants are evaluated at a "lower-level" of theory. There are several approaches to combining force constants. The approaches can be classified based upon whether they make the following two assumptions: i) The anharmonic coupling is well described at the lower-level of theory. ii) The normal coordinates are the same at both levels of theory. Both assumptions are generally valid, if very high levels of theory can be applied to both the harmonic and anharmonic parts of the force field. If this is the case, then details of how the hybrid approximation is applied are unimportant. This is not the case for the molecules discussed in this

dissertation. Ordinarily the higher and lower levels of theory are CCSD(T)/ANO1 and CCSD(T)/ANO0, respectively, and the combination of both into a hybrid force field will be indicated as CCSD(T)/ANO[1,0].

The first approach, denoted "additive," makes both assumptions. The VPT2 equations are solved with the non-hybrid (i.e. pure), lower-level quartic force field, and additive anharmonic corrections are determined. These are simply the difference between the VPT2 frequency and the harmonic frequency. The corrections are then applied to the higher-level harmonic frequencies. This approach is not recommended, as the first assumption is particularly poor when dealing with CH stretches. In this spectral region, the most important couplings occur between singly excited CH stretches and doubly excited HCH bends; however, the basis set requirements are much greater for CH stretches than for HCH bends. If the Fermi coupling problem is solved in a small one-electron basis set (e.g. using CCSD(T)/ANO0), the CH stretching harmonic frequencies will be systematically too high (10-20 cm^{-1} or more), but the HCH bending harmonic frequencies will be fairly well converged. The stretch-bend coupling will not be accurately described; it's strength is typically underestimated. A further concern arises with additive anharmonicity corrections derived from effective Hamiltonian treatments. Since the final states can be of significantly mixed character, but the corrections are applied to pure, harmonic states, the additive approach can be unsatisfying.

The second approach is denoted "substituted," and it makes only the second assumption. The lower-level harmonic force constants are first replaced with their higher-level analogues, in the quartic force field. Then the VPT2 equations are solved with the modified force field. This approach is generally recommended, as it has no additional cost, and the two problems discussed with the additive approach are completely overcome. The substituted approach allows for more natural effective Hamiltonian treatments. However the second assumption may still cause

problems for larger, lower symmetry systems, where the localized vs. delocalized nature of the normal coordinates becomes more sensitive to the level of theory.

The third approach, denoted “transformed,” discards the second assumption, eliminating error due to differences in the normal coordinates. It achieves this by a transformation of the lower-level cubic/quartic force constants into the higher-level normal coordinates. This implies that the harmonic force constants have also been substituted as in the second approach. The transformation procedure is further motivated and discussed in detail in Chapter 6. The disadvantage of the transformed approach is that it requires a full quartic force field as opposed to the more common “semi-diagonal” quartic force field. The computation of a full quartic force field can be several times more expensive; however, it can still be less expensive than using the higher-level of theory for all force constants.

3.8. Illustrative Examples

This section introduces the first two example systems in this chapter, using them to illustrate some of the considerations involved in performing VPT simulations. This sets a precedent for the structure of the remainder of the chapter; further aspects of VPT2 simulations are discussed with reference to these examples and others. For instance, the formaldehyde example in Section 3.8.2 motivates the introduction of the Darling-Dennison resonance constants in Section 3.9, seeing VPT2 extended fully to VPT2+K.

3.8.1. Simulation of the CH Stretches of Cyclopentadiene

Cyclopentadiene is an 11-atom system (3N-6 = 27 normal modes) with C_{2v} symmetry. In a semi-rigid system like this, the CH stretch transitions are often the most anharmonic and therefore the most interesting to model. Vibrational states with 1-quantum of CH stretch excitation frequently fall close in energy to states with 2-quanta of CH bending and/or C=C stretching excitation. When those stretching and bending normal modes primarily involve motion

of the same atoms, the force constants can also be quite large. The procedure for predicting the infrared spectrum is divided into six steps.

Step 1: Compute the anharmonic force field. This example uses a semi-diagonal hybrid quartic force field. In this force field, the quadratic force constants are computed at the CCSD(T)/ANO1 level of theory, and the cubic and quartic force constants are computed at the CCSD(T)/ANO0 level of theory (a smaller basis set). The substituted hybrid scheme is employed. This force field contains 990 unique cubic force constants and 2548 unique quartic force constants (of which 368 are sufficient for VPT2). The C_{2v} symmetry of the system is taken into account during the calculation, so many force constants are rigorously zero. This has significantly reduced the size of the force field.

Step 2: Calculate the anharmonicity constants. The full VPT2 spectrum of the CH stretching fundamentals is shown in Figure 3.1. Harmonic oscillator intensity is used, based upon a linear expansion of the transition dipole moment. This choice is likely not the most accurate option, but it avoids overcomplicating the discussion. Something is so wrong that an axis break is necessary. Frequency predictions that are hundreds or thousands of wavenumbers outside of the normal range, such as the 4700 cm^{-1} CH stretching fundamental here, usually indicate an untreated Fermi resonance. Now it should be considered whether Fermi resonances are active.

Step 3: Establish a list of resonances. This should reveal why there is a CH stretch fundamental at 4700 cm^{-1}. Using the Martin Test with a 1 cm^{-1} threshold, which is typical, four Fermi resonances are identified: three Type I and one Type II (Table 3.1). Refer to the list of normal coordinates to decide which resonances are relevant for the CH stretching region (Table 3.2). The CH stretching modes are highlighted. Four are linear combinations of the CH stretches on the ring, and the other two correspond to the symmetric and antisymmetric stretches of the CH_2 group. Inspecting the resonance list, note that the first two do not affect the CH stretches. They manifest in anharmonicity constants that are not present in the energy expressions for the

CH stretch fundamentals. As long as only CH stretch transitions are desired, these resonances can be ignored. The last two resonances directly involve CH stretches. The highest frequency CH stretch states are strongly coupled to doubly-excited C=C stretching states. The first resonance occurs between B_2 states and the second between A_1 states.

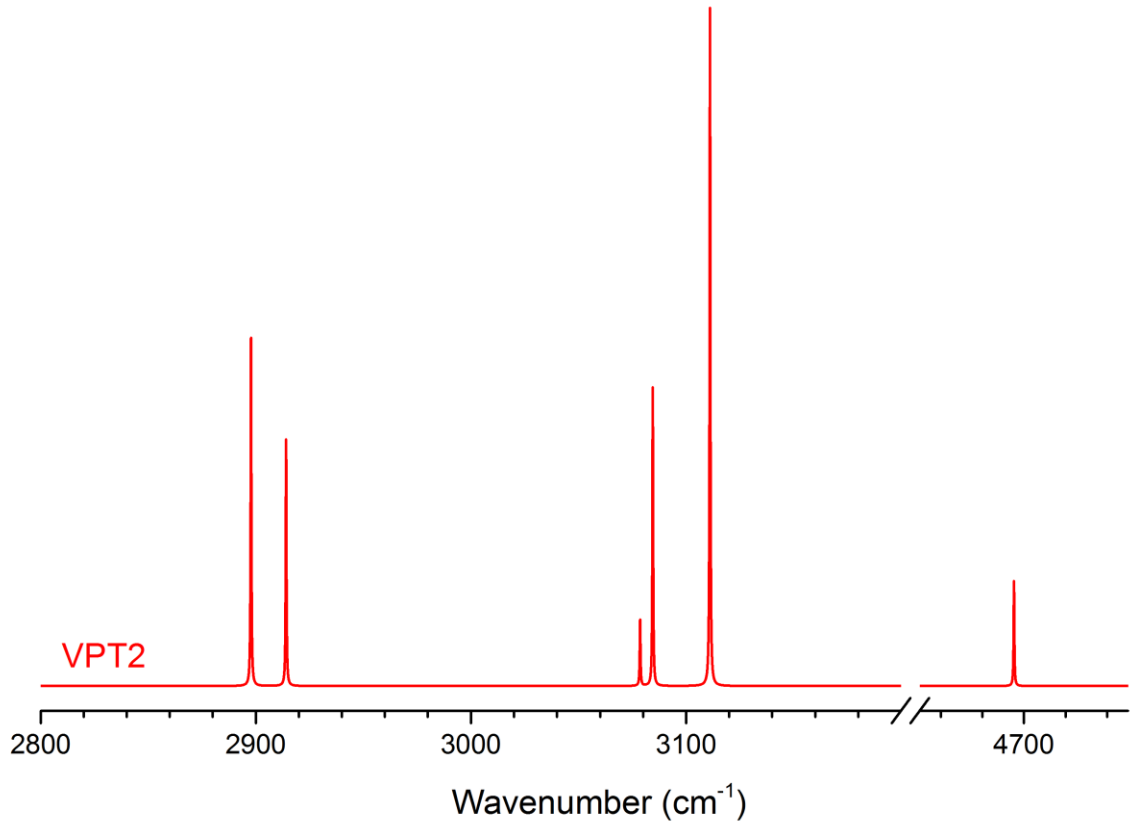

Figure 3.1. Full VPT2 simulation of the CH stretching fundamentals of cyclopentadiene. Quartic force field was determined using the CCSD(T)/ANO[1,0] hybrid model.

Table 3.1. Fermi resonances in cyclopentadiene. All quantities are given in wavenumbers. Resonances were identified with a 1 cm^{-1} threshold Martin Test, shown in the last column.

Resonance	Γ	Energy Separation	Cubic Force Constant	Variational - Perturbational
$\omega_8 \approx 2\omega_{14}$	A_1	10.9	-31.6	1.6
$\omega_6 \approx 2\omega_{13}$	A_1	2.4	-11.2	1.4
$\omega_{20} \approx \omega_4 + \omega_{22}$	B_2	64.6	-89.7	2.6
$\omega_1 \approx 2\omega_{22}$	A_1	0.3	88.1	1567.2

Table 3.2. Normal coordinates of cyclopentadiene. Modes are ordered in the standard spectroscopic convention. Symmetries and qualitative descriptions are given.

#	Γ	Description	#	Γ	Description	#	Γ	Description
1	A_1	v_s^{in}(CH)	10	A_1	δ_s(ring)	19	B_1	ring puckering
2	A_1	v_{as}^{in}(CH)	11	A_2	τ(CH_2)	20	B_2	v_s^{out}(CH)
3	A_1	v_s(CH_2)	12	A_2	$\rho_{w,as}^{out}$(CH)	21	B_2	v_{as}^{out}(CH)
4	A_1	v_s(C=C)	13	A_2	$\rho_{w,s}^{out}$(CH)	22	B_2	v_{as}(C=C)
5	A_1	δ_{as}^{in}(CH)	14	A_2	τ(ring)	23	B_2	δ_{as}^{out}(CH)
6	A_1	δ(CH_2)	15	B_1	v_{as}(CH_2)	24	B_2	ρ_w(CH_2)
7	A_1	δ_s^{in}(CH)	16	B_1	$\rho_{w,as}^{in}$(CH)	25	B_2	δ_s^{out}(CH)
8	A_1	v(C-C)	17	B_1	ρ_r(CH_2)	26	B_2	v_{as}(C-C-C)
9	A_1	v_s(C-C-C)	18	B_1	$\rho_{w,s}^{in}$(CH)	27	B_2	δ_{as}(ring)

Step 4: Deperturb the anharmonicity constants accordingly. The consequences of deperturbing the anharmonicity constants for the B_2 resonance are shown below.

$$\chi_{4,20} = 15.3 \rightarrow \chi^*_{4,20} = \text{-}0.3, \qquad \chi_{20,22} = 15.6 \rightarrow \chi^*_{20,22} = 0.0,$$

$$\chi_{4,22} = \text{-}32.2 \rightarrow \chi^*_{4,22} = \text{-}16.7$$

Deperturbing the anharmonicity constants for the A_1 resonance has the following effects.

$$\chi_{22,22} = -798.3 \rightarrow \chi^*_{22,22} = -3.7, \qquad \chi_{1,22} = 3177.1 \rightarrow \chi^*_{1,22} = -1.1$$

Step 5: Treat the resonances. This anharmonic coupling problem is quite simple, and it requires only two 2x2 effective Hamiltonians. The solutions of matrix eigenvalue problems will be presented in a form that simplifies their interpretation. The rows of the eigensolution represent the "unmixed" DVPT2 basis functions, in the same order as they were arranged in the effective Hamiltonian. Each column corresponds to a final vibrational state, headed by its eigenvalue. The numbers within the matrix are the squared eigenvector coefficients. They are interpreted as the fraction of each original DVPT2 vibrational state that is present in the final states. Variational treatment of the B_2 symmetry resonance is detailed below (Eqn. 3.47-3.49).

$$H_{eff} = \begin{pmatrix} v^*_{20} & \frac{1}{2\sqrt{2}}\phi_{20,4,22} \\ \frac{1}{2\sqrt{2}}\phi_{20,4,22} & (v_4 + v_{22})^* \end{pmatrix} \tag{3.47}$$

$$H_{eff} = \begin{pmatrix} 3095.5 & -31.7 \\ -31.7 & 3068.0 \end{pmatrix} \tag{3.48}$$

$$\begin{bmatrix} & \mathbf{3116.3} & \mathbf{3047.2} \\ |v_{20}\rangle & 0.70 & 0.30 \\ |v_4 + v_{22}\rangle & 0.30 & 0.70 \end{bmatrix} \tag{3.49}$$

As a result of the B_2 resonance, the fundamental is pushed up, and the combination is pushed down in frequency by 21 wavenumbers (Eqn. 3.49). The states mix considerably, but the transition at 3116.3 cm^{-1} is best described as a CH stretch fundamental, and the transition at

3047.2 cm^{-1} is primarily the symmetric + antisymmetric C=C stretch combination. Treatment of the A_1 resonance proceeds similarly (Eqn. 3.50-3.52).

$$H_{eff} = \begin{pmatrix} v_1^* & \frac{1}{4}\phi_{1,22,22} \\ \frac{1}{4}\phi_{1,22,22} & 2v_{22}^* \end{pmatrix} \tag{3.50}$$

$$H_{eff} = \begin{pmatrix} 3106.1 & 22.0 \\ 22.0 & 3152.0 \end{pmatrix} \tag{3.51}$$

$$\begin{bmatrix} & \mathbf{3160.8} & \mathbf{3097.2} \\ |v_1\rangle & 0.14 & 0.86 \\ |2v_{22}\rangle & 0.86 & 0.14 \end{bmatrix} \tag{3.52}$$

The overtone is pushed up, and the fundamental is pushed down in frequency by 9 cm^{-1}. They mix more weakly than the B_2 states, so the transitions are still well described as a CH stretch fundamental at 3097.2 cm^{-1} and the first overtone of the antisymmetric C=C stretch at 3160.8 cm^{-1}.

These results illustrate that the variational-perturbational difference from the Martin Test is not always reflective of how strong the mixing will be, as it is based upon a two-state interaction of zeroth-order harmonic oscillator states. Whereas, the final mixing occurs after the diagonal elements have been "dressed" to account for weak interactions with other states. Note also that the A_1 resonance is predicted to be so strong because the zeroth order states are less than 1 cm^{-1} apart. The harmonic frequencies of these states are not fully converged, and they might change by 10 cm^{-1} or more if they are computed with more complete basis sets. Small changes could lead to a much smaller value of the resonance diagnostic.

Step 6: Simulate the spectrum. As with the full VPT2 spectrum, harmonic intensity is used. In the case of resonant interactions, the harmonic intensity can be distributed proportional to the state-mixing. For example, the B_2 effective Hamiltonian gives transitions at 3047.2 and 3116.3 cm^{-1}. The lower frequency transition, $v_4 + v_{22}$, steals 30% of the intensity from v_{20},

which is left with 70%. In this model, mixing is necessary to confer intensity to combinations and overtones.

Figure 3.2 shows the variationally-corrected simulation. This type of simulation has occasionally been called VPT2+F, where the F indicates some explicit treatment of Fermi coupling.[59] It would be interesting to see how this simulation compares to a scaled harmonic spectrum, which is a far simpler and cheaper alternative. The scaling factor for the harmonic spectrum is chosen to best reproduce the experimental band origins of the two non-resonant fundamentals centered around 2900 cm^{-1}. Additionally, a DVPT2 simulation in included in the comparison (Fig. 3.2).

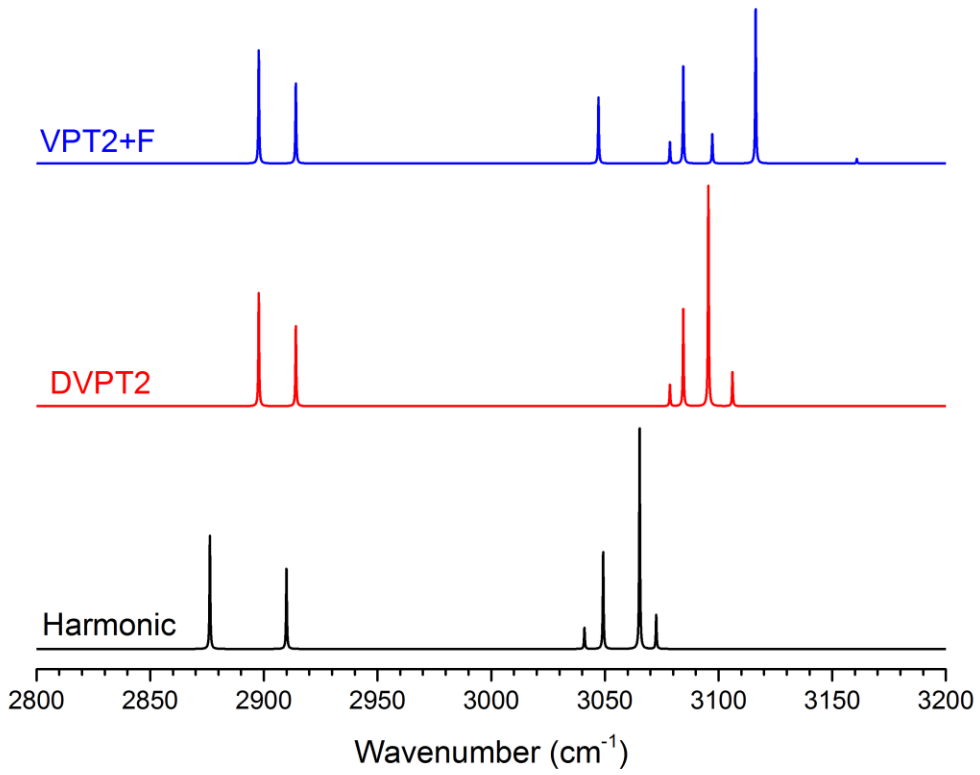

Figure 3.2. Various anharmonic simulations of the cyclopentadiene CH stretching region.

The structure of the harmonic and DVPT2 spectra are very similar. They each have only six transitions because we have provided no mechanism for dark states to borrow intensity. The effective Hamiltonian procedure from VPT2+F simultaneously corrects the frequencies of the fundamentals and the strongly-coupled 2-quanta states and also lights up the dark 2-quanta transitions, giving intensity predictions that are usually qualitatively correct. Observe that the combination transition at 3047 cm^{-1} is actually more intense than some of the fundamentals.

The theoretical transitions are now compared to experimental values. The experimental frequencies come from a series of gas and liquid phase studies conducted at room temperature. Band origins derived from these measurements are not highly accurate (~ 10 cm^{-1} uncertainty). For some transitions, their symmetries could be experimentally deduced based upon Raman depolarization ratios and gas-phase rotational contours. This is especially useful for assigning the transitions above 3000 cm^{-1}, which are somewhat dense but can be distinguished as being either A_1 or B_2 symmetry.

The lowest frequency transitions are the A_1 and B_1 symmetry CH_2 stretches. They have been observed as two medium-strength bands at 2886 and 2900 cm^{-1}, respectively. Nothing else is observed in the vicinity of these. The simulation places these in the correct order, at 2905 and 2914 cm^{-1}. In this spectral region, VPT2+F offers no advantage over VPT2, and even an assignment based upon harmonic frequencies will be successful. On the high frequency side, the first overtone of the antisymmetric C=C stretch was assigned as a weak feature at 3161 cm^{-1}. The VPT2+F simulation also places it at 3161 cm^{-1}. Two medium-strength A_1 transitions were observed at 3091 and 3075 cm^{-1} and were assigned to the fundamentals. The lower transition from the A_1 effective Hamiltonian is predicted at 3097 cm^{-1}. This is a good candidate for the higher frequency transition. The 3075 cm^{-1} transition probably corresponds to the in-phase antisymmetric CH stretch fundamental, predicted at 3084 cm^{-1}.

One medium-strength B_2 band was observed at 3105 cm^{-1} and assigned to the symmetric out-of-phase CH stretch. This same transition is predicted at 3116 cm^{-1} from diagonalization of the effective Hamiltonian. The other transition that is predicted from the B_2 effective Hamiltonian is the combination band at 3047 cm^{-1}. This matches well with another medium-strength experimental band found at 3043 cm^{-1}. This feature was previously assigned to the other B_2 fundamental; however, assignment to the combination band is also consistent with the symmetry. Of the methods compared, only VPT2+F predicts intense transitions in the vicinity of both experimental bands. It is plausible that the remaining B_2 fundamental was too weak to observe and/or obscured by other spectral features. VPT2 predicts that it occurs at 3079 cm^{-1} and that it is the least intense of all the fundamentals.

Several more transitions have been observed in this spectral region. For example, the first overtone of the symmetric C=C stretch was assigned as a weak feature at 2994 cm^{-1}. Since no resonances are associated with it, full VPT2 should provide a reasonable description. It places it at 2996 cm^{-1}. This agreement is as good as could be hoped for, considering the experimental uncertainty. In the remainder of this chapter, further example problems are discussed for several small molecules (ethylene, formaldehyde, and water). These systems exhibit more complicated resonance interactions.

3.8.2. Out-of-Phase Symmetric CH_2 Stretch of Ethylene

The anharmonic coupling in ethylene was the subject of a 1995 paper by J. M. L. Martin et al.[13] This was the same study that proposed the Martin Test for Fermi resonances. In their work, they discuss a resonance triad involving v_{11}, $v_2 + v_{12}$, and $2v_{10} + v_{12}$. These states are the out-of-phase symmetric CH_2 stretch fundamental, [C=C stretch + out-of-phase CH_2 scissor], and [2(in-phase CH_2 rock) + out-of-phase CH_2 scissor], respectively. The smallest effective Hamiltonian that can describe their interaction will be a 3x3. When more than two vibrational states are mutually coupled in an effective Hamiltonian, this is referred to as a resonance polyad.

Ethylene will be described using a CCSD(T)/cc-pVTZ force field, similar to that used by Martin. This semi-diagonal quartic force field contains only 60 unique cubic and 115 unique quartic force constants. This time, the procedure will begin with computation of the Martin Diagnostics for all two-state interactions (Table 3.3).

Table 3.3. Fermi resonances in ethylene. All quantities are given in wavenumbers. Resonances were identified with a 1 cm^{-1} threshold Martin Test, shown in the last column.

Resonance	Γ	Energy Separation	Cubic Force Constant	Variational - Perturbational
$\omega_{11} \approx \omega_2 + \omega_{12}$	B_{3u}	11.7	125.7	130.2
$\omega_2 \approx 2\omega_{10}$	B_{3u}	25.7	-53.0	1.2

Using a cut-off value of 1 cm^{-1}, two resonances are identified. These are the same resonances that give rise to the polyad discussed by Martin. It may not be immediately obvious why this is the case. The first resonance directly involves the CH stretch fundamental. In isolation, it could be treated by diagonalizing the 2x2 matrix of v_{11}^* and $(v_2 + v_{12})^*$. However the anharmonicity constants will have been deperturbed for the second resonance as well. This deperturbs $v_2 + v_{12}$ for an additional interaction: with $2v_{10} + v_{12}$. This state also must be included in the effective Hamiltonian in order for the VPT2+F treatment of the coupling to be complete.

To understand the origin of the 3-quanta state above, it may also be helpful to recall that, in VPT2, the vibrational energies of multiply-excited states can be expressed as a sum of energies of singly-excited states and certain anharmonicity constants. By deperturbing v_2 for its

interaction with $2v_{10}$, the analogous interaction between $v_2 + v_{12}$ and $2v_{10} + v_{12}$ is also deperturbed, or more generally all interactions between the states: $v_2 + v_n$ and $2v_{10} + v_n$. When multiple resonances are connected to each other in this way, the complexity of the effective Hamiltonian can increase significantly. This phenomenon of "connected" resonances is discussed further in Section 3.14. Now calculate the anharmonicity constants and deperturb for these two resonances. The effect of the $\omega_{11} \approx \omega_2 + \omega_{12}$ resonance is shown below.

$$\chi_{2,11} = \text{-}177.4 \rightarrow \chi^*_{2,11} = \text{-}8.2, \qquad \chi_{11,12} = \text{-}182.3 \rightarrow \chi^*_{11,12} = \text{-}13.1,$$

$$\chi_{2,12} = 166.1 \rightarrow \chi^*_{2,12} = \text{-}3.0$$

The effect of the $\omega_2 \approx 2\omega_{10}$ resonance is shown below.

$$\chi_{2,2} = 1.2 \rightarrow \chi^*_{2,2} = 4.6, \qquad \chi_{2,10} = 5.9 \rightarrow \chi^*_{2,10} = \text{-}7.8$$

Resonance treatment is shown below (Eqn. 3.53-3.55). This resonance polyad might be described as $v_2 + v_{12}$ simultaneously participating in a Fermi Type II interaction with v_{11} and a Fermi Type I interaction with $2v_{10} + v_{12}$. State mixing is extensive; although, the transition at 2978.4 cm^{-1} arguably remains pure enough to be called the CH stretch fundamental (Eqn. 3.55).

$$H_{eff} = \begin{pmatrix} v^*_{11} & \frac{1}{2\sqrt{2}}\phi_{2,11,12} & \approx 0 \\ \frac{1}{2\sqrt{2}}\phi_{2,11,12} & (v_2 + v_{12})^* & \frac{1}{4}\phi_{2,10,10} \\ \approx 0 & \frac{1}{4}\phi_{2,10,10} & (2v_{10} + v_{12})^* \end{pmatrix} \tag{3.53}$$

$$H_{eff} = \begin{pmatrix} 3001.8 & 44.4 & 0 \\ 44.4 & 3064.6 & -13.3 \\ 0 & -13.3 & 3085.4 \end{pmatrix} \tag{3.54}$$

$$\begin{bmatrix} & \mathbf{3098.5} & \mathbf{3074.9} & \mathbf{2978.4} \\ |v_{11}\rangle & 0.09 & 0.12 & 0.78 \\ |v_2 + v_{12}\rangle & 0.45 & 0.34 & 0.22 \\ |2v_{10} + v_{12}\rangle & 0.46 & 0.54 & 0.00 \end{bmatrix} \tag{3.55}$$

This spectral region has been measured with high resolution, in the gas phase. Bands having rotational structure consistent with a B_{3u} symmetry vibration have been observed at 2988.6, 3078.5, and 3104.3 cm^{-1}. This agreement is quite good. VPT2+F predicts all three transitions to within just about 10 cm^{-1}. This simulation can be taken a bit farther by populating the zero matrix elements of the effective Hamiltonian.

3.9. Darling-Dennison Resonance Constants

Consider the vibrational states v_{11} and $2v_{10} + v_{12}$. Their net difference in vibrational quanta is two. More specifically, when considering the normal coordinates separately, the number of quanta in q_{12} changes by ± 1, the number of quanta in q_{10} changes by ± 2, the number of quanta in q_{11} changes by ∓ 1, and the number of quanta in all other normal coordinates changes by 0. In order for a force constant to couple these states, it must contain an odd number of 11 and 12 indices, an even number (at least two) of q_{10} indices, and an even number (or zero) of other indices. Only one force constant in the anharmonic force field satisfies these criteria, the quartic constant, $\phi_{10,10,11,12}$, of the form ϕ_{rrst}.

In VPT2, these states do not interact, as all coupling between different vibrational states is through cubic terms in the potential. These can connect states differing by 1 and 3 net quanta only. States differing by an even number of net quanta (and zero net quanta) do not interact until VPT4, when off-diagonal quartic terms first enter into the expressions.

In the VPT2+F effective Hamiltonian, these states still do not directly interact; however, they interact indirectly through their mutual coupling to $v_2 + v_{12}$. The matrix element directly coupling these states has been approximated as zero. Since the force field contains some information about higher-order coupling that is not currently being taken advantage of, it may be desirable to introduce some of this coupling into the model. A simple solution would be to populate this matrix element with $\frac{1}{4\sqrt{2}}\phi_{10,10,11,12}$, where the numerical factor is the usual product

of the harmonic oscillator matrix elements, $\frac{1}{2\sqrt{2}}$, the Taylor series coefficient, $\frac{1}{24}$, and the degeneracy of the force constant, twelve.

A more rigorous approach is to use one of the Darling-Dennison resonance constants, K_{rstu}.[60-63] There are eight types of these. The leading term of each is a quartic force constant (multiplied by the Taylor series coefficient and its degeneracy factor). The remaining terms involve cubic force constants, Coriolis constants, and resonance denominators. These additional terms are derived from perturbation theory (hence the resonance denominators). Their inclusion incorporates more of the correlation effects from VPT4 and is thus more balanced than simply using the quartic force constant (i.e. the cubic and quartic contributions arise at the same order in perturbation theory).

In the ethylene situation, the 1:3 resonance constant, $K_{11;10,10,12}$, is appropriate. Its leading term is $\frac{1}{2}\phi_{10,10,11,12}$, the quartic force constant that couples these vibrational states (without the harmonic oscillator matrix element factor). Before this can be used, it needs to be deperturbed. To do this, search it for resonant terms and zero them out. It is reasonable to use the same diagnostic that is used to deperturb the anharmonicity constants. Resonance constants are kept deperturbed. There is no follow-up matrix-diagonalization step. This particular resonance constant takes the following form (Eqn. 3.56).

$$K_{r;sst} = \frac{1}{2}\phi_{rsst} - \frac{1}{4}\sum_u \phi_{rsu}\phi_{rst}\left(\frac{1}{\omega_r-\omega_s+\omega_u} + \frac{1}{-\omega_r+\omega_s+\omega_u} + \frac{1}{\omega_s+\omega_t+\omega_u} + \frac{1}{-\omega_s-\omega_t+\omega_u}\right) - \frac{1}{8}\sum_u \phi_{rtu}\phi_{ssu}\left(\frac{1}{\omega_r-\omega_t+\omega_u} + \frac{1}{-\omega_r+\omega_t+\omega_u} + \frac{1}{\omega_u+2\omega_s} + \frac{1}{\omega_u-2\omega_s}\right) + 2\left(A_e\zeta_{rs}^a\zeta_{st}^a + B_e\zeta_{rs}^b\zeta_{st}^b + C_e\zeta_{rs}^c\zeta_{st}^c\right)\frac{(\omega_r+\omega_s)(\omega_s-\omega_t)}{\omega_s\sqrt{\omega_r\omega_t}} \quad (3.56)$$

The $K_{r;sst}$ resonance constant connects vibrational states that differ by the annihilation of one quantum in one mode, the creation of one quantum in a different mode, and the creation of

two quanta in a third mode. The expressions for all of the resonance constants (and general formulas for all Darling-Dennison matrix elements) can be found in the 2014 paper by Rosnik & Polik.[60] The final matrix element will be the product of this resonance constant and the harmonic oscillator matrix elements. The improved effective Hamiltonian and resonance treatment are shown below (Eqn. 3.57-3.59).

$$H_{eff} = \begin{pmatrix} v_{11}^{*} & \frac{1}{2\sqrt{2}}\phi_{2,11,12} & \frac{1}{2\sqrt{2}}K_{11;10,10,12} \\ \frac{1}{2\sqrt{2}}\phi_{2,11,12} & (v_2 + v_{12})^{*} & \frac{1}{4}\phi_{2,10,10} \\ \frac{1}{2\sqrt{2}}K_{11;10,10,12} & \frac{1}{4}\phi_{2,10,10} & (2v_{10} + v_{12})^{*} \end{pmatrix} \tag{3.57}$$

$$H_{eff} = \begin{pmatrix} 3001.8 & 44.4 & -3.5 \\ 44.4 & 3064.6 & -13.3 \\ -3.5 & -13.3 & 3085.4 \end{pmatrix} \tag{3.58}$$

$$\begin{bmatrix} & \mathbf{3100.0} & \mathbf{3073.1} & \mathbf{2978.7} \\ |v_{11}\rangle & 0.10 & 0.11 & 0.79 \\ |v_2 + v_{12}\rangle & 0.44 & 0.35 & 0.21 \\ |2v_{10} + v_{12}\rangle & 0.46 & 0.54 & 0.00 \end{bmatrix} \tag{3.59}$$

The result does not appear to be worth the extra effort. The highest frequency transition now agrees a bit better, the middle transition agrees a bit worse, and the lowest frequency transition is almost unchanged. Approximating this matrix element as 0 was fine, in this situation. The simulation can now be called VPT2+K.[60] It is differentiated from VPT2+F in that its effective Hamiltonians contain not only the standard Fermi-type matrix elements composed of cubic force constants but also Darling-Dennison matrix elements with leading quartic force constants. It provides one of the best and most affordable descriptions of anharmonic coupling possible with a quartic expansion of the potential.

3.10. Antisymmetric CH_2 Stretch of Formaldehyde

The anharmonic coupling in formaldehyde is well-understood.[22] It is accepted that the antisymmetric CH_2 stretch, v_5, is involved in resonance triad with two combination states:

$v_2 + v_6$ and $v_3 + v_6$. These are [C=O stretch + CH_2 wag] and [CH_2 scissor + CH_2 wag], respectively. As with ethylene, this interaction will require at least a 3x3 effective Hamiltonian for a proper description. It will be described with a CCSD(T)/ANO2 force field, containing 22 unique cubic and 45 unique quartic force constants. Begin with the Martin Test (Table 3.4).

Table 3.4. Fermi resonances in formaldehyde. All quantities are given in wavenumbers. Resonances were identified with a 1 cm^{-1} threshold Martin Test, shown in the last column.

Resonance	Γ	Energy Separation	Cubic Force Constant	Variational - Perturbational
$\omega_5 \approx \omega_2 + \omega_6$	B_2	37.8	-146.7	34.8
$\omega_5 \approx \omega_3 + \omega_6$	B_2	202.9	185.8	1.9

With a cut-off value of 1 cm^{-1}, the two resonances identified are precisely the same ones discussed in the literature. Calculate the anharmonicity constants and deperturb for these two resonances. Notice that both resonances necessitate removal of terms from $\chi_{5,6}$. The effect of the $\omega_5 \approx \omega_2 + \omega_6$ resonance on the constants is given below.

$$\chi_{2,6} = 64.2 \rightarrow \chi^*_{2,6} = \text{-}6.8, \qquad \chi_{2,5} = \text{-}72.2 \rightarrow \chi^*_{2,5} = \text{-}1.1, \qquad \chi_{5,6} = \text{-}80.2 \rightarrow \chi^*_{5,6} = \text{-}9.1$$

The effect of the $\omega_5 \approx \omega_3 + \omega_6$ resonance on the constants is given below.

$$\chi_{3,6} = \text{-}19.4 \rightarrow \chi^*_{3,6} = 1.9, \qquad \chi_{3,5} = \text{-}12.8 \rightarrow \chi^*_{3,5} = \text{-}34.0, \qquad \chi_{5,6} = \text{-}80.2 \rightarrow \chi^*_{5,6} = \text{-}101.5$$

And the net effect of both resonances on the $\chi_{5,6}$ constant is shown below.

$$\chi_{5,6} = \text{-}80.2 \rightarrow \chi^*_{5,6} = \text{-}30.4$$

The structure of this effective Hamiltonian is analogous to the B_2 example from cyclopentadiene. Here, the singly-excited vibrational state directly interacts with two doubly-excited states via matrix elements containing cubic force constants. This VPT2+F simulation gives very good agreement with experiment (Eqn. 3.60-3.62). The stretch fundamental is observed at 2843 cm^{-1}, and the two combination bands are observed at 3000 and 2719 cm^{-1}. Filling in the 0's of this effective Hamiltonian will be somewhat more involved than in the previous example.

$$H_{eff} = \begin{pmatrix} v_5^* & \frac{1}{2\sqrt{2}}\phi_{2,5,6} & \frac{1}{2\sqrt{2}}\phi_{3,5,6} \\ \frac{1}{2\sqrt{2}}\phi_{2,5,6} & (v_2+v_6)^* & \approx 0 \\ \frac{1}{2\sqrt{2}}\phi_{3,5,6} & \approx 0 & (v_3+v_6)^* \end{pmatrix} \tag{3.60}$$

$$H_{eff} = \begin{pmatrix} 2828.0 & -51.8 & 65.7 \\ -51.8 & 2987.4 & 0 \\ 65.7 & 0 & 2751.9 \end{pmatrix} \tag{3.61}$$

$$\begin{bmatrix} & \mathbf{3004.3} & \mathbf{2851.5} & \mathbf{2711.5} \\ |v_5\rangle & 0.10 & 0.63 & 0.27 \\ |v_2+v_6\rangle & 0.90 & 0.09 & 0.01 \\ |v_3+v_6\rangle & 0.01 & 0.28 & 0.72 \end{bmatrix} \tag{3.62}$$

3.11. Derivation of a Darling-Dennison Matrix Element

Consider the doubly-excited vibrational states $v_2 + v_6$ and $v_3 + v_6$. Their net difference in quanta is zero. More specifically, when considering the normal coordinates separately, the number of quanta in q_2 changes by ± 1, the number of quanta in q_3 changes by ∓ 1, and the number of quanta in q_6 (and all other normal coordinates) changes by 0. Force constants capable of coupling these states will contain an odd number of 2 and 3 indices and an even number (or zero) of all other indices.

In contrast to the 1:3 resonance example in ethylene, there are now multiple quartic force constants that can couple these states. Every constant of the form $\phi_{2,n,3,n}$ can contribute to this

matrix element. This matrix element will be a sum of 3N-6 resonance constants. It will be simpler to evaluate the harmonic oscillator matrix element "q-factors" separately for each resonance constant that appears. It is important to be aware that, in force constants, the order of the indices does not matter. For resonance constants, the order of the indices (i.e. which side of the semi-colon they appear on) does matter. Four possible cases are shown below.

$n = 2$:	Resonance constant: $K_{3,2;2,2}$	q-factor: $\frac{3}{4}$
$n = 3$:	Resonance constant: $K_{2,3;3,3}$	q-factor: $\frac{3}{4}$
$n = 6$:	Resonance constant: $K_{2,6;3,6}$	q-factor: $\frac{3}{4}$
$n \neq \{2,3,6\}$:	Resonance constant: $K_{2,n;3,n}$	q-factor: $\frac{1}{4}$

The final matrix element is defined with all numerical factors absorbed into it.

$$D_{2,6;3,6} = \frac{3}{4}K_{2,3;3,3} + \frac{3}{4}K_{3,2;2,2} + \frac{3}{4}K_{2,6;3,6} + \frac{1}{4}\sum_{n\neq\{2,3,6\}} K_{2,n;3,n} \tag{3.63}$$

The first two terms in Eqn. 3.63 are instances of the $K_{rs;ss}$ resonance constant; whereas, the third term and the summation use $K_{rt;st}$ constants. This matrix element is similar to the matrix element for resonance between singly-excited states; the extra excitation in q_6 simply leads to a higher weight for the $K_{2,6;3,6}$ resonance constant. There is no generally accepted notation for these matrix elements; here they will be denoted by *D*, for Darling-Dennison. Since formaldehyde is small, the fully expanded matrix element is shown (Eqn. 3.64).

$$D_{2,6;3,6} = \frac{1}{4}K_{2,1;3,1} + \frac{3}{4}K_{3,2;2,2} + \frac{3}{4}K_{2,3;3,3} + \frac{1}{4}K_{2,4;3,4} + \frac{1}{4}K_{2,5;3,5} + \frac{3}{4}K_{2,6;3,6} \tag{3.64}$$

$$D_{2,6;3,6} = \frac{1}{4}(32.9) + \frac{3}{4}(-7.4) + \frac{3}{4}(-3.7) + \frac{1}{4}(-3.1) + \frac{1}{4}(36.9) + \frac{3}{4}(-7.9)$$

$$\boxed{D_{2,6;3,6} = 2.5 \text{ cm}^{-1}}$$

The VPT2+K effective Hamiltonian and resonance treatment are shown below (Eqn. 3.65-3.67). Including the Darling-Dennison matrix element changes almost nothing. It is desirable to now discuss an example where higher-order effects are important (Section 3.12).

$$H_{eff} = \begin{pmatrix} v_5^* & \frac{1}{2\sqrt{2}}\phi_{2,5,6} & \frac{1}{2\sqrt{2}}\phi_{3,5,6} \\ \frac{1}{2\sqrt{2}}\phi_{2,5,6} & (v_2 + v_6)^* & D_{2,6;3,6} \\ \frac{1}{2\sqrt{2}}\phi_{3,5,6} & D_{2,6;3,6} & (v_3 + v_6)^* \end{pmatrix} \tag{3.65}$$

$$H_{eff} = \begin{pmatrix} 2828.0 & -51.8 & 65.7 \\ -51.8 & 2987.4 & 2.5 \\ 65.7 & 2.5 & 2751.9 \end{pmatrix} \tag{3.66}$$

$$\begin{bmatrix} & \mathbf{3003.9} & \mathbf{2852.3} & \mathbf{2711.1} \\ |v_5\rangle & 0.09 & 0.63 & 0.27 \\ |v_2 + v_6\rangle & 0.90 & 0.09 & 0.01 \\ |v_3 + v_6\rangle & 0.00 & 0.28 & 0.72 \end{bmatrix} \tag{3.67}$$

3.12. Doubly and Triply Excited Stretching Levels of Water

This example is borrowed from Matthews, Vazquez, and Stanton.[7] A CCSD(T)/ANO1 quartic force field is used, identical to theirs. Because water has fewer than four vibrational degrees of freedom, note that a semi-diagonal quartic force field is identical to a full quartic force field. It contains 6 unique cubic and 9 unique quartic force constants. In accordance with the spectroscopic convention, the symmetric stretch will be referred to as v_1, and the antisymmetric stretch will be called v_3.

Begin by computing the Martin diagnostics. Nothing is flagged with a cut-off value of 1 cm^{-1}. If the threshold is loosened to 0.5 cm^{-1}, the symmetric stretch and the bend overtone show up as a resonance. However, an effective Hamiltonian treatment of this interaction will not be necessary. Indeed, if this "resonance" were to be treated, the fundamental would remain 97% pure. The discussion will proceed without any Fermi resonances. Calculate the anharmonicity constants. Contrary to the Fermi resonances encountered earlier, the Darling-Dennison

resonances important in this system do not lead to near-zero denominators in the anharmonicity constants. There is nothing that needs to be deperturbed.

The doubly excited stretching levels are well-separated in energy from all triply-excited levels. On the basis of their energy differences, it will be a good approximation to separate excited stretching levels into polyads by their net excitation level. Accordingly, the first effective Hamiltonian will contain $2v_1$, $v_1 + v_3$, and $2v_3$. Symmetry makes this problem rather easy. Only the matrix element connecting the two A_1 states can be non-zero. This matrix element uses the $K_{rr;ss}$ resonance constant because these states are connected by the annihilation of 2 quanta in one mode and the creation of 2 quanta in a different mode.

Resonance treatment is shown below (Eqn. 3.68-3.70). To understand the effect of treating the Darling-Dennison resonance, the VPT2+K eigenvalues can be directly compared to the diagonal values (which correspond to the full VPT2 prediction). The Darling-Dennison interaction causes the first overtones to repel each other by 30 cm^{-1}. This pushes them into excellent agreement with the experimental values of 7202 and 7445 cm^{-1}. The uncoupled B_2 combination also matches experiment (7251 cm^{-1}).

$$H_{eff} = \begin{pmatrix} 2v_1 & 0 & \frac{1}{2}K_{1,1;3,3} \\ 0 & v_1 + v_3 & 0 \\ \frac{1}{2}K_{1,1;3,3} & 0 & 2v_3 \end{pmatrix} \tag{3.68}$$

$$H_{eff} = \begin{pmatrix} 7233.6 & 0 & -80.4 \\ 0 & 7250.5 & 0 \\ -80.4 & 0 & 7416.1 \end{pmatrix} \tag{3.69}$$

$$\begin{bmatrix} & \mathbf{7446.4} & \mathbf{7250.5} & \mathbf{7203.2} \\ |2v_1\rangle & 0.12 & 0 & 0.88 \\ |v_1 + v_3\rangle & 0 & 1.00 & 0 \\ |2v_3\rangle & 0.88 & 0 & 0.12 \end{bmatrix} \tag{3.70}$$

Resonance treatment for the v = 3 polyad is detailed below (Eqn. 3.71-3.73). Again, symmetry helps here. This problem can be block-diagonalized into one 2x2 block of each

symmetry type (A_1 and B_2). Notice that these matrix elements involve the very same resonance constant from the v = 2 polyad, as the coupled states still differ by creation/annihilation of 2 quanta in two modes. However, the harmonic oscillator integral factors are larger as a consequence of the greater excitation.

$$H_{eff} = \begin{pmatrix} 3v_1 & 0 & \frac{3}{2\sqrt{3}}K_{1,1;3,3} & 0 \\ 0 & 2v_1 + v_3 & 0 & \frac{3}{2\sqrt{3}}K_{1,1;3,3} \\ \frac{3}{2\sqrt{3}}K_{1,1;3,3} & 0 & v_1 + 2v_3 & 0 \\ 0 & \frac{3}{2\sqrt{3}}K_{1,1;3,3} & 0 & 3v_3 \end{pmatrix} \tag{3.71}$$

$$H_{eff} = \begin{pmatrix} 10722.2 & 0 & -139.3 & 0 \\ 0 & 10658.6 & 0 & -139.3 \\ -139.3 & 0 & 10743.6 & 0 \\ 0 & -139.3 & 0 & 10977.2 \end{pmatrix} \tag{3.72}$$

$$\begin{bmatrix} & \mathbf{11029.6} & \mathbf{10872.6} & \mathbf{10606.3} & \mathbf{10593.2} \\ |3v_1\rangle & 0 & 0.46 & 0 & 0.54 \\ |2v_1 + v_3\rangle & 0.12 & 0 & 0.88 & 0 \\ |v_1 + 2v_3\rangle & 0 & 0.51 & 0 & 0.46 \\ |3v_3\rangle & 0.88 & 0 & 0.12 & 0 \end{bmatrix} \tag{3.73}$$

The B_2 states mix modestly with each other and are corrected by 52 cm^{-1}. However, the uncoupled A_1 states were much closer to each other, so they receive corrections of 129 cm^{-1} and mix thoroughly. The B_2 transitions have been observed at 10,613 and 11,032 cm^{-1}, and A_1 transitions have been identified at 10,600 and 10,869 cm^{-1}. The agreement is less good, but VPT2+K is still capable of predicting these transitions to within 10 cm^{-1}.

By v = 3, it is clear that unacceptable error is introduced by neglecting the Darling-Dennison interaction. And as the excitation level increases, both the density of states and the magnitude of the Darling-Dennison matrix elements increase. With increasing energy and excitation, all simulations based upon VPT2 will eventually break down; however, VPT2+K remains useful for longer.

3.13. A Simpler Procedure for Deperturbation

For systems that involve many resonances, the standard deperturbation procedure entails many manipulations to the anharmonicity constants and becomes cumbersome and error-prone. There is a much more straightforward alternative to deperturbing the anharmonicity constants. It requires is that VPT2 be understood in both its sum-over-states formulation and in its anharmonicity constant based formulation. First, the structure of the effective Hamiltonian matrices must be deduced from the list of defined Fermi resonances. Then, the fully perturbed diagonal elements are evaluated with the anharmonicity constant based expression, as this is much faster than performing the sum-over-states. Now, the diagonal elements themselves can simply be adjusted by subtracting the SoS VPT2 correction (Eqn. 3.74) for their interaction with all other states, c, involved in the effective Hamiltonian.

$$\sum_{c \neq a} \frac{|\langle a|\hat{H}_1|c\rangle|^2}{\epsilon_a - \epsilon_c} \tag{3.74}$$

Now it is not necessary to even use the term “deperturb.” It is also appealing that every interaction takes the same form, as opposed to applying tailored corrections for Type I and Type II Fermi resonances to different numbers of anharmonicity constants as is done in the standard procedure. Another advantage of this approach is that it allows for easier modification of the list of resonances and the effective Hamiltonians. One might consider this approach to prioritize solution of the reduced dimensional coupling problem(s) over all else. As a takeaway message, it is often useful to consider the sensitivity of anharmonic predictions to the choice of resonances and to the extent of effective Hamiltonian treatment. The resonance treatment should be understood as an additional source of uncertainty when critically evaluating VPT predictions.

3.14. Systems of Interacting Resonances

The purpose of this section is to further discuss the relationships between Fermi resonances and to illustrate a few more complicated resonance situations. It is useful to consider

the structure of effective Hamiltonian matrices that are implied by certain definitions of resonances. As was seen in the various examples above, when several Fermi resonances are active in a system, and these resonances involve some of the same normal coordinates, complicated resonance polyads may result. We might say that the resonances are "connected" to each other through their shared normal coordinates. The ethylene example illustrates a "vertical" connected resonance: necessitating an effective Hamiltonian that couples a 1-quantum state to a 2-quanta state to a 3-quanta state. In contrast, the formaldehyde example shows a "horizontal" connected resonance: implying an effective Hamiltonian treatment of a 1-quantum state coupled to two different 2-quanta states. These cases can be combined and/or extended to include several different tiers of coupling. For example, consider the following case of a two-level vertical resonance system, having the following active Fermi resonances.

$$\omega_a \approx 2\omega_b \quad \text{and} \quad \omega_b \approx 2\omega_c$$

In complicated situations such as the above, it is most useful to think about the list of resonances as a list of replacement rules. Iterate through the states in the effective Hamiltonian, replacing indices with resonant indices to generate new states, until all possible resonant states are present. An effective Hamiltonian that simultaneously couples all of these states will provide a theoretically "complete" treatment of the resonance system. Equations 3.75 and 3.76 show how predictions for various states might be made, in the presence of this resonance system. Treatment of vertical resonances demands the coupling of states with successively higher levels of excitation. Discussion of the treatment of complicated resonance polyads is scarce in the literature; however, an example can be found in the supporting information of Reference 59.

$$H_{eff} = \begin{pmatrix} v_b^* & \frac{1}{4}\phi_{bcc} \\ \frac{1}{4}\phi_{bcc} & 2v_c^* \end{pmatrix} \tag{3.75}$$

$$H_{eff} = \begin{pmatrix} v_a^* & \frac{1}{4}\phi_{abb} & \frac{1}{2\sqrt{2}}K_{a;bcc} & 0 \\ \frac{1}{4}\phi_{abb} & 2v_b^* & \frac{1}{2\sqrt{2}}\phi_{bcc} & 0 \\ \frac{1}{2\sqrt{2}}K_{a;bcc} & \frac{1}{2\sqrt{2}}\phi_{bcc} & (v_b + 2v_c)^* & \frac{\sqrt{3}}{2\sqrt{2}}\phi_{bcc} \\ 0 & 0 & \frac{\sqrt{3}}{2\sqrt{2}}\phi_{bcc} & 4v_c^* \end{pmatrix} \tag{3.76}$$

In some automated implementations of variationally-corrected VPT2, the couplings to excited states of three-quanta and greater are not treated in a variational framework; rather, the two-quantum states are left partially deperturbed.[25] While it is more appealing to treat the couplings, it is doubtful that very high levels of excitation (e.g. couplings with 6-quantum states and higher) will lead to higher accuracy predictions, as the description of increasingly higher excited states, based merely upon a quartic expansion of the potential, becomes increasingly poor. Sometimes it may be wise to truncate the list of resonances in order to prevent the effective Hamiltonian from becoming too large. Complicated resonance treatments should not always be avoided; however, they should be taken with a grain of salt. If a system is subjected to various reasonable resonance treatments, and a particular transition frequency shows high sensitivity, then that prediction should be taken to be less certain.

Finally, it is an interesting fact that certain systems of resonances are impossible to treat in a complete and satisfying manner. Consider below the case of the cyclic resonance.

$$\omega_a \approx \omega_b + \omega_c, \qquad \omega_b \approx \omega_a + \omega_c, \qquad \omega_c \approx \omega_a + \omega_b$$

Attempting to build an effective Hamiltonian to treat this system of resonances leads to an infinite number of substitutions and inclusion of states that are infinitely excited. There are few, if any, real systems where a cyclic resonance would be a reasonable model of the anharmonic coupling. However, the Martin Test has a tendency to identify cyclic resonances in systems with low frequency modes (e.g. alkyl radicals). By combining the Martin Test with an energy window test, as done in Chapter 8, cyclic resonances are effectively eliminated.[64]

3.15. Large Effective Hamiltonian Simulations

3.15.1. Description

This section discusses a philosophy and standard procedure for predicting the CH stretching (~ 2700-3150 cm^{-1}) spectra of hydrocarbons, which employs VPT2+K with large effective Hamiltonians. This is a particularly robust and accurate approach for small alkenes, where it allows for excellent quality intensity predictions, even when using harmonic oscillator transition moments. An application to isoprene is made in Section 3.15.2. Variations of this approach are applied in Chapters 4, 5 and 6 and in several additional manuscripts.[65-67]

The use of large VPT2+K effective Hamiltonians was inspired by work in the Sibert group[68] on modeling CH stretch Fermi coupling with local mode models (Chapter 4). The most significant anharmonic interactions involving CH stretch fundamentals are assumed to be their couplings with doubly-excited HCH bending states (sometimes called scissors). The most basic local-mode model of Sibert and coworkers, referred to as the "simple model," will be the subject of all further discussion of local mode models.[68] In this model, a methyl group contributes three scissor coordinates, a methylene group (either bridging or terminal radical) contributes one scissor coordinate, and other functional groups do not contribute. From the pool of X scissoring coordinates generated, all possible doubly-excited scissoring states are generated, totaling (1/2)X(X+1) states, where X states are overtones, and the remainder are combinations. These are mutually coupled together and with the CH stretch fundamentals in an effective Hamiltonian.

When this large effective Hamiltonian treatment of anharmonic coupling is adapted for VPT2+K in normal coordinates, the resulting model is more flexible; however, it produces more complicated effective Hamiltonians. The increased flexibility is a consequence of its *ab initio* nature, contrasting with the semi-empirical local-mode model. This allows for couplings to other kinds of coordinates to be treated straightforwardly without requiring parameterization. For

instance, coupling to [HCH scissor + C=C stretch] states proves to be quite important in alkenes (Section 3.15.2 and Chapter 5), and it can be accounted for by simply expanding the pool of coordinates to include the C=C stretch.[66] The option to include Darling-Dennison coupling also increases the model's flexibility; however, the significance of these couplings in the CH stretching region is generally minor (Chapter 4). More complicated effective Hamiltonians often arise due to the explicit consideration of Fermi resonances other than those between CH stretches and HCH bends. As described in Section 3.14, connected Fermi resonances necessitate the consideration of additional coordinates and the explicit coupling of multiply-excited states.

3.15.2. Application to *trans*-Isoprene

A final example is presented in this section. A comparison is made between VPT2 simulations of the CH stretching region of isoprene with varying extents of effective Hamiltonian resonance treatment. In order to make this comparison as fair as possible, VPT2-quality transition moments are used in all simulations (except the last) for 1- and 2-quanta transitions. This entails that the intensities of all "resonant" transitions are obtained from diagonalized-projected DVPT2 transition moments, [22] and "non-resonant" transition intensities are obtained directly from VPT2 transition moments. A CCSD(T)/ANO[1,0] semi-diagonal quartic force field is used, with the substituted hybrid scheme. Dipole derivatives are determined at the CCSD(T)/ANO0 level of theory. Small amounts of *gauche*-isoprene are present in the experimental HENDI spectrum, but no attempt is made here to account for its absorptions. Transitions of *gauche*-isoprene are identified in three regions of the spectrum and are indicated with arrows. From left to right, the arrows designate: i) The small peak with low S/N. ii) Either the weaker, sharper peak or the red shoulder on the stronger peak. iii) Both the weak peak and the blue shoulder on the strong peak. See Chapter 5 for a more detailed treatment of the conformers, including assignments, magnified spectral regions, and VPT2+K predictions for *gauche*-isoprene.

To start, it is desirable to show a simulation that is representative of the minimalist treatment of anharmonic resonances that prevails in the literature. In order to do this, a more primitive resonance diagnostic is used for Fermi resonances. The zeroth-order states are considered to be in resonance if two conditions are met: i) They are separated in energy by less than fifty wavenumbers. ii) The cubic force constant that couples them has a magnitude of greater than fifty wavenumbers. This diagnostic identifies three Fermi resonances; five vibrational states receive effective Hamiltonian treatment. Below, the corresponding VPT2+F simulation is compared to an experimental spectrum (Fig. 3.3).

This simulation fails to capture the spectral complexity—especially in the regions centered around 2900 and 3050 cm^{-1}. These regions are predicted to have single, strong transitions; however, the experiment contains many weaker transitions instead. The two strong, high frequency features correspond to the antisymmetric CH_2 stretches, and these are predicted accurately. Also, the strong experimental transition at 2958 cm^{-1} corresponds to the strong theoretical prediction at 2950 cm^{-1}. This is the sole fundamental of *a″* symmetry and does not participate in extensive resonances. A detailed discussion of spectral assignments is available in Section 5.4.4. The remaining discussion in this section will evaluate how well VPT2 models the spectral patterns, with only little regard for what the underlying transitions are assigned to.

It is reasonable to think that a better description might be achieved by using the Martin Test to identify the Fermi resonances (*vide supra*). With the standard 1cm^{-1} threshold, a total of 17 resonances are identified, which are relevant to the CH stretching region. An effective Hamiltonian treatment of these resonances involves the coupling of 20 vibrational states. A comparison between a VPT2+F simulation based on this list of resonances and the previous VPT2+F simulation is given below (Fig. 3.4). The simulation changes dramatically for the better. The 3050 cm^{-1} region is now well-populated by weak transitions; these generally agree well with

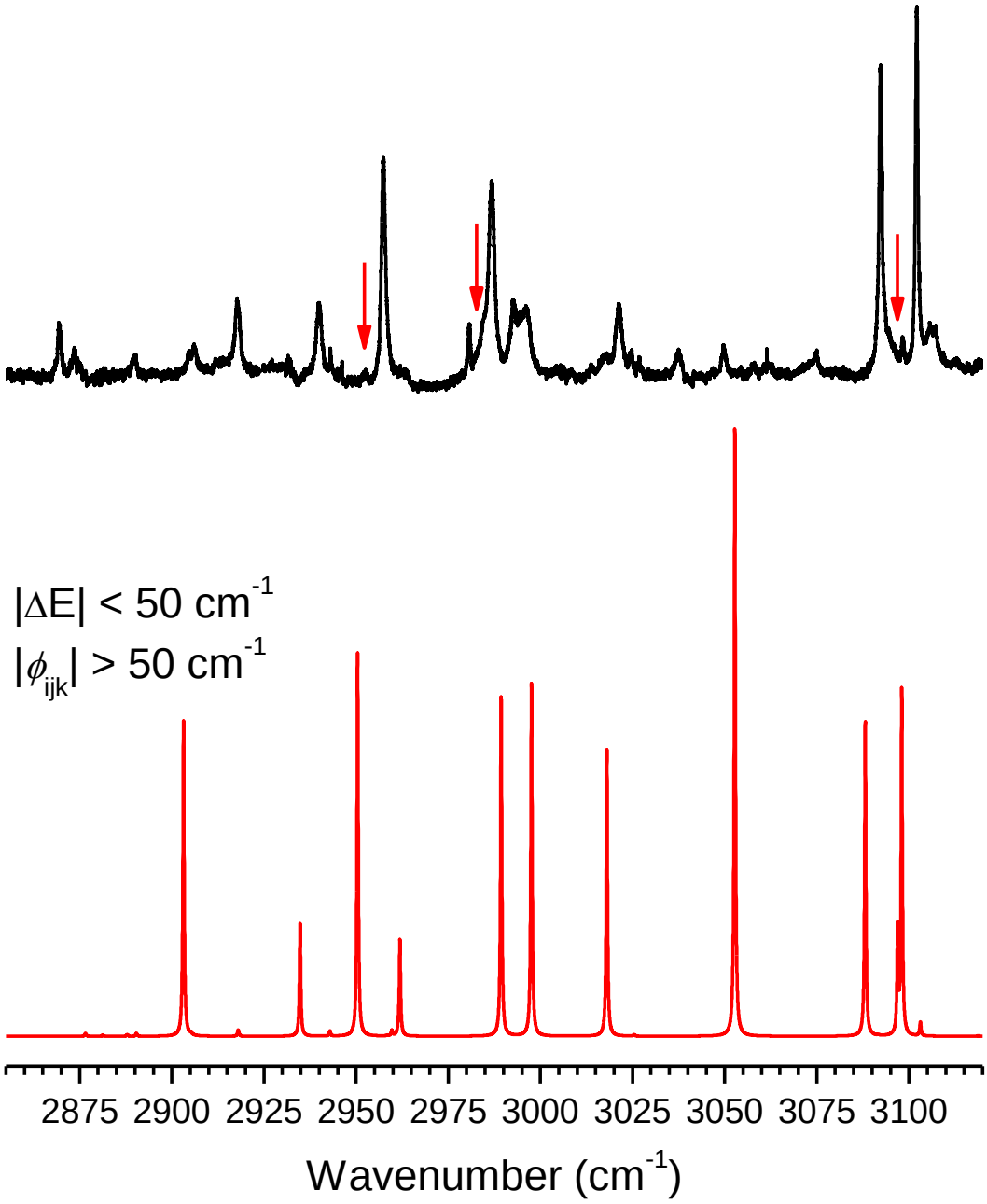

Figure 3.3. Infrared spectrum of isoprene compared to a VPT2+F simulation based on individual energy difference and force constant magnitude tests.

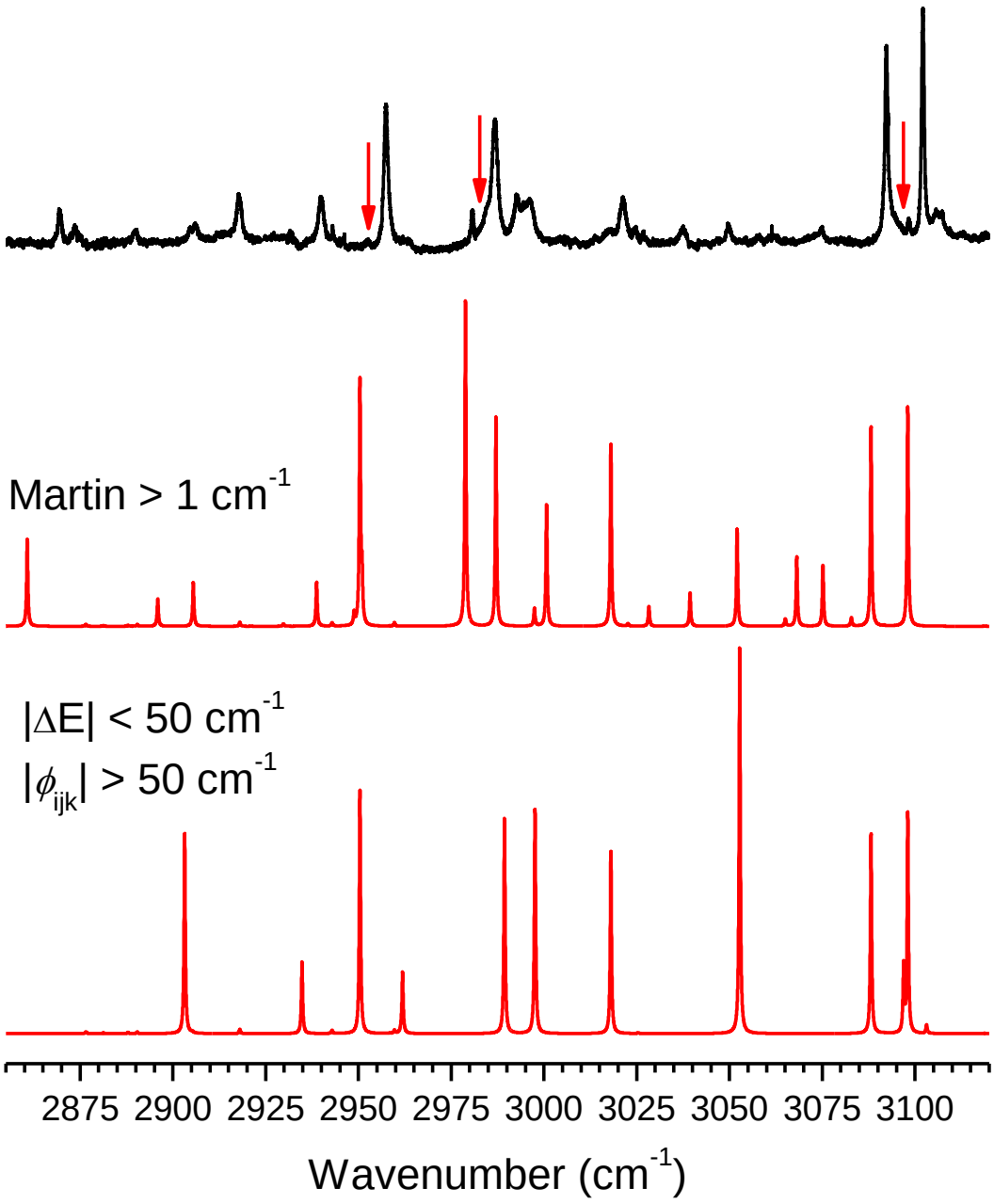

Figure 3.4. Infrared spectrum of isoprene compared to VPT2+F simulations based on individual energy difference and force constant magnitude tests and the Martin Test.

experiment. Similar changes are observed in the 2900 cm^{-1} region; although, the agreement is less good. Lastly, the spectral patterns also change on both sides of the spectral valley at 2970 cm^{-1}.

Next, the large effective Hamiltonian model is applied, combined with the 1 cm^{-1} Martin Test to identify connected resonances. In this mode, the effective Hamiltonian mutually couples 8 one-quantum states, 45 two-quanta states, 60 three-quanta states, and 20 four-quanta states, for a total of 133 vibrational states. It is compared to the previous Martin Test only simulation (Fig. 3.5). The features from 2970-3030 cm^{-1} are much better described with the larger Hamiltonian. Moreover, inspection of the effective Hamiltonian eigenvectors suggests that these features are highly anharmonic, involving complicated mixtures of four of the zeroth-order CH stretches. The mixing of the CH stretches is achievable entirely through indirect coupling, as the 1:1 Darling-Dennison matrix elements have not yet been included. The lone fundamental of *a''* symmetry now agrees better with experiment. The low frequency region is also improved; roughly the correct number of intense transitions are now predicted in this region. This comparison is somewhat qualitative, of course, as the low-frequency experimental transitions are weak and difficult to identify. Also note the large effective Hamiltonian model predicts the doublet feature centered around 2870 cm^{-1}; whereas, the Martin Test simulation predicts only a single, strong transition.

Darling-Dennison couplings are then introduced into the large effective Hamiltonian, upgrading VPT2+F to VPT2+K. It is compared with the previous simulation in Figure 3.6. Only the frequency predictions of the 3020 cm^{-1} feature prove sensitive to the inclusion of Darling-Dennison coupling. This feature arises from several partially overlapping transitions. Because of the variable broadening in the experimental spectrum, it is difficult to judge which of the two simulations is more accurate here. The relative intensities of the two predicted transitions around 2980 cm^{-1} also switch. This is a result of the coupling between two close-lying states being slightly adjusted by small Darling-Dennison terms. Intensity predictions are often sensitive in regions where the density of vibrational states is high.

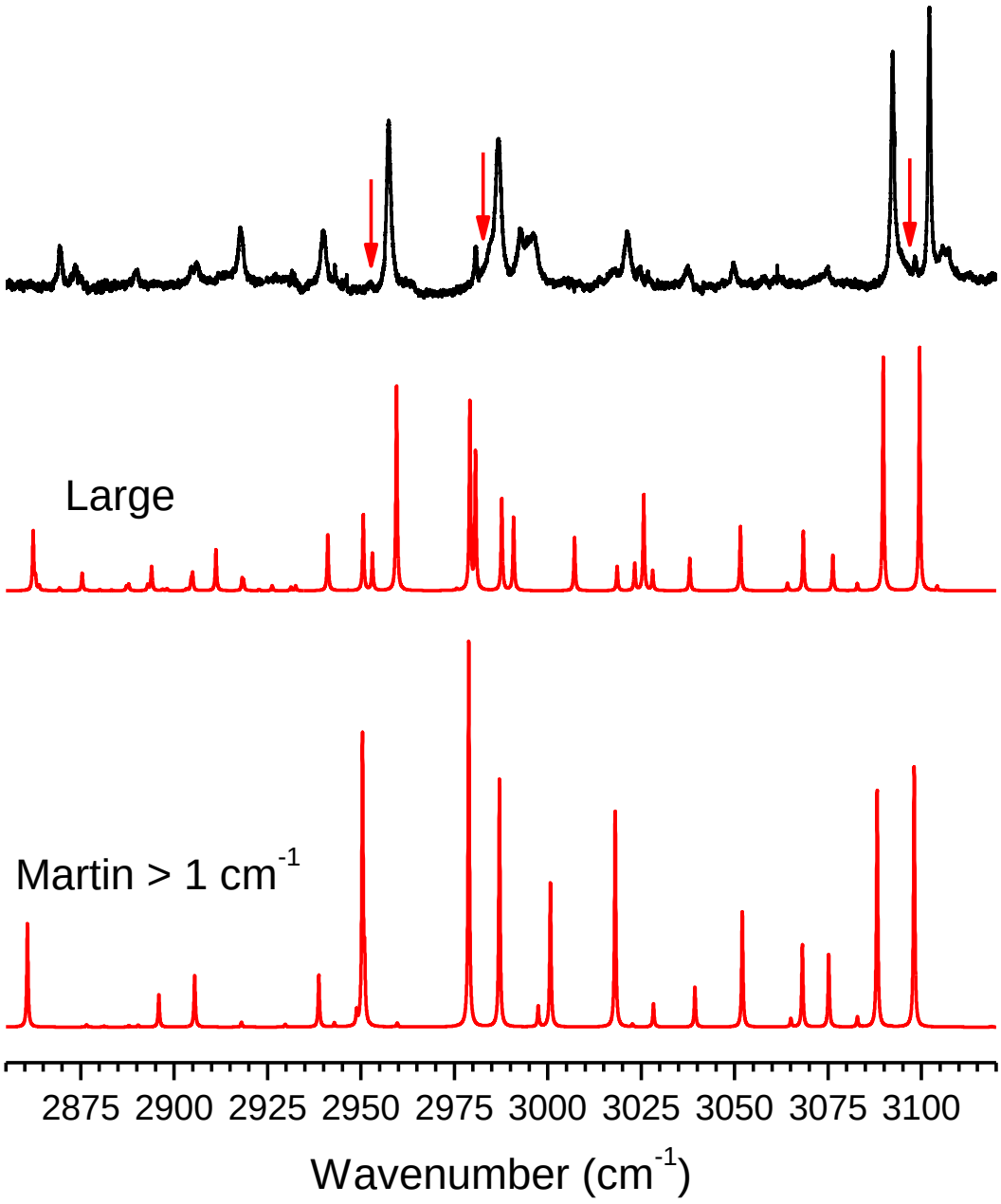

Figure 3.5. Infrared spectrum of isoprene compared to VPT2+F simulations based on the Martin Test and the large effective Hamiltonian model.

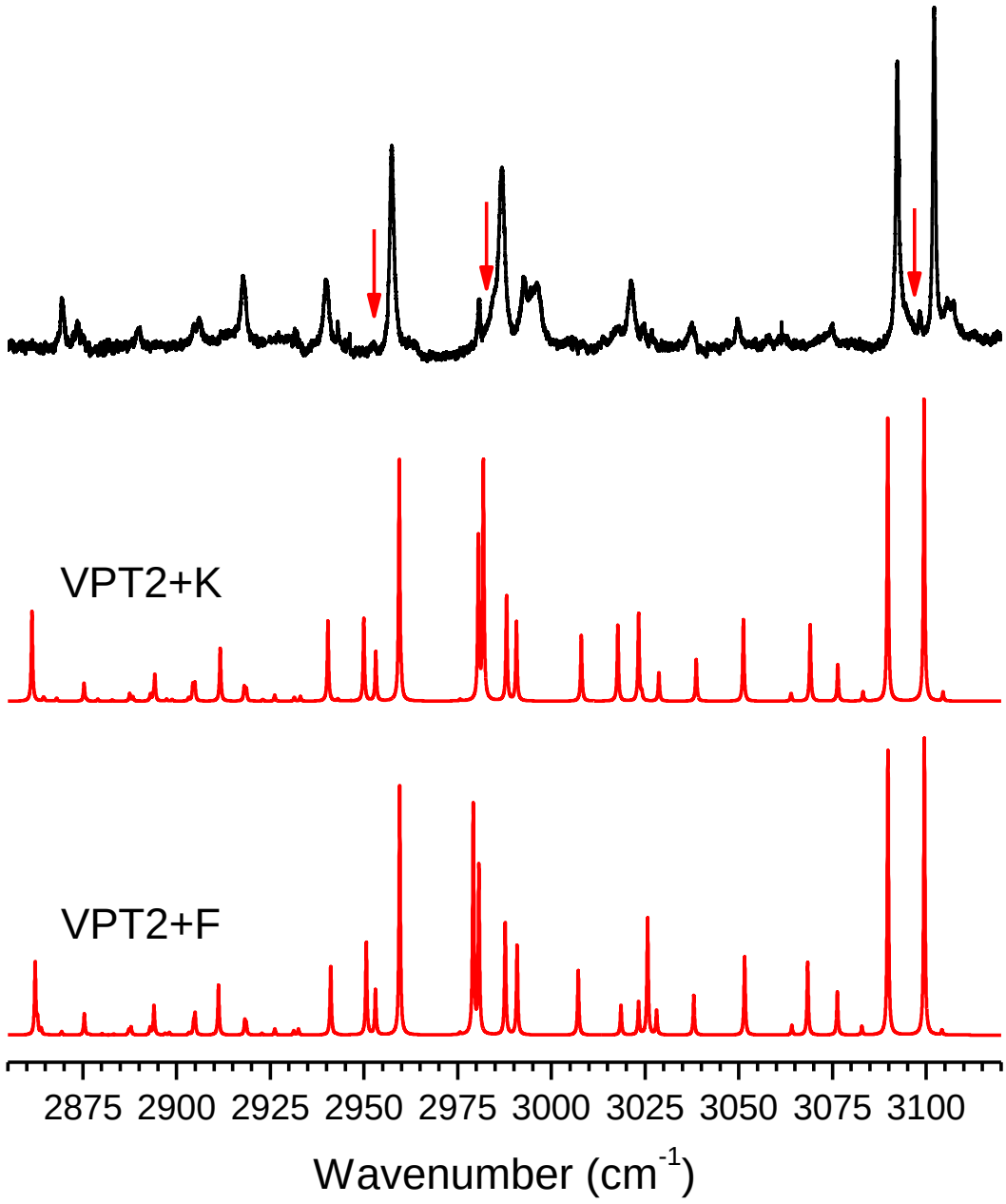

Figure 3.6. Infrared spectrum of isoprene compared to large effective Hamiltonian VPT2+F and VPT2+K simulations.

Clearly, the VPT2 simulations for isoprene, based on large effective Hamiltonians, are far superior to those that opt to treat only the most severe Fermi resonances. Specifically, large effective Hamiltonian VPT2 simulations provide much more accurate intensity predictions than standard VPT2, even when the intensities are determined from VPT2 transition moments. It is interesting to compare the current "best" large effective Hamiltonian VPT2+K simulation to a simulation in which the intensity is derived from only linear harmonic oscillator transition moments. This comparison is provided in Figure 3.7. A qualitative comparison of the two simulations reveals that the VPT2 transition moments are indeed better, except perhaps for the two transitions predicted around 3060 cm^{-1}, where harmonic intensity provides a closer match to experiment. However, the intensity predictions are not sufficiently better with VPT2 transition moments such that it changes the interpretation of the spectrum (i.e. the assignments of the experimental bands). The far simpler harmonic intensity is arguably "good enough" for the purposes of assigning the HENDI spectrum. Considering that VPT2 transition moments are highly resonance-prone, this can make them difficult to trust. This is especially true for larger molecular systems with high densities of states. Although it is possible to eliminate resonance denominators from VPT2 transition moments with carefully chosen numerical thresholds, harmonic intensity is appealing for its simplicity. The use of harmonic oscillator transition moments combined with large effective Hamiltonians is thus generally recommended for the prediction of CH stretches. VPT2 transition moments are recommended if very high accuracy is desired.

Similar to VPT2 transition moments, the inclusion of Darling-Dennison couplings in the CH stretching region may also be considered optional. The expressions for the Darling-Dennison resonance constants are algebraically complicated and require deperturbation; although, they are all simpler in both respects than the 1- and 3-quanta VPT2 transition moments. The accuracy of VPT2+F is not greatly inferior to VPT2+K in the CH stretching fundamental region.

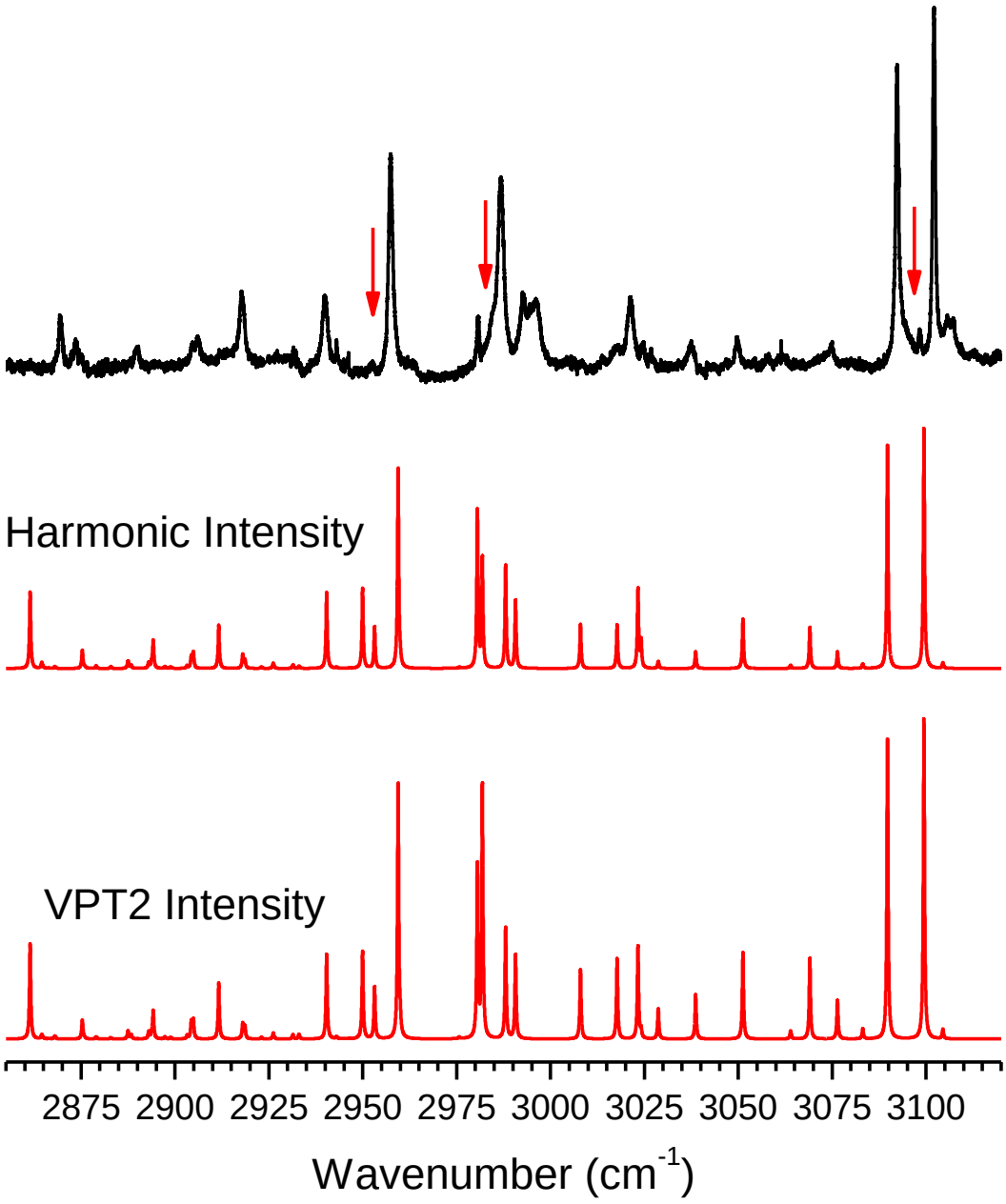

Figure 3.7. Infrared spectrum of isoprene compared to large effective Hamiltonian VPT2+K simulations with intensities determined from VPT2-quality transition moments and less rigorous linear harmonic oscillator transition moments.

References

(1) Nielsen, H. H. The Vibration-Rotation Energies of Molecules. *Rev. Mod. Phys.* **1951**, *23*, 90-136.

(2) Mills, I. M. *Vibration-Rotation Structure in Asymmetric and Symmetric Top Molecules*. Academic Press: 1972; p 115-140.

(3) Watson, J. K. G. Simplification of the Molecular Vibration-Rotation Hamiltonian. *Mol. Phys.* **1968**, *15*, 479-490.

(4) Meyer, H. The Molecular Hamiltonian. *Annu. Rev. Phys. Chem.* **2002**, *53*, 141-172.

(5) Wilson, E. B.; Howard, J. B. The Vibration-Rotation Energy Levels of Polyatomic Molecules I. Mathematical Theory of Semirigid Asymmetrical Top Molecules. *J. Chem. Phys.* **1936**, *4*, 260-268.

(6) Colbert, D. T.; Sibert, E. L. Variable Curvature Coordinates for Molecular Vibrations. *J. Chem. Phys.* **1989**, *91*, 350-363.

(7) Matthews, D. A.; Vazquez, J.; Stanton, J. F. Calculated Stretching Overtone Levels and Darling-Dennison Resonances in Water: A Triumph of Simple Theoretical Approaches. *Mol. Phys.* **2007**, *105*, 2659-2666.

(8) Wilson, E. B., Jr.; Decius, J. C.; Cross, P. C. *Molecular Vibrations: The Theory of Infrared and Raman Vibrational Spectra*; McGraw-Hill, 1955, p 388.

(9) Califano, S. *Vibrational States*; John Wiley & Sons, Ltd., 1976, p 335.

(10) Carbonniere, P.; Barone, V. Coriolis Couplings in Variational Computations of Vibrational Spectra Beyond the Harmonic Approximation: Implementation and Validation. *Chem. Phys. Lett.* **2004**, *392*, 365-371.

(11) Gong, J. Z.; Matthews, D. A.; Changala, P. B.; Stanton, J. F. Fourth-Order Vibrational Perturbation Theory with the Watson Hamiltonian: Report of Working Equations and Preliminary Results. *J. Chem. Phys.* **2018**, *149*, 114102.

(12) Piccardo, M.; Bloino, J.; Barone, V. Generalized Vibrational Perturbation Theory for Rotovibrational Energies of Linear, Symmetric and Asymmetric tops: Theory,

Approximations, and Automated Approaches to Deal with Medium-to-Large Molecular Systems. *Int. J. Quantum Chem.* **2015**, *115*, 948-982.

(13) Martin, J. M. L.; Lee, T. J.; Taylor, P. R.; Francois, J. P. The Anharmonic-Force Field of Ethylene, C_2H_4, by Means of Accurate Ab Initio Calculations. *J. Chem. Phys.* **1995**, *103*, 2589-2602.

(14) J. F. Stanton, J. Gauss, L. Cheng, M. E. Harding, D. A. Matthews, and P. G. Szalay, CFOUR, Coupled-cluster techniques for computational chemistry, a quantum-chemical program package, With contributions from A. A. Auer, R. J. Bartlett, U. Benedikt, C. Berger, D. E. Bernholdt, Y. J. Bomble, O. Christiansen, F. Engel, R. Faber, M. Heckert, O. Heun, M. Hilgenberg, C. Huber, T.-C. Jagau, D. Jonsson, J. Jusélius, T. Kirsch, K. Klein, W. J. Lauderdale, F. Lipparini, T. Metzroth, L. A. Mück, D. P. O'Neill, D. R. Price, E. Prochnow, C. Puzzarini, K. Ruud, F. Schiffmann, W. Schwalbach, C. Simmons, S. Stopkowicz, A. Tajti, J. Vázquez, F. Wang, J. D. Watts and the integral packages MOLECULE (J. Almlöf and P. R. Taylor), PROPS (P. R. Taylor), ABACUS (T. Helgaker, H. J. Aa. Jensen, P. Jørgensen, and J. Olsen), and ECP routines by A. V. Mitin and C. van Wüllen, for the current version, see http://www.cfour.de.

(15) Matthews, D. A.; Stanton, J. F. Quantitative Analysis of Fermi Resonances by Harmonic Derivatives of Perturbation Theory Corrections. *Mol. Phys.* **2009**, *107*, 213-222.

(16) Barone, V. Anharmonic Vibrational Properties by a Fully Automated Second-Order Perturbative Approach. *J. Chem. Phys.* **2005**, *122*, 014108.

(17) McCoy, A. B.; Guasco, T. L.; Leavitt, C. M.; Olesen, S. G.; Johnson, M. A. Vibrational Manifestations of Strong Non-Condon Effects in the $H_3O^+ \bullet X_3$ (X = Ar, N_2, CH_4, H_2O) Complexes: A Possible Explanation for the Intensity in the "Association Band" in the Vibrational Spectrum of Water. *Phys. Chem. Chem. Phys.* **2012**, *14*, 7205-7214.

(18) Kjaergaard, H. G.; Garden, A. L.; Chaban, G. M.; Gerber, R. B.; Matthews, D. A.; Stanton, J. F. Calculation of Vibrational Transition Frequencies and Intensities in Water Dimer: Comparison of Different Vibrational Approaches. *J. Phys. Chem. A* **2008**, *112*, 4324-4335.

(19) Vazquez, J.; Stanton, J. F. Simple(r) Algebraic Equation for Transition Moments of Fundamental Transitions in Vibrational Second-Order Perturbation Theory. *Mol. Phys.* **2006**, *104*, 377-388.

(20) Bloino, J.; Biczysko, M.; Barone, V. Anharmonic Effects on Vibrational Spectra Intensities: Infrared, Raman, Vibrational Circular Dichroism, and Raman Optical Activity. *J. Phys. Chem. A* **2015**, *119*, 11862-11874.

(21) Bloino, J.; Barone, V. A Second-Order Perturbation Theory Route to Vibrational Averages and Transition Properties of Molecules: General Formulation and Application to Infrared and Vibrational Circular Dichroism Spectroscopies. *J. Chem. Phys.* **2012**, *136*, 124108.

(22) Vazquez, J.; Stanton, J. F. Treatment of Fermi Resonance Effects on Transition Moments in Vibrational Perturbation Theory. *Mol. Phys.* **2007**, *105*, 101-109.

(23) Neese, F. The ORCA Program System. *Wiley Interdiscip. Rev.: Comput. Mol. Sci.* **2012**, *2*, 73-78.

(24) Neese, F. Software Update: The ORCA Program System, Version 4.0. *Wiley Interdiscip. Rev.: Comput. Mol. Sci.* **2018**, *8*, e1327.

(25) J. Frisch, G. W. Trucks, H. B. Schlegel, G. E. Scuseria, M. A. Robb, J. R. Cheeseman, G. Scalmani, V. Barone, B. Mennucci, G. A. Petersson, H. Nakatsuji, M. Caricato, X. Li, H. P. Hratchian, A. F. Izmaylov, J. Bloino, G. Zheng, J. L. Sonnenberg, M. Hada, M. Ehara, K. Toyota, R. Fukuda, J. Hasegawa, M. Ishida, T. Nakajima, Y. Honda, O. Kitao, H. Nakai, T. Vreven, J. A. Montgomery, Jr., J. E. Peralta, F. Ogliaro, M. J. Bearpark, J. Heyd, E. N. Brothers, K. N. Kudin, V. N. Staroverov, R. Kobayashi, J. Normand, K. Raghavachari, A. P. Rendell, J. C. Burant, S. S. Iyengar, J. Tomasi, M. Cossi, N. Rega, N. J. Millam, M. Klene, J. E. Knox, J. B. Cross, V. Bakken, C. Adamo, J. Jaramillo, R. Gomperts, R. E. Stratmann, O. Yazyev, A. J. Austin, R. Cammi, C. Pomelli, J. W. Ochterski, R. L. Martin, K. Morokuma, V. G. Zakrzewski, G. A. Voth, P. Salvador, J. J. Dannenberg, S. Dapprich, A. D. Daniels, Ö . Farkas, J. B. Foresman, J. V. Ortiz, J. Cioslowski, and D. J. Fox, Gaussian 09, Revision E.01, Gaussian, Inc., Wallingford, CT, USA, 2009.

(26) Roos, B. O.; Taylor, P. R.; Siegbahn, P. E. M. A Complete Active Space SCF Method (CASSCF) Using a Density-Matrix Formulated Super-CI Approach. *Chem. Phys.* **1980**, *48*, 157-173.

(27) Siegbahn, P. E. M.; Almlof, J.; Heiberg, A.; Roos, B. O. The Complete Active Space SCF (CASSCF) Method in a Newton-Raphson Formulation with Application to The HNO Molecule. *J. Chem. Phys.* **1981**, *74*, 2384-2396.

(28) Lee, T. J.; Taylor, P. R. A Diagnostic for Determining the Quality of Single-Reference Electron Correlation Methods. *Int. J. Quantum Chem.* **1989**, 199-207.

(29) Cheng, L.; Gauss, J.; Ruscic, B.; Armentrout, P. B.; Stanton, J. F. Bond Dissociation Energies for Diatomic Molecules Containing 3d Transition Metals: Benchmark Scalar-Relativistic Coupled-Cluster Calculations for 20 Molecules. *J. Chem. Theory Comput.* **2017**, *13*, 1044-1056.

(30) Bally, T.; Borden, W. Calculations on Open-Shell Molecules: A Beginner's Guide. In *Rev. Comput. Chem.*, John Wiley & Sons, Inc.: 2007; Vol. 13, pp 1-97.

(31) Krylov, A. I. The Quantum Chemistry of Open-Shell Species. In *Rev. Comput. Chem.*, First ed.; Parrill, A. L.; Lipkowitz, K. B., Eds. John Wiley & Sons, Inc.: 2017; Vol. 30.

(32) Szalay, P. G.; Gauss, J. Spin-Restricted Open-Shell Coupled-Cluster Theory for Excited States. *J. Chem. Phys.* **2000**, *112*, 4027-4036.

(33) Stanton, J. F. On the Extent of Spin Contamination in Open-Shell Coupled-Cluster Wave Functions. **1994**, *101*, 371-374.

(34) Crawford, T. D.; Stanton, J. F.; Allen, W. D.; Schaefer, H. F. Hartree-Fock Orbital Instability Envelopes in Highly Correlated Single-Reference Wave Functions. *J. Chem. Phys.* **1997**, *107*, 10626-10632.

(35) Szalay, P. G.; Vazquez, J.; Simmons, C.; Stanton, J. F. Triplet Instability in Doublet Systems. *J. Chem. Phys.* **2004**, *121*, 7624-7631.

(36) Stanton, J. F.; Gauss, J. A Discussion of Some Problems Associated with the Quantum Mechanical Treatment of Open-Shell Molecules. In *Adv. Chem. Phys.*, Prigogine, I.; Rice, S. A., Eds. John Wiley & Sons, Inc.: 2003; Vol. 125.

(37) Margraf, J. T.; Perera, A.; Lutz, J. J.; Bartlett, R. J. Single-Reference Coupled Cluster Theory for Multi-Reference Problems. *J. Chem. Phys.* **2017**, *147*, 184101.

(38) Dykstra, C. E. Examination of Brueckner Condition for Selection of Molecular-Orbitals in Correlated Wavefunctions. *Chem. Phys. Lett.* **1977**, *45*, 466-469.

(39) Krylov, A. I. Equation-of-Motion Coupled-Cluster Methods for Open-Shell and Electronically Excited Species: The Hitchhiker's Guide to Fock Space. *Annu. Rev. Phys. Chem.* **2008**, *59*, 433-462.

(40) Howard, J. C.; Gray, J. L.; Hardwick, A. J.; Nguyen, L. T.; Tschumper, G. S. Getting down to the Fundamentals of Hydrogen Bonding: Anharmonic Vibrational Frequencies of $(HF)_2$ and $(H2O)_2$ from Ab Initio Electronic Structure Computations. *J. Chem. Theory Comput.* **2014**, *10*, 5426-5435.

(41) Tajti, A.; Szalay, P. G.; Csaszar, A. G.; Kallay, M.; Gauss, J.; Valeev, E. F.; Flowers, B. A.; Vazquez, J.; Stanton, J. F. HEAT: High Accuracy Extrapolated Ab Initio Thermochemistry. *J. Chem. Phys.* **2004**, *121*, 11599-11613.

(42) Karton, A.; Rabinovich, E.; Martin, J. M. L.; Ruscic, B. W4 Theory for Computational Thermochemistry: In Pursuit of Confident sub-kJ/mol Predictions. *J. Chem. Phys.* **2006**, *125*, 144108.

(43) Allinger, N. L.; Fermann, J. T.; Allen, W. D.; Schaefer, H. F. The Torsional Conformations of Butane: Definitive Energetics from Ab Initio Methods. *J. Chem. Phys.* **1997**, *106*, 5143-5150.

(44) Schuurman, M. S.; Muir, S. R.; Allen, W. D.; Schaefer, H. F. Toward Subchemical Accuracy in Computational Thermochemistry: Focal Point Analysis of the Heat of Formation of NCO and H,N,C,O Isomers. *J. Chem. Phys.* **2004**, *120*, 11586-11599.

(45) Sylvetsky, N.; Peterson, K. A.; Karton, A.; Martin, J. M. L. Toward a W4-F12 Approach: Can Explicitly Correlated and Orbital-Based Ab Initio CCSD(T) Limits Be Reconciled? *J. Chem. Phys.* **2016**, *144*, 214101.

(46) Almlöf, J.; Taylor, P. R. General Contraction of Gaussian-Basis Sets .I. Atomic Natural Orbitals for 1st-Row and 2nd-Row Atoms. *J. Chem. Phys.* **1987**, *86*, 4070-4077.

(47) Martin, J. M. L.; Taylor, P. R.; Lee, T. J. The Harmonic Frequencies of Benzene. A Case for Atomic Natural Orbital Basis Sets. *Chem. Phys. Lett.* **1997**, *275*, 414-422.

(48) McCaslin, L.; Stanton, J. Calculation of Fundamental Frequencies for Small Polyatomic Molecules: A Comparison Between Correlation Consistent and Atomic Natural Orbital Basis Sets. *Mol. Phys.* **2013**, *111*, 1492-1496.

(49) Gaw, J. F.; Yamaguchi, Y.; Schaefer, H. F.; Handy, N. C. Generalization of Analytic Energy 3rd Derivatives for the RHF Closed-Shell Wave-Function - Derivative Energy and Integral Formalisms and the Prediction of Vibration-Rotation Interaction Constants. *J. Chem. Phys.* **1986**, *85*, 5132-5142.

(50) Colwell, S. M.; Jayatilaka, D.; Maslen, P. E.; Amos, R. D.; Handy, N. C. Higher Analytic Derivatives .1. A New Implementation for the 3rd Derivative of the SCF Energy. *Int. J. Quantum Chem.* **1991**, *40*, 179-199.

(51) Maslen, P. E.; Jayatilaka, D.; Colwell, S. M.; Amos, R. D.; Handy, N. C. Higher Analytic Derivatives .2. The 4th Derivative of Self-Consistent-Field Energy. *J. Chem. Phys.* **1991**, *95*, 7409-7417.

(52) Ringholm, M.; Jonsson, D.; Bast, R.; Gao, B.; Thorvaldsen, A. J.; Ekstrom, U.; Helgaker, T.; Ruud, K. Analytic Cubic and Quartic Force Fields Using Density-Functional Theory. *J. Chem. Phys.* **2014**, *140*, 034103.

(53) Matthews, D. A.; Cheng, L.; Harding, M. E.; Lipparini, F.; Stopkowicz, S.; Jagau, T. C.; Szalay, P. G.; Gauss, J.; Stanton, J. F. Coupled-Cluster Techniques for Computational Chemistry: The CFOUR Program Package. *J. Chem. Phys.* **2020**, *152*, 214108.

(54) Breidung, J.; Thiel, W.; Gauss, J.; Stanton, J. F. Anharmonic Force Fields from Analytic CCSD(T) Second Derivatives: HOF and F_2O. *J. Chem. Phys.* **1999**, *110*, 3687-3696.

(55) Gauss, J.; Stanton, J. F. Analytic CCSD(T) Second Derivatives. *Chem. Phys. Lett.* **1997**, *276*, 70-77.

(56) MRCC, a quantum chemical program suite written by M. Kállay, Z. Rolik, J. Csontos, P. Nagy, G. Samu, D. Mester, I. Ladjánszki, L. Szegedy, B. Ladóczki, K. Petrov, M. Farkas, B. Hégely. See also. Z. Rolik, L. Szegedy, I. Ladjánszki, B. Ladóczki, and M. Kállay,. J. Chem. Phys. **139**, 094105 (2013), as well as: www.mrcc.hu.

(57) Kallay, M.; Nagy, P. R.; Mester, D.; Rolik, Z.; Samu, G.; Csontos, J.; Csoka, J.; Szabo, P. B.; Gyevi-Nagy, L.; Hegely, B., et al. The MRCC Program System: Accurate Quantum Chemistry from Water to Proteins. *J. Chem. Phys.* **2020**, *152*, 074107.

(58) Allen, W. D.; Csaszar, A. G. On the Ab Initio Determination of Higher-Order Force-Constants at Nonstationary Reference Geometries. *J. Chem. Phys.* **1993**, *98*, 2983-3015.

(59) Schneider, H.; Vogelhuber, K. M.; Schinle, F.; Stanton, J. F.; Weber, J. M. Vibrational Spectroscopy of Nitroalkane Chains Using Electron Autodetachment and Ar Predissociation. *J. Phys. Chem. A* **2008**, *112*, 7498-7506.

(60) Rosnik, A. M.; Polik, W. F. VPT2+K Spectroscopic Constants and Matrix Elements of the Transformed Vibrational Hamiltonian of a Polyatomic Molecule with Resonances Using Van Vleck Perturbation Theory. *Mol. Phys.* **2014**, *112*, 261-300.

(61) Lehmann, K. K. Beyond the χ-K Relations - Calculations of 1-1 and 2-2 Resonance Constants with Application to HCN and DCN. *Mol. Phys.* **1989**, *66*, 1129-1137.

(62) Darling, B. T.; Dennison, D. M. The Water Vapor Molecule. *Phys. Rev.* **1940**, *57*, 128-139.

(63) Martin, J. M. L.; Taylor, P. R. Accurate Ab Initio Quartic Force Field for *trans*-HNNH and Treatment of Resonance Polyads. *Spectrochim. Acta, Part A* **1997**, *53*, 1039-1050.

(64) Misiewicz, J. P.; Moore, K. B.; Franke, P. R.; Morgan, W. J.; Turney, J. M.; Douberly, G. E.; Schaefer, H. F. Sulfurous and Sulfonic Acids: Predicting the Infrared Spectrum and Setting the Surface Straight. *J. Chem. Phys.* **2020**, *152*, 024302.

(65) Brown, A. R.; Franke, P. R.; Douberly, G. E. Helium Nanodroplet Isolation of the Cyclobutyl, 1-Methylallyl, and Allylcarbinyl Radicals: Infrared Spectroscopy and Ab Initio Computations. *J. Phys. Chem. A* **2017**, *121*, 7576-7587.

(66) Pullen, G. T.; Franke, P. R.; Lee, Y. P.; Douberly, G. E. Infrared Spectroscopy of Propene in Solid *para*-Hydrogen and Helium Droplets: The Role of Matrix Shifts in the Analysis of Anharmonic Resonances. *J. Mol. Spectrosc.* **2018**, *354*, 7-14.

(67) Brown, A. R.; Brice, J. T.; Franke, P. R.; Douberly, G. E. Infrared Spectrum of Fulvenallene and Fulvenallenyl in Helium Droplets. *J. Phys. Chem. A* **2019**, *123*, 3782-3792.

(68) Tabor, D. P.; Hewett, D. M.; Bocklitz, S.; Korn, J. A.; Tomaine, A. J.; Ghosh, A. K.; Zwier, T. S.; Sibert, E. L. Anharmonic Modeling of the Conformation-Specific IR Spectra of Ethyl, *n*-Propyl, and *n*-Butylbenzene. *J. Chem. Phys.* **2016**, *144*, 224310.

CHAPTER 4

INFRARED LASER SPECTROSCOPY OF THE N-PROPYL AND I-PROPYL RADICALS: STRETCH-BEND FERMI COUPLING IN THE ALKYL CH STRETCH REGION[1]

[1] Reprinted from Franke, P.R.; Tabor, D.P.; Moradi, C.P.; Douberly, G.E.; Agarwal, J.; Schaefer, H.F.; Sibert, E.L. 2016. *Journal of Chemical Physics*. 145:224304 DOI: 10.1063/1.4971239, AIP Publishing.

The *n*-propyl and *i*-propyl radicals were generated in the gas phase via pyrolysis of *n*-butyl nitrite [$CH_3(CH_2)_3ONO$] and *i*-butyl nitrite [$(CH_3)_2CHCH_2ONO$], respectively. Nascent radicals were promptly solvated by a beam of He nanodroplets, and the infrared spectra of the radicals were recorded in the CH stretching region. Several previously unreported bands are observed between 2800 and 3150 cm^{-1}. The CH stretching modes observed above 3000 cm^{-1} are in excellent agreement with CCSD(T) anharmonic frequencies computed using second-order vibrational perturbation theory. However, between 2800 and 3000 cm^{-1}, the spectra of *n*- and *i*-propyl radicals become congested and difficult to assign due to the presence of multiple anharmonic resonance polyads. To model the spectrally congested region, Fermi and Darling-Dennison resonances are treated explicitly using "dressed" Hamiltonians and CCSD(T) quartic force fields in the normal mode representation, and the agreement with experiment is less than satisfactory. Computations employing local mode effective Hamiltonians reveal the origin of the spectral congestion to be strong coupling between the high frequency CH stretching modes and the lower frequency CH_n bending/scissoring motions. The most significant coupling is between stretches and bends localized on the same CH_2/CH_3 group. Spectral simulations using the local mode approach are in excellent agreement with experiment.

4.1. Introduction

Propyl is archetypical of the alkyl radicals prevalent in combustion systems. The barrierless association of propyl and O_2 produces an oxygen-centered $C_3H_7OO^{\bullet}$ peroxy radical, which can decompose to bimolecular products or undergo unimolecular rearrangements to produce carbon-centered radicals, such as the β- or γ-hydroperoxy propyl (i.e. QOOH) species.[1-5] Propyl peroxy radicals are the smallest alkyl species that can isomerize to QOOH via intramolecular H-atom transfer pathways having barriers that lie *below* the alkyl + O_2 reaction asymptote.[6-7] The propyl + O_2 reaction is therefore a prototype of low-temperature hydrocarbon oxidation chemistry, as it represents the prototypical alkyl system undergoing transformations

characteristic of larger species.[8] Indeed, many experimental and computational studies have been reported with the aim of characterizing the potential energy surface and detailed kinetics of the propyl + O_2 reaction.[9-14] On the other hand, detailed spectroscopic analyses of isolated propyl and propyl peroxy radicals remain incomplete.[15] Here, we present a mid-infrared (IR) spectroscopic characterization of the *n*- and *i*-propyl radicals in the CH stretching region, which is complicated by the presence of multiple anharmonic resonance polyads.

Fessenden reported in the 1960s a series of seminal electron spin resonance (ESR) studies of alkyl radicals produced via photolysis of precursors dissolved in liquid cyclopropane solution at -140 °C.[16-17] Comparing the relative magnitudes of β-proton hyperfine coupling constants extracted from pentyl, butyl and propyl ESR spectra, they arrived at the *n*-propyl equilibrium structure shown in Scheme 4.1, in which the singly occupied *p*-orbital makes a π/6 angle with the β-CH bonds. Moreover, from the temperature dependence of the β-coupling constants, a barrier to hindered rotation between equivalent C_s structures was estimated to be ~140 cm^{-1}. Using the stationary photolytic technique,[18-19] Krusic and co-workers assigned line broadening in their ESR spectra to the exchange of magnetically non-equivalent α hydrogen atoms,[20] an interpretation which is consistent with the *n*-propyl structure proposed by Fessenden. The equilibrium structure of *n*-propyl and the barrier to internal rotation were the focus of several early electronic structure computations, which gave qualitatively different results depending on the level of theory, often in conflict with conclusions arrived at via experimental ESR spectra.[21-24] Modern, coupled-cluster theory was recently applied to the *n*-propyl system,[25] and a zero-Kelvin enthalpic barrier of 137 cm^{-1} was found for hindered rotation. Moreover, the equilibrium structure at zero Kelvin was predicted to have C_s symmetry. Both findings are in remarkable agreement with the experimental results inferred from the 1960s ESR spectra of alkyl radicals produced in liquid cyclopropane solutions.

Scheme 4.1.

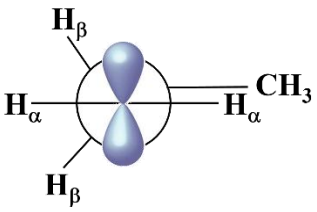

Other than the aforementioned ESR studies, Pacansky's argon matrix isolation experiments represent the only other spectroscopic work carried out on propyl radicals.[26-27] In separate experiments, dibutyryl peroxide and diisobutyryl peroxide precursors were co-deposited with argon on a cold window and photolyzed to form the *n*- and *i*-propyl radicals (and CO_2), respectively. Infrared spectra were measured with a dispersive instrument, and a few bands could be definitively assigned to propyl radicals. For *n*-propyl, the α-CH_2 wagging mode was observed at 530 cm^{-1}. Two other strong bands at 3100 and 3118 cm^{-1} were assigned to symmetric and antisymmetric stretching vibrations of the α-CH_2 group. These three features were later described as being the characteristic signatures of primary alkyl radicals.[28] The remaining spectrum was congested and more difficult to assign, especially in the CH stretching region. However, Pacansky did note an "anomalous band" located near 2812 cm^{-1}. This rather strong band in the CH stretch region was viewed as "anomalous" simply due to its characteristically large redshift from typical alkyl CH stretch vibrations. Pacansky assigned this band to the symmetric β-CH_2 stretch and rationalized the red shift as being due to a hyperconjugative stabilization and softening of the β-CH bonds, i.e., an electron transfer from β-CH σ-bonding orbitals into the half-filled *p*-orbital localized on the α carbon atom.

Ultraviolet absorption spectra that probe the $\tilde{B}$-$\tilde{X}$ transition have been reported for gas-phase propyl peroxy radicals, and these are broad and featureless due to the dissociative nature of the excited state.[29-30] More recently, a near-IR study was reported by Miller and co-workers,[15] in which cavity ringdown spectroscopy was used to probe the non-dissociative $\tilde{A}$-$\tilde{X}$ transition. This

study was followed by a detailed theoretical analysis of the interconversion pathways connecting the various rotamers of the *n*- and *i*-propyl peroxy systems.[31]

In contrast to the peroxy species, spectroscopic studies of gas-phase propyl radicals are completely lacking. Here we report IR spectra in the CH stretching region for both the *n*- and *i*-propyl radicals, which have been produced in the gas-phase by flash-vacuum pyrolysis and isolated in helium nanodroplets. The spectra are sufficiently resolved so as to reveal a vibrational complexity that can be assigned to strong anharmonic coupling between the CH stretches and the overtones and combinations of CH_n bends (referred to here as scissor modes). Resonance polyads are characterized with effective Hamiltonian approaches that are constructed in either a normal or local mode representation. The origin of the extensive anharmonic coupling is revealed via comparisons of experimental spectra to local mode Hamiltonian predictions.[32-38] The weakly interacting nature of superfluid helium allows for a direct comparison between experimental band origins and computed spectra. Moreover, the helium droplet spectra reported here provide a robust starting point for future high resolution gas-phase spectroscopic studies.

4.2. Experimental Methods

The details of the helium droplet methodology have been discussed elsewhere.[39-42] Liquid He droplets consisting of 4500 He atoms on average are formed in a cryogenic nozzle expansion (35 bar, 17 K, 5 μm orifice diameter).[43] The droplet expansion is collimated into a beam by a 0.4 mm conical skimmer prior to entering a differentially pumped chamber containing propyl radicals at a density of about 10^{10} cm^{-3} over an ~1 cm path. Propyl radicals are generated in a high-temperature, effusive, flash-vacuum pyrolysis source consisting of a quartz tube wrapped with a Ta filament.[41, 44] Precursor molecules colliding with the hot tube decompose, and the products of this decomposition (referred to hereafter as the pyrolysate) effuse through the droplet beam path. Collisions between droplets and gas-phase pyrolysate molecules result in solvation and cooling to ~ 0.4 K via He atom evaporation.[45-46]

The precursor molecule used for the production of *n*-propyl radicals is *n*-butyl nitrite (*n*-BN), which was synthesized by $NaNO_2$ addition to an aqueous solution of *n*-butanol and sulfuric acid.[47] The pyrolysis of R−CH_2ONO nitrite molecules has been shown to lead to the formation of NO, H_2CO, and R radicals (R = C_2H_5, C_3H_3, C_3H_5).[44, 48-49] Thermal decomposition of *n*-BN produces the *n*-propyl radical, as shown in Eq. 4.1. Gas-phase *i*-propyl radicals were produced similarly via the thermal decomposition *i*-butyl nitrite (*i*-BN).

$$i,n\text{-BN} \xrightarrow{\Delta} \cdot\mathrm{NO} + i,n\text{-}\mathrm{C_3H_7} + \mathrm{H_2CO} \tag{4.1}$$

Droplets are detected by electron ionization in a quadrupole mass spectrometer equipped with a crossed-beam ionizer. The mechanism for dopant ionization via He^+ charge transfer has been described elsewhere.[46] Ionization and fragmentation of dopant molecules yields desolvated, gas-phase ions that provide mass spectrometer signatures of the upstream droplet doping process. Moreover, the cross-section for droplet ionization provides the action necessary for measuring IR spectra of He-solvated molecules and clusters.

The mid-IR idler output from a continuous-wave optical parametric oscillator (cw-OPO) is spatially overlapped with the droplet beam in a counter-propagating configuration. The tuning and calibration of the cw-OPO is discussed elsewhere.[50] Vibrational excitation of dopant molecules affects a geometric cross-section reduction of the droplet via evaporative cooling. Because this cooling is fast in comparison to the time between excitation and mass spectrometer detection, resonant vibrational excitation is measured as a reduction in the average ionization cross-section of the helium droplets, which can be detected in judiciously chosen mass channels to provide quasi-species-selective IR spectra. The laser beam is mechanically chopped at 80 Hz, and the mass spectrometer ion current is processed with a lock-in amplifier, providing background-free laser-induced depletion signals as the IR radiation is tuned with approximately 20 MHz resolution. Infrared spectra are normalized to the mid-IR idler power.

4.3. Theoretical Methods

4.3.1. Second Order Vibrational Perturbation Theory with Resonances (VPT2+K)

Geometric parameters at the electronic global minima were optimized using CFOUR software[51] at the CCSD(T)/ANO0 (*n*-propyl) and CCSD(T)/ANO1 (*i*-propyl) levels of theory. The electronic global minima for *n*- and *i*-propyl radicals have C_1 and C_s symmetry, respectively; however, we note that the minimum energy structures on the zero-Kelvin enthalpic surfaces have C_s and C_{2v} symmetry, respectively. The zero-Kelvin enthalpic surface is defined as the vibrationally adiabatic surfaces for large-amplitude motion about the high-symmetry structures; these motions correspond to either CH_3 hindered rotation for *n*-propyl[25] or out-of-plane CH_α bending for *i*-propyl (See Section 4.5.1). For the *n*-propyl radical, the C_1 electronic global minimum structure differs from the zero-Kelvin most probable structure by an ~8° pyramidal distortion and an ~25° internal rotation of the methylene group (α-CH_2).[25] The C_s symmetry *i*-propyl electronic minimum differs from the most probable C_{2v} structure by an ~17° distortion of the CH_α bond out of the plane containing the three carbon atoms, along with an ~11° rotation of the methyl groups in the opposite sense of the CH_α distortion. On the *n*-propyl zero-Kelvin enthalpic surface, the energy of the C_1 structure described above lies only 10 cm^{-1} above the C_s structure, indicative of the rather floppy nature for motion about the high-symmetry geometry.[25] Similarly for *i*-propyl, at zero-Kelvin, the C_s electronic minimum lies ~35 cm^{-1} above the C_{2v} structure. For each electronic global minimum structure, harmonic vibrational frequencies and a semi-diagonal quartic force field were computed at the same level of theory. Additionally, to obtain infrared active transition intensities, a geometry optimization followed by a harmonic frequency computation was performed using the next largest size of ANO basis set: ANO1 for *n*-propyl[25] and ANO2 for *i*-propyl.

An Intrinsic Reaction Path (IRP) was computed in Gaussian 09 at the CCSD(T)/aug-cc-pVTZ//MP2/6-311++G** level of theory. It was expected that the MP2/6-311++G** geometries would be reasonable for non-stationary points along the IRP because its electronic global minimum geometry agrees with the CCSD(T)/ANO1 result to within 5 degrees for the CHα out-of-plane angle and to within 1 degree for the methyl torsional angle. Various DFT functionals were first considered for the geometries; however, all of them severely under-predicted the degree of pyramidalization at the radical center. Additionally zero-point vibrational energy was, of course, computed at the MP2/6-311++G** level of theory, and the appropriate[52] projection was carried out at non-stationary points, namely the built-in Freq=Projected procedure.

Second order vibrational perturbation theory with resonances (VPT2+K)[53] was implemented using an in-house script written in *Mathematica*.[54] Historically, anharmonic resonances have been identified by an inspection of the force constant magnitudes and zeroth-order energy differences between states. Often an arbitrary threshold is set that weighs one or both of these factors. There are, however, less arbitrary ways to decide when the interaction between vibrational states is strong.[55-56] The Martin test is one of these.[56] It provides an estimate of how the frequencies of two interacting states would be affected if their interaction were to be treated explicitly. Another more sophisticated scheme for resonance identification would be to use the harmonic derivatives method developed by Matthews and Stanton.[57] Simulations were performed, identifying resonances on the basis of their Martin test values. Tables 4.1 and 4.2 contain harmonic and VPT2 computational results for the CH stretch vibrations of *i*- and *n*-propyl radicals, respectively, along with the eigenvalues of resonance polyads identified via the Martin test.

To facilitate a fair comparison to the local mode Hamiltonian procedure described in Section 4.3.2, the anharmonic couplings in *n*-propyl and *i*-propyl were modeled via effective Hamiltonians with 22 and 28 coupled vibrational states, respectively. The associated basis states

Table 4.1. Harmonic and VPT2+K frequencies of the *i*-propyl radical (cm^{-1}).[a]

Mode	**Γ(C_s)**	**Γ(C_{2v})**	**ω(C_s)**	**ω(C_{2v})**	**Δω**	**Description**
1	a'	a_1	3187.04	3209.38	22.33	CHα str.
2	a'	a_1	3110.98	3116.11	5.13	CH_β sym. str.
3	a'	b_1	3048.97	3025.46	-23.51	CHγ asym. str. in-phase
4	a'	a_1	2974.15	2988.57	14.42	CHγ sym. str. in-phase
14	a''	b_2	3111.58	3117.02	5.44	CH_β asym. str.
15	a''	a_2	3048.89	3026.66	-22.23	CHγ asym. str. out-of-phase
16	a''	a_2	2971.28	2985.22	13.94	CHγ sym. str. out-of-phase
Mode	**Γ(C_s)**	**VPT2 w/ Torsion**	**VPT2 w/o Torsion**	**Δ**	**Intensity**	
1	a'	3066.99	3055.81	-11.18	21.32	
2	a'	2963.13	2960.92	-2.21	15.00	
3	a'	2894.18	2901.03	6.84	35.82	
4[b]	a'	2844.58	2834.42	-10.17	31.86	
14	a''	2963.07	2961.20	-1.87	21.05	
15[c]	a''	2878.68	2885.14	6.45	4.81	
16[c]	a''	2830.94	2820.80	-10.13	19.73	

[a] The modes are ordered, in the Herzberg convention, based on the symmetries at the electronic global minimum. The harmonic frequencies and quartic force field were computed at the CCSD(T)/ANO1 level of theory. Harmonic intensities (km/mol) were computed at the CCSD(T)/ANO2 level of theory. Resonances were identified with the Martin test.[56]

[b] Deperturbed value is given; involved in a resonance polyad (torsional modes kept) with eigenvalues: 2911.26, 2894.31, 2884.87, 2877.96, 2831.86 cm^{-1}.

[c] Deperturbed value is given; involved in a resonance polyad (torsional modes kept) with eigenvalues: 2929.58, 2899.83, 2881.66, 2868.52, 2844.29, 2834.55, 2742.65 cm^{-1}.

Table 4.2. Harmonic and VPT2+K frequencies of the *n*-propyl radical (cm^{-1}).[a]

Mode	**Γ(C_1)**	**Γ(C_s)**	**ω(C_1)**	**ω(C_s)**	**Δω**	**Description**
1	*a*	*a′*	3262.40	3267.67	5.27	α-CH_2 asym. str.
2	*a*	*a′*	3152.94	3157.75	4.81	α-CH_2 sym. str.
3	*a*	*a′*	3131.91	3131.29	-0.62	γ-CH_3 asym. str.
4	*a*	*a″*	3126.13	3126.59	0.46	γ-CH_3 asym. str.
5	*a*	*a′*	3059.98	3043.68	0.58	γ-CH_3 sym. str.
6	*a*	*a″*	3043.10	3027.92	-15.18	β-CH_2 asym. str.
7	*a*	*a′*	2981.93	3000.37	18.44	β-CH_2 sym. str.
Mode	**Γ(C_1)**	**VPT2 w/ Torsion**	**VPT2 w/o Torsion**	**Δ**	**Intensity**	
1	*a*	3116.34	3090.04	-26.30	12.28	
2[b]	*a*	3015.96	3012.29	-3.67	13.80	
3	*a*	2982.70	2983.31	0.61	26.12	
4	*a*	2979.61	2978.87	-0.74	32.88	
5	*a*	2898.05	2915.33	17.28	17.14	
6[c]	*a*	2897.27	2896.23	-1.05	21.26	
7[d]	*a*	2844.54	2833.43	-11.11	25.54	

[a] The modes are ordered, in the Herzberg convention, based on the symmetries at the electronic global minimum. The harmonic frequencies and quartic force field were computed at the CCSD(T)/ANO0 level of theory. Harmonic intensities (km/mol) were computed at the CCSD(T)/ANO1 level of theory. Note that our *n*-propyl force field was identical to the one used by Li et al.[25] It can be seen that the frequencies in their Table S3 are exactly reproduced, except for the resonant modes, to which we give different treatment. Resonances were identified with the Martin test.[56]

[b] Deperturbed value is given; involved in a Fermi resonance (torsional modes kept) with eigenvalues: 3033.89, 2856.51 cm^{-1}.

[c] Deperturbed value is given; involved in a resonance polyad (torsional modes kept) with eigenvalues: 3004.69, 2941.88, 2895.41, 2742.37 cm^{-1}.

[d] Deperturbed value is given; involved in a resonance polyad (torsional modes kept) with eigenvalues: 2936.81, 2931.23, 2880.74, 2824.80 cm^{-1}.

are the CH stretching fundamentals and all overtones/combinations of normal modes that have primarily CH_n scissoring character. The energies of these states were first computed via the full VPT2 treatment. Anharmonicity constants were then "deperturbed", which was accomplished by removing all terms in the summation that couple states explicitly included within each effective Hamiltonian. Deperturbed VPT2 frequencies were subsequently computed using the modified anharmonicity constants and placed along the diagonals of the Hamiltonian matrices.

Fermi-type coupling was accounted for by cubic force constants multiplied by the appropriate numerical factors. Higher-order coupling was included via the Darling-Dennison resonance constants proposed by Lehmann.[58] The function of these is to recover some of the correlation from the fourth order of vibrational perturbation theory. Expressions for the resonance constants that allow for high-order coupling between fundamentals and between two quanta states were (carefully) obtained from the literature.[57, 59-61] It is important to realize that the resonance constants have denominators containing differences of harmonic frequencies, just as the anharmonicity constants do; thus, they also require deperturbation, or else artefactual values will be obtained. This scheme for treating resonances is known as the VPT2+K method.[60]

In the course of computing the anharmonicity constants required for the VPT2 treatment, the formulae derived by Martin were used to identify strongly-coupled states.[56] We chose to classify the interaction between a CH stretching fundamental and a two-quantum CH bending state as a Fermi resonance if these formulae gave a value of 0.5 cm^{-1} or greater. The Martin test has a different expression for the interaction between a fundamental and an overtone,

$$-\frac{\phi_{ijj}{}^4}{256\Delta^3}, \tag{4.2}$$

and for the interaction between a fundamental and a combination tone,

$$-\frac{\phi_{ijk}{}^4}{64\Delta^3}, \tag{4.3}$$

where Δ is the difference in energy between two zeroth-order states, and (ϕ_{ijj} and ϕ_{ijk}) are the cubic force constants that couple them. Some examples of the Martin test applied to interacting vibrational states of *n*-propyl are provided below (Table 4.3).

Table 4.3. Martin test values (cm^{-1}), differences between the perturbation theory correction and the (2x2) variational correction to the vibrational frequency (cm^{-1}), the percentage of wavefunction mixing, the difference in zeroth-order energies (cm^{-1}), and the relevant force constant (cm^{-1}), for a subset of interactions between the vibrational modes of *n*-propyl.

State a	State b	|Martin Test|	|VPT2 − Var|	Mixing	Force Constant	Δ
v_{12}	$v_7 + v_{11}$	31162.49	178.97	52/48	-43.17	1.20
v_{16}	$v_7 + v_{14}$	572.57	55.345	59/41	-85.08	11.27
v_{25}	$2v_{23}$	62.02	16.62	67/33	-102.70	19.14
v_{24}	$2v_{21}$	56.63	15.89	68/32	104.40	20.16
v_{25}	$2v_{22}$	16.74	7.56	75/25	-108.15	31.72
v_{14}	$v_7 + v_{12}$	1.50	1.11	88/12	-53.00	43.50
v_{13}	$v_7 + v_{11}$	1.07	0.81	88/12	40.72	34.24
v_{24}	$v_{20} + v_{21}$	0.44	0.36	91/9	-30.01	30.58
v_{26}	$2v_{21}$	0.27	0.24	95/5	89.58	98.21
v_{10}	$v_7 + v_8$	0.13	0.12	96/4	42.11	73.20
v_{11}	$v_9 + v_{10}$	0.04	0.04	98/2	30.22	68.54

A very clear relationship can be seen between the Martin test value, the variational/perturbational frequency difference, and the extent of wavefunction mixing. As the coupling between states grows stronger, the Martin test overestimates, with increasing severity, the change that would be brought about by treating the interaction explicitly. However, this does not present a problem because the Martin test is rather accurate at the cut-off we used (0.5 cm^{-1}). This cut-off value was chosen to be approximately the value for which one state is predicted to mix and take on 10% of the character of another state. It is not apparent that reliance on the Martin test could have led to false negatives in our resonance search. We do acknowledge the

possibility of neglected resonant interactions with three-quanta states; the Martin test does not identify these types of resonances. However, three-quanta states do not interact with fundamentals at second order in perturbation theory. In VPT2+K, their effects would only be felt in the effective Hamiltonians, where they could either directly couple to fundamentals via quartic force constants (or the related 1:3 resonance constants) or couple to the two-quanta states.[60]

When Fermi resonances were identified, they were treated systematically in the following manner. Denominators corresponding to the resonant interactions were removed from the anharmonicity constants. The VPT2 frequencies calculated using the modified anharmonicity constants are then said to be "deperturbed." An effective Hamiltonian matrix was built, placing the deperturbed values along the diagonal. In cases where two fundamentals were involved in Fermi resonances with the same state, they were all placed into the same effective Hamiltonian, and their frequencies were further deperturbed, if necessary, for interactions with all other states in that matrix. Zeroth-order states in the effective Hamiltonian are coupled by cubic and quartic terms in the force field expansion.

A reduced-dimensional variational treatment of the anharmonicity was performed by simply diagonalizing each effective Hamiltonian. The eigenvalues are the corrected anharmonic frequencies. We assume that transitions to dark states derive their intensity entirely via intensity-borrowing from "bright" fundamental CH stretch basis states. In this simple scheme, transition intensities were obtained by summing the squared eigenvector components, which are multiplied by their associated harmonic intensities. Moreover, we did not account for intensity arising from higher-order terms in the dipole moment expansion, i.e., we assumed electrical harmonicity.

4.3.2. Local Mode Effective Hamiltonian

The local mode approach employed here has been described previously,[33-34] and we provide only a brief overview. As a starting point, harmonic frequencies were computed for the

high-symmetry structures of *n*-propyl (C_s) and *i*-propyl (C_{2v}), which were obtained via symmetry-constrained geometry optimizations. Computations were carried out at the B3LYP/6-311++G(d,p) level of theory, using the Gaussian 09 suite of programs.[62] The procedure described below for constructing the local mode effective Hamiltonian is analogous to the "simple model" described in Reference 34.

We performed an orthogonal transformation of the normal modes to obtain a set of local CH stretch and HCH scissor modes. A central step in constructing this transformation is a series of intermediate computations that involve calculating normal modes that have been localized.[38] This simply involves increasing by a factor of two the masses of atoms *not* involved in the local motions. The quadratic force constant matrix was then re-mass-weighted and diagonalized, and this procedure was repeated to localize all CH stretch and HCH scissor modes. The resulting set of *localized* modes are used to transform the quadratic normal mode Hamiltonian and dipole derivatives.[38]

The effective Hamiltonian in the local mode basis was constructed by including only those states necessary for a satisfactory simulation of the CH stretching region. Based on experience developed over several investigations,[32-33, 34] the basis states required are the CH stretch fundamentals and the HCH scissor overtones/combinations. The combination tones are composed of one quantum in each of two scissor modes. The resulting effective Hamiltonians for *n*-propyl and *i*-propyl contain 22 and 28 vibrational states, respectively.

In the localized representation, basis states are coupled by both quadratic and higher-order terms. Quadratic couplings were determined directly from the normal mode calculations. However, anharmonic terms, which include couplings between CH stretches and scissor overtones/combinations were not evaluated for either *n*- or *i*-propyl. Instead, these couplings have been calculated previously using 4th order perturbation theory for a set of model systems.[35] The couplings have been found to be similar for all model systems studied. Due to this similarity,

average values of these coupling terms were inserted into the local mode Hamiltonians as non-adjustable parameters. For example, the cubic coupling term that mixes a CH stretch with its contiguous HCH scissor overtone is set equal to 22 cm^{-1}. The magnitude of the various stretch-scissor coupling terms are tabulated elsewhere.[34]

To incorporate the effects of missing basis functions, CH stretch anharmonicities, and deficiencies in the electronic structure calculations used to determine the normal modes, we apply select scaling factors to the CH stretch and HCH scissor frequencies. All of the scalings were refined in a previous study of alkylbenzene chains and are not altered for the present study.[34] The effective Hamiltonians were diagonalized to determine the transition energies and intensities. The localized CH stretch fundamentals are the only basis states that contribute oscillator strength, and the dipole derivatives are not scaled.

4.4. Experimental Results

4.4.1. Mass Spectra

Droplet beam mass spectra were measured for both the *n*-BN precursor flowing through the room-temperature pyrolysis source and with the pyrolysis source operated at approximately 1000 K (Fig. 4.1). In addition to $(He_n)^+$ ions originating from the ionization of neat droplets,[46] various peaks between 27 and 72 u are observed due to the ionization and fragmentation of He-solvated *n*-BN. As the pyrolysis source is heated, notable changes in the mass spectrum include reduced intensity at 41 and 43 u and enhanced intensity at 15, 27, 29, 30 and 39 u, all of which is consistent with *n*-BN thermal decomposition (Eqn. 1) and He droplet solvation of the pyrolysate. This pyrolysis signature is similar to that previously observed for other nitrite precursors used to generate ethyl, propargyl and allyl radicals.[44, 48-49] We find difference mass spectra (*vide infra*) that the measurement of laser-induced depletion signal in channel 39 u proves effective at discriminating against droplets that contain pyrolytic decomposition products other than propyl

radicals. It is important to emphasize that the density of molecules in the pyrolysis tube is optimized to dope droplets with single molecules. Under these source conditions, we expect less than five percent of the droplet ensemble to capture more than one molecule. Therefore, cluster formation is not expected to appreciably contribute to the infrared spectra reported here.

4.4.2. *n*-propyl Infrared Spectrum and Difference Mass Spectra

The laser-induced depletion spectrum of the precursor molecule shown at the bottom of Fig. 4.2. was measured with the quadrupole set to pass only ions having *m/z* = 43 u, which is one of the most intense peaks in the MS recorded with cold pyrolysis conditions. The precursor absorptions lie between 2850 and 3000 cm^{-1} and exhibit relatively weak and broad features. Because the *m/z* = 39 u signal is significantly enhanced upon *n*-BN pyrolysis, this mass channel was chosen to record the depletion spectrum of the *n*-BN decomposition products (top spectrum of Fig. 4.2). Finally, the middle spectrum of Fig. 4.2 is that of the C_3H_6 molecule, which was recorded by metering a pure propene sample into a differentially pumped pickup cell.

The top spectrum in Fig. 4.2 shows weak signals (marked by *) that correspond to the positions of the most intense propene vibrations; however, the vast majority of the "pyrolysis-on" spectrum cannot be explained by either *n*-BN precursor or propene vibrations. There are two intense vibrations above 3000 cm^{-1} that are in the vicinity of symmetric and antisymmetric α-CH_2 stretch vibrations previously assigned to the *n*-propyl radical in Pacansky's solid-Ar matrix isolation study.[26] A third distinct vibration falls near 2823 cm^{-1}, which is near the alkyl radical "anomalous band".[26-28] The congestion between these two regions, however, is difficult to interpret. We considered the possibility of a droplet sequentially capturing both an *n*-propyl radical and another component of the pyrolysate. However, when the flux through the pyrolysis source is reduced by ~40%, all bands between 2810 and 2960 cm^{-1} decrease in intensity together (but do not disappear entirely), indicating that the spectrum arises predominantly from the pickup

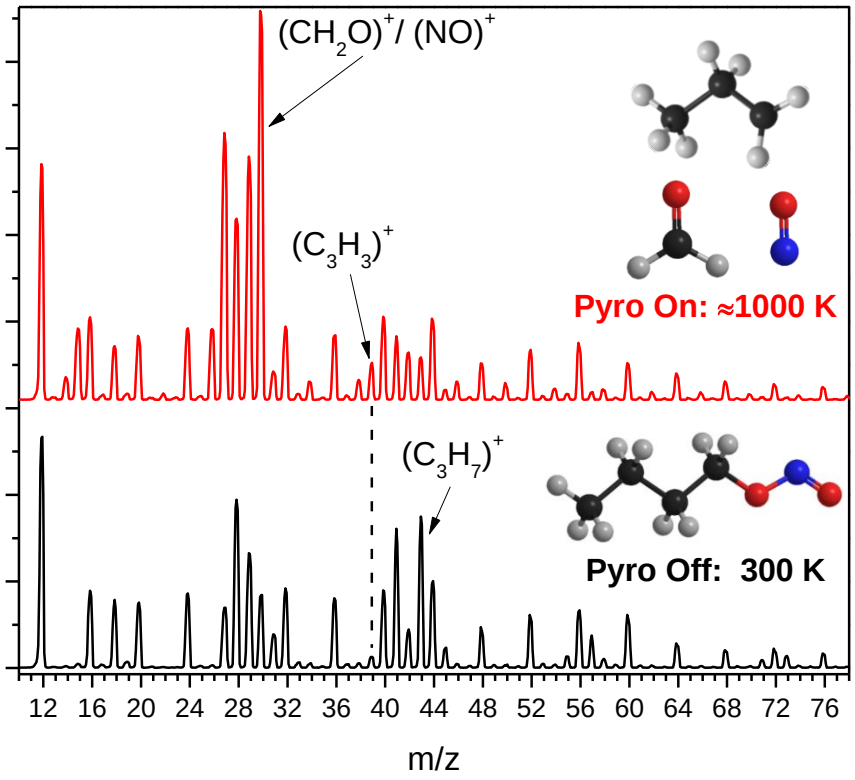

Figure 4.1. Mass spectra of droplets doped with the *n*-BN precursor (bottom) and its pyrolysate (top). Reduced ion signal in m/z = 41 and 43 u and enhanced ion signal at masses between 27 and 30 u are indicative of *n*-BN decomposition. The enhancement of m/z = 39 u (denoted by the dashed line) results largely from ionization and fragmentation of the *n*-propyl radical.

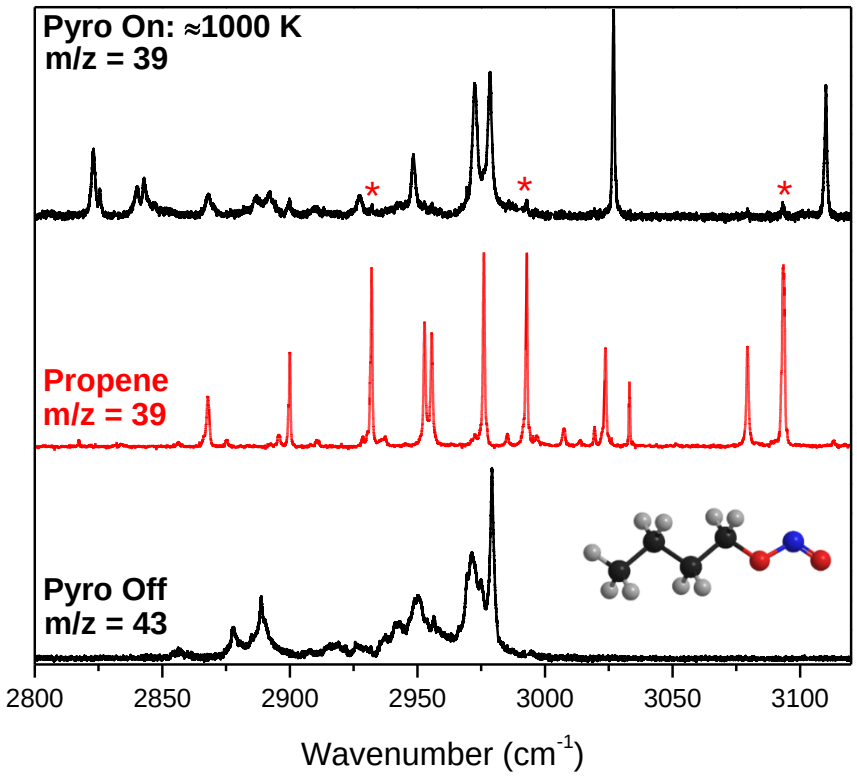

Figure 4.2. IR spectra measured in the CH stretching region. The spectrum of the precursor (bottom) was recorded with *n*-BN flowing through the room-temperature pyrolysis source. The spectrum attributed to the *n*-propyl radical (top) was measured with *n*-BN flowing through the hot (1000 K) pyrolysis source. The middle spectrum was measured with propene gas metered from a lecture bottle into a differentially pumped pickup cell. Peaks marked by * in the *n*-propyl spectrum are attributed to the formation of a small fraction of propene during the precursor decomposition process.

of a single molecule. We therefore conclude that the features in the congested "pyrolysis-on" spectrum in Fig. 4.2 are due mostly to the pickup and detection of a single *n*-propyl radical.

Figure 4.3 shows Difference Mass Spectra (DMS) obtained by fixing the laser frequency to the peak of an isolated vibrational band and scanning the quadrupole from 10 to 82 u in 0.01 u increments. The ion signal is processed with a lock-in amplifier, giving the difference in the

overall mass spectrum with and without laser excitation. This modulation scheme provides an essentially background-free mass spectrum of helium droplets containing the species being resonantly excited by the laser. The bottom DMS corresponds to the most intense precursor vibration at 2979 cm^{-1} (cold pyrolysis source condition), revealing significant depletion signal on masses greater than 43 u (the mass of the *n*-propyl radical). The top DMS was measured with the laser frequency fixed to the symmetric α-CH_2 stretch of *n*-propyl near 3026.9 cm^{-1} (hot pyrolysis source condition), and this DMS shows no significant depletion signal beyond 43 u, with the exception of $(He_n)^+$ ($n \geq 11$) peaks. DMS scans were obtained for each band in the *n*-propyl radical spectrum (top of Fig. 4.2), and each of these bands shows a similar intensity pattern between *m/z* = 39 and 43 u, with no significant contribution from higher mass channels. This confirms that the spectrum obtained in mass channel 39 u with hot pyrolysis source conditions is due almost entirely to the *n*-propyl radical.

4.4.3. *i*-Propyl Infrared Spectrum

The successful detection of the *n*-propyl radical led to the expectation that pyrolysis of isobutyl nitrite [*i*-BN, $(CH_3)_2CHCH_2ONO$] under the same experimental conditions would yield a clean IR spectrum of the *i*-propyl radical. The IR spectra shown in Fig. 4.4 correspond to the precursor, propene, and pyrolytic decomposition products (bottom, middle, and top, respectively). The "pyrolysis-on" spectrum (recorded on *m/z* = 39 u) contains many sharp bands that can be assigned to propene (marked by asterisks) and many others that cannot. The IR spectrum of *i*-BN decomposition products contains an intense absorption at 3062 cm^{-1} consistent with the lone CH_α stretch of the *i*-propyl radical, as assigned in Pacansky's solid-Ar matrix isolation study.[27] The propene spectrum was scaled and subtracted from the "pyrolysis-on" spectrum, and a series of DMS and pressure dependence studies (as discussed above) indicates that the remaining absorptions arise predominantly from droplets containing single *i*-propyl radicals. Figure 4.5 displays both the *n*-propyl (top) and subtracted *i*-propyl (bottom) spectra.

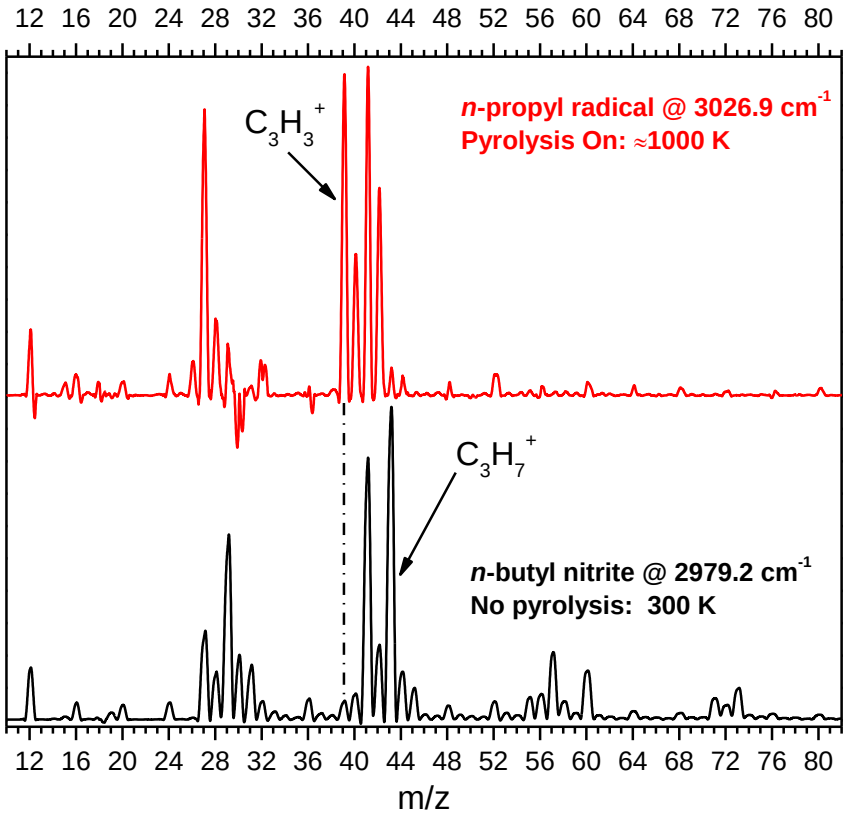

Figure 4.3. Difference mass spectra for the *n*-BN precursor and the *n*-propyl radical. The precursor DMS (bottom) shows laser depletion at masses greater than that of the *n*-propyl radical (43 u), whereas the band assigned to *n*-propyl shows depletion only at masses up to 43 u. The dashed line indicates the mass channel (39 u) used to record the entire laser-induced depletion spectrum shown at the top of Fig. 4.2.

It is perhaps not unreasonable to expect propene to be produced more efficiently via thermal decomposition of *i*-BN (i.e. compared to *n*-BN), as the mechanism is likely due to the unimolecular dissociation of the propyl radicals themselves. Miller and Klippenstein have reported the C_3H_7 potential surface and theoretical kinetics of propyl radical dissociation.[63] Although the barrier height for dissociation via C-H beta scission to produce propene + H is

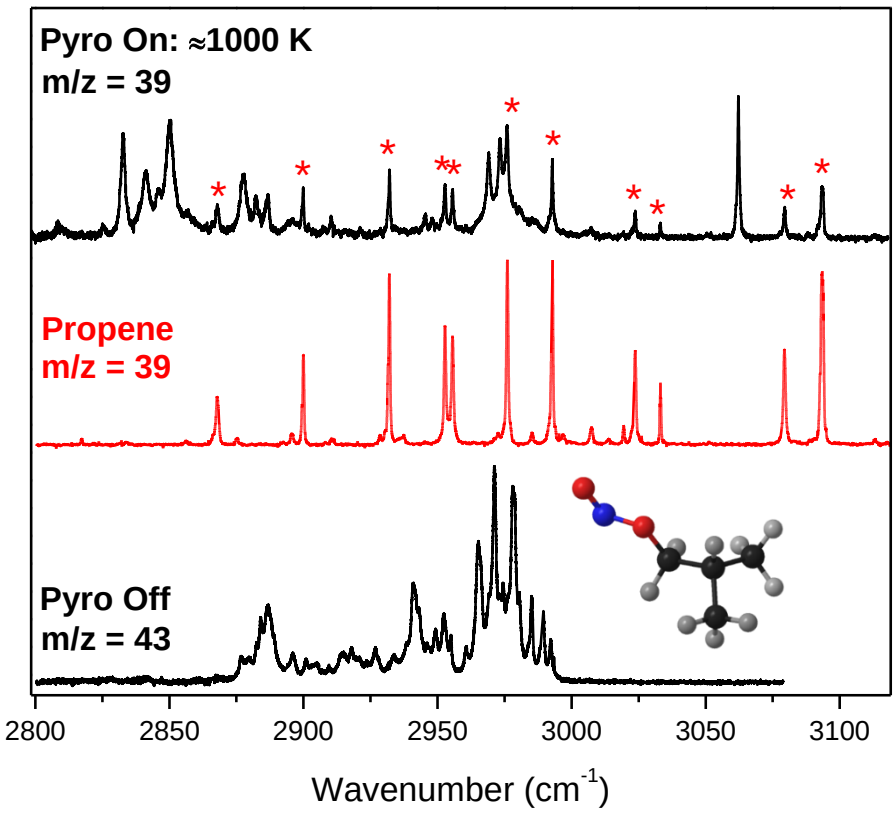

Figure 4.4. IR spectra measured in the CH stretching region. The spectrum of the precursor (bottom) was recorded with *i*-BN flowing through the room-temperature pyrolysis source. The spectrum mostly attributed to the *i*-propyl radical and propene (top) was measured with *i*-BN flowing through the hot (1000 K) pyrolysis source. The middle spectrum was measured with propene gas metered from a lecture bottle into a differentially pumped pickup cell. Peaks marked by * in the *i*-propyl spectrum are attributed to the formation of propene during the precursor decomposition process.

approximately the same for both *n*- and *i*-propyl radicals, *n*-propyl can dissociate via a low barrier C-C beta scission pathway to produce ethylene and methyl radical; in contrast, *i*-propyl cannot. For *n*-propyl dissociation, theory finds the C-C beta scission pathway to dominate at the temperature and pressure conditions relevant to the pyrolysis source used here. Indeed, the C-C

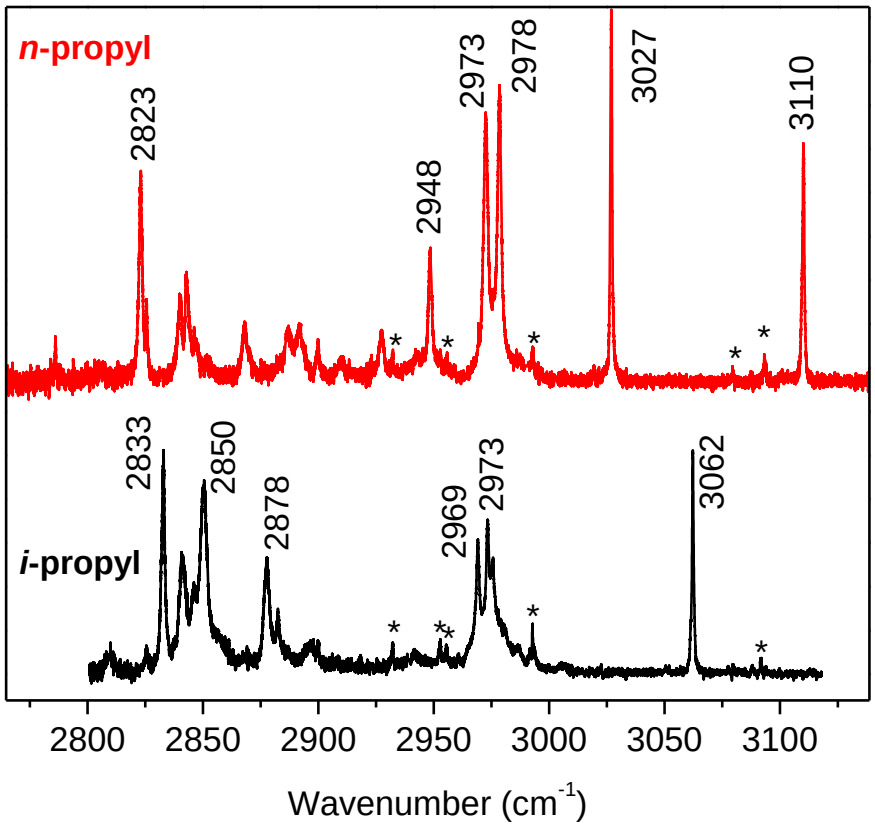

Figure 4.5. IR spectra of the *n*-propyl and *i*-propyl radicals in the CH stretching region. Propene bands have been subtracted from the *i*-propyl spectrum. Residual propene bands are marked by asterisks.

beta scission barrier lies 5 kcal/mol below that for C-H beta scission. The appearance of moderately intense MS features at 15 and 28 u following the thermal decomposition of *n*-BN provides some experimental evidence for this (see top of Fig. 4.1). We note, however, that the vibrational bands of the *n*-propyl dissociation products (C_2H_4 and CH_3) do not appear in the spectrum because they are discriminated against by the choice of mass channel (39 u) to record the laser-induced depletion. In contrast, vibrational excitation of helium-solvated propene results in a large depletion signal in channel 39 u.

4.5. Theoretical Results & Discussion

4.5.1. Harmonic Frequencies

Full tables of CCSD(T)/ANO1 normal coordinates and harmonic frequencies are provided below to assist in interpretation (Tables 4.4-4.5). Values and symmetry labels are given for both the electronic equilibrium structure and for the higher symmetry transition states. The differences between harmonic frequencies at the high and low symmetry structures are also given in the tables. In addition to the changes in the CH stretches, indicated in Tables 4.1-4.2, several of the low frequency modes also display significant changes. However, it should be noted that the correspondences between the normal modes of different structures are determined by best match; thus, any comparisons between their frequencies are necessarily approximate.

4.5.2. Intrinsic Reaction Path Connecting (C_s) *i*-Propyl and (C_{2v}) *i*-Propyl

The IRP corresponds to the black, "electronic" curve in Figure 4.6. The zero-point corrected IRP corresponds to the red, "enthalpic" curve. Here we see a simplification of the potential energy surface when vibrational zero-point effects are accounted for, similarly to what was seen for *n*-propyl.[25] In the case of *i*-propyl, the two wells at C_s symmetry merge into a single well with C_{2v} symmetry, implying that it may be reasonable to treat the system as having higher symmetry.

4.5.3. Comparisons to VPT2+K Computations

4.5.3.1. General Comparisons and Assignments

Figures 4.7-4.10 compare experimental spectra of the *i*- and *n*-propyl radicals to computations employing VPT2+K effective Hamiltonians. The theoretical spectra presented here were produced with a VPT2 treatment that includes all vibrational modes. We note however, that it is sometimes useful to ignore contributions from torsional modes in the VPT2 treatment,

Table 4.4. Qualitative descriptions, symmetries, and CCSD(T)/ANO1 harmonic frequencies of the normal modes of vibration of *i*-propyl radical. The modes are ordered, in the Herzberg convention, based on the symmetries at the electronic global minimum. Symmetry labels at the C_{2v} geometry are also provided.

#	$\Gamma(C_s)$	$\Gamma(C_{2v})$	$\omega(C_s)$	$\omega(C_{2v})$	$\Delta\omega$	Description
1	a'	a_1	3187.05	3209.38	22.33	CHα stretch
2	a'	a_1	3110.98	3116.11	5.13	CH_β symmetric stretch
3	a'	b_1	3048.97	3025.46	-23.51	CHγ antisymmetric stretch in-phase
4	a'	a_1	2974.15	2988.57	14.42	CHγ symmetric stretch in-phase
5	a'	a_1	1495.23	1498.27	3.04	CH_3 in-phase asymmetric bend
6	a'	b_1	1485.62	1482.60	-3.02	CH_3 in-phase asymmetric bend
7	a'	a_1	1412.34	1413.49	1.15	CH_3 umbrella in-phase
8	a'	a_1	1183.57	1185.72	2.15	CH_3 rocking in-plane in-phase
9	a'	b_1	1038.53	1015.05	-23.48	CH_3 rocking out-of-plane in-phase
10	a'	a_1	890.72	895.49	4.77	C-C symmetric stretch
11	a'	b_1	407.82	245.14	-162.68	skeletal bend out-of-plane
12	a'	a_1	347.45	359.64	12.19	skeletal bend in-plane
13	a'	b_1	143.30	174.93	31.63	CH_3 torsion in-phase
14	a''	b_2	3111.58	3117.02	5.44	CH_β antisymmetric stretch
15	a''	a_2	3048.89	3026.66	-22.23	CHγ antisymmetric stretch out-of-phase
16	a''	b_2	2971.28	2985.22	13.94	CHγ symmetric stretch out-of-phase
17	a''	b_2	1484.08	1483.00	-1.09	CH_3 out-of-phase asymmetric bend
18	a''	a_2	1474.22	1470.10	-4.12	CH_3 out-of-phase asymmetric bend
19	a''	b_2	1416.49	1420.37	3.88	CH_3 umbrella out-of-phase
20	a''	b_2	1366.85	1363.06	-3.79	CHα bend in-plane
21	a''	b_2	1150.53	1149.47	-1.06	C-C antisymmetric stretch
22	a''	a_2	945.67	959.12	13.45	CH_3 rocking out-of-plane out-of-phase
23	a''	b_2	934.55	937.14	2.59	CH_3 rocking in-plane out-of-phase
24	a''	a_2	121.65	92.77	-28.88	CH_3 torsion out-of-phase

Table 4.5. Qualitative descriptions, symmetries, and CCSD(T)/ANO0 harmonic frequencies of the normal modes of vibration of *n*-propyl radical. The modes are ordered, in the Herzberg convention, based on the symmetries at the electronic global minimum. Symmetry labels at the C_s geometry are also provided.

#	$\Gamma(C_s)$	$\omega(C_1)$	$\omega(C_s)$	$\Delta\omega$	Description
1	a'	3262.40	3267.67	5.27	α-CH_2 antisymmetric stretch
2	a'	3152.94	3157.75	4.81	α-CH_2 symmetric stretch
3	a'	3131.91	3131.29	-0.62	γ-CH_3 antisymmetric stretch
4	a''	3126.13	3126.59	0.46	γ-CH_3 antisymmetric stretch
5	a'	3059.98	3043.68	0.58	γ-CH_3 symmetric stretch
6	a''	3043.10	3027.92	-15.18	β-CH_2 antisymmetric stretch
7	a'	2981.93	3000.37	18.44	β-CH_2 symmetric stretch
8	a'	1511.98	1512.78	0.80	γ-CH_3 in-plane asymmetric bend
9	a''	1505.69	1505.90	0.21	γ-CH_3 out-of-plane asymmetric bend
10	a'	1480.89	1480.69	-0.20	β-CH_2 scissor
11	a'	1470.47	1470.50	0.03	α-CH_2 scissor
12	a'	1415.31	1417.10	1.79	γ-CH_3 umbrella
13	a'	1363.03	1364.94	1.91	β-CH_2 wagging
14	a''	1279.99	1276.65	-3.34	β-CH_2 and γ-CH_3 out-of-phase rocking
15	a'	1177.42	1167.83	-9.59	collective in-phase in-plane rocking
16	a'	1091.71	1093.47	1.76	C-C antisymmetric stretch
17	a''	1059.14	1054.56	-4.58	β-CH_2 and γ-CH_3 in-phase rocking
18	a'	919.12	924.61	5.49	collective out-of-phase in-plane rocking
19	a'	886.08	879.92	-6.16	C-C symmetric stretch
20	a''	755.33	764.07	8.74	out-of-plane skeletal bend
21	a''	459.26	395.67	-63.59	α-CH_2 wagging
22	a'	364.61	372.09	7.48	in-plane skeletal bend
23	a''	256.51	255.44	-1.07	γ-CH_3 torsion
24	a''	129.55	124.27	-5.28	α-CH_2 torsion

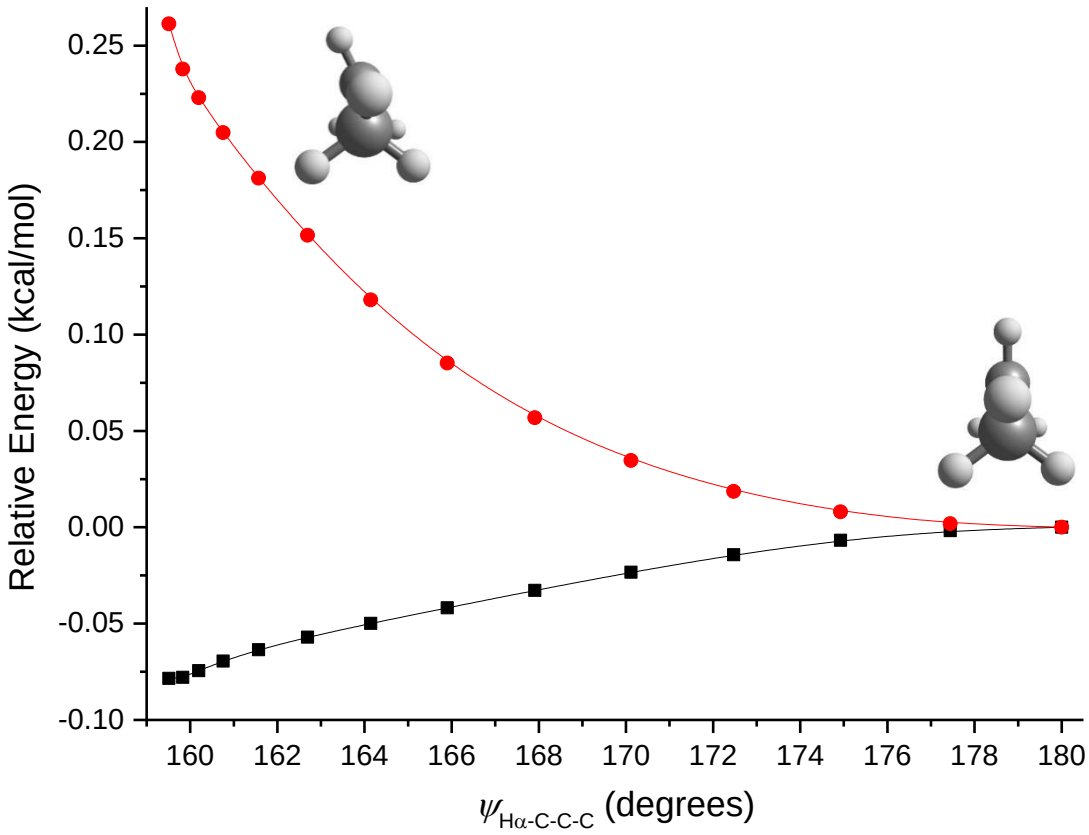

Figure. 4.6. Electronic and enthalpic intrinsic reaction paths. The IRP connects the C_s electronic global minimum of *i*-propyl with its C_{2v} first-order saddle-point geometry, and thus the motion is largely characterized by the out-of-plane bending of the CH_α hydrogen. The value of the dihedral bending angle between the symmetrically-equivalent Hα-C-C planes is plotted on the x-axis, rather than the mass-weighted intrinsic reaction coordinate because its physical meaning is more obvious. Note that the relative energy of each curve is defined to be zero at the C_{2v} geometry, so direct comparisons between energies on different curves are not meaningful.

because torsional modes are often poorly approximated as harmonic oscillators at zeroth-order and can have unphysically large force constants. The difference between anharmonic frequencies obtained with and without the treatment of torsions may be taken as a measure of how strongly coupled a vibration is to the torsional degrees of freedom.[44] By extension, the frequency difference is a metric of the inaccuracy of VPT2 for those transitions, brought about by the poor theoretical treatment of torsional modes.[25] When we exclude low frequency torsional modes, the

simulated CH stretch spectra do not change qualitatively, although the magnitudes of a few frequencies change by as much as 10-25 cm^{-1} (Tables 4.1 and 4.2).[25, 44] A detailed discussion of simulations that employ both approaches can be found in Section 4.5.3.2.

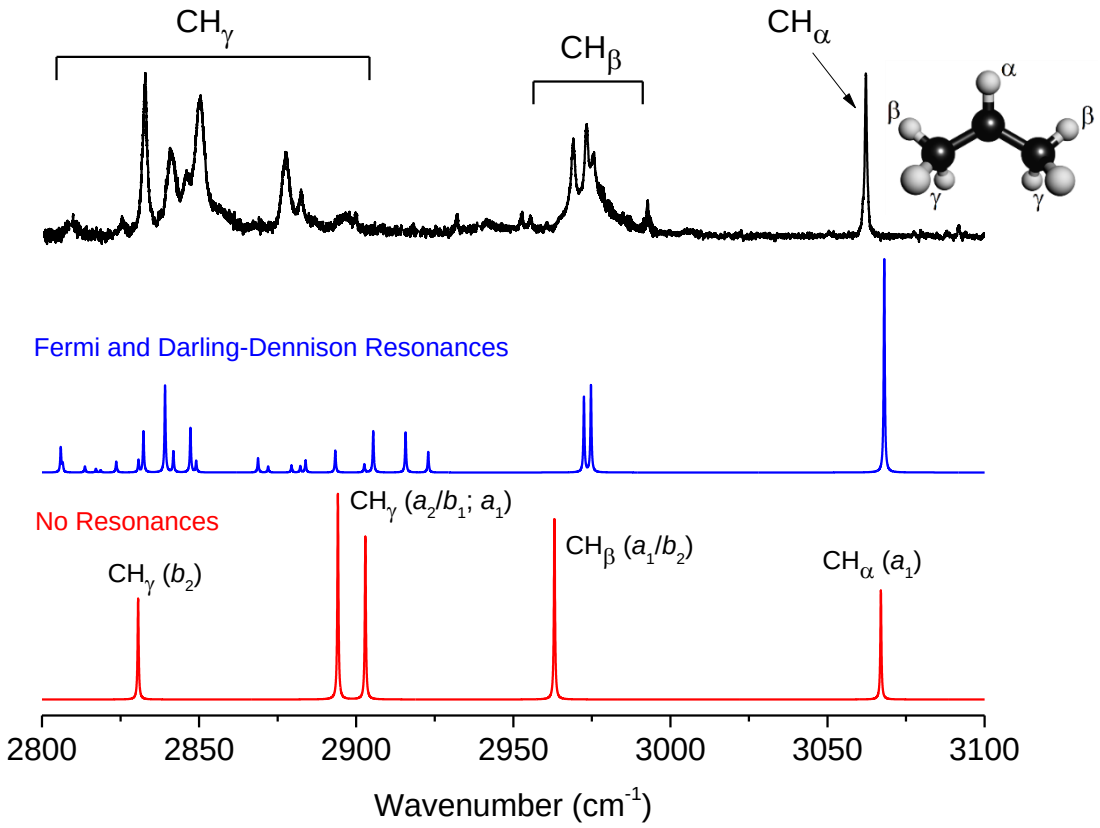

Figure 4.7. Comparison of the experimental *i*-propyl spectrum (top, black) to VPT2 simulated spectra. The bottom (red) trace is the result of a full VPT2 treatment with no consideration of resonances. The blue trace includes explicit theoretical treatment of Fermi and Darling-Dennison resonances. Labels correspond to the hydrogen atoms primarily involved in the motion, although the normal modes are observed to be rather mixed linear combinations of individual CH oscillators, with the exception being the lone CH_α stretch. The frequencies are the eigenvalues of a 28-state effective Hamiltonian. Symmetry labels are included on the bottom trace; these are for the C_{2v} average structure (minimum energy structure on the zero-Kelvin enthalpic surface), although we note that the computation is carried out at the C_s symmetry electronic global minimum structure. When fundamental transitions are nearly degenerate, symmetry labels are separated by a slash.

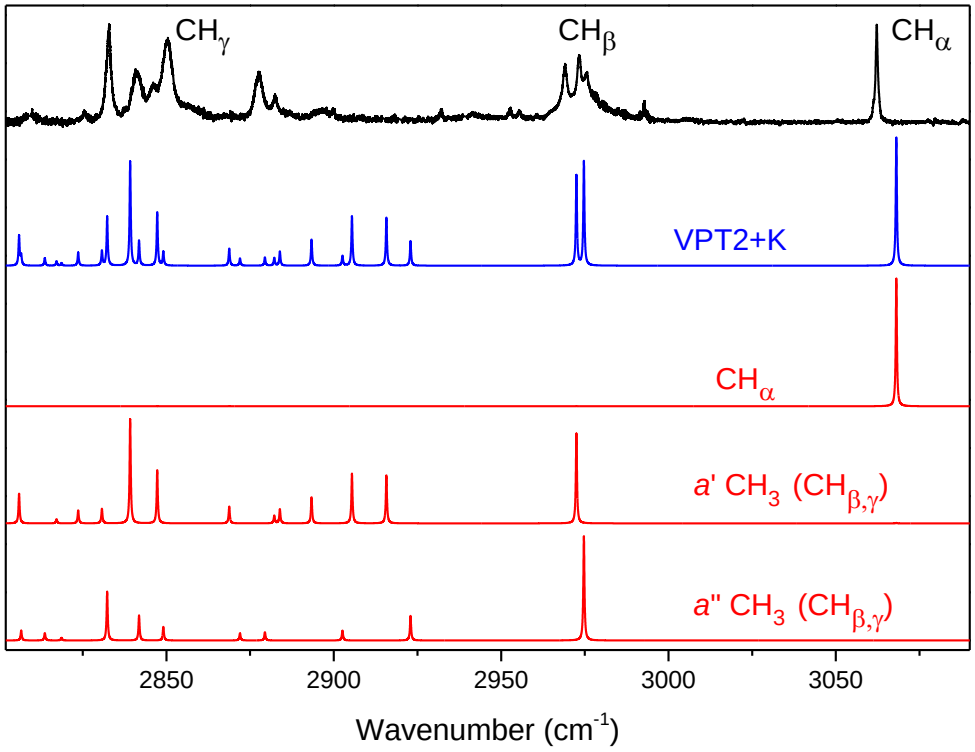

Figure 4.8. Dipole decomposition of VPT2+K simulation (*i*-propyl). The experimental spectrum, the complete VPT2+K simulation, and the dipole decomposed simulations are shown as black, blue, and red traces, respectively. Contributions from methyl CH oscillators are separated by symmetry due to the non-local nature of the analysis. Symmetry labels are associated with the C_s symmetry electronic global minimum of *i*-propyl.

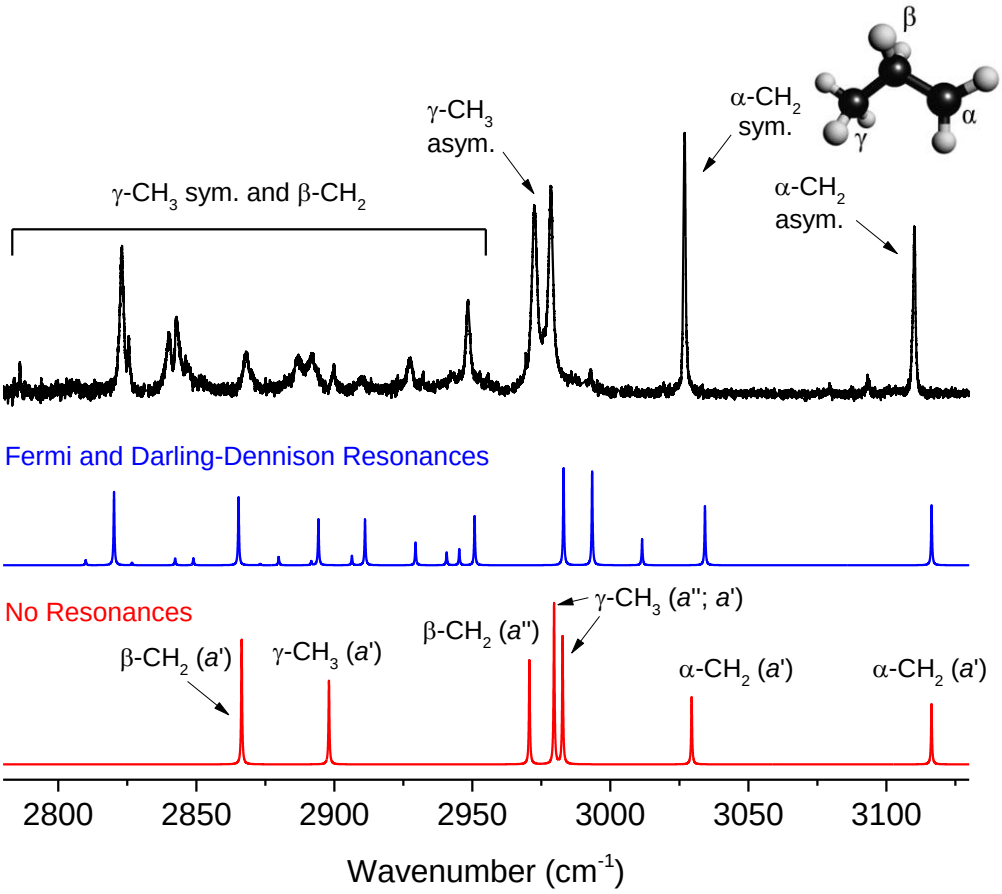

Figure 4.9. Comparison of the experimental *n*-propyl spectrum (top, black) to VPT2 simulated spectra. The bottom (red) trace represents a full VPT2 treatment with no resonance treatments whatsoever. The blue trace includes explicit treatment of Fermi and Darling-Dennison resonances. Labels correspond to the carbon atoms around which the vibrations are localized. The frequencies are the eigenvalues of a 22-state effective Hamiltonian. Symmetry labels are included on the bottom trace; these are for the C_s average structure (minimum energy structure on the zero-Kelvin enthalpic surface), although we note that the computation is carried out at the C_1 symmetry electronic global minimum structure.

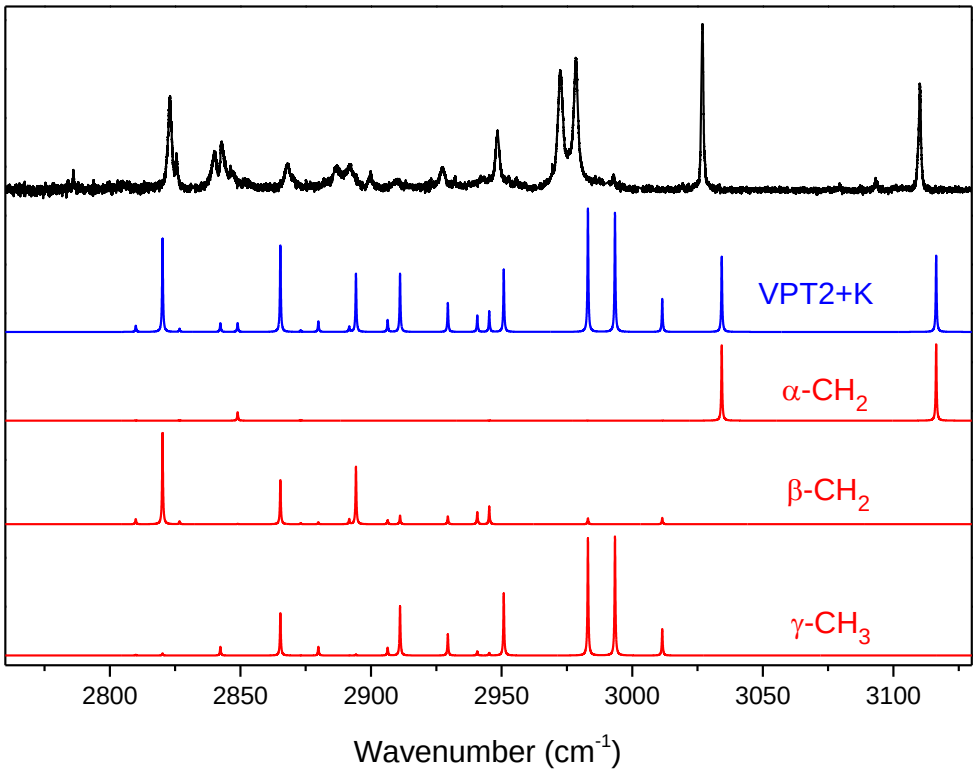

Figure 4.10. Dipole decomposition of VPT2+K simulation (*n*-propyl). The experimental spectrum, the complete VPT2+K simulation, and the dipole decomposed simulations are shown as black, blue, and red traces, respectively. As a result of the somewhat local nature of the *n*-propyl CH stretches, bright state normal modes are assigned as either α-CH_2, β-CH_2 or γ-CH_3.

Figure 4.7 compares the VPT2 (red) and VPT2+K (blue) simulations to the experimental (black) *i*-propyl spectrum. The higher frequency region of the simulated spectrum (above 2950 cm^{-1}) has a similar appearance with and without resonance treatments. The VPT2 analysis alone is capable of reproducing the band origin for the lone CH_α stretch. With an explicit resonance treatment, the near degeneracy of the two CH_β transitions is lifted, and the transitions are blue shifted into rather good agreement with the experimental spectral features. The lower frequency CH_γ region changes dramatically after resonant interactions are taken into account. This illustrates that the VPT2 analysis is insufficient for this spectral region; mechanical

anharmonicity and intensity borrowing must be explicitly accounted for when modeling the low frequency CH stretching regions of hydrocarbons. Indeed, it is well-known that this spectral region is prone to resonance interactions involving CH stretches and overtones/combinations of CH_n bending modes that have fundamentals in the 1350 to 1500 cm^{-1} range.[32, 34, 36-37]

In presenting our effective Hamiltonians, we adopt the omega notation of Stanton and Matthews[57] for our deperturbed frequencies, where the vibrational modes are in subscript and the number of quanta in each mode are written as a secondary subscript. Fundamentals have no second subscript. Numerical factors are products of harmonic oscillator integrals, Taylor series coefficients, and the number of times the given force constant appears in the potential expansion Additional commas and semicolons are included in resonance constant subscripts when helpful to eliminate ambiguity with double-digit mode numbers. Between any two fundamentals, between two combination tones with a shared quantum, and between an overtone and a combination tone that share a quantum, the coupling matrix element is a sum of resonance *K* constants.[60] When matrix elements of this form are required, they are indicated by a capital *D*, with any numerical factors absorbed into them. They take the following forms.

$$D_{i,j} = \frac{3}{4}\left(K_{i,i;i,j} + K_{i,j;j,j}\right) + \frac{1}{4}\sum_{k\neq\{i,j\}}^{3N-6} K_{i,k;j,k} \tag{4.4}$$

$$D_{i,i;i,j} = \frac{3}{2\sqrt{2}}\left(2K_{i,i;i,j} + K_{i,j;j,j}\right) + \frac{1}{2\sqrt{2}}\sum_{k\neq\{i,j\}}^{3N-6} K_{i,l;j,l} \tag{4.5}$$

$$D_{i,k;j,k} = \frac{3}{4}\left(K_{i,i;i,j} + K_{i,j;j,j} + K_{i,k;j,k}\right) + \frac{1}{4}\sum_{l\neq\{i,j,k\}}^{3N-6} K_{i,l;j,l} \tag{4.6}$$

The effective Hamiltonians used to model *n*-propyl's CH stretching region are given below (Eqn. 4.7-4.8). They are separated into a' and a'' blocks, respectively.

$$\begin{pmatrix} \Omega_{6_1 5_1} & \frac{\phi_{654}}{2\sqrt{2}} & \frac{1}{2\sqrt{2}}K_{17,17;6,5} & D_{66,65} & D_{55,56} \\ \frac{\phi_{654}}{2\sqrt{2}} & \Omega_4 & \frac{\phi_{17,17,4}}{4} & \frac{\phi_{664}}{4} & \frac{\phi_{554}}{4} \\ \frac{1}{2\sqrt{2}}K_{17,17;6,5} & \frac{\phi_{17,17,4}}{4} & \Omega_{17_2} & \frac{1}{2}K_{17,17;6,6} & \frac{1}{2}K_{17,17;5,5} \\ D_{66,65} & \frac{\phi_{664}}{4} & \frac{1}{2}K_{17,17;6,6} & \Omega_{6_2} & \frac{1}{2}K_{66,55} \\ D_{55,56} & \frac{\phi_{554}}{4} & \frac{1}{2}K_{17,17;5,5} & \frac{1}{2}K_{66,55} & \Omega_{5_2} \end{pmatrix} \tag{4.7}$$

$$\begin{pmatrix} \Omega_{16} & \frac{\phi_{19,16,7}}{2\sqrt{2}} & \frac{\phi_{18,16,5}}{2\sqrt{2}} & \frac{\phi_{18,16,6}}{2\sqrt{2}} & D_{16,15} & \frac{\phi_{17,16,6}}{2\sqrt{2}} & \frac{\phi_{17,16,5}}{2\sqrt{2}} \\ \frac{\phi_{19,16,7}}{2\sqrt{2}} & \Omega_{19_1 7_1} & 0 & 0 & \frac{\phi_{19,15,7}}{2\sqrt{2}} & 0 & 0 \\ \frac{\phi_{18,16,5}}{2\sqrt{2}} & 0 & \Omega_{18_1 5_1} & D_{19,7;18,6} & \frac{\phi_{18,15,5}}{2\sqrt{2}} & 0 & D_{18,5;17,5} \\ \frac{\phi_{18,16,6}}{2\sqrt{2}} & 0 & D_{19,7;18,6} & \Omega_{18_1 6_1} & \frac{\phi_{18,15,6}}{2\sqrt{2}} & D_{18,6;17,6} & 0 \\ D_{16,15} & \frac{\phi_{19,15,7}}{2\sqrt{2}} & \frac{\phi_{18,15,5}}{2\sqrt{2}} & \frac{\phi_{18,15,6}}{2\sqrt{2}} & \Omega_{15} & \frac{\phi_{17,15,6}}{2\sqrt{2}} & \frac{\phi_{17,15,5}}{2\sqrt{2}} \\ \frac{\phi_{17,16,6}}{2\sqrt{2}} & 0 & 0 & D_{18,6;17,6} & \frac{\phi_{17,15,6}}{2\sqrt{2}} & \Omega_{17_1 6_1} & D_{17,6;17,5} \\ \frac{\phi_{17,16,5}}{2\sqrt{2}} & 0 & D_{18,5;17,5} & 0 & \frac{\phi_{17,15,5}}{2\sqrt{2}} & D_{17,6;17,5} & \Omega_{17_1 5_1} \end{pmatrix} \tag{4.8}$$

The effective Hamiltonian used for *i*-propyl can be separated into three blocks (Eqn. 4.9-4.11).

$$\begin{pmatrix} \Omega_2 & \frac{\phi_{11,11,2}}{4} \\ \frac{\phi_{11,11,2}}{4} & \Omega_{11_2} \end{pmatrix} \tag{4.9}$$

$$\begin{pmatrix} \Omega_{10_2} & \frac{\phi_{10,10,7}}{4} & \frac{1}{2\sqrt{2}}K_{10,10;11,8} & D_{10,10;10,8} \\ \frac{\phi_{10,10,7}}{4} & \Omega_7 & \frac{\phi_{11,8,7}}{2\sqrt{2}} & \frac{\phi_{10,8,7}}{2\sqrt{2}} \\ \frac{1}{2\sqrt{2}}K_{10,10;11,8} & \frac{\phi_{11,8,7}}{2\sqrt{2}} & \Omega_{11_1 8_1} & D_{11,8;10,8} \\ D_{10,10;10,8} & \frac{\phi_{10,8,7}}{2\sqrt{2}} & D_{11,8;10,8} & \Omega_{10_1 8_1} \end{pmatrix} \tag{4.10}$$

$$\begin{pmatrix} \Omega_{12_2} & \frac{1}{2}K_{12,12;9,9} & \frac{1}{2}K_{12,12;8,8} & \frac{\phi_{12,12,6}}{4} \\ \frac{1}{2}K_{12,12;9,9} & \Omega_{9_2} & \frac{1}{2}K_{99,88} & \frac{\phi_{996}}{4} \\ \frac{1}{2}K_{12,12;8,8} & \frac{1}{2}K_{99,88} & \Omega_{8_2} & \frac{\phi_{886}}{4} \\ \frac{\phi_{12,12,6}}{4} & \frac{\phi_{996}}{4} & \frac{\phi_{886}}{4} & \Omega_6 \end{pmatrix} \tag{4.11}$$

Dipole decomposition[34] offers a useful way to interpret the results of the VPT2+K simulations (Figs. 4.8 and 4.9). This entails separating the total intensity of each peak into

contributions from different bright state CH oscillators. In the *i*-propyl spectrum (Fig. 4.8), the *a'* CH_α oscillator located at the radical site gives rise to the single peak at highest frequency. The next highest frequency features are assigned to fundamental transitions of the methyl CH_β oscillators, the higher frequency transition having *a''* symmetry and the lower frequency transition having *a'* symmetry. These fundamentals do not exhibit strong coupling to any two-quanta states; and thus, they are qualitatively reproduced by all of our simulations. The lower frequency CH_γ region proves to be a challenge for the VPT2+K approach. A significant portion of the total transition intensity is distributed between 2900 and 2930 cm^{-1}. The experimental spectrum, however, contains no spectral features in this region. The spectral pattern below 2950 cm^{-1} is rather sensitive to the resonance criteria and to the values of the Darling-Dennison resonance constants. Many examples of this sensitivity can be found in Section 4.5.3.2.

Figure 4.9 compares the VPT2 (red) and VPT2+K (blue) simulations to the experimental *n*-propyl spectrum (black). The two highest frequency peaks at 3027 and 3110 cm^{-1} are well-predicted, and as with *i*-propyl, these features have a similar appearance with and without the explicit resonance treatment. These bands are definitively assigned to the symmetric and antisymmetric α-CH_2 stretching fundamentals localized on the radical center. The antisymmetric γ-CH_3 stretch fundamentals around 2975 cm^{-1} agree well with predictions from full VPT2; however, the predicted frequencies are blue-shifted when resonances are considered, and an additional low intensity peak is predicted near 3010 cm^{-1}, which is not observed experimentally. In contrast to predictions for *i*-propyl, VPT2+K does a reasonable job of simulating the lower frequency region.

As a result of the more local nature of the *n*-propyl CH stretches, we can assign labels to the bright state normal modes that correspond to either α-CH_2, β-CH_2 or γ-CH_3. The dipole decomposition shown in Fig. 4.10 is obtained by analyzing the various α, β, γ- bright state contributions to the eigenvalues obtained from the VPT2+K analysis. From this we find that the

n-propyl spectral complexity between 2800 and 2960 cm^{-1} derives from resonant interactions involving either the β-CH_2 or γ-CH_3 oscillators. Contributions from oscillators localized on the β and γ carbons are spread out, but in general, β-CH_2 contributions are observed in the lower frequency region, with the γ-CH_3 intensity contributions falling largely between 2900 cm^{-1} and 3000 cm^{-1}. For a few of the simulated peaks that closely match experiment, 2827 cm^{-1}, 2951 cm^{-1}, and 2873 cm^{-1}, dipole decomposition indicates that they derive their transition intensity from the β-CH_2 oscillators, the γ-CH_3 oscillators, and a mixture of both, respectively. The remaining peaks are predicted less confidently, and definitive assignments of these are not possible with the normal mode VPT2+K treatment.

For the case of VPT2+K, increasing the number of states in the effective Hamiltonian can improve the description of the anharmonic coupling that dominates in the low frequency CH stretching region (for both *n*- and *i*-propyl; results shown in Figs. 4.6 and 4.8). However this can come at the cost of accurate high frequency stretch predictions. This point has been made by Stanton and co-workers.[57] It is appealing to think that, as the effective Hamiltonian matrix grows in size, and the eigenvalues approach the variational solution to the semi-diagonal quartic potential, the accuracy would improve, but this is often not the case. The reduced accuracy of frequencies computed with large effective Hamiltonians, for relatively uncoupled CH stretching modes (e.g. α-CH_2 modes in *n*-propyl), can be rationalized as owing to an upset of the fortuitous error-cancellation, from which the full VPT2 treatment benefits. Also, using our effective Hamiltonians, some interactions with states of lower frequency than the CH stretch fundamentals are treated variationally, yet all interactions with higher frequency states (excluding the typically negligible 1:1 resonances with other single-quantum CH stretching states) are still treated perturbatively. This has a biasing effect upon the anharmonic corrections because interactions that raise and lower the energy of the vibrational states are treated in different ways. Perhaps the best example of this effect, in our study, is seen for the γ-CH_3 asymmetric stretching modes of *n*-

propyl, which are observed experimentally at 2973 and 2978 cm^{-1}. When relying upon the Martin test to identify resonances,[56] requiring smaller effective Hamiltonians, these modes are predicted rather accurately (Fig. 4.12). The Martin test with a threshold value of 0.5 cm^{-1} does not predict any resonances involving these modes, so they receive the full VPT2 treatment, not requiring deperturbation. Expansion of the effective Hamiltonian to include all CH stretch fundamentals and scissor overtones/combinations significantly degrades the quality by which these transitions are predicted (Fig. 4.10).

4.5.3.2. Hamiltonian Size and Influence of Torsional Couplings

We present the full tables of anharmonic frequencies (Tables 4.6-4.7) and theoretical spectra (Figures 4.11-4.12) generated for all variations and modifications of the VPT2 procedure employed in this study (with/without torsion, resonance treatment, and Darling-Dennison coupling).

The spectral complexity of *i*-propyl's CH stretching region is not well reproduced by VPT2 (Figure 4.11). For the simulations that include torsion, the lone CH stretch at 3062.2 cm^{-1} is predicted at 3067.0 cm^{-1}, blue shifted by 4.8 cm^{-1}. When methylene torsion is ignored, it is predicted at 3055.8 cm^{-1}, redshifted by 6.4 cm^{-1}. The shapes and positions of the lower frequency bands are not reproduced. Consistently it is seen that ignoring the torsional modes worsens the agreement, sometimes by more than ten wavenumbers. Inclusion of Darling-Dennison couplings does not obviously lead to a better agreement; in fact, their inclusion tends to produce only small shifts in the frequency regime that we are concerned with. However their implementation is relatively simple and does not add significant computational time, as the required force constants are already computed by CFOUR (with the exception of force constants of the form, ϕ_{ijkl}). Elsewhere, a strong case has been made for the effectiveness of the resonance constants, for predicting the stretching overtone frequencies of water.[57]

Table. 4.6. Harmonic and VPT2+K frequencies of the *i*-propyl radical (cm^{-1}). Harmonic intensities were computed at the CCSD(T)/ANO2 level of theory. Resonances were identified with the Martin test. Symmetry labels given are for the electronic minimum.

Mode	Γ	Harmonic	VPT2 w/ Torsion	VPT2 w/o Torsion	Difference	Intensity (km/mol)
1	A'	3187.05	3066.99	3055.81	-11.18	21.32
2	A'	3110.98	2963.13	2960.92	-2.21	15.00
3	A'	3048.97	2894.18	2901.03	6.84	35.82
4[a]	A'	2974.15	2844.58	2834.42	-10.17	31.86
5	A'	1495.23	1454.80	1451.43	-3.37	5.01
6	A'	1485.62	1441.40	1440.97	-0.43	13.74
7	A'	1412.34	1379.87	1379.11	-0.76	3.87
8	A'	1183.57	1309.57	1154.60	-154.97	2.49
9	A'	1038.53	1001.66	1012.13	10.48	0.05
10	A'	890.72	876.57	874.67	-1.90	1.42
11	A'	407.82	249.25	318.67	69.42	16.09
12	A'	347.45	315.59	329.18	13.59	11.14
13	A'	143.30	66.32	N/A	N/A	0.32
14	A''	3111.58	2963.07	2961.20	-1.87	21.05
15[b]	A''	3048.89	2878.68	2885.14	6.45	4.81
16[b]	A''	2971.28	2830.94	2820.80	-10.13	19.73
17	A''	1484.08	1440.23	1439.46	-0.77	0.44
18	A''	1474.22	1432.96	1430.09	-2.87	0.90
19	A''	1416.49	1385.53	1382.36	-3.17	9.08
20	A''	1366.85	1342.55	1343.31	0.76	2.13
21	A''	1150.53	1124.90	1125.17	0.27	0.09
22	A''	945.67	937.01	927.69	-9.33	0.90
23	A''	934.55	925.17	920.76	-4.41	0.02
24	A''	121.65	82.25	N/A	N/A	0.01

[a] Deperturbed value is given; involved in a resonance polyad (torsional modes kept) with eigenvalues: 2911.26, 2894.31, 2884.87, 2877.96, 2831.86 (cm^{-1}).

[b] Deperturbed value is given; involved in a resonance polyad (torsional modes kept) with eigenvalues: 2929.58, 2899.83, 2881.66, 2868.52, 2844.29, 2834.55, 2742.65 (cm^{-1}).

Table. 4.7. Harmonic and VPT2+K frequencies of the *n*-propyl radical (cm^{-1}). Harmonic intensities were computed at the CCSD(T)/ANO1 level of theory. Note that our *n*-propyl force field was identical to the one used by Li et al.[25] It can be seen that the frequencies in their Table S3 are exactly reproduced, except for the resonant modes, to which we give different treatment. Resonances were identified with the Martin test.[56]

Mode	Harmonic	VPT2 w/ Torsion	VPT2 w/o Torsion	Difference	Intensity (km/mol)
1	3262.40	3116.34	3090.04	-26.30	12.28
2[a]	3152.94	3015.96	3012.29	-3.67	13.80
3	3131.91	2982.70	2983.31	0.61	26.12
4	3126.13	2979.61	2978.87	-0.74	32.88
5	3059.98	2898.05	2915.33	17.28	17.14
6[b]	3043.10	2897.27	2896.23	-1.05	21.26
7[c]	2981.93	2844.54	2833.43	-11.11	25.54
8	1511.98	1500.29	1499.69	-0.59	3.25
9	1505.69	1463.90	1463.77	-0.12	6.00
10	1480.89	1434.16	1435.18	1.02	1.23
11	1470.47	1437.76	1436.92	-0.84	2.15
12	1415.31	1384.76	1381.60	-3.16	1.99
13	1363.03	1327.56	1329.23	1.66	2.14
14	1279.99	1243.61	1246.61	3.00	0.13
15	1177.42	1059.04	1150.31	91.27	0.33
16	1091.71	1067.52	1066.95	-0.57	0.14
17	1059.14	1073.10	1042.69	-30.41	1.34
18	919.12	947.47	939.38	-8.09	1.29
19	886.08	1061.08	869.79	-191.28	0.11
20	755.33	750.59	744.45	-6.14	0.87
21	459.26	418.23	433.74	15.51	45.24
22	364.61	370.08	365.11	-4.96	3.03
23	256.51	233.17	242.81	9.64	0.07
24	129.55	15.32	N/A	N/A	0.24

[a] Deperturbed value is given; involved in a Fermi resonance (torsional modes kept) with eigenvalues: 3033.89, 2856.51 (cm^{-1}).

[b] Deperturbed value is given; involved in a resonance polyad (torsional modes kept) with eigenvalues: 3004.69, 2941.88, 2895.41, 2742.37 (cm^{-1}).

[c] Deperturbed value is given; involved in a resonance polyad (torsional modes kept) with eigenvalues: 2936.81, 2931.23, 2880.74, 2824.80 (cm^{-1}).

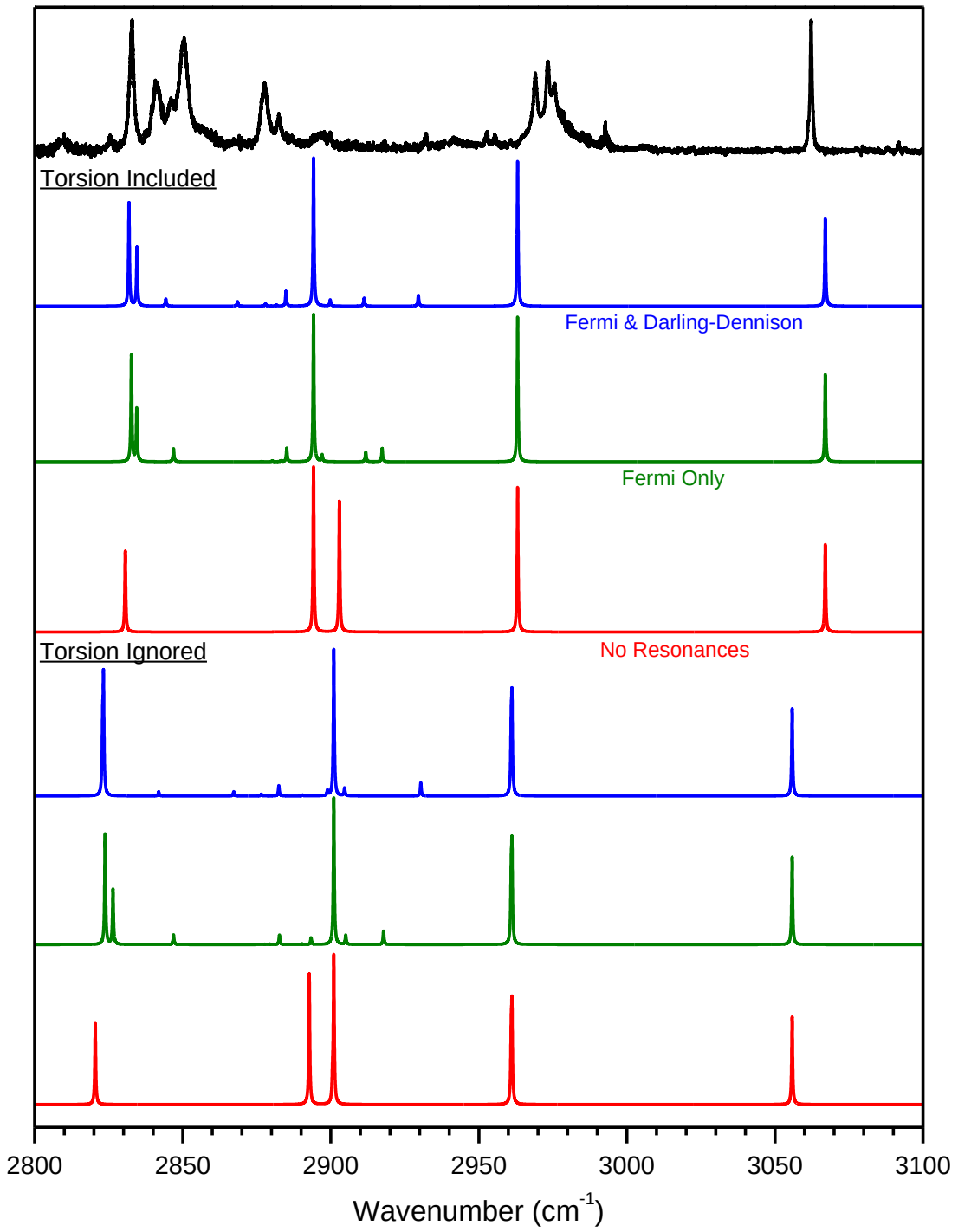

Figure. 4.11. Simulated *i*-propyl spectra with and without the methyl torsional modes, ν_{13} and ν_{24}, included in the VPT2 procedure, and with and without treatment of Fermi resonances or inclusion of Darling-Dennison resonance constants. Resonances were identified with the Martin test.

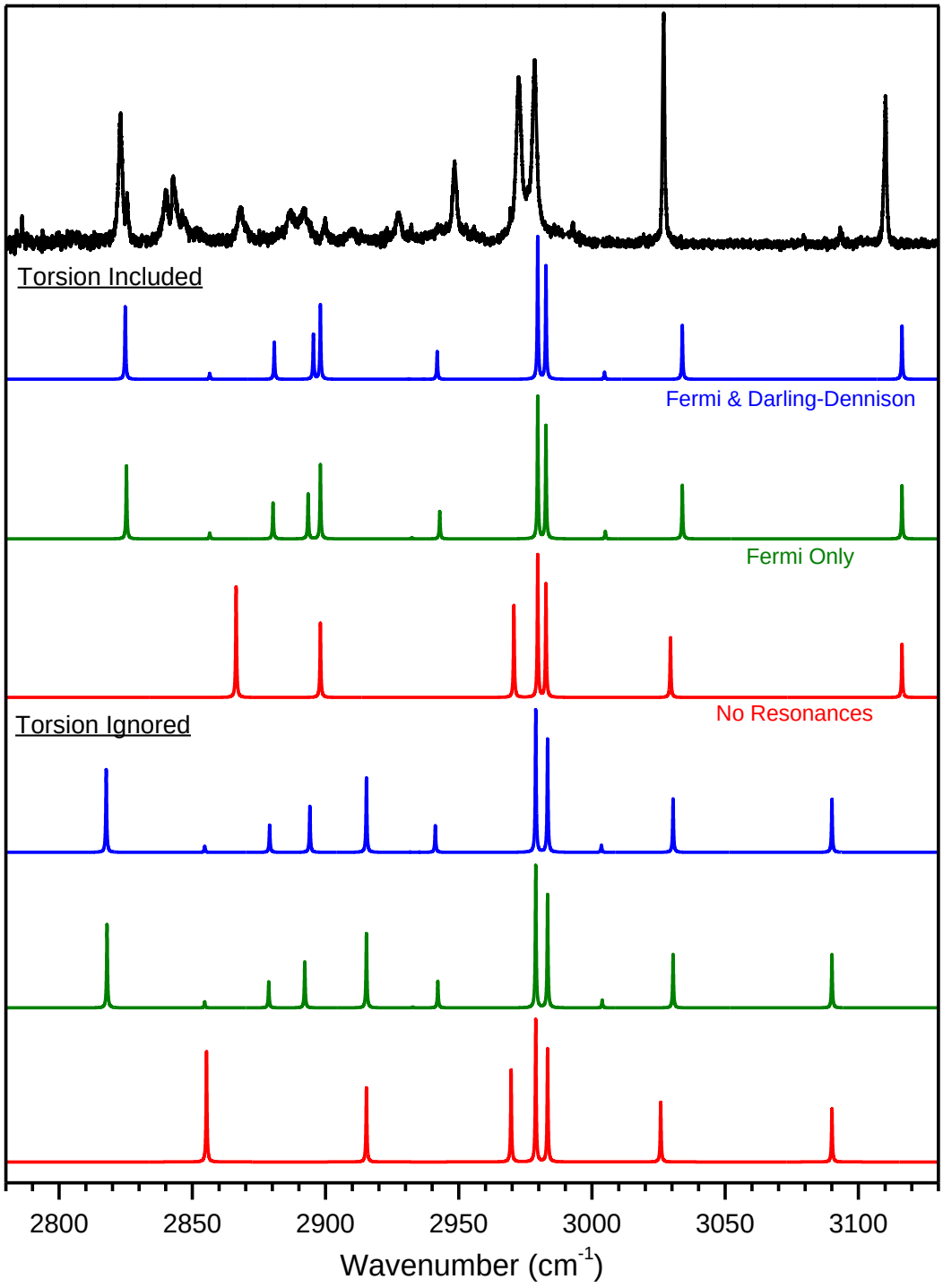

Figure. 4.12. Simulated *n*-propyl spectra with and without the methylene torsional mode, ν_{24}, included in the VPT2 procedure, and with and without treatment of Fermi resonances or inclusion of Darling-Dennison resonance constants. Resonances were identified with the Martin test.

As seen with *i*-propyl, neglect of torsion in *n*-propyl (Figure 4.12) leads to quantitatively worse frequency agreement. Consider the frequency difference between the α-CH_2 transitions. Experimentally, they are separated by 83 cm^{-1}, and the simulations with torsion correctly predict that to within 1 cm^{-1}. Simulations that neglect torsion instead predict that those transitions are separated by 60 cm^{-1}. However unlike with *i*-propyl, VPT2+K does a reasonable job at simulating *n*-propyl's CH stretches, with the strong transitions at 2823.0 cm^{-1} and 2948.5 cm^{-1} being some of the most consistently predicted by different simulations. For the resonance treatment scheme using smaller effective Hamiltonians, the same types of comparisons with and without torsions were generated. They are presented on the following pages (Figures 4.13 and 4.14).

4.5.4. Comparisons to Local Mode Hamiltonian Predictions

Figures 4.15 and 4.16 compare the local mode model Hamiltonian predictions to the experimental *n*- and *i*-propyl spectra, respectively. As described in Section 4.3.2, the basis states consist of the entire set of localized CH stretch fundamentals and the overtones/combinations of localized HCH scissor modes. The size of the effective Hamiltonians are the same as for the VPT2+K treatment, namely 22 states and 28 states for *n*- and *i*-propyl, respectively. We emphasize again that both the scale factors and the Fermi coupling parameters used to generate the effective Hamiltonians were refined in previous studies of alkyl CH stretch spectra,[34] and they are used here *without* modification.

For the *n*-propyl spectra shown in Fig. 4.15, the format is the same as in Fig. 4.10. The dipole decompositions for each CH_n group are shown as red traces, and the blue trace corresponds to the results from the "Full Model" local mode predictions. Overall, there is good agreement between experiment and theory, with the largest differences being in the higher frequency region (above 3000 cm^{-1}). The quality of the agreement in the high frequency region is a measure of the transferability of the scale factors that adjust the harmonic frequencies.[34] We find the local mode frequencies of the α-CH_2 group to be underestimated using these scale factors. In addition, the

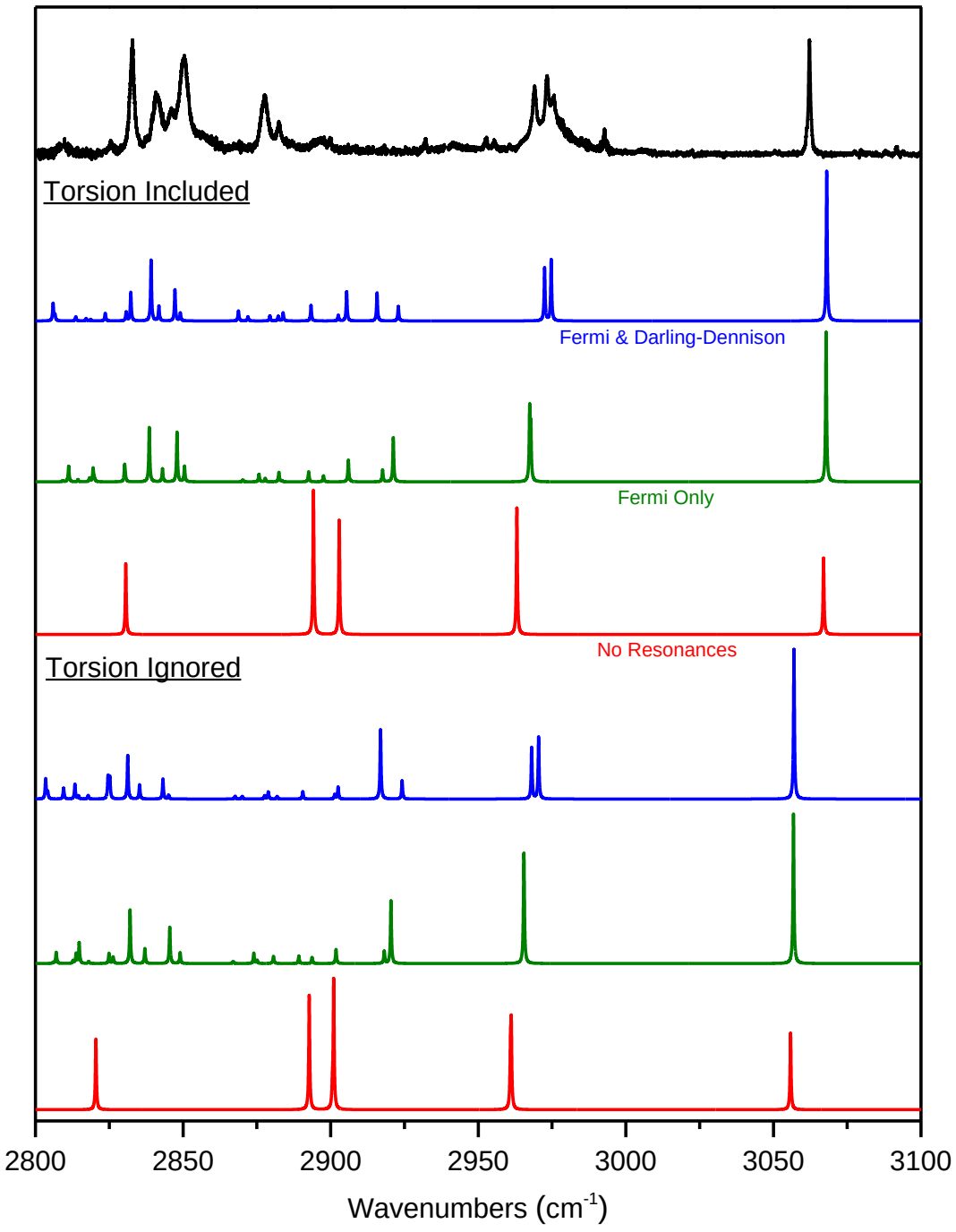

Figure. 4.13. Simulated *i*-propyl spectra with and without the methyl torsional modes, ν_{13} and ν_{24}, included in the VPT2 procedure, and with and without treatment of Fermi resonances or inclusion of Darling-Dennison resonance constants. Frequencies are eigenvalues of a 28-state effective Hamiltonian.

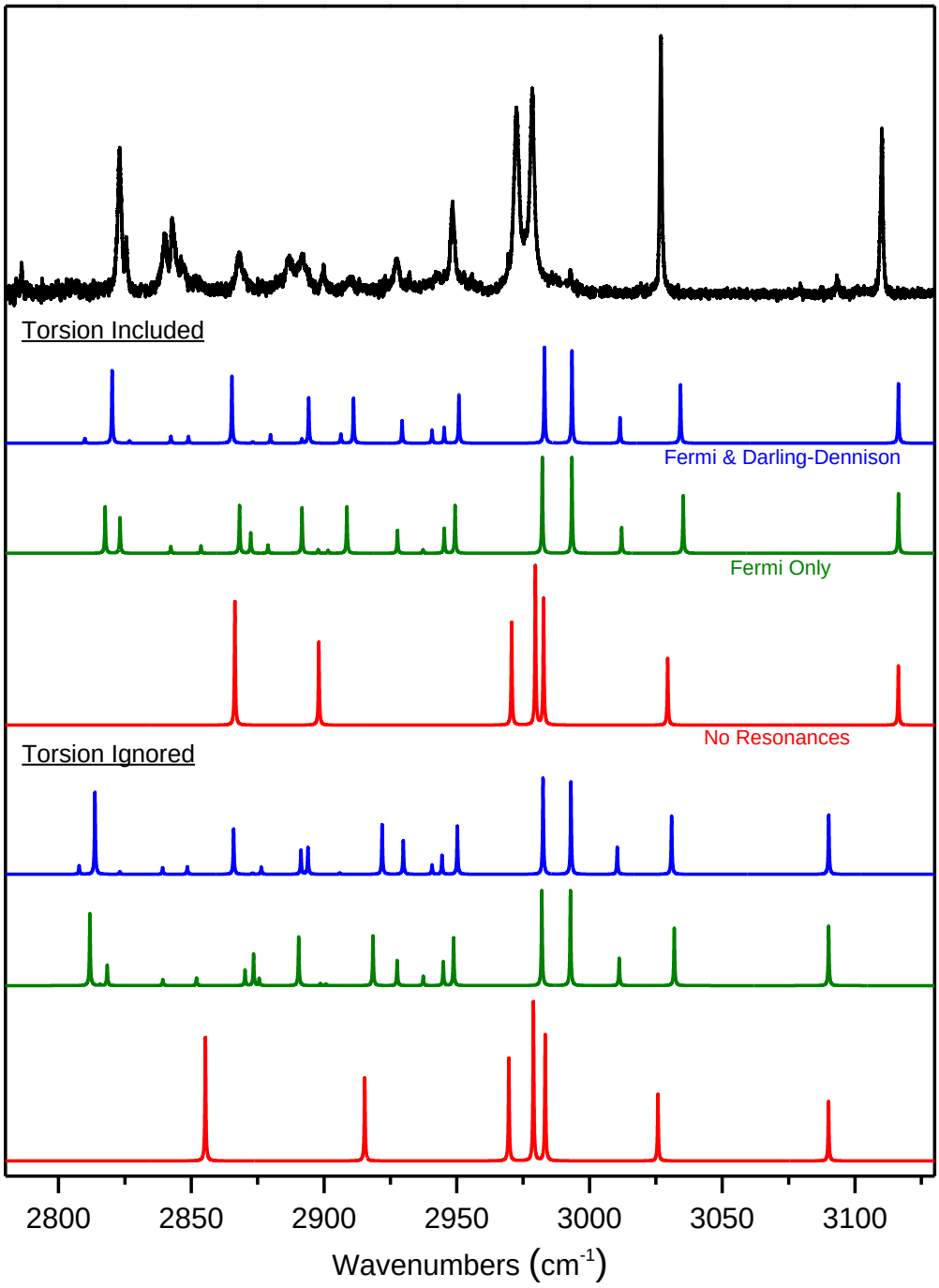

Figure. 4.14. Simulated *n*-propyl spectra with and without the methylene torsional mode, ν_{24}, included in the VPT2 procedure, and with and without treatment of Fermi resonances or inclusion of Darling-Dennison resonance constants. Frequencies are eigenvalues of a 22-state effective Hamiltonian.

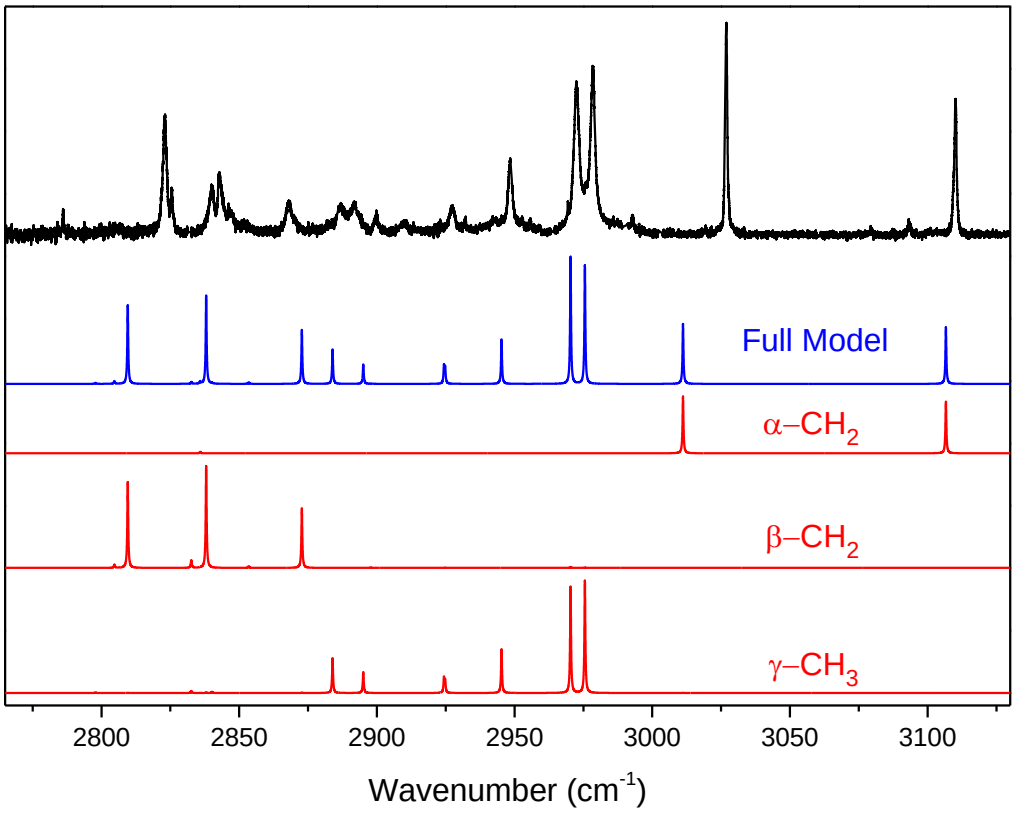

Figure 4.15. Dipole decomposition of local mode Hamiltonian simulations (*n*-propyl). The experimental spectrum, the full model local mode simulation, and the dipole decomposed simulations are shown as black, blue, and red traces, respectively.

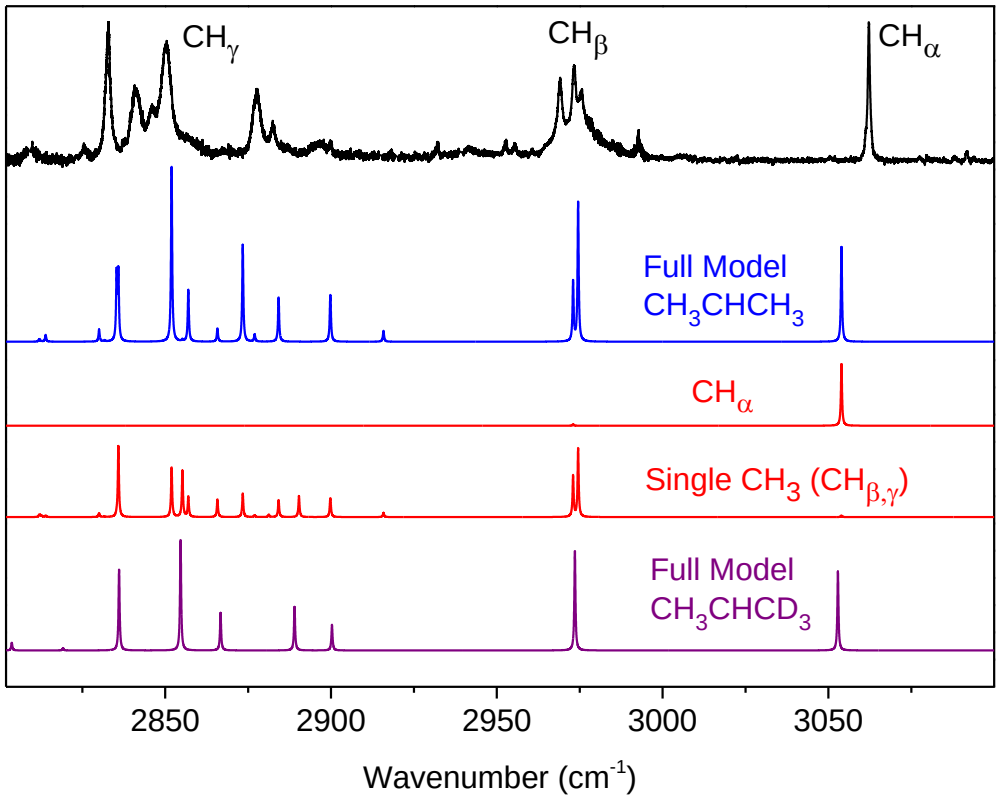

Figure 4.16. Dipole decomposition of local mode Hamiltonian simulations (*i*-propyl). The experimental spectrum, the full model local mode simulation (CH_3CHCH_3), and the dipole decomposed simulations are shown as black, blue, and red traces, respectively. The full model local mode simulation for CH_3CHCD_3 is shown as the purple trace.

splitting between the symmetric and antisymmetric α-CH_2 stretches is overestimated, indicating that the model overestimates the quadratic coupling between stretches localized on the radical site. The agreement in the low frequency region is sensitive to both the transferability of the scale factors and the accuracy of the Fermi coupling parameters. The local mode model successfully predicts the number of lower frequency features in the spectrum. Other than the lowest frequency band at 2820 cm^{-1}, which is underestimated by the model, the agreement is very good below 3000 cm^{-1}, despite there being zero adjustable parameters.

Figure 4.16 compares the local mode model to the experimental *i*-propyl spectrum. Overall, the local mode Full Model spectrum (blue) satisfactorily reproduces most of the spectral features, although the CH_α stretch is underestimated, and the agreement in the lower frequency region is less quantitative than observed for *n*-propyl. In general, the relative intensities of bands comprising the lower frequency region are predicted by the model, although a few discrepancies are apparent in the ordering of the higher and lower intensity transitions. In comparison to the VPT2+K approach, the local mode model is far better at predicting the lower frequency region of the *i*-propyl spectrum. Again, this lower frequency region is especially sensitive to stretch-scissor anharmonic coupling interactions, as illustrated by the VPT2+K simulations shown in Figure 4.7.

The red traces in Figure 4.16 correspond to dipole decompositions for the CH_α bright state and one of the equivalent CH_3 groups (i.e. $CH_{\beta,\gamma}$). To highlight the spectral features arising from the coupling between CH_3 groups, we constructed a local mode effective Hamiltonian for the CH_3CHCD_3 isotopologue. For the latter isotopologue, the Hamiltonian matrix is of reduced size; it includes only those basis states associated with the CH_α group and the CH_3 group. Comparing the resulting spectrum (purple trace) to the CH_3CHCH_3 Full Model (blue trace), we see that many of the finer features arising in the 2800-2900 cm^{-1} region are the result of mixing between the two CH_3 groups. As discussed below, these states mix extensively despite the relatively small coupling terms that directly connect them.

The local mode model Hamiltonian allows for a detailed analysis of characteristic alkyl radical signatures present in the CH stretch region, some of which were described qualitatively by Pacansky in his matrix isolation study.[26] The open shell nature of the system can be appreciated in a qualitative sense via inspection of the *n*-propyl dipole decompositions (Fig. 4.15), where the radical site leads to distinct α,β,γ-CH stretch contributions to the spectrum. In previous work on α-alkyl benzyl radicals,[64] the radical site has been shown to dramatically influence the CH oscillators localized on adjacent carbon atoms. For CH oscillators localized on non-adjacent

carbon atoms, the radical effect was observed to be far smaller. The CH stretch Hamiltonian for *n*-propyl is given below.

$$H_{\mathrm{str}}^{n} = \begin{pmatrix} 2952(\gamma) & & & & & & \\ -21 & 2942(\gamma) & & & & & \\ -21 & -21 & 2942(\gamma) & & & & \\ 4 & -8 & 5 & 2840(\beta) & & & \\ 4 & 5 & -8 & -2 & 2840(\beta) & & \\ 0 & 2 & 2 & -4 & -4 & 3059(\alpha) & \\ 0 & 1 & 1 & 3 & 3 & -51 & 3059(\alpha) \end{pmatrix} \quad (4.12)$$

Descending along the diagonal, the first three states correspond to the local mode γ-CH stretches (the 2952 cm^{-1} mode corresponds to the in-plane stretch), the fourth and fifth states are the β-CH stretches, and the last two states correspond to the α-CH stretches. The local mode α-CH stretches are >100 cm^{-1} higher in frequency than is "typical" for alkyl CH stretches (i.e. ~2950 cm^{-1}). Moreover, the quadratic coupling between the α-CH stretches is more than twice the magnitude observed for alkyl moieties within closed shell systems.[34] In contrast, β-CH frequencies are >100 cm^{-1} below what is typically observed for alkyl CH stretches, and the coupling between them is reduced to almost zero. The former effect was recently noted for α-alkyl benzyl radicals and was shown to depend sensitively on the orientation of the CH stretch relative to the radical site.[64] Finally, we find the 3×3 γ-CH stretch block to be typical of the CH_3 stretch Hamiltonians constructed for closed shell systems.[34] As observed in the α-alkyl benzyl study,[64] the *n*-propyl radical site significantly affects only those CH oscillators localized on or adjacent to it. We turn now to the *i*-propyl CH stretch Hamiltonian.

$$H_{\mathrm{str}}^{i} = \begin{pmatrix} 3052(\alpha) & & & & & & \\ -4 & 2855(\gamma) & & & & & \\ 8 & -21 & 2963(\beta) & & & & \\ -4 & -6 & -21 & 2855(\gamma) & & & \\ -4 & 1 & 0 & 2 & 2855(\gamma) & & \\ 8 & 0 & 0 & 0 & -21 & 2963(\beta) & \\ -4 & 2 & 0 & 1 & -6 & -21 & 2855(\gamma) \end{pmatrix} \quad (4.13)$$

The first state in the *i*-propyl CH stretch Hamiltonian corresponds to the lone CH_α stretch; whereas, the remaining states are due to the methyl groups. The CH_3 blocks have two different types of stretches, an in-plane (CH_β) stretch and two out-of-plane (CH_γ) stretches. Here we see many of the same effects due to the radical site. The CH_γ stretches are shifted down in frequency to 2855 cm^{-1}. This shift is close in magnitude to the shift observed for the β-CH stretches in the *n*-propyl Hamiltonian (Eqn. 4.12). On the other hand, the CH_β stretches at 2963 cm^{-1} fall in the range typical of CH_3 stretches in closed shell systems. These differences in the $CH_{\beta,\gamma}$ stretch frequencies are a direct manifestation of the orientation dependence described above. The in-plane CH_β oscillators are oriented perpendicular to the singly occupied *p*-orbital localized on the α carbon, whereas each CH_γ oscillator makes an ~π/3 angle with the symmetry plane. These observations are consistent with the hyperconjugative stabilization hypothesis, in which electron density in CH_γ σ-bonds is partially transferred to the half-filled *p*-orbital, leading to a concomitant reduction in the CH_γ oscillator's quadratic force constant.

The 3×3 CH_3 stretch block reveals an interesting result associated with the intramonomer quadratic couplings. The down-shifted CH_γ states are coupled to each other by only 6 cm^{-1}, which is similar in magnitude to the coupling observed between the *n*-propyl β-CH oscillators. However, the CH_γ stretches are still strongly coupled to the "unshifted" CH_β stretch (21 cm^{-1}). The larger coupling constant is identical to the matrix elements that couple the three γ-CH oscillators in the *n*-propyl radical, showing that the presence of one unshifted CH stretch is sufficient to produce unmodified intramonomer couplings. Finally, we note that the direct coupling between the two CH_3 group stretches is relatively small (with a maximum of 2 cm^{-1}), yet the final spectra are still clearly sensitive to the combined presence of both CH_3 groups, as shown in Figure 4.16. Rather than being due to direct stretch-stretch couplings, this mixing appears to arise from the coupling between scissor combination modes that involve both CH_3 groups. The coupling between the harmonic local mode scissors is much larger (near 6 cm^{-1}). The effects of

these scissor combination couplings appear to be the primary mechanism by which the two CH_3 groups are mixed.

4.6. Summary and Comparison of Theoretical Methods

High-quality infrared spectra of *n*- and *i*-propyl radicals in the CH stretching region were obtained via the helium droplet isolation method. Quasi-species-selective spectroscopy was achieved through the detection of ionization cross-section modulations in judiciously chosen mass channels. Assignments of spectral features to propyl radicals were confirmed by recording the difference in the mass spectrum with and without laser excitation. In the limit of $3N-6$ uncoupled oscillators, one predicts seven CH stretch vibrations for both *n*- and *i*-propyl. However, the resolution achieved in the experiment reveals a vibrational complexity that demands a treatment beyond the harmonic approximation.

Second-order vibrational perturbation theory, VPT2, accurately predicts the high-frequency stretching vibrations localized on the radical site (α-CH_2 for *n*-propyl; CH_α for *i*-propyl). The CH stretch vibrations localized on carbon atoms adjacent to the radical center are red shifted, due to a hyperconjugative stabilization of the system and concomitant softening of the CH oscillators (β-CH_2 for *n*-propyl; CH_γ for *i*-propyl). The associated red shifts drive these CH stretch modes into resonance with the overtones and combination tones of CH_n bending modes. This effect contributes substantially to the spectral complexity observed between 2800 to 3000 cm^{-1}. Clearly, VPT2 alone cannot account for the complexity that emerges in this lower frequency region.

The pervasive anharmonic coupling and intensity borrowing evident in the CH stretch region is modeled with two separate effective Hamiltonian approaches. 1) The VPT2+K approach treats Fermi and Darling-Dennison resonances explicitly via the diagonalization of an effective Hamiltonian matrix. The matrix contains deperturbed diagonal elements and off-diagonal

coupling terms derived from quartic force fields computed at the CCSD(T)/ANO0 (*n*-propyl) or CCSD(T)/ANO1 (*i*-propyl) levels of theory. The effective Hamiltonian is represented in a normal mode basis consisting of CH_n stretching fundamentals and CH_n bending overtones/combinations. 2) The local mode effective Hamiltonian approach employs a localization scheme that takes as input a harmonic frequency computation at the B3LYP/6-311++G(d,p) level of theory. The localized basis states correspond to CH stretching fundamentals and overtones/combinations of HCH scissor modes. Refined harmonic scale factors and anharmonic coupling terms are taken from previous studies of closed shell hydrocarbon CH stretch spectra and are transferred to the local mode model *without* modification.[34] Both approaches generate Hamiltonian matrices that contain 22-states for *n*-propyl and 28-states for *i*-propyl. The computational cost of the local mode approach is far lower than the VPT2+K method, because it does not require a quartic force field as input.

Local mode predictions are generally in very good agreement with experiment, despite there being zero adjustable parameters in the model. The success of the local mode model indicates a rather robust transferability of the anharmonic coupling terms.[34] The presence of a radical center apparently does not significantly affect the cubic coupling between localized CH stretch and HCH scissor modes. On the other hand, the quadratic force field is strongly affected by the radical site. For example, the two α-CH_2 stretches are shifted to higher energy and coupled more strongly by quadratic terms in the Hamiltonian. In contrast, the β-CH_2 stretches are largely decoupled from each other and shifted to lower energy. Both observations are completely consistent with the hybridization (α-CH_2) and hyperconjugation (β-CH_2) arguments put forth by Pacansky to rationalize the matrix IR spectra of *n*-propyl.[26-27]

With regard to predicting the number and relative intensities of transitions within the spectrally congested 2800 to 3000 cm^{-1} region, the local mode approach is generally superior to VPT2+K. This is especially evident in the *i*-propyl spectrum, where VPT2+K distributes the

transition intensity in a qualitatively incorrect manner, a fairly large portion of it being between 2910 and 2925 cm^{-1}, where nothing is observed experimentally. The discrepancy may partly be due to the fact that the local model Hamiltonians are evaluated at the C_s (*n*-propyl) and C_{2v} (*i*-propyl) geometries, whereas the VPT2+K computations were carried out at the C_1 (*n*-propyl) and C_s (*i*-propyl) electronic minima. We chose the high-symmetry structures for the local mode approach because these are the most probable structures and the minima on the zero-Kelvin enthalpic surfaces, and the model only requires as input a harmonic frequency calculation of localized CH stretch and HCH scissor vibrations. Moreover, the impact of methyl torsions are expected to be somewhat mitigated by computing frequencies at the most probable structure.

The geometries for the VPT2+K procedure were fixed to the electronic minima out of necessity because performing VPT2 with anharmonic force fields computed at non-minimum energy structures is not a well-defined practice. The frequencies of CH stretches depend on the dihedral angle of the CH bond to the radical site and thus the model spectrum is sensitive to the geometry. For example, the computed CH stretch harmonic frequencies at the CCSD(T) level of theory are shown in Tables 4.1 and 4.2 for both geometries considered here (see also Tables 4.4 and 4.5). The average deviation in going from the electronic minimum to the high-symmetry structure is 15.3 cm^{-1} for *i*-propyl and 6.5 cm^{-1} for *n*-propyl. It is less obvious how the force fields should depend on this geometry change; however, we note again that in a previous study of closed shell alkyl benzene systems, it was found that the anharmonic contributions to the spectra were very similar for all molecules and conformations.[34] Therefore, the choice of geometry is likely not the only factor leading to the observed discrepancy between the two effective Hamiltonian approaches; for example, the choice of representation, local versus normal mode, should result in different convergence behavior. The coupling between basis states in the local mode model more accurately reflects the salient interactions responsible for the experimental spectral complexity (stretch-scissor coupling), and is therefore more easily converged.

Collectively, these observations suggest that we should expect the local mode model to accurately predict the CH stretch spectra of larger alkyl radical systems, and because of the low cost of such computations, this approach provides an excellent alternative to the more expensive VPT2+K method.

References

(1) Westbrook, C. K. Chemical Kinetics of Hydrocarbon Ignition in Practical Combustion Systems. *P. Combust. Inst.* **2000**, *28*, 1563-1577.

(2) Miller, J. A.; Pilling, M. J.; Troe, E. Unravelling Combustion Mechanisms Through a Quantitative Understanding of Elementary Reactions. *P. Combust. Inst.* **2005**, *30*, 43-88.

(3) Taatjes, C. A. Uncovering the Fundamental Chemistry of Alkyl Plus O_2 Reactions via Measurements of Product Formation. *J. Phys. Chem. A* **2006**, *110*, 4299-4312.

(4) Zador, J.; Taatjes, C. A.; Fernandes, R. X. Kinetics of Elementary Reactions in Low-Temperature Autoignition Chemistry. *Prog. Energy Combust. Sci.* **2011**, *37*, 371-421.

(5) Wilke, J. J.; Allen, W. D.; Schaefer, H. F. Establishment of the C_2H_5+O_2 Reaction Mechanism: A Combustion Archetype. *J. Chem. Phys.* **2008**, *128*, 074308.

(6) Hoobler, P. R.; Turney, J. M.; Schaefer, H. F. Investigating the Ground-State Rotamers of *n*-Propylperoxy Radical. *J. Chem. Phys.* **2016**, *145*, 174301.

(7) Goldsmith, C. F.; Green, W. H.; Klippenstein, S. J. Role of O_2 + QOOH in Low-Temperature Ignition of Propane. 1. Temperature and Pressure Dependent Rate Coefficients. *J. Phys. Chem. A* **2012**, *116*, 3325-3346.

(8) Huynh, L. K.; Carstensen, H. H.; Dean, A. M. Detailed Modeling of Low-Temperature Propane Oxidation: 1. The Role of the Propyl + O_2 Reaction. *J. Phys. Chem. A* **2010**, *114*, 6594-6607.

(9) Baldwin, R. R.; Walker, R. W.; Yorke, D. A. Reaction of *n*-Propyl Radicals with Oxygen, Hydrogen and Deuterium. *J. Chem. Soc., Faraday Trans. 1* **1973**, *69*, 826-832.

(10) Ruiz, R. P.; Bayes, K. D. Rates of Reaction of Propyl Radicals with Molecular Oxygen. *J. Phys. Chem.* **1984**, *88*, 2592-2595.

(11) DeSain, J. D.; Taatjes, C. A.; Miller, J. A.; Klippenstein, S. J.; Hahn, D. K. Infrared Frequency-Modulation Probing of Product Formation in Alkyl + O_2 Reactions. Part IV. Reactions of Propyl and Butyl Radicals with O_2. *Faraday Discuss.* **2002**, *119*, 101-120.

(12) DeSain, J. D.; Klippenstein, S. J.; Miller, J. A.; Taatjes, C. A. Measurements, Theory, and Modeling of OH Formation in Ethyl + O_2 and Propyl + O_2 Reactions. *J. Phys. Chem. A* **2003**, *107*, 4415-4427.

(13) Merle, J. K.; Hayes, C. J.; Zalyubovsky, S. J.; Glover, B. G.; Miller, T. A.; Hadad, C. M. Theoretical Determinations of the Ambient Conformational Distribution and Unimolecular Decomposition of *n*-Propylperoxy Radical. *J. Phys. Chem. A* **2005**, *109*, 3637-3646.

(14) Huang, H. F.; Merthe, D. J.; Zador, J.; Jusinski, L. E.; Taatjes, C. A. New Experiments and Validated Master-Equation Modeling for OH Production in Propyl + O_2 Reactions. *P. Combust. Inst.* **2011**, *33*, 293-299.

(15) Zalyubovsky, S. J.; Glover, B. G.; Miller, T. A.; Hayes, C.; Merle, J. K.; Hadad, C. M. Observation of the $\tilde{A}$-$\tilde{X}$ Electronic Transition of the 1-$C_3H_7O_2$ and 2-$C_3H_7O_2$ Radicals Using Cavity Ringdown Spectroscopy. *J. Phys. Chem. A* **2005**, *109*, 1308-1315.

(16) Fessenden, R. W.; Schuler, R. H. Electron Spin Resonance Studies of Transient Alkyl Radicals. *J. Chem. Phys.* **1963**, *39*, 2147-2195.

(17) Fessenden, R. ESR Studies of Internal Rotation in Radicals. *J. Chim. Phys. Phys.- Chim. Biol.* **1964**, *61*, 1570-1575.

(18) Kochi, J. K.; Krusic, P. J. Electron Spin Resonance of Primary Alkyl Radicals. Photolysis of Acyl Peroxides. *J. Am. Chem. Soc.* **1969**, *91*, 3940.

(19) Krusic, P. J.; Kochi, J. K. Conformational Effects of Sulfur, Silicon, Germanium, and Tin on Alkyl Radicals - Electron Spin Resonance Study of Barriers to Internal Rotation. *J. Am. Chem. Soc.* **1971**, *93*, 846-860.

(20) Krusic, P. J.; Jesson, J. P.; Meakin, P. Electron Spin Resonance Studies of Conformations and Hindered Internal Rotation in Transient Free Radicals. *J. Phys. Chem.* **1971**, *75*, 3438-3453.

(21) Ellinger, Y.; Subra, R.; Levy, B.; Millie, P.; Berthier, G. Ab-Initio Study of Electronic-Structure and Hyperfine Coupling Properties in Simple Hydrocarbon Radicals .2. Short-Range and Long-Range Interactions in Alkyl Free-Radicals. *J. Chem. Phys.* **1975**, *62*, 10-29.

(22) Pacansky, J.; Dupuis, M. Ab Initio Study for the Structure of Propane and the Normal-Propyl Radical. *J. Chem. Phys.* **1979**, *71*, 2095-2098.

(23) Claxton, T. A.; Graham, A. M. Ab Initio Study of Propyl Radicals. *J. Chem. Soc., Faraday Trans. 2* **1988**, *84*, 121-134.

(24) Turovtsev, V. V.; Orlov, Y. D. Study of Internal Rotation of Radical Center in *n*-Alkyl Radicals. *Russ. J. Gen. Chem.* **2010**, *80*, 749-755.

(25) Li, C. Y.; Agarwal, J.; Wu, C. H.; Allen, W. D.; Schaefer, H. F. Intricate Internal Rotation Surface and Fundamental Infrared Transitions of the *n*-Propyl Radical. *J. Phys. Chem. B* **2015**, *119*, 728-735.

(26) Pacansky, J.; Horne, D. E.; Gardini, G. P.; Bargon, J. Matrix-Isolation Studies of Alkyl Radicals - Characteristic Infrared-Spectra of Primary Alkyl Radicals. *J. Phys. Chem.* **1977**, *81*, 2149-2154.

(27) Pacansky, J.; Coufal, H. The Photochemistry and Infrared-Spectrum of the Isopropyl Radical. *J. Chem. Phys.* **1980**, *72*, 3298-3303.

(28) Pacansky, J.; Brown, D. W.; Chang, J. S. Infrared-Spectra of the Isobutyl and Neopentyl Radicals - Characteristic Spectra of Primary, Secondary, and Tertiary Alkyl Radicals. *J. Phys. Chem.* **1981**, *85*, 2562-2567.

(29) Lightfoot, P. D.; Cox, R. A.; Crowley, J. N.; Destriau, M.; Hayman, G. D.; Jenkin, M. E.; Moortgat, G. K.; Zabel, F. Organic Peroxy-Radicals - Kinetics, Spectroscopy and Tropospheric Chemistry. *Atmos. Environ., Part A* **1992**, *26*, 1805-1961.

(30) Wallington, T. J.; Dagaut, P.; Kurylo, M. J. Ultraviolet-Absorption Cross-Sections and Reaction-Kinetics and Mechanisms for Peroxy-Radicals in the Gas-Phase. *Chem. Rev.* **1992**, *92*, 667-710.

(31) Tarczay, G.; Zalyubovsky, S. J.; Miller, T. A. Conformational Analysis of the 1- and 2-Propyl Peroxy Radicals. *Chem. Phys. Lett.* **2005**, *406*, 81-89.

(32) Sibert, E. L.; Kidwell, N. M.; Zwier, T. S. A First-Principles Model of Fermi Resonance in the Alkyl CH Stretch Region: Application to Hydronaphthalenes, Indanes, and Cyclohexane. *J. Phys. Chem. B* **2014**, *118*, 8236-8245.

(33) Sibert, E. L.; Tabor, D. P.; Kidwell, N. M.; Dean, J. C.; Zwier, T. S. Fermi Resonance Effects in the Vibrational Spectroscopy of Methyl and Methoxy Groups. *J. Phys. Chem. A* **2014**, *118*, 11272-11281.

(34) Tabor, D. P.; Hewett, D. M.; Bocklitz, S.; Korn, J. A.; Tomaine, A. J.; Ghosh, A. K.; Zwier, T. S.; Sibert, E. L. Anharmonic Modeling of the Conformation-Specific IR Spectra of Ethyl, *n*-Propyl, and *n*-Butylbenzene. *J. Chem. Phys.* **2016**, *144*, 224310.

(35) Sibert, E. L. Dressed Local Mode Hamiltonians for CH Stretch Vibrations. *Mol. Phys.* **2013**, *111*, 2093-2099.

(36) Buchanan, E. G.; Sibert, E. L.; Zwier, T. S. Ground State Conformational Preferences and CH Stretch-Bend Coupling in a Model Alkoxy Chain: 1,2-Diphenoxyethane. *J. Phys. Chem. A* **2013**, *117*, 2800-2811.

(37) Buchanan, E. G.; Dean, J. C.; Zwier, T. S.; Sibert, E. L. Towards a First-Principles Model of Fermi Resonance in the Alkyl CH Stretch Region: Application to 1,2-Diphenylethane and 2,2,2-Paracyclophane. *J. Chem. Phys.* **2013**, *138*, 064308.

(38) Tabor, D. P.; Kusaka, R.; Walsh, P. S.; Zwier, T. S.; Sibert, E. L. Local Mode Approach to OH Stretch Spectra of Benzene-$(H_2O)_n$ Clusters, n=2-7. *J. Phys. Chem. A* **2015**, *119*, 9917-9930.

(39) Callegari, C.; Lehmann, K. K.; Schmied, R.; Scoles, G. Helium Nanodroplet Isolation Rovibrational Spectroscopy: Methods and Recent Results. *J. Chem. Phys.* **2001**, *115*, 10090-10110.

(40) Toennies, J. P.; Vilesov, A. F. Superfluid Helium Droplets: A Uniquely Cold Nanomatrix for Molecules and Molecular Complexes. *Angew. Chem., Int. Ed.* **2004**, *43*, 2622-2648.

(41) Choi, M. Y.; Douberly, G. E.; Falconer, T. M.; Lewis, W. K.; Lindsay, C. M.; Merritt, J. M.; Stiles, P. L.; Miller, R. E. Infrared Spectroscopy of Helium Nanodroplets: Novel Methods for Physics and Chemistry. *Int. Rev. Phys. Chem.* **2006**, *25*, 15-75.

(42) Stienkemeier, F.; Lehmann, K. K. Spectroscopy and Dynamics in Helium Nanodroplets. *J. Phys. B: At., Mol. Opt. Phys.* **2006**, *39*, R127-R166.

(43) Callegari, A.; Merker, U.; Engels, P.; Srivastava, H. K.; Lehmann, K. K.; Scoles, G. Intramolecular Vibrational Redistribution in Aromatic Molecules. I. Eigenstate Resolved CH Stretch First Overtone Spectra of Benzene (vol 113, pg 10583, 2000). *J. Chem. Phys.* **2001**, *114*, 3344-3344.

(44) Raston, P. L.; Agarwal, J.; Turney, J. M.; Schaefer, H. F.; Douberly, G. E. The Ethyl Radical in Superfluid Helium Nanodroplets: Rovibrational Spectroscopy and Ab Initio Computations. *J. Chem. Phys.* **2013**, *138*, 194303.

(45) Hartmann, M.; Miller, R. E.; Toennies, J. P.; Vilesov, A. Rotationally Resolved Spectroscopy of SF_6 in Liquid-Helium Clusters - A Molecular Probe of Cluster Temperature. *Phys. Rev. Lett.* **1995**, *75*, 1566-1569.

(46) Scheidemann, A.; Schilling, B.; Toennies, J. P. Anomalies in the Reactions of He^+ with SF_6 Embedded in Large ^4He Clusters. *J. Phys. Chem.* **1993**, *97*, 2128-2138.

(47) Noyes, W. A. *n*-Butyl Nitrite. *Org. Synth.* **1936**, *16*, 7.

(48) Moradi, C. P.; Morrison, A. M.; Klippenstein, S. J.; Goldsmith, C. F.; Douberly, G. E. Propargyl + O_2 Reaction in Helium Droplets: Entrance Channel Barrier or Not? *J. Phys. Chem. A* **2013**, *117*, 13626-13635.

(49) Leavitt, C. M.; Moradi, C. P.; Acrey, B. W.; Douberly, G. E. Infrared Laser Spectroscopy of the Helium-Solvated Allyl and Allyl Peroxy Radicals. *J. Chem. Phys.* **2013**, *139*, 234301.

(50) Morrison, A. M.; Liang, T.; Douberly, G. E. Automation of an "Aculight" Continuous-Wave Optical Parametric Oscillator. *Rev. Sci. Instrum.* **2013**, *84*, 013102.

(51) J. F. Stanton, J. Gauss, L. Cheng, M. E. Harding, D. A. Matthews, and P. G. Szalay, CFOUR, Coupled-cluster techniques for computational chemistry, a quantum-chemical program package, With contributions from A. A. Auer, R. J. Bartlett, U. Benedikt, C. Berger, D. E. Bernholdt, Y. J. Bomble, O. Christiansen, F. Engel, R. Faber, M. Heckert, O. Heun, M. Hilgenberg, C. Huber, T.-C. Jagau, D. Jonsson, J. Jusélius, T. Kirsch, K. Klein, W. J. Lauderdale, F. Lipparini, T. Metzroth, L. A. Mück, D. P. O'Neill, D. R. Price, E. Prochnow, C. Puzzarini, K. Ruud, F. Schiffmann, W. Schwalbach, C. Simmons, S. Stopkowicz, A. Tajti, J. Vázquez, F. Wang, J. D. Watts and the integral packages MOLECULE (J. Almlöf and P. R. Taylor), PROPS (P. R. Taylor), ABACUS (T. Helgaker, H. J. Aa. Jensen, P. Jørgensen, and J. Olsen), and ECP routines by A. V. Mitin and C. van Wüllen, for the current version, see http://www.cfour.de.

(52) Allen, W. D.; Bodi, A.; Szalay, V.; Csaszar, A. G. Adiabatic Approximations to Internal Rotation. *J. Chem. Phys.* **2006**, *124*.

(53) Nielsen, H. H. The Vibration-Rotation Energies of Molecules. *Rev. Mod. Phys.* **1951**, *23*, 90-136.

(54) *Mathematica*, 9; Wolfram Research Inc.: Champaign, IL, 2012.

(55) Matthews, D. A.; Stanton, J. F. Quantitative Analysis of Fermi Resonances by Harmonic Derivatives of Perturbation Theory Corrections. *Mol. Phys.* **2009**, *107*, 213-222.

(56) Martin, J. M. L.; Lee, T. J.; Taylor, P. R.; Francois, J. P. The Anharmonic-Force Field of Ethylene, C_2H_4, by Means of Accurate Ab Initio Calculations. *J. Chem. Phys.* **1995**, *103*, 2589-2602.

(57) Matthews, D. A.; Vazquez, J.; Stanton, J. F. Calculated Stretching Overtone Levels and Darling-Dennison Resonances in Water: A Triumph of Simple Theoretical Approaches. *Mol. Phys.* **2007**, *105*, 2659-2666.

(58) Lehmann, K. K. Beyond the χ-K Relations - Calculations of 1-1 and 2-2 Resonance Constants with Application to HCN and DCN. *Mol. Phys.* **1989**, *66*, 1129-1137.

(59) Martin, J. M. L.; Taylor, P. R. Accurate Ab Initio Quartic Force Field for *trans*-HNNH and Treatment of Resonance Polyads. *Spectrochim. Acta, Part A* **1997**, *53*, 1039-1050.

(60) Rosnik, A. M.; Polik, W. F. VPT2+K Spectroscopic Constants and Matrix Elements of the Transformed Vibrational Hamiltonian of a Polyatomic Molecule with Resonances Using Van Vleck Perturbation Theory. *Mol. Phys.* **2014**, *112*, 261-300.

(61) Hanninen, V.; Halonen, L. Calculation of Spectroscopic Parameters and Vibrational Overtones of Methanol. *Mol. Phys.* **2003**, *101*, 2907-2916.

(62) J. Frisch, G. W. Trucks, H. B. Schlegel, G. E. Scuseria, M. A. Robb, J. R. Cheeseman, G. Scalmani, V. Barone, B. Mennucci, G. A. Petersson, H. Nakatsuji, M. Caricato, X. Li, H. P. Hratchian, A. F. Izmaylov, J. Bloino, G. Zheng, J. L. Sonnenberg, M. Hada, M. Ehara, K. Toyota, R. Fukuda, J. Hasegawa, M. Ishida, T. Nakajima, Y. Honda, O. Kitao, H. Nakai, T. Vreven, J. A. Montgomery, Jr., J. E. Peralta, F. Ogliaro, M. J. Bearpark, J. Heyd, E. N. Brothers, K. N. Kudin, V. N. Staroverov, R. Kobayashi, J. Normand, K. Raghavachari, A. P. Rendell, J. C. Burant, S. S. Iyengar, J. Tomasi, M. Cossi, N. Rega, N. J. Millam, M. Klene, J. E. Knox, J. B. Cross, V. Bakken, C. Adamo, J. Jaramillo, R. Gomperts, R. E. Stratmann, O. Yazyev, A. J. Austin, R. Cammi, C. Pomelli, J. W. Ochterski, R. L. Martin, K. Morokuma, V. G. Zakrzewski, G. A. Voth, P. Salvador, J. J. Dannenberg, S. Dapprich, A. D. Daniels, Ö . Farkas, J. B. Foresman, J. V. Ortiz, J. Cioslowski, and D. J. Fox, Gaussian 09, Revision E.01, Gaussian, Inc., Wallingford, CT, USA, 2009.

(63) Miller, J. A.; Klippenstein, S. J. Dissociation of Propyl Radicals and Other Reactions on a C_3H_7 Potential. *J. Phys. Chem. A* **2013**, *117*, 2718-2727.

(64) Korn, J. A.; Tabor, D. P.; Sibert, E. L.; Zwier, T. S. Conformation-Specific Spectroscopy of Alkyl Benzyl Radicals: Effects of a Radical Center on the CH Stretch Infrared Spectrum of an Alkyl Chain. *J. Chem. Phys.* **2016**, *145*, 124314.

CHAPTER 5

ROTAMERS OF ISOPRENE: INFRARED SPECTROSCOPY IN HELIUM DROPLETS AND AB INITIO THERMOCHEMISTRY[1]

[1] Reproduced with permission from Franke, P.R. and Douberly, G.E. 2018. *Journal of Physical Chemistry A*. 122:148-158. DOI: 10.1021/acs.jpca.7b10260 Copyright 2018 American Chemical Society.

Isoprene (C_5H_8) is an abundant, reactive tropospheric hydrocarbon, derived from biogenic emissions. A detailed understanding of the spectroscopy of isoprene is therefore desirable. Isoprene monomer is isolated in helium droplets and its infrared spectrum is measured in the CH stretching region. Anharmonic frequencies are predicted by VPT2+K simulations employing CCSD(T) force fields with quadratic (cubic and quartic) force constants computed using the ANO1 (ANO0) basis set. The vast majority of the spectral features can be assigned to *trans*-isoprene on the basis of these computations. Some features of the higher energy *gauche* conformer are also assignable, by comparison to experiments using heated isoprene. Convergent *ab initio* thermochemistry is presented for the isomerization pathway, for which the partition function explicitly accounts for the eigenstates associated with separate, uncoupled one-dimensional potential surfaces for methyl torsion and internal rotation between rotamers. The respective 0 K and 298.15 K *trans*/*gauche* energy differences are 2.82 and 2.52 kcal/mol, which implies a room temperature *gauche* population of 2.8%.

5.1. Introduction

Isoprene annually comprises ~500 Tg of biogenic emissions into the troposphere, which represents 44% of total emissions of non-methane volatile organic compounds (VOCs).[1] Isoprene has a daytime half-life of less than 2 hours, and its oxidation is the dominant source of summertime tropospheric ozone.[2-3] Indeed, accurate models of tropospheric oxidative capacity will demand a thorough understanding of the OH initiated oxidation of isoprene and monoterpenes, which is still incomplete.[1, 4] Moreover, isoprene is believed to be a significant contributor to secondary organic aerosol (SOA) formation via pathways beginning with the OH addition reaction.[5-10] Isoprene-derived SOA influences the global radiation budget and can act as cloud condensation nuclei.[11] The tropospheric chemistry of isoprene is initiated largely by the electrophilic addition of OH to double bonds, leading to hydroxyalkyl adduct formation. These adducts react with O_2, forming hydroxyperoxy radicals, which are involved in a series of complex

reaction pathways leading to a variety of products.[12-13] Because isoprene is the starting point for these complex oxidation pathways, an accurate determination of its conformer populations (*trans* and *gauche*) is necessary, as different conformers may follow different pathways.[13] In this report, we present a detailed analysis of the infrared (IR) spectrum in the CH stretching region and analyze the spectral complexity that emerges due to the anharmonic coupling of stretching fundamentals and bending overtone/combination states. Moreover, convergent theoretical thermochemistry for the isomerization pathway is presented.

The IR spectrum of isoprene has been measured in the gas phase at room temperature[14] and in Ar[14] and N_2 matrices.[15] However, a spectrum that is simultaneously cold and minimally-perturbed, with sub-wavenumber resolution, is currently absent from the literature. Measurements of cold, vibrationally-resolved spectra are expected to reveal the multitude of bending overtone and combination bands that cohabitate with CH stretch fundamentals, particularly in the region from 2800 to 3000 cm^{-1}.[16] This region is home to groups of strongly-interacting vibrational states, called polyads, of which the complexity grows rapidly with the size of the molecule.[17-19] This provides challenging test cases for anharmonic theory.[20] The helium nanodroplet isolation technique allows for the acquisition of the vibrationally-resolved IR spectrum of isoprene in the CH stretching region. Indeed, the low temperature and weak matrix interactions afforded by this technique yield a spectrum whose analysis requires an explicit treatment of anharmonic coupling.[16] Here we apply the VPT2+K approach in a normal mode representation,[21] which provides a detailed picture of the polyad structure associated with this wavelength region.

To our knowledge, the highest level theoretical study of isoprene's rotamers was reported by Allodi *et. al.*[13] Their investigation was focused on the various OH-addition adducts and pre-reactive complexes, but they also studied the *trans*/*gauche* isomerization potential of isoprene at the CCSD(T)/aug-cc-pVTZ//BHandHLYP/6-311G** level of theory. The lowest lying

conformer was the familiar *trans* structure, and the enthalpy for interconversion to the *gauche* structure, ΔH_0, was predicted to be 2.66 kcal/mol.[13] On the basis of a theoretical ΔG_{298} of 2.45 kcal/mol, the *trans* structure was determined to be far more abundant (96.8%) at 298.15 K than the higher energy *gauche* structure (3.2%). Squillacote and Liang[15] computed thermochemical parameters with the G3 composite method for various methyl-substituted dienes, including isoprene (ΔH_0 = 2.73 kcal/mol). These authors also derived an experimental interconversion enthalpy (2.46 kcal/mol) from a van't Hoff analysis of solid-N_2 matrix isolation spectra. Here we apply convergent electronic structure theory (i.e. focal point analysis)[22-24] to improve upon the previously reported theoretical thermochemistry, which includes explicit analysis of the partition functions associated with methyl torsion and the *trans*/*gauche* interconversion pathway.

5.2. Experimental Methods

Details of the helium droplet methodology can be found elsewhere.[25-26] Ultrapure (99.9995%) helium at 35 bar is continuously expanded through a 5 μm, 17 K nozzle to form He nanodroplets, producing a distribution of droplets containing 4000-6000 He atoms on average.[27] Droplets are skimmed into a beam and passed into a second vacuum chamber and through a pick up cell (PUC). Vapor from a glass bulb of liquid isoprene (99%, Sigma Aldrich) is metered into the PUC. Helium droplets collide with gas phase isoprene molecules; and following solvation, the molecules are rapidly cooled to the droplet temperature of ~0.4 K.[25-26] The PUC pressure is adjusted to be less than that necessary to optimize single molecule pick up. Based on the Poisson capture statistics[28] and the log-normal distribution of droplet sizes,[27] 18% of the droplet ensemble is doped with isoprene monomer, and 2.3% of the droplet ensemble picks up two isoprene molecules that cluster within the droplet to form an isoprene dimer. A negligible fraction of the ensemble picks up three or more isoprene molecules.

After being doped, the droplet beam interacts with the mid-IR beam of an optical parametric oscillator (OPO), which propagates antiparallel to the droplet beam. The tuning and

calibration of this laser system are discussed elsewhere.[29] Upon excitation, the vibrational energy of the molecule is quenched by the evaporation of He atoms from the droplet. Evaporation of one helium atom carries away approximately 5 cm^{-1} of vibrational energy.[30] Loss of helium reduces the average geometric cross section of the droplets, decreasing the cross section for electron impact ionization, which is detected with a quadrupole mass spectrometer tuned to pass only ions within a particular mass channel. The IR beam is mechanically chopped at 80 Hz, and the ion current is processed with a lock-in amplifier. The resulting IR spectrum is a laser on *vs*. laser off difference spectrum associated with the chosen mass channel, and the signal is normalized to the power of the laser beam. The mass spectrometry scheme by which action spectra are recorded and the choice of mass channel is discussed in detail below.

The mechanism by which doped helium droplets are ionized by electron bombardment has been discussed in detail elsewhere.[26] Electron impact ionization of pure droplets leads to a distribution of helium cluster ions via the mechanism shown in Equation 5.1.

$$(He)_n + e^- \rightarrow He^+(He)_{n-1} + 2e^- \rightarrow (He)_2^+(He)_{n-2} + 2e^- \rightarrow (He)_m^+ + (n-m)(He) + 2e^- \quad (5.1)$$

Dopants are ionized via charge-transfer from He^+, because the IP difference between He and the molecular dopant is typically 10 to 15 eV.

$$(M)(He)_m + e^- \rightarrow (M)He^+(He)_{m-1} + 2e^- \rightarrow (M)^{+*} + m(He) + 2e^- \quad (5.2)$$

Despite the presence of the helium bath, this large IP mismatch leads to the fragmentation of the ionized dopant, $(M)^{+*}$ and its ejection into the gas phase, where it is detected with quadrupole mass spectrometry. The observed fragmentation pathways are typically analogous to those observed in gas-phase electron impact ionization, when comparisons are available. Indeed, from the NIST webbook, one finds the electron ionization mass spectrum (EI-MS) of gas-phase isoprene, and it is evident that the most abundant fragment ions (m/z = 27, 39, 41, 53, 67, 68) are the same as those in the droplet mass spectrum shown in Figure 5.1A, although some of the relative abundances are modified (e.g. the fragmentation pathway leading the allyl cation, m/z =

41, is apparently favored by the He^+ charge transfer mechanism; whereas, m/z = 41 is no more abundant than 39 in the gas-phase EI-MS).

The mass spectrum of only those droplets containing single isoprene molecules can, in principle, be recorded via a *difference depletion mass spectrometry* technique, the results from which are shown in Figure 5.1. The IR laser is tuned to 2957.28 cm^{-1}, i.e. a resonant frequency for isoprene monomer. The laser frequency is fixed and amplitude modulated at 80 Hz while the quadrupole mass spectrometer is slowly scanned across all mass channels. When processed with a lock-in amplifier, the resulting *difference* mass spectrum corresponds to the EI-MS of *only* the subset of droplets that contain resonantly excited molecules. In Figure 5.1B, mass channels 27, 39, 41, 53, 65, and 68 u are the most intense, indicating that these channels carry the largest laser-induced ion depletion signal at 2957.28 cm^{-1}, i.e. indicating that these are the largest mass channels associated with isoprene doped helium droplets. We chose to record the IR spectrum of isoprene as a depletion in channel 67 u, $C_5H_7^+$. Our decision is based on signal to noise considerations, arrived at through some trial and error, and the fact that the molecular ion, m/z = 68 u, $C_5H_8^+$, is also a helium peak, $(He)_{17}^+$, which could potentially carry depletion signal from other species in the beam, such as isoprene dimers. This species-selective mass spectrometry was used throughout and provides a two-dimensional approach for assigning bands in the IR spectrum of isoprene.

For temperature-dependence experiments, the gas phase isoprene was heated within the PUC to increase the population of the higher energy rotamer while maintaining a fixed number density of isoprene molecules within the PUC. This was accomplished by tightly packing the PUC with copper wool, two 125 Watt cartridge heaters, and a K-type thermocouple. Gas-phase isoprene molecules had to pass through the copper wool prior to interacting with the droplet beam. Variable current was applied to the cartridge heaters, and the temperature of the isoprene was taken from the thermocouple reading (~700 K). Previous studies of multi-conformer systems

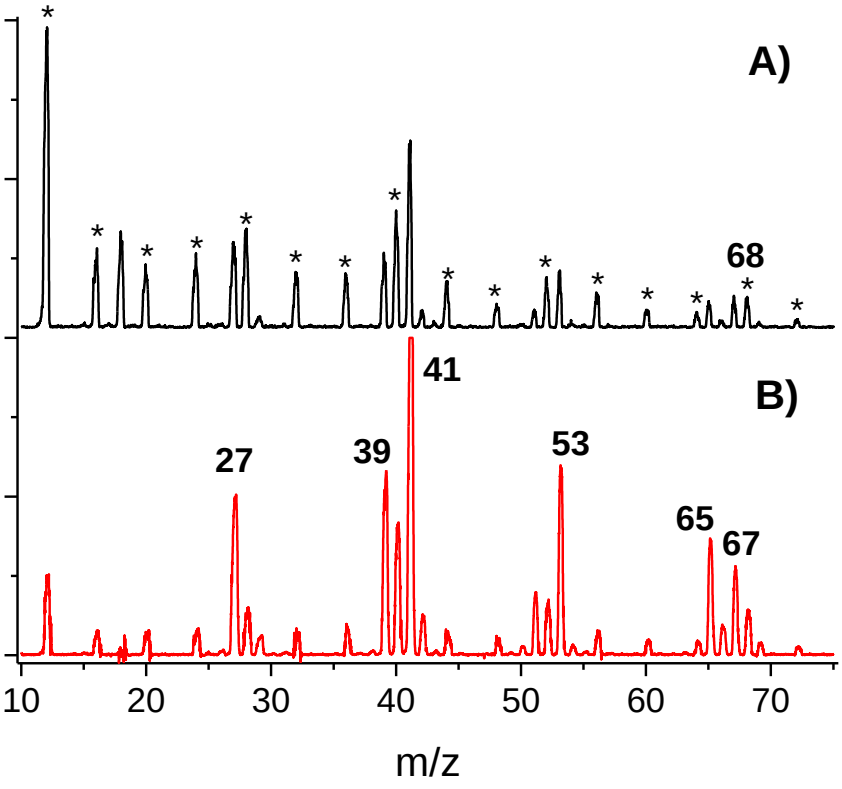

Figure 5.1. (A) Mass spectrum of a droplet beam doped with isoprene (black). The isoprene pressure is first adjusted to optimize the probability that droplets pick up single molecules, and then the pressure is reduced by a factor of approximately two. This procedure minimizes the probability associated with a single droplet picking up multiple isoprene molecules. Peaks marked by * indicate mass channels coincident with $(He)_n^+$ ions. (B) Difference mass spectrum (red) with the laser fixed at 2957.28 cm^{-1}. Here the quadrupole is scanned, and the ion signal depletion, as processed by a lock-in amplifier, is recorded.

have shown that the gas-phase conformer ratio is preserved upon helium solvation,[31-32] because the helium cooling is sufficiently rapid such that interconversion is prevented within the droplet. We note that thermal equilibration by collisions with the hot copper wool in the PUC prior to droplet pick up is not essential in our analysis. In general, we find that the CH stretching region is too congested to provide highly accurate *trans*:*gauche* intensity ratios. Therefore, our scheme is

simply set up to enhance the population of the higher energy *gauche* rotamer to aid in its spectral assignment, and we do not attempt here to vary the PUC temperature and derive an experimental enthalpy of interconversion via van't Hoff analysis of the *trans*:*gauche* ratio.

5.3. Theoretical Methods

5.3.1. Relative Enthalpy

Four stationary points were characterized: a C_s electronic minimum (*trans*) and first-order saddle point (*cis*), and a C_1 electronic minimum (*gauche*) and first-order saddle point. Geometries were optimized using the CCSD(T)[33-38] method combined with the ANO0 and ANO1 basis sets,[39] as implemented in CFOUR.[40] Unless otherwise noted, the frozen-core approximation was made, i.e. the carbon 1s electrons were not included in the post-HF treatment. Energies were obtained at the CCSD(T)/ANO1 geometries by extrapolation to the complete basis set limit. The HF-SCF energy was extrapolated with a 3-point formula from cc-pVXZ (X = 4,5,6) energy calculations.[41] The correlation energies were extrapolated using a 2-point formula from cc-pVXZ (X = various) energy calculations.[42] The points used in the correlation energy extrapolations were those with the largest basis sets: X = 5,6 for MP2, X=4,5 for CCSD, and X=3,4 for CCSD(T). All energy calculations used in extrapolations were performed in Gaussian 09,[43] while energy calculations using the ANO0 basis were performed in CFOUR.

The anharmonic ZPVE, excluding contributions from the isomerization and methyl torsion modes, was computed using a resonance-free formula.[44] The zero-point energies associated with the methyl torsion and isomerization coordinates were determined by 1D variational solutions of relaxed CCSD(T)/ANO1//CCSD(T)/ANO0 potentials using the procedure of Laane and coworkers.[45-46] The methyl torsion is allowed to relax in the isomerization potential; however, the skeletal torsion is frozen in the methyl torsional potentials. It follows from this that the coupling between the two coordinates is largely ignored. Three additional corrections were

appended to the CCSD(T)/CBS energies. First, the effects of core correlation were accounted for by differencing all-electron and frozen-core energies using CCSD(T) with the cc-pCVTZ basis set.[47] Secondly, diagonal Born-Oppenheimer corrections (DBOC) were computed at the HF/ANO1 level of theory.[48-49] Finally, corrections for post-CCSD(T) electron correlation effects were added. CCSDT(Q) energies were computed only with the ANO0 basis set, and the [CCSDT/ANO0 - CCSD(T)/ANO0] and [CCSDT(Q)/ANO0 – CCSDT/ANO0] increments were assumed to be additive. These are included in the focal point tables (Tables 5.1, 5.2, and 5.3) alongside the extrapolated energies.

Previous work has shown that the higher-order electron correlation correction can be expected to be reasonably close to the basis set limit, even with small basis sets such as ANO0.[50-52] CCSDT(Q)[53-55] energy calculations were performed using the MRCC program.[56] This scheme for evaluating the electronic energies is a form of focal point analysis (FPA) originally proposed by Allen and coworkers.[22-24]

Table. 5.1. Incremented FPA of the *gauche* minimum relative to the *trans* minimum.

Basis Set	**ΔE_{HF}**	**δMP2**	**δCCSD**	**δCCSD(T)**	**δCCSDT**	**δCCSDT(Q)**	**$\Delta E_{CCSDT(Q)}$**
ANO0	+2.74	+0.31	-0.39	+0.15	+0.01	+0.02	[+2.84]
cc-pVTZ	+2.74	+0.25	-0.22	+0.15	[+0.01]	[+0.02]	[+2.95]
cc-pVQZ	+2.76	+0.27	-0.23	+0.16	[+0.01]	[+0.02]	[+3.00]
cc-pV5Z	+2.77	+0.30	-0.23	[+0.16]	[+0.01]	[+0.02]	[+3.03]
cc-pV6Z	+2.77	+0.31	[-0.23]	[+0.16]	[+0.01]	[+0.02]	[+3.04]
CBS limit	[+2.77]	[+0.32]	[-0.23]	[+0.16]	[+0.01]	[+0.02]	[+3.06]

ΔH (0K) = $\Delta E_{electronic} + \Delta_{ZPVE} + \Delta_{core} + \Delta_{DBOC}$ = 3.06 – 0.24 + 0.01 + 0.00 = **2.82 kcal/mol**

Table. 5.2. Incremented FPA of the *gauche* TS relative to the *trans* minimum.

Basis Set	**ΔE_{HF}**	**δMP2**	**δCCSD**	**δCCSD(T)**	**δCCSDT**	**δCCSDT(Q)**	**$\Delta E_{CCSDT(Q)}$**
ANO0	+5.30	+0.80	-0.82	+0.33	+0.02	+0.05	[+5.69]
cc-pVTZ	+5.40	+0.80	-0.69	+0.34	[+0.02]	[+0.05]	[+5.92]
cc-pVQZ	+5.41	+0.84	-0.68	+0.35	[+0.02]	[+0.05]	[+6.00]
cc-pV5Z	+5.42	+0.86	-0.67	[+0.35]	[+0.02]	[+0.05]	[+6.04]
cc-pV6Z	+5.42	+0.88	[-0.67]	[+0.35]	[+0.02]	[+0.05]	[+6.06]
CBS limit	[+5.43]	[+0.91]	[-0.67]	[+0.35]	[+0.02]	[+0.05]	[+6.09]

ΔH (0K) = $\Delta E_{electronic} + \Delta_{ZPVE} + \Delta_{core} + \Delta_{DBOC}$ = 6.09 – 0.53 + 0.01 + 0.00 = **5.57 kcal/mol**

Table. 5.3. Incremented FPA of the *cis* TS relative to the *trans* minimum.

Basis Set	**ΔE_{HF}**	**δMP2**	**δCCSD**	**δCCSD(T)**	**δCCSDT**	**δCCSDT(Q)**	**$\Delta E_{CCSDT(Q)}$**
ANO0	+4.01	-0.10	-0.36	+0.02	-0.02	+0.00	[+3.55]
cc-pVTZ	+4.01	+0.00	-0.33	+0.02	[-0.02]	[+0.00]	[+3.68]
cc-pVQZ	+4.04	+0.02	-0.32	+0.02	[-0.02]	[+0.00]	[+3.74]
cc-pV5Z	+4.04	+0.03	-0.32	[+0.02]	[-0.02]	[+0.00]	[+3.75]
cc-pV6Z	+4.04	+0.03	[-0.32]	[+0.02]	[-0.02]	[+0.00]	[+3.75]
CBS lim.	[+4.04]	[+0.03]	[-0.32]	[+0.02]	[-0.02]	[+0.00]	[+3.75]

ΔH (0K) = $\Delta E_{electronic} + \Delta_{ZPVE} + \Delta_{core} + \Delta_{DBOC}$ = 3.75 – 0.41 + 0.01 + 0.01 = **3.35 kcal/mol**

5.3.2. Relative Free Energy

The aforementioned focal point analysis and anharmonic ZPVE treatment provides the *trans/gauche* interconversion enthalpy at zero Kelvin. To compute the free-energy at 298.15 K, a fairly traditional analysis was conducted.[57] Due to the nature of the structures being compared,

relative free-energy requires only that the rotational entropy, vibrational entropy, and vibrational thermal energy contributions be evaluated. Free energy of isomerization is defined as,

$$\Delta G = \Delta H + \Delta E_{vib} - T(\Delta S_{vib} + \Delta S_{rot}) , \quad (5.3)$$

where ΔH represents the 0 K enthalpy and ΔE_{vib} is relative to v=0, i.e. it does not include the zero-point energy. The rigid-rotor approximation was invoked for the rotational entropy. The harmonic oscillator approximation was used for the vibrational thermal energy and entropy of the 3N-8 highest vibrational degrees of freedom. We decided against an anharmonic treatment of the ΔE_{vib} and ΔS_{vib} terms due to challenges associated with accounting for resonances and the observation that nearly half of all 298.15 K thermal contributions are derived from the torsional modes. For the isomerization and methyl torsion degrees of freedom, partition functions were computed by a direct eigenstate count from the torsional potentials (Fig. 5.3-5.7). In the instance of methyl torsion, a factor of 1/3 appears in front of the partition function expressions, given by the following.

$$Q_{tors}^{CH_3}(T) = \frac{1}{3}\sum_{n=1}^{\infty} e^{\left(-\frac{E_n - E_1}{k_B T}\right)} \quad (5.4)$$

This is because the torsional motion interconverts three indistinguishable versions of isoprene. Eigenstates were summed until the partition functions converged.

Calculating the skeletal torsional partition function for the *trans* conformer is straightforward. All eigenstates localized in the *trans* well were counted. In the energy regime above the *trans-gauche* barrier, where the eigenstates are nearly degenerate pairs, all states were counted toward both *trans* and *gauche*. At 298.15 K, the contribution of these levels to the *trans* partition function is minimal. The distinguishable (enantiomeric) nature of the *gauche* conformers can be accounted for in two equivalent ways. First, the enantiomers can be considered separately. All *gauche* eigenstates can be summed, and a factor of 1/2 can be introduced in front of the

gauche skeletal torsional partition function to prevent overcounting. The fraction of *gauche* isoprene is calculated as follows.

$$\frac{2e^{\left(-\frac{\Delta G}{k_B T}\right)}}{1+2e^{\left(-\frac{\Delta G}{k_B T}\right)}} \tag{5.5}$$

This is the approach used in this study. Alternatively, the *gauche* enantiomers can be considered together, from the beginning, leaving out the 1/2 factor. This is intuitively more appealing at high temperatures, where large fractions of *gauche*-isoprene would be found in excited skeletal torsional states lying above the *gauche-gauche* barrier (*cis*). With this approach, the calculated ΔG is lower and can be interpreted as a *trans-cis* free-energy difference. The fraction of higher energy conformers is then calculated as follows.

$$\frac{e^{\left(-\frac{\Delta G}{k_B T}\right)}}{1+e^{\left(-\frac{\Delta G}{k_B T}\right)}} \tag{5.6}$$

where the factors of 2 are now absent. Both approaches differ only in their interpretation. They give identical population ratios. Subsequently, all thermodynamic quantities were computed directly from the torsional partition functions using standard expressions.[57] This information is collected below (Tables 5.4-5.7).

Table 5.4. Theoretical Torsional Partition Functions (v=0) at 298.15 K.

	Harmonic Oscillator		**Hindered Rotor**	
Rotamer	**Q_{tors} (CC)**	**Q_{tors} (CH_3)**	**Q_{tors} (CC)**	**Q_{tors} (CH_3)**
trans	1.8804	1.5561	1.9119	1.6889
gauche (TS)	0	1.5891	0	1.7027
gauche	2.3957	1.6987	2.6396	1.8774
cis (TS)	0	1.6549	0	1.8229

Table 5.5. Theoretical Entropies at 298.15 K (cal/mol·K).

		Harmonic Oscillator			Hindered Rotor	
Rotamer	**S_{rot}**	**S_{vib} (3N-8)**	**S_{vib} (CC)**	**S_{vib} (CH_3)**	**S_{vib} (CC)**	**S_{vib} (CH_3)**
trans	25.5581	5.6577	2.5825	2.0157	2.6933	2.4175
gauche (TS)	25.6300	6.2390	0	2.0821	0	2.4474
gauche	25.5955	5.9185	3.2346	2.2865	3.5202	2.7224
cis (TS)	25.5981	5.7875	0	2.2074	0	2.6500

Table 5.6. Theoretical Vibrational Thermal Corrections (v=0) at 298.15 K (kcal/mol).

	Harmonic Oscillator			Hindered Rotor	
Rotamer	**E_{vib} (3N-8)**	**E_{vib} (CC)**	**E_{vib} (CH_3)**	**E_{vib} (CC)**	**E_{vib} (CH_3)**
trans	1.1842	0.3958	0.3390	0.4190	0.4103
gauche (TS)	1.2692	0	0.3464	0	0.4144
gauche	1.2220	0.4468	0.3678	0.4745	0.4385
cis (TS)	1.2103	0	0.3597	0	0.4344

Table 5.7. Theoretical Zero Point Vibrational Energies (kcal/mol).

	Harmonic Oscillator			Resonance Free VPT2			Hindered Rotor	
Rotamer	**E(3N-8)**	**E(CC)**	**E(CH_3)**	**E(3N-8)**	**E(CC)**	**E(CH_3)**	**E(CC)**	**E(CH_3)**
trans	70.4329	0.2248	0.3048	69.4952	0.2185	0.2981	0.2279	0.3014
gauche (TS)	70.1502	0	0.2940	69.2046	0	0.2848	0	0.2897
gauche	70.2961	0.1601	0.2432	69.3559	0.1560	0.2522	0.1647	0.2592
cis (TS)	70.2827	0	0.2746	69.3458	0	0.2657	0	0.2710

5.3.3. Anharmonic Theory

The local mode Hamiltonian model developed by Sibert and coworkers is an appealing approach for dealing with anharmonic coupling in the CH stretch spectral region.[16, 18-20] However, their model relies upon parameterization. To our knowledge, Sibert's local mode model in its current form cannot handle the CH stretch / (C=C stretch + HCH bend) interactions that are so important (*vide infra*) for isoprene and indeed for other unsaturated hydrocarbons.[58] Predictions

of the isoprene vibrational spectra were made using the VPT2+K method.[21, 59-61] Quadratic force constants and first derivatives of the dipole moment were computed at CCSD(T)/ANO1 by numerical differentiation of analytic gradients. Cubic and semi-diagonal quartic force constants were computed by numerical differentiation of CCSD(T)/ANO0 analytic second derivatives.[62] These force constants were combined into a hybrid force field.[17] The standard VPT2 procedure was carried out, using scripts written in Mathematica.[63]

Similar effective Hamiltonians were built for both *trans* and *gauche* conformers. All of the CH stretching fundamentals were included (8 states). Then 2-quanta vibrational states were chosen in a systematic way, on the basis of zeroth-order energies and Martin diagnostic values.[64] The Martin diagnostic used here is not the approximate formula; rather, it is the exact difference between the second-order perturbation theory correction and the variational correction resulting from a 2-state interaction.[64] All possible 2-quanta states were built from the following 9 normal coordinates: three CH_3 scissors, two CH_2 scissors, one CH in-plane bend, one skeletal bend, and the symmetric and antisymmetric C=C stretches (45 states). The complete list of normal modes is available in Tables 5.8-5.9. The diagonal elements of the effective Hamiltonian were the VPT2 frequencies of each state, deperturbed for interactions with all other states within the effective Hamiltonian. Off-diagonal matrix elements involve cubic and quartic force constants and provide explicit Fermi and Darling-Dennison couplings. Diagonalization of the effective Hamiltonian yields the anharmonic transition frequencies. Anharmonic intensities are determined from the CCSD(T)/ANO1 harmonic intensities, where the intensity of each anharmonic transition is simply proportional to the fraction of each zeroth-order CH stretching state that it contains.

Connected resonances are also present in these systems. These can complicate the polyads, and they require more careful treatment. These are instances where a fundamental of one of the 9 normal coordinates that were selected to populate the list of 2-quanta states is in Fermi resonance with some further 2-quanta state. This 2-quanta state is typically characterized by

Table. 5.8. Qualitative descriptions, symmetries, and CCSD(T)/ANO1 harmonic frequencies and intensities of the *a′* normal modes of vibration of *trans*-isoprene.

Mode	ω (cm^{-1})	I (km/mol)	Shorthand	Description
1	3244.5603	10.6243	$\nu_{as}(CH_2)$	antisymmetric CH_2 stretch (vinyl)
2	3234.3193	9.9565	$\nu_{as}(CH_2)$	antisymmetric CH_2 stretch (methylene)
3	3162.0021	4.1880	$\nu^{in}(CH_2)$	symmetric vinyl stretch in-phase
4	3151.5980	10.2346	$\nu^{out}(CH_2)$	symmetric vinyl stretch out-of-phase
5	3144.9542	4.1569	$\nu_s(CH_2)$	symmetric methylene stretch
6	3129.8661	15.8022	$\nu_{as}(CH_3)$	antisymmetric CH_3 stretch
7	3033.6159	15.8656	$\nu_s(CH_3)$	symmetric CH_3 stretch
8	1693.0579	1.4442	ν_s(C=C)	symmetric C=C stretch
9	1644.0767	19.5574	ν_{as}(C=C)	antisymmetric C=C stretch
10	1503.1165	6.0597	$\delta_{as}(CH_3)$	antisymmetric CH_3 scissor
11	1459.0536	1.4189	$\delta^{in}(CH_2)$	CH_2 scissor in-phase
12	1431.7524	3.1731	$\delta^{out}(CH_2)$	CH_2 scissor out-of-phase
13	1406.6981	5.6469	$\delta_s(CH_3)$	CH_3 symmetric scissor (umbrella)
14	1334.3384	0.7874	δ(skeletal)	skeletal bend (central)
15	1314.2937	0.1379	δ(CH)	CH bend
16	1084.0800	3.1146	$\rho_r(CH_2+CH_3)$	methylene CH_2 and CH_3 rock
17	1004.9739	0.2257	$\rho_r(CH_2+CH_3)$	vinyl CH_2 and CH_3 rock
18	964.4903	0.7134	ν_{as}(C-C)	antisymmetric C-C stretch
19	792.1836	0.1036	ν_s(C-C)	symmetric C-C stretch
20	527.7516	0.0427	δ(skeletal)	skeletal bend (vinyl, center)
21	415.9823	1.5062	δ(skeletal)	skeletal bend (methylene, methyl)
22	277.8314	0.7880	δ(skeletal)	skeletal bend (vinyl, methyl)

Table. 5.9. Qualitative descriptions, symmetries, and CCSD(T)/ANO1 harmonic frequencies and intensities of the *a″* normal modes of vibration of *trans*-isoprene.

Mode	ω (cm^{-1})	I (km/mol)	Shorthand	Description
23	3096.7754	13.1548	$\nu_{as}(CH_3)$	antisymmetric CH_3 stretch
24	1484.6844	7.7274	$\delta_{as}(CH_3)$	antisymmetric CH_3 scissor
25	1066.1355	0.1490	$\rho_r(CH_3)$	CH_3 rock
26	1016.4185	16.9475	$\delta(CH)$	CH bend
27	923.3859	31.6880	$\rho_w(CH_2)$	CH_2 wag (vinyl)
28	910.7999	40.9321	$\rho_w(CH_2)$	CH_2 wag (methylene)
29	777.5147	0.5691	$\rho_t^{in}(CH_2)$	twisting in-phase (vinyl, methylene)
30	639.7732	0.2006	$\rho_t^{out}(CH_2)$	twisting out-of-phase (vinyl, methylene)
31	398.5607	9.4163	ρ_w(skeletal)	central carbon wag
32	213.2430	0.2929	$\tau(CH_3)$	methyl torsion
33	157.2597	0.1045	$\tau(CC)$	skeletal torsion

skeletal bending and/or CH wagging/rocking/twisting. This resonance affects the energies of the 2-quanta states in the effective Hamiltonian, which in-turn affects the 1-quantum CH stretches. Correction for this necessitates the addition of 3-quanta states to the effective Hamiltonian. The Martin diagnostic with a threshold of 1 cm^{-1} was used to identify such connected resonances: seven are found for *trans* and five are found for *gauche*. By inspection of the normal modes involved in each resonance, three of them are found to involve very closely the same motions in both conformers. It was endeavored to make the simulations for both conformers comparable, so as to facilitate a fair comparison of band positions. Based on further comparisons of the normal modes, 2 resonances were added to the *trans* list, and 4 were added to the *gauche* list, bringing the total to 9 connected resonances apiece (72 states).

Identified resonances involving torsionally-excited states were ignored; these interactions were kept perturbed. This practice was helpful for reducing the complexity of the effective Hamiltonian; and in our experience, there really is no good way to handle torsions within the framework of VPT2+K. However, very large Martin diagnostic values for these stretch-torsion couplings should be a cause for concern. The Martin diagnostic does not turn up any strong (> 10 cm^{-1}) stretch-torsion resonances in the *trans* conformer, but the *gauche* conformer exhibits 22 cm^{-1} and 14 cm^{-1} resonances that affect the $\rho_t^{out}(CH_2)$ and the methylene $\rho_w(CH_2)$ fundamentals, respectively. These resonances weakly affect the $\delta_s(CH_3)$ and $\delta^{out}(CH_2)$ fundamentals, which are rather important, and they more strongly affect the highest frequency δ(skeletal) fundamental, which is the least important of the 9 selected normal coordinates. Through Fermi-coupling, this affects $\nu_s(CH_2)$ and a'-$\nu_{as}(CH_3)$, which contribute primarily to the middle region of the spectrum (~ 2950-3030 cm^{-1}).

A common feature of both conformers is a medium-valued Martin diagnostic (5 cm^{-1} in *trans* and 8 cm^{-1} in *gauche*) for the interaction between $\nu_s(CH_3)$ and $2\tau(CH_3)$. We note that it is commonplace for these kinds of states, i.e. a torsional overtone and the corresponding symmetric stretch, to experience strong potential coupling. This is a feature of the rectilinear normal coordinate system.[65] Because the $\nu_s(CH_3)$ transition intensity tends to be distributed in the lower regions of the CH stretch spectrum, we might expect the predictions in that region to be less reliable on account of this.

5.4. Results and Discussion

5.4.1. Interconversion Potential

A potential surface for rotation about the central carbon-carbon single bond is given in Figure 5.2. The potential was generated via Fourier fit to 61 evenly-spaced points at the CCSD(T)/ANO1//CCSD(T)/ANO0 level of theory. Structures of the various stationary points are

superimposed. Additionally, each stationary point is labeled with its 0 K enthalpy and 298.15 K free energy, based on the electronic energies from focal point analysis. The relaxed skeletal torsional potential, with squared torsional wavefunctions, is presented below (Fig. 5.3). The one-dimensional torsional problems were solved variationally in a free-rotor basis.[46] The Hamiltonian used was the general internal motion Hamiltonian, originally derived by Meyer and Günthard.[45] It is has the following form,

$$\widehat{\mathrm{H}} = -\frac{\partial}{\partial\tau}\mathrm{B}(\tau)\frac{\partial}{\partial\tau} - \frac{1}{4}\frac{\partial}{\partial\tau}\mathrm{B}(\tau)\frac{\partial \ln|\mathrm{G}(\tau)|}{\partial\tau} + \frac{1}{16}\mathrm{B}(\tau)\left(\frac{\partial \ln|\mathrm{G}(\tau)|}{\partial\tau}\right)^2 + \mathrm{V}(\tau) \tag{5.7}$$

where $\mathrm{B}(\tau)$ represents the internal rotation constant, $|\mathrm{G}(\tau)|$ is the determinant of the rovibrational G-matrix, and $\mathrm{V}(\tau)$ is the *ab initio* potential. Inverse G-matrices were calculated numerically from the optimized Cartesian coordinates at each point along the relaxed scan.

$$G(\tau)^{-1} = \begin{pmatrix} I_{xx} & -I_{xy} & -I_{xz} & X_{x1} \\ -I_{yx} & I_{yy} & -I_{yz} & X_{y1} \\ -I_{zx} & -I_{zy} & I_{zz} & X_{z1} \\ X_{1x} & X_{1y} & X_{1z} & Y_{11} \end{pmatrix} \tag{5.8}$$

The first, pure-rotational block of the matrix is the traditional moment of inertia tensor, the X elements are rotation-vibration couplings, and Y_{11} is the pure vibrational term, defined below.

$$X_{\alpha 1} = \sum_{i=1}^{N} m_i \left[r_i \times \left(\frac{\partial r_i}{\partial q_1}\right)\right]_\alpha \tag{5.9}$$

$$Y_{11} = \sum_{i=1}^{N} m_i \left(\frac{\partial r_i}{\partial q_1}\right)^2 \tag{5.10}$$

In these expressions, sums are over all atoms in the system, q_1 is the torsional coordinate, and r_i is the Cartesian displacement of atom *i* from the center of mass. The inverse G-matrices were inverted to obtain G-matrices.

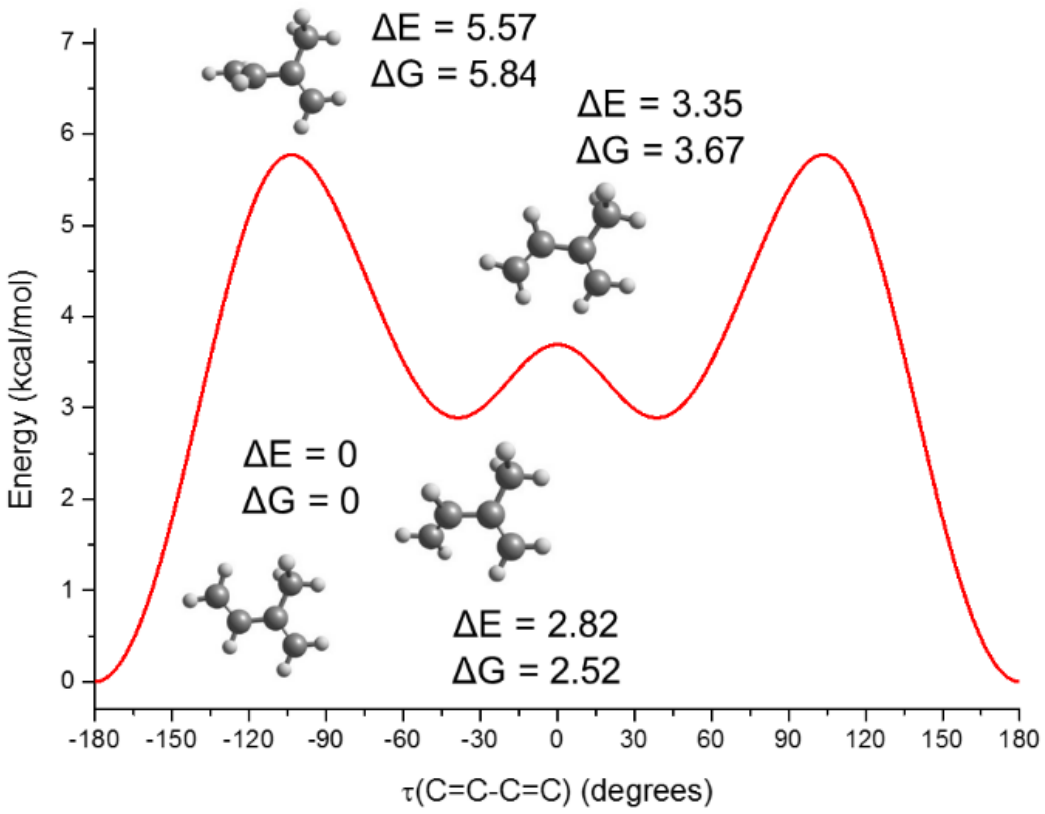

Figure 5.2. Relaxed torsional potential about the isoprene single C-C bond at the CCSD(T)/ANO1//CCSD(T)/ANO0 level of theory. The energy axis corresponds to the electronic energy differences at this level of theory, but the more rigorous determinations of the 0 K enthalpy and 298.15 K free energy are shown in text for each stationary point (also given in kcal/mol).

$$G(\tau) = \begin{pmatrix} g_{11} & g_{12} & g_{13} & g_{14} \\ g_{21} & g_{22} & g_{23} & g_{24} \\ g_{31} & g_{32} & g_{33} & g_{34} \\ g_{41} & g_{42} & g_{43} & g_{44} \end{pmatrix} \tag{5.11}$$

The internal rotation constant (Eqn. 5.12) was obtained directly from these.

$$\mathrm{B}(\tau) = \frac{\hbar^2}{2} g_{44} \tag{5.12}$$

Then $B(\tau)$, $\ln|G(\tau)|$, and $V(\tau)$ were expanded in Fourier series. It is common to define the last two terms in the kinetic energy part of the Hamiltonian as a pseudopotential because of their resemblance to the actual potential.[46] The effect of the pseudopotential on the final eigenvalues is often insignificant, especially for larger systems. It was evaluated regardless and added to the potential, forming an effective potential. Then the Hamiltonian matrix was built and diagonalized, using the published matrix element expressions.[46]

Relaxed methyl torsional potentials for the *trans* and *gauche* minima and the *cis* and *gauche* saddle points are presented below (Fig. 5.4-5.7). Squared torsional wavefunctions are plotted on each potential. A savvy reader will notice that the wavefunctions do not have the correct symmetry properties. This is because the threefold symmetry of these torsional problems was not respected (or enforced). While the potentials do display threefold symmetry, at least within the requested precision of the *ab initio* calculations, the reduced mass functions deviate slightly from this, and they are only rigorously symmetric about 0 and π. This is because the rotation of each methyl group was described by a single (C=C-C-H) dihedral angle. A symmetry-conserving coordinate would involve an average of three dihedral angles, in effect, following all three methyl hydrogens simultaneously. A more in-depth discussion of this problem is provided by Allen and coworkers.[66] The consequence of this is that the 0 degree well is considered nonequivalent to the ± 120 degree wells, and a subset of the torsional states below the barrier which should be doubly degenerate are only approximately so. We considered a few crude procedures for symmetrizing our reduced mass functions. We ultimately found that the asymmetry introduced a negligible amount of error into the partition functions, since partition functions are computed only from the eigenvalues and do not depend on amplitudes.

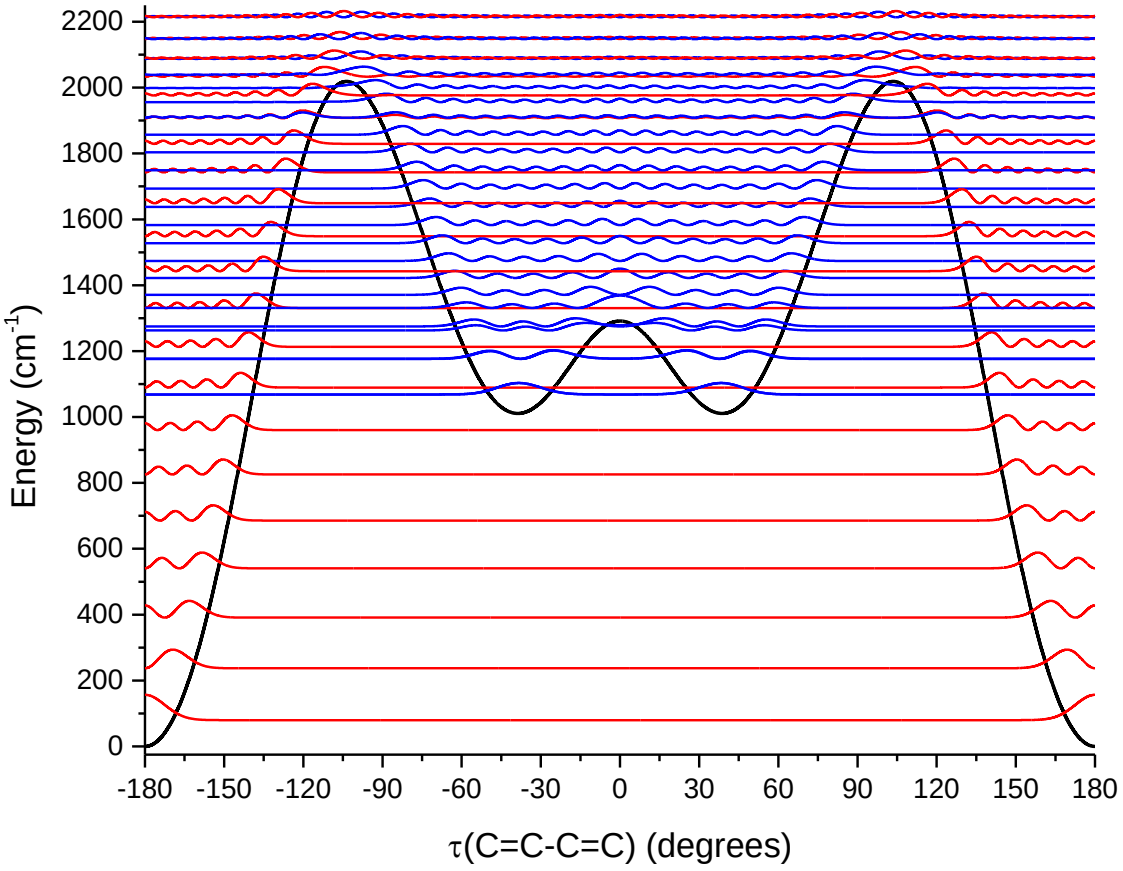

Figure 5.3. Relaxed skeletal torsional PES. The fundamental torsional transitions are 158 cm^{-1} for the *trans* conformer and 108/109 cm^{-1} for the *gauche* conformer. The *trans* levels are red, and *gauche* levels are blue.

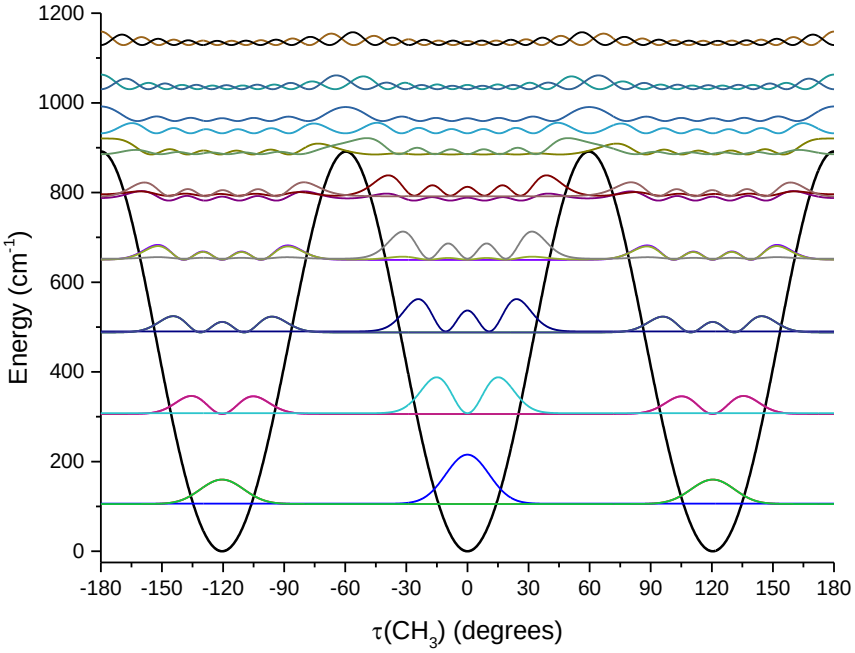

Figure 5.4. Semi-relaxed methyl torsional PES of *trans*-isoprene. The fundamental methyl torsional transition is 202 cm^{-1}.

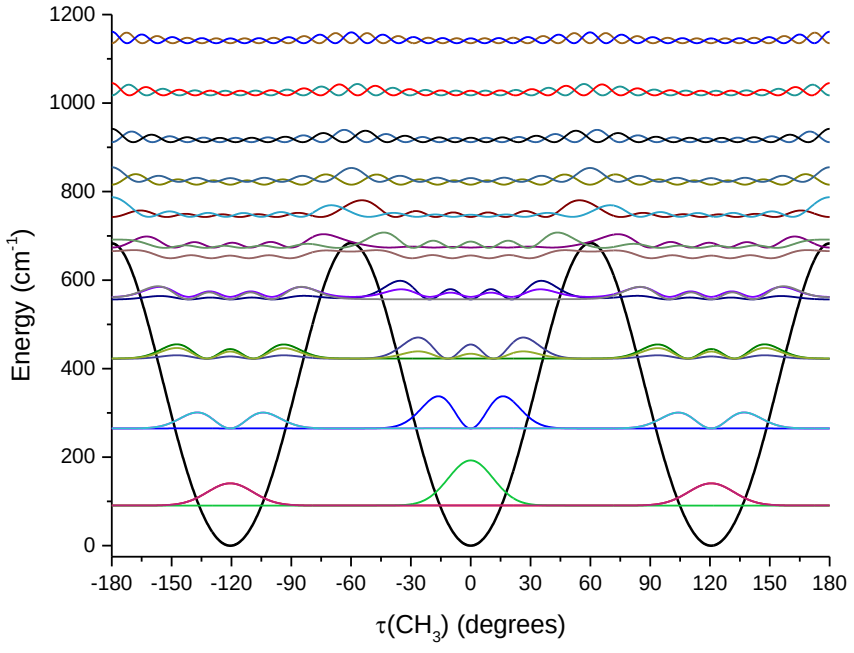

Figure 5.5. Semi-relaxed methyl torsional PES of *gauche*-isoprene. The fundamental methyl torsional transition is 174 cm^{-1}.

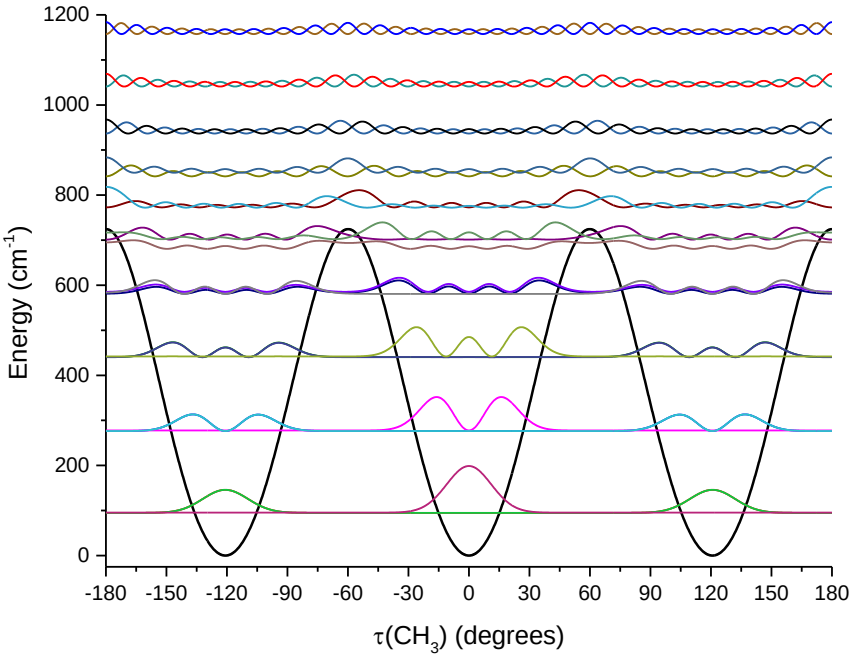

Figure 5.6. Semi-relaxed methyl torsional PES of the *cis*-isoprene TS.

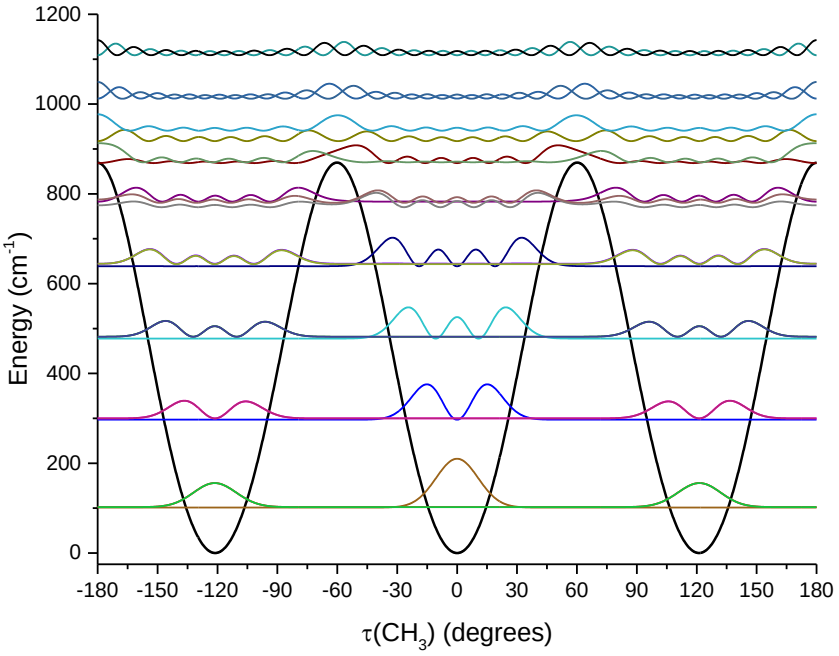

Figure 5.7. Semi-relaxed methyl torsional PES of the *gauche*-isoprene TS.

5.4.2. Thermochemistry

The results of focal point analyses are found in Tables 5.1, 5.2, and 5.3. These tables report the extrapolated electronic energy differences from *trans*-isoprene (defined as 0) to *gauche*, *gauche* (TS), and *cis* (TS) isoprene, respectively. Calculations of the enthalpy differences are shown below each table. The HF energy differences are seen to converge to within 0.01 kcal/mol on all three tables. The net electron correlation energy converges somewhat slowly [see δMP2], but the convergence of correlation energy increments [see δCCSD and δCCSD(T)] is more rapid. These increments all converge to ± 0.01 kcal/mol. It is clear that the convergence of the electronic energy is least complete for the *gauche* transition state. Convergence of the MP2 correlation energy is incomplete even with the large cc-pV6Z basis set, and this stationary point also possesses a large (+0.05 kcal/mol) CCSDT(Q) increment. This is not altogether surprising, as transition states often exhibit more multiconfigurational character than potential minima. It is reasonable then, that more thorough treatments of electron correlation, post-CCSDT(Q), would be necessary to describe it to our desired accuracy.

The *cis* transition state is comparatively very well-described, showing ± 0.01 kcal/mol convergence by CCSD/cc-pV5Z owing to a cancellation of small, higher-order CC contributions. The superior convergence of the *cis* TS relative to the *gauche* TS can be rationalized as due to two competing effects which give rise to these saddle points.[15] Conjugation of the C=C-C=C backbone is stabilizing, and steric repulsion, between hydrogens on separate CH_2 groups, is destabilizing. The *cis* transition state is stabilized by conjugation of its bonds; but by deforming slightly, to *gauche* with a dihedral angle of 38.7 degrees, it alleviates steric strain and achieves a lower energy. The *gauche* TS, however, arises from a profound breaking of the π-conjugation. At this geometry, the C=C bonds are nearly orthogonal to each other, τ(C=C-C=C) = 103.6 degrees, the central C-C bond is at its longest, the C=C bonds are shortest, and the electronic structure is quite different. No further discussion of the geometries will be given; however, a table of selected

CCSD(T)/ANO1 internal coordinates is provided below (Table 5.10). The FPA convergence of the *gauche* minimum is intermediate between the two transition states, and this structure exhibits an intermediate degree of conjugation-breaking. For all stationary points, the contributions from core-correlation corrections (Δ_{core}) and adiabatic corrections (Δ_{DBOC}) are small ($\leq$ 0.01 kcal/mol). Conservative error bars for the relative electronic energies would be ± 0.1 kcal/mol.

Relative enthalpies and free energies of isomerization, in addition to hindered-rotor corrections, are given in Table 5.11. It can be seen that the 1D variational treatment of the torsional modes leads to large entropic corrections. However, corrections for the methyl torsional degree of freedom are similarly valued for all rotamers; thus, they do not contribute greatly to relative free energies. This seems reasonable. All four structures possess methyl groups in similar chemical environments. In contrast, the hindered-rotor correction for skeletal torsion increases the entropy of the *gauche* conformer by 0.18 cal/mol·K relative to the *trans* conformer. Combined with the methyl torsion correction, the net hindered-rotor correction to the entropy is +0.22 cal/mol·K. This stabilizes *gauche*-isoprene by 0.06 kcal/mol relative to *trans*-isoprene, at room temperature. Because the skeletal torsional mode does not contribute to the free-energy of the transition states, the hindered-rotor treatment destabilizes *gauche* (TS) by only 0.02 kcal/mol relative to *trans*. The relative free energy of *cis*-isoprene is insensitive to hindered-rotor treatment.

Our relative 0 K enthalpy and 298.15 K free energies are generally close to the values computed by Allodi and coworkers. [13] This is particularly evident for the *trans*-*cis* differences. In part due to the previously discussed cancellation of higher-order CC contributions and the rapid basis set convergence, our 0 K enthalpy change of 3.35 kcal/mol differs from their result by only about 0.01 kcal/mol, and our 298.15 K free energy change is 3.68 kcal/mol, identical to two decimal places. For the *trans-gauche* interconversion enthalpy, they computed 2.66 kcal/mol, somewhat lower than our 2.82 kcal/mol. Partly due to their harmonic treatment of the torsional

Table 5.10. Selected Internal Coordinates. Angles are measured in degrees, and bond distances are expressed in Angstroms.

Rotamer	**τ(C=C-C=C)**	**r(C-C)$_{central}$**	**r(C=C)$_{vinyl}$**	**r(C=C)$_{methylene}$**
trans	180.000	1.4687	1.3429	1.3454
gauche (TS)	103.587	1.4920	1.3379	1.3394
gauche	38.670	1.4791	1.3405	1.3424
cis (TS)	0.000	1.4816	1.3415	1.3429

Table. 5.11. Contributions to the Relative Free Energies (kcal/mol) at 298.15 K.[a]

Rotamer	**ΔH_0**	**E_{vib}**	**δE(CC)**	**δE(CH_3)**	**S_{vibrot}**	**δS(CC)**	**δS(CH_3)**	**δ*G***	**ΔG_{298}**
trans	**0**	1.92	+0.02	+0.07	35.81	+0.11	+0.40	0	**0**
gauche (TS)	**+5.57**	1.62	0	+0.07	33.95	0	+0.37	+0.02	**+5.84**
gauche	**+2.82**	2.04	+0.03	+0.07	37.04	+0.29	+0.44	-0.06	**+2.52**
cis (TS)	**+3.35**	1.57	0	+0.07	33.59	0	+0.44	+0.00	**+3.67**

[a] Enthalpic corrections are given in kcal/mol, and entropic corrections are in cal/mol·K. The δE, δS, and δG quantities are hindered-rotor corrections at 298.15 K, defined as [(hindered-rotor) – (harmonic oscillator)].

contributions, they underestimate the stabilizing effect of free-energy upon *gauche*-isoprene by nearly 0.1 kcal/mol. Overall, our calculations agree that thermal/entropic effects should stabilize *gauche*-isoprene and destabilize both of the transition states, relative to *trans*-isoprene. We stress that the focal point approach allows us to observe the convergence of the electronic energies (the largest contribution to all relative energetics) and to estimate the errors associated with basis set incompleteness and deficiency in electron correlation. The CCSD(T)/aug-cc-pVTZ// BHandHLYP/6-311G** model chemistry used by Allodi and coworkers, chosen for its suitability not only for isoprene but also for various complexes/adducts with hydroxyl radical, appears to

have been a wise choice. However, we feel that our convergent *ab initio* approach, with consideration of anharmonic effects, should be preferred for the isomerization of neat isoprene.

We now consider a comparison of our computed *trans-gauche* thermochemistry to the experimentally-derived interconversion enthalpy of Squillacote and Liang.[15] In their report, a series of IR spectra were obtained by changing the temperature of the source used to co-deposit isoprene and N_2 onto a cold CsI window. The *trans-gauche* interconversion enthalpy was obtained via a van't Hoff analysis (2.46 kcal/mol), and it was compared to a computed ΔH_0 (2.73 kcal/mol) obtained with the composite G3 method. However, the van't Hoff analysis provides an average interconversion enthalpy, over the range 300-800 K, assuming no isoprene interconversion on the timescale of cooling in the solid-N_2 matrix. To justify direct comparison to their theoretical ΔH_0 value, they noted that (harmonic) thermal corrections to the interconversion enthalpy of *(E)*-pentadiene were insignificant, never exceeding 0.015 kcal/mol over the same temperature range. We must assume that similar insensitivity was seen for isoprene. This does not agree with our calculations. We predict a far greater temperature dependence in isoprene's ΔH over this range, varying 0.533 kcal/mol in a nonlinear manner (Figure 5.8). Furthermore, even harmonic thermal corrections at the CCSD(T)/ANO1 level of theory show a modest temperature dependence, 0.042 kcal/mol, about 3 times higher than what was implied by Squillacote and Liang.[15] We are unconvinced that the experimental number can be meaningfully compared to any 0 K theoretical value. The average (anharmonic) thermal correction over the 300-800 K temperature range is -0.079 kcal/mol. Using this to correct our 0 K value (2.82 kcal/mol), we obtain an average enthalpy change, $\Delta\overline{H}$, of 2.74 kcal/mol. This is 0.28 kcal/mol higher than the experimental value.

Squillacote and Liang reported,[15] for *(E)*-pentadiene, that ΔH varied about ± 0.3 kcal/mol depending on which *gauche* and *trans* vibrational bands were chosen for van't Hoff analysis. However, they did not report an error bar for their isoprene experiment, and we again assume that

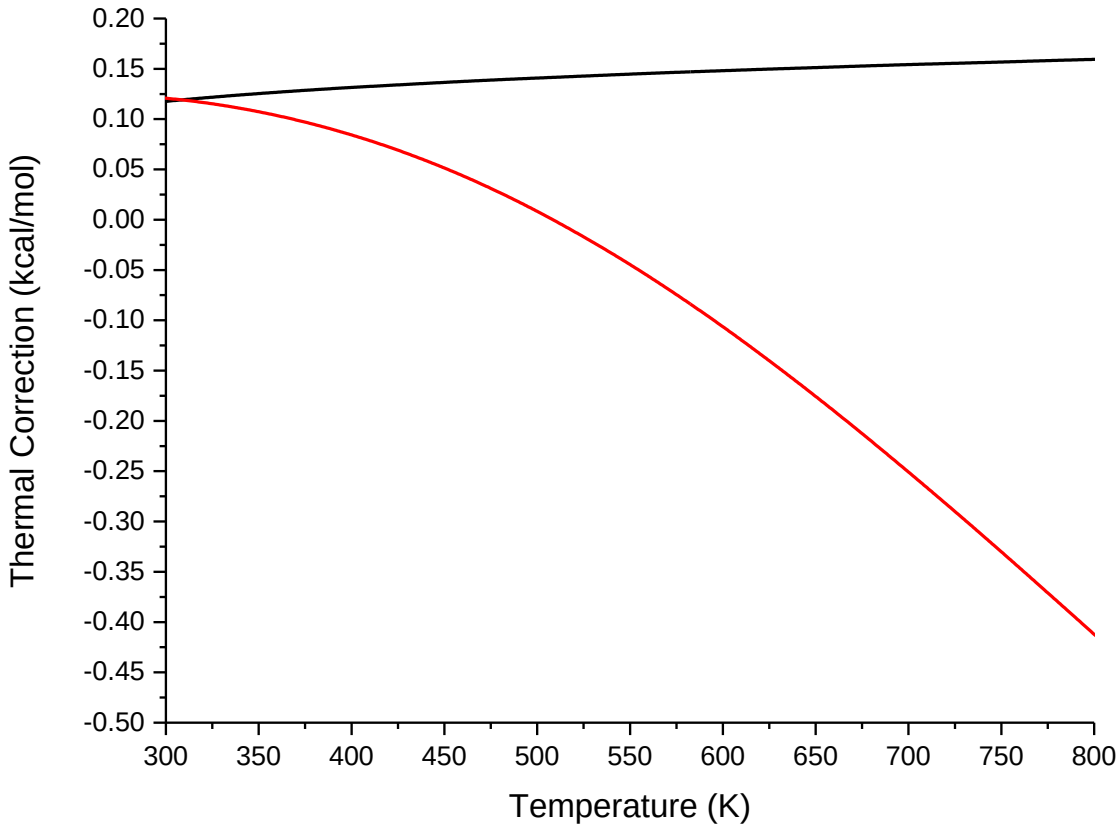

Figure 5.8. Plot of the thermal correction to the enthalpy of isomerization over the temperature range: 300-800K. (black) 3N-6 harmonic. (red) 3N-8 harmonic with anharmonic/hindered rotor treatment of torsional degrees of freedom.

a similar deviation was observed. Our $\Delta\bar{H}$ value then falls just within the upper bound of the experimental error bars. As noted above, the error in our calculations is lower than the reported experimental error by at least a factor of three. We suggest that our computed results represent the most accurate thermochemistry on the isoprene system, at present.

5.4.3. Infrared Spectroscopy

The experimental IR spectrum and VPT2+K simulations for both isoprene rotamers are presented in Figure 5.9. On the basis of the computed thermodynamics, both *gauche* and *trans*

species should contribute to the experimental spectrum; although, *trans* should dominate (97.2% abundance). The spectrum was measured with the quadrupole mass spectrometer tuned to pass ions of only m/z = 67, as described in Section 5.2. There is generally good agreement between the experimental spectrum and the VPT2+K predictions for the *trans* rotamer; and as discussed below, a few weaker features can be confidently assigned to the *gauche* rotamer. Although the PUC pressure conditions and choice of mass channel minimize the presence of features due to isoprene dimers, some of the weak, broad spectral features are potentially due to these low abundance dimers, which could feasibly have several isomeric structures. The nature of these species is not considered in this report.

The scaled harmonic spectrum of the *trans*-isoprene species (black) is compared to the full VPT2+K treatment (red) in Figure 5.10. The polyads of *a'* and *a''* symmetry are separated for clarity. It is evident from this comparison that the anharmonic coupling predicted by VPT2+K leads to a spectral complexity in the CH stretch region that disagrees qualitatively with the predictions of the harmonic oscillator model. A detailed discussion of polyad membership is provided in the following section.

5.4.4. Detailed Spectroscopic Assignments

5.4.4.1. Antisymmetric CH_2 Stretches

The two most prominent experimental transitions at 3102 and 3092 cm^{-1} are clearly assignable to the antisymmetric CH_2 stretches of *trans*-isoprene. The corresponding theoretical transitions fall at 3099 and 3090 cm^{-1}. The higher frequency transition is mostly localized on the vinyl CH_2; whereas, the lower is localized on the methylene CH_2. There appear to be several more transitions in this region. Comparison to a high temperature scan of this region (Fig. 5.11) suggests that the small band at 3098 cm^{-1} and the partially-resolved features at 3096 and 3094 cm^{-1} derive from the *gauche* conformer. The *gauche* simulation predicts that this region contains

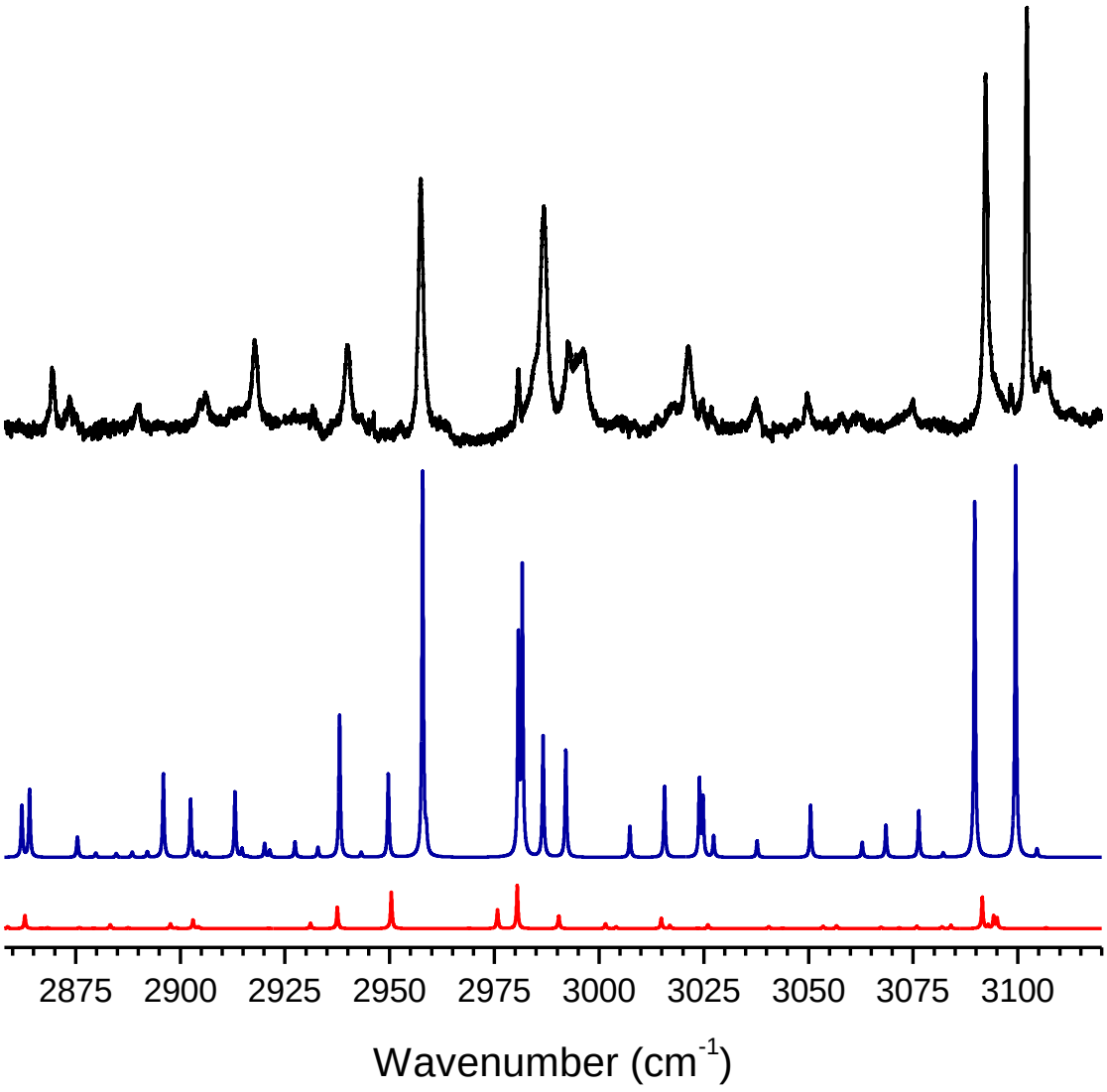

Figure 5.9. Experimental spectrum (black) and theoretical spectra of *trans* (blue) and *gauche* (red) isoprene. The intensities are scaled to reflect the relative populations at room temperature, but *gauche* has been additionally magnified three times to improve visibility.

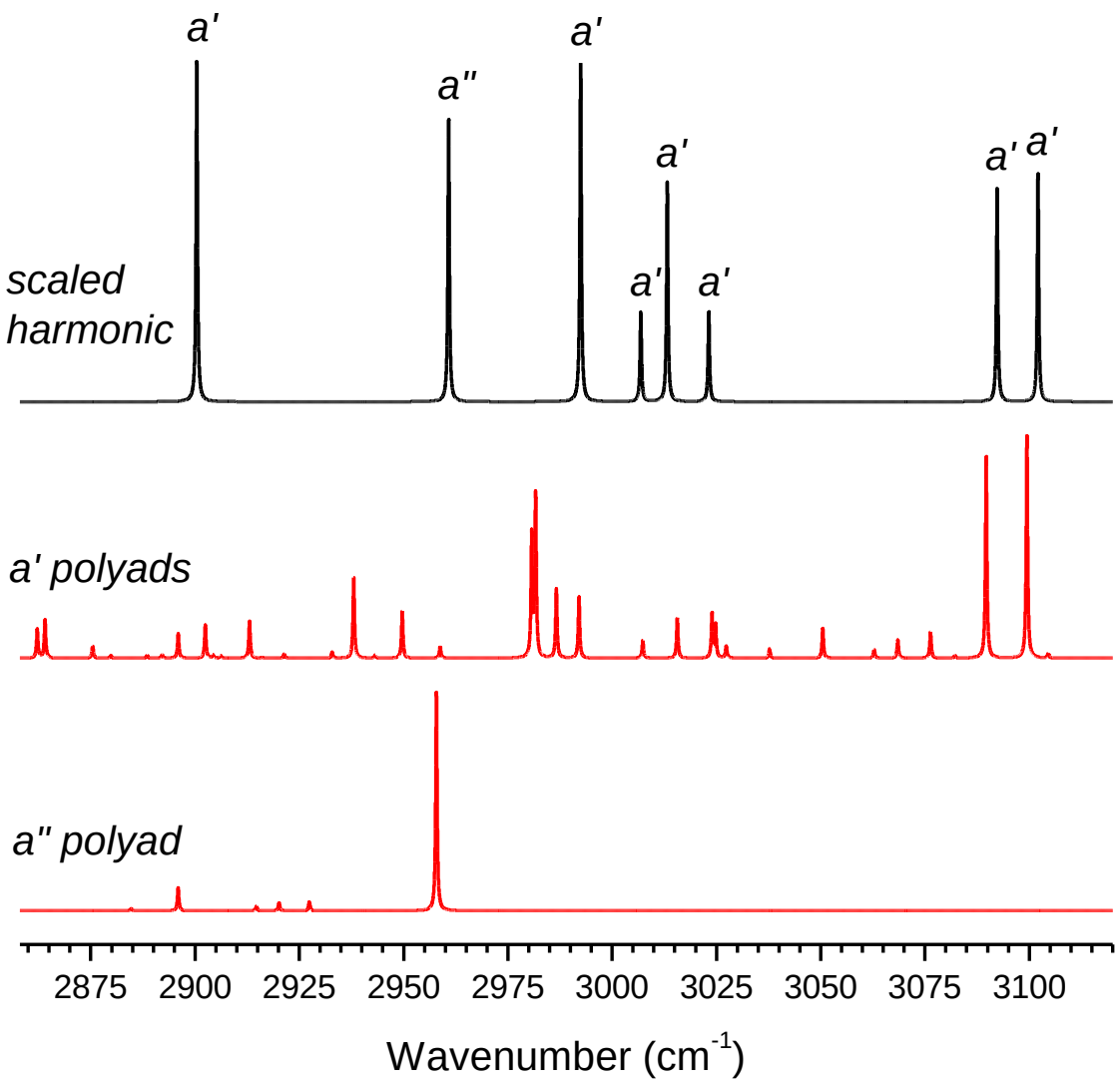

Figure 5.10. Comparison of scaled CCSD(T)/ANO1 harmonic frequencies with VPT2+K frequencies, separated by symmetry, for *trans*-isoprene. The scaling factor is chosen to best match the experimental antisymmetric CH_2 stretch frequencies.

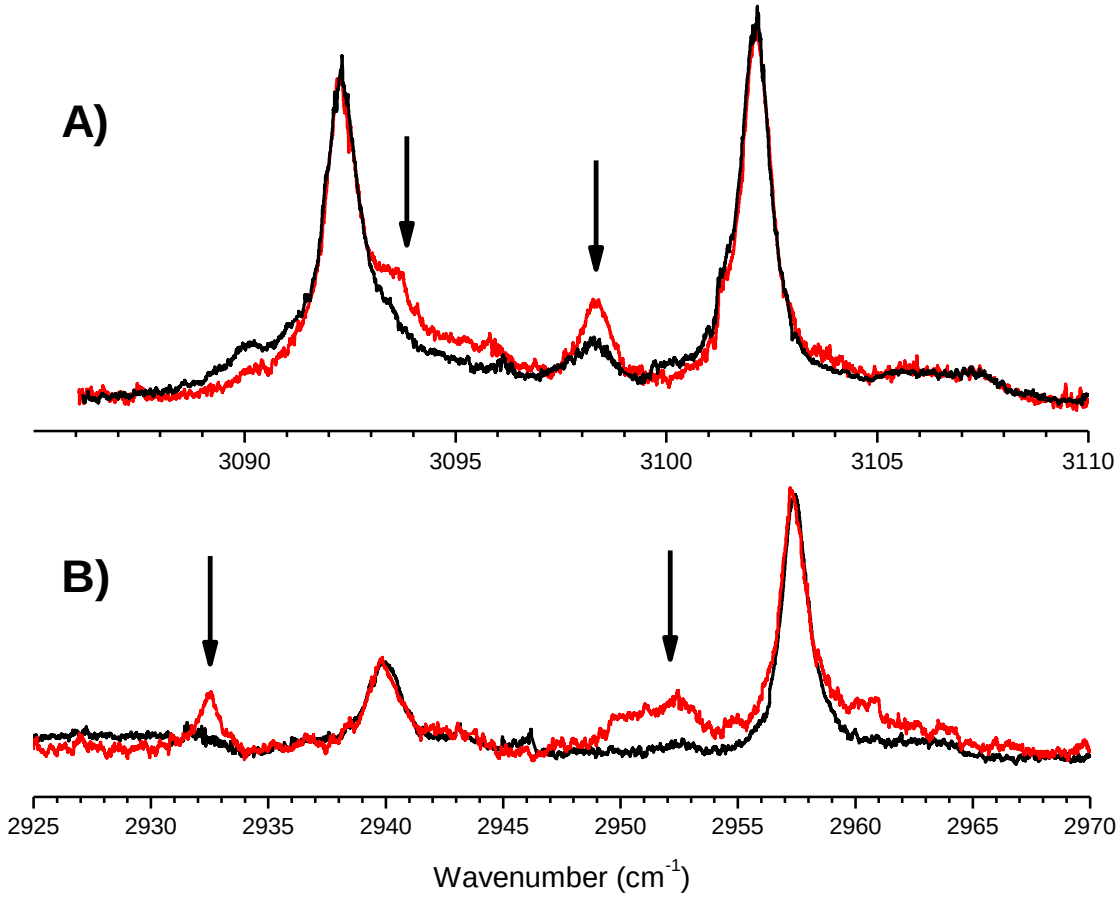

Figure 5.11. (A) Comparison of antisymmetric stretching region with isoprene samples at approximately 300 K (black) and 700 K (red). Spectra are scaled to maximize overlap of the intense *trans* transitions at 3092 and 3102 cm^{-1}. (B) Comparison of lower frequency region with isoprene samples at approximately 300 K (black) and 700 K (red). Spectra are scaled to maximize overlap of the *trans* fundamental at 2958 cm^{-1}. Candidate *gauche* bands are indicated by the black arrows.

multiple resonances, with the vinyl $\nu_{as}(CH_2)$ being split into peaks at 3095 and 3094 cm^{-1} via mixing with the nearby [$\nu_{as}(C=C)$ + a''-$\delta_{as}(CH_3)$] combination. The methylene $\nu_{as}(CH_2)$ is 80% pure, having 10% of the [$\nu_s(C=C)$ + a' -$\delta_{as}(CH_3)$] combination. It is predicted at 3091.5 cm^{-1}. An additional feature arises at 3093 cm^{-1} that borrows small amounts (5%) of both antisymmetric

CH_2 stretches, but is primarily [ν_s(C=C) + δ(skeletal) + $\rho_r(CH_3)$]. This feature loses much of its intensity if Darling-Dennison couplings are neglected. It seems reasonable that the peak at 3098 cm^{-1} holds most of the vinyl $\nu_{as}(CH_2)$ intensity, the shoulder at 3094 cm^{-1} is the methylene $\nu_{as}(CH_2)$ fundamental, and the weak feature at 3096 cm^{-1} is a combination that borrows a bit of intensity from both. Additional features at 3106 and 3090 cm^{-1} do not have clear assignments. These could correspond to low intensity *trans* features or may be signatures of strong antisymmetric stretches of low-abundance dimers having several conceivable structures.

Most of the remaining transitions are also of mixed character in the simulations, and sometimes the mixing is so extensive that a meaningful description or assignment is not possible. We will move from high to low frequency and focus the discussion on the high intensity features and on those that can be described in less than one paragraph of text.

5.4.4.2. High Frequency Combination Tones

There are three weak features measured at 3075, 3062, and 3058 cm^{-1}. The *trans* simulation finds three transitions at 3076, 3068, and 3063 cm^{-1}. They all borrow intensity from the out-of-phase vinyl stretch (about 20% in total). Together they participate in a somewhat isolated resonance polyad. Their largest components are 50% [ν_s(C=C) + $\delta_s(CH_3)$], 50% [ν_{as}(C=C) + $\delta_s(CH_3)$], and 40% [ν_s(C=C) + *a″*-$\rho_r(CH_3)$ + ρ_w(skeletal)] respectively. Two transitions are measured at 3050 and 3037 cm^{-1}. Their theoretical counterparts are at 3050 and 3038 cm^{-1}. They are both highly mixed. Intensities come from the in- and out-of-phase vinyl stretches and the symmetric methylene stretch.

5.4.4.3. Middle Region

The majority (75%) of the intensity of the in-phase vinyl stretch is predicted as a doublet feature at (3025, 3024) cm^{-1}, where it mixes most strongly with the [$\delta_s(CH_3)$ + ν_s(C=C)] state. This is in the vicinity of the experimental band at 3021 cm^{-1}. In this region from about 3010-3030

cm^{-1}, theory predicts roughly the same number of bands as are observed experimentally, but overlap and the variable broadening from the helium makes detailed assignments more difficult. The predicted transition at 3016 cm^{-1} is roughly 30% of the symmetric methylene stretch and 30% of [$\nu_{as}(C=C) + \delta^{out}(CH_2)$]. It may correspond to the broad feature at 3018 cm^{-1}.

The region 2970-3000 cm^{-1} holds four prominent bands around 2981 cm^{-1}. VPT2+K also predicts four bands. The broad doublet feature at (2996, 2993) cm^{-1} matches most closely to the predictions at (2992, 2987) cm^{-1}. These transitions derive intensity from a mixture of the *a′*-$\nu_{as}(CH_3)$ and the methylene $\nu_s(CH_2)$. The intense feature at 2987 cm^{-1} is predicted at 2982 cm^{-1} and has the character of 40% *a′*-$\nu_{as}(CH_3)$ 15% and $\nu^{out}(CH_2)$. The theory predicts an additional band at 2981 cm^{-1} comprising 20% *a′*-$\nu_{as}(CH_3)$ and 25% $\nu^{out}(CH_2)$. This could either be assigned to the shoulder of the 2987 cm^{-1} feature or to the smaller, sharper feature at 2981 cm^{-1}, with the nearby intense *gauche* peak assigned to the other. While it is difficult to judge the effect of temperature on intensity where features from multiple conformers overlap, the 2987 and 2981 cm^{-1} features appear to behave similarly; thus, we assign the shoulder (2985 cm^{-1}) to the *gauche* conformer. This gauche transition is the rather pure (85%) *a′*-like $\nu_{as}(CH_3)$ fundamental.

5.4.4.4. Lower Frequency Region

A paradigm shift occurs around 2970 cm^{-1}. For all of the previously discussed transitions, the most significant two- and three-quanta states all involved 1 quantum of C=C stretch excitation and 1-2 quanta of bend excitation. On the lower frequency side of this spectral valley, the important couplings are all to pure bending states. The two CH stretches that contribute to this region are *a″*-$\nu_{as}(CH_3)$ and $\nu_s(CH_3)$.

The *a″* manifold is far simpler than the *a′* manifold. We assign the intense transition at 2957 cm^{-1} to the $\nu_{as}(CH_3)$ fundamental. In this simulation, it appears at 2958 cm^{-1} and is 80% pure. It also contains 20% [*a′*-$\delta_{as}(CH_3)$ + *a″*-$\delta_{as}(CH_3)$]. An additional band appears at 2896 cm^{-1} as

a result of this Fermi resonance, composed of 10% $\nu_{as}(CH_3)$ and 60% of the two-quanta scissor combination. This is best assigned to the experimental band at 2890 cm^{-1}. In this region, the *gauche* analog of the *a″*-$\nu_{as}(CH_3)$ fundamental has high predicted intensity and thus may be visible in the spectrum. It is predicted at 2950 cm^{-1} and may be one of the weak features on either side of the *trans* fundamental. Assignment to the 2952 cm^{-1} feature is most consistent with the theoretical predictions; furthermore, this feature gains intensity at higher isoprene temperatures (Fig. 5.11).

Lastly $\nu_s(CH_3)$ is by far the most thoroughly mixed. Its intensity is distributed into various weak transitions between 2970 and 2850 cm^{-1}. None of them can reasonably be called the fundamental transition. The first transition in this polyad is predicted to hold 15% of the intensity and fall at 2950 cm^{-1}. It probably contributes to the broad features underlying the 2940 cm^{-1} band. The theoretical band at 2938 cm^{-1} holds 25% of $\nu_s(CH_3)$ and falls 2 cm^{-1} to the red of the experimental band center. These two transitions have dark states in common. Their dark-state components are predominantly the *a′*-$\delta_{as}(CH_3)$ overtone and [*a′*-$\delta_{as}(CH_3)$ + δ(skeletal) + *a′*-$\rho_r(CH_3)$]. The higher frequency transition is composed of 60% of the three-quanta state, and the lower frequency transition is more mixed: having about 20% of the two-quanta and 30% of the three-quanta components. Figure 5.11 also reveals a band with a strong temperature dependence at 2932.5 cm^{-1} Theory predicts a very similar pair of transitions for the *gauche* conformer in this frequency region, composed of zeroth order states that are analogous to those in *trans*. Here, the primarily three-quanta transition falls at 2931 cm^{-1} with the more mixed transition at 2938 cm^{-1}. The assignment of this band should be to one of these *gauche* transitions; however, the observation of only a single band here and only one well-defined band for *trans* should cast some doubt upon the validity of the anharmonic coupling picture for this region. Perhaps the mixing between these zeroth-order states is exaggerated here; and in fact, only one transition should possess significant intensity. This experiment cannot confidently answer that question. In this

region of the spectrum that contains multiple resonances, discriminating between weak *trans* transitions and strong *gauche* transitions is challenging.

The next notable experimental band is found at 2918 cm^{-1}. The simulation predicts a band at 2913 cm^{-1} to hold 10% of the $\nu_s(CH_3)$ intensity. The remaining components of this transition are the overtones of both a'-$\delta_{as}(CH_3)$ and a''-$\delta_{as}(CH_3)$ and three-quanta states connected to them. A doublet is found at (2906, 2905) cm^{-1}. There is a theoretical band at 2902 cm^{-1}, but it is not split. The transition contains 10% $\nu_s(CH_3)$ and 65% [a''-$\delta_{as}(CH_3)$ + ρ_w(skeletal) + a'-$\rho_r(CH_3)$]. The remaining experimental features are: a broad feature at 2874 and a peak at 2869.5 cm^{-1} with a shoulder at 2868.5 cm^{-1}. The best match to the broad 2874 cm^{-1} feature are the overlapping predicted transitions at 2876 cm^{-1}. These are highly mixed, in general and with each other; together they contain 45% [δ(CH) + ν_{as}(C=C)], 35% [ν_{as}(C=C) + ρ_w(skeletal) + $\rho_w(CH_2)$], and 25% [$\delta^{in}(CH_2)$ + a'-$\delta_{as}(CH_3)$], amongst other things.

The lowest frequency peak and its shoulder match best to the VPT2+K transitions at 2864 and 2862 cm^{-1} respectively. As with some of the previous transitions, these two share many dark-state components. The primary ones are the overtone of a''-$\delta_{as}(CH_3)$, the combination [a'-$\delta_{as}(CH_3)$ + $\delta^{out}(CH_2)$], and the three-quanta combination [a'-$\delta_{as}(CH_3)$ + $\rho_t^{in}(CH_2)$ + $\rho_t^{out}(CH_2)$]. This feature, with its shoulder, is predicted to hold 20% of the $\nu_s(CH_3)$ intensity.

Overall the predictions in this region are less satisfactory than in other regions of the spectrum. This can be attributed to the inherently higher complexity/dimensionality of the polyads here. There are more states involved, and high accuracy in the force constants becomes more necessary to achieve a qualitatively correct description of the coupling. It is possible that the polyad description needs to be extended even further to include states having 4-quanta of excitation. This is not presently implemented in our VPT2+K scripts. Somewhat more quantifiable than that is the “resonance” between the symmetric stretch and the methyl torsional overtone, as revealed by the Martin diagnostic. This cannot be treated in a satisfying way.

5.5. Conclusions

In conclusion, a detailed vibrational spectrum has been measured for the CH stretching region of isoprene. The various polyad transitions are well-simulated by the VPT2+K method. Some features in the spectrum are best assigned to the higher energy *gauche* conformer rather than to low intensity combinations/overtones of *trans*. Computations utilizing CBS extrapolation, corrections for post-CCSD(T) correlation, core-correlation, adiabatic effects, and anharmonicity predict respective 0 K and 298.15 K *trans*/*gauche* energy differences of 2.82 and 2.52 kcal/mol and a room temperature *gauche* population of 2.8%. Hindered-rotor corrections are found to be important for the *trans*/*gauche* relative free energy, predicting a 0.06 kcal/mol stabilizing effect upon *gauche*-isoprene. These theoretical values are generally in agreement with previous computations, but the error associated with our numbers is lower and more clear. Our *trans* to *gauche* $\Delta\overline{H}$ value over the 300 to 800 K range falls just within the error bar associated with a previously reported experimental interconversion enthalpy. The error in our calculations is lower than the reported experimental error by at least a factor of three. We suggest that our computed results represent the most accurate thermochemistry on the isoprene system, at present. A rigorous 2D variational treatment of the methyl and skeletal torsional modes would improve upon the separate 1D treatments described in this study. This would eliminate the assumption of uncoupled rotors, allowing for even more confident determinations of the free energy of isomerization.

References

(1) Guenther, A.; Hewitt, C. N.; Erickson, D.; Fall, R.; Geron, C.; Graedel, T.; Harley, P.; Klinger, L.; Lerdau, M.; McKay, W. A., et al. A Global-Model of Natural Volatile Organic-Compound Emissions. *J. Geophys. Res.: Atmos.* **1995**, *100*, 8873-8892.

(2) Chameides, W. L.; Fehsenfeld, F.; Rodgers, M. O.; Cardelino, C.; Martinez, J.; Parrish, D.; Lonneman, W.; Lawson, D. R.; Rasmussen, R. A.; Zimmerman, P., et al. Ozone Precursor Relationships in the Ambient Atmosphere. *J. Geophys. Res.: Atmos.* **1992**, *97*, 6037-6055.

(3) Stone, D.; Evans, M. J.; Edwards, P. M.; Commane, R.; Ingham, T.; Rickard, A. R.; Brookes, D. M.; Hopkins, J.; Leigh, R. J.; Lewis, A. C., et al. Isoprene Oxidation Mechanisms: Measurements and Modelling of OH and HO_2 over a South-East Asian Tropical Rainforest During the OP3 Field Campaign. *Atmos. Chem. Phys.* **2011**, *11*, 6749-6771.

(4) Monks, P. S. Gas-Phase Radical Chemistry in the Troposphere. *Chem. Soc. Rev.* **2005**, *34*, 376-395.

(5) Claeys, M.; Graham, B.; Vas, G.; Wang, W.; Vermeylen, R.; Pashynska, V.; Cafmeyer, J.; Guyon, P.; Andreae, M. O.; Artaxo, P., et al. Formation of Secondary Organic Aerosols Through Photooxidation of Isoprene. *Science* **2004**, *303*, 1173-1176.

(6) Edney, E. O.; Kleindienst, T. E.; Jaoui, M.; Lewandowski, M.; Offenberg, J. H.; Wang, W.; Claeys, M. Formation of 2-Methyl Tetrols and 2-Methylglyceric Acid in Secondary Organic Aerosol from Laboratory Irradiated Isoprene/NO(X)/SO(2)/Air Mixtures and Their Detection in Ambient PM(2.5) Samples Collected in the Eastern United States. *Atmos. Environ.* **2005**, *39*, 5281-5289.

(7) Paulot, F.; Crounse, J. D.; Kjaergaard, H. G.; Kurten, A.; St Clair, J. M.; Seinfeld, J. H.; Wennberg, P. O. Unexpected Epoxide Formation in the Gas-Phase Photooxidation of Isoprene. *Science* **2009**, *325*, 730-733.

(8) Surratt, J. D.; Murphy, S. M.; Kroll, J. H.; Ng, N. L.; Hildebrandt, L.; Sorooshian, A.; Szmigielski, R.; Vermeylen, R.; Maenhaut, W.; Claeys, M., et al. Chemical Composition of Secondary Organic Aerosol Formed from the Photooxidation of Isoprene. *J. Phys. Chem. A* **2006**, *110*, 9665-9690.

(9) Kroll, J. H.; Ng, N. L.; Murphy, S. M.; Flagan, R. C.; Seinfeld, J. H. Secondary Organic Aerosol Formation from Isoprene Photooxidation. *Environ. Sci. Technol.* **2006**, *40*, 1869-1877.

(10) Henze, D. K.; Seinfeld, J. H. Global Secondary Organic Aerosol from Isoprene Oxidation. *Geophys. Res. Lett.* **2006**, *33*.

(11) Kleindienst, T. E. Epoxying Isoprene Chemistry. *Science* **2009**, *325*, 687-688.

(12) Greenwald, E. E.; North, S. W.; Georgievskii, Y.; Klippenstein, S. J. A Two Transition State Model for Radical-Molecule Reactions: Applications to Isomeric Branching in the OH-Isoprene Reaction. *J. Phys. Chem. A* **2007**, *111*, 5582-5592.

(13) Allodi, M. A.; Kirschner, K. N.; Shields, G. C. Thermodynamics of the Hydroxyl Radical Addition to Isoprene. *J. Phys. Chem. A* **2008**, *112*, 7064-7071.

(14) Compton, D. A. C.; George, W. O.; Maddams, W. F. Conformations of Conjugated Hydrocarbons .1. Spectroscopic and Thermodynamic Study of Buta-1,3-Diene and 2-Methylbuta-1,3-Diene (Isoprene). *J. Chem. Soc., Perkin Trans. 2* **1976**, 1666-1671.

(15) Squillacote, M. E.; Liang, F. T. Conformational Thermodynamic and Kinetic Parameters of Methyl-Substituted 1,3-Butadienes. *J. Org. Chem.* **2005**, *70*, 6564-6573.

(16) Franke, P. R.; Tabor, D. P.; Moradi, C. P.; Douberly, G. E.; Agarwal, J.; Schaefer, H. F.; Sibert, E. L. Infrared Laser Spectroscopy of the *n*-Propyl and *i*-Propyl Radicals: Stretch-Bend Fermi Coupling in the Alkyl CH Stretch Region. *J. Chem. Phys.* **2016**, *145*, 224304.

(17) Schneider, H.; Vogelhuber, K. M.; Schinle, F.; Stanton, J. F.; Weber, J. M. Vibrational Spectroscopy of Nitroalkane Chains Using Electron Autodetachment and Ar Predissociation. *J. Phys. Chem. A* **2008**, *112*, 7498-7506.

(18) Tabor, D. P.; Hewett, D. M.; Bocklitz, S.; Korn, J. A.; Tomaine, A. J.; Ghosh, A. K.; Zwier, T. S.; Sibert, E. L. Anharmonic Modeling of the Conformation-Specific IR Spectra of Ethyl, *n*-Propyl, and *n*-Butylbenzene. *J. Chem. Phys.* **2016**, *144*, 224310.

(19) Korn, J. A.; Tabor, D. P.; Sibert, E. L.; Zwier, T. S. Conformation-Specific Spectroscopy of Alkyl Benzyl Radicals: Effects of a Radical Center on the CH Stretch Infrared Spectrum of an Alkyl Chain. *J. Chem. Phys.* **2016**, *145*, 124314.

(20) Sibert, E. L.; Kidwell, N. M.; Zwier, T. S. A First-Principles Model of Fermi Resonance in the Alkyl CH Stretch Region: Application to Hydronaphthalenes, Indanes, and Cyclohexane. *J. Phys. Chem. B* **2014**, *118*, 8236-8245.

(21) Rosnik, A. M.; Polik, W. F. VPT2+K Spectroscopic Constants and Matrix Elements of the Transformed Vibrational Hamiltonian of a Polyatomic Molecule with Resonances Using Van Vleck Perturbation Theory. *Mol. Phys.* **2014**, *112*, 261-300.

(22) Gonzales, J. M.; Pak, C.; Cox, R. S.; Allen, W. D.; Schaefer, H. F.; Csaszar, A. G.; Tarczay, G. Definitive Ab Initio Studies of Model S_N2 reactions CH_3X+F^- (X = F, Cl, CN, OH, SH, NH_2, PH_2). *Chem. - Eur. J.* **2003**, *9*, 2173-2192.

(23) Csaszar, A. G.; Allen, W. D.; Schaefer, H. F. In Pursuit of the Ab Initio Limit for Conformational Energy Prototypes. *J. Chem. Phys.* **1998**, *108*, 9751-9764.

(24) Allinger, N. L.; Fermann, J. T.; Allen, W. D.; Schaefer, H. F. The Torsional Conformations of Butane: Definitive Energetics from Ab Initio Methods. *J. Chem. Phys.* **1997**, *106*, 5143-5150.

(25) Toennies, J. P.; Vilesov, A. F. Superfluid Helium Droplets: A Uniquely Cold Nanomatrix for Molecules and Molecular Complexes. *Angew. Chem., Int. Ed.* **2004**, *43*, 2622-2648.

(26) Choi, M. Y.; Douberly, G. E.; Falconer, T. M.; Lewis, W. K.; Lindsay, C. M.; Merritt, J. M.; Stiles, P. L.; Miller, R. E. Infrared Spectroscopy of Helium Nanodroplets: Novel Methods for Physics and Chemistry. *Int. Rev. Phys. Chem.* **2006**, *25*, 15-75.

(27) Lewerenz, M.; Schilling, B.; Toennies, J. P. A New Scattering Deflection Method for Determining and Selecting the Sizes of Large Liquid Clusters of ^{4}He. *Chem. Phys. Lett.* **1993**, *206*, 381-387.

(28) Lewerenz, M.; Schilling, B.; Toennies, J. P. Successive Capture and Coagulation of Atoms and Molecules to Small Clusters in Large Liquid-Helium Clusters. *J. Chem. Phys.* **1995**, *102*, 8191-8207.

(29) Morrison, A. M.; Liang, T.; Douberly, G. E. Automation of an "Aculight" Continuous-Wave Optical Parametric Oscillator. *Rev. Sci. Instrum.* **2013**, *84*, 013102.

(30) Chin, S. A.; Krotscheck, E. Systematics of Pure and Doped ^{4}He Clusters. *Phys. Rev. B* **1995**, *52*, 10405-10428.

(31) Leavitt, C. M.; Moore, K. B.; Raston, P. L.; Agarwal, J.; Moody, G. H.; Shirley, C. C.; Schaefer, H. F.; Douberly, G. E. Liquid Hot NAGMA Cooled to 0.4 K: Benchmark Thermochemistry of a Gas-Phase Peptide. *J. Phys. Chem. A* **2014**, *118*, 9692-9700.

(32) Skvortsov, D. S.; Vilesov, A. F. Using He Droplets for Measurements of Interconversion Enthalpy of Conformers in 2-Chloroethanol. *J. Chem. Phys.* **2009**, *130*, 151101.

(33) Raghavachari, K.; Trucks, G. W.; Pople, J. A.; Headgordon, M. A 5th-Order Perturbation Comparison of Electron Correlation Theories. *Chem. Phys. Lett.* **1989**, *157*, 479-483.

(34) Hampel, C.; Peterson, K. A.; Werner, H. J. A Comparison of the Efficiency and Accuracy of the Quadratic Configuration-Interaction (QCISD), Coupled Cluster (CCSD), and Brueckner Coupled Cluster (BCCD) Methods. *Chem. Phys. Lett.* **1992**, *190*, 1-12.

(35) Watts, J. D.; Gauss, J.; Bartlett, R. J. Coupled-Cluster Methods with Noniterative Triple Excitations for Restricted Open-Shell Hartree-Fock and Other General Single

Determinant Reference Functions - Energies and Analytical Gradients. *J. Chem. Phys.* **1993**, *98*, 8718-8733.

(36) Watts, J. D.; Gauss, J.; Bartlett, R. J. Open-Shell Analytical Energy Gradients for Triple Excitation Many-Body, Coupled-Cluster Methods - MBPT(4), CCSD+T(CCSD), CCSD(T), and QCISD(T). *Chem. Phys. Lett.* **1992**, *200*, 1-7.

(37) Deegan, M. J. O.; Knowles, P. J. Perturbative Corrections to Account for Triple Excitations in Closed and Open-Shell Coupled-Cluster Theories. *Chem. Phys. Lett.* **1994**, *227*, 321-326.

(38) Stanton, J. F. Why CCSD(T) Works: A Different Perspective. *Chem. Phys. Lett.* **1997**, *281*, 130-134.

(39) Almlöf, J.; Taylor, P. R. General Contraction of Gaussian-Basis Sets .I. Atomic Natural Orbitals for 1st-Row and 2nd-Row Atoms. *J. Chem. Phys.* **1987**, *86*, 4070-4077.

(40) J. F. Stanton, J. Gauss, L. Cheng, M. E. Harding, D. A. Matthews, and P. G. Szalay, CFOUR, Coupled-cluster techniques for computational chemistry, a quantum-chemical program package, With contributions from A. A. Auer, R. J. Bartlett, U. Benedikt, C. Berger, D. E. Bernholdt, Y. J. Bomble, O. Christiansen, F. Engel, R. Faber, M. Heckert, O. Heun, M. Hilgenberg, C. Huber, T.-C. Jagau, D. Jonsson, J. Jusélius, T. Kirsch, K. Klein, W. J. Lauderdale, F. Lipparini, T. Metzroth, L. A. Mück, D. P. O'Neill, D. R. Price, E. Prochnow, C. Puzzarini, K. Ruud, F. Schiffmann, W. Schwalbach, C. Simmons, S. Stopkowicz, A. Tajti, J. Vázquez, F. Wang, J. D. Watts and the integral packages MOLECULE (J. Almlöf and P. R. Taylor), PROPS (P. R. Taylor), ABACUS (T. Helgaker, H. J. Aa. Jensen, P. Jørgensen, and J. Olsen), and ECP routines by A. V. Mitin and C. van Wüllen, for the current version, see http://www.cfour.de.

(41) Feller, D. The Use of Systematic Sequences of Wave-Functions for Estimating the Complete Basis Set, Full Configuration-Interaction Limit in Water. *J. Chem. Phys.* **1993**, *98*, 7059-7071.

(42) Helgaker, T.; Klopper, W.; Koch, H.; Noga, J. Basis-Set Convergence of Correlated Calculations on Water. *J. Chem. Phys.* **1997**, *106*, 9639-9646.

(43) J. Frisch, G. W. Trucks, H. B. Schlegel, G. E. Scuseria, M. A. Robb, J. R. Cheeseman, G. Scalmani, V. Barone, B. Mennucci, G. A. Petersson, H. Nakatsuji, M. Caricato, X. Li, H. P. Hratchian, A. F. Izmaylov, J. Bloino, G. Zheng, J. L. Sonnenberg, M. Hada, M. Ehara, K. Toyota, R. Fukuda, J. Hasegawa, M. Ishida, T. Nakajima, Y. Honda, O. Kitao, H. Nakai, T. Vreven, J. A. Montgomery, Jr., J. E. Peralta, F. Ogliaro, M. J. Bearpark, J. Heyd, E. N. Brothers, K. N. Kudin, V. N. Staroverov, R. Kobayashi, J. Normand, K. Raghavachari, A. P. Rendell, J. C. Burant, S. S. Iyengar, J. Tomasi, M. Cossi, N. Rega, N. J. Millam, M. Klene, J. E. Knox, J. B. Cross, V. Bakken, C. Adamo, J. Jaramillo, R.

Gomperts, R. E. Stratmann, O. Yazyev, A. J. Austin, R. Cammi, C. Pomelli, J. W. Ochterski, R. L. Martin, K. Morokuma, V. G. Zakrzewski, G. A. Voth, P. Salvador, J. J. Dannenberg, S. Dapprich, A. D. Daniels, Ö . Farkas, J. B. Foresman, J. V. Ortiz, J. Cioslowski, and D. J. Fox, Gaussian 09, Revision E.01, Gaussian, Inc., Wallingford, CT, USA, 2009.

(44) Schuurman, M. S.; Allen, W. D.; Schleyer, P. V.; Schaefer, H. F. The Highly Anharmonic BH_5 Potential Energy Surface Characterized in the Ab Initio Limit. *J. Chem. Phys.* **2005**, *122*, 104302.

(45) Meyer, R.; Gunthard, H. H. General Internal Motion of Molecules Classical Quantum-Mechanical Hamiltonian. *J. Chem. Phys.* **1968**, *49*, 1510.

(46) Lewis, J. D.; Malloy, T. B.; Chao, T. H.; Laane, J. Periodic Potential Functions for Pseudorotation and Internal-Rotation. *J. Mol. Struct.* **1972**, *12*, 427.

(47) Woon, D. E.; Dunning, T. H. Gaussian-Basis Sets for Use in Correlated Molecular Calculations .V. Core-Valence Basis-Sets for Boron Through Neon. *J. Chem. Phys.* **1995**, *103*, 4572-4585.

(48) Handy, N. C.; Yamaguchi, Y.; Schaefer, H. F. The Diagonal Correction to the Born-Oppenheimer Approximation - Its Effect on the Singlet-Triplet Splitting of CH_2 and Other Molecular Effects. *J. Chem. Phys.* **1986**, *84*, 4481-4484.

(49) Sellers, H.; Pulay, P. The Adiabatic Correction to Molecular-Potential Surfaces in the SCF Approximation. *Chem. Phys. Lett.* **1984**, *103*, 463-465.

(50) Boese, A. D.; Oren, M.; Atasoylu, O.; Martin, J. M. L.; Kallay, M.; Gauss, J. W3 Theory: Robust Computational Thermochemistry in the kJ/mol Accuracy Range. *J. Chem. Phys.* **2004**, *120*, 4129-4141.

(51) Ruden, T. A.; Helgaker, T.; Jorgensen, P.; Olsen, J. Coupled-Cluster Connected-Quadruples Corrections to Atomization Energies. *Chem. Phys. Lett.* **2003**, *371*, 62-67.

(52) Tajti, A.; Szalay, P. G.; Csaszar, A. G.; Kallay, M.; Gauss, J.; Valeev, E. F.; Flowers, B. A.; Vazquez, J.; Stanton, J. F. HEAT: High Accuracy Extrapolated Ab Initio Thermochemistry. *J. Chem. Phys.* **2004**, *121*, 11599-11613.

(53) Kállay, M.; Gauss, J. Approximate Treatment of Higher Excitations in Coupled-Cluster Theory. *J. Chem. Phys.* **2005**, *123*, 214105.

(54) Kállay, M.; Gauss, J. Approximate Treatment of Higher Excitations in Coupled-Cluster Theory. II. Extension to General Single-Determinant Reference Functions and Improved Approaches for the Canonical Hartree-Fock Case. *J. Chem. Phys.* **2008**, *129*, 144101.

(55) Bomble, Y. J.; Stanton, J. F.; Kállay, M.; Gauss, J. Coupled-Cluster Methods Including Noniterative Corrections for Quadruple Excitations. *J. Chem. Phys.* **2005**, *123*, 054101

(56) MRCC, a quantum chemical program suite written by M. Kállay, Z. Rolik, J. Csontos, P. Nagy, G. Samu, D. Mester, I. Ladjánszki, L. Szegedy, B. Ladóczki, K. Petrov, M. Farkas, B. Hégely. See also. Z. Rolik, L. Szegedy, I. Ladjánszki, B. Ladóczki, and M. Kállay,. J. Chem. Phys. **139**, 094105 (2013), as well as: www.mrcc.hu.

(57) McQuarrie, D. A. *Statistical Mechanics*; Harper Collins: New York, N.Y., 1976, p 641.

(58) Brown, A. R.; Franke, P. R.; Douberly, G. E. Helium Nanodroplet Isolation of the Cyclobutyl, 1-Methylallyl, and Allylcarbinyl Radicals: Infrared Spectroscopy and Ab Initio Computations. *J. Phys. Chem. A* **2017**, *121*, 7576-7587.

(59) Nielsen, H. H. The Vibration-Rotation Energies of Molecules. *Rev. Mod. Phys.* **1951**, *23*, 90-136.

(60) Matthews, D. A.; Vazquez, J.; Stanton, J. F. Calculated Stretching Overtone Levels and Darling-Dennison Resonances in Water: A Triumph of Simple Theoretical Approaches. *Mol. Phys.* **2007**, *105*, 2659-2666.

(61) Clabo, D. A.; Allen, W. D.; Remington, R. B.; Yamaguchi, Y.; Schaefer, H. F. A Systematic Study of Molecular Vibrational Anharmonicity and Vibration-Rotation Interaction by Self-Consistent-Field Higher-Derivative Methods - Asymmetric-Top Molecules. *Chem. Phys.* **1988**, *123*, 187-239.

(62) Gauss, J.; Stanton, J. F. Analytic CCSD(T) Second Derivatives. *Chem. Phys. Lett.* **1997**, *276*, 70-77.

(63) Mathematica, Version 11, Wolfram Research, Inc., Champaign, IL (2016).

(64) Martin, J. M. L.; Lee, T. J.; Taylor, P. R.; Francois, J. P. The Anharmonic-Force Field of Ethylene, C_2H_4, by Means of Accurate Ab Initio Calculations. *J. Chem. Phys.* **1995**, *103*, 2589-2602.

(65) Colbert, D. T.; Sibert, E. L. Variable Curvature Coordinates for Molecular Vibrations. *J. Chem. Phys.* **1989**, *91*, 350-363.

(66) Allen, W. D.; Bodi, A.; Szalay, V.; Csaszar, A. G. Adiabatic Approximations to Internal Rotation. *J. Chem. Phys.* **2006**, *124*.

CHAPTER 6

ETHYL + O_2 IN HELIUM NANODROPLETS: INFRARED SPECTROSCOPY OF THE ETHYLPEROXY RADICAL[1]

[1] Reproduced with permission from Franke, P.R.; Brice, J.T.; Moradi, C.P.; Schaefer, H.F.; Douberly, G.E. 2019. *Journal of Physical Chemistry A*. 123:3558-3568. DOI: 10.1021/acs.jpca.9b01867 Copyright 2019 American Chemical Society.

Helium-solvated ethylperoxy radicals ($CH_3CH_2OO^{\bullet}$) are formed *via* the *in situ* reaction between $^2A'$ ethyl radical and $^3\Sigma_g^-$ dioxygen. The reactants are captured sequentially through the droplet pick-up technique. Helium droplets are doped with ethyl radical *via* pyrolysis of di-*tert*-amyl peroxide or *n*-propylnitrite in an effusive, low-pressure source. An infrared spectrum of ethylperoxy, in the CH stretching region, is recorded with species-selective droplet beam depletion spectroscopy. Spectral assignments are made *via* comparisons to second-order vibrational perturbation theory with resonances (VPT2+K) based on coupled-cluster full quartic force fields. Cubic and quartic force constants, evaluated using a small basis set, are transformed into the normal coordinate system of the higher level quadratic force constants. This transformation procedure eliminates the mismatch between normal modes, which is a source of error whenever normal coordinate force constants from different levels of theory are combined. The spectrum shows signatures of both the C_1 *gauche* and C_s *trans* rotamers in an approximate 2:1 ratio; this is despite the prediction that the *gauche* rotamer lies 44 cm^{-1} lower on the zero-Kelvin enthalpic potential surface for torsional interconversion. Helium droplets are 0.4 K at equilibrium; therefore, *in situ* ethylperoxy production is highly non-thermal.

6.1. Introduction

The ethyl + O_2 reaction has proven to be prototypical for the study of low temperature hydrocarbon combustion.[1-2] It has been the subject of extensive experimental kinetics studies[3-16] and theoretical computations.[17-25] The peroxy radical intermediate is of particular interest, because its dissociation *via* concerted elimination of HO_2 is predicted to be the main source of products in the bimolecular ethyl + O_2 reaction.[24] Although the ethylperoxy radical has been probed spectroscopically with many complementary methods,[26-32] ground-state vibrational spectroscopy is for the most part missing. We report here an infrared (IR) spectrum in the CH stretching region for *trans*- and *gauche*-ethylperoxy, which are formed *via* barrierless association of ethyl and O_2 in helium droplets. The spectra are challenging to assign due to the presence of

strong anharmonic resonances. Nevertheless, progress is made *via* comparisons to anharmonic frequency computations that employ effective Hamiltonian models (VPT2+K) that use as input full quartic force fields computed *ab initio*.

A pioneering study by Hunziker and Wendt provided the first measurements of the richly structured Ã←X̃ electronic absorption band for hydroperoxy, methylperoxy, and the *gauche* rotamer of ethylperoxy.[30] In the ethylperoxy spectrum, vibronic bands were assigned to the O-O stretch in the Ã state. Vibrational progressions were also observed in the negative-ion photoelectron spectroscopy study by Blanksby *et al*.; these were assigned to O-O stretches and low frequency bending vibrations of *gauche*-ethylperoxy in both its ground and first electronically excited state.[29] High resolution cavity ring-down studies of the ethylperoxy Ã←X̃ electronic bands were undertaken by Miller and co-workers,[26-28] and the band origin for the *trans* rotamer were observed for the first time.[28] In addition to this, they assigned several vibronic transitions for each rotamer, involving excitation in the O-O stretch and low frequency bends; they also analyzed various CH_3 and CO torsional hot bands and partially-resolved rotational structure.[28]

As early as 1987, an infrared spectrum was obtained by Chettur and Snelson in a low temperature argon matrix.[32] They assigned several transitions to ethylperoxy, including one CH stretch band at 3016 cm^{-1}. Mah *et al*. measured the gas phase IR spectrum of room temperature ethylperoxy.[31] A few vibrational bands were assignable, although spectral overlap with ethane prevented assignments in the CH stretch region; however, they noted rovibrational transitions at 2999, 2988, and 2964 cm^{-1}.

Rienstra-Kiracofe, Allen, and Schaefer published an exhaustive computational study of the $CH_3CH_2 + O_2$ reaction thermochemistry.[23] They considered various pathways, and concluded that the most favorable, under low temperature combustion conditions, was the concerted elimination of HO_2 from the ethylperoxy radical intermediate. Wilke, Allen, and Schaefer probed this concerted elimination pathway at higher levels of electronic structure theory.[24] They used the

focal point analysis technique to compute the transition state for concerted elimination, which was found to lie below the reaction asymptote, in excellent agreement with previous master equation modeling.[18] Such a submerged barrier is consistent with the negative temperature dependence observed in kinetic studies.[10, 18] More recently, it has become possible to apply these theoretical techniques to the larger *n*-propyl + O_2 system; the longer carbon chain of propyl grants it access to additional reaction pathways.[33-34]

The most comprehensive computational study of the ethylperoxy rotamers was recently reported by Launder *et al*.[35] They studied both rotamers in their ground and first excited electronic states, computing relative energetics, relaxed C-O torsional potentials, vibrational frequencies, and adiabatic electronic transition energies. According to their extrapolated electronic energies with harmonic ZPVE corrections, ground state *gauche*-ethylperoxy lies only 44 cm^{-1} lower in energy than *trans*-ethylperoxy at 0 K.

6.2. Experimental Methods

The Helium Nanodroplet Isolation (HENDI) methodology has been thoroughly reviewed.[36-39] Only details relevant to the present experiment will be reproduced here. Ultrapure helium (99.9999%) is continuously expanded from a 5 μm pinhole nozzle, forming helium droplets consisting, on average, of a several thousand atoms.[40] The nozzle temperature is held at 15 K for the experiments described here. The droplet expansion is skimmed into a beam by a conical skimmer. Ethyl radical is produced by flash pyrolysis of either di-*tert*-amyl peroxide (DTAP) or *n*-propylnitrite (PRONO) in an orthogonally-oriented load-lockable source that has previously been described in detail.[41] It comprises a quartz tube, the end of which is wrapped in tantalum wire and resistively heated. Precursor molecules flow through the quartz tube and decompose when they make collisions with the hot quartz. The pyrolysate expands into the vacuum chamber, where the decomposition products are picked up by the droplet beam *via* gas

phase collisions. Dopants are rapidly cooled to the 0.4 K droplet temperature.[36-37] Following this, the beam enters a differentially-pumped gas cell and picks up molecular oxygen.

To observe the ethylperoxy radical, a droplet must pick up a single ethyl radical followed by a single O_2 molecule; the reaction to form ethylperoxy then proceeds barrierlessly.[23, 35] The pick-up process is statistical, and these conditions will only be achieved in a small number of droplets in the ensemble. This fraction is optimized by adjusting the pressures of oxygen and the ethyl radical precursor. The precursor pressure is chosen to be slightly lower than is optimal for the doping of a single ethyl radical; this ensures that the probability of recombination reactions, either inside the pyrolysis region or following pick-up, is exceedingly low.[42-44] The O_2 pressure is adjusted to maximize the ethylperoxy monomer signal. The dissipation of approximately 2700 He atoms is required to quench the reaction enthalpy associated with ethylperoxy formation.[24] Each helium atom carries with it approximately 5 cm^{-1} of energy.[45]

Droplets exit the pick-up chamber and enter a detection chamber, where they are electron-impact ionized, and the fragments are detected by quadrupole mass spectrometry. Details concerning the mechanism of dopant ionization and fragmentation have been discussed in detail elsewhere.[38] Ion current on a single mass peak is monitored, while a continuous-wave IR OPO, aligned in a counter-propagating orientation to the droplet beam, is scanned continuously through the CH stretching region. Details concerning the tuning and automation of the laser scans can be found in a previous article.[46] Upon absorption of an IR photon by the helium-solvated dopant, the energy is transferred to the bath of helium droplet modes and dissipated by helium atom evaporation. The evaporative loss of helium (~600 atoms) reduces the size of the droplets and therefore reduces the efficiency by which they are ionized. This is observed as a depletion in the ion signal. The laser is mechanically chopped at 80 Hz, and the ion signal modulated *via* laser excitation is processed with lock-in-amplification, allowing for the acquisition of a background-free IR action spectrum.

Thermal decomposition of DTAP produces two molecules of acetone and two ethyl radicals; whereas, PRONO produces one formaldehyde, one nitric oxide, and one ethyl radical. It is crucial, therefore, to discriminate against signals from droplets containing acetone, formaldehyde, NO, or precursor contaminants. This is largely achieved by mass-selection; when measuring the depletion of one nominal mass peak, only dopants that produce fragment ions of that mass will contribute spectroscopic signatures. This is imperfect; the possibility for other molecules or molecular clusters to contribute fragment ions to the detection channel motivates our use of multiple pyrolytic precursors. The spectra obtained *via* pyrolysis of DTAP and PRONO are compared to rule out spectral assignments to species other than ethylperoxy.

6.3. Theoretical Methods

6.3.1. Electronic Structure Calculations

The geometries and frequencies of *trans*- and *gauche*-ethylperoxy were probed with several levels of *ab initio* electronic structure theory. For all computations, the frozen-core approximation was made, and Unrestricted Hartree-Fock (UHF) references were used. The selection of UHF was motivated by the negligible spin contamination in alkyl peroxy radicals and the absence of orbital near-instabilities.[47] Optimized geometries and semi-diagonal quartic force fields were first computed at the CCSD(T)/ANO0 level of theory.[48-55] Geometries, harmonic frequencies, and harmonic intensities were additionally computed using two larger basis sets: the ANO1 basis set and the "heavy-augmented" cc-pVTZ basis set, consisting of cc-pVTZ on hydrogen and aug-cc-pVTZ on carbon and oxygen, hereafter referred to as haug-cc-pVTZ.[48, 56-57] All computations were performed using the CFOUR package.[58]

Geometries and harmonic frequencies were additionally computed at the CCSD(T)-F12/cc-pVDZ-F12 level of theory in ORCA.[59-64] Because no analytic derivatives are yet implemented for this method, the optimizations and frequency calculations were performed externally by finite differences of energies. Related to this, the lack of a CCSD(T)-F12 density

left us with the option to compute intensities using the finite field approach. Instead we opted to substitute the CCSD(T)/haug-cc-pVTZ harmonic intensities from CFOUR. Since CCSD(T)-F12/cc-pVDZ-F12 was expected to provide harmonic frequencies similar in quality to aug-cc-pVQZ, nearer to the complete basis set limit than either ANO1 or haug-cc-pVTZ,[65] only the "lower level" CCSD(T)/ANO0 results and the "higher level" CCSD(T)-F12/cc-pVDZ-F12 results will be discussed in depth. For the sake of readability in the ensuing discussion, CCSD(T)/ANO0 will often be shortened to "ANO0," and CCSD(T)-F12/cc-pVDZ-F12 will be shortened to "F12."

6.3.2. Quartic Force Fields

To improve the ANO0 quartic force field, the quadratic force constants of the ANO0 force field were directly substituted with the quadratic force constants (*i.e.* harmonic frequencies) evaluated with CCSD(T)-F12.[66] For this to be a good approximation, the two sets of normal coordinates must not be greatly dissimilar. We have seen before, in other peroxy radicals, that the O-O stretch has a greater basis set dependence than other vibrations. It is not uncommon for the harmonic frequency to shift 50 cm^{-1} or more between a double zeta and triple zeta basis set, often changing the frequency ordering of the normal modes. This is easily accounted for by permuting the normal mode labels. However, it is also possible that a change in basis alters the degree to which the O-O stretching coordinate mixes with other coordinates. Using the C-O stretching coordinate as an example, there are two limiting cases of this mixing: individual C-O and O-O stretching normal coordinates and symmetric and antisymmetric C-O-O stretching normal coordinates. This mixing does not change greatly for the *gauche* rotamer upon change of basis, but the mixing changes noticeably for the *trans* rotamer, where the normal modes determined with more complete basis sets tend to contain a more localized O-O stretch. The simple hybrid force field approximation will be less valid in situations like this. As a consequence of this observation, we sought to combine force constants from different levels of theory in a more robust manner: to represent them in the same set of normal coordinates.[67]

To have all force constants expressed in the same normal coordinates, we decided to compute CCSD(T)/ANO0 full quartic force fields for both rotamers, in internal coordinates, and then to transform each force field into the CCSD(T)-F12/cc-pVDZ-F12 normal coordinates. The non-linear transformation from curvilinear internal to rectilinear normal coordinates, to a given order, is only possible if all force constants of that order are known.[68] Although the cubic force field is already complete, allowing for its transformation directly into the CCSD(T)-F12 normal coordinates, the quartic part of the "semi-diagonal" force field lacks force constants with four unique normal mode indices (*ijkl*). The quartic part of the force field is essentially stuck in the CCSD(T)/ANO0 normal coordinate system unless/until it can be made complete. These missing quartic force constants are numerous and add considerable computational expense. Moreover, because they are not required for standard VPT2, they are usually not calculated.

To obtain full quartic force fields, we made small displacements from the ANO0 optimized geometries in up to 3 different internal coordinates simultaneously. At each displaced structure, we computed analytic energy gradients, in the internal coordinate representation, using CFOUR. The ANO0 structure was chosen as the reference structure for the expansion, instead of the more accurate F12 structure, to avoid complications arising from non-zero forces.[69] Then we obtained the quadratic, cubic, and quartic force constants in internal coordinates by numerically differentiating the analytic gradients. The transformation of each ANO0 quartic force field into the F12 normal coordinates was performed using published formulae.[68] These formulae involve the elements of the *L*-tensor, which are first, second, and third derivatives of the internal coordinates with respect to the normal coordinates. For simplicity, the *L*-tensor elements were also determined numerically, with central finite differences; although, analytic expressions are given for common internal coordinate types.[68] All numerical force field calculations and transformations were performed using Mathematica.[70] The remainder of this section gives a more detailed account of our protocol for computing full quartic force fields.

To compute full quartic force fields of *trans*- and *gauche*-ethylperoxy, displacements were made in all 3N-6 internal (z-matrix) coordinates. Step sizes used were 0.005 Å for bond lengths and 0.25 degrees for bond angles and dihedral angles. Up to two positive and negative steps were taken in single internal coordinates, and single positive and negative steps were taken simultaneously in two and three internal coordinates. No advantage was taken of symmetry to reduce the number of displacements needed; although, abelian computational symmetry could be used for all of the C_s symmetry displacements of the *trans* conformer. A total of 11564 displaced gradients were computed for each conformer. CFOUR was directed to compute analytic energy gradients and to transform them into z-matrix coordinates by providing z-matrix coordinate input, requesting geometry optimization, and including the keyword GEO_MAXSTEP=1. Gradients were read from the GRDINT files written by CFOUR.

An analytic gradient vector of length 3N-6 is determined at each displacement. For each component of this vector, 1D, 2D, and 3D, in internal coordinates, were constructed from its values at equilibrium (effectively zero) and at displacements along all 3N-6 internal coordinates. These grids were constructed for every possible combination of 1, 2, and 3 different internal coordinates. In Mathematica, low-order polynomial interpolation was applied to each rectangular grid with the "Interpolation" function. A necessary condition to use Mathematica's interpolation function on multidimensional data is that the grids be rectangular. This implies that the grids in 2 and 3 normal modes may only include the gradients from points displaced by ± 1 units. For each interpolated grid, a Taylor series expansion was constructed about the equilibrium using the "Series" function. Then quadratic, cubic, and quartic force constants are extracted from each Taylor series. Once this has been performed on all possible grids, some types of force constants will have been determined redundantly; these are averaged together. Comparing the values of these force constants also provides a numerical consistency check on the force field. This kind of diagnostic is also reported by CFOUR for quartic force constants of the iijj type. We found that

this interpolation scheme allows for accurate determination of force constants. It is not as sensitive to step size or the number of grid points as direct least squares fitting of Taylor polynomials, and it is more straightforward to apply than central difference formulas.

The internal coordinate force constants are converted into atomic units. The L-tensor elements are then evaluated via central finite differences. Up to third derivatives of the internal coordinates with respect to the normal coordinates are necessary to transform a full quartic force field.[68] In order to evaluate these, the dimensionless normal coordinates, in the form of Cartesian displacement vectors, are read from the QUADRATURE file that CFOUR writes after a harmonic frequency calculation. Small steps in the normal coordinates are made by adding the normal coordinate vectors to the Cartesian coordinates of the equilibrium geometry. About 0.001 units is found to be satisfactory. The values of the internal coordinates are measured at these displaced geometries. Once all elements of the L-tensor are determined, the force constants in normal coordinates are straightforwardly determined using algebraic equations.[68]

6.3.3. Anharmonic Simulations

The vibrational spectra of the ethylperoxy rotamers were modeled with second-order vibrational perturbation theory with resonances (VPT2+K).[71-73] This approach has been well-documented, and we have utilized it several times in recent years.[74-76] It is a combination of vibrational perturbation theory and the variational method, using a (typically) semi-diagonal quartic expansion of the potential, and it was applied with in-house scripts written in Mathematica.[70] Applied judiciously, it describes the vast majority of interactions using VPT2, and repairs any deficiencies arising from near-singularities. It requires a decision to be made about which couplings should be treated with VPT2 and which should be left out, to be treated instead by diagonalizing an effective Hamiltonian matrix of the deperturbed VPT2 states.

In our application of VPT2+K to model CH stretching vibrations, we typically choose the one-quantum CH stretches and the two-quanta CH bends to be mutually in resonance. We

compute their VPT2 energies, deperturb them accordingly, set up the appropriate effective Hamiltonian, and diagonalize. Other resonant interactions are possible; and, rather than relying on intuition to identify those, we use the Martin test.[73] Sometimes this will reveal additional resonances between one-quantum CH bends and two-quanta states composed of lower frequency vibrations, such as wagging, which will impact the resonances in the fundamental CH stretch region. These connected resonances can be included in the effective Hamiltonian to account for these types of interactions.[74] In the case of the ethylperoxy rotamers, connected resonances are not found to be important; spectral simulations were insensitive to the explicit inclusion of these couplings. The salient interactions appear to occur only between one-quantum stretches and two-quanta bends. The VPT2+K procedure ensures that every vibrational interaction that would have been accounted for by VPT2 is still accounted for, but only once, either by VPT2 or explicitly in the effective Hamiltonian. The effective Hamiltonian treatment then includes some higher-order effects. These arise from both the indirect variational mixing between states and from some new interaction terms, the resonance K constants, that directly couple states that do not interact in VPT2.

For anharmonic intensities, we start from the harmonic intensities of the fundamental transitions, and then we distribute some of their intensity into multi-quanta transitions, proportional to the degree of variational mixing in the effective Hamiltonian. This provides simple anharmonic intensities that are immune to resonance singularities and are usually in good agreement with our experiments, keeping in mind that the band intensities determined experimentally do not precisely correspond to the direct absorption intensities calculated *ab initio*. Indeed, accurate theoretical transition intensities are not a major aim of this study because of the lack of accurate experimental intensities and the sensitivity of intensity-sharing to level of theory.

6.4. Results and Discussion

6.4.1. Theoretical Structures and Harmonic Frequencies

We choose to make comparisons only between our highest level theoretical results (UHF-CCSD(T)-F12/cc-pVDZ-F12) and the highest level results of Launder *et al*. (ROHF-CCSD(T)/ANO2).[35] The optimized geometries are in excellent agreement. Bond lengths and angles agree within ± 0.001 Å and ± 0.1 degrees, respectively. Agreement between our harmonic frequencies (Table 6.1) and the frequencies from Ref. 35 is generally good. The maximum difference from those of Launder *et al*. is found to be 6 cm^{-1} between an *a″* CH stretch of the *trans* rotamer. In general, the CH stretches and bends, most important for accurate modeling of the CH stretching region, are the modes that agree least well. The differences between our frequencies can be ascribed to remaining basis set incompleteness, remaining dependence on the reference wavefunction, and neglected contributions from post-CCSD(T) electron correlation and core correlation, motivating even higher level studies of the harmonic frequencies of ethylperoxy. We stress that it is not the goal of our study to predict accurate fundamental frequencies for the remainder of the mid-IR region. Nevertheless, we provide VPT2 predictions for these (Table 6.1).

6.4.2. Mass Spectrometry

Mass spectra collected under various experimental conditions, using the DTAP precursor, are shown in Figure 6.1. The neat droplet beam displays the characteristic helium peaks separated by 4 u. When droplets are doped with the DTAP precursor, signal appears on 87 u corresponding to $CH_3CH_2(CH_3)_2CO^+$ ions, a significant fragmentation product of ionized di-*tert*-amyl peroxide. This peak diminishes when current flows through the pyrolysis source, indicating that the majority of the DTAP has decomposed prior to intersecting the droplet beam. An increase in signal is observed on 43 u, 29 u, and 27 u. The two decomposition products, acetone and ethyl radical contribute to much of the signal on 43 u and 27 u, respectively. Mass channel 29 u contains a combination of the two and also some amount of unpyrolyzed DTAP. The further addition of O_2, in the uppermost trace, contributes most notably to the 32 u signal. The signal on

Table 6.1. Descriptions, symmetries (*trans*), CCSD(T)-F12/cc-pVDZ-F12 harmonic frequencies (ω), VPT2 fundamental frequencies (*ν*), and CCSD(T)/haug-cc-pVTZ harmonic intensities (km/mol) of the normal modes of vibration of both rotamers of ethylperoxy. The normal vibrations of *gauche* are arranged by their best matches to the *trans* vibrations. The labels "in" and "out" represent in- and out-of-phase, respectively.

#	Γ	*trans*			*gauche*			Description
		ω(cm^{-1})	***ν*(cm^{-1})**	**I(km/mol)**	**ω(cm^{-1})**	***ν*(cm^{-1})**	**I(km/mol)**	
1	a'	3132.83	2980.4	14.09	3131.67	2979.6	7.66	$\nu_{as}(CH_3)$
2	a'	3070.87	2894.2[b]	12.05	3075.21	2902.7[b]	18.79	$\nu_{s}(CH_2)$
3	a'	3052.33	2891.0[b]	9.68	3049.81	2892.6[b]	10.86	$\nu_{s}(CH_3)$
4	a'	1520.33	1478.0	5.52	1515.48	1473.1	3.89	$\delta(CH_2)$ out
5	a'	1508.55	1464.9	1.58	1497.88	1456.3	2.55	$\delta(CH_2)$ in
6	a'	1427.60	1391.5	14.81	1417.49	1384.3	9.55	$\delta_{s}(CH_3)$
7	a'	1385.16	1351.1	13.84	1385.46	1355.0[a]	5.54	$\rho_{w}(CH_2)$
8	a'	1186.36	1169.2	19.72	1159.85	1134.8	11.00	ν(O-O)
9	a'	1148.41	1117.6	8.31	1110.23	1083.4	5.90	$\rho_{r}(CH_3)$
10	a'	1044.41	1024.3	17.12	1016.38	987.9	15.75	ν_{as}(C-C-O)
11	a'	865.53	844.6	3.50	865.73	844.2	4.52	ν_{s}(C-C-O)
12	a'	507.10	500.3	9.56	531.10	528.8	4.03	δ(C-O-O)
13	a'	308.75	295.7	1.27	363.06	360.8	4.93	δ(C-C-O)
14	a''	3143.41	2986.5	25.71	3149.61	2995.8	17.70	$\nu_{as}(CH_2)$ in
15	a''	3120.34	2964.1	0.08	3125.49	2973.3	8.61	$\nu_{as}(CH_2)$ out
16	a''	1496.54	1455.6	6.00	1493.40	1452.1	5.88	$\delta_{as}(CH_3)$
17	a''	1285.25	1256.3	0.36	1314.85	1280.1	4.10	$\rho_{t}(CH_2)$
18	a''	1162.85	1135.4	4.00	1207.18	1179.5	9.86	$\rho_{t}(CH_2)$
19	a''	806.31	798.5	0.78	804.42	796.6	2.08	$\rho_{r}(CH_2) + \rho_{r}(CH_3)$
20	a''	230.91	214.1	0.34	235.47	214.0	0.46	$\tau(CH_3)$
21	a''	86.21	73.1	0.37	124.56	112.4	0.43	τ(C-O)

[a] Corrected for Fermi resonance between v_7 and $v_{10} + v_{13}$ (combination appears at 1342.7 cm^{-1}).
[b] Highly anharmonic; diagonal effective Hamiltonian value is given but is not recommended.

the small 45 u peak ($C_2H_5O^+$) also increases, which is barely perceptible on this scale. The ethylperoxy parent ion, $CH_3CH_2OO^+$, is not observed at 61 u. This is consistent with our previous work on methylperoxy, where the parent ion was also not observed; rather, ionization and fragmentation of the neutral dopant largely produced HCO^+.[42]

A series of mass spectra for the *n*-propylnitrite (PRONO) experiments are presented below (Fig. 6.2). Trace (a) shows the neat droplet beam. When droplets are doped with the PRONO precursor (trace b), some parent ion signal appears at 90 u and also deprotonated signals

at 89 and 88 u. These signals diminish when the precursor is decomposed in the heated pyrolysis source (trace c). Also note the increase in 27 u and 30 u upon heating the source. The only obvious change upon adding O_2 (trace d) is the growth of 32 u; the enhancement of 45 u, the chosen mass channel for ethylperoxy spectroscopy, is slight. The pyrolysis current was chosen to maximize the ethylperoxy depletion signal; the optimal value for PRONO was found to be 30 A, somewhat higher than for the di-*tert*-amyl peroxide (DTAP) precursor, which optimized at 20 A.

6.4.3. Infrared Spectroscopy

An infrared spectrum of the *n*-propylnitrite precursor was collected (Fig. 6.3). Several skeletal and nitrite torsional isomers are expected to be populated in the PRONO sample. This spectrum could be modeled as the sum of several conformer specific spectra, with appropriate Boltzmann weights. We make no attempt to assign these features.

Preliminary depletion spectra were recorded on several mass channels to find ethylperoxy spectroscopy signal, including 27, 29, 30, 32, and 43 u. However, 45 u, corresponding to the $C_2H_5O^+$ ion, turned out to provide the greatest signal while also being relatively free from other absorbers. DTAP and PRONO precursors do not contribute to depletion signal on 45 u, neither with nor without added O_2.

Because of the greater fractional production of ethyl radical by DTAP (50%) compared to PRONO (33%), it produced spectra with superior signal-to-noise ratios. Scans with PRONO were primarily undertaken to corroborate spectral features found with DTAP. Because the precursors have only ethyl radical as a common decomposition product, features that appear with both precursors are strong candidates for ethylperoxy radical absorptions.

A survey spectrum was measured between 2880 cm^{-1} and 3050 cm^{-1} with each precursor, as shown in Figure 6.4. The spectra are similar in appearance. The most obvious differences (marked by asterisks) are the presence of a peak at 2979 cm^{-1} that is unique to the PRONO

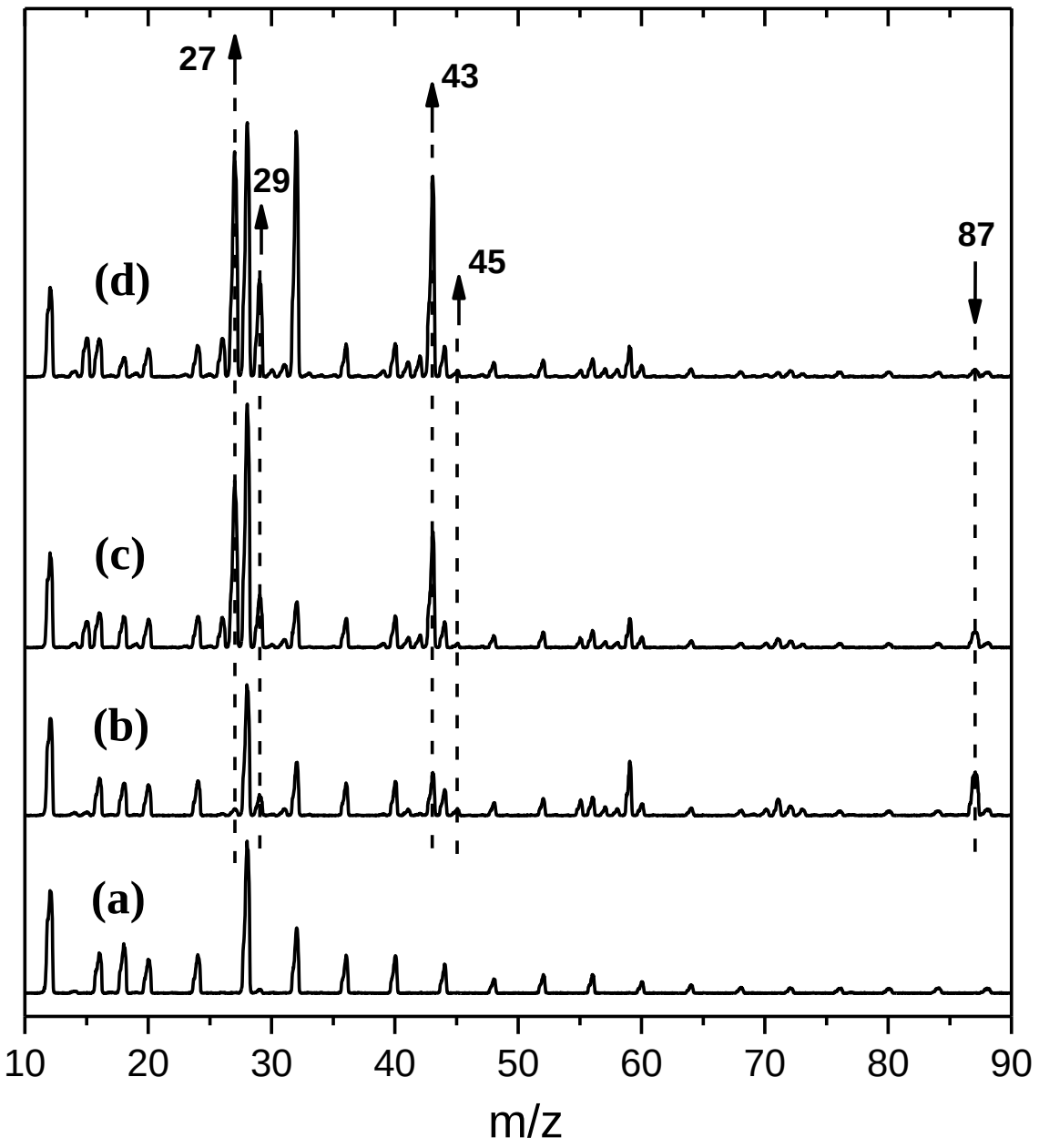

Figure 6.1. HENDI mass spectra of (a) neat droplet beam (b) cold DTAP (c) DTAP with 20 A pyrolysis current (d) DTAP with 20 A pyrolysis current with O_2.

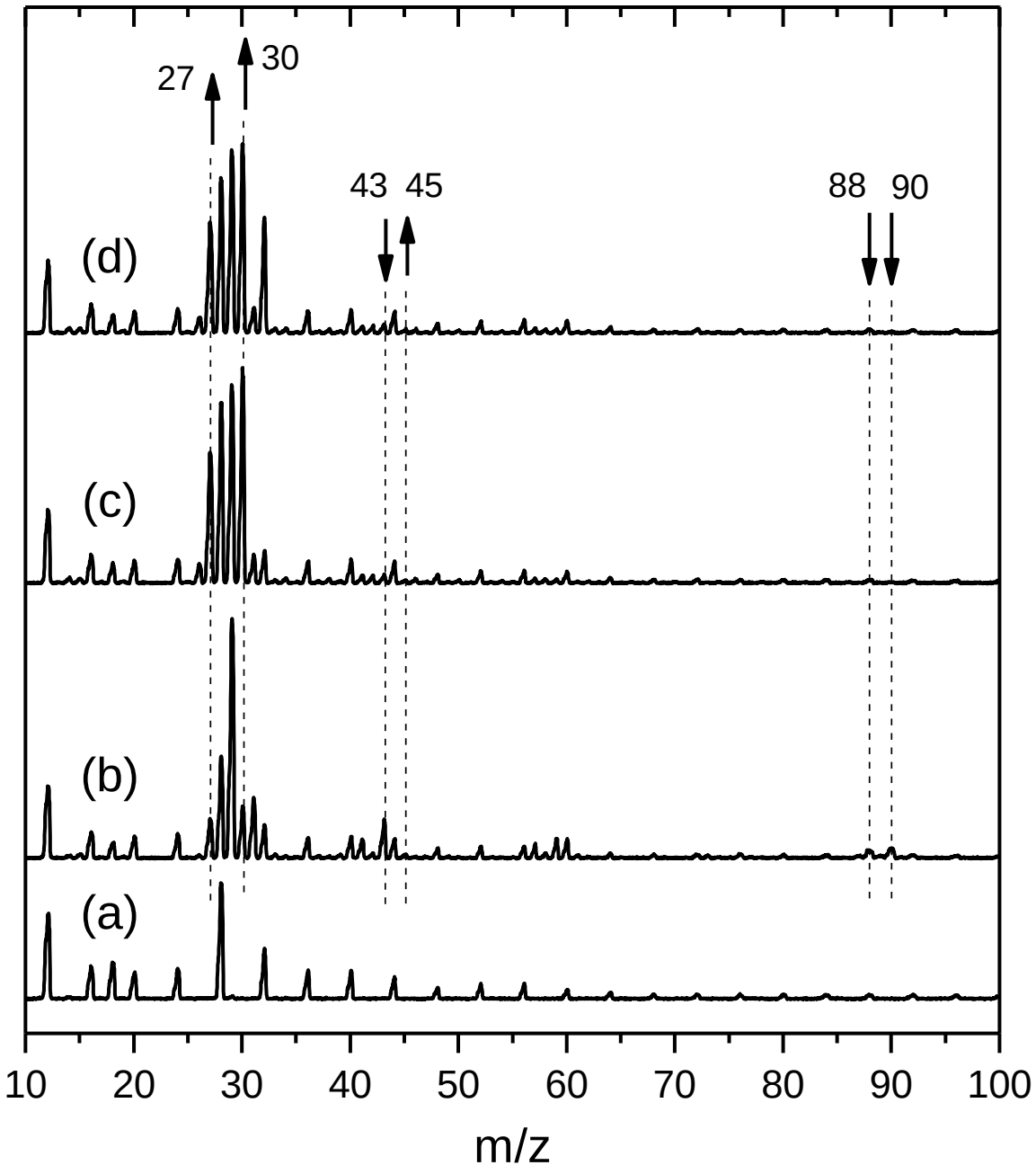

Figure 6.2. HENDI mass spectra of (a) neat droplet beam (b) cold PRONO (c) PRONO with 30 A pyrolysis current (d) PRONO with 30 A pyrolysis current with O_2.

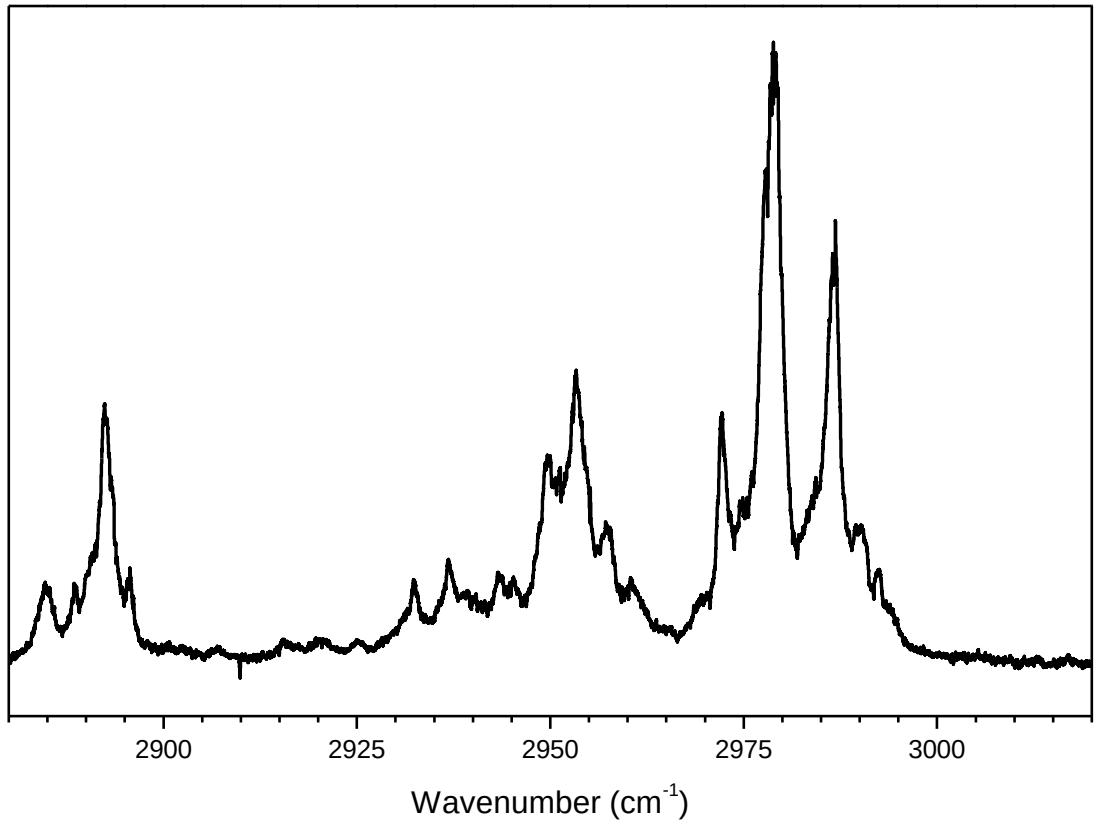

Figure 6.3. Infrared spectrum of the *n*-propylnitrite precursor, measured on mass channel 29 u, in the region hosting ethylperoxy radical features. It is likely that several rotamers are contributing to this spectrum.

precursor and a peak at 3030 cm^{-1} that is unique to DTAP. Also of note are the differences in band shape of the 2970 and 2985 cm^{-1} features. In the DTAP spectrum, each one appears to be two overlapping bands; one of each pair has an approximate band center that matches up nicely with the band centers in the PRONO spectrum, as indicated by the dotted lines. Overall, the majority of the peaks on 45 u appear to be due to ethylperoxy. The peaks unique to DTAP may arise from clusters containing acetone. The PRONO unique peak could similarly arise from clusters containing formaldehyde.

Two ponderous “negative-going” peaks appear at 2964.1 and 3010.9 cm^{-1}, with a possible third one appearing at 2952.1 cm^{-1}. These features are reproducible and appear, with both precursors, under various experimental conditions. Negative signals such as these are made possible by our lock-in detection scheme. In our experiments, a phase angle describes the time relationship between laser amplitude modulation and ion current modulation. The phase is chosen to optimize the positive signals that we associate with ethylperoxy. If another feature displays an optimal phase that is greater than 90 degrees different from the chosen phase, it may appear negative. The identity of these features will be the subject of a future investigation. In the ensuing discussion, it will be assumed that the optimal phases of all ethylperoxy absorptions are similar and so they all contribute positive signals.

6.4.4. Anharmonic Force Fields

6.4.4.1. Numerical Accuracy

The numerical accuracy of our normal coordinate force constants, which were determined by numerical differentiation of analytic internal coordinate gradients, followed by numerical transformation into normal coordinates, was benchmarked against CFOUR’s standard semi-diagonal quartic force field recipe, based upon analytic second derivatives. We computed quartic normal coordinate force fields for several small molecules: water, formaldehyde, hydrogen peroxide, and formic acid. The differences between our force constants and CFOUR’s force constants were about ± 0.01 cm^{-1} for quadratic and ± 0.2 cm^{-1} for cubic and quartic. We also checked the correctness of the ethylperoxy anharmonic internal force constants by simply transforming them into the CCSD(T)/ANO0 normal coordinates. The agreement with CFOUR’s force constants was excellent.

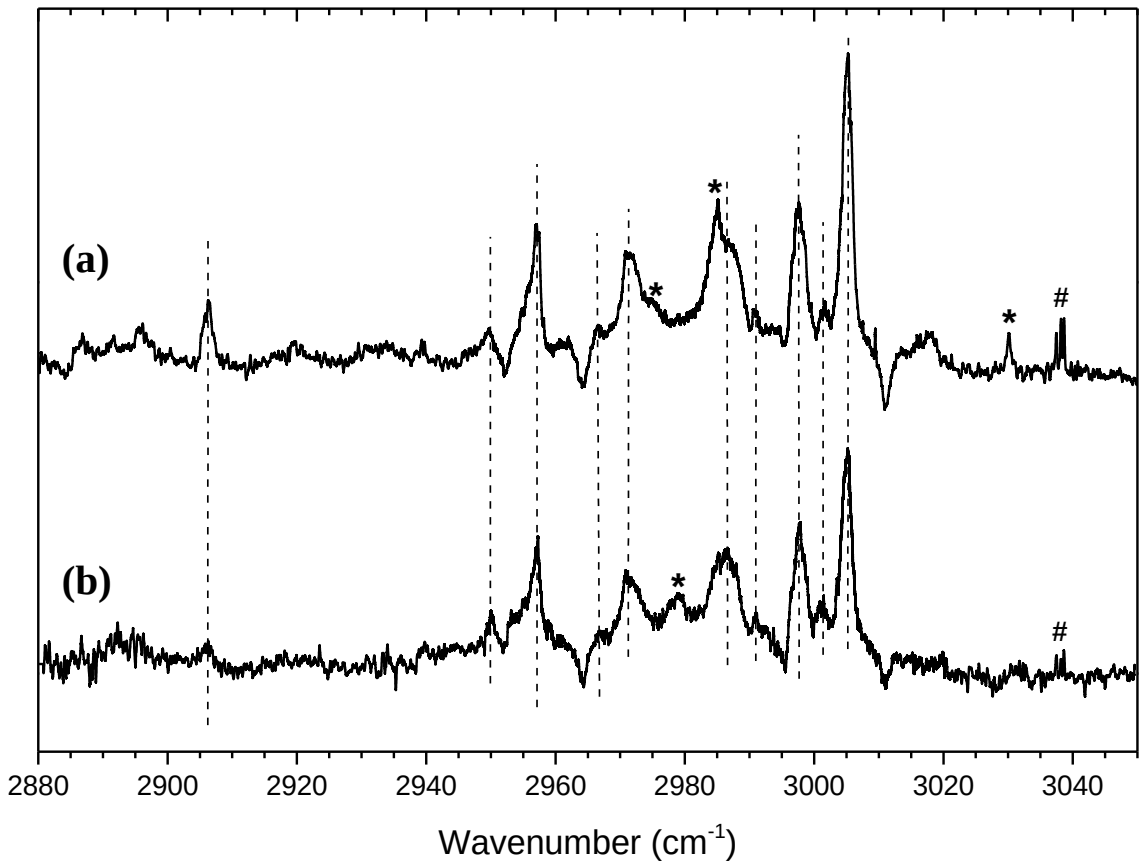

Figure 6.4. Infrared depletion spectra measured on mass channel 45 u with (a) DTAP (b) PRONO as the pyrolytic precursor. Common features assigned to ethylperoxy are indicated by dotted lines. The strongest rovibrational lines of ethyl radical in this region (marked with #) are visible in the spectra centered around 3038 cm^{-1}, but other ethyl transitions are too weak to be observed.[77] Contaminant absorptions are marked with asterisks.

6.4.4.2. Sensitivity to Harmonic Frequencies

Sensitivity of the VPT2+K predictions to the harmonic frequencies was explored (Fig. 6.5). The four simulations for each conformer are completely analogous to each other, aside from using a different set of harmonic frequencies and intensities. We also note that these simulations are performed with semi-diagonal quartic force fields, where the cubic and quartic force constants are in the CCSD(T)/ANO0 normal coordinates. The number of bands from each conformer is nearly unchanged for the three levels of theory, and the relative intensities are also similar. However the

differences in the zeroth-order frequencies influence the ordering of the bands. Between the hybrid simulations, which use at least triple-zeta quality harmonic frequencies, the position of any given transition changes by less than 10 cm^{-1}. It can be seen that CCSD(T)/ANO0 harmonic frequencies lead to a (sometimes) severe overestimation of the transition frequencies.

6.4.4.3. Transformation & Resonance Treatment

Subtly different ways of transforming the ANO0 force constants into the F12 normal coordinates were considered. Four approaches were identified. They are characterized by which of the two equilibrium geometries is used to evaluate the *L*-tensor elements and which of the two sets of quadratic internal force constants is used during the transformation (either F12 or ANO0). It was feasible to obtain the one-mode cubic (ϕ_{iii}) and quartic (ϕ_{iiii}) force constants at the CCSD(T)-F12/cc-pVDZ-F12 level of theory from the same grid of energy points that was used to determine the quadratic force constants. These were used as reference values in a series of comparisons between the ANO0 force constants, in their original normal coordinates, and the same force constants transformed (four different ways) into the F12 normal coordinates (Tables 6.2-6.5).

In these tables, the column "ANO0" contains the CCSD(T)/ANO0 force constants in their original normal coordinates, ordered by best match to the CCSD(T)-F12 normal coordinates. Four different variations of the transformation into the CCSD(T)-F12 normal coordinates are defined by the reference structure used to compute the L-tensor elements and by the set of quadratic internal force constants used in the transformation equations. These four variations are named as follows: ANO0 reference structure and ANO0 quadratic force constants (var-1), F12 reference structure and F12 quadratic force constants (var-2), F12 reference structure and ANO0 quadratic force constants (var-3), ANO0 reference structure and F12 internal quadratic force constants (var-4). The column labeled "F12" contains anharmonic normal coordinate force constants evaluated via finite differences of CCSD(T)-F12/cc-pVDZ-F12 energies. Cubic

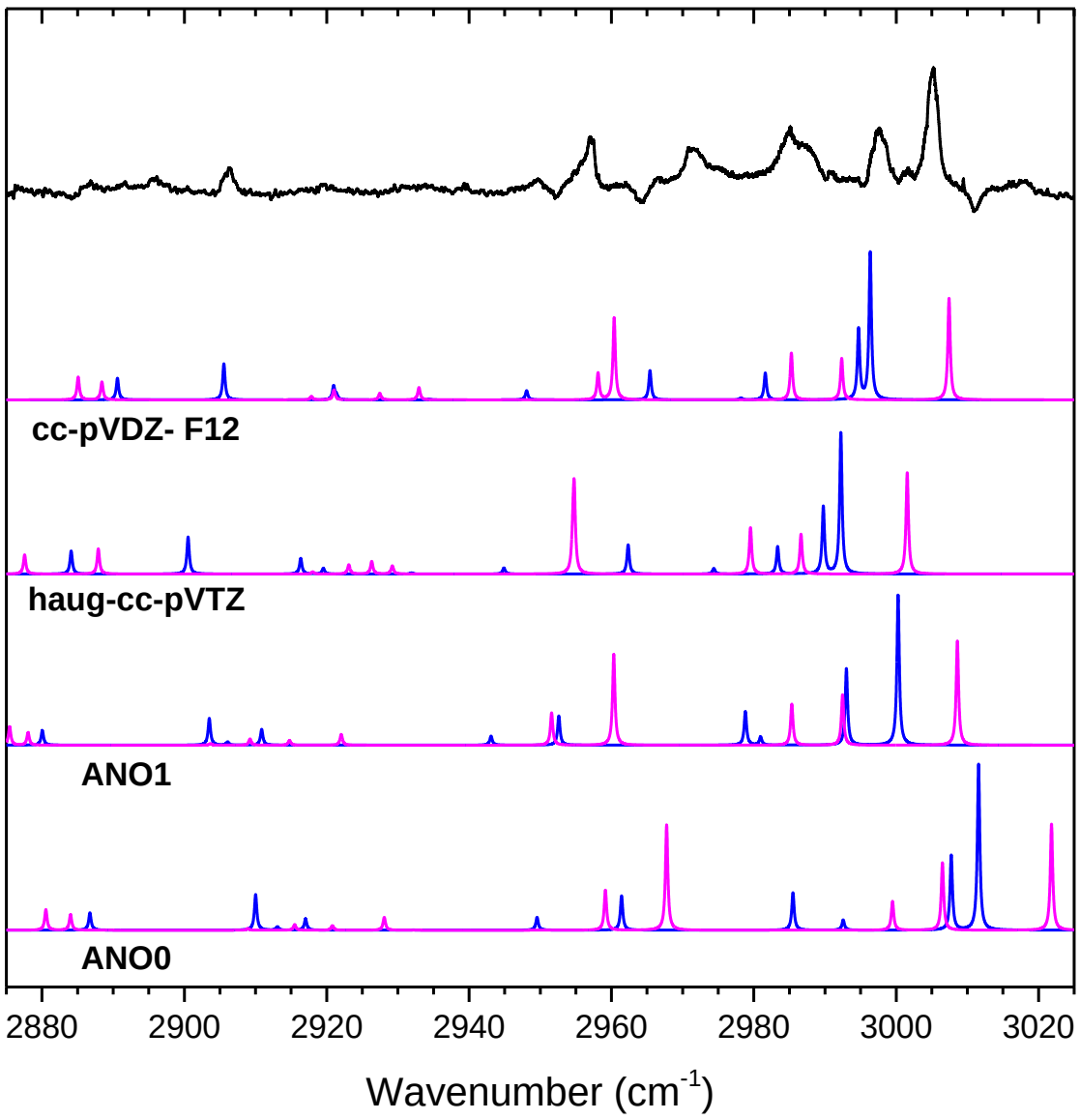

Figure 6.5. Infrared depletion spectrum of ethylperoxy, measured on mass channel 45 u, using DTAP, and VPT2+K simulations. The basis sets used for the harmonic frequencies and intensities are indicated for each pair of simulations (with the exception that the cc-pVDZ-F12 simulations used the haug-cc-pVTZ intensities). The *trans* simulations are in blue, while the *gauche* simulations are in pink.

Table 6.2. Comparisons of *trans* ϕ_{iii} (cm^{-1}) for four methods of transforming from internal to normal coordinate force constants. RMSD excludes the O-O stretch (i = 8).

i	**Γ**	**ANO0**	**var-1**	**var-2**	**var-3**	**var-4**	**F12**
1	a'	-787.3	-796.3	-794.0	-794.1	-796.3	-783.1
2	a'	1335.8	1351.2	1351.0	1351.0	1351.2	1332.4
3	a'	1051.6	1067.2	1067.3	1067.3	1067.2	1054.9
4	a'	35.1	18.3	17.4	16.8	18.8	17.3
5	a'	-62.1	-63.2	-62.3	-63.3	-62.3	-62.4
6	a'	-101.4	-109.4	-107.1	-109.9	-106.6	-106.2
7	a'	-12.4	-14.9	-16.0	-19.6	-11.4	-21.4
8	a'	334.1	346.9	345.8	346.5	346.2	410.9
9	a'	95.6	-86.0	-89.3	-90.2	-85.2	-86.9
10	a'	-93.2	-90.2	-87.3	-87.3	-90.2	-83.3
11	a'	131.6	144.0	132.8	134.5	142.2	134.0
12	a'	59.0	57.8	60.0	61.2	56.8	58.2
13	a'	-10.7	-1.2	-9.8	-11.1	0.4	-11.6
RMSD		53.1	9.1	7.5	7.5	9.3	-

Table 6.3. Comparisons of *trans* ϕ_{iii} (cm^{-1}) for four methods of transforming from internal to normal coordinate force constants. RMSD excludes the O-O stretch (i = 8).

i	**Γ**	**ANO0**	**var-1**	**var-2**	**var-3**	**var-4**	**F12**
1	a'	553.3	558.4	557.8	557.8	558.4	548.8
2	a'	512.2	521.3	521.1	521.2	521.3	510.6
3	a'	322.6	328.5	328.5	328.5	328.5	322.9
4	a'	15.3	12.5	11.6	12.1	12.0	1.5
5	a'	13.6	14.3	13.6	14.1	13.9	2.4
6	a'	32.3	34.0	32.7	32.9	33.8	31.9
7	a'	66.5	71.6	70.9	71.4	71.0	69.7
8	a'	106.0	106.8	106.3	106.3	106.8	120.1
9	a'	12.6	14.7	14.6	14.7	14.7	13.8
10	a'	37.8	42.1	41.4	41.4	42.1	39.6
11	a'	97.7	99.1	99.6	100.1	98.5	99.2
12	a'	6.3	5.9	6.7	6.4	6.1	6.0
13	a'	69.4	68.0	71.3	69.3	69.9	70.8
14	a''	302.8	314.7	314.8	314.9	314.7	309.7
15	a''	310.9	323.7	324.1	324.0	323.8	318.1
16	a''	6.3	5.7	4.6	4.4	5.8	-9.7
17	a''	57.2	58.3	57.3	58.9	57.5	56.6
18	a''	67.9	64.3	63.4	64.2	63.5	61.5
19	a''	293.9	295.8	297.1	299.2	293.7	296.7
20	a''	3234.8	3474.0	3509.2	3520.2	3463.2	3502.2
21	a''	541.3	628.5	744.0	652.2	716.7	746.7
RMSD		77.2	27.9	6.3	22.4	12.7	-

Table 6.4. Comparisons of *gauche* ϕ_{iii} (cm^{-1}) for four methods of transforming from internal to normal coordinate force constants. RMSD excludes the O-O stretch (i = 8).

i	**Γ**	**ANO0**	**var-1**	**var-2**	**var-3**	**var-4**	**F12**
1	a'	258.3	165.1	165.7	165.7	165.1	162.8
2	a'	-1329.9	-1338.4	-1337.8	-1337.8	-1338.4	-1321.7
3	a'	-1063.7	-1078.7	-1078.7	-1078.7	-1078.7	-1065.9
4	a'	-55.0	-54.5	-53.5	-54.5	-53.6	-53.2
5	a'	19.4	29.8	29.2	29.5	29.5	30.8
6	a'	-100.2	-108.3	-107.7	-110.3	-105.8	-107.4
7	a'	-2.6	2.1	-9.4	-10.5	3.1	-10.5
8	a'	241.7	197.8	199.2	199.4	197.6	242.6
9	a'	-100.3	130.3	128.0	129.9	128.4	125.7
10	a'	-11.7	-28.8	-30.4	-30.6	-28.6	-25.2
11	a'	139.1	146.7	145.8	147.6	145.0	145.8
12	a'	40.2	43.3	42.8	43.0	43.1	39.8
13	a'	54.5	53.8	56.2	56.2	53.7	57.0
14	a''	344.9	260.5	261.4	261.4	260.5	257.2
15	a''	227.7	210.0	209.4	209.4	210.0	206.0
16	a''	11.3	-8.9	-10.5	-10.7	-8.7	-9.8
17	a''	-9.0	13.5	13.3	14.7	12.2	17.4
18	a''	-12.4	42.9	38.7	39.5	41.9	47.0
19	a''	22.0	18.0	18.4	19.6	16.8	16.0
20	a''	9.3	158.3	7.9	7.4	158.2	7.0
21	a''	41.9	43.2	46.8	47.2	46.5	43.7
RMSD		60.7	34.4	5.5	5.6	34.4	-

Table 6.5. Comparisons of *gauche* ϕ_{iiii} (cm^{-1}) for four methods of transforming from internal to normal coordinate force constants. RMSD excludes the O-O stretch (i = 8).

i	Γ	ANO0	var-1	var-2	var-3	var-4	F12
1	a'	309.2	323.4	323.3	323.3	323.4	318.3
2	a'	509.7	515.1	514.8	514.8	515.1	506.0
3	a'	332.3	338.1	338.2	338.1	338.1	332.6
4	a'	8.9	8.5	7.5	7.8	8.2	-3.9
5	a'	5.7	8.3	7.6	7.9	7.9	-1.1
6	a'	34.1	35.6	34.8	35.0	35.3	34.3
7	a'	70.1	73.8	72.7	73.4	73.1	71.0
8	a'	69.5	60.6	60.7	60.8	60.5	69.0
9	a'	23.7	28.3	28.2	28.3	28.2	27.2
10	a'	21.1	24.4	24.1	24.1	24.4	22.3
11	a'	59.0	60.5	60.7	60.8	60.4	60.5
12	a'	41.4	41.4	43.2	42.4	42.1	42.4
13	a'	49.6	44.8	45.9	45.5	45.1	45.9
14	a''	332.1	313.5	314.2	314.1	313.5	309.5
15	a''	314.0	333.2	333.2	333.2	333.2	328.1
16	a''	8.2	5.6	4.9	5.1	5.5	-3.8
17	a''	62.7	64.6	63.4	64.4	63.6	61.1
18	a''	28.1	20.9	20.6	21.0	20.6	21.3
19	a''	230.2	238.2	239.2	241.2	236.2	239.0
20	a''	3370.0	3574.3	3611.3	3626.0	3559.8	3607.3
21	a''	407.6	401.2	441.8	414.4	427.5	439.3
RMSD		54.2	12.4	5.0	8.6	12.1	-

and quartic force constants calculated in this manner are typically accurate to 1 cm^{-1} (sometimes more numerical error for very low frequency coordinates, such as the torsions 20 and 21).

The force constants transformed with the var-2 procedure are usually very similar to those transformed with var-3; likewise, var-1 force constants are similar to var-4. This indicates that the contribution to these higher order force constants from the quadratic internal coordinate force constants is small. Procedures var-2 and var-3 are quite a bit better overall than var-1 and var-4. It is apparent that their use of the ANO0 equilibrium geometry for determination of the L-tensor elements is largely responsible for their deficiencies. For many normal coordinates, it can be seen that the transformed force constants are not greatly different. This is generally because

the two sets of normal coordinates are very similar. Sometimes the transformed force constants are superior, and sometimes the force constants expressed in the original ANO0 normal coordinates are superior. For certain force constants, the advantages of coordinate transformation are striking, such as for the antisymmetric CH stretching (i=14,15) cubic force constants of the *gauche* conformer (Table 6.4). In this instance, the transformation puts the force constants into excellent agreement with the true CCSD(T)-F12 values.

It was found that when the F12 equilibrium structure was used to determine the L-tensor elements and the F12 quadratic force constants were used in the transformation equations, the resulting anharmonic force constants consistently had the smallest RMSD from the true CCSD(T)-F12 values. This suggests that performing the coordinate transformation in this manner produces a force field that more closely approximates a CCSD(T)-F12 full quartic force field. This particular version of the transformation also happens to be the most physically satisfying, as it directly reproduces the CCSD(T)-F12 harmonic frequencies, and all mixed normal coordinate second derivatives are zero. This set of transformed force constants will be used in all subsequent discussions and comparisons to experiment.

The substitution of lower level cubic and quartic force constants into a higher level quadratic force field is done in the interest of cost-effectiveness. It is typically best to use computing resources to improve the quality of the quadratic force constants, which can require very large basis sets to achieve an adequately-converged description. In contrast, an investment in higher level cubic and quartic force constants usually only gives modest returns and requires many more energy derivatives. Oftentimes, a level of theory that is affordable for the quadratic force constants is rendered intractable for the cubic and quartic force constants by the sheer number of displaced energy and/or energy derivative calculations required. In different situations, the hybrid approximation for anharmonic force fields can be thought of as either a more

economical means of calculating the anharmonic part of the potential or as enabling the harmonic part to be described with the level of accuracy that it demands.

Expounding on the validity of the coordinate transformation, the CCSD(T)/ANO0 full quartic force field (in internal coordinates) and the CCSD(T)-F12/cc-pVDZ-F12 quadratic force fields (transformed into internal coordinates) are each rigorously correct, at least at their respective levels of theory. Likewise, transforming those force fields between the internal and normal coordinate representations is valid and reversible. The procedure that we use can be viewed as making one central approximation; it comes into play during the transformation. We essentially say that the CCSD(T)/ANO0 cubic and quartic force constants, in internal coordinates, can be treated as if they are actually CCSD(T)-F12 force constants.

The consequences of transforming the force constants can be seen in Figure 6.6, where identical VPT2+K simulations are performed with both sets of anharmonic force constants; additionally these are compared with two simpler models: a deperturbed VPT2 (DVPT2) of only the CH stretch fundamentals and a scaled harmonic spectrum.

The scaled harmonic treatment is acceptable for the two prominent high frequency transitions. Its ability to predict their frequencies should not be viewed as a success of the harmonic model, as the scaling factor is chosen to reproduce these. The experimental splitting (7.2 cm^{-1}) is predicted accurately at the harmonic level (6.2 cm^{-1}), though this worsens slightly after scaling (5.9 cm^{-1}). This suggests that a harmonic description of these transitions is reasonable and that their anharmonicities are similar. The lower frequency region is not well described, but we did not expect this to succeed here. Deperturbed second-order vibrational perturbation theory (DVPT2) also fails here because of its neglect of strong anharmonic couplings. However it does correctly place a strong feature around 2960 cm^{-1}. Many small splittings and additional anharmonic features are introduced by the VPT2+K effective Hamiltonian approach. Now the region around 2900 cm^{-1} bears some resemblance to experiment. In the top trace, where all force constants are expressed in the F12 normal coordinates, the

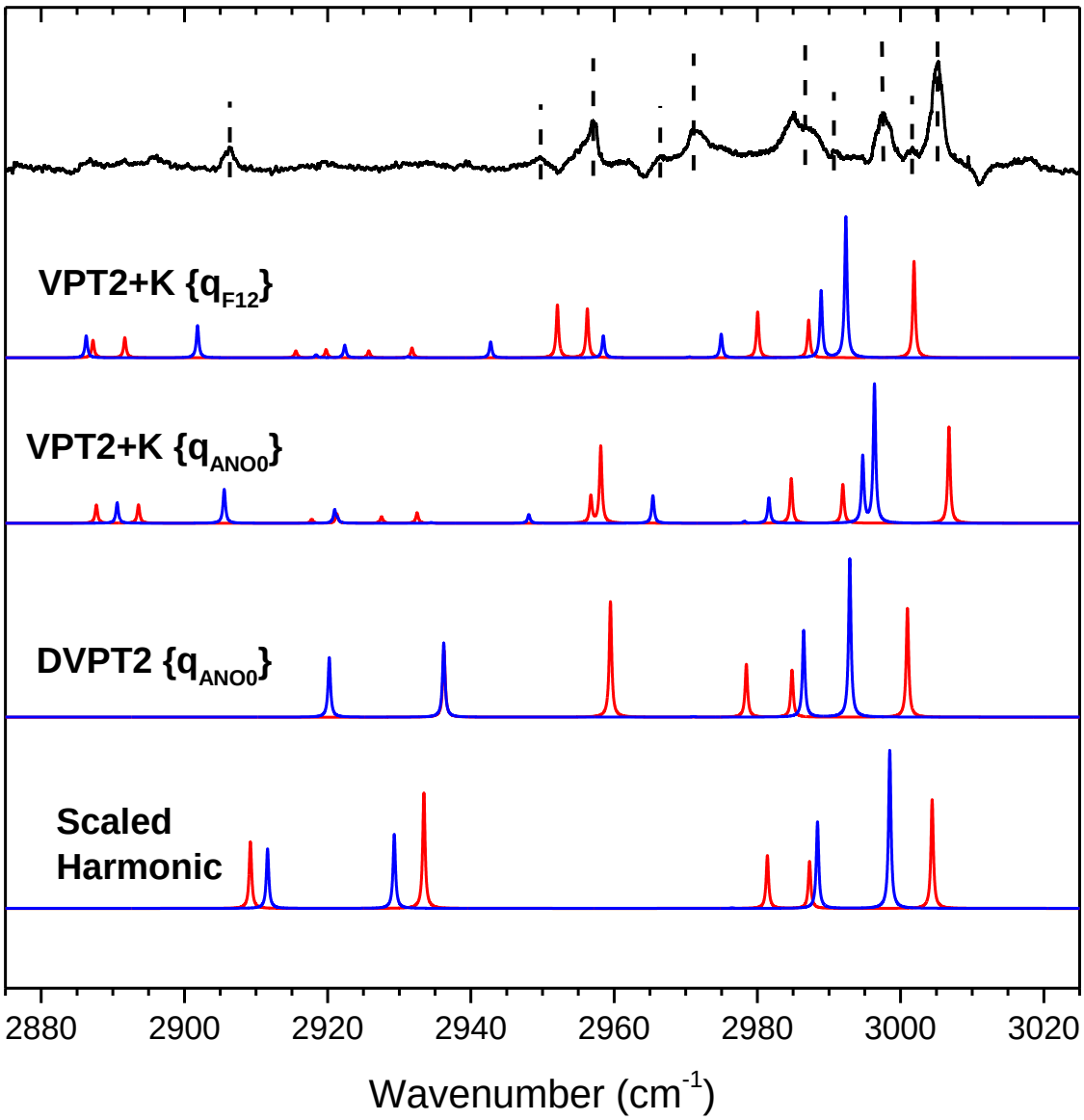

Figure 6.6. Infrared depletion spectrum of ethylperoxy, measured on mass channel 45 u, using DTAP, and various theoretical simulations (*gauche* in red; *trans* in blue). Ethylperoxy peaks are indicated with dotted lines. The simulations labeled VPT2+K $\{q_{F12}\}$ combine CCSD(T)-F12/cc-pVDZ-F12 quadratic force constants and CCSD(T)/ANO0 cubic and quartic force constants (in the same set of normal coordinates). VPT2+K $\{q_{ANO0}\}$ represents the cubic and quartic force constants in the CCSD(T)/ANO0 normal coordinates. DVPT2 deperturbs the strongest resonances involving the CH stretch fundamentals but does not treat those couplings. The harmonic simulations scale the CCSD(T)-F12 frequencies by 0.954 to best reproduce the intense high-frequency transitions. All simulations use CCSD(T)/haug-cc-pVTZ harmonic intensities.

changes are less striking than between other models. There is an overall red shift of the higher frequency transitions, putting them back into quite good fortuitous agreement with the predictions of DVPT2. There is a great change in intensity-sharing between the pair of *gauche* features around 2955 cm^{-1}. This is largely a consequence of the deperturbed frequencies (the diagonal elements of the effective Hamiltonian) moving closer together. The relative intensities of closely spaced transitions (of the same symmetry) are always very sensitive to the force field and to the choice of states for the effective Hamiltonian.

Unfortunately, the match to experiment is not overwhelmingly better with the transformed force constants (VPT2+K $\{q_{F12}\}$). The higher and lowest frequency features appear to be in slightly worse agreement, but now more intensity is correctly distributed around 2970-2980 cm^{-1}, where it was lacking with the original force field (VPT2+K $\{q_{ANO0}\}$). This suggests that there is still some room for the *ab initio* force field to be improved. Still, we anticipate that a VPT2+K simulation done with higher quality cubic and quartic force constants would most closely resemble the upper (VPT2+K $\{q_{F12}\}$) trace.

6.4.5. Spectroscopic Assignments

Figure 6.7 shows a comparison between the VPT2+K simulations, using the CCSD(T)-F12 harmonic frequencies and normal coordinates, and the ethylperoxy spectrum produced from the DTAP precursor. Between the two rotamers, effort is made to make the anharmonic simulations comparable. The number of states in each rotamer's VPT2+K effective Hamiltonian is the same, and they were chosen to be similar in character, bearing in mind that the normal modes are not the same, and so the simulations cannot be completely equivalent.

Much of the spectrum is congested with broad, overlapping features, owing to the presence of contaminants and to both ethylperoxy rotamers. In most cases, specific conformer assignments should be considered tentative. A summary of the ethylperoxy experimental bands

and their assignments is given in Table 6.6. To aid in assignment, a list of normal modes and harmonic frequencies is also made available (Table 6.1).

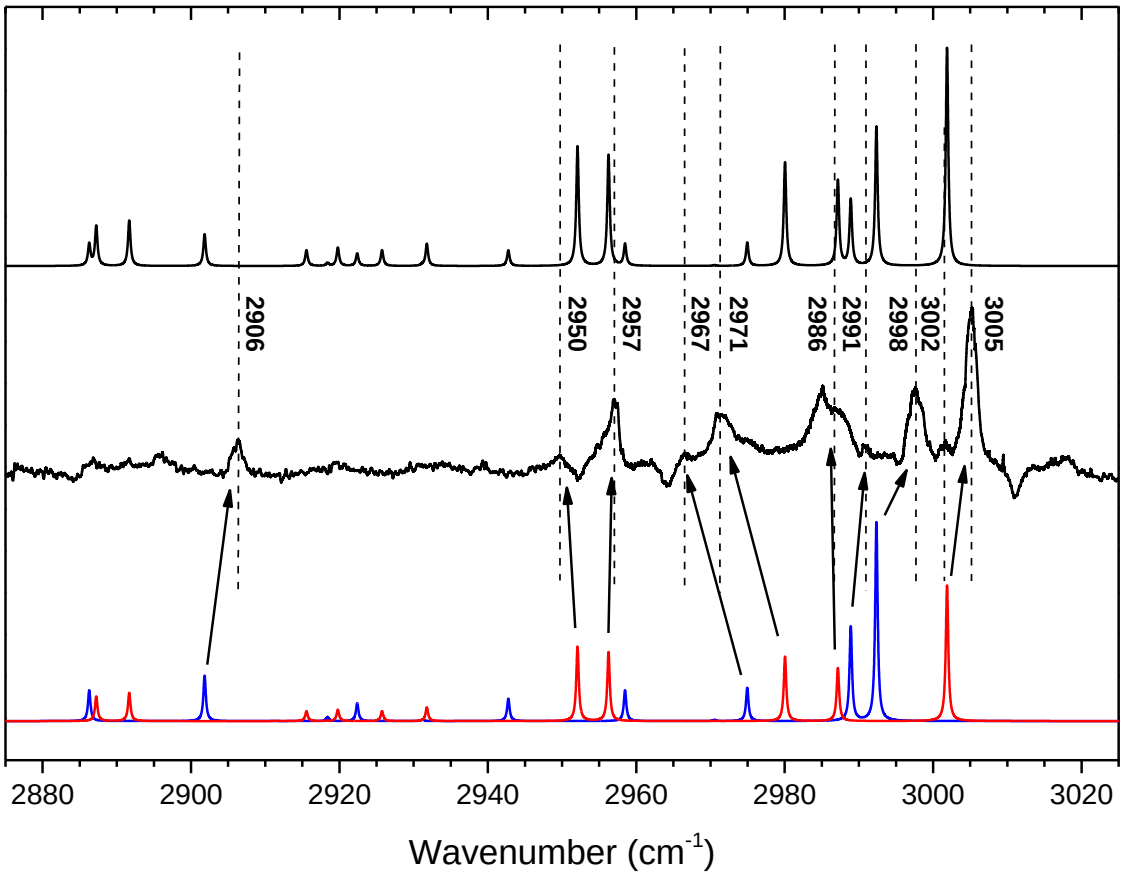

Figure 6.7. Infrared depletion spectrum of ethylperoxy, measured on mass channel 45 u, using DTAP, and VPT2+K simulations (*gauche* in red; *trans* in blue) that combine CCSD(T)-F12/cc-pVDZ-F12 quadratic force constants, CCSD(T)/ANO0 cubic and quartic force constants (expressed in the F12 normal coordinates), and CCSD(T)/haug-cc-pVTZ harmonic intensities. Ethylperoxy peaks are indicated with dotted lines and labeled with their frequencies. Suggested assignments are shown with arrows. The top simulation shows the sum of the separate conformer simulations, with *gauche* features scaled to reflect a 2.3x greater abundance.

Table 6.6. Experimental bands assigned to ethylperoxy, conformer assignments, CCSD(T) anharmonic frequencies (parenthetical anharmonic intensities in km/mol), and descriptions. Listed VPT2+K transition components are the largest squared eigenvector coefficients of the stretch/bend effective Hamiltonians. VPT2+K frequencies are computed using the force field with the cubic/quartic force constants transformed into the CCSD(T)-F12 normal coordinates.

Expt. (cm^{-1})	VPT2+K (cm^{-1})	Rotamer	VPT2+K Transition Components
-	2886.3 (3.6)	*trans*	44% $2v_{16}$+ 23% v_3
-	2887.2 (2.8)	*gauche*	40% $2v_{16}$+ 19% v_3+ 18% $2v_5$
-	2891.7 (3.3)	*gauche*	49% $(v_5 + v_{16})$ + 13% v_2
2906.2	2901.8 (5.2)	*trans*	43% v_2+ 19% $(v_4 + v_5)$ + 10% $2v_5$
-	2942.8 (2.6)	*trans*	57% $2v_5$+ 17% v_3+ 12% $2v_4$
2950.0	2952.1 (8.6)	*gauche*	32% v_2+ 20% $(v_5 + v_{16})$ + 17% v_3 + 16% $2v_4$
2957.0	2956.3 (8.0)	*gauche*	35% v_2+ 34% $2v_4$+ 10% v_3
-	2958.5 (3.6)	*trans*	33% $(v_4 + v_5)$ + 21% v_3 + 14% $2v_4$ +14% $2v_{16}$
2966.6	2975.0 (3.9)	*trans*	53% $2v_4$+ 30% v_2+ 11% $(v_4 + v_5)$
2971.4	2980.0 (7.4)	*gauche*	80% v_{15}
2986.2	2987.2 (6.1)	*gauche*	78% v_1+ 13% $2v_4$
2990.8	2988.9 (10.9)	*trans*	75% v_1+ 14% $(v_4 + v_5)$
2997.6	2992.4 (22.9)	*trans*	89% v_{14}
3001.5	-	-	-
3005.2	3001.9 (15.7)	*gauche*	87% v_{14}

6.4.5.1. Low Frequency Region (Below 2950 cm^{-1})

There are several weak, anharmonic features predicted around 2890 cm^{-1}. The experimental spectrum in this vicinity has some semblance of structure, but the signal to noise ratio is too low for us to be comfortable making any assignment. The lowest frequency band appears at 2906.2 cm^{-1} and lies in the cleanest region of the spectrum. It is fit well to a single Lorentzian line shape. Comparisons with theory motivate the assignment of this band to the *trans* conformer. This feature, predicted at 2901.8 cm^{-1}, carries about half of the symmetric CH_2 stretch intensity; the rest of its composition is overtones and combinations of a' scissoring vibrations. For the next 40 cm^{-1}, there are again many low intensity, highly anharmonic features predicted. Experimentally, the spectrum is devoid of assignable band structure.

6.4.5.2. High Frequency Region (Above 2950 cm^{-1})

While the lower frequency region contains mostly weak, unresolved features and one definitive peak, the higher frequency part of the spectrum contains many intense bands, at least nine of which derive from ethylperoxy radical. Two of the most Lorentzian features appear at high frequency; namely 3005.2 and 2997.6 cm^{-1}. Theory predicts that *gauche* should possess the highest frequency absorption, at 3001.9 cm^{-1}; whereas, the highest frequency *trans* band should lie at 2992.4 cm^{-1}. On the basis of this ordering, consistent at various levels of theory (Fig. 6.5), and the splitting between these features (experimentally 7.6 cm^{-1} and theoretically 9.5 cm^{-1}), we assign the higher frequency feature to the *gauche* conformer and the lower feature to *trans*. Both transitions are well described as CH stretch fundamentals. They correspond to an in-phase antisymmetric stretching motion of the two CH_2 moieties, bisected by the symmetry plane in the C_s *trans* conformer, and approximately the same motion in the C_1 *gauche* conformer. A consideration of the intensities of these features can provide a rough estimate of the rotamer populations. By fitting this region with three Lorentzian functions (the third fits the weaker peak at 3001.5 cm^{-1}), we estimate that the 2997.6 cm^{-1} band is 60% as intense as the 3005.2 cm^{-1} band. The theoretical intensity of the *gauche* feature is about 70% as great as the *trans* feature; thus, there is ~ 2.3 times as much *gauche*-ethylperoxy present as *trans*-ethylperoxy. On this basis, assignment of the remaining intense peaks to *gauche* would seem most reasonable. Note that this population ratio implies the conformers do not exist in thermal equilibrium at the droplet temperature (*gauche* should comprise essentially 100% of the population at 0.4 K). In the helium droplet community, it is well known that association processes in droplets do not, in general, yield products in thermal equilibrium.

At 2957 cm^{-1} we observe an intense band with an asymmetric shape, possibly obtaining its low frequency shoulder from an overlapping feature. We assign this to the *gauche* conformer. Theory predicts a pair of *gauche* bands near here, and each carries a mixture of symmetric CH_2 stretch intensity and a smaller amount of symmetric CH_3 stretch intensity. Their intensity ratio is

quite sensitive to the level of theory (Fig. 6.5 and 6.6). The two nearby *trans* transitions have similar compositions. One of the *gauche* symmetric stretches likely dominates this feature. Its shoulder and the broad feature at 2950 cm^{-1} probably correspond to the other *gauche* transition and one or both of the similar *trans* symmetric stretches.

A prominent band is centered at 2971.4 cm^{-1}, which likely originates from the *gauche* rotamer. It overlaps with a weaker band, centered at 2966.6 cm^{-1}, which may derive from the *trans* rotamer. A good candidate for the weak feature is the first overtone of the out-of-phase CH_2 scissor, predicted at 2975.0 cm^{-1}, which borrows considerable intensity from the symmetric CH_3 stretch. The nearest *gauche* feature is predicted at 2980.0 cm^{-1}, and it represents the most likely assignment for the main peak at 2971.4 cm^{-1}. This *gauche* transition represents the lower frequency "degenerate" antisymmetric stretch fundamental of the CH_3 group. The higher frequency antisymmetric CH_3 stretch is predicted at 2987.2 cm^{-1}. We assign the next highest frequency ethylperoxy feature, at 2986.2 cm^{-1}, to this.

An analogous antisymmetric stretch of the *trans* conformer may additionally be visible. While the *gauche* conformer has two antisymmetric CH_3 stretching fundamentals of similar intensity, *trans* has one that is nearly dark (0.1 km/mol). The bright transition (10.9 km/mol) is predicted at 2988.9 cm^{-1}. Based on the theoretical frequency ordering, this is assigned to the weak 2990.8 cm^{-1} feature. This leaves the 3001.5 cm^{-1} peak unassigned. Although theory predicts that the surrounding strong features are relatively unmixed, a weak resonance with some three- or four-quanta vibrational state absent from the VPT2+K effective Hamiltonian could still give rise to the 3001.5 cm^{-1} peak. Such a thing is thought to occur with the high frequency CH stretches of allyl radical.[43] In its spectrum, several low intensity transitions with identical rotational structure were found to cluster around the high frequency CH stretches.

6.4.6. Comparison to Previous Spectroscopy

We now compare our experimental ethylperoxy transitions to the room temperature gas phase work of Mah *et al*.[31] In the CH stretch region, they noted that their ethyl radical precursor,

ethane, showed absorptions much more intense than in the rest of their coverage region. The ethane transitions were sufficiently intense that they fell in the non-linear absorption regime. They found it necessary to use a lower ethane concentration, to bring the absorption back into the linear regime, when measuring this region. Despite their efforts, they were still unable to completely subtract out the ethane signal. Furthermore, by using lowered ethane concentration, their peroxy radical signals were diminished. They were able to assign three rovibrational lines to the peroxy radical, but determination of accurate band origin(s) was not possible. Their rovibrational lines were measured at 2964, 2988, and 2999 cm^{-1}. They assigned these lines to rovibrational transitions belonging to specific CH stretching bands on the basis of B3LYP/6-311G scaled harmonic frequency computations. The theoretical calculations appear to be for the *gauche* rotamer only; although, they made no mention of rotamers in their work. Because of the much different temperatures, and because it is not completely clear what their computations correspond to, it is not easy to compare our assignments to theirs. The higher frequency lines in the gas-phase work matches most closely with our intense bands centered at 2986.2 cm^{-1} and 2997.6 cm^{-1}. The identity of their 2964 cm^{-1} transition is less clear. It is closest in frequency to the weak 2966.6 cm^{-1} feature, yet it is amidst the strong 2957.0 cm^{-1} and 2971.4 cm^{-1} features. Unfortunately, a more detailed comparison is not possible.

The only comparison that we are able to make to the work of Chettur and Snelson is to the CH stretching peak that they observed at 3016 wavenumbers.[32] This most likely represents the same transition as our 3005 cm^{-1} band; although, it is unusual for an argon matrix absorption to be blue shifted 11 cm^{-1} relative to band origins observed using helium droplet isolation. We base this partly upon the prominence of this feature in our experiment. The region of their spectrum to the blue of the 3016 cm^{-1} peak is also relatively free of vibrational bands, suggesting that the 3016 cm^{-1} peak is the highest frequency ethylperoxy transition in argon. To the red of this peak, strong absorptions of ethane are indicated, and they likely obscure the remainder of the CH stretches.

6.5. Conclusions

Ethylperoxy radical was produced in helium droplets *via* the barrierless association reaction: $CH_3CH_2 + O_2$. The radical was interrogated with IR spectroscopy. Through the use of two different ethyl radical precursors, several experimental bands could be assigned to the ethylperoxy radical. The spectrum is most readily interpreted as having both *gauche* and *trans* rotamers in appreciable abundance. The IR spectra of both rotamers were modeled with VPT2+K using high quality quadratic force constants and various approximations for transition intensities and the anharmonic part of the potential. The simple approach of combining force constants from different levels of theory, represented in their respective normal coordinates, was compared to transformation of force constants into the same normal coordinate system. It was found that when lower level cubic and quartic force constants were transformed into the same normal coordinates as the quadratic force constants, they more closely approximated higher level cubic and quartic force constants. Effects on the simulation were modest but not insignificant, typically red-shifting the transitions. We cannot state with certainty how much this improves the predictive ability of the simulations, due to the difficulty of making confident conformer-specific assignments. The quality of VPT2 simulations using lower-level, transformed anharmonic force constants needs to be assessed by detailed comparisons to the spectra of well-understood small molecules in the gas phase.

The finding of multiple rotamers represents a novel departure from our previous work on multi-conformer peroxy radical systems, in which analogous association reactions were carried out inside helium droplets, and only a single conformer of the product was observed.[43-44] In this previous work, we exclusively observed the lowest energy allylperoxy and propargylperoxy rotamers, and we rationalized this by suggesting a solvent-assisted adiabatic funneling mechanism. In this mechanism, upon association, the high frequency stretch vibrations cool slowly in comparison to the low frequency torsional modes (most importantly the highly excited

C-OO stretch most closely associated with the R + O_2 reaction path). It is reasonable to expect torsional cooling to be comparatively fast due to *i*) the smaller associated energy gaps and *ii*) the stronger coupling of torsional motion to the collective excitations of the helium droplet. As a nascent peroxy radical cools, it is annealed (i.e. "funneled") into the torsional minimum that appears first (i.e. the first to appear as the excitation along the "C-OO" reaction coordinate is quenched). Clearly, this mechanism cannot explain the ethylperoxy experimental results, for which we observe both *gauche* and *trans* rotamers in appreciable abundance (however, *gauche* is about twice as abundant as *trans*). For allylperoxy and propargylperoxy (i.e. in the acetylenic part of the potential), the barriers to isomerization were predicted to be about 300 cm^{-1} and 100 cm^{-1}, respectively.[78-79] Similarly, interconversion from *trans*- to *gauche*-ethylperoxy occurs via an ~ 300 cm^{-1} barrier on the ground state potential. The more important comparison, however, is the torsional interconversion barriers that exist at long-range, consistent with high degrees of inter-fragment excitation (i.e. C-OO stretching). Perhaps the adiabatic funneling mechanism can still be viewed as realistic; but for ethylperoxy, kinetic trapping in the *trans* minimum occurs due to it being formed earlier during the dynamical cooling process. All of this discussion is necessarily qualitative, but these results comprise a set of systems that can be tested against future quantitative models of the dynamical processes that are operative during bimolecular association reactions within helium droplets.

References

(1) Naik, C. V.; Dean, A. M. Detailed Kinetic Modeling of Ethane Oxidation. *Combust. Flame* **2006**, *145*, 16-37.

(2) Stark, M. S. Addition of Peroxyl Radicals to Alkenes and the Reaction of Oxygen with Alkyl Radicals. *J. Am. Chem. Soc.* **2000**, *122*, 4162-4170.

(3) Baldwin, R. R.; Dean, C. E.; Walker, R. W. Relative Rate Study of the Addition of HO_2 Radicals to C_2H_4 and C_3H_6. *J. Chem. Soc., Faraday Trans. 2* **1986**, *82*, 1445-1455.

(4) Kaiser, E. W. Mechanism of the Reaction $C_2H_5+O_2$ from 298 to 680 K. *J. Phys. Chem. A* **2002**, *106*, 1256-1265.

(5) Kaiser, E. W. Temperature and Pressure-Dependence of the C_2H_4 Yield from the Reaction $C_2H_5+O_2$. *J. Phys. Chem.* **1995**, *99*, 707-711.

(6) Kaiser, E. W.; Wallington, T. J.; Andino, J. M. Pressure-Dependence of the Reaction $C_2H_5+O_2$. *Chem. Phys. Lett.* **1990**, *168*, 309-313.

(7) Kaiser, E. W.; Lorkovic, I. M.; Wallington, T. J. Pressure-Dependence of the C_2H_4 Yield from the Reaction $C_2H_5+O_2$. *J. Phys. Chem.* **1990**, *94*, 3352-3354.

(8) DeSain, J. D.; Klippenstein, S. J.; Miller, J. A.; Taatjes, C. A. Measurements, Theory, and Modeling of OH Formation in Ethyl + O_2 and Propyl + O_2 Reactions. *J. Phys. Chem. A* **2003**, *107*, 4415-4427.

(9) Carstensen, H. H.; Naik, C. V.; Dean, A. M. Detailed Modeling of the Reaction of $C_2H_5+O_2$. *J. Phys. Chem. A* **2005**, *109*, 2264-2281.

(10) Slagle, I. R.; Feng, Q.; Gutman, D. Kinetics of the Reaction of Ethyl Radicals with Molecular-Oxygen from 294 K to 1002 K. *J. Phys. Chem.* **1984**, *88*, 3648-3653.

(11) Clifford, E. P.; Farrell, J. T.; DeSain, J. D.; Taatjes, C. A. Infrared Frequency-Modulation Probing of Product Formation in Alkyl Plus O_2 Reactions: I. The Reaction of C_2H_5 with O_2 Between 295 and 698 K. *J. Phys. Chem. A* **2000**, *104*, 11549-11560.

(12) Plumb, I. C.; Ryan, K. R. Kinetic-Studies of the Reaction of C_2H_5 with O_2 at 295 K. *Int. J. Chem. Kinet.* **1981**, *13*, 1011-1028.

(13) McAdam, K. G.; Walker, R. W. Arrhenius Parameters for the Reaction $C_2H_5+O_2 \rightarrow C_2H_4+HO_2$. *J. Chem. Soc., Faraday Trans. 2* **1987**, *83*, 1509-1517.

(14) Dobis, O.; Benson, S. W. Reaction of the Ethyl Radical with Oxygen at Millitorr Pressures at 243-368 K and a Study of the Cl+HO_2, Ethyl+HO_2, and HO_2+HO_2 Reactions. *J. Am. Chem. Soc.* **1993**, *115*, 8798-8809.

(15) Atkinson, D. B.; Hudgens, J. W. Chemical Kinetic Studies Using Ultraviolet Cavity Ring-Down Spectroscopic Detection: Self-Reaction of Ethyl and Ethylperoxy Radicals and the Reaction $O_2+C_2H_5 \rightarrow C_2H_5O_2$. *J. Phys. Chem. A* **1997**, *101*, 3901-3909.

(16) Wagner, A. F.; Slagle, I. R.; Sarzynski, D.; Gutman, D. Experimental and Theoretical-Studies of the $C_2H_5+O_2$ Reaction-Kinetics. *J. Phys. Chem.* **1990**, *94*, 1853-1868.

(17) Miller, J. A.; Klippenstein, S. J.; Robertson, S. H. A Theoretical Analysis of the Reaction Between Ethyl and Molecular Oxygen. *P. Combust. Inst.* **2000**, *28*, 1479-1486.

(18) Miller, J. A.; Klippenstein, S. J. The Reaction between Ethyl and Molecular Oxygen II: Further Analysis. *Int. J. Chem. Kinet.* **2001**, *33*, 654-668.

(19) Bozzelli, J. W.; Dean, A. M. Hydrocarbon Radical Reactions with O_2 - Comparison of Allyl, Formyl, and Vinyl to Ethyl. *J. Phys. Chem.* **1993**, *97*, 4427-4441.

(20) Ignatyev, I. S.; Xie, Y. M.; Allen, W. D.; Schaefer, H. F. Mechanism of the $C_2H_5+O_2$ Reaction. *J. Chem. Phys.* **1997**, *107*, 141-155.

(21) Quelch, G. E.; Gallo, M. M.; Shen, M. Z.; Xie, Y. M.; Schaefer, H. F.; Moncrieff, D. Aspects of the Reaction-Mechanism of Ethane Combustion .2. Nature of the Intramolecular Hydrogen-Transfer. *J. Am. Chem. Soc.* **1994**, *116*, 4953-4962.

(22) Quelch, G. E.; Gallo, M. M.; Schaefer, H. F. Aspects of the Reaction-Mechanism of Ethane Combustion - Conformations of the Ethylperoxy Radical. *J. Am. Chem. Soc.* **1992**, *114*, 8239-8247.

(23) Rienstra-Kiracofe, J. C.; Allen, W. D.; Schaefer, H. F. The $C_2H_5+O_2$ Reaction Mechanism: High-Level Ab Initio Characterizations. *J. Phys. Chem. A* **2000**, *104*, 9823-9840.

(24) Wilke, J. J.; Allen, W. D.; Schaefer, H. F. Establishment of the $C_2H_5+O_2$ Reaction Mechanism: A Combustion Archetype. *J. Chem. Phys.* **2008**, *128*, 074308.

(25) Villano, S. M.; Huynh, L. K.; Carstensen, H. H.; Dean, A. M. High-Pressure Rate Rules for Alkyl + O_2 Reactions. 1. The Dissociation, Concerted Elimination, and Isomerization Channels of the Alkyl Peroxy Radical. *J. Phys. Chem. A* **2011**, *115*, 13425-13442.

(26) Melnik, D.; Thomas, P. S.; Miller, T. A. Electronic Transition Moment for the 0_0^0 Band of the Ã←X̃ Transition in the Ethyl Peroxy Radical. *J. Phys. Chem. A* **2011**, *115*, 13931-13941.

(27) Just, G. M. P.; Rupper, P.; Miller, T. A.; Meerts, W. L. High-Resolution Cavity Ringdown Spectroscopy of the Jet-Cooled Ethyl Peroxy Radical $C_2H_5O_2$. *J. Chem. Phys.* **2009**, *131*, 11, 184303.

(28) Rupper, P.; Sharp, E. N.; Tarczay, G.; Miller, T. A. Investigation of Ethyl Peroxy Radical Conformers via Cavity Ringdown Spectroscopy of the $\tilde{A}\leftarrow\tilde{X}$ Electronic Transition. *J. Phys. Chem. A* **2007**, *111*, 832-840.

(29) Blanksby, S. J.; Ramond, T. M.; Davico, G. E.; Nimlos, M. R.; Kato, S.; Bierbaum, V. M.; Lineberger, W. C.; Ellison, G. B.; Okumura, M. Negative-Ion Photoelectron Spectroscopy, Gas-Phase Acidity, and Thermochemistry of the Peroxyl Radicals CH_3OO and CH_3CH_2OO. *J. Am. Chem. Soc.* **2001**, *123*, 9585-9596.

(30) Hunziker, H. E.; Wendt, H. R. Electronic Absorption-Spectra of Organic Peroxyl Radicals in Near-Infrared. *J. Chem. Phys.* **1976**, *64*, 3488-3490.

(31) Mah, D. A.; Cabrera, J.; Nation, H.; Ramos, M.; Sharma, S.; Nickolaisen, S. L. Mid-Infrared Spectrum of the Gas-Phase Ethyl Peroxy Radical: C_2H_5OO. *J. Phys. Chem. A* **2003**, *107*, 4354-4359.

(32) Chettur, G.; Snelson, A. Alkylperoxy and Alkyl Radicals .IV. Matrix IR-Spectra and UV Photolysis of $C_2H_5O_2$ and C_2H_5 Radicals. *J. Phys. Chem.* **1987**, *91*, 3483-3488.

(33) Bartlett, M. A.; Liang, T.; Pu, L.; Schaefer, H. F.; Allen, W. D. The Multichannel *n*-Propyl + O_2 Reaction Surface: Definitive Theory on a Model Hydrocarbon Oxidation Mechanism. *J. Chem. Phys.* **2018**, *148*, 094303.

(34) Huynh, L. K.; Carstensen, H. H.; Dean, A. M. Detailed Modeling of Low-Temperature Propane Oxidation: 1. The Role of the Propyl + O_2 Reaction. *J. Phys. Chem. A* **2010**, *114*, 6594-6607.

(35) Launder, A. M.; Turney, J. M.; Agarwal, J.; Schaefer, H. F. Ethylperoxy Radical: Approaching Spectroscopic Accuracy via Coupled-Cluster Theory. *Phys. Chem. Chem. Phys.* **2017**, *19*, 15715-15723.

(36) Choi, M. Y.; Douberly, G. E.; Falconer, T. M.; Lewis, W. K.; Lindsay, C. M.; Merritt, J. M.; Stiles, P. L.; Miller, R. E. Infrared Spectroscopy of Helium Nanodroplets: Novel Methods for Physics and Chemistry. *Int. Rev. Phys. Chem.* **2006**, *25*, 15-75.

(37) Toennies, J. P.; Vilesov, A. F. Superfluid Helium Droplets: A Uniquely Cold Nanomatrix for Molecules and Molecular Complexes. *Angew. Chem., Int. Ed.* **2004**, *43*, 2622-2648.

(38) Mauracher, A.; Echt, O.; Ellis, A. M.; Yang, S.; Bohme, D. K.; Postler, J.; Kaiser, A.; Denifl, S.; Scheier, P. Cold Physics and Chemistry: Collisions, Ionization and Reactions Inside Helium Nanodroplets Close to Zero K. *Phys. Rep.* **2018**, *751*, 1-90.

(39) Verma, D.; Tanyag, R. M. P.; O'Connell, S. M. O.; Vilesov, A. F. Infrared Spectroscopy in Superfluid Helium Droplets. *Adv. Phys.: X* **2019**, *4*, 1553569.

(40) Lewerenz, M.; Schilling, B.; Toennies, J. P. A New Scattering Deflection Method for Determining and Selecting the Sizes of Large Liquid Clusters of ^{4}He. *Chem. Phys. Lett.* **1993**, *206*, 381-387.

(41) Kupper, J.; Merritt, J. M.; Miller, R. E. Free Radicals in Superfluid Liquid Helium Nanodroplets: A Pyrolysis Source for the Production of Propargyl Radical. *J. Chem. Phys.* **2002**, *117*, 647-652.

(42) Morrison, A. M.; Agarwal, J.; Schaefer, H. F.; Douberly, G. E. Infrared Laser Spectroscopy of the CH_3OO Radical Formed from the Reaction of CH_3 and O_2 within a Helium Nanodroplet. *J. Phys. Chem. A* **2012**, *116*, 5299-5304.

(43) Leavitt, C. M.; Moradi, C. P.; Acrey, B. W.; Douberly, G. E. Infrared Laser Spectroscopy of the Helium-Solvated Allyl and Allyl Peroxy Radicals. *J. Chem. Phys.* **2013**, *139*, 234301.

(44) Moradi, C. P.; Morrison, A. M.; Klippenstein, S. J.; Goldsmith, C. F.; Douberly, G. E. Propargyl + O_2 Reaction in Helium Droplets: Entrance Channel Barrier or Not? *J. Phys. Chem. A* **2013**, *117*, 13626-13635.

(45) Chin, S. A.; Krotscheck, E. Systematics of Pure and Doped ^{4}He Clusters. *Phys. Rev. B* **1995**, *52*, 10405-10428.

(46) Morrison, A. M.; Liang, T.; Douberly, G. E. Automation of an "Aculight" Continuous-Wave Optical Parametric Oscillator. *Rev. Sci. Instrum.* **2013**, *84*, 013102.

(47) Crawford, T. D.; Stanton, J. F.; Allen, W. D.; Schaefer, H. F. Hartree-Fock Orbital Instability Envelopes in Highly Correlated Single-Reference Wave Functions. *J. Chem. Phys.* **1997**, *107*, 10626-10632.

(48) Almlöf, J.; Taylor, P. R. General Contraction of Gaussian-Basis Sets .I. Atomic Natural Orbitals for 1st-Row and 2nd-Row Atoms. *J. Chem. Phys.* **1987**, *86*, 4070-4077.

(49) Kállay, M.; Gauss, J. Approximate Treatment of Higher Excitations in Coupled-Cluster Theory. *J. Chem. Phys.* **2005**, *123*, 214105.

(50) Stanton, J. F. Why CCSD(T) Works: A Different Perspective. *Chem. Phys. Lett.* **1997**, *281*, 130-134.

(51) Helgaker, T.; Klopper, W.; Koch, H.; Noga, J. Basis-Set Convergence of Correlated Calculations on Water. *J. Chem. Phys.* **1997**, *106*, 9639-9646.

(52) Deegan, M. J. O.; Knowles, P. J. Perturbative Corrections to Account for Triple Excitations in Closed and Open-Shell Coupled-Cluster Theories. *Chem. Phys. Lett.* **1994**, *227*, 321-326.

(53) Watts, J. D.; Gauss, J.; Bartlett, R. J. Coupled-Cluster Methods with Noniterative Triple Excitations for Restricted Open-Shell Hartree-Fock and Other General Single Determinant Reference Functions - Energies and Analytical Gradients. *J. Chem. Phys.* **1993**, *98*, 8718-8733.

(54) Hampel, C.; Peterson, K. A.; Werner, H. J. A Comparison of the Efficiency and Accuracy of the Quadratic Configuration-Interaction (QCISD), Coupled Cluster (CCSD), and Brueckner Coupled Cluster (BCCD) Methods. *Chem. Phys. Lett.* **1992**, *190*, 1-12.

(55) Raghavachari, K.; Trucks, G. W.; Pople, J. A.; Headgordon, M. A 5th-Order Perturbation Comparison of Electron Correlation Theories. *Chem. Phys. Lett.* **1989**, *157*, 479-483.

(56) Dunning, T. H. Gaussian-Basis Sets for Use in Correlated Molecular Calculations .I. The Atoms Boron Through Neon and Hydrogen. *J. Chem. Phys.* **1989**, *90*, 1007-1023.

(57) Howard, J. C.; Gray, J. L.; Hardwick, A. J.; Nguyen, L. T.; Tschumper, G. S. Getting down to the Fundamentals of Hydrogen Bonding: Anharmonic Vibrational Frequencies of $(HF)_2$ and $(H2O)_2$ from Ab Initio Electronic Structure Computations. *J. Chem. Theory Comput.* **2014**, *10*, 5426-5435.

(58) J. F. Stanton, J. Gauss, L. Cheng, M. E. Harding, D. A. Matthews, and P. G. Szalay, CFOUR, Coupled-cluster techniques for computational chemistry, a quantum-chemical program package, With contributions from A. A. Auer, R. J. Bartlett, U. Benedikt, C. Berger, D. E. Bernholdt, Y. J. Bomble, O. Christiansen, F. Engel, R. Faber, M. Heckert, O. Heun, M. Hilgenberg, C. Huber, T.-C. Jagau, D. Jonsson, J. Jusélius, T. Kirsch, K. Klein, W. J. Lauderdale, F. Lipparini, T. Metzroth, L. A. Mück, D. P. O'Neill, D. R. Price, E. Prochnow, C. Puzzarini, K. Ruud, F. Schiffmann, W. Schwalbach, C. Simmons, S. Stopkowicz, A. Tajti, J. Vázquez, F. Wang, J. D. Watts and the integral packages MOLECULE (J. Almlöf and P. R. Taylor), PROPS (P. R. Taylor), ABACUS (T. Helgaker, H. J. Aa. Jensen, P. Jørgensen, and J. Olsen), and ECP routines by A. V. Mitin and C. van Wüllen, for the current version, see http://www.cfour.de.

(59) Neese, F. The ORCA Program System. *Wiley Interdiscip. Rev.: Comput. Mol. Sci.* **2012**, *2*, 73-78.

(60) Peterson, K. A.; Adler, T. B.; Werner, H. J. Systematically Convergent Basis Sets for Explicitly Correlated Wavefunctions: The Atoms H, He, B-Ne, and Al-Ar. *J. Chem. Phys.* **2008**, *128*, 12, 084102.

(61) Pavosevic, F.; Pinski, P.; Riplinger, C.; Neese, F.; Valeev, E. F. SparseMaps-A Systematic Infrastructure for Reduced-Scaling Electronic Structure Methods. IV. Linear-Scaling Second-Order Explicitly Correlated Energy with Pair Natural Orbitals. *J. Chem. Phys.* **2016**, *144*, 13, 144109.

(62) Liakos, D. G.; Izsak, R.; Valeev, E. F.; Neese, F. What Is the Most Efficient Way to Reach the Canonical MP2 Basis Set Limit? *Mol. Phys.* **2013**, *111*, 2653-2662.

(63) Weigend, F.; Kohn, A.; Hattig, C. Efficient Use of the Correlation Consistent Basis Sets in Resolution of the Identity MP2 Calculations. *J. Chem. Phys.* **2002**, *116*, 3175-3183.

(64) Neese, F. Software Update: The ORCA Program System, Version 4.0. *Wiley Interdiscip. Rev.: Comput. Mol. Sci.* **2018**, *8*, e1327.

(65) Hollman, D. S.; Schaefer, H. F. In Search of the Next Holy Grail of Polyoxide Chemistry: Explicitly Correlated Ab Initio Full Quartic Force Fields for HOOH, HOOOH, HOOOOH, and Their Isotopologues. *J. Chem. Phys.* **2012**, *136*, 084302.

(66) Schneider, H.; Vogelhuber, K. M.; Schinle, F.; Stanton, J. F.; Weber, J. M. Vibrational Spectroscopy of Nitroalkane Chains Using Electron Autodetachment and Ar Predissociation. *J. Phys. Chem. A* **2008**, *112*, 7498-7506.

(67) Begue, D.; Carbonniere, P.; Pouchan, C. Calculations of Vibrational Energy Levels by Using a Hybrid Ab Initio and DFT Quartic Force Field: Application to Acetonitrile. *J. Phys. Chem. A* **2005**, *109*, 4611-4616.

(68) Hoy, A. R.; Mills, I. M.; Strey, G. Anharmonic Force Constant Calculations. *Mol. Phys.* **1972**, *24*, 1265-1290.

(69) Allen, W. D.; Csaszar, A. G. On the Ab Initio Determination of Higher-Order Force-Constants at Nonstationary Reference Geometries. *J. Chem. Phys.* **1993**, *98*, 2983-3015.

(70) Mathematica, Version 11, Wolfram Research, Inc., Champaign, IL (2016).

(71) Rosnik, A. M.; Polik, W. F. VPT2+K Spectroscopic Constants and Matrix Elements of the Transformed Vibrational Hamiltonian of a Polyatomic Molecule with Resonances Using Van Vleck Perturbation Theory. *Mol. Phys.* **2014**, *112*, 261-300.

(72) Matthews, D. A.; Vazquez, J.; Stanton, J. F. Calculated Stretching Overtone Levels and Darling-Dennison Resonances in Water: A Triumph of Simple Theoretical Approaches. *Mol. Phys.* **2007**, *105*, 2659-2666.

(73) Martin, J. M. L.; Lee, T. J.; Taylor, P. R.; Francois, J. P. The Anharmonic-Force Field of Ethylene, C_2H_4, by Means of Accurate Ab Initio Calculations. *J. Chem. Phys.* **1995**, *103*, 2589-2602.

(74) Franke, P. R.; Douberly, G. E. Rotamers of Isoprene: Infrared Spectroscopy in Helium Droplets and Ab Initio Thermochemistry. *J. Phys. Chem. A* **2018**, *122*, 148-158.

(75) Brown, A. R.; Franke, P. R.; Douberly, G. E. Helium Nanodroplet Isolation of the Cyclobutyl, 1-Methylallyl, and Allylcarbinyl Radicals: Infrared Spectroscopy and Ab Initio Computations. *J. Phys. Chem. A* **2017**, *121*, 7576-7587.

(76) Franke, P. R.; Tabor, D. P.; Moradi, C. P.; Douberly, G. E.; Agarwal, J.; Schaefer, H. F.; Sibert, E. L. Infrared Laser Spectroscopy of the *n*-Propyl and *i*-Propyl Radicals: Stretch-Bend Fermi Coupling in the Alkyl CH Stretch Region. *J. Chem. Phys.* **2016**, *145*, 224304.

(77) Raston, P. L.; Agarwal, J.; Turney, J. M.; Schaefer, H. F.; Douberly, G. E. The Ethyl Radical in Superfluid Helium Nanodroplets: Rovibrational Spectroscopy and Ab Initio Computations. *J. Chem. Phys.* **2013**, *138*, 194303.

(78) Thomas, P. S.; Miller, T. A. Cavity Ringdown Spectroscopy of the NIR $\tilde{A}$ - $\tilde{X}$ Electronic Transition of Allyl Peroxy Radical (H_2C=CH-CH_2OO·). *Chem. Phys. Lett.* **2010**, *491*, 123-131.

(79) Thomas, P. S.; Kline, N. D.; Miller, T. A. $\tilde{A}$ - $\tilde{X}$ Absorption of Propargyl Peroxy Radical (H-C=C-CH_2OO) A Cavity Ring-Down Spectroscopic and Computational Study. *J. Phys. Chem. A* **2010**, *114*, 12437-12446.

CHAPTER 7

TERT-BUTYL PEROXY RADICAL: GROUND AND FIRST EXCITED STATE ENERGETICS AND FUNDAMENTAL FREQUENCIES[1]

[1] Reproduced from Franke, P.R.; Moore, K.B.; Schaefer, H.F.; Douberly, G.E. 2019. *Physical Chemistry Chemical Physics*. 21:9747-9758. DOI: 10.1039/c9cp01476d with permission from the PCCP Owner Societies.

Alkylperoxy radicals ($RO_2^{\bullet}$) are key intermediates in combustion and atmospheric oxidation processes. As such, reliable detection and monitoring of these radicals can provide a wealth of information about the underlying chemistry. The *tert*-butyl peroxy radical is the archetypal tertiary peroxy radical, yet its vibrational spectroscopy is largely unexplored. To aid in future experimental investigations, we have performed high-level theoretical studies of the fundamental vibrational frequencies of the ground- and first excited states. A conformer search on both electronic surfaces reveals single minimum-energy structures. We predict an $\tilde{A}^2A' \leftarrow \tilde{X}^2A''$ adiabatic excitation energy of 7738 cm^{-1} via focal point analysis, approximating the CCSDT(Q)/CBS level of theory. This excitation energy agrees to within 17 cm^{-1} of the most accurate experimental measurement. We compute CCSD(T) fundamental vibrational frequencies via second-order vibrational perturbation theory (VPT2), using a hybrid force field in which the quadratic (cubic/quartic) force constants are evaluated with the ANO1 (ANO0) basis set. Anharmonic resonance polyads are treated with the VPT2 + K effective Hamiltonian approach. Among the predicted fundamental frequencies, the ground state O-O stretch, excited state O-O stretch, and excited state C-O-O bend fundamentals are predicted at 1138, 959, and 490 cm^{-1}, respectively. Basis set sensitivity is found to be particularly great for the O-O stretches, similar to what has already been noted in smaller, unbranched peroxy radicals. Exempting these O-O stretches, agreement with the available experimental fundamentals is generally good (± 10 cm^{-1}).

7.1. Introduction

Peroxy radicals ($RO_2^{\bullet}$) are integral species to low-temperature oxidation processes that occur in terrestrial combustion environments and in the troposphere. The kinetics of peroxy radical isomerizations often dictate pre-ignition and engine knock events.[1-2] In the atmosphere, the oxidation of alkanes proceeds via hydrogen abstraction by OH, followed by reaction with O_2, forming a peroxy radical intermediate. Peroxy radicals have implications for air quality, as 90% of tropospheric ozone is thought to derive from reactions involving them.[3] Tracking the formation

and decomposition of peroxy radicals is thus key to understanding these processes. Of particular utility is the use of species-selective electronic absorptions to monitor the kinetics of specific peroxy radicals.[4]

Early attempts at spectroscopic characterization of peroxy radicals utilized ultraviolet $\tilde{B} \leftarrow \tilde{X}$ transitions.[5] Each such transition corresponds to a $\pi \rightarrow \pi^*$ excitation within the C-O-O moiety of most peroxy radicals.[6-8] Increased occupation of the π* orbital makes the $\tilde{B}$ state dissociative along the C-O and O-O coordinates.[9-11] As such, these transitions yield largely structureless absorption peaks, which prevent unambiguous assignment to specific R groups of a peroxy radical.

Work on the vibrational spectroscopy of *tert*-butyl peroxy radical remains limited. The earliest bands were identified by Parkes and Donovan.[12-13] They produced *tert*-butyl peroxy radical from photolysis of azoisobutane and subsequently reacted it with molecular oxygen; they observed two gas-phase transitions at 693.7 ± 0.5 cm^{-1} and 760 ± 2 cm^{-1}. Parkes and Donovan argued that these transitions could derive from *tert*-butyl peroxy radical by comparisons to the known vibrational frequencies of other molecules containing a *tert*-butyl group bonded to oxygen. The next development was an argon matrix-isolation study by Chettur and Snelson.[14] They identified nine vibrational transitions in the 200-1200 cm^{-1} range, which they assigned to the O-O stretch (1124 ± 2 cm^{-1}), C-O stretch (730 ± 2 cm^{-1}), and C-C stretches (808 ± 2 cm^{-1}), as well as H-C-H bends (1187 and 1139 ± 2 cm^{-1}) and various skeletal bending vibrations (< 539 cm^{-1}). To aid in these assignments, Chettur and Snelson performed isotopic substitution experiments wherein they deposited a mixture of $^{16}O_2$ and $^{18}O_2$ onto the matrix.

Another attractive spectroscopic approach probes the $\tilde{A} \leftarrow \tilde{X}$ vibronic transitions. For alkyl peroxy radicals, these are $n \rightarrow \pi^*$ transitions localized on the peroxy moiety. Such transitions enabled the observation of excited state O-O stretching progressions of alkyl radicals[15]

early on; however, this approach is generally limited by the small $\tilde{A} \leftarrow \tilde{X}$ absorption cross-sections, which are 10^4 to 10^5 times weaker than $\tilde{B} \leftarrow \tilde{X}$ transitions.[11] Cavity Ringdown Spectroscopy (CRDS) alleviates these issues by increasing the effective optical path length.[16-19] The Miller group has reviewed energetic trends in small peroxy radicals by using computational chemistry to supplement and explain their CRDS experiments.[11] They found that branching at the α carbon atom had the most significant effect on the energy of the $\tilde{A} \leftarrow \tilde{X}$ electronic transition: tertiary peroxy radicals absorb further to the blue than secondary radicals, which absorb further to the blue than primary radicals.

Glover and Miller[20] employed CRDS to measure the $\tilde{A} \leftarrow \tilde{X}$ band of the *tert*-butyl peroxy radical between 7250-8750 cm^{-1}. The peroxy radical was formed via the reaction of O_2 with *tert*-butyl, which was produced from two different sources: chlorine-initiated hydrogen-abstraction from isobutane and photolysis of *tert*-butyl bromide. They assigned bands at 7757, 8242, and 8695 cm^{-1} to the $\tilde{A} \leftarrow \tilde{X}$ band origin and to the simultaneous excitation of one quantum of excited state C-O-O bending and O-O stretching, respectively. The presence of the latter two bands was attributed to favorable Franck-Condon overlap, which results from the large geometric change in the C-O-O moiety where the $\tilde{A} \leftarrow \tilde{X}$ transition is localized. They also observed two triplets of bands at (7895, 7994, 8094 cm^{-1}) and (8358, 8476, and 8523 cm^{-1}). They speculated that these bands could correspond to the band origins and the C-O-O bend fundamentals of additional conformers. One plausible way in which this could be achieved is if the three-fold symmetric peroxy torsional potential possesses additional shallower wells capable of supporting bound states. Glover and Miller suggested that the six equivalent points, over the full 360 degree rotation, at which the peroxy group eclipses the hydrogen atom of a methyl group, might correspond to equivalent transition states. The potential would then contain two sets of three equivalent minima. Similar characteristics have been predicted for the CH_2-torsional potential of the *n*-propyl radical; however, the shallower wells disappear after correcting for zero-point

energy, leaving the torsional potential with a single minimum at the *Cs* geometry.[21] As an alternative to the additional conformers hypothesis, they also posited that these triplets could arise from the hindered rotation of the peroxy moiety.

The Miller group soon returned to *tert*-butyl peroxy to answer these lingering questions.[22] Sharp, Rupper, and Miller improved upon their experimental spectrum, refining the frequency of the origin transition to 7755 ± 10 cm^{-1} and reporting B3LYP/6-31+G* computations of the ground state peroxy torsional potential and ground and excited state harmonic frequencies. Their relaxed torsional potential displayed simple three-fold symmetry, overturning their additional conformers hypothesis. By comparisons to the $\tilde{A}$ harmonic frequencies, they were able to assign their observed vibrational structure to simultaneous excitation in three low frequency bending degrees of freedom and the O-O stretching degree of freedom. The four fundamentals were assigned at (240, 340, 481, and 934) ± 10 cm^{-1}, respectively. By applying a recommended scaling factor to their harmonic frequencies, their predictions were slightly to the red of the bend fundamentals but significantly to the blue (24 cm^{-1}) for the O-O stretch fundamental.

Anion photoelectron spectroscopy (APES) was used by Ellison, Lineberger, and coworkers to probe the vibronic states of the peroxy radical.[23-24] In these experiments, *tert*-butyl hydroperoxide [$(CH_3)_3COOH$] was deprotonated by O^- anions, followed by electron detachment via an argon ion laser. A flow tube surrounded by liquid N_2 was used to cool ions to 200 ± 30 K to reduce rotational broadening. Two peaks were assigned to separate 0_0^0 transitions, allowing for a determination of an $\tilde{A} \leftarrow \tilde{X}$ adiabatic electronic excitation energy (T_0) of 7800 ± 90 cm^{-1}. An $\tilde{X}$ state band at 1130 ± 90 cm^{-1} was assigned to the O-O stretch through analogy with the HO_2 frequency; this assignment agrees well with the O-O stretch fundamental measured by Chettur and Snelson.[14] An $\tilde{A}$ state band at 930 ± 90 cm^{-1} was also assigned to the O-O stretch. There were also 245 ± 90 cm^{-1} and 240 ± 90 cm^{-1} bands found for the $\tilde{X}$ and $\tilde{A}$ states, respectively. These transitions were not assigned to specific vibrations.

Most recently, Neumark and co-workers[25] performed cryo-SEVI photoelectron spectroscopy experiments. In their experiments, $(CH_3)_3COO^-$ anions were guided into a cryogenically cooled octupole ion trap with 20% H_2 in He, wherein the $(CH_3)_3COO^-$ ions were cooled to 10 K via collisions with the buffer gas. The measured photoelectron spectrum was fit using Franck–Condon simulations that employed B3LYP/6-311+G* scaled vibrational frequencies to compute the Franck-Condon overlap and EOMIP-CCSD/6-311+G* Dyson orbital computations to determine photodetachment cross sections as functions of the energy. Neumark and co-workers obtained O–O stretch fundamentals of 1129 ± 22 cm^{-1} and 939 ± 14 cm^{-1} for the $\tilde{X}^2A''$ and $\tilde{A}^2A'$ electronic states, respectively, which compare favorably to the corresponding values of Chettur and Snelson[14] and Sharp, Rupper, and Miller.[22] They also located the 245 (240) cm^{-1} band for the $\tilde{X}^2A''$ ($\tilde{A}^2A'$) state observed by Ellison, Lineberger, and co-workers.[24] They assigned the $\tilde{X}$ state transition to the ν_{22} fundamental. They did not observe the $\tilde{A}$ δ(C-O-O) fundamental measured by Sharp, Rupper, and Miller; however, they assigned two new fundamental transitions in the $\tilde{X}$-state: 279(21) cm^{-1} to ν_{21} and 1254(26) cm^{-1} to ν_{12}. They measured similar energies for the $\tilde{A} \leftarrow \tilde{X}$ origin transition as Ellison, Lineberger, and co-workers and Sharp, Rupper, and Miller. Neumark and co-workers did, however, note issues with their B3LYP frequencies, which had to be adjusted at times, so that their Franck-Condon simulations could adequately reproduce their experimental spectra.

Despite decades of careful experimental study, there are still many vibrational fundamentals of the *tert*-butyl peroxy radical that have not been observed. In addition, there is a conspicuous absence of any sophisticated, high-level theoretical treatment that could help confirm these assignments as well as predict the energies of yet-unidentified vibrational transitions. Our group has recently demonstrated the efficacy of extrapolated coupled cluster treatments for predicting the ground- and first excited state fundamental vibrational transitions for a number of radicals, including the methylperoxy,[26-28] ethylperoxy,[29] propylperoxy,[30] peroxyacetyl,[31] and

formylperoxy[32] radicals. This work seeks to expand this success to branched alkyl systems, which have not yet been addressed. We also wish to establish whether current coupled-cluster techniques can be applied to a system of this size and still achieve the same level of accuracy as in our previous research.[33]

7.2. Theoretical Methods

7.2.1. Peroxy Torsional Potential

To explore the conformational space in the $\tilde{X}$ and $\tilde{A}$ electronic states, we computed torsional potentials describing the rotation of the peroxy moiety about the C-O bond. To preserve the three-fold dynamical symmetry, the scans were carried out in the following way. One of three possible (bonded) C-C-O-O dihedral angles was scanned from 0 degrees (corresponding to the torsional transition state) to 55 degrees, in 5 degree increments. All other internal coordinates, including the other two bonded C-C-O-O dihedral angles, were optimized. Then, at each scan point, the average of the three C-C-O-O angles, τ_{CCOO}, was determined, and this was chosen to represent the true torsional coordinate. A final 60 degree point, corresponding to the equilibrium geometry, was optimized by constraining the in-plane dihedral angle to be 180 degrees while relaxing all other coordinates. The increments of the torsional scan then become only approximately 5 degrees, correcting for the asymmetry introduced by singling out one of three dynamically indistinguishable methyl groups in the original scan.

The geometries were optimized with the CCSD(T) method[34-36] in CFOUR.[37] The 1s-electrons of carbon and oxygen were not correlated in the CCSD(T) computations. An unrestricted Hartree-Fock (UHF) reference wavefunction was used. The atoms were described with the ANO0 truncation (H:[2s1p]; C,O:[3s2p1d]) of the atomic natural orbital (ANO) basis sets of Almlöf and Taylor.[38-39] During optimization, the SCF and CC energies were converged to 10^{-10} E_h. At each of the optimized geometries, the electronic energy was refined by performing a

CCSD(T) single-point energy computation with the larger ANO1 truncation (H:[4s2p1d]; C,O:[4s3p2d1f]) of the atomic natural orbital (ANO) basis set.[38]

Along most of the peroxy torsional potential, there is no molecular symmetry that can be exploited to uniquely target a reference wavefunction for the $\tilde{A}$ electronic state, and variational collapse may be a problem. As is the case with all alkylperoxy radicals, the $\tilde{X}$ and $\tilde{A}$ electronic configurations of *tert*-butyl peroxy radical differ, in zeroth-order, by a simple rotation of two molecular orbitals. For example, the electron configurations at the C_s equilibrium structure of *tert*-butyl peroxy radical can be described as,

$$\tilde{X}^2A'':[\text{core}](17a')^2(8a'')^1 \quad \tilde{A}^2A':[\text{core}]\,(17a')^1(8a'')^2$$

where $17a'$ and $8a''$ are the ground-state HOMO-1 and HOMO, respectively. The $17a'$ and $8a''$ orbitals are depicted in Fig. 7.1. The HOMO-1 can be thought of as bonding with respect to C-O and nonbonding with respect to O-O, while the HOMO is predominantly antibonding with respect to O-O.[11] In a zeroth-order picture, where $\tilde{A} \leftarrow \tilde{X}$ excitation does not involve substantial orbital mixing/relaxation, the $\tilde{A}$ state simply corresponds to a rotation of these orbitals. In this study we did not find it necessary to rotate the orbitals. Instead we were able to target the excited state wavefunction by using, as a guess at all asymmetric points, the converged orbitals from the nearest symmetric structure.

7.2.2. $\tilde{A} \leftarrow \tilde{X}$ Transition Origin

The adiabatic $\tilde{A} \leftarrow \tilde{X}$ excitation energy (T_0) was obtained with the following series of computations. First, we computed the adiabatic $\tilde{A} \leftarrow \tilde{X}$ electronic transition energy ($T_{e,\text{CBS}}$) via the focal point approach of Allen and co-workers, closely approximating a CCSDT(Q) treatment of electron correlation at the complete basis set (CBS) limit.[40-43] Herein, the relative HF and MP2 energies were computed directly with the cc-pVXZ basis sets[44] up through cc-pVQZ and cc-pV5Z. The relative HF/CBS energy (E_{HF}^{∞}) and MP2/CBS correlation energy ($\varepsilon_{MP2}^{\infty}$) were then

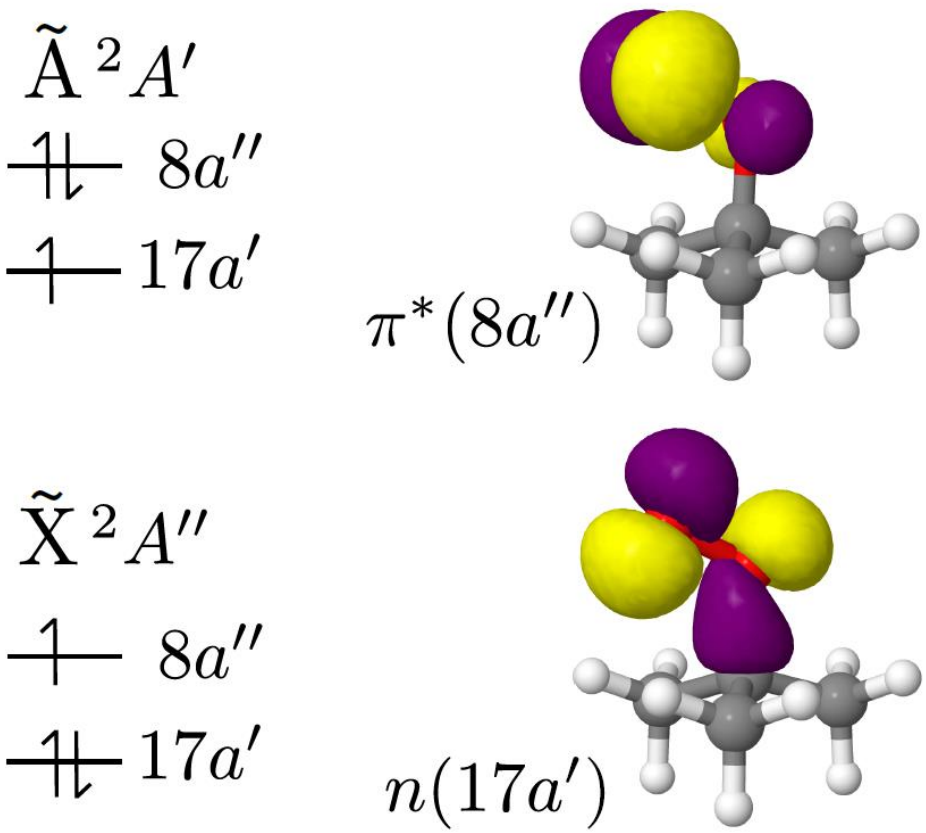

Figure 7.1. Depiction of the HOMO-1[n($17a'$)] and HOMO[$\pi^*(8a'')$] involved in the $\tilde{A}^2A' \leftarrow \tilde{X}^2A''$ transition of *tert*-butyl peroxy radical. Shown here are state-averaged CASSCF natural orbitals.

obtained by using the values from these latter two basis sets in the two-point extrapolation formulas of Karton and Martin [45] and Helgaker,[46] respectively:

$$E_{HF}(X) = E_{HF}^{\infty} + A(X+1)e^{-9\sqrt{X}} \tag{7.1}$$

$$\varepsilon_{MP2}(X) = \varepsilon_{MP2}^{\infty} + AX^{-3} \tag{7.2}$$

The CCSD and CCSD(T) energies were computed with up to the cc-pVQZ basis set. The cc-pV5Z and CBS values were obtained by assuming additivity; wherein, the CCSD and CCSD(T) increments from cc-pVQZ are assumed to be the same with larger basis sets.

The uncertainty in the electronic energies was assessed by computing the HF and MP2 correlation energies with other extrapolation schemes. Various combinations of HF extrapolations (exp,[47] expGauss,[48] and SchwenkeHF[49]) and correlation energy extrapolations (Schwartz4 and Schwartz6)[50] were tested. Collectively, the $T_{e,CBS}$ values computed with these combinations had a mean value of 7817 cm^{-1} and a standard deviation of 2 cm^{-1}.

Auxiliary corrections were then appended to $T_{e,CBS}$ to account for certain approximations. We computed the energetic contributions of full-triple and perturbative quadruple excitations using the 6-31G* basis set[51-52] via the following expression:

$$\Delta_T = \Delta E_{\mathrm{CCSDT}} - \Delta E_{\mathrm{CCSD(T)}} \tag{7.3}$$

$$\Delta_{(Q)} = \Delta E_{\mathrm{CCSDT(Q)}} - \Delta E_{\mathrm{CCSDT}} \tag{7.4}$$

A core-correlation correction (Δ_{CORE}) accounts for not correlating the 1s-electrons of carbon and oxygen:

$$\Delta_{CORE} = \Delta E_{\mathrm{AE\text{-}CCSD(T)}} - \Delta E_{\mathrm{FC\text{-}CCSD(T)}} \tag{7.5}$$

where AE and FC denote the all-electron and frozen-core methods, respectively. The cc-pCVTZ basis set[53] was used. To assess the validity of the separability of the electronic and nuclear coordinates, we computed ROHF/ANO1 Diagonal Born-Oppenheimer Corrections (Δ_{DBOC}):[54-55]

$$\Delta_{DBOC} = \langle \Psi_e(r;R) | \hat{T}_N | \Psi_e(r;R) \rangle \tag{7.6}$$

where $\Psi_e(r;R)$ is the electronic wavefunction and $\hat{T}_N$ is the nuclear kinetic energy operator. A relativistic correction (Δ_{REL}), including a Darwin term and one-electron and two-electron mass-velocity terms, accounts for scalar relativistic effects at first-order with direct perturbation theory (DPT):[56-57]

$$\Delta_{REL} = \Delta E_{\mathrm{AE\text{-}CCSD(T)/DPT}} - \Delta E_{\mathrm{AE\text{-}CCSD(T)}} \tag{7.7}$$

This relativistic correction was evaluated with all-electron CCSD(T)/cc-pCVTZ wavefunctions. Lastly, we appended the relative anharmonic zero-point vibrational energies (Δ_{ZPVE}) to the corrected $T_{e,CBS}$, which were obtained using the quartic force field described below and a resonance-free expression.[58] In summary, adiabatic $\tilde{A} \leftarrow \tilde{X}$ transition energy is expressed fully as:

$$T_0 = T_{e,CBS} + \Delta_T + \Delta_{(Q)} + \Delta_{CORE} + \Delta_{DBOC} + \Delta_{REL} + \Delta_{ZPVE} \quad (7.8)$$

Using this approach, we obtain a CCSDT(Q)/CBS T_0 value. The incremental nature of the focal point analysis allows us to assess the convergence toward the CBS and full configuration interaction (FCI) limits as well as the limitations of single-reference, non-relativistic, Born-Oppenheimer wavefunctions. All of the above energy computations employed an ROHF reference. Each energy was converged to within 10^{-10} E_h. The Δ_T and $\Delta_{(Q)}$ corrections were computed with the MRCC program.[59-60] All other energies were computed with CFOUR. Lastly, we emphasize that all of the energy computations were performed at the CCSD(T)/ANO1 equilibrium structures described in Section 7.2.3.

7.2.3. Anharmonic Vibrational Frequencies

Anharmonic vibrational frequencies were determined for both the $\tilde{X}^2A''$ and $\tilde{A}^2A'$ equilibrium structures with second-order vibrational perturbation theory (VPT2).[61] We employed a semidiagonal quartic force field that includes all force constants up to ϕ_{ijkk} quartic terms. For this research, we constructed a "hybrid" force field where the force constants were computed with the following mixture of levels of theory:

Harmonic frequencies (ω_i): UHF-CCSD(T)/ANO1

Cubic force constants (ϕ_{ijk}): UHF-CCSD(T)/ANO0

Quartic force constants (ϕ_{ijkk}): UHF-CCSD(T)/ANO0,

where the indices i, j, k correspond to the normal modes of vibration.

A UHF reference was used throughout to take advantage of the parallelized, analytic CCSD(T) energy derivatives within CFOUR.[62] To obtain all of the force constants, optimized geometries were obtained at the UHF-CCSD(T)/ANO1 and UHF-CCSD(T)/ANO0 levels. Tight convergence parameters were used for all of the optimization and frequency computations described: the SCF densities, CC amplitudes, and Lambda coefficients were converged to 10^{-10} E_h, and the RMS forces were converged to 10^{-9} E_h/a_0.

Harmonic vibrational frequencies were obtained by finite differences of UHF-CCSD(T)/ANO1 analytic gradients; harmonic intensities were obtained from finite differences of dipole moments. The cubic and quartic force constants were obtained at the UHF-CCSD(T)/ANO0 level. To obtain these derivatives, displacements were made in the CCSD(T)/ANO0 normal coordinates, and analytic second derivatives were evaluated. Finite differences were then used to obtain the anharmonic force constants.[63]

Anharmonic vibrational frequencies were evaluated via Second-Order Vibrational Perturbation Theory with Resonances (VPT2+K).[61, 64-65] For this research, we employed the diagnostic of Martin, Lee, Taylor, and François[66] to determine if a Fermi Type I ($\omega_i \approx 2\omega_j$) or Type II ($\omega_i \approx \omega_j + \omega_k$) resonance was severe enough to warrant the reduced-dimensional variational treatment (essentially the +K). We chose the cut-off for stretching and bending modes to be 1 cm^{-1} and elected to not treat stretch-torsion resonances explicitly, as our previous attempts to do this generally worsened agreement with experiment.[67-68] Indeed, this has been recognized by other researchers.[69] The Martin diagnostic is sometimes used in conjunction with simpler energy gap and force constant magnitude tests, with the energy gap test ensuring that stretch-torsion interactions will not be flagged as Fermi resonances.[69] We made one exception to this rule, for a resonance polyad involving ν_{21}, ν_{22}, and $2\nu_{39}$. The diagnostic for the interaction between ν_{21} and $2\nu_{39}$ (161 cm^{-1}) was simply too large to ignore. The resonance diagnostics are given in Table 7.1. After being identified, resonances were treated by building and diagonalizing effective

Hamiltonians. For these cases, we approximate the anharmonic intensities of the final transitions to be simply fractions of the harmonic intensity of the participating fundamentals, proportional to the squared eigenvector coefficients. In this way, we model the effects of mechanical anharmonicity but not electrical anharmonicity. Symbolic Hamiltonian matrices (Eqn. 7.12-7.22) and expressions for relevant types of Darling-Dennison matrix elements (Eqn. 7.9-7.11) are given below.

$$D_{r;s} = \frac{3}{4}\left(K_{rr;rs} + K_{ss;sr}\right) + \frac{1}{4}\sum_{t\neq\{r,s\}}^{3N-6} K_{rt;st} \tag{7.9}$$

$$D_{rt;st} = \frac{3}{4}\left(K_{rr;rs} + K_{ss;sr} + K_{rt;st}\right) + \frac{1}{4}\sum_{u\neq\{r,s,t\}}^{3N-6} K_{ru;su} \tag{7.10}$$

$$D_{rst;rsu} = \frac{1}{4}\left(K_{rt;ru} + K_{st;su}\right) + \frac{1}{8}\sum_{v\neq\{r,s\}}^{3N-6} K_{vt;vu} \tag{7.11}$$

The effective Hamiltonians used to describe the $\tilde{X}$-state are given below (Eqn. 7.12-7.19).

$$\begin{pmatrix} \nu_4^* & \frac{\phi_{4,6,6}}{4} & 0 & 0 \\ \frac{\phi_{4,6,6}}{4} & 2\nu_6^* & \frac{\phi_{6,13,20}}{2} & 0 \\ 0 & \frac{\phi_{6,13,20}}{2} & \begin{pmatrix}\nu_6+\nu_{13}\\+\nu_{20}\end{pmatrix}^* & \frac{\phi_{6,13,20}}{2\sqrt{2}} \\ 0 & 0 & \frac{\phi_{6,13,20}}{2\sqrt{2}} & (2\nu_{13}+2\nu_{20})^* \end{pmatrix} \tag{7.12}$$

$$\begin{pmatrix} \nu_{26}^* & \frac{\phi_{26,6,27}}{2\sqrt{2}} & \frac{\phi_{26,6,28}}{2\sqrt{2}} & 0 & 0 & 0 & 0 \\ \frac{\phi_{26,6,27}}{2\sqrt{2}} & \begin{pmatrix}\nu_6\\+\nu_{27}\end{pmatrix}^* & D_{27,6;28,6} & \frac{\phi_{6,13,20}}{2\sqrt{2}} & 0 & \frac{\phi_{27,18,34}}{2\sqrt{2}} & 0 \\ \frac{\phi_{26,6,28}}{2\sqrt{2}} & D_{27,6;28,6} & \begin{pmatrix}\nu_6\\+\nu_{28}\end{pmatrix}^* & 0 & \frac{\phi_{6,13,20}}{2\sqrt{2}} & \frac{\phi_{28,18,34}}{2\sqrt{2}} & 0 \\ 0 & \frac{\phi_{6,13,20}}{2\sqrt{2}} & 0 & \begin{pmatrix}\nu_{13}\\+\nu_{20}\\+\nu_{27}\end{pmatrix}^* & D_{\substack{13,20,27;\\13,20,28}} & 0 & \frac{\phi_{27,18,34}}{2\sqrt{2}} \\ 0 & 0 & \frac{\phi_{6,13,20}}{2\sqrt{2}} & D_{\substack{13,20,27;\\13,20,28}} & \begin{pmatrix}\nu_{13}\\+\nu_{20}\\+\nu_{28}\end{pmatrix}^* & 0 & \frac{\phi_{28,18,34}}{2\sqrt{2}} \\ 0 & \frac{\phi_{27,18,34}}{2\sqrt{2}} & \frac{\phi_{28,18,34}}{2\sqrt{2}} & 0 & 0 & \begin{pmatrix}\nu_6\\+\nu_{18}\\+\nu_{34}\end{pmatrix}^* & \frac{\phi_{6,13,20}}{2\sqrt{2}} \\ 0 & 0 & 0 & \frac{\phi_{27,18,34}}{2\sqrt{2}} & \frac{\phi_{28,18,34}}{2\sqrt{2}} & \frac{\phi_{6,13,20}}{2\sqrt{2}} & \begin{pmatrix}\nu_{13}\\+\nu_{18}\\+\nu_{20}\\+\nu_{34}\end{pmatrix}^* \end{pmatrix} \tag{7.13}$$

$$\begin{pmatrix} \nu_5^* & \frac{\phi_{5,6,8}}{2\sqrt{2}} & 0 & 0 & 0 \\ \frac{\phi_{5,6,8}}{2\sqrt{2}} & (\nu_6+\nu_8)^* & \frac{\phi_{8,15,18}}{2\sqrt{2}} & \frac{\phi_{6,13,20}}{2\sqrt{2}} & 0 \\ 0 & \frac{\phi_{8,15,18}}{2\sqrt{2}} & \begin{pmatrix}\nu_6+\nu_{15}\\+\nu_{18}\end{pmatrix}^* & 0 & \frac{\phi_{6,13,20}}{2\sqrt{2}} \\ 0 & \frac{\phi_{6,13,20}}{2\sqrt{2}} & 0 & \begin{pmatrix}\nu_8+\nu_{13}\\+\nu_{20}\end{pmatrix}^* & \frac{\phi_{8,15,18}}{2\sqrt{2}} \\ 0 & 0 & \frac{\phi_{6,13,20}}{2\sqrt{2}} & \frac{\phi_{8,15,18}}{2\sqrt{2}} & \begin{pmatrix}\nu_{13}+\nu_{15}\\+\nu_{18}+\nu_{20}\end{pmatrix}^* \end{pmatrix} \tag{7.14}$$

$$\begin{pmatrix} \nu_6^* & \frac{\phi_{6,13,20}}{2\sqrt{2}} \\ \frac{\phi_{6,13,20}}{2\sqrt{2}} & (\nu_{13}+\nu_{20})^* \end{pmatrix} \tag{7.15}$$

$$\begin{pmatrix} \nu_{27}^* & D_{27;28} & \frac{\phi_{27,18,34}}{2\sqrt{2}} \\ D_{27;28} & \nu_{28}^* & \frac{\phi_{28,18,34}}{2\sqrt{2}} \\ \frac{\phi_{27,18,34}}{2\sqrt{2}} & \frac{\phi_{28,18,34}}{2\sqrt{2}} & (\nu_{18}+\nu_{34})^* \end{pmatrix} \tag{7.16}$$

$$\begin{pmatrix} \nu_7^* & D_{7;8} & \frac{\phi_{7,15,18}}{2\sqrt{2}} \\ D_{7;8} & \nu_8^* & \frac{\phi_{8,15,18}}{2\sqrt{2}} \\ \frac{\phi_{7,15,18}}{2\sqrt{2}} & \frac{\phi_{8,15,18}}{2\sqrt{2}} & (\nu_{15}+\nu_{18})^* \end{pmatrix} \tag{7.17}$$

$$\begin{pmatrix} \nu_{10}^* & \frac{\phi_{10,16,18}}{2\sqrt{2}} \\ \frac{\phi_{10,16,18}}{2\sqrt{2}} & (\nu_{16}+\nu_{18})^* \end{pmatrix} \tag{7.18}$$

$$\begin{pmatrix} \nu_{21}^* & D_{21;22} & \frac{\phi_{21,39,39}}{4} \\ D_{21;22} & \nu_{22}^* & \frac{\phi_{22,39,39}}{4} \\ \frac{\phi_{21,39,39}}{4} & \frac{\phi_{22,39,39}}{4} & 2\nu_{39}^* \end{pmatrix} \tag{7.19}$$

The effective Hamiltonians used to describe the $\tilde{A}$-state are given below (Eqn. 7.20-7.22).

$$\begin{pmatrix} \nu_4^* & \frac{\phi_{4,6,6}}{4} \\ \frac{\phi_{4,6,6}}{4} & 2\nu_6^* \end{pmatrix} \tag{7.20}$$

$$\begin{pmatrix} \nu_5^* & \frac{\phi_{5,6,8}}{2\sqrt{2}} \\ \frac{\phi_{5,6,8}}{2\sqrt{2}} & (\nu_6+\nu_8)^* \end{pmatrix} \tag{7.21}$$

$$\begin{pmatrix} \nu_{26}^{*} & \frac{\phi_{26,28,6}}{2\sqrt{2}} \\ \frac{\phi_{26,28,6}}{2\sqrt{2}} & (\nu_{28}+\nu_{6})^{*} \end{pmatrix} \tag{7.22}$$

Table 7.1. Martin diagnostics for identifying Fermi resonances. Values are in wavenumbers.

Vibrational States		**Diagnostic**	**Vibrational States**		**Diagnostic**
$\widetilde{X}^2A''$			$\widetilde{A}^2A'$		
v_{22}	$2v_{39}$	160.8	v_4	$2v_6$	20.3
v_4	$2v_6$	81.1	v_5	v_6+v_8	3.1
v_{10}	$v_{16}+v_{18}$	26.7	v_{26}	v_6+v_{28}	2.5
v_{27}	$v_{11}+v_{38}$	11.1	v_5	$v_{37}+v_{38}$	1.9
v_{28}	$v_{18}+v_{34}$	4.2	v_{37}	v_5+v_{38}	1.2
v_5	v_6+v_8	4.0	v_{11}	$v_{13}+v_{22}$	1.1
v_8	$v_{15}+v_{18}$	3.7	v_{38}	v_5+v_{37}	1.1
v_{21}	$2v_{39}$	2.9			
v_{26}	v_6+v_{28}	2.8			
v_{26}	$v_{22}+v_{38}$	1.1			
v_{26}	v_6+v_{27}	1.0			
v_7	$v_{15}+v_{18}$	1.0			

Previous research[26, 31-32, 70] has found small differences (1–10 cm^{-1}) in harmonic frequencies predicted with a UHF reference, compared with ROHF, due in part to its improper treatment of spin. To correct for these deficiencies, optimized geometries and harmonic vibrational frequencies were also computed at the CCSD(T)/ANO0 level with an ROHF reference. The harmonic vibrational frequencies were then used to compute a small correction:

$$\delta\omega = \omega^{ROHF}_{\text{CCSD(T)/ANO0}} - \omega^{UHF}_{\text{CCSD(T)/ANO1}} \quad (7.23)$$

This $\delta\omega$ was added to the final anharmonic vibrational frequencies. In the case of resonance polyads, the diagonal values of the effective Hamiltonians were corrected in this manner.

7.2.4. Reliability of the Methods

We checked for substantial deviations of $\langle \hat{S}^2 \rangle_{UHF}$ from the proper value (0.75 in atomic units). Additionally, the single reference character of the HF wavefunctions was confirmed by inspecting the squares of the three leading CASCI coefficients from a complete active-space SCF (CASSCF) wavefunction[71-72] that was computed with the ANO1 basis set. The active space consisted of 11 electrons distributed among $6a'$ and $6a''$ symmetry orbitals around the HOMO-LUMO gap. These diagnostics are available in Table 7.2.

7.3. Results and Discussion

7.3.1. Peroxy Torsional Potential

Figure 7.2 depicts the C-C-O-O torsional potential for the $\tilde{X}$ and $\tilde{A}$ electronic states. The shape of the curve illustrates that the potential for peroxy torsion displays simple three-fold symmetry for both electronic states, rather than possessing additional finer structure (including extra wells) akin to *n*-propyl radical's CH_2 torsional potential.[21] The appearance of the torsional potential, in the ground state, is consistent with what was previously computed.[22] Each curve contains maxima at τ_{CCOO} = 0, 120° that correspond to equivalent structures where the peroxy group is eclipsed with respect to the methyl groups. The minimum of each curve (τ_{CCOO} = 60°) corresponds to a structure where the peroxy group is staggered with respect to the methyl groups.

The two potential curves differ in the height of the peroxy torsion barrier, which is 828 cm^{-1} and 1523 cm^{-1} in the $\tilde{X}$ and $\tilde{A}$ electronic states, respectively. Launder et al.[29] computed peroxy torsional potentials for the $\tilde{X}$ and $\tilde{A}$ states of the ethyl peroxy radical. These are similar in

Table 7.2. Diagnostics for the reference wavefunction used for the CCSD(T) computations. Diagnostics were obtained at the UHF-CCSD(T)/ANO1 equilibrium structures. The CASCI coefficients come from CASSCF(11,12)/ANO1 wavefunctions.

	$\langle \hat{S}^2 \rangle_{UHF}$	C_0^2	C_1^2	C_2^2
$\tilde{X}^2A''$	0.76	0.95	0.00	0.00
$\tilde{A}^2A'$	0.77	0.93	0.02	0.01

that the barriers for the $\tilde{A}$ state are also about twice as high as those for the $\tilde{X}$ state. Note that the torsional potential of ethyl peroxy radical possesses lower symmetry; it displays two distinct conformers. They found that the torsional transition states corresponded to structures where the peroxy moiety eclipsed some other part of the molecule (either the β-methyl group or the α-hydrogen). Similar trends in computed torsional potentials were also found by Miller and co-workers for other peroxy radicals, including: methyl, allyl and cyclopentadienyl peroxy.[73-75]

For the methyl peroxy radical, Just, McCoy, and Miller explain the higher barriers in the excited state based upon destabilization of the HOMO[π*(a'')].[73] They argue that, when the peroxy radical is in a staggered orientation, the HOMO[π*(a'')] experiences favorable delocalization (i.e. hyperconjugation) over the adjacent C-H bonds; however, this delocalization is mostly lost when it assumes an eclipsed orientation. The energy stabilization should be enhanced when the HOMO[π*(a'')] is doubly occupied, as it is in the $\tilde{A}$ state. Miller and co-workers also note that the HOMO-1[n(a')] and other orbitals of a' symmetry do not noticeably change from one orientation to the other. Similar arguments also apply to *tert*-butyl peroxy; however, in the staggered configuration, its HOMO[π*($8a''$)] is delocalized over the adjacent C-C bonds. In the $\tilde{A}$-state, the decreased occupation of the HOMO-1[n($17a'$)] also decreases the length of the C-O bond, and the C-O bond has to elongate more along the potential in the $\tilde{A}$-state, in response to repulsion from the methyl groups. From the bottom of the well to the top of the barrier, the C-O bond elongates by 0.009 and 0.019 Å for the $\tilde{X}$ and $\tilde{A}$ states, respectively.

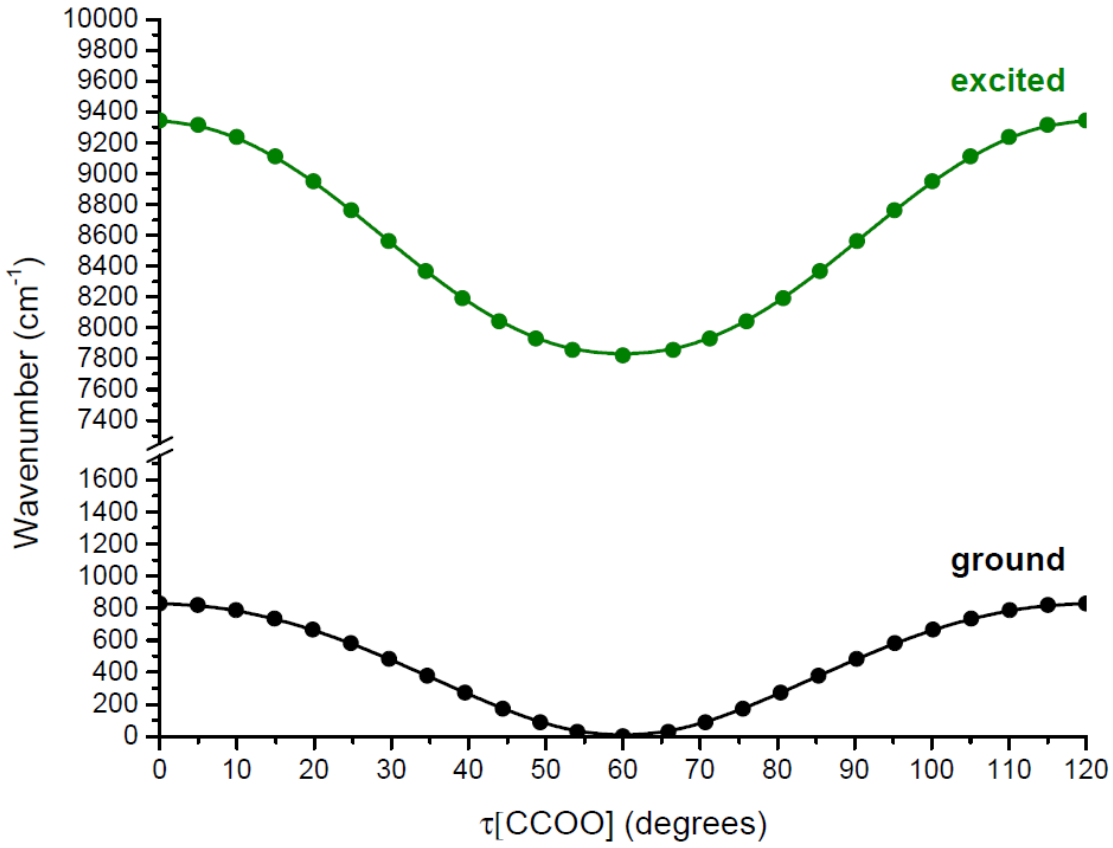

Figure 7.2. Three-fold symmetric C-C-O-O torsional potentials for the $\tilde{X}$ and $\tilde{A}$ electronic states obtained at the UHF-CCSD(T)/ANO1//UHF-CCSD(T)/ANO0 level of theory. The $\tilde{A}$ energies are offset by the $T_{e,CBS}$ value from Table 7.7.

7.3.2. Equilibrium Structures

Figure 7.3 depicts the UHF-CCSD(T)/ANO1 equilibrium structure of the *tert*-butyl peroxy radical, with select geometrical parameters, for the $\tilde{X}^2A''$ and $\tilde{A}^2A'$ electronic states. For both states, the peroxy moiety is staggered with respect to the methyl groups. The $\tilde{A}^2A' \leftarrow \tilde{X}^2A''$ transition (Fig. 7.1) primarily involves the excitation of a single electron from the HOMO-1[n(17a')] to the HOMO[π*(8a'')], which are localized on the peroxy moiety. As such, this transition only induces significant changes in the C-O and O-O bonds. The $\tilde{A} \leftarrow \tilde{X}$ transition

induces an elongation of the O-O bond (Δr_e = 0.074 Å) and contraction of the C-O bond (Δr_e = -0.017 Å). In contrast, the C-C bond lengths shift only very slightly: the in-plane C-C bond and out-of-plane C-C bonds elongate by only 0.004 Å and 0.001 Å, respectively. These structural changes induced by the $\tilde{A} \leftarrow \tilde{X}$ excitation are remarkably similar to those computed for the methyl peroxy[26] and ethyl peroxy[29] radicals, as shown in Table 7.3. It is also noteworthy that the 6-3-4 C-C-C angle and the C-O-O angle both contract by 2.7 degrees upon excitation.

Energetic trends of peroxy radical conformers have already been discussed in the article by Sharp, Rupper, and Miller.[11] Some discussion was also devoted to geometric trends. They argue that the hyperconjugating effect is weakened in peroxy radicals that are branched at the carbon atom adjacent to the peroxy group. They show that the SOMO (in the ground electronic state) of primary peroxy radicals is delocalized over the nearby C-H bonds; however, in secondary and tertiary peroxy radicals, the SOMO is more localized on the peroxy moiety. Miller and co-workers expected that this hyperconjugation should stabilize the C-O bond. The greater lengthening of the C-O bond that we find in *tert*-butyl peroxy versus the primary peroxy radicals is consistent with the arguments put forth by Sharp, Rupper, and Miller.[11]

7.3.3. $\widetilde{A} \leftarrow \widetilde{X}$ Transition Origin

7.3.3.1. Primary Extrapolation and Discussion of Schemes

Extrapolation schemes are described and summarized in Tables 7.4-7.6. The CBS extrapolation and the auxiliary corrections used to obtain the final adiabatic $\tilde{A} \leftarrow \tilde{X}$ excitation energy (T_0) are given in Table 7.7. We predict a T_0 value of 7738 cm^{-1}. The difference between the CCSD(T) energies with the cc-pVQZ and CBS limits shows good convergence with respect to the basis set. The sum of the post-CCSD(T) corrections (47 cm^{-1}) is very close to the analogous correction determined for the methyl peroxy radical (56 cm^{-1}).[26] This is promising since Copan et al. computed that the difference between perturbative and full quadruples was only 10 cm^{-1} in

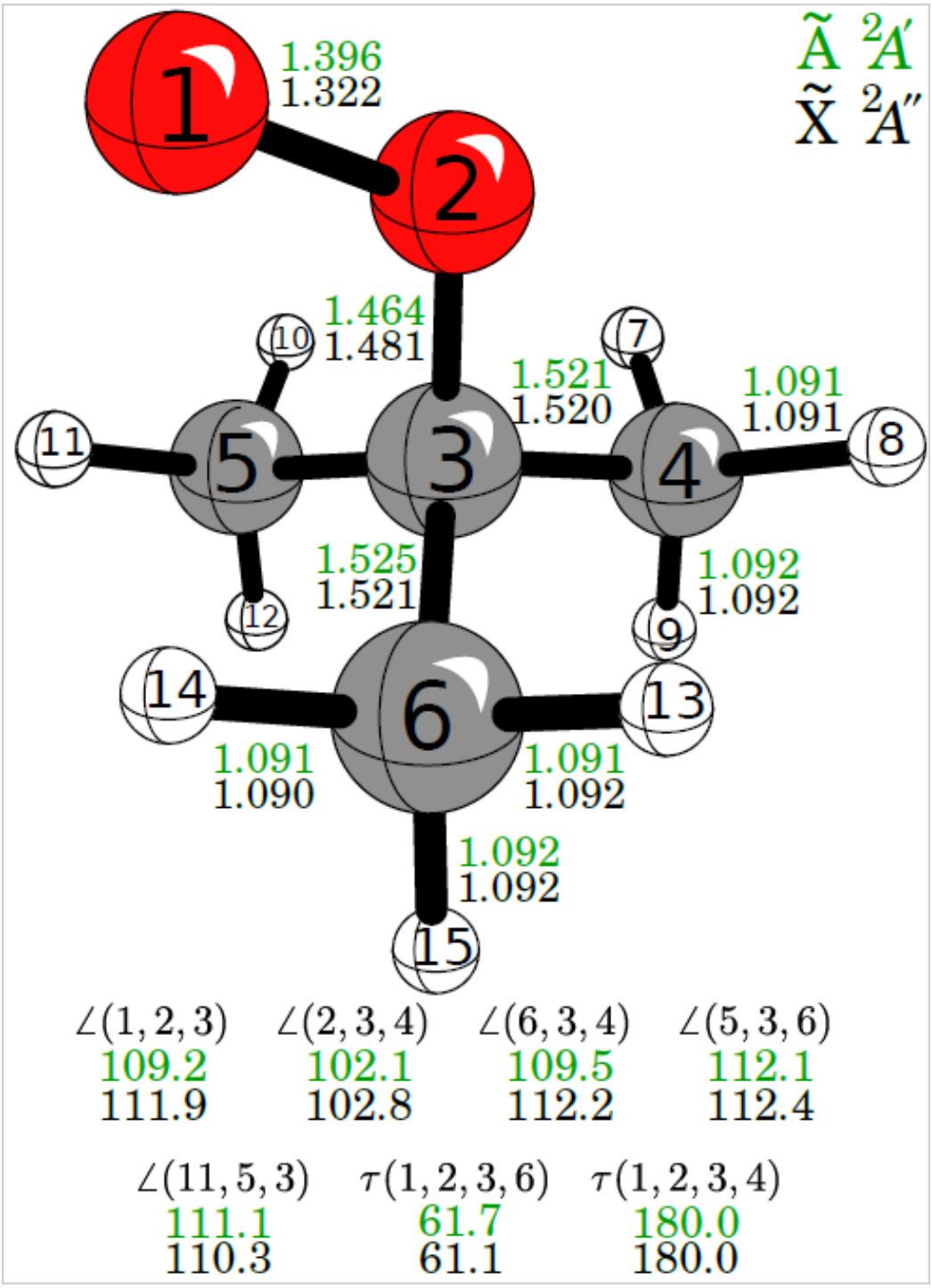

Figure 7.3. Optimized equilibrium structure for the $\tilde{X}^2A''$ and $\tilde{A}^2A'$ electronic states of the *tert*-butyl peroxy radical obtained at the UHF-CCSD(T)/ANO1 level of theory. The bond distances are in angstroms, and the angles are in degrees.

Table 7.3. Comparison of predicted geometric parameters, transition energies, and vibrational frequencies for the *tert*-butyl peroxy radical, ethyl peroxy radical, and methyl peroxy radical. In all cases, geometries were optimized with the CCSD(T) method and a basis set of at least triple zeta quality. Transition energies were evaluated with Focal Point Analysis (FPA).

Parameter[a]	***tert*-Butyl**	***gauche*-Ethyl**[29]	***trans*-Ethyl**[29]	**Methyl**[26]
Δr_e(C-O)	-0.017	-0.012	-0.012	-0.012
Δr_e(O-O)	+0.074	+0.073	+0.074	+0.075
Δa_e(C-O-O)	-2.7	-3.6	-4.7	-4.8
T_0	7738	7583	7363	7374
$\widetilde{X}$: ν(O-O)	1138	1123	1152	1186, 1128
$\widetilde{A}$: ν(O-O)	959	920	-	1008, 910
$\widetilde{X}$: δ(C-O-O)	541	529	500	493
$\widetilde{A}$: δ(C-O-O)	490	-	-	379

[a] Distances in Å, angles in degrees, T_0 in cm^{-1}, and frequencies in cm^{-1}.

methyl peroxy. It is important to ask whether a good quality prediction of the $\tilde{A} \leftarrow \tilde{X}$ origin can be achieved using an ANO0 optimized geometry. At the CCSD(T)/cc-pVQZ//CCSD(T)/ANO0 level, we calculate a T_e value of 7828 cm^{-1}, which differs somewhat from the 7792 cm^{-1} T_e value obtained at the CCSD(T)/ANO1 geometry.

Table 7.3 shows that the T_0 of *tert*-butyl peroxy radical (7738 cm^{-1}) is appreciably greater than T_0 of the ethyl peroxy (*gauche*: 7583 cm^{-1}, *trans*: 7363 cm^{-1})[29] and methyl peroxy radicals (7374 cm^{-1}),[26] which highlights the utility of these $\tilde{A} \leftarrow \tilde{X}$ transitions for specific identification of peroxy radicals. Sharp, Rupper, and Miller previously explored these trends, concluding that α-branching induced the greatest blueshift to T_0, followed by *gauche* orientation of τ_{CCOO}.[11]

Table 7.4. Extrapolation Schemes for Hartree-Fock Energy.

Method	Formula	X Points[a]	Ref.
exp	$E(X) = E_{HF}^{\infty} + Ae^{-BX}$	[3,4,5]	47
expGauss	$E(X) = E_{HF}^{\infty} + Ae^{-(X-1)} + Be^{-(X-1)^2}$	[3,4,5]	48
exp-2	$E_{HF}(X) = E_{HF}^{\infty} + A(X+1)e^{-9\sqrt{X}}$	[4,5]	45
SchwenkeHF	$E_{HF}^{\infty} = E(X_1) + [E(X_2) - E(X_1)]F_{X_2}$	[4,5]	49

[a] X = 3, 4, and 5 denote the use of the cc-pVTZ, cc-pVQZ, and cc-pV5Z basis sets, respectively.

Table 7.5. Extrapolation Schemes for Correlation Energy.

Method	Formula	X Points[a]	Ref.
X^{-3}	$\epsilon(X) = \epsilon^{\infty} + AX^{-3}$	[3,4,5]	46
Schwartz4	$\epsilon(X) = \epsilon^{\infty} + A\left(X + {}^{1}/_{2}\right)^{-4}$	[3,4,5]	50
Schwartz6	$\epsilon(X) = \epsilon^{\infty} + A\left(X + {}^{1}/_{2}\right)^{-4} + B\left(X + {}^{1}/_{2}\right)^{-6}$	[3,4,5]	50
SchwenkeCCSD[b]	$\epsilon^{\infty} = \epsilon(X_1) + [\epsilon(X_2) - \epsilon(X_1)]F_{X_2}$	[4,5]	49
SchwenkeCCSD(T)[b]	$\epsilon^{\infty} = \epsilon(X_1) + [\epsilon(X_2) - \epsilon(X_1)]F_{X_2}$	[4,5]	49

[a] X = 3, 4, and 5 denote the use of the cc-pVTZ, cc-pVQZ, and cc-pV5Z basis sets, respectively.

[b] Not used in this study; CCSD and CCSD(T) correlation energies were obtained by additivity.

We now compare our predicted T_0 value (7738 cm^{-1}) to previous experimental values. We observe excellent agreement with the available experimental values from Sharp, Rupper, and Miller (7755 ± 10 cm^{-1})[22] and Neumark and co-workers (7744 ± 19 cm^{-1}).[25] Our value also falls well within the error bars of the value from Ellison, Lineberger, and co-workers (7799 ± 90 cm^{-1}).[24] To the best of our knowledge, the only other attempt to compute T_0 was performed by

Table 7.6. Extrapolated T_e via different schemes. Mean is 7817 cm^{-1}, and std. deviation is 2 cm^{-1}.

Scheme	E[HF]	ϵ[MP2]	$T_{e,CBS}$ (cm^{-1})
1	exp	X^{-3}	7817
2	expGauss	X^{-3}	7820
3[a]	exp-2	X^{-3}	7820
4	exp	Schwartz6	7813
5	expGauss	Schwartz6	7816
6	exp-2	Schwartz6	7816
7	exp	Schwartz4	7813
8	expGauss	Schwartz4	7816
9	exp-2	Schwartz4	7817
10	SchwenkeHF	X^{-3}	7820

[a] Chosen for the final analysis.

Table 7.7. The adiabatic $\tilde{A} \leftarrow \tilde{X}$ origin transition energy (T_0), obtained at the CCSDT(Q)/CBS//CCSD(T)/ANO1 level. Bracketed values were obtained by additivity or extrapolation assumptions. All energies are in cm^{-1}, and extrapolation scheme 3 is used.

	ROHF	+δMP2	+δCCSD	+δCCSD(T)	NET
cc-pVDZ	4685	+2529	+87	+201	7503
cc-pVTZ	4732	+2570	+71	+311	7684
cc-pVQZ	4758	+2614	+86	+334	7792
cc-pV5Z	4758	+2628	[+86]	[+334]	7805
CBS LIMIT	[4758]	[+2643]	[+86]	[+334]	7820

$$T_0 = T_{e,CBS} + \Delta_T + \Delta_{(Q)} + \Delta_{CORE} + \Delta_{DBOC} + \Delta_{REL} + \Delta_{ZPVE}$$

T_0 = 7820 - 0.6 + 47.5 + 23.5 + 0.5 - 5.1 - 147.3 cm^{-1}. T_0 = 7738 cm^{-1}.

Neumark and co-workers, who predicted this energy to be 7933 cm^{-1} at the B3LYP/6-311+G* level of theory. The excitation energy cannot be predicted accurately by DFT (and without considering, at minimum, the effect of core-valence correlation). Our higher level determination signals a coalescence of theory and experiment regarding the energy of the $\tilde{A} \leftarrow \tilde{X}$ origin transition and shows that accuracy approaching the best quality experimental measurements may indeed be achieved for larger peroxy radicals.

7.3.3.2. Alternative Extrapolation Schemes

For reference, the focal point tables for all alternative extrapolation schemes not selected are given below (Tables 7.8-7.16). Differing with the presentation of similar information in Table 7.7, the non-electronic contributions are omitted in these tables. It is important to note that the cc-pVDZ results, while computed, are not actually used in any of the extrapolation formulas or indeed even in additivity approximations. It is generally accepted that cc-pVDZ energies perform poorly in basis set extrapolations; although, they are frequently used for additive post-CCSD(T) correlation corrections.

Table 7.8. The electronic $\tilde{A} \leftarrow \tilde{X}$ transition energy (T_e), in wavenumbers, obtained with extrapolation scheme 1 at the CCSDT(Q)/CBS//CCSD(T)/ANO1 level of theory.

	ROHF	**+δMP2**	**+δCCSD**	**+δCCSD(T)**	**NET**
cc-pVDZ	4685	+2529	+87	+201	7503
cc-pVTZ	4732	+2570	+71	+311	7684
cc-pVQZ	4758	+2614	+86	+334	7792
cc-pV5Z	4758	+2628	[+86]	[+334]	7805
CBS LIMIT	[4755]	[+2643]	[+86]	[+334]	7817

Table 7.9. The electronic $\tilde{A} \leftarrow \tilde{X}$ transition energy (T_e), in wavenumbers, obtained with extrapolation scheme 2 at the CCSDT(Q)/CBS//CCSD(T)/ANO1 level of theory.

	ROHF	**+δMP2**	**+δCCSD**	**+δCCSD(T)**	**NET**
cc-pVDZ	4685	+2529	+87	+201	7503
cc-pVTZ	4732	+2570	+71	+311	7684
cc-pVQZ	4758	+2614	+86	+334	7792
cc-pV5Z	4758	+2628	[+86]	[+334]	7805
CBS LIMIT	[4758]	[+2643]	[+86]	[+334]	7820

Table 7.10. The electronic $\tilde{A} \leftarrow \tilde{X}$ transition energy (T_e), in wavenumbers, obtained with extrapolation scheme 4 at the CCSDT(Q)/CBS//CCSD(T)/ANO1 level of theory.

	ROHF	**+δMP2**	**+δCCSD**	**+δCCSD(T)**	**NET**
cc-pVDZ	4685	+2529	+87	+201	7503
cc-pVTZ	4732	+2570	+71	+311	7684
cc-pVQZ	4758	+2614	+86	+334	7792
cc-pV5Z	4758	+2628	[+86]	[+334]	7805
CBS LIMIT	[4755]	[+2639]	[+86]	[+334]	7813

Table 7.11. The electronic $\tilde{A} \leftarrow \tilde{X}$ transition energy (T_e), in wavenumbers, obtained with extrapolation scheme 5 at the CCSDT(Q)/CBS//CCSD(T)/ANO1 level of theory.

	ROHF	**+δMP2**	**+δCCSD**	**+δCCSD(T)**	**NET**
cc-pVDZ	4685	+2529	+87	+201	7503
cc-pVTZ	4732	+2570	+71	+311	7684
cc-pVQZ	4758	+2614	+86	+334	7792
cc-pV5Z	4758	+2628	[+86]	[+334]	7805
CBS LIMIT	[4758]	[+2639]	[+86]	[+334]	7816

Table 7.12. The electronic $\tilde{A} \leftarrow \tilde{X}$ transition energy (T_e), in wavenumbers, obtained with extrapolation scheme 6 at the CCSDT(Q)/CBS//CCSD(T)/ANO1 level of theory.

	ROHF	**+δMP2**	**+δCCSD**	**+δCCSD(T)**	**NET**
cc-pVDZ	4685	+2529	+87	+201	7503
cc-pVTZ	4732	+2570	+71	+311	7684
cc-pVQZ	4758	+2614	+86	+334	7792
cc-pV5Z	4758	+2628	[+86]	[+334]	7805
CBS LIMIT	[4758]	[+2639]	[+86]	[+334]	7816

Table 7.13. The electronic $\tilde{A} \leftarrow \tilde{X}$ transition energy (T_e), in wavenumbers, obtained with extrapolation scheme 7 at the CCSDT(Q)/CBS//CCSD(T)/ANO1 level of theory.

	ROHF	**+δMP2**	**+δCCSD**	**+δCCSD(T)**	**NET**
cc-pVDZ	4685	+2529	+87	+201	7503
cc-pVTZ	4732	+2570	+71	+311	7684
cc-pVQZ	4758	+2614	+86	+334	7792
cc-pV5Z	4758	+2628	[+86]	[+334]	7805
CBS LIMIT	[4758]	[+2643]	[+86]	[+334]	7820

Table 7.14. The electronic $\tilde{A} \leftarrow \tilde{X}$ transition energy (T_e), in wavenumbers, obtained with extrapolation scheme 8 at the CCSDT(Q)/CBS//CCSD(T)/ANO1 level of theory.

	ROHF	**+δMP2**	**+δCCSD**	**+δCCSD(T)**	**NET**
cc-pVDZ	4685	+2529	+87	+201	7503
cc-pVTZ	4732	+2570	+71	+311	7684
cc-pVQZ	4758	+2614	+86	+334	7792
cc-pV5Z	4758	+2628	[+86]	[+334]	7805
CBS LIMIT	[4755]	[+2639]	[+86]	[+334]	7813

Table 7.15. The electronic $\tilde{A} \leftarrow \tilde{X}$ transition energy (T_e), in wavenumbers, obtained with extrapolation scheme 9 at the CCSDT(Q)/CBS//CCSD(T)/ANO1 level of theory.

	ROHF	**+δMP2**	**+δCCSD**	**+δCCSD(T)**	**NET**
cc-pVDZ	4685	+2529	+87	+201	7503
cc-pVTZ	4732	+2570	+71	+311	7684
cc-pVQZ	4758	+2614	+86	+334	7792
cc-pV5Z	4758	+2628	[+86]	[+334]	7805
CBS LIMIT	[4758]	[+2639]	[+86]	[+334]	7816

Table 7.16. The electronic $\tilde{A} \leftarrow \tilde{X}$ transition energy (T_e), in wavenumbers, obtained with extrapolation scheme 10 at the CCSDT(Q)/CBS//CCSD(T)/ANO1 level of theory.

	ROHF	**+δMP2**	**+δCCSD**	**+δCCSD(T)**	**NET**
cc-pVDZ	4685	+2529	+87	+201	7503
cc-pVTZ	4732	+2570	+71	+311	7684
cc-pVQZ	4758	+2614	+86	+334	7792
cc-pV5Z	4758	+2628	[+86]	[+334]	7805
CBS LIMIT	[4758]	[+2639]	[+86]	[+334]	7817

7.3.4. Vibrational Frequencies

7.3.4.1. Harmonic Frequencies

For all combinations of reference wavefunction and basis set used in this study, harmonic frequencies and intensities are tabulated (Tables 7.17-7.18). Differences between ANO0 and ANO1 are most pronounced in the CH and OO stretching modes. This highlights the shortcomings of an entirely ANO0 description of anharmonic coupling, as the HCH bending harmonic frequencies are comparatively less sensitive to the basis set. Differences between

ROHF and UHF references are generally small, except for modes involving motion of the peroxy moiety, as seen in Section 7.3.4.2 and Table 7.19.

7.3.4.2. Assessing the Quality of the Force Field

One potential shortcoming of our force field is the use of a UHF reference determinant, which does not properly handle spin, for the cubic and quartic force constants. Table 7.2 shows that the UHF reference is only minimally spin-contaminated, so we should not expect significant errors in the vibrational frequencies due to this. Indeed, this is largely the case when we consider the $\delta\omega$ corrections obtained with the ROHF reference. Nearly all corrections are less than 1 cm^{-1}. The more substantial corrections are tabulated in Table 7.19. The most notable of these are for the O-O stretch in the $\tilde{X}$-state (ν13) and $\tilde{A}$-state (ν14), which amount to ± 4 cm^{-1} and 8 cm^{-1}, respectively. While these corrections largely align with similar corrections in previous research,[26, 31-32, 70] the $\tilde{A}$-state correction is particularly large; this may result from its slightly higher spin contamination. However, it is not surprising that only modes involving the C-O-O moiety are greatly affected, because the spin density is largely localized there. Finally we note that differences in force constants, based upon different reference wavefunctions, can also be due to orbital near-instabilities (in the references).[76] This is more frequently a concern in systems that possess double- and triple-bonds; however, we cannot completely rule this out as an explanation for these differences.

Other issues may arise from our combination of CCSD(T)/ ANO1 quadratic and CCSD(T)/ANO0 cubic/quartic force constants. A central assumption made in most hybrid force fields is that the normal modes do not differ between the two levels of theory (in this case the different basis sets). The extent to which this condition is met depends strongly upon the type of normal coordinate; moreover, this approximation is generally less sound for larger molecules with lower symmetry. Changes in the potential energy surface, at different levels of theory, will influence how the internal coordinates couple together into normal coordinates. We have found

Table 7.17. CCSD(T) harmonic frequencies (ω) and intensities (I) for $\tilde{X}$-state *tert*-butyl peroxy.

#	ANO1 (UHF)		ANO0 (UHF)		ANO0 (ROHF)	
	ω (cm^{-1})	**I (km/mol)**	**ω (cm^{-1})**	**I (km/mol)**	**ω (cm^{-1})**	**I (km/mol)**
1	3144.7	14.9	3161.2	14.1	3161.1	14.2
2	3132.1	29.5	3148.8	29.1	3148.8	29.1
3	3125.2	3.6	3142.1	3.7	3142.1	3.7
4	3049.2	8.0	3058.1	7.6	3058.1	7.6
5	3044.2	8.5	3052.2	10.8	3052.2	10.9
6	1523.4	10.7	1527.0	9.4	1527.0	9.4
7	1499.9	3.7	1503.7	2.5	1503.7	3.2
8	1489.3	0.2	1493.1	0.0	1493.1	0.1
9	1422.7	6.2	1425.9	5.6	1425.9	5.6
10	1401.9	23.4	1404.7	19.8	1404.7	19.8
11	1308.4	11.9	1305.6	14.0	1305.6	14.0
12	1221.0	26.4	1217.0	33.2	1217.1	33.3
13	1167.4	18.1	1101.9	17.1	1097.6	16.8
14	1056.3	0.3	1054.3	0.4	1054.1	0.5
15	938.3	0.6	936.0	0.3	936.0	0.3
16	852.8	6.8	851.4	7.8	851.7	7.8
17	751.0	1.8	742.1	2.2	742.3	2.2
18	549.2	6.3	543.5	6.0	543.6	5.9
19	399.4	0.5	399.9	0.4	399.9	0.4
20	360.7	2.4	360.3	2.1	360.3	2.1
21	273.0	1.8	271.2	1.7	271.1	1.7
22	253.7	0.1	256.0	0.0	256.0	0.0
23	3141.3	3.4	3157.9	2.8	3157.8	2.8
24	3131.0	19.5	3146.8	19.2	3146.8	19.2
25	3123.3	3.8	3140.3	2.9	3140.3	2.9
26	3044.5	14.4	3053.3	16.7	3053.2	16.7
27	1499.4	3.3	1503.7	3.2	1503.7	2.5
28	1489.8	0.0	1493.9	0.1	1493.9	0.0
29	1471.2	0.0	1476.4	0.0	1476.4	0.0
30	1398.2	19.0	1401.2	16.2	1401.2	16.2
31	1279.6	12.2	1278.0	15.8	1278.0	15.8
32	1045.1	0.4	1044.0	0.5	1044.0	0.5
33	964.8	0.0	963.4	0.0	963.4	0.0
34	936.4	0.2	934.9	0.1	934.9	0.1
35	438.3	3.1	437.9	3.1	438.0	3.1
36	333.3	1.1	332.9	1.2	332.9	1.2
37	247.9	0.0	252.4	0.0	252.4	0.0
38	190.7	0.0	197.1	0.0	197.1	0.0
39	126.6	0.2	126.1	0.1	126.1	0.1

Table 7.18. CCSD(T) harmonic frequencies (ω) and intensities (I) for $\tilde{A}$-state *tert*-butyl peroxy.

#	ANO1 (UHF)		ANO0 (UHF)		ANO0 (ROHF)	
	ω (cm^{-1})	**I (km/mol)**	**ω (cm^{-1})**	**I (km/mol)**	**ω (cm^{-1})**	**I (km/mol)**
1	3137.6	21.8	3153.1	21.1	3153.1	21.1
2	3133.2	28.4	3150.0	27.8	3149.9	27.8
3	3125.9	7.0	3142.8	7.3	3142.8	7.3
4	3049.4	7.3	3057.7	6.9	3057.7	6.9
5	3044.7	10.1	3052.8	12.6	3052.8	12.6
6	1521.0	7.5	1524.7	6.6	1524.7	6.6
7	1498.6	5.1	1502.8	4.4	1502.8	4.4
8	1488.4	0.0	1492.3	0.0	1492.3	0.0
9	1424.2	8.9	1427.9	8.2	1427.9	8.2
10	1401.3	18.0	1403.8	14.3	1403.8	14.3
11	1297.1	9.5	1294.4	11.3	1294.2	11.3
12	1215.3	59.2	1218.4	60.6	1218.4	60.6
13	1050.6	0.4	1050.1	0.3	1049.9	0.3
14	969.0	33.6	912.1	35.5	894.2	46.8
15	933.7	4.2	940.4	6.1	938.2	2.1
16	864.0	24.1	860.5	12.2	852.1	4.9
17	739.7	6.9	732.7	5.7	731.6	5.2
18	495.3	4.8	495.4	3.5	494.8	3.4
19	403.4	0.6	403.6	0.5	403.4	0.5
20	347.1	1.7	347.1	1.3	346.9	1.3
21	254.5	1.0	251.1	1.2	250.8	1.2
22	250.4	0.7	255.5	0.1	255.5	0.1
23	3137.3	24.1	3152.6	22.5	3152.6	22.5
24	3133.3	0.0	3149.0	0.2	3149.0	0.2
25	3123.4	2.5	3140.3	2.1	3140.3	2.1
26	3043.0	11.1	3051.5	13.3	3051.5	13.3
27	1498.2	2.4	1502.6	1.7	1502.6	1.7
28	1486.7	0.1	1490.8	0.2	1490.8	0.2
29	1470.2	0.1	1475.9	0.1	1475.9	0.1
30	1402.6	20.3	1405.8	16.6	1405.8	16.6
31	1283.2	15.9	1281.1	19.8	1281.1	19.8
32	1049.7	0.9	1049.1	1.0	1049.1	1.0
33	964.3	0.0	963.1	0.0	963.1	0.0
34	927.3	0.0	926.1	0.0	926.1	0.0
35	457.5	4.1	455.8	3.8	455.8	3.8
36	337.8	1.0	336.8	1.0	336.8	1.0
37	254.8	0.0	258.5	0.0	258.5	0.0
38	197.1	0.0	202.2	0.0	202.2	0.0
39	112.2	0.1	111.3	0.2	111.2	0.2

Table 7.19. Non-negligible δω values denoting the errors from using a UHF reference. Similar values were computed in previous research.[26, 31-32, 70]

$\widetilde{X}^2A''$			$\widetilde{A}^2A'$	
Mode	**δω**		**Mode**	**δω**
ω_{13}	-4		ω_{14}	-18
			ω_{15}	-2
			ω_{16}	-8
			ω_{17}	-1
			ω_{18}	-1

that the O-O and C-O stretch coordinates of peroxy radicals are particularly sensitive to the level of theory and basis set size. These oscillators have similar masses; depending on the potential, they may remain decoupled, or they may couple into symmetric and antisymmetric C-O-O stretch normal coordinates. By visual inspection of the normal mode displacements, the extent of coupling between the two stretches changes between the different levels of theory; this occurs to a greater extent in the $\tilde{A}$ state.

For the ethyl peroxy radical, we recently showed that transformation of the cubic/quartic force constants into the same normal coordinates as the quadratic force constants makes them very closely approximate the values of the analogous force constants at a higher level of theory.[77] This suggests that the normal-mode mismatching is largely responsible for the disagreement between force constants computed at different levels of theory. Despite its general success, the aforementioned transformation did not improve the agreement for the O-O stretching force constants. This degree of freedom, in addition to being impacted by the normal-mode mismatching, evidently requires a more complete basis set than ANO0 to describe accurately.[4] Both of these factors are implicated in the lower accuracy predictions of the O-O stretch

fundamentals for the *tert*-butyl peroxy radical; unfortunately, the necessary corrections were deemed too expensive for this (15-atom) system. As a follow-up, we feel that it would be of great practical value to conduct a dedicated study of O-O stretch transitions of peroxy radicals, in order to evaluate their sensitivity to various aspects of the one-electron basis set (diffuse functions, high angular momentum functions), reference wavefunction (UHF vs. ROHF vs. Brückner), correlation treatment (core-correlation, post- CCSD(T) correlation), and anharmonicity treatment (empirical scaling vs. VPT2).

7.3.4.3. Fermi Resonances

Using the threshold described in the Methods section, several Type I and Type II Fermi resonances were identified. Resonances with diagnostic values exceeding the threshold are given in the Table 7.1. The Fermi resonances are primarily isolated in the C-H stretching (3145-3044 cm^{-1}) and H-C-H bending regions (1523-1400 cm^{-1}). The only exception is a Fermi triad involving the ν_{21}, ν_{22}, and $2\nu_{39}$ states in the $\tilde{X}$ electronic state. These are both regions for which there is presently no experimental information. As seen in Table 7.1, there are several vibrational states that strongly interact. The variational mixing between deperturbed vibrational states is sometimes as high as 50/50, resulting in vibrational states that can no longer be correlated with any zeroth-order harmonic oscillator states. Several large resonance polyads exist in the $\tilde{X}$ state, as the C-H stretching states are sometimes in resonance with doubly-excited H-C-H bending states, and these are, in turn, in resonance with more highly-excited low-frequency bending states.

7.3.4.4. Comparison to Previous Research

Six previous experimental studies[12-14, 20, 22, 24-25] have measured bands of the *tert*-butyl peroxy radical. In total, fifteen distinct fundamental transitions have been assigned. Eleven of these transitions are associated with the $\tilde{X}$ state and four with the $\tilde{A}$ state. Our predictions for the fundamental transitions of the $\tilde{X}$ and $\tilde{A}$ states are listed in Tables 7.20-7.23. When there is a

consensus between the assignments of theory and experiment, and exempting the pathological O-O stretches, there is good agreement with the predicted frequencies (± 10 cm^{-1}). Regarding our calculated intensities, recall that these are infrared absorption intensities based upon geometric derivatives of the dipole moment; as such, these can only be meaningfully compared to the infrared absorption experiments. The mechanism that gives rise to transition intensity in the CRDS experiment[20, 22] is, instead, favorable Franck-Condon overlap between the ground and excited state vibrational wavefunctions. Similarly, the active vibrations in the APES experiments[24-25] are those with favorable overlap between the closed shell anion and either the ground or the excited state of the neutral radical.

7.3.4.5. Comparison to $\tilde{X}^2A''$ Experimental Fundamentals

The most recent experiment from Neumark and co-workers[25] observed six fundamental vibrations for the $\tilde{X}$ state. Three fundamentals can readily be compared to our predicted values: ν_{13}, ν_{17}, and ν_{19}. We predict frequencies for these transitions of 1138, 737, and 401 cm^{-1}, which agree with the 1129, 740, and 410 cm^{-1} values observed in the experiment. Note however that the fundamental at 740 cm^{-1} was not directly observed; rather, it was estimated by subtracting the value of ν_{13} from a combination band assigned as $\nu_{13} + \nu_{17}$. It should, therefore, not be considered as accurate as the others. Chettur and Snelson[14] measured similar bands at 1124, 730, and 403 cm^{-1}, which they attributed to O-O stretching, C-O stretching, and skeletal bending, respectively. Their assignments, based off isotopic shifts, align well with the amount of oxygen motion that occurs in ν_{13}, ν_{17}, and ν_{19}. Therefore, theory and experiment appear to align nicely for these three fundamental transitions. The slight red shifts of the frequencies of Chettur and Snelson are consistent with typical argon matrix perturbations.

Neumark and co-workers also reported vibrational bands at 236 cm^{-1} and 279 cm^{-1}, which they assigned to ν_{21} and ν_{22}, respectively. These values nearly match two of the frequencies of

Table 7.20. Fundamental vibrational frequencies (ν) of a' symmetry for the $\tilde{X}^2A''$ state of the *tert*-butyl peroxy radical. All theoretical results are from the present research.

		Theory			Expt.[d]		
Mode[a]		**ω**[b]	**ν**[c]	**Int.**[b]	**Ref. 25**[f]	**Ref. 24**[f]	**Ref. 14**[g]
1	$\nu_{as}(CH_3)_2$	3145	2996	14.9	-	-	-
2	$\nu_{as}(CH_3)_3$	3132	2985	29.5	-	-	-
3	$\nu_{as}(CH_3)_3$	3125	2978	3.6	-	-	-
4	$\nu_{s}(CH_3)_3$	3049	2930, 2970	6.6, 1.1	-	-	-
5	$\nu_{s}(CH_3)_3$	3044	2908, 2953	4.2, 3.7	-	-	-
6	$\delta_{as}(CH_3)_3$	1523	1482	10.5	-	-	-
7	$\delta_{as}(CH_3)_2$	1500	1454, 1469	1.8, 1.8	-	-	-
8	$\delta_{as}(CH_3)_3$	1489	1449, 1454	0.2, 1.8	-	-	-
9	$\delta_{s}(CH_3)_3$	1423	1391	6.2	-	-	-
10	$\delta_{s}(CH_3)_3$	1402	1361, 1369	1.7, 21.8	-	-	-
11	$\delta_{as}(CC_3)$	1308	1269	11.9	1254 ± 26[e]	-	-
12	$\delta_{s}(CC_3)$	1221	1190	26.4	-	-	1187 ± 2
13	ν(OO)	1167	1138	18.1	1129 ± 22	1130 ± 90	1124 ± 2
14	$\rho_{r}(CH_3)_3$	1056	1031	0.3	-	-	-
15	ν_{as}(CC)	938	920	0.6	-	-	-
16	ν_{as}(CC/CO)	853	823	6.8	-	-	808 ± 2
17	ν_{s}(CC/CO)	751	737	1.8	740 ± 26[e]	-	730 ± 2
18	δ(COO)	549	541	6.3	-	-	539 ± 2
19	δ_{as}(CCC)	399	401	0.5	410 ± 29	-	403 ± 2
20	δ(CCO/COO)	361	358	2.4	-	-	361 ± 2
21	δ(COO/CCO)	273	229, 247, 275	0.2, 0.2, 1.5	279 ± 21	-	-
22	$\tau(CH_3)_2$	254	229, 247, 275	0.2, 0.2, 1.5	236 ± 21	245 ± 90	-

[a] A qualitative description of each ANO1 normal coordinate is given. Abbreviations used: ν: stretch, δ: deformation, ρ_r: rock, τ: torsion, s: symmetric, as: antisymmetric. [b] Computed at UHF-CCSD(T)/ANO1 level of theory. [c] For participants in a resonance polyad, transitions comprised of greater than 10% of fundamental character are shown here. [d] Unclear assignments: 1139 cm^{-1} [$\delta(CH_3)$].[14] [e] Estimated from measured overtone or combination transition. [f] Gas phase, anion photoelectron spectroscopy. [g] Argon matrix, infrared absorption spectroscopy.

Table 7.21. Fundamental vibrational frequencies (ν) of a'' symmetry for the $\tilde{X}^2A''$ state of the *tert*-butyl peroxy radical. All theoretical results are from the present research.

		Theory			Expt.[d]
Mode[a]		**ω**[b]	**ν**[c]	**Int.**[b]	**Ref. 14**[f]
23	$\nu_{as}(CH_3)_2$	3141	2993	3.4	-
24	$\nu_{as}(CH_3)$	3131	2983	19.5	-
25	$\nu_{as}(CH_3)_2$	3123	2977	3.8	-
26	$\nu_{s}(CH_3)_2$	3045	2906, 2943, 2962	6.7, 2.7, 2.8	-
27	$\delta_{as}(CH_3)$	1499	1460, 1475	0.4, 2.9	-
28	$\delta_{as}(CH_3)_3$	1490	1445, 1460	0.0, 0.4	-
29	$\delta_{as}(CH_3)_3$	1471	1432	0.0	-
30	$\delta_{s}(CH_3)_2$	1398	1365	19.0	-
31	$\delta_{as}(CC_3)$	1280	1245	12.2	-
32	$\rho_{r}(CH_3)_3$	1045	1020	0.4	-
33	$\rho_{r}(CH_3)_3$	965	949	0.0	-
34	$\nu_{as}(CC)$	936	919	0.2	-
35	$\delta(COO)$	438	434	3.1	-
36	$\delta_{as}(CCC)$	333	333	1.1	337 ± 2
37	$\tau(CH_3)_3$	248	236	0.0	-
38	$\tau(CH_3)_3$	191	185	0.0	-
39	$\tau(CCOO)$	127	122	0.2	-

[a] A qualitative description of each ANO1 normal coordinate is given. Abbreviations used: ν: stretch, δ: deformation, ρ_r: rock, τ: torsion, s: symmetric, as: antisymmetric. [b] Computed at UHF-CCSD(T)/ANO1 level of theory. [c] For participants in a resonance polyad, transitions comprised of greater than 10% of fundamental character are shown here. [d] Unclear assignments: 1139 cm^{-1} [$\delta(CH_3)$].[14] [e] Estimated from measured overtone or combination transition. [f] Argon matrix, infrared absorption spectroscopy.

Table 7.22. Fundamental vibrational frequencies (ν) of a' symmetry for the $\tilde{A}^2A'$ state of the *tert*-butyl peroxy radical. All theoretical results are from the present research.

		Theory			Expt.		
Mode[a]		**ω**[b]	**ν**[c]	**Int.**[b]	**Ref. 25**[e]	**Ref. 24**[e]	**Ref. 22**[f]
1	$\nu_{as}(CH_3)_2$	3138	2990	21.8	-	-	-
2	$\nu_{as}(CH_3)_3$	3133	2986	28.4	-	-	-
3	$\nu_{as}(CH_3)_3$	3126	2979	7.0	-	-	-
4	$\nu_{s}(CH_3)_3$	3049	2930, 2970	6.0, 1.3	-	-	-
5	$\nu_{s}(CH_3)_3$	3045	2909, 2953	5.1, 5.0	-	-	-
6	$\delta_{as}(CH_3)_3$	1521	1483	7.5	-	-	-
7	$\delta_{as}(CH_3)_2$	1499	1462	5.1	-	-	-
8	$\delta_{as}(CH_3)_3$	1488	1452	0.0	-	-	-
9	$\delta_{s}(CH_3)_3$	1424	1390	8.9	-	-	-
10	$\delta_{s}(CH_3)$	1401	1368	18.0	-	-	-
11	$\delta_{as}(CC_3)$	1297	1257	9.5	-	-	-
12	$\delta_{s}(CC_3)$	1215	1182	59.2	-	-	-
13	$\rho_{r}(CH_3)_3$	1051	1026	0.4	-	-	-
14	ν(OO)	969	959	33.6	939 ± 14	-	934 ± 10
15	ν_{as}(CC)	934	919	4.2	-	-	-
16	ν_{as}(CC/CO)	864	842	24.1	-	-	-
17	ν_{s}(CC/CO)	740	727	6.9	-	-	-
18	δ(COO)	495	490	4.8	-	-	481 ± 10
19	δ(CCO)	403	405	0.6	-	-	-
20	δ_{as}(CCC)	347	347	1.7	-	-	340 ± 10
21	δ(COO/CCO)	254	252	1.0	244 ± 15[d]	240 ± 90[d]	240 ± 10[d]
22	$\tau(CH_3)_2$	250	239	0.7	244 ± 15[d]	240 ± 90[d]	240 ± 10[d]

[a] A qualitative description of each ANO1 normal coordinate is given. Abbreviations used: ν: stretch, δ: deformation, ρ_r: rock, τ: torsion, s: symmetric, as: antisymmetric. [b] Computed at UHF CCSD(T)/ANO1 level of theory. [c] For participants in a resonance polyad, transitions comprised of greater than 10% of fundamental character are shown here. [d] Indicates several reasonable assignments. [e] Gas phase, anion photoelectron spectroscopy. [f] Gas phase, cavity ringdown spectroscopy.

Table 7.23. Fundamental vibrational frequencies (ν) of a'' symmetry for the $\tilde{A}^2A'$ state of the *tert*-butyl peroxy radical. All theoretical results are from the present research. No experimental comparisons are available for these fundamentals.

		Theory		
Mode[a]		**ω**[b]	**ν**[c]	**Int.**[b]
23	$\nu_{as}(CH_3)_3$	3137	2989	24.1
24	$\nu_{as}(CH_3)_3$	3133	2985	0.0
25	$\nu_{as}(CH_3)_2$	3123	2977	2.5
26	$\nu_{s}(CH_3)_2$	3043	2910, 2951	5.4, 5.6
27	$\delta_{as}(CH_3)_3$	1498	1461	2.4
28	$\delta_{as}(CH_3)_2$	1487	1451	0.1
29	$\delta_{as}(CH_3)_3$	1470	1435	0.1
30	$\delta_{s}(CH_3)_2$	1403	1369	20.3
31	$\delta_{as}(CC_3)$	1283	1249	15.9
32	$\rho_{r}(CH_3)_3$	1050	1024	0.9
33	$\rho_{r}(CH_3)_3$	964	947	0.0
34	$\nu_{as}(CC)$	927	909	0.0
35	$\delta(COO)$	457	456	4.1
36	$\delta_{as}(CCC)$	338	337	1.0
37	$\tau(CH_3)_3$	255	243	0.0
38	$\tau(CH_3)_3$	197	191	0.0
39	$\tau(CCOO)$	112	118	0.1

[a] A qualitative description of each ANO1 normal coordinate is given. Abbreviations used: ν: stretch, δ: deformation, ρ_r: rock, τ: torsion, s: symmetric, as: antisymmetric. [b] Computed at UHF CCSD(T)/ANO1 level of theory. [c] For participants in a resonance polyad, transitions comprised of greater than 10% of fundamental character are shown here.

the $v_{21}/v_{22}/2v_{39}$ Fermi triad: 229, 247, and 275 cm^{-1}. The 236 cm^{-1} also matches our predicted value for v_{37} of 236 cm^{-1}; however, this vibration is antisymmetric and is unlikely to be active in their experiment. As noted by Neumark and co-workers,[25] their 236 cm^{-1} band may correspond with the 245 cm^{-1} band measured by Lineberger, Ellison, and co-workers.[24]

The last $\tilde{X}$ vibrational transition reported by Neumark and co-workers was at 1254 cm^{-1}, which they assigned to the CC_3 symmetric bend (i.e. skeletal umbrella) fundamental (v_{12}). As with v_{17}, the value of this fundamental was estimated from a combination band which they assigned as $v_{12} + v_{13}$. According to our calculations, it is more likely that the combination band corresponds to $v_{11} + v_{12}$, and their fundamental should instead be considered an estimate of the a' CC_3 antisymmetric bend fundamental, v_{11}, which we predict at 1269 cm^{-1}. The only observation of v_{12} appears to be by Chettur and Snelson[14] at 1187 cm^{-1}. This agrees much better with our prediction (1190 cm^{-1}) for the CC_3 symmetric bend fundamental. To corroborate this, we predict $v_{12} + v_{13}$ at 2326 cm^{-1} and $v_{11} + v_{13}$ at 2405 cm^{-1}; Neumark and co-workers' experimental band at 2382 cm^{-1} agrees better with the latter.

The last set of measured $\tilde{X}$ bands were those from Chettur and Snelson, corresponding to various bends and stretches below 1000 cm^{-1}. We find, for each experimental band, a predicted frequency in close agreement (Tables 7.20-7.21). Moreover, the isotopic shifts are consistent with the amount of O-O motion in each normal mode.[14]

7.3.4.6. Comparison to $\tilde{A}^2A'$ Experimental Fundamentals

Neumark and co-workers[25] also measured $\tilde{A}$-state fundamentals. They found, for the O-O stretch, a frequency of 939 ± 14 cm^{-1}, in excellent agreement with the 934 ± 10 cm^{-1} reported by Sharp, Rupper, and Miller.[22] Our prediction of 959 cm^{-1} deviates somewhat from these. We have already discussed the difficulties associated with accurately modeling the O-O stretching degree of freedom.

This transition represents the most significant disagreement between our predicted values and experiment. Notably, similar issues have been observed for the methyl and ethyl peroxy radicals, despite their relative simplicity and treatments with higher levels of theory. For the methyl peroxy radical, normal mode analysis does not predict a localized O-O stretch, but the predicted values of the $\tilde{A}$ symmetric and antisymmetric C-O-O stretches deviate from gas-phase measurements by 12 cm^{-1} and 14 cm^{-1}, respectively. For the ethyl peroxy radical, the $\tilde{X}$-state O-O stretch deviates by at least 11 cm^{-1} (assignment of O-O is ambiguous) from the gas phase value. This is unfortunate, as the O-O stretch is among the most easily measured transitions for the $\tilde{X}$ and $\tilde{A}$ states due to its high Franck-Condon activity (in both direct vibronic absorption and anion photoelectron spectroscopies). Additionally, it is sensitive to the peroxy radical R-group and can serve as another valuable identification aid (in addition to the band origin).

Sharp, Rupper, and Miller also assigned a transition at 481 ± 10 cm^{-1} to the $\tilde{A}$-state C-O-O bending fundamental.[22] For this, we find good agreement with our predicted ν18 fundamental of 490 cm^{-1}. This mode is reasonably described as C-O-O bending. At 340 ± 10 cm^{-1} they assigned a band as C-C-C bending; this agrees with our prediction of 347 cm^{-1}.

The only other measured $\tilde{A}$ transitions were 244 cm^{-1} from Neumark and co-workers[25] and two 240 cm^{-1} bands from Sharp, Rupper, and Miller[22] and Lineberger, Ellison, and co-workers.[24] Neumark and co-workers did not offer a definitive assignment for their band; they stated that either v_{21} or v_{22} was reasonable based on their Franck–Condon simulations. Our theory is also not conclusive; while there is not a strongly interacting Fermi triad in this range (as in the $\tilde{X}$ state), our predicted v_{21}, v_{22}, and v_{37} frequencies all are in good agreement with this mode. We find assignment to v_{37} less likely since it is an antisymmetric vibration.[22] These two bands do not necessarily have to correspond to the same transition, as the two types of experiments do not light up exactly the same vibrations. Hence, in agreement with Neumark and co-workers, we would assign these two observed transitions to either v_{21} or v_{22}.

7.3.4.7. Experimental Bands Without Clear Assignments

Parkes and Donovan[12-13] measured the first infrared spectrum of the *tert*-butyl peroxy radical in the gas phase. They observed two bands at 693.7 ± 0.5 and 760 ± 2 cm^{-1}. Neither of these transitions align with our predicted vibrational fundamentals or with bands measured in subsequent experiments. Our prediction for v_{17} (at 737 cm^{-1}) comes closest to the latter band; however, the respective 740 ± 26 cm^{-1} and 730 ± 2 cm^{-1} bands of Neumark and co-workers[25] and Chettur and Snelson,[14] taken with the theoretical predictions of this research, make Parkes and Donovan's assignment of this band to *tert*-butyl peroxy tenuous. It is possible that the bands instead belong to the product of the photolysis + oxidation process carried out on azoisobutane.

Lastly, we discuss an $\tilde{X}$ band at 1139 cm^{-1} measured by Chettur and Snelson. This value only aligns with our predicted 1138 cm^{-1} frequency for the O-O stretch; however, as discussed earlier, we agree with the conclusions of Chettur and Snelson that their 1124 cm^{-1} band corresponds to the O-O stretch. This is most clearly seen by the isotopic shifts Chettur and Snelson measured for the 1139 cm^{-1} and 1124 cm^{-1} bands. Upon $^{18}O_2$ substitution, the 1139 cm^{-1} shifts by only 2 cm^{-1}, while the 1124 cm^{-1} band shifts by 54 cm^{-1}. Unfortunately, this makes one wonder exactly what the 1138 cm^{-1} band corresponds to. An intense combination or overtone band is the first reasonable guess; however, there are many possibilities that could explain this, and assigning a certain combination or overtone transition is not possible, given the data.

7.4. Conclusions

High accuracy theoretical predictions have been made for the fundamental vibrational transitions of the $\tilde{X}^2A''$ and $\tilde{A}^2A'$ electronic states of *tert*-butyl peroxy radical. A UHF-CCSD(T)/ANO1//UHF-CCSD(T)/ANO0 peroxy torsional potential shows three equivalent minima for both electronic states, in which the peroxy moiety is staggered with respect to the methyl groups. An eclipsed structure corresponds to a transition state at an energy relative to the

minimum of 828 cm^{-1} and 1523 cm^{-1} in the $\tilde{X}$ and $\tilde{A}$ electronic states, respectively. Equilibrium structures were obtained for the $\tilde{X}$ and $\tilde{A}$ electronic states at the UHF-CCSD(T)/ANO1 level of theory. The optimized geometries show that the $\tilde{A} \leftarrow \tilde{X}$ [n-π^*] transition induces appreciable changes in the peroxy moiety. The O-O bond elongates (Δr_e = +0.074), and the C-O bond contracts (Δr_e = -0.017). These shifts are very similar to those of methyl peroxy radical[26] and ethyl peroxy radicals.[29] The $\tilde{A} \leftarrow \tilde{X}$ origin transition (T_0) was computed by extrapolating CCSD(T)/cc-pVXZ energies to the complete basis set limit and adding auxiliary corrections for full triples and perturbative quadruple excitations, core-correlation, relativistic effects, and the Born-Oppenheimer approximation. We predict a T_0 value of 7738 cm^{-1}, which is in excellent agreement with the transitions measured by Sharp, Rupper, and Miller[22] (7755 ± 10 cm^{-1}); Neumark and co-workers[25] (7744 ± 19 cm^{-1}); and Ellison, Lineberger, and co-workers[24] (7799 ± 90 cm^{-1}). Comparison with the values for the methyl peroxy radical (7374 cm^{-1})[26] and ethyl peroxy radical (7363 and 7583 cm^{-1})[29] reflect the trends found in the previous computations of Sharp, Rupper, and Miller.[11] Anharmonic vibrational frequencies for both electronic states were computed using VPT2 + K in conjunction with a hybrid, semi-diagonal quartic force field. Fourteen of the predicted fundamentals (for both the $\tilde{X}$ and $\tilde{A}$ states) could be directly matched to measured transitions. Among these transitions, there was good agreement between theory and experiment. The most notable discrepancy was the $\tilde{A}$-state O-O stretch, which deviated by 25 cm^{-1}. This is ascribed to a combination of basis set incompleteness error and normal mode mismatching, impacting the force constants associated with the O-O stretching and the O-O and C-O stretching degrees of freedom, respectively. The two transitions, at 693 and 760 cm^{-1}, measured in the gas phase infrared study, deviate at least 44 cm^{-1} and 23 cm^{-1} from our fundamentals, respectively, and do not have obvious assignments.

References

(1) Pilling, M. J.; Smith, I. W. M. *Modern Gas Kinetics: Theory, Experiment, and Application*; Blackwell Scientific Publications: Oxford, UK, 1987.

(2) Robertson, S. H.; Seakins, P. W.; Pilling, M. J. *Low-Temperature Combustion and Autoignition*; Elsevier: San Diego, CA, 1997.

(3) Wallington, T.; Nielsen, O.; Sehested, J. In *Reactions of Organic Peroxy Radicals in the Gas Phase*, Alfassi, Z., Ed. Wiley: 1997; pp 113-172.

(4) Rupper, P.; Sharp, E. N.; Tarczay, G.; Miller, T. A. Investigation of Ethyl Peroxy Radical Conformers via Cavity Ringdown Spectroscopy of the Ã←X̃ Electronic Transition. *J. Phys. Chem. A* **2007**, *111*, 832-840.

(5) Wallington, T. J.; Dagaut, P.; Kurylo, M. J. Ultraviolet-Absorption Cross-Sections and Reaction-Kinetics and Mechanisms for Peroxy-Radicals in the Gas-Phase. *Chem. Rev.* **1992**, *92*, 667-710.

(6) Lightfoot, P. D.; Cox, R. A.; Crowley, J. N.; Destriau, M.; Hayman, G. D.; Jenkin, M. E.; Moortgat, G. K.; Zabel, F. Organic Peroxy-Radicals - Kinetics, Spectroscopy and Tropospheric Chemistry. *Atmos. Environ., Part A* **1992**, *26*, 1805-1961.

(7) Tyndall, G. S.; Cox, R. A.; Granier, C.; Lesclaux, R.; Moortgat, G. K.; Pilling, M. J.; Ravishankara, A. R.; Wallington, T. J. Atmospheric Chemistry of Small Organic Peroxy Radicals. *J. Geophys. Res.: Atmos.* **2001**, *106*, 12157-12182.

(8) Maric, D.; Crowley, J. N.; Burrows, J. P. Application of a Gaussian Distribution Function to Describe Molecular UV-Visible Absorption Continua .2. The UV Spectra of RO_2• Radicals. *J. Phys. Chem. A* **1997**, *101*, 2561-2567.

(9) Jafri, J. A.; Phillips, D. H. Ground and Lower Excited-States of Methyl Peroxy, CH_3O_2, Radical - A Computational Investigation. *J. Am. Chem. Soc.* **1990**, *112*, 2586-2590.

(10) Nielsen, O. J.; Wallington, T. J. *Ultraviolet Absorption Spectra of Peroxy Radicals in the Gas Phase*; John Wiley & Sons: Chichester, UK, 1997.

(11) Sharp, E. N.; Rupper, P.; Miller, T. A. The Structure and Spectra of Organic Peroxy Radicals. *Phys. Chem. Chem. Phys.* **2008**, *10*, 3955-3981.

(12) Parkes, D. A.; Donovan, R. J. Infrared-Absorption Spectrum of *tert*-Butylperoxy Radicals in Gas-Phase. *Chem. Phys. Lett.* **1975**, *36*, 211-214.

(13) Parkes, D. A.; Donovan, R. J. *Chem. Phys. Lett.* **1976**, *37*, 198.

(14) Chettur, G.; Snelson, A. Alkylperoxy and Alkyl Radicals .V. Infrared-Spectra and Ultraviolet Photolysis of *t*-$C_4H_9O_2$ Radicals in Argon Plus Oxygen Matrices. *J. Phys. Chem.* **1987**, *91*, 5873-5875.

(15) Hunziker, H. E.; Wendt, H. R. Electronic Absorption-Spectra of Organic Peroxyl Radicals in Near-Infrared. *J. Chem. Phys.* **1976**, *64*, 3488-3490.

(16) Chung, C. Y.; Cheng, C. W.; Lee, Y. P.; Liao, H. Y.; Sharp, E. N.; Rupper, P.; Miller, T. A. Rovibronic Bands of the $\tilde{A} \leftarrow \tilde{X}$ Transition of CH_3OO and CD_3OO Detected with Cavity Ringdown Absorption near 1.2-1.4 μm. *J. Chem. Phys.* **2007**, *127*, 044311.

(17) Wu, S.; Dupre, P.; Rupper, P.; Miller, T. A. The vibrationless $\tilde{A} \leftarrow \tilde{X}$ Transition of the Jet-Cooled Deuterated Methyl Peroxy Radical CD_3O_2 by Cavity Ringdown Spectroscopy. *J. Chem. Phys.* **2007**, *127*, 224305.

(18) Atkinson, D. B.; Spillman, J. L. Alkyl Peroxy Radical Kinetics Measured Using Near-Infrared CW-Cavity Ring-Down Spectroscopy. *J. Phys. Chem. A* **2002**, *106*, 8891-8902.

(19) Pushkarsky, M. B.; Zalyubovsky, S. J.; Miller, T. A. Detection and Characterization of Alkyl Peroxy Radicals Using Cavity Ringdown Spectroscopy. *J. Chem. Phys.* **2000**, *112*, 10695-10698.

(20) Glover, B. G.; Miller, T. A. Near-IR Cavity Ringdown Spectroscopy and Kinetics of the Isomers and Conformers of the Butyl Peroxy Radical. *J. Phys. Chem. A* **2005**, *109*, 11191-11197.

(21) Li, C. Y.; Agarwal, J.; Wu, C. H.; Allen, W. D.; Schaefer, H. F. Intricate Internal Rotation Surface and Fundamental Infrared Transitions of the *n*-Propyl Radical. *J. Phys. Chem. B* **2015**, *119*, 728-735.

(22) Sharp, E. N.; Rupper, P.; Miller, T. A. Observation of the $\tilde{A}$ - $\tilde{X}$ Electronic Transition of the Isomers and Conformers of Pentyl Peroxy Radical Using Cavity Ringdown Spectroscopy. *J. Phys. Chem. A* **2008**, *112*, 1445-1456.

(23) Blanksby, S. J.; Ramond, T. M.; Davico, G. E.; Nimlos, M. R.; Kato, S.; Bierbaum, V. M.; Lineberger, W. C.; Ellison, G. B.; Okumura, M. Negative-Ion Photoelectron

Spectroscopy, Gas-Phase Acidity, and Thermochemistry of the Peroxyl Radicals CH_3OO and CH_3CH_2OO. *J. Am. Chem. Soc.* **2001**, *123*, 9585-9596.

(24) Clifford, E. P.; Wenthold, P. G.; Gareyev, R.; Lineberger, W. C.; DePuy, C. H.; Bierbaum, V. M.; Ellison, G. B. Photoelectron Spectroscopy, Gas Phase Acidity, and Thermochemistry of *tert*-Butyl Hydroperoxide: Mechanisms for the Rearrangement of Peroxyl Radicals. *J. Chem. Phys.* **1998**, *109*, 10293-10310.

(25) DeVine, J. A.; Weichman, M. L.; Babin, M. C.; Neumark, D. M. Slow Photoelectron Velocity-Map Imaging of Cold *tert*-Butyl Peroxide. *J. Chem. Phys.* **2017**, *147*, 013915.

(26) Copan, A. V.; Schaefer, H. F.; Agarwal, J. Examining the Ground and First Excited States of Methyl Peroxy Radical with High-Level Coupled-Cluster Theory. *Mol. Phys.* **2015**, *113*, 2992-2998.

(27) Agarwal, J.; Simmonett, A. C.; Schaefer, H. F. Fundamental Vibrational Frequencies and Spectroscopic Constants for the Methylperoxyl Radical, CH_3O_2, and Related Isotopologues $^{13}CH_3OO$, $CH_3{}^{18}O{}^{18}O$, and CD_3OO. *Mol. Phys.* **2012**, *110*, 2419-2427.

(28) Morrison, A. M.; Agarwal, J.; Schaefer, H. F.; Douberly, G. E. Infrared Laser Spectroscopy of the CH_3OO Radical Formed from the Reaction of CH_3 and O_2 within a Helium Nanodroplet. *J. Phys. Chem. A* **2012**, *116*, 5299-5304.

(29) Launder, A. M.; Turney, J. M.; Agarwal, J.; Schaefer, H. F. Ethylperoxy Radical: Approaching Spectroscopic Accuracy via Coupled-Cluster Theory. *Phys. Chem. Chem. Phys.* **2017**, *19*, 15715-15723.

(30) Hoobler, P. R.; Turney, J. M.; Schaefer, H. F. Investigating the Ground-State Rotamers of *n*-Propylperoxy Radical. *J. Chem. Phys.* **2016**, *145*, 174301.

(31) Copan, A. V.; Wiens, A. E.; Nowara, E. M.; Schaefer, H. F.; Agarwal, J. Peroxyacetyl Radical: Electronic Excitation Energies, Fundamental Vibrational Frequencies, and Symmetry Breaking in the First Excited State. *J. Chem. Phys.* **2015**, *142*, 054303.

(32) Elliott, S. N.; Turney, J. M.; Schaefer, H. F. The *cis*- and *trans*-Formylperoxy Radical: Fundamental Vibrational Frequencies and Relative Energies of the $\tilde{X}^2A''$ and $\tilde{A}^2A'$ States. *Rsc Adv* **2015**, *5*, 107254-107265.

(33) Moore, K. B.; Turney, J. M.; Schaefer, H. F. The Fate of the *tert*-Butyl Radical in Low-Temperature Autoignition Reactions. *J. Chem. Phys.* **2017**, *146*, 194304.

(34) Knowles, P. J.; Hampel, C.; Werner, H. J. Coupled-Cluster Theory for High-Spin, Open-Shell Reference Wave-Functions (vol 99, pg 5219, 1993). *J. Chem. Phys.* **2000**, *112*, 3106.

(35) Knowles, P. J.; Hampel, C.; Werner, H. J. Coupled-Cluster Theory for High-Spin, Open-Shell Reference Wave-Functions. *J. Chem. Phys.* **1993**, *99*, 5219-5227.

(36) Watts, J. D.; Gauss, J.; Bartlett, R. J. Coupled-Cluster Methods with Noniterative Triple Excitations for Restricted Open-Shell Hartree-Fock and Other General Single Determinant Reference Functions - Energies and Analytical Gradients. *J. Chem. Phys.* **1993**, *98*, 8718-8733.

(37) J. F. Stanton, J. Gauss, L. Cheng, M. E. Harding, D. A. Matthews, and P. G. Szalay, CFOUR, Coupled-cluster techniques for computational chemistry, a quantum-chemical program package, With contributions from A. A. Auer, R. J. Bartlett, U. Benedikt, C. Berger, D. E. Bernholdt, Y. J. Bomble, O. Christiansen, F. Engel, R. Faber, M. Heckert, O. Heun, M. Hilgenberg, C. Huber, T.-C. Jagau, D. Jonsson, J. Jusélius, T. Kirsch, K. Klein, W. J. Lauderdale, F. Lipparini, T. Metzroth, L. A. Mück, D. P. O'Neill, D. R. Price, E. Prochnow, C. Puzzarini, K. Ruud, F. Schiffmann, W. Schwalbach, C. Simmons, S. Stopkowicz, A. Tajti, J. Vázquez, F. Wang, J. D. Watts and the integral packages MOLECULE (J. Almlöf and P. R. Taylor), PROPS (P. R. Taylor), ABACUS (T. Helgaker, H. J. Aa. Jensen, P. Jørgensen, and J. Olsen), and ECP routines by A. V. Mitin and C. van Wüllen, for the current version, see http://www.cfour.de.

(38) Almlöf, J.; Taylor, P. R. General Contraction of Gaussian-Basis Sets .I. Atomic Natural Orbitals for 1st-Row and 2nd-Row Atoms. *J. Chem. Phys.* **1987**, *86*, 4070-4077.

(39) McCaslin, L.; Stanton, J. Calculation of Fundamental Frequencies for Small Polyatomic Molecules: A Comparison Between Correlation Consistent and Atomic Natural Orbital Basis Sets. *Mol. Phys.* **2013**, *111*, 1492-1496.

(40) Schuurman, M. S.; Muir, S. R.; Allen, W. D.; Schaefer, H. F. Toward Subchemical Accuracy in Computational Thermochemistry: Focal Point Analysis of the Heat of Formation of NCO and H,N,C,O Isomers. *J. Chem. Phys.* **2004**, *120*, 11586-11599.

(41) Gonzales, J. M.; Pak, C.; Cox, R. S.; Allen, W. D.; Schaefer, H. F.; Csaszar, A. G.; Tarczay, G. Definitive Ab Initio Studies of Model S_N2 reactions CH_3X+F^- (X = F, Cl, CN, OH, SH, NH_2, PH_2). *Chem. - Eur. J.* **2003**, *9*, 2173-2192.

(42) Csaszar, A. G.; Allen, W. D.; Schaefer, H. F. In Pursuit of the Ab Initio Limit for Conformational Energy Prototypes. *J. Chem. Phys.* **1998**, *108*, 9751-9764.

(43) East, A. L. L.; Allen, W. D. The Heat of Formation of NCO. *J. Chem. Phys.* **1993**, *99*, 4638-4650.

(44) Dunning, T. H. Gaussian-Basis Sets for Use in Correlated Molecular Calculations .I. The Atoms Boron Through Neon and Hydrogen. *J. Chem. Phys.* **1989**, *90*, 1007-1023.

(45) Karton, A.; Martin, J. M. L. Comment on: "Estimating the Hartree-Fock Limit from Finite Basis Set Calculations" Jensen F (2005) Theor Chem Acc 113, 267. *Theor. Chem. Acc.* **2006**, *115*, 330-333.

(46) Helgaker, T.; Klopper, W.; Koch, H.; Noga, J. Basis-Set Convergence of Correlated Calculations on Water. *J. Chem. Phys.* **1997**, *106*, 9639-9646.

(47) Feller, D. Application of Systematic Sequences of Wave-Functions to the Water Dimer. *J. Chem. Phys.* **1992**, *96*, 6104-6114.

(48) Peterson, K. A.; Woon, D. E.; Dunning, T. H. Benchmark Calculations with Correlated Molecular Wave-Functions .IV. The Classical Barrier Height of the $H+H_2 \rightarrow H_2+H$ Reaction. *J. Chem. Phys.* **1994**, *100*, 7410-7415.

(49) Schwenke, D. W. The Extrapolation of One-Electron Basis Sets in Electronic Structure Calculations: How It Should Work and How It Can Be Made to Work. *J. Chem. Phys.* **2005**, *122*, 014107.

(50) Martin, J. M. L. Ab Initio Total Atomization Energies of Small Molecules - Towards the Basis Set Limit. *Chem. Phys. Lett.* **1996**, *259*, 669-678.

(51) Hehre, W. J.; Ditchfield, R.; Pople, J. A. Self-Consistent Molecular-Orbital Methods .XII. Further Extensions of Gaussian-Type Basis Sets for Use in Molecular-Orbital Studies of Organic-Molecules. *J. Chem. Phys.* **1972**, *56*, 2257-2261.

(52) Harihara.Pc; Pople, J. A. Influence of Polarization Functions on Molecular-Orbital Hydrogenation Energies. *Theor. Chim. Acta* **1973**, *28*, 213-222.

(53) Woon, D. E.; Dunning, T. H. Gaussian-Basis Sets for Use in Correlated Molecular Calculations .V. Core-Valence Basis-Sets for Boron Through Neon. *J. Chem. Phys.* **1995**, *103*, 4572-4585.

(54) Handy, N. C.; Yamaguchi, Y.; Schaefer, H. F. The Diagonal Correction to the Born-Oppenheimer Approximation - Its Effect on the Singlet-Triplet Splitting of CH_2 and Other Molecular Effects. *J. Chem. Phys.* **1986**, *84*, 4481-4484.

(55) Sellers, H.; Pulay, P. The Adiabatic Correction to Molecular-Potential Surfaces in the SCF Approximation. *Chem. Phys. Lett.* **1984**, *103*, 463-465.

(56) Tarczay, G.; Csaszar, A. G.; Klopper, W.; Quiney, H. M. Anatomy of Relativistic Energy Corrections in Light Molecular Systems. *Mol. Phys.* **2001**, *99*, 1769-1794.

(57) Klopper, W. Simple Recipe for Implementing Computation of First-Order Relativistic Corrections to Electron Correlation Energies in Framework of Direct Perturbation Theory. *J. Comput. Chem.* **1997**, *18*, 20-27.

(58) Schuurman, M. S.; Allen, W. D.; Schleyer, P. V.; Schaefer, H. F. The Highly Anharmonic BH_5 Potential Energy Surface Characterized in the Ab Initio Limit. *J. Chem. Phys.* **2005**, *122*, 104302.

(59) MRCC, a quantum chemical program suite written by M. Kállay, Z. Rolik, J. Csontos, P. Nagy, G. Samu, D. Mester, I. Ladjánszki, L. Szegedy, B. Ladóczki, K. Petrov, M. Farkas, B. Hégely. See also. Z. Rolik, L. Szegedy, I. Ladjánszki, B. Ladóczki, and M. Kállay,. J. Chem. Phys. **139**, 094105 (2013), as well as: www.mrcc.hu.

(60) Rolik, Z.; Szegedy, L.; Ladjanszki, I.; Ladoczki, B.; Kallay, M. An Efficient Linear-Scaling CCSD(T) Method Based on Local Natural Orbitals. *J. Chem. Phys.* **2013**, *139*, 094105.

(61) Clabo, D. A.; Allen, W. D.; Remington, R. B.; Yamaguchi, Y.; Schaefer, H. F. A Systematic Study of Molecular Vibrational Anharmonicity and Vibration-Rotation Interaction by Self-Consistent-Field Higher-Derivative Methods - Asymmetric-Top Molecules. *Chem. Phys.* **1988**, *123*, 187-239.

(62) Watts, J. D.; Gauss, J.; Bartlett, R. J. Open-Shell Analytical Energy Gradients for Triple Excitation Many-Body, Coupled-Cluster Methods - MBPT(4), CCSD+T(CCSD), CCSD(T), and QCISD(T). *Chem. Phys. Lett.* **1992**, *200*, 1-7.

(63) Breidung, J.; Thiel, W.; Gauss, J.; Stanton, J. F. Anharmonic Force Fields from Analytic CCSD(T) Second Derivatives: HOF and F_2O. *J. Chem. Phys.* **1999**, *110*, 3687-3696.

(64) Rosnik, A. M.; Polik, W. F. VPT2+K Spectroscopic Constants and Matrix Elements of the Transformed Vibrational Hamiltonian of a Polyatomic Molecule with Resonances Using Van Vleck Perturbation Theory. *Mol. Phys.* **2014**, *112*, 261-300.

(65) Matthews, D. A.; Vazquez, J.; Stanton, J. F. Calculated Stretching Overtone Levels and Darling-Dennison Resonances in Water: A Triumph of Simple Theoretical Approaches. *Mol. Phys.* **2007**, *105*, 2659-2666.

(66) Martin, J. M. L.; Lee, T. J.; Taylor, P. R.; Francois, J. P. The Anharmonic-Force Field of Ethylene, C_2H_4, by Means of Accurate Ab Initio Calculations. *J. Chem. Phys.* **1995**, *103*, 2589-2602.

(67) Franke, P. R.; Tabor, D. P.; Moradi, C. P.; Douberly, G. E.; Agarwal, J.; Schaefer, H. F.; Sibert, E. L. Infrared Laser Spectroscopy of the *n*-Propyl and *i*-Propyl Radicals: Stretch-Bend Fermi Coupling in the Alkyl CH Stretch Region. *J. Chem. Phys.* **2016**, *145*, 224304.

(68) Raston, P. L.; Agarwal, J.; Turney, J. M.; Schaefer, H. F.; Douberly, G. E. The Ethyl Radical in Superfluid Helium Nanodroplets: Rovibrational Spectroscopy and Ab Initio Computations. *J. Chem. Phys.* **2013**, *138*, 194303.

(69) Barone, V. Anharmonic Vibrational Properties by a Fully Automated Second-Order Perturbative Approach. *J. Chem. Phys.* **2005**, *122*, 014108.

(70) Estep, M. L.; Schaefer, H. F. The Methylsulfinyl Radical CH_3SO Examined. *Phys. Chem. Chem. Phys.* **2016**, *18*, 22293-22299.

(71) Werner, H. J.; Knowles, P. J. A 2nd Order Multiconfiguration SCF Procedure with Optimum Convergence. *J. Chem. Phys.* **1985**, *82*, 5053-5063.

(72) Busch, T.; Degli Esposti, A.; Werner, H. J. Analytical Energy Gradients for Multiconfigurational Self-Consistent Field Wave-Functions with Frozen Core Orbitals. *J. Chem. Phys.* **1991**, *94*, 6708-6715.

(73) Just, G. M. P.; McCoy, A. B.; Miller, T. A. Effect of Methyl Rotation on the Electronic Spectrum of the Methyl Peroxy Radical. *J. Chem. Phys.* **2007**, *127*, 044310.

(74) Thomas, P. S.; Miller, T. A. Cavity Ringdown Spectroscopy of the NIR $\tilde{A}$ - $\tilde{X}$ Electronic Transition of Allyl Peroxy Radical (H_2C=CH-CH_2OO·). *Chem. Phys. Lett.* **2010**, *491*, 123-131.

(75) Thomas, P. S.; Miller, T. A. The $\tilde{A}$ - $\tilde{X}$ Electronic Absorption of Cyclopentadienyl Peroxy Radical (*c*-C_5H_5OO·): A Cavity Ringdown Spectroscopic and Computational Study. *Chem. Phys. Lett.* **2011**, *514*, 196-201.

(76) Crawford, T. D.; Stanton, J. F.; Allen, W. D.; Schaefer, H. F. Hartree-Fock Orbital Instability Envelopes in Highly Correlated Single-Reference Wave Functions. *J. Chem. Phys.* **1997**, *107*, 10626-10632.

(77) Franke, P. R.; Brice, J. T.; Moradi, C. P.; Schaefer, H. F.; Douberly, G. E. Ethyl + O_2 in Helium Nanodroplets: Infrared Spectroscopy of the Ethylperoxy Radical. *J. Phys. Chem. A* **2019**, *123*, 3558-3568.

CHAPTER 8

INFRARED PHOTODISSOCIATION SPECTROSCOPY AND ANHARMONIC VIBRATIONAL STUDY OF THE HO_4^+ MOLECULAR ION[1]

[1] Reprinted from Franke, P.R.; Duncan, M.A.; Douberly, G.E. 2020. *Journal of Chemical Physics*. 152:174309 DOI: 10.1063/5.0005975, AIP Publishing.

Molecular cations of HO_4^+ and DO_4^+ are produced in a supersonic expansion. They are mass-selected, and infrared photodissociation spectra of these species are measured with the aid of argon-tagging. Although previous theoretical studies have modeled these systems as proton-bound dimers of molecular oxygen, infrared spectra have free OH stretching bands, suggesting other isomeric structures. As a consequence, we undertook extensive computational studies. Our conformer search used a composite method based on an economical combination of single- and multi-reference theories. Several conformers were located on the quintet, triplet, and singlet surfaces, spanning in energy only a few thousand wavenumbers. Most of the singlet and triplet conformers have pronounced multiconfigurational character. Previously unidentified covalent-like structures (H-O-O-O-O) on the singlet and triplet surfaces likely represent the global minima. In our experiments, HO_4^+ is formed in a relatively hot environment, and similar experiments have been shown capable of producing multiple conformers in low-lying electronic states. None of the predicted HO_4^+ isomers can be ruled out *a priori* based on energetic arguments. We interpret our argon-tagged spectra with Second-Order Vibrational Perturbation Theory with Resonances (VPT2+K). The presence of one or more covalent-like isomers is the only reasonable explanation for the spectral features observed.

8.1. Introduction

Proton-Bound Dimers (PBD) are of fundamental interest, as they serve as useful model systems for proton transfer.[1] The structural motif of a shared proton is perhaps best known in the Zundel form of protonated water clusters.[2-3] In reactions in the Interstellar Medium (ISM), neutral systems are protonated by the abundant H_3^+ ion.[4-5] Then the reaction between the protonated monomer and a neutral typically proceeds barrierlessly.[6-11] In many cases, a PBD represents the thermodynamically most favorable reaction product. A characteristic spectroscopic feature of a PBD is the shared proton stretch or proton shuttle vibration. This transition is expected to be strongly infrared active and to show up at around 1000 cm^{-1}, when the proton is shared by

equivalent monomers.[12] The frequency can be greatly different when the monomers are not equivalent. In this case, it has been shown to correlate with the difference in proton affinities of the monomers.[12-13]

Proton-bound dimers of molecular hydrogen, nitrogen, and carbon-dioxide have been studied in our laboratory, using Infrared Photodissociation (IRPD) spectroscopy.[14-17] We have measured PBD formation in larger systems, such as the protonated formaldehyde and acetone dimers and the protonated dimers and trimers of ethylenediamine.[18-20] Of these, we see evidence for PBD formation under our experimental conditions, except in the case of formaldehyde; nevertheless, formaldehyde PBD is predicted to be the global minimum on its potential surface. Other laboratories have contributed numerous IRPD studies of protonated dimers, including ethanol and various ether PBDs.[12, 21-23] The smallest PBD species consist of rare gas dimers, such as protonated argon and helium dimers.[24-25] These triatomic PBD have been the subjects of recent theoretical attention.[26-27] They are excellent theoretical model systems for the proton shuttle, whose vibrational problems can be routinely tackled with exact variational methods. The structurally analogous bihalide anions have a long theoretical history as well.[28]

The HO_4^+ potential energy surface encompasses the proton-bound dimer of molecular oxygen; however, this system has received relatively little experimental or theoretical attention. It has been postulated by Hernández-Lamoneda and coworkers that HO_4^+ may act as a sink for oxygen in the ISM, providing a solution to the so-called oxygen problem.[29-30] However the authors admitted that the lack of evidence for HO_2^+ in the ISM makes this unlikely, as it leaves no viable mechanism for HO_4^+ formation.[31] This is additionally complicated by the fact that reaction between O_2 and H_3^+ is known to be mildly endothermic and to possess an activation barrier of 80 cm^{-1}.[4, 32-34] HO_2^+, however, has been observed in the D-region of the ionosphere, and a replacement reaction with atmospheric N_2 has been discussed.[35] Little attention appears to have been paid to the reaction between HO_2^+ and atmospheric O_2. Another possible formation

mechanism is the reaction between O_2^+ and HO_2, both of which are known to exist in the upper atmosphere.[35-36] A third option is $O_3 + OH^+$; both reactants have been detected in the ISM.[37-38] It is therefore plausible that HO_4^+ may form as an intermediate in atmospheric ion chemistry or in the ISM.

The mass 65 ion corresponding to HO_4^+ has been detected in mass spectrometry experiments.[39-40] Recently, in helium droplets, it was a particularly abundant fragmentation product of ionized droplets containing many H_2 and O_2 molecules.[39] Prior to this, the mass 65 ion was also detected in the gas phase in a high-pressure mass spectrometry study.[40] The authors performed a van't Hoff analysis to determine thermodynamic quantities for clustering reactions of O_2 with a proton, finding the clustering of two O_2 molecules to be highly favorable in terms of enthalpy and free energy, much more so than clustering of CO or N_2. They also conducted the earliest *ab initio* computations on HO_4^+, at the HF/STO-3G level of theory, finding C_{2h} PBD structures in the quintet and singlet multiplicities, the singlet lying nearly 100 kcal/mol higher in energy than the quintet.

The earliest dedicated theoretical study of HO_4^+ by Leszczynski and coworkers focused on the high spin quintet state.[41] A C_2 minimum energy structure was found for HO_4^+ at various levels of theory: UHF, MP2, B3LYP, and CASSCF combined with the aug-cc-pVDZ and aug-cc-pVTZ basis sets. This is best described as a proton-bound dimer of molecular oxygen. Addition of further O_2 was found to solvate the HO_4^+ core ion. Two recent computational studies by Hernández-Lamoneda and coworkers provided the first predictions for the triplet isomers of the system and refined predictions for the singlet surface.[29-30] The authors discussed the severe multiconfigurational nature of the singlet and triplet PBD isomers, applying CASSCF and MRCI to predict equilibrium structures, energetics, harmonic infrared transitions, and various 1D potential energy curves. They determined that the quintet C_2 PBD identified by Leszczynski and coworkers represents the highest energy conformer. Somewhat lower in energy were two triplet

PBD isomers, with C_{2h} and C_{2v} point group symmetry, and lowest were the singlet PBD isomers. In the singlet multiplicity, C_{2h} and C_{2v} PBD structures analogous to the triplets were identified; additionally, a cyclic PBD species was found to be the global minimum.

No spectroscopy has been reported for HO_4^+. In this study we present the first vibrational spectroscopy results for this system in the region between 900 and 3600 cm^{-1}. We support our assignments with *ab initio* computations. We also report the most complete conformer search and highest quality theoretical structures thus far for this challenging system. Our study reveals several previously unidentified isomers of HO_4^+, which are low in energy and cannot be described as proton-bound dimers (see Section 8.3.2).

8.2. Methods

8.2.1. Infrared Photodissociation Spectroscopy

Ions are formed in a pulsed electric discharge of a few percent of O_2 and H_2 seeded in argon. The molecular beam is skimmed, and cations are extracted orthogonally into a reflectron TOF mass spectrometer. HO_4^+-Ar ions are mass-selected with pulsed deflection plates prior to entering the reflectron. An infrared OPO (LaserVision) is directed into the turning point of the reflectron region. When resonant excitation of the mass-selected ion imparts sufficient internal energy to eliminate an argon atom, the signal associated with the HO_4^+ ion appears on a zero background. A mid-infrared action spectrum is measured by monitoring the HO_4^+ ion signal as the laser wavelength is tuned from 900 to 4000 cm^{-1}. Resolution is limited by the linewidth of the laser system (1-2 cm^{-1}), and intensities are not normalized to laser power. Previous investigations into the spectroscopy of small organic cations, including proton-bound dimers, have been conducted using a similar methodology.[14-15, 18, 42] For a detailed review, see Reference 43.

8.2.2. Electronic Structure and Thermochemistry

Single-reference coupled cluster calculations, including semi-diagonal quartic force fields, were computed with the CFOUR 2.1 package.[44] Multi-reference energy computations, with

CASSCF and NEVPT2-F12, and single-reference UHF-CCSD(T)-F12 energy computations were performed with ORCA 4.0.1.2.[45-49] All optimizations and harmonic frequency calculations used CFOUR for generation of symmetry displacements. When necessary, energies for composite methods were determined by running multiple jobs at each displaced geometry and summing and differencing the appropriate energies, depending on the definition of the composite method. Then the final composite energies were communicated to CFOUR. A similar procedure was used in a recent article.[50]

All isomers of HO_4^+, without argon tags, were described with a composite single-reference/multi-reference approach, based on a previously tested methodology.[30, 51-53] These kinds of methods compute the energy of the single-configurational quintet state with the reliable CCSD(T) method and then add the energy gap between the quintet and either the singlet or triplet, evaluated by multi-reference approaches. A similar composite approach has been applied to determine relative energies for HO_4^+ proton-bound dimers.[30] Here, we apply a composite method, defined as,

$$E(\text{comp.}) = E(\text{CCSD(T)-F12/cc-pVDZ-F12}) + \delta[E(\text{CASSCF(16,13)/aug-cc-pVTZ})] \quad (8.1)$$

to determine the equilibrium geometries and harmonic frequencies of the entire set of HO_4^+ isomers, including covalent-like conformers. Single point energies were computed at the optimized structures by replacing CASSCF/aug-cc-pVTZ with NEVPT2-F12/cc-pVDZ-F12, in the composite method. In the special case of the quintet isomer, the multireference energy difference component is zero, so it is simply described with UHF-CCSD(T)-F12/cc-pVDZ-F12. Similarly, HO_2 radical and O_2 cation were optimized with CCSD(T)-F12/cc-pVDZ-F12 to allow for structural comparisons with the various HO_4^+ isomers. The composite geometry and energy methods will be shortened to CCSD(T)+δ[CASSCF] and CCSD(T)+δ[NEVPT2], respectively, for the remainder of the manuscript.

The active space chosen to describe HO_4^+ included 16 electrons in 13 orbitals. This corresponds to the valence space, with the exception of the low energy sigma orbitals, which are comprised mostly of oxygen 2s basis functions. CASSCF orbitals are state-specific rather than state-averaged. The Resolution of the Identity (RI) approximation is applied, as implemented in ORCA, to speed up CASSCF and CCSD(T)-F12 computations without any significant loss of accuracy.

8.2.3. Quartic Force Fields and Anharmonic Frequencies

In addition to the application of composite methods for relative energetics, all covalent-like isomers on the triplet surface, with and without an argon tag, were optimized with ROHF-CCSD(T) combined with the ANO-VT-DZ and ANO-VT-TZ basis sets.[54-55] Harmonic frequencies were computed at the ANO-VT-TZ structures, and quartic force fields were computed at the ANO-VT-DZ structures. The TZ harmonic frequencies and dipole moment first derivatives were substituted for their DZ counterparts, forming hybrid force fields, and Second-Order Vibrational Perturbation Theory with Resonances (VPT2+K) was applied to predict the infrared spectra.[56-58] The hybrid force fields will be denoted CCSD(T)/ANO-VT-[T,D]Z and sometimes shortened to simply CCSD(T). Anharmonic infrared intensities were evaluated for all 1- and 2-quantum transitions and additionally for the 3-quantum ν(O-H) + 2ν(H···Ar) transition. For transitions to states not involved in anharmonic resonances, intensities were determined from VPT2 transition moments; whereas, if the target state participates in a resonance with close-lying state(s), its transition intensity is evaluated by transformation of deperturbed VPT2 transition moments into the VPT2+K eigenvector basis.[59-62]

Resonance treatments were conducted in an *ad hoc* manner. In most cases, a list of Fermi resonances was identified using the Martin test,[63] with a standard threshold value of 1 cm^{-1}, combined with the requirement that the zeroth order states fall within a 250 cm^{-1} energy window. The energy window test prevents most interactions between vibrations and low frequency

torsional/intermolecular modes from showing up as resonances.[64] The first "harmonic derivatives" were evaluated for some systems, as implemented in the GUINEA module of CFOUR 2.1.[65] It was observed that a threshold value of 1 unit predicts a similar but slightly more conservative set of resonances as the combined Martin and energy window tests. The sensitivity of the VPT2 transition moments to the resonance treatment was also carefully checked. VPT2 intensities are somewhat more sensitive to the effects of resonance than VPT2 frequencies. Sometimes unusually small or large VPT2 intensities are obtained until an additional resonance is taken into consideration. Caution is exercised whenever the anharmonic intensity based on VPT2 transition moments differs greatly from intensity based on harmonic oscillator transition moments.

An important resonance case occurs whenever the O-H stretching fundamental is found to be involved in a resonance. In addition to treating that resonance by diagonalization of an effective Hamiltonian matrix, analogous resonances were treated between states with the mutual addition of 1 and 2 quanta of ν(H···Ar) excitation.[58-59] For example, if the interaction ν(O-H) ~ 2ν(O-O) is treated explicitly, ν(O-H) + ν(H···Ar) ~ 2ν(O-O) + ν(H···Ar) and ν(O-H) + 2ν(H···Ar) ~ 2ν(O-O) + 2ν(H···Ar) should also be treated. To be completely rigorous, the resonance must be treated between every possible pair of states of the form ν(O-H) + X ~ 2ν(O-O) + X. In practice, few multi-quanta transitions aside from combinations of ν(O-H) with ν(H···Ar) have appreciable intensity in our experiment, so it is not necessary to treat a resonance absolutely everywhere that it may manifest.

For the lowest energy triplet HO_4^+ isomer, denoted ^{3}*tc* (*trans-cis*), higher levels of theory were applied to gauge the convergence to the FCI and CBS limits. The quartic force fields, with and without an argon tag, were evaluated with the ANO-VT-TZ basis set, which allowed us to test the accuracy of the [T,D]Z hybrid approximation. The geometry and harmonic frequencies of the untagged ion were also improved, first by use of the ANO-VT-QZ basis set and then by

applying additive corrections for core-correlation and post-CCSD(T) electron correlation. With additive corrections, all gradients and frequencies were evaluated by numerical differentiation of energies. ROHF-CCSDT and ROHF-CCSDT(Q)/B energy computations were performed using the CFOUR interface to MRCC.[66]

The contribution of core-core and core-valence correlation was evaluated using the cc-pwCVTZ basis set by differencing frozen-core computations and computations that correlate all electrons.[67] Our best single-reference description of the ^3tc system is then given by,

$$E(\text{CCSD(T)/ANO-VT-QZ}) + \delta E(\text{CCSD(T)/cc-pwCVTZ}) + \delta E(\text{CCSDT(Q)/ANO-VT-DZ}) \quad (8.2)$$

where all contributions are based on an ROHF reference. Note that dipole derivatives were not evaluated with this method; for the highest-level treatments, the CCSD(T)/ANO-VT-TZ values are used. As these computations, particularly the CCSDT(Q) correction, were intractable for the argon-tagged ion, its harmonic frequencies were estimated by applying a scaling,

$$\omega^{\text{tagged}}_{\text{corrected}} \approx \omega^{\text{tagged}}_{\text{CCSD(T)/TZ}} \left[\frac{\omega^{\text{untagged}}_{\text{corrected}}}{\omega^{\text{untagged}}_{\text{CCSD(T)/TZ}}} \right] \quad (8.3)$$

based on the harmonic frequencies of the untagged ion.

8.3. Results and Discussion

8.3.1. Infrared Spectroscopy

The experimental infrared spectra are presented in Figure 8.1. A few comments can be made before any comparison to theory. Common features are seen at approximately 1170, 1580, 1950, 2760, 3090, and 3145 cm^{-1} for protonated and deuterated systems. As these are minimally shifted, these likely represent oxygen vibrations. The lack of a bright proton-shuttling band around 1000 cm^{-1} suggests that proton-bound dimers are not produced in our experiment. Furthermore, many intense transitions are centered around 2900 cm^{-1} in the protonated system and around 2200 cm^{-1} in the deuterated system. On the basis of the isotopic shift, these transitions likely have O-H and

O-D stretching character, respectively. They are red-shifted by several 100 cm^{-1} due to the argon atom, which is typical. As in other ionic systems, e.g. hydronium, the argon tag preferentially sits on an O-H bond (parallel to the bond axis).[68] Furthermore, the structures of the 2200 and 2900 cm^{-1} bands are also related to the argon tag. Weaker transitions are seen to the blue of the strong O-H and O-D stretching fundamentals, which likely have additional excitation in the intermolecular ν(H···Ar) or ν(D···Ar) modes. This is most clearly seen in the $ArDO_4^+$ spectrum. Other tagging isomers, where argon is not parallel to the O-H or O-D bond axis, may be possible. We expect that the O-H and O-D stretches of these would be minimally shifted from the stretches for the untagged ion, appearing around 3300 and 2400 cm^{-1}, respectively (Section 8.3.6). As no strong transitions are observed in those regions, it does not appear that these kinds of isomers are formed.

8.3.2. Conformers and Energetics

The isomers of HO_4^+ are studied on the lowest-lying singlet, triplet, and quintet potential energy surfaces. They can be divided into two classes: proton-bound dimers (PBD), which have two O=O units that share a proton between them, and covalent-like structures that are more similar to O_2^+ interacting with HO_2, through a very long (1.7-2.1 Å) central O-O bond. Figure 8.2 shows a potential curve for the dissociation of the lowest energy triplet isomer of HO_4^+ into O_2^+ and HO_2, illustrating a smooth dissociation. This potential can be classified as semi-relaxed. The system was constrained to C_s symmetry, and the two angles that transition into intermolecular degrees of freedom were frozen to their equilibrium values. These conditions were imposed to prevent the system from trying to rearrange into a PBD at separations greater than ~ 3 Å. Bound states were computed variationally in a basis set of harmonic oscillator wavefunctions. The kinetic and potential energy operators were expanded in Hermite polynomials. Large changes in the CC amplitudes are not found to occur over the dissociation curve, so this does not appear to be a multireference process.

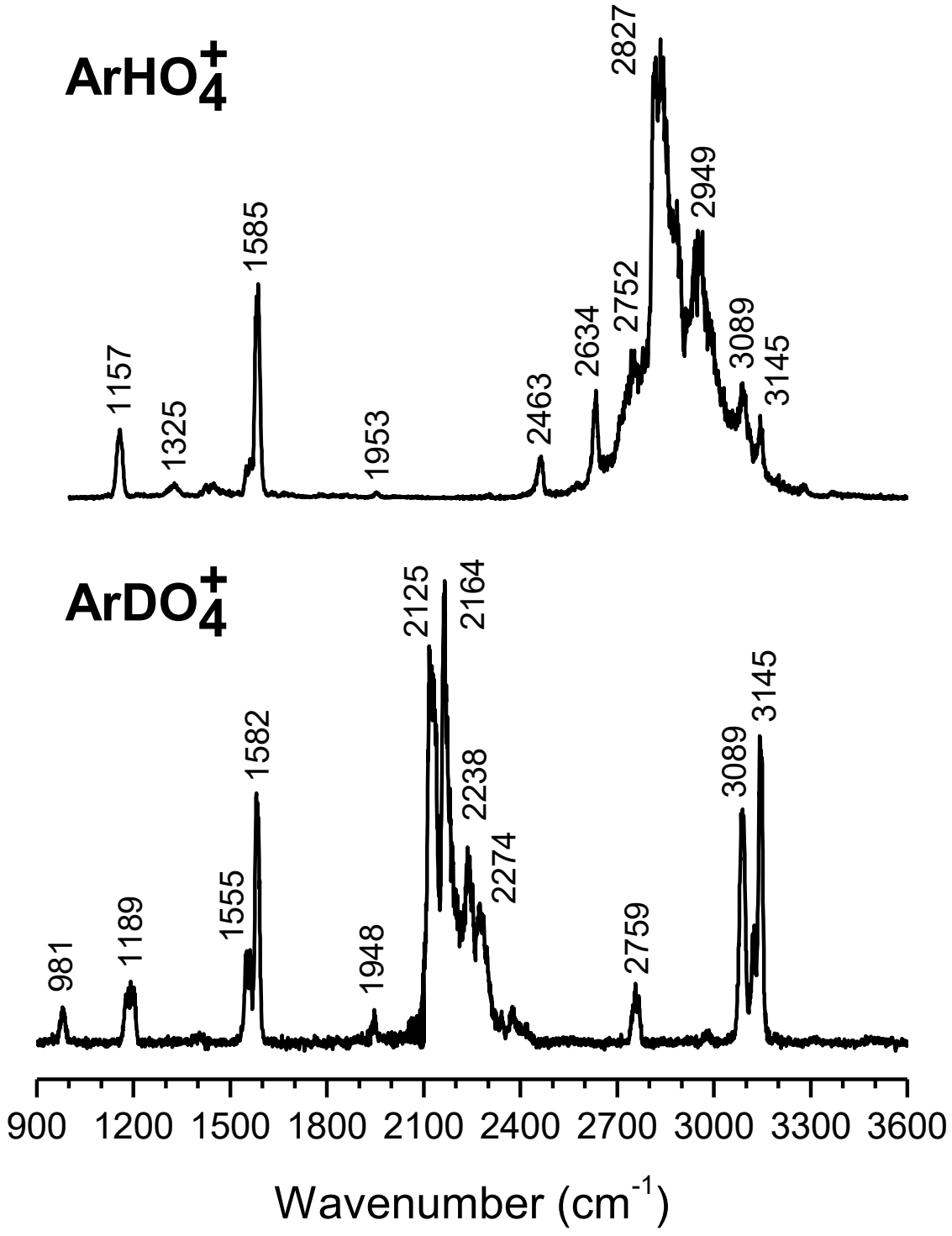

Figure 8.1. Experimental IRPD spectra for both protonated and deuterated systems. The $ArHO_4^+$ labels 2827 and 2949 represent the average centers of two closely spaced doublets (Table 8.2).

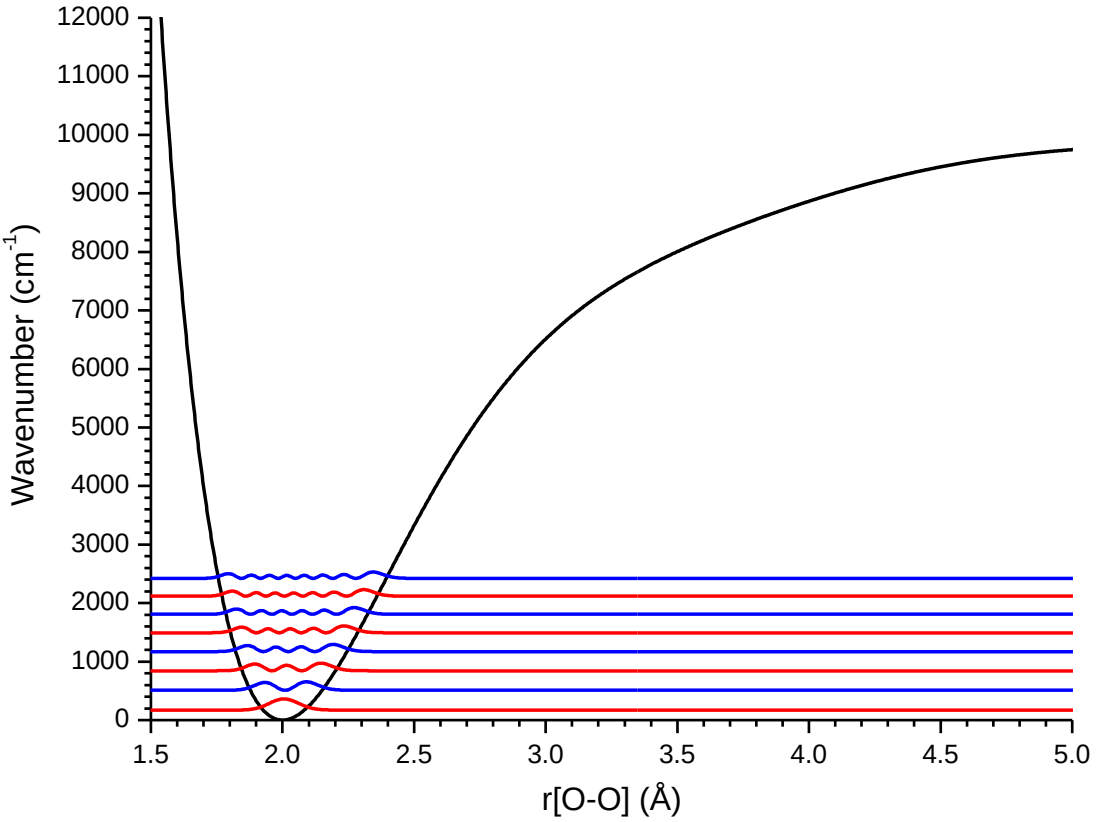

Figure 8.2. Central O-O dissociation potential of ^{3}*tc* HO_4^+ at ROHF-CCSD(T)/ANO-VT-TZ //ROHF-CCSD(T)/ANO-VT-DZ level of theory. Zero point energy is 171 cm^{-1} and fundamental frequency is 339 cm^{-1}. Squared wavefunctions are shown for the lowest eight vibrational states. At this level of theory, D_e = 11,113 cm^{-1}.

Structures and energetics of all isomers are given in Figure 8.3. We adopt different naming conventions for the different classes of structure. The covalent-like isomers that possess the central O-O bond are named for the values of the bonded H-O-O-O dihedral angle and the adjacent, bonded O-O-O-O dihedral angle. These isomers are thus named *cis-cis*, *trans-cis*, *trans-cis*, and *trans-trans* and shortened to simply *cc*, *tc*, *ct*, and *tt*, with their multiplicities given in superscript. The latter three are found to always adopt C_s symmetry structures. Proton-bound dimers are named by their point group symmetries and multiplicities. We note that the C_{2v}

isomers and the *cc* isomers are somewhat similar to one another; however, they are distinguishable by the distance between the two oxygen atoms farthest from the proton.

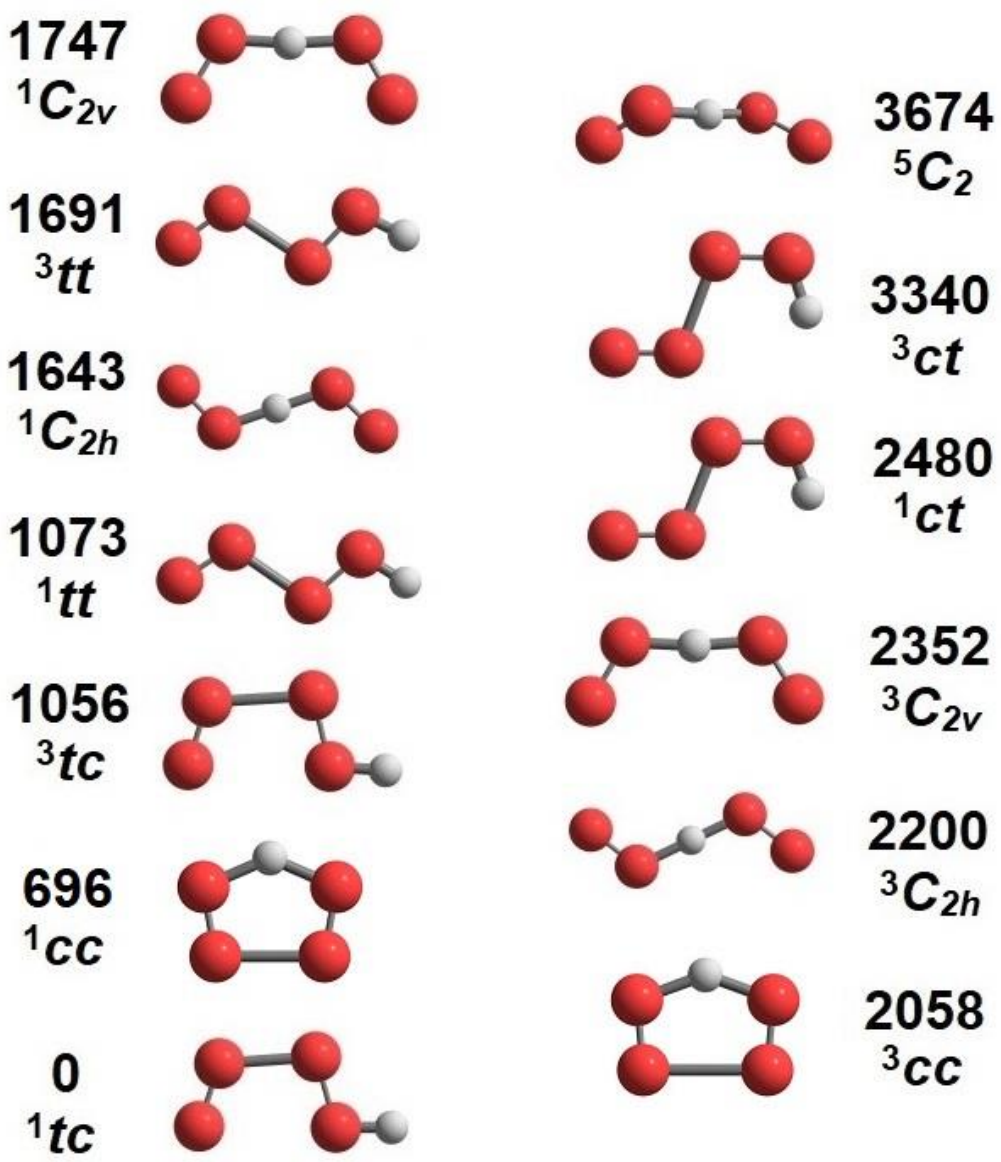

Figure 8.3. Composite structures, conformer labels, and relative electronic energies (cm^{-1}) for HO_4^+ stationary points. Relative energies are evaluated at UHF-CCSD(T)-F12/cc-pVDZ-F12 + δ[NEVPT2(16,13)-F12/cc-pVDZ-F12)].

Only one minimum is located on the quintet surface; it is the C_2 symmetry PBD and is the highest energy isomer. The singlet and triplet surfaces are found to have six isomers each: two PBD, three covalent-like, and one having characteristics of both, perhaps best described as a cyclic PBD. These six isomers are qualitatively the same on the two surfaces. The most notable difference between the singlet and triplet multiplicities is seen for the isomers with covalent-like structures. The central O-O bond is somewhat longer on the triplet surface, causing the triplets to more closely resemble a $HO_2 + O_2^+$ complex. The *tc*, *tt*, and *cc* isomers represent the lowest energy conformers on the singlet and triplet surfaces, followed by the C_{2h} and C_{2v} PBD, followed by the considerably less stable *ct* isomers. We note that a $^3C_{2v}$ well does not exist at CCSD(T)+δ[CASSCF]; rather, $^3C_{2v}$ is a transition state with a small imaginary torsional frequency. However at other levels of theory, a shallow $^3C_{2v}$ well exists. See Section 8.3.3 for a potential curve and discussion of this.

In Table 8.1, relative energies are also provided with NEVPT2-F12/cc-pVDZ-F12, as it is a component of the CCSD(T)+δ[NEVPT2] energy. NEVPT2 and CCSD(T)+δ[NEVPT2] agree on the two lowest energy isomers and predict a similar energetic ordering for the remaining isomers, never differing by more than 500 cm^{-1}. This comparison provides some idea of the accuracy of the energy predictions. The precise energetic ordering is still uncertain, but the stability of the covalent-like isomers is likely to hold true in the event that a more sophisticated level of theory can be applied to the system.

Relaxed torsional potential energy curves are given in Figures 8.4-8.5. These show the O-O torsional interconversion pathways for $^3tc \leftrightarrow {}^3tt$ and $^3cc \leftrightarrow {}^3ct$. While the O-O torsional curves of the covalent-like isomers were difficult to obtain, owing to the existence of several SCF solutions at C_1 geometries, the torsions themselves are not multireference processes. The O-H torsional pathways, $^3cc \leftrightarrow {}^3$tc and $^3ct \leftrightarrow {}^3tt$, were not explored in as much depth. In these cases, the character of the electronic wavefunction is significantly different at the halfway point

compared to at the endpoints, similar to the rotation about a double bond. The magnitudes of largest T_1 amplitudes were found to be in excess of 0.4 for 90 degree twisted structures. As we

Table 8.1. Squares of CASCI coefficients (large contributions bold), ground-state electronic symmetries, and relative electronic energies (cm^{-1}) for various stationary points on HO_4^+ potential surfaces, optimized with UHF-CCSD(T)-F12/cc-pVDZ-F12 + δ[CASSCF(16,13)/aug-cc-pVTZ)].

Isomer	$\Gamma(\Psi_{el})$	ΔE(MR/SR)[a]	ΔE(MR)[b]	C_0^2	C_1^2	C_2^2	C_3^2	C_4^2	C_5^2
^1tc	A'	0	0	**0.64**	**0.18**	0.03	0.02	0.01	0.01
^1cc	A_1	696	198	**0.57**	**0.21**	0.04	0.03	0.03	0.01
^3tc	A'	1056	1313	**0.84**	0.03	0.01	0.01	0.01	0.01
^1tt	A'	1073	1162	**0.58**	**0.24**	0.03	0.03	0.02	0.01
$^1C_{2h}$	A_g	1643	1246	**0.28**	**0.23**	**0.16**	**0.12**	**0.11**	0.01
^3tt	A'	1691	1901	**0.83**	0.04	0.01	0.01	0.01	0.01
$^1C_{2v}$	A_1	1747	1328	**0.28**	**0.22**	**0.16**	**0.12**	**0.11**	0.01
^3cc	B_2	2058	1607	**0.73**	**0.11**	0.02	0.02	0.01	0.01
$^3C_{2h}$	B_u	2200	1796	**0.40**	**0.18**	**0.17**	**0.15**	0.01	0.01
$^3C_{2v}$	B_2	2352	1934	**0.40**	**0.18**	**0.17**	**0.15**	0.01	0.01
^1ct	A'	2480	2690	**0.58**	**0.22**	0.03	0.03	0.02	0.01
^3ct	A'	3340	3631	**0.81**	0.06	0.01	0.01	0.01	0.01
$^5C_2$	A	3674	3303	**0.90**	0.01	0.00	0.00	0.00	0.00

[a] Evaluated at UHF-CCSD(T)-F12/cc-pVDZ-F12 + δ[NEVPT2(16,13)-F12/cc-pVDZ-F12)]

[b] Evaluated at NEVPT2(16,13)-F12/cc-pVDZ-F12

do not trust that these potential curves are accurate, we do not report them. Reasonable description of the OH torsional curves or of the 2D coupled torsional surface would require multireference approaches. Bound states were computed for the torsional curves using the variational approach described in Reference 57.

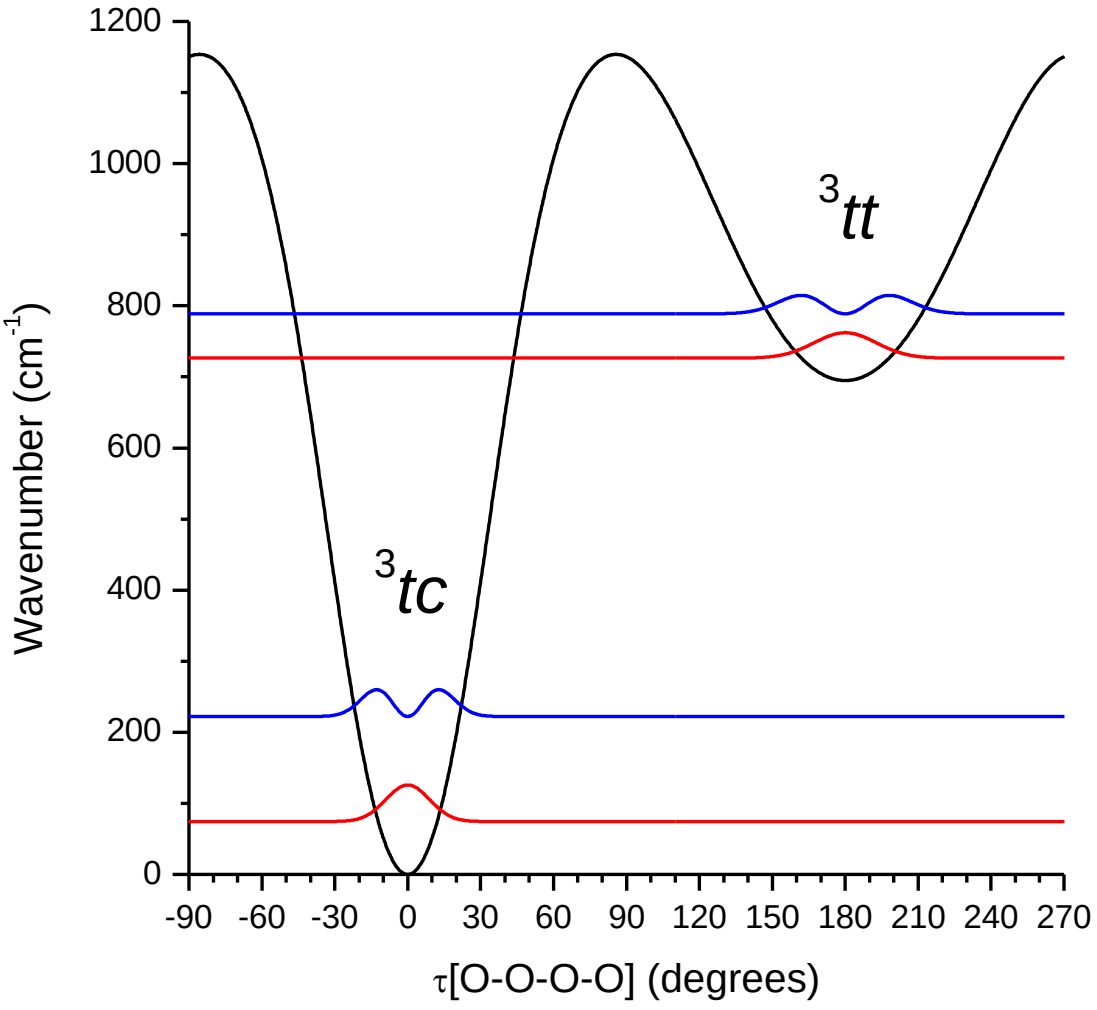

Figure 8.4. Relaxed O-O torsional potential at ROHF-CCSD(T)/ANO-VT-TZ//ROHF-CCSD(T)/ANO-VT-DZ level of theory showing interconversion of ^3tc and ^3tt HO_4^+ isomers. Zero point energies are 74 cm^{-1} and 31 cm^{-1} and fundamental frequencies are 148 cm^{-1} and 62 cm^{-1} for ^3tc and ^3tt, respectively. Squared wavefunctions are shown for the lowest two states associated with each conformer.

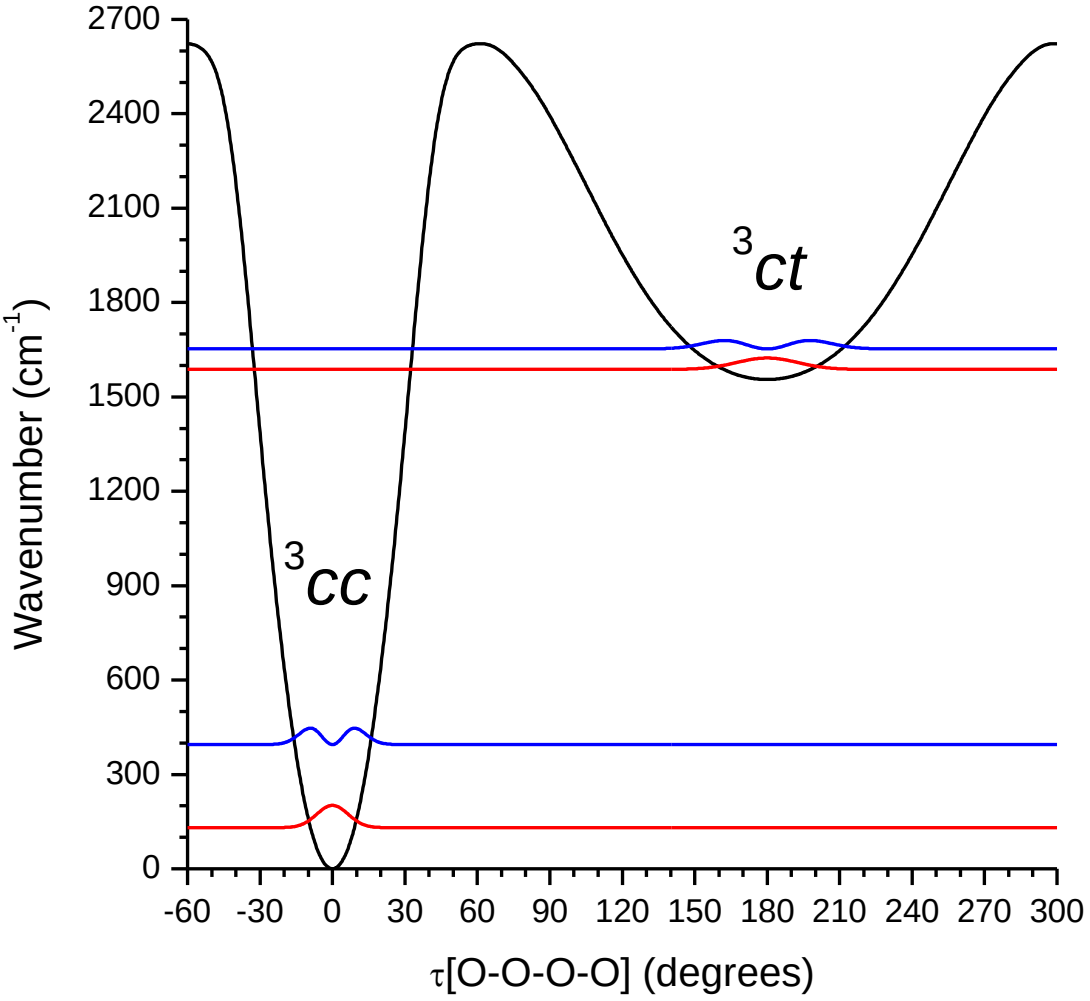

Figure 8.5. Relaxed O-O torsional potential at ROHF-CCSD(T)/ANO-VT-TZ//ROHF-CCSD(T)/ANO-VT-DZ level of theory showing interconversion of ^3cc and ^3ct HO_4^+ isomers. Zero point energies are 131 cm^{-1} and 32 cm^{-1} and fundamental frequencies are 264 cm^{-1} and 65 cm^{-1} for ^3cc and ^3ct, respectively. Squared wavefunctions are shown for the lowest two states associated with each conformer.

8.3.3. Geometric Structures

Some further structural comparisons are useful to understand the nature of HO_4^+. The various PBD, including ^1cc and ^3cc, have very similar bond lengths, varying between 1.21-1.22 Å, for the O=O distance. For comparison, the bond length of $^3\Sigma_g^-$ O_2 is 1.21 Å, with CCSD(T)-

F12. The O-H-O distances range from 1.22 Å in the singlet and triplet PBD, to 1.23 Å in the quintet, to 1.24 Å in the symmetrical ^{1}*cc* and ^{3}*cc*.

For the ^{3}*tc*, ^{3}*ct*, and ^{3}*tt* isomers, CCSD(T)+δ[CASSCF] bond distances are very similar to ROHF-CCSD(T)/ANO-VT-TZ values, differing by at most 0.01 Å. The exception to this is the central O-O distance, which is consistently 0.10 Å longer with ROHF-CCSD(T), demonstrating its high sensitivity to method. As stated above, the singlet and triplet *tc*, *ct*, and *tt* isomers resemble $^2\Pi_g$ O_2^+ interacting with $^2A''$ HO_2. In this analogy, the singlet HO_4^+ isomers arise from spin-paired reactants, and the triplets arise from a parallel spin coupling. The O-O farthest from the hydrogen atom has a bond length between 1.16-1.17 Å for all isomers and methods. With CCSD(T)-F12, O_2^+ has a bond length of 1.12 Å, so the far O-O bond length in HO_4^+ falls right between the values for O_2^+ and O_2. The O-O bond distance nearest to the hydrogen is between 1.29-1.30 Å, and the O-H bond distance is 0.99 Å for all isomers and methods. For comparison, HO_2 has O-O and O-H bond lengths of 1.33 Å and 0.97 Å, using CCSD(T)-F12. The argon tag, though it strongly perturbs the O-H and O-D stretching frequencies of the covalent-like isomers, has little influence on the geometry. The only notable change is a small (0.01-0.02 Å) lengthening of the O-H bond. The argon tag sits approximately parallel to the bond axis in ^{3}*tc*, ^{3}*ct*, and ^{3}*tt*, at distances of about 2.0 Å from the hydrogen in ^{3}*tc* and 2.1 Å from the hydrogen in ^{3}*ct* and ^{3}*tt*, at the CCSD(T)/ANO-VT-TZ level of theory. At the same level of theory, the tag sits farther away from the hydrogen in ^{3}*cc* (2.5 Å) and does not align with the O-H axis.

The ^{1}*cc* isomer corresponds to the lowest energy structure located by Hernández-Lamoneda and coworkers.[29-30] However, the remaining covalent-like isomers have not been identified before. The single-reference/multi-reference composite energy scheme chosen for optimization allows for all isomers to be treated at a similar level of approximation. The composite geometries are also expected to be more accurate than CASSCF geometries, one of the few alternatives that is both balanced and affordable. Indeed, we find that CASSCF(16,13)/aug-

cc-pVTZ has difficulty describing the triplet covalent-like isomers, generally underestimating the strength of the $HO_2 + O_2^+$ interaction. The central O-O bond-length it predicts for ^3tc is 2.3 Å, which is 0.4 Å longer than the prediction of the CCSD(T)+δ[CASSCF] composite model and 0.3 Å longer than the ROHF-CCSD(T) prediction.

We now briefly consider the barriers that separate the triplet covalent-like isomers (*cc*, *tc*, *ct*, and *tt*), the PBD isomers (C_2, C_{2v} and C_{2h}), and the two types of isomers from one another. First, the covalent-like isomers are well-separated from one-another. Figures 8.4 and 8.5 show that barriers of several hundred wavenumbers separate ^3tc from ^3tt and ^3cc from ^3ct, respectively, along the O-O torsional coordinate. Each well is capable of supporting several localized bound states. Although we do not report the O-H torsional potentials or transition states associated with the $^3cc \leftrightarrow {}^3tc$ and $^3ct \leftrightarrow {}^3tt$ isomerizations, the large harmonic frequencies (300-500 cm^{-1}) suggest that the O-H torsional barriers should be even higher.

The singlet and triplet C_{2h} and C_{2v} isomers are related by torsion of the O=O units about the central O-H-O. For the singlets, the torsional transition state is electronically 127 cm^{-1} above C_{2v} and 231 cm^{-1} above C_{2h} with the CCSD(T)+δ[NEVPT2]//CCSD(T)+δ[CASSCF] model and 100 cm^{-1} above C_{2v} and 212 cm^{-1} above C_{2h} when the torsional ZPVE is included, indicating that $^1C_{2v}$ and $^1C_{2h}$ are energetically separated. For the triplets, Figure 8.6 shows a relaxed potential for the $^3C_{2v} \leftrightarrow {}^3C_{2h}$ interconversion, at CCSD(T)+δ[NEVPT2]//CCSD(T)+δ[CASSCF]. The scan coordinate involves a dummy atom in the plane of the central O-H-O unit. Twice the value of this coordinate is approximately equivalent to the O=O-(H)-O=O torsional dihedral angle. The potential curve is fitted from only 7 grid points (30 degree steps) which are shown. Although a $^3C_{2v}$ well does not exist with the CCSD(T)+δ[CASSCF] model, it reappears when higher quality CCSD(T)+δ[NEVPT2] single point energies are used. This well is actually too shallow to support a localized bound-state. The first wavefunction with significant amplitude in the $^3C_{2v}$ well degrees also has amplitude in the $^3C_{2h}$ well. Therefore $^3C_{2v}$ may not correspond to a conformer of HO_4^+ despite being a minimum on the potential surface, at some levels of theory.

Finally, we consider the PBD ↔ covalent-like isomerization. The most obvious pathway that could connect these two classes of isomers would seem to be a ring-opening of the ^1cc and ^3cc isomers to the corresponding C_{2v} isomers. Both the singlet and triplet ring-opening transition states were characterized with CCSD(T)+δ[NEVPT2]//CCSD(T)+δ[CASSCF]. On the singlet surface, the C_{2v} → TS → *cc* pathway is completely downhill. Electronically, the stationary points are at 1747 cm^{-1}, 1706 cm^{-1}, and 696 cm^{-1} (relative to ^1tc in Fig. 8.3), and ZPVE does not change the qualitative ordering. Similarly to $^3C_{2v}$, these energetics suggest that $^1C_{2v}$ also cannot support localized bound states; although, a ring opening potential surface would be useful to confirm this. In contrast, the triplet ring-opening possesses a real barrier. In terms of electronic energy, the triplet transition state is 93 cm^{-1} above $^3C_{2v}$ and 387 cm^{-1} above ^3cc. The ZPVE associated with the ring-opening coordinate lowers these to 42 cm^{-1} and 283 cm^{-1}, respectively.

8.3.4. Electronic Structures

Squared CASCI coefficients are given in Table 8.1. Inspection of the CASSCF and ROHF-CCSD wavefunctions suggests that it may be reasonable to treat the covalent-like triplet isomers as single-configurational systems. With the exception of the ^3cc isomer, which is somewhat multiconfigurational, the CASSCF wavefunctions of the covalent-like triplets are all dominated by single determinants, and the magnitudes of the largest T_1 and T_2 amplitudes are ~ 0.2 and ~ 0.1, respectively. The UHF-CCSD wavefunctions, however, exhibit one very large T_1 amplitude of 0.6 and cannot be considered reliable. The covalent-like singlets, in contrast, are all emphatically two-configurational biradical systems. The quintet PBD is single-configurational, and finally the singlet and triplet PBD are all highly multi-configurational (5 and 4 configuration state functions with significant weights, respectively). Because of the greater availability of analytic derivatives for single-reference methods, we chose to compute quartic force fields only for the triplet covalent-like isomers. In principle, accurate quartic force fields could be obtained

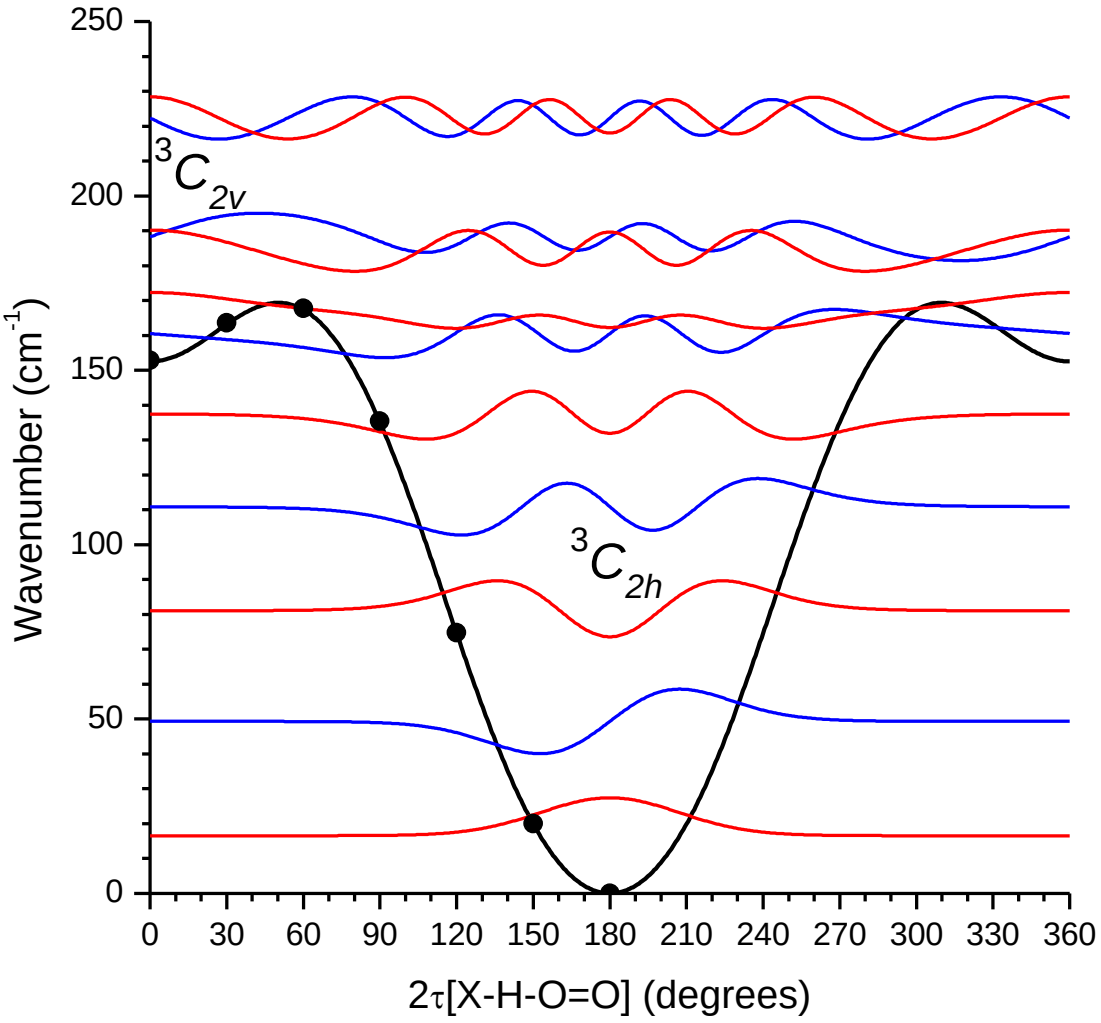

Figure 8.6. Relaxed torsional potential, using CCSD(T)+δ[NEVPT2]//CCSD(T)+δ[CASSCF] composite method, showing the interconversion of $^3C_{2v}$ and $^3C_{2h}$ HO_4^+ isomers. For the $^3C_{2h}$ isomer, the zero point energy is 17 cm^{-1} and the fundamental frequency is 33 cm^{-1}. The first six symmetric wavefunctions (red) and the first five antisymmetric wavefunctions (blue) are shown.

with multi-reference approaches for the other isomers; however, this would come at far greater computational expense.

The important electronic configurations for the ground states of all HO_4^+ isomers arise from a "4 electrons in 4 orbitals" coupling. These can be viewed as linear combinations of the π* orbitals of two oxygen molecules and the four electrons that occupy them (Fig. 8.7). Since the π*

orbitals are exactly degenerate in the limit of two infinitely-separated oxygen molecules, this explains how certain isomers of HO_4^+ can be so highly multiconfigurational. Forming the molecular orbitals entails taking in-phase and out-of-phase combinations of the in-plane π* orbitals, denoted *a′*(+) and *a′*(-), and of the out-of-plane π* orbitals, *a″*(+) and *a″*(-). These are labeled in C_s symmetry such that they are applicable to all conformers, except for $^5C_2$, which simply has one electron in each orbital; all four electrons have parallel spins, producing a single important configuration for the quintet. The covalent-like triplets, in this case including ^3cc, place one electron into each *a″*(+) and *a″*(-). Then, the dominant configuration doubly occupies *a′*(+), which is sigma-bonding with respect to the central O-O; the less dominant configuration instead doubly occupies *a′*(-), which has sigma-antibonding character.

The covalent-like singlets, ^1tc, ^1ct, ^1tt, and ^1cc, are all strongly two-configurational. They are not totally analogous to the triplets. In their dominant configurations, *a′*(+) is always doubly occupied and *a′*(-) is always unoccupied. The two leading configurations differ by doubly occupying either *a″*(+) or *a″*(-). Because *a″*(+) is π-bonding with respect to the central O-O, the configuration that occupies it is slightly more dominant; however, the energetic difference between filling *a″*(+) and *a″*(-) is small, as the central O-O is so long. The similar energy of their out-of-plane π* orbitals is the origin of their biradical character.

The remaining PBD isomers are strongly multiconfigurational. Similar to the covalent-like triplets, a leading configuration for the $^3C_{2h}$ and $^3C_{2v}$ isomers has *a″*(+) and *a″*(-) singly occupied and *a′*(+) doubly occupied; however, the *a′*(+) and *a′*(-) orbitals are now much closer in energy. The preference to doubly occupy the more bonding orbital is weak, so doubly-occupying *a′*(-) is now much more viable. The *a′* and *a″* orbitals are closer in energy as well, and the two configurations with *a′*(+) and *a′*(-) singly occupied and either *a″*(+) or *a″*(-) doubly occupied also contribute significantly to the total wavefunction, making the ground states four-configurational. Finally, the $^1C_{2v}$ and $^1C_{2h}$ isomers each possess four important closed shell configurations. Each

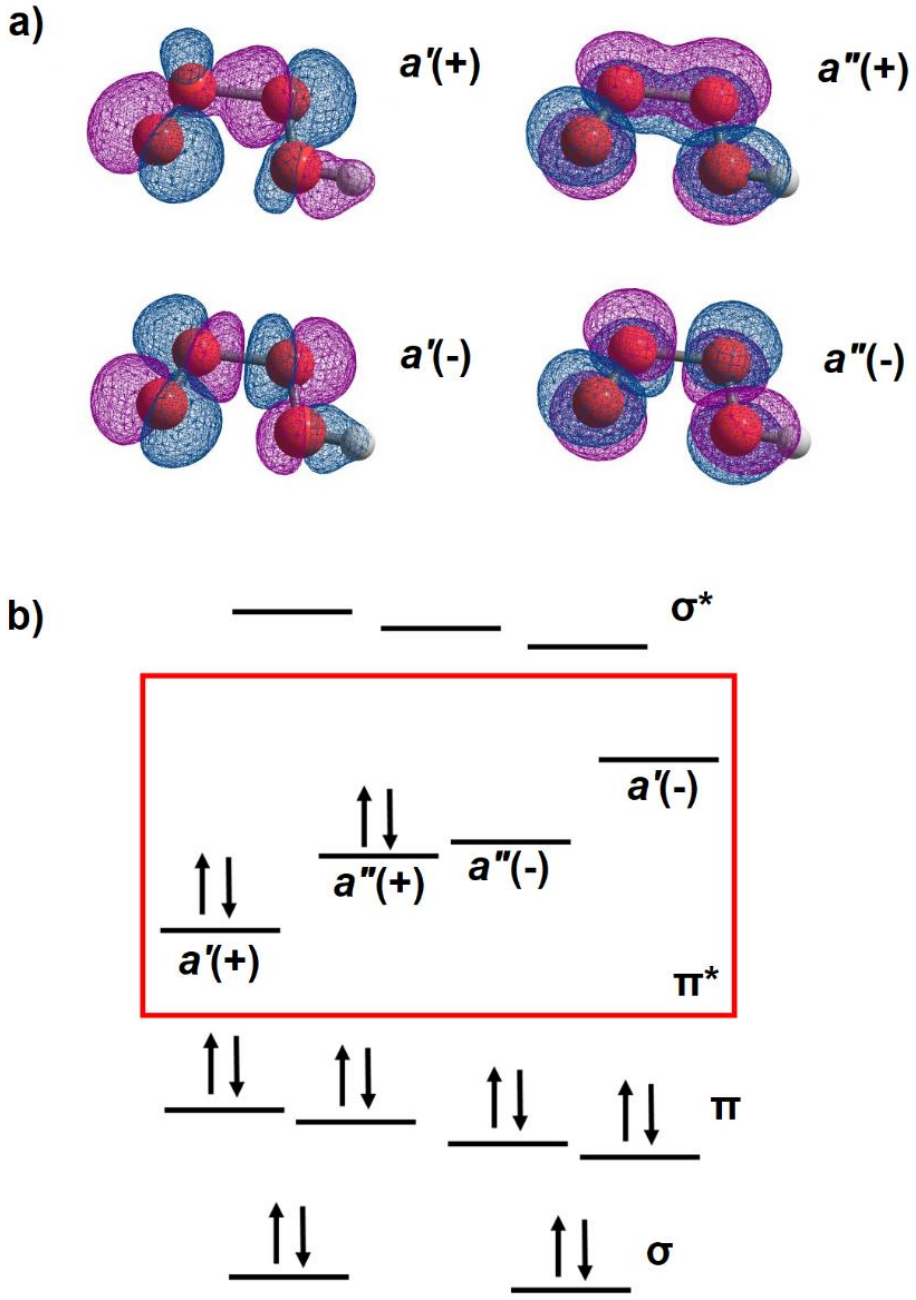

Figure 8.7. a) Variable occupation molecular orbitals referred to in the text. Depicted are 98% isodensity surface CASSCF(16,13)/aug-cc-pVTZ natural orbitals of ^1tc, at its equilibrium geometry. **b)** Generic molecular orbital diagram for HO_4^+. The (16,13) active space orbitals are shown with approximate bonding/antibonding descriptions. Orbital energies are not to scale; energy gaps are chosen to exaggerate the near-degeneracy of *a″*(+) and *a″*(-). The horizontal positions of the orbitals are chosen to resemble a $2O_2 + H^+$ system. The box contains the "four-electrons in four-orbitals." The configuration written corresponds to that with the largest weight for the ^1tc isomer.

configuration doubly occupies one *a′* orbital and one a″ orbital. There is a further fifth configuration with large weight, in which all four electrons are unpaired.

8.3.5. Symmetry and Anharmonicity

The proton shuttling motion in a PBD is often associated with small changes in energy; furthermore, theory has a propensity for predicting double-well features on the potential surface. In other PBD systems, the equilibrium structure has either a symmetrically or asymmetrically shared proton, depending on the level of theory. For example, the proton-bound N_2 dimer (HN_4^+) possesses a $D_{\infty h}$ equilibrium structure at the CCSD(T)/ANO0 and CCSD(T)/ANO2 levels of theory yet a $C_{\infty v}$ equilibrium structure at CCSD(T)/ANO1. To determine whether a proton is shared or localized, it is not sufficient to consider only the equilibrium structure(s). Even when the potential displays a double well feature, the shuttling barrier may be below the zero-point energy of the coordinate, causing the ground state wavefunction to be delocalized over it.

In accordance with this, the PBD isomers (here including the *cc* isomers) display flat potential energy surfaces for proton-shuttling. At some levels of theory, multiple well features are predicted. Hernández-Lamoneda and coworkers found this to be the case for ^{1}*cc* at the CASSCF(24,17)/aug-cc-pVTZ level of theory.[29] We find with CCSD(T)+δ[CASSCF] that the ^{1}*cc* isomer possesses an unusual potential surface with three wells: a C_{2v} minimum and lower energy C_s minima. When ^{3}*cc* is described with CCSD(T)+δ[CASSCF], it instead has a single C_{2v} minimum. With ROHF-CCSD(T), the ^{3}*cc* isomer is predicted to have a C_s equilibrium structure, with and without the argon tag present. The anharmonic nature of the proton shuttling often causes significant errors whenever VPT2 is applied to proton-bound dimers.[23] As a consequence, our ^{3}*cc* VPT2 predictions should be considered less accurate than those for the ^{3}*tc*, ^{3}*ct*, and ^{3}*tt* isomers. A further problem affecting the ^{3}*cc* isomer is the large C_1^2 value, indicating some degree of two-configurational character. This also degrades the quality of ROHF-CCSD(T) computations.

The interaction between HO_4^+ and argon is quite strong, lowering the predicted frequency of the O-H and O-D stretches by several hundred wavenumbers. The low frequency intermolecular vibrations associated with the argon-tagged species do not appear to cause a problem for VPT2. The ionic nature of the $Ar\cdots HO_4^+$ interaction leads to a potential energy surface that is more akin to a rigid molecular system than to a weakly bound complex. In previous studies, VPT2 has performed well for other argon-tagged ions.[68-70] Notably, strongly red-shifted, argon-tagged X-H stretches were predicted no less accurately than free X-H stretches. Some additional discussion of symmetry-breaking and orbital near-instabilities[71] is given below.

Symmetry breaking was also observed for the singlet C_{2v} PBD. The optimized structure possesses one non-symmetric imaginary frequency (b_2 O=O bend). We did not attempt to follow this normal coordinate to obtain a lower energy symmetry-broken structure, nor did we investigate the nature of the symmetry breaking. Hernández-Lamoneda and coworkers discussed similar problems with symmetry-breaking.[30] They found that a full-valence active space (i.e. 24 electrons in 17 orbitals) was more resistant to this; however, such a thing was not tractable for our numerical optimizations and NEVPT2 energy computations. It will suffice to say that a lower energy structure may exist for this isomer, but it may not be physically meaningful.

For the $^1C_{2h}$ isomer, a suspicious b_u harmonic frequency of 1975 cm^{-1} was determined, corresponding to the in-plane bending of the proton. This frequency is several hundred wavenumbers higher than the frequencies of all other PBD, where an O=O stretching vibration has the highest frequency, at around 1550-1620 cm^{-1}. We suspect that this is the manifestation of a near-instability in either the UHF orbitals or the CASSCF orbitals. This is known to cause unphysically large frequencies that are highly sensitive to the basis set and electron correlation treatment.[71] As a test, we changed the CASSCF basis set from aug-cc-pVTZ to cc-pVDZ-F12, reoptimized, and reevaluated the CCSD(T)+δ[CASSCF] harmonic frequencies. While most frequencies are minimally shifted, the highest frequency changes to 2105 cm^{-1}. From this simple

test, we cannot conclude that a near-instability is present in the CASSCF orbitals, as this changes the geometry, which would also affect the proximity to any UHF instability. This reflects a weakness of composite energy methods, as they use more than one reference wavefunction, multiplying the chance that a near-instability will be encountered. To obtain reliable frequency predictions for this isomer, a careful convergence study, involving several methods and basis sets, would likely be needed. The CASSCF and MRCI harmonic predictions of Hernández-Lamoneda and coworkers do not appear to suffer from near instabilities and should be preferred over our predictions for the $^1C_{2h}$ isomer.[30] We are, however, skeptical of the usefulness of harmonic predictions for the bending vibrations of the shared proton.

To summarize, the HO_4^+ system displays numerous challenges in both its electronic and vibrational structure, and our study does not address all of these. The symmetry-breaking and orbital near-instabilities appear to only impact the proton-bound dimers, which are also the only species to behave so anharmonically as to render VPT2 untrustworthy. The ^3tc, ^3ct, and ^3tt isomers, on the other hand, are relatively untouched by these issues and by the multiconfigurational problems of the covalent-like singlets. For these reasons, we now narrow our vibrational discussion to these well-behaved isomers.

8.3.6. Anharmonic Frequencies

We now compare CCSD(T) VPT2+K simulations for the argon-tagged triplet covalent-like isomers to the experimental spectra. The comparisons for $ArHO_4^+$ and $ArDO_4^+$ are given in Figures 8.8 and 8.9, respectively. We note that the CCSD(T)+δ[CASSCF] O-H stretch harmonic frequencies of the analogous singlet isomers are 10-20 cm^{-1} to the blue of the triplets. On this basis, we anticipate that VPT2+K predictions for the argon-tagged ^1tc, ^1ct, and ^1tt isomers would match the experiment somewhat less well. Predictions for the bare ions were also performed. To aid in detection of HO_4^+ in the upper atmosphere and/or interstellar medium, we provide VPT2+K

predictions for the untagged isomers for which we expect VPT2 based on single-reference force fields will be accurate and appropriate, namely: ^3tc, ^3ct, and ^3tt (Fig. 8.10-8.11).

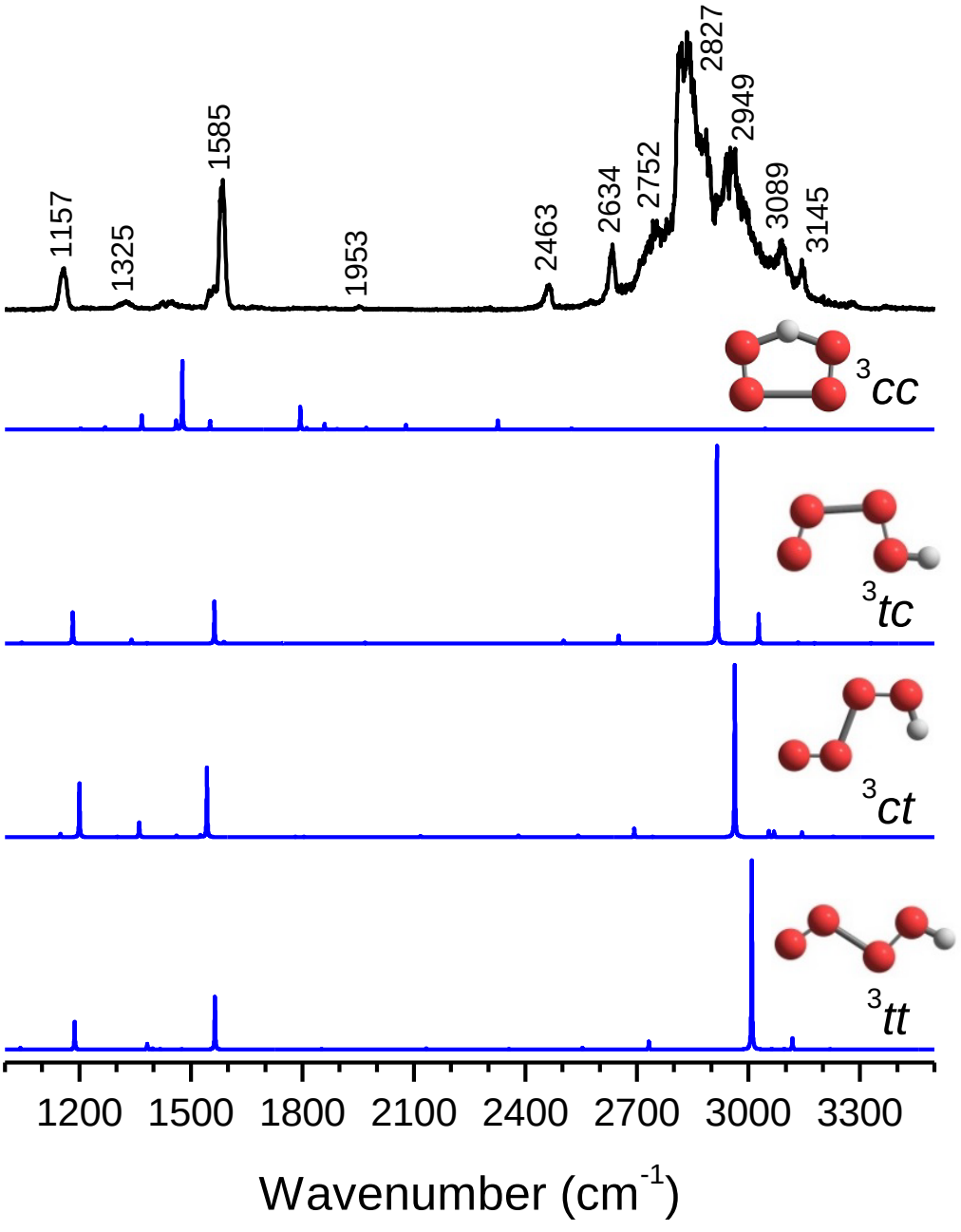

Figure 8.8. Experimental spectrum of $ArHO_4^+$ compared to CCSD(T) VPT2+K simulations of triplet $ArHO_4^+$. Band intensities of theoretical simulations are scaled to improve visibility.

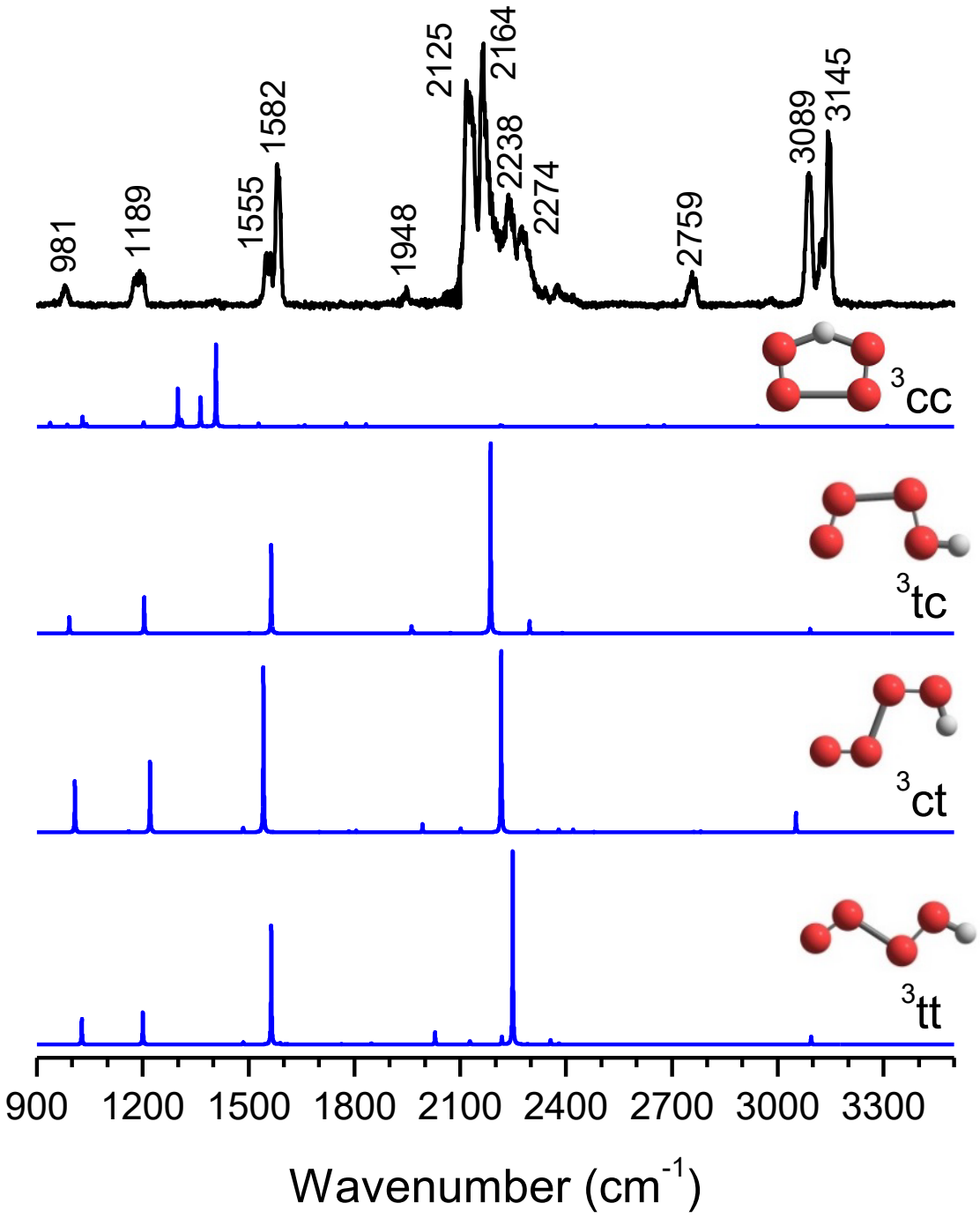

Figure 8.9. Experimental spectrum of $ArDO_4^+$ compared to CCSD(T) VPT2+K simulations of triplet $ArDO_4^+$. Band intensities of theoretical simulations are scaled to improve visibility.

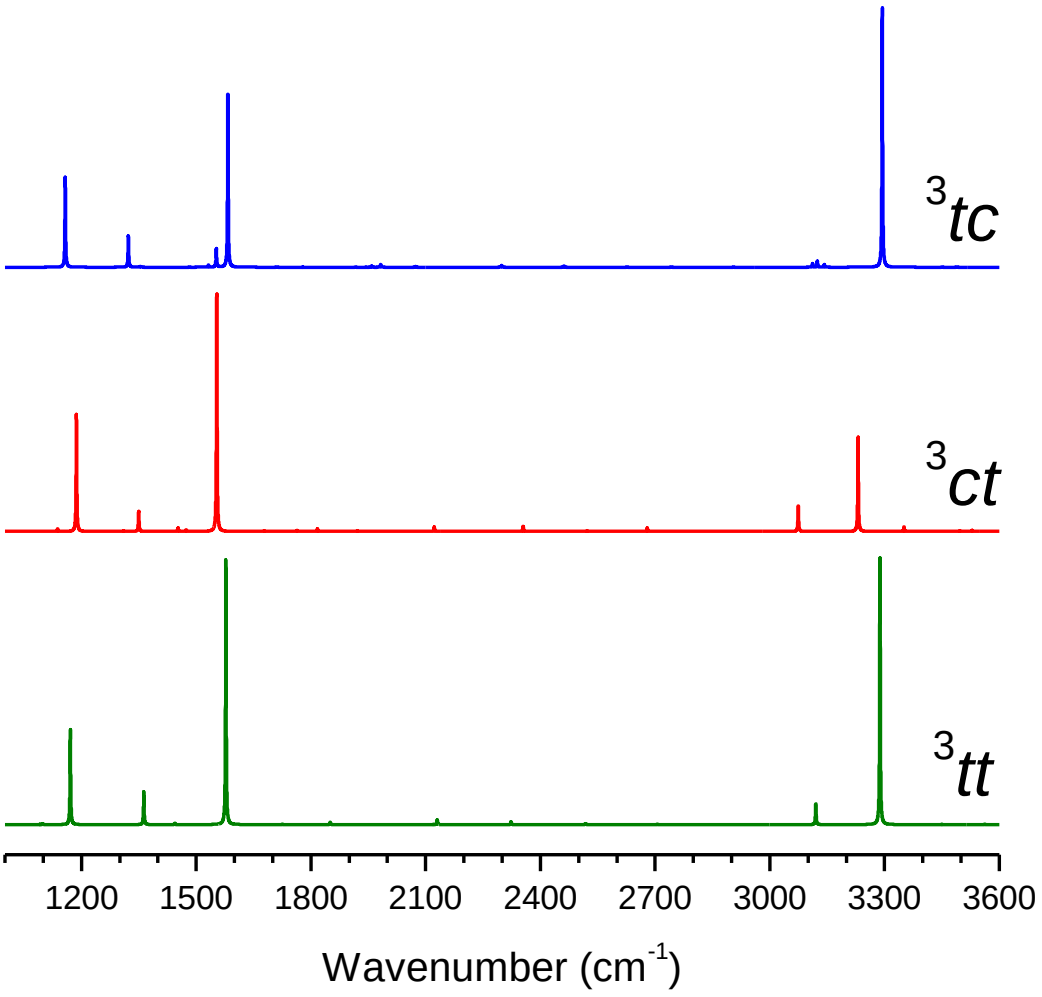

Figure 8.10. VPT2+K simulations of ^3tc, ^3ct, and ^3tt HO_4^+ based on ROHF-CCSD(T)/ANO-VT-[T,D]Z force fields.

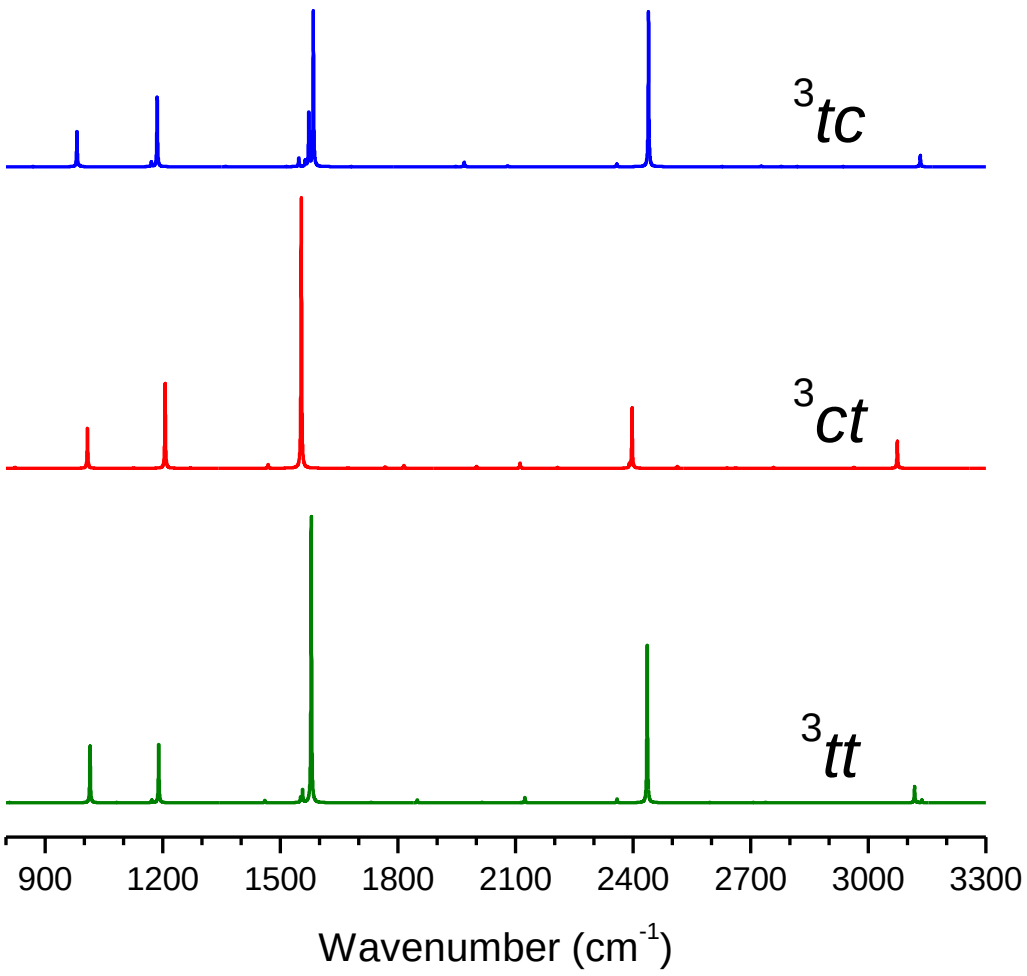

Figure 8.11. VPT2+K simulations of ^3tc, ^3ct, and ^3tt DO_4^+ based on ROHF-CCSD(T)/ANO-VT-[T,D]Z force fields.

Simulations using composite harmonic frequencies, instead of CCSD(T)/ANO-VT-TZ, are presented and discussed briefly. Overall, these are similar to the CCSD(T) simulations; however, the agreement is slightly worse. CCSD(T)+δ[CASSCF] is apparently less accurate than straightforward CCSD(T) for harmonic frequency predictions of these chemical species.

The composite-hybrid simulations were performed in the following manner. For each conformer of HO_4^+ and DO_4^+ (*trans-cis*, *cis-trans*, and *trans-trans*), the normal coordinates of the bare ion at ROHF-CCSD(T)/ANO-VT-TZ, the bare ion at UHF-CCSD(T)-F12/cc-pVDZ-F12 + δ[CASSCF(16,13)/aug-cc-pVTZ)], the tagged ion at ROHF-CCSD(T)/ANO-VT-DZ, and the tagged ion at ROHF-CCSD(T)/ANO-VT-TZ were inspected and arranged into a consistent order. Here, we assumed that the bare ion's normal coordinates were independent of the level of theory and were unaffected by argon-tagging. This was qualitatively the case. Because the single-reference *cis-cis* simulations in the main text bear little resemblance to the experimental spectra, we made no attempt to test composite-hybrid force fields for the *cis-cis* isomer. Ratios were taken between the harmonic frequencies of the bare ion at UHF-CCSD(T)-F12/cc-pVDZ-F12 + δ[CASSCF(16,13)/aug-cc-pVTZ)] and ROHF-CCSD(T)/ANO-VT-TZ. The harmonic frequencies of the tagged ion, at ROHF-CCSD(T)/ANO-VT-TZ, were then scaled by those ratios, and the scaled frequencies were substituted into the ROHF-CCSD(T)/ANO-VT-DZ quartic force field. The dipole derivatives were not adjusted any further, as no dipole moments were evaluated with composite methods. The same ROHF-CCSD(T)/ANO-VT-[T,D]Z dipole moment function was used for the primary simulations (Fig 8.8-8.9).

The theoretical comparisons for the protonated and deuterated systems are presented in Figures 8.12 and 8.13, respectively. For $ArHO_4^+$, composite-hybrid predictions for the O-H stretch are a bit worse, and predictions for the lower frequency far O-O stretch are considerably worse, and predictions for the H-O-O bend and near O-O stretch are moderately worse than the ROHF-CCSD(T)/ANO-VT-[T,D]Z hybrid predictions. The situation is similar for $ArDO_4^+$, where

O-D stretch predictions are nearly unchanged, far O-O stretch predictions are significantly worse, and D-O-O bend and near O-O stretch predictions are moderately worse. That the far O-O stretch shows the most sensitivity to level of theory is unsurprising, as it is short (~ 1.2 Å), possessing some multiple bond character. Unfortunately, it was not tractable for us to obtain geometries and harmonic frequencies with UHF-CCSD(T)-F12/cc-pVDZ-F12 + δ[NEVPT2(16,13)-F12/cc-pVDZ-F12)], but we would expect those frequencies to be of higher quality, having both improved dynamical correlation and basis set completeness. Other notable improvements to the composite method would be consideration of core correlation and higher-order electron correlation, in both the SR and MR components. It is interesting to note that the far O-O stretch frequencies obtained by the MR/SR composite approach are similar to the SR frequencies that include CCSDT(Q) corrections.

Most of the features in the $ArHO_4^+$ spectrum can be explained by the presence of one of the covalent-like isomers. The region around 2900 cm^{-1} is congested and difficult to assign; however, the lower frequency region is much simpler. There are about three strong transitions here, which is what is predicted for the ^3tc, ^3ct, and ^3tt isomers. The experimental spectrum does not resemble the predictions for the ^3cc isomer. This isomer does not have a free O-H; therefore, its strongest transitions are centered around 1500 cm^{-1}. The other PBD isomers are expected to have similar infrared spectra. Harmonic predictions for these isomers, with CASSCF and MRCI, were reported by Hernández-Lamoneda and coworkers.[29-30] Simulation of the other PBD spectra is therefore unnecessary for interpreting our experimental results. Overall the best match is to the lowest energy ^3tc isomer; however, we are not able to make a confident assignment or to rule out the possibility of small amounts of ^3tt and ^3ct contributing to the spectrum.

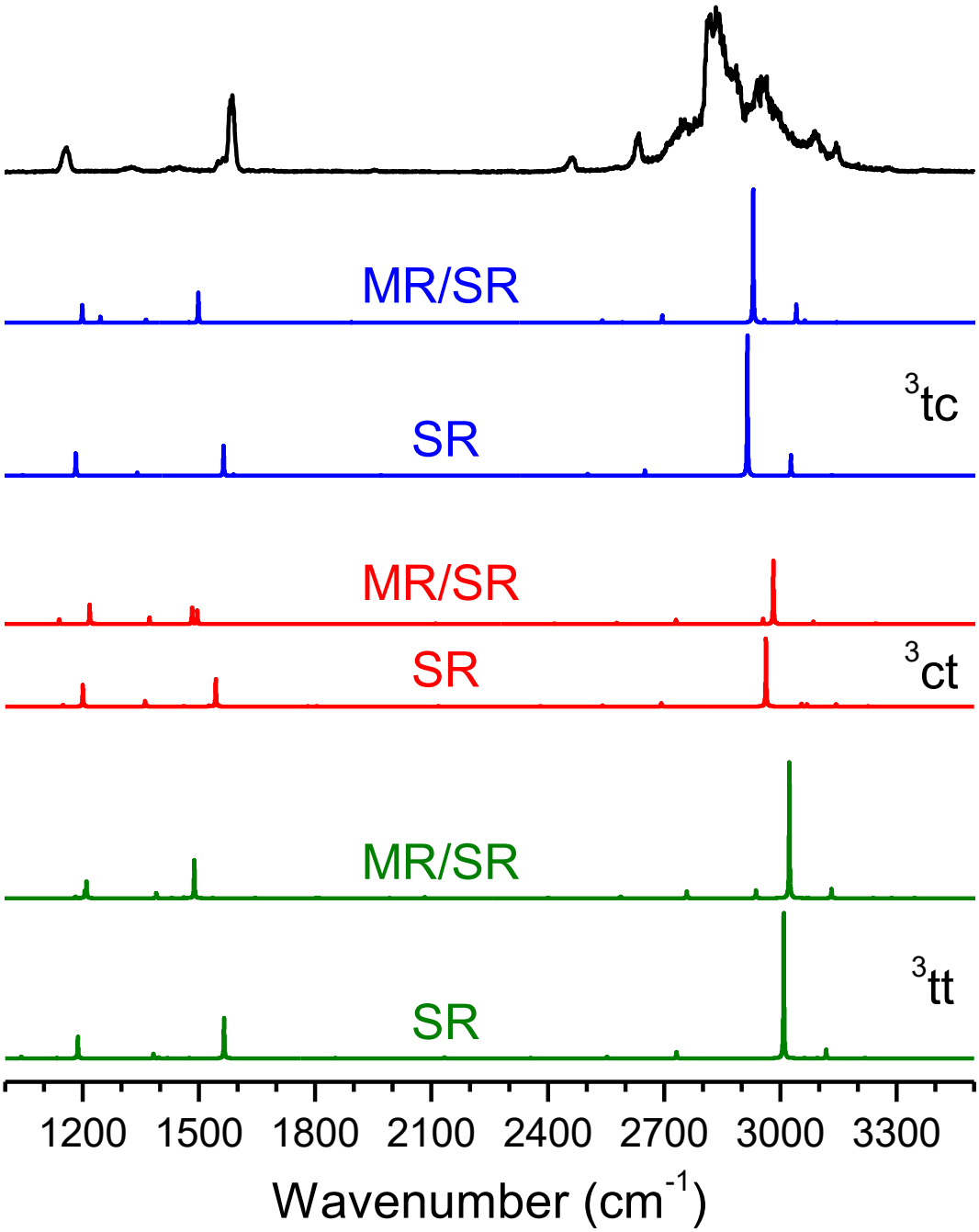

Figure 8.12. Experimental $ArHO_4^+$ spectrum compared to VPT2+K simulations using the ROHF-CCSD(T)/ANO-VT-[T,D]Z force fields (SR) and the composite force fields described in the text (MR/SR).

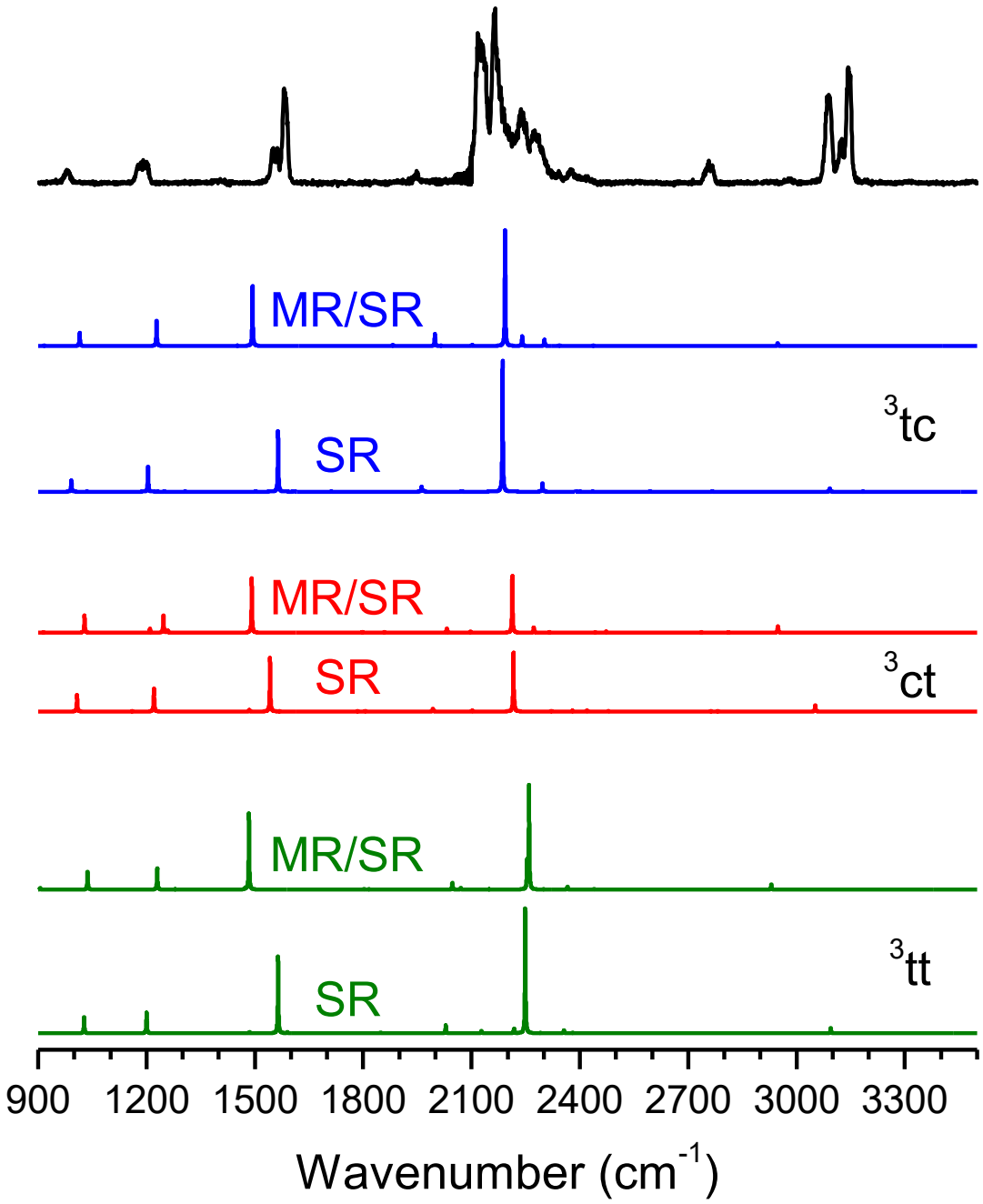

Figure 8.13. Experimental $ArDO_4^+$ spectrum compared to VPT2+K simulations using the ROHF-CCSD(T)/ANO-VT-[T,D]Z force fields (SR) and the composite force fields described in the text (MR/SR).

In the spectrum of $ArDO_4^+$, the ^3cc isomer is again a poor match; however, based on splittings in the ν(O-D) + n[ν(D···Ar)] bands *ca.* 2200 cm^{-1}, the presence of two distinct bands at 1555 and 1582 cm^{-1}, and the broadening of the 1189 cm^{-1} band, this spectrum is best explained by the presence of two covalent-like isomers (Fig. 8.9). The best matches are to the ^3tc and ^3ct isomers. For both systems, we are not able to make a confident assignment to the *tc*, *ct*, and/or *tt* covalent-like isomers, nor can we confidently determine whether the spin state(s) prepared are singlets or triplets. It is worthwhile to note that some transitions, e.g. those around 3100 cm^{-1} and the overtone and combination tone transitions on the red edge of the multiplets centered around 2900 cm^{-1}, are quite a bit more intense in the experiment relative to the theoretical predictions. Enhanced intensities for high frequency bands are often seen because of enhanced laser power and fragmentation efficiency in this region. This has been consistently seen in our infrared photodissociation experiments.[18, 70, 72] It is also noteworthy that our experimental intensity does not precisely correspond with the theoretical intensity, which is calculated for direct absorption events.

8.3.7. Detailed Spectroscopic Assignments

Despite our uncertainty regarding the multiplicity and the identities of the conformers, some assignments can nevertheless be made, as the vibrational modes of different conformers are generally similar. The normal coordinates of the ^3tc, ^3ct, and ^3tt isomers include three localized O-O stretches. These modes will be referred to as far, central, and near, based on their proximity to the hydrogen or deuterium atom. Stated theoretical frequencies will refer to the ^3tc conformer, as its predictions match most closely to the experiment, and it is lowest in electronic energy. Assignments of experimental bands are collected in Tables 8.2 and 8.3. In these tables, it is indicated whenever ^3tt or ^3ct predictions provide a better match to experiment.

8.3.7.1. $ArHO_4^+$ Assignments

The lowest frequency experimental transitions are at 1157, 1325, and 1585 cm^{-1}. These are best assigned to the O-O stretch fundamental nearest to the hydrogen (predicted at 1182 cm^{-1}), the H-O-O bend fundamental (predicted at 1341 cm^{-1}), and the O-O stretch fundamental farthest from the hydrogen (predicted at 1563 cm^{-1}), respectively. A weak transition at 1953 cm^{-1} is assigned to the combination of the far O-O stretch and central O-O stretch, predicted at 1969 cm^{-1}. Somewhat stronger experimental transitions are seen at 2463 and 2634 cm^{-1}, on the red edge of the features centered around 2900 cm^{-1}. These are best assigned to the combination of the near O-O stretch and H-O-O bend (predicted at 2503 cm^{-1}) and to the first overtone of the H-O-O bend (predicted at 2651 cm^{-1}), respectively.

The most intense features are difficult to disentangle. The first strong feature shows up around 2752 cm^{-1}. As a similar feature can be seen in $ArDO_4^+$ (predicted at 2759 cm^{-1}), one possible assignment is to the combination of the near O-O stretch + far O-O stretch (predicted at 2743 cm^{-1}); although, this has very low predicted intensity. The most intense feature is split into 2816 and 2838 cm^{-1} peaks; similarly, the second most intense feature is split into 2939 and 2959 cm^{-1} peaks. The splitting between the centers of both features is about 120 cm^{-1}, and the splittings within each feature are about 20 cm^{-1}. Based on previous studies and the theoretical predictions, the most sensible interpretation of the 120 cm^{-1} splitting is that it separates a strong ν(O-H) transition from a weaker ν(O-H) + ν(H···Ar) transition. For comparison, the theoretical frequency difference between these transitions is 112 cm^{-1}. Although the splitting is predicted accurately, the absolute positions of these transitions (2915 cm^{-1} and 3027 cm^{-1}) are roughly 100 cm^{-1} to the blue of experiment. With regard to the 20 cm^{-1} splitting and broadening, this may be caused by the presence of two conformers, but this is unclear. Lastly, the feature at 3089 cm^{-1}, which appears at the same frequency in the $ArDO_4^+$ spectrum, can be assigned to the first overtone of the far O-O stretch, predicted at 3091 cm^{-1}. The 3145 cm^{-1} peak lacks an obvious assignment. It is close to the

Table 8.2. Assignments for $ArHO_4^+$ experimental bands. CCSD(T) VPT2+K frequencies are given in cm^{-1} with parenthetical intensities given in km/mol. Best conformer matches are bolded.

Expt.	ν **(I)**			Description
	^{3}***tc***	^{3}***ct***	^{3}***tt***	
1157	**1182 (407)**	1200 (388)	1187 (390)	$\nu(O\text{-}O)_{near}$
1325	**1341 (56)**	1361 (105)	1382 (82)	δ(H-O-O)
1585	1563 (546)	1543 (502)	**1565 (739)**	$\nu(O\text{-}O)_{far}$
1953	1969 (12)	1804[a] (6)	1851[b] (7)	$\nu(O\text{-}O)_{far} + \nu(O\text{-}O)_{central}$
2463	**2503 (40)**	2542 (14)	2553 (29)	$\nu(O\text{-}O)_{near}$ + δ(H-O-O)
2634	**2651 (105)**	2693 (60)	2732 (114)	2δ(H-O-O)
2752	2743 (2)	2742 (3)	**2752 (0)**	$\nu(O\text{-}O)_{near} + \nu(O\text{-}O)_{far}$
2816	**2915 (2558)**	2963 (1238)	3009 (2656)	ν(O-H)
2838				
2939	**3027 (381)**	3069 (39)	3118 (162)	ν(O-H) + ν(H···Ar)
2959				
3089	**3091 (3)**	3055 (46)	3096 (10)	$2\nu(O\text{-}O)_{far}$
3145	**3133 (15)**	3174 (0)	3230[c] (0)	ν(O-H) + 2ν(H···Ar)

[a] Better match to δ(H-O-O) + δ_s(O-O-O-O) at 1939 cm^{-1} (2 km/mol).

[b] Better match to δ(H-O-O) + δ_s(O-O-O-O) at **1954 cm^{-1} (3 km/mol)**.

[c] Better match to ν(O-H) + δ_{as}(O-O-O-O) at 3219 cm^{-1} (11 km/mol).

Table 8.3. Assignments for $ArDO_4^+$ experimental bands. CCSD(T) VPT2+K frequencies are given in cm^{-1} with parenthetical intensity given in km/mol. Best conformer matches are bolded.

Expt.	ν (I)			Description
	^3tc	^3ct	^3tt	
981	**992 (111)**	1008 (165)	1027 (163)	δ(D-O-O)
1189	1204 (250)	1221 (229)	**1200 (208)**	$\nu(O\text{-}O)_{near}$
1555	**1564 (605)**	1542 (533)	**1564 (762)**	$\nu(O\text{-}O)_{far}$
1582				
1948	**1962 (50)**	1993 (28)	2029 (78)	2δ(D-O-O)
2125	**2186 (1240)**	2216 (575)	2249 (1240)	ν(O-D)
2164				
2238	**2297 (84)**	2320 (6)	2356 (30)	ν(O-D) + ν(D···Ar)
2274				
2341	**2401 (1)**	2425 (0)	2464 (0)	ν(O-D) + 2ν(D···Ar)
2375				
2759	2767 (2)	**2762 (3)**	2764 (1)	$\nu(O\text{-}O)_{near} + \nu(O\text{-}O)_{far}$
3089	**3092 (30)**	3052 (64)	3095 (52)	$2\nu(O\text{-}O)_{far}$
3145	**3184 (1)**	3227 (0)	3279 (1)	ν(O-D) + δ(D-O-O)

prediction for ν(O-H) + 2ν(H···Ar) (3133 cm^{-1}); however, such a close match to ν(O-H) + 2ν(H···Ar) seems implausible, as the predictions for ν(O-H) + ν(H···Ar) and ν(O-H) are both greatly overestimated.

8.3.7.2. $ArDO_4^+$ Assignments

The lowest frequency feature is observed at 981 cm^{-1}, followed by a broad feature at 1189 cm^{-1}, and a doublet at 1555 and 1582 cm^{-1}. Two of these closely match the 1157 and 1585 cm^{-1} features of $ArHO_4^+$, and they are readily assigned to the near O-O stretch and far O-O stretch. The far O-O stretch (1582 cm^{-1}) is closer in frequency to the $ArHO_4^+$ transition, as it is farther away and more kinetically decoupled from the motion of the hydrogen/deuterium atom, compared to the near O-O stretch at 1189 cm^{-1}. Their theoretical predictions are 1564 and 1204 cm^{-1}, which are both reasonable. The 981 cm^{-1} transition (predicted at 992 cm^{-1}) corresponds to the D-O-O bend fundamental, which is understandably red-shifted compared to the H-O-O bend in $ArHO_4^+$. The extra 1555 cm^{-1} peak and the broadening of the 1189 cm^{-1} peak probably arise from a second conformer (*vide infra*).

The transition at 1948 cm^{-1} (compare to 1953 cm^{-1} in $ArHO_4^+$) could be analogously assigned to the combination of the far O-O stretch and central O-O stretch, predicted here at 1966 cm^{-1}. However, there is a second assignment that is also reasonable. The first overtone of the D-O-O bend is predicted to be a factor of three more intense and to appear at 1962 cm^{-1}. The O-D stretching features are far better resolved than the O-H stretching features. Two progressions of similar intensity are clearly visible at 2125, 2238, 2341 cm^{-1} and 2164, 2274, 2375 cm^{-1}; although, the last member in each progression is weak and uncertain. The large frequency difference, corresponding to changes in ν(D···Ar) excitation, is about 111 cm^{-1} (theoretically 108 cm^{-1}). The small frequency difference is 37 cm^{-1}, and this separates different conformers. As with $ArHO_4^+$, the absolute predictions for the transitions in the ν(O-D) + n[ν(D···Ar)] series are less accurate than the frequency differences, and the predictions are greatly blueshifted. Predictions for the ^{3}*tc* isomer are 2186, 2297, and 2401 cm^{-1}. Similar to $ArHO_4^+$, the 2759 cm^{-1} feature is assigned to the combination of the near O-O stretch + far O-O stretch (predicted at 2767 cm^{-1}), and the 3089 cm^{-1} feature is assigned to the first overtone of the far O-O stretch, (predicted at

3092 cm^{-1}). The 3145 cm^{-1} feature is tentatively assigned to the combination of the D-O-O bend and the O-D stretch (predicted at 3184 cm^{-1}).

8.3.8. Systematic Improvement of ^{3}*tc* Frequency Predictions.

It can be demonstrated that the accuracy of O-H stretch predictions for ^{3}*tc* improves greatly with more complete basis sets and treatment of electron correlation. At the same time, the quality of predictions for other transitions, which were already good with CCSD(T)/ANO-VT-[T,D]Z, does not degrade, with one exception. The most important results are summarized now. Consideration of core-correlation and electron correlation up to CCSDT(Q) and employing a larger basis set improves the agreement for the O-H stretch fundamental by more than 30 cm^{-1} compared to CCSD(T)/ANO-VT-[T,D]Z. Agreement of other transitions improves modestly; however, the agreement for the far O-O stretching fundamental is worsened by 20 cm^{-1} by the collective effects of the various corrections. It is apparent that the description of the far O-O stretch is converged neither with respect to the basis set nor the correlation treatment. Particularly large is the (Q) correction, which lowers the harmonic frequency by 50 cm^{-1}.

Figure 8.14 shows the evolution of the VPT2+K prediction as the force field is improved; likewise, Figure 8.15 shows a similar comparison for untagged ^{3}*tc* HO_4^+. All VPT2+K simulations for each set of comparisons used an equivalent set of resonance definitions and effective Hamiltonian matrices, in order to permit a fair comparison. The simulations are arranged in order of sophistication.

The $ArHO_4^+$ VPT2+K simulation using an ROHF-CCSD(T)/ANO-VT-DZ quartic force field is labeled "DZ" (Fig. 8.14). This yields by far the highest prediction for the O-H stretch (2988 cm^{-1}), which is over 150 cm^{-1} higher than the most intense experimental band in the vicinity. As expected, the most substantial correction to this frequency is achieved by introducing ANO-VT-TZ harmonic frequencies, with a simple substitution adjusting the prediction to 2915 cm^{-1}. The accuracy of the hybrid force field approximation can be judged by the closeness of the

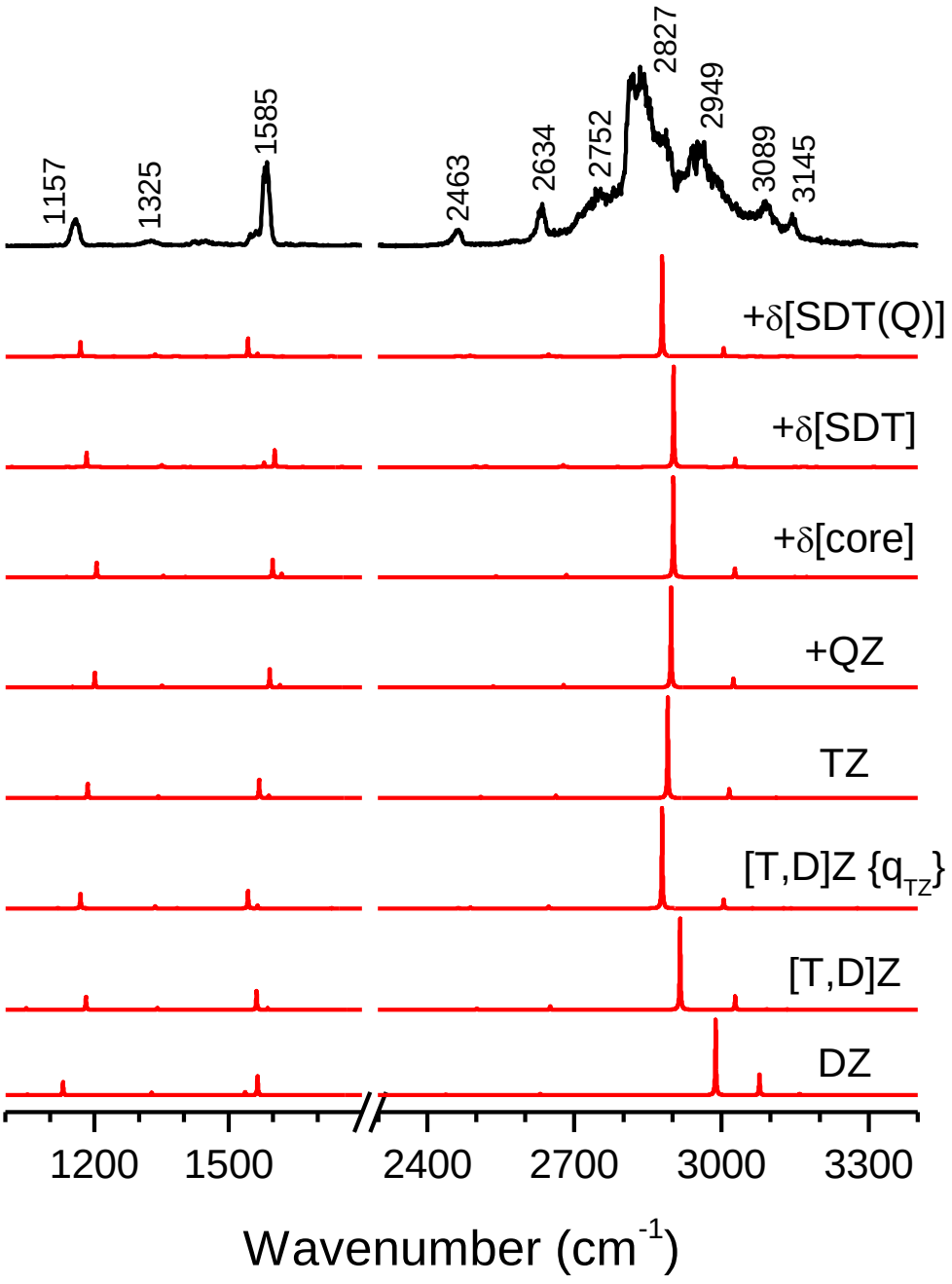

Figure 8.14. Experimental spectrum of $ArHO_4^+$ compared to VPT2+K simulations of ^{3}*tc* $ArHO_4^+$ using various levels of theory. The simulation labeled "+QZ" scales the ANO-VT-TZ harmonic frequencies of $ArHO_4^+$ based on the ANO-VT-QZ harmonic frequencies of HO_4^+, as described in Section 8.2.3. Simulations denoted by "+δ" also use scaled harmonic frequencies but with additional additive corrections appended to CCSD(T)/ANO-VT-QZ. The additive corrections are successive, i.e. the +δ[SDT] simulation contains +δ[core], and the +δ[SDT(Q)] simulation contains both +δ[SDT] and +δ[core]. The simulation labeled [T,D]Z $\{q_{TZ}\}$ is an extension of the [T,D]Z force field in which the DZ cubic/quartic force constants are transformed into the TZ normal coordinates; this uses the procedure described in Reference 50.

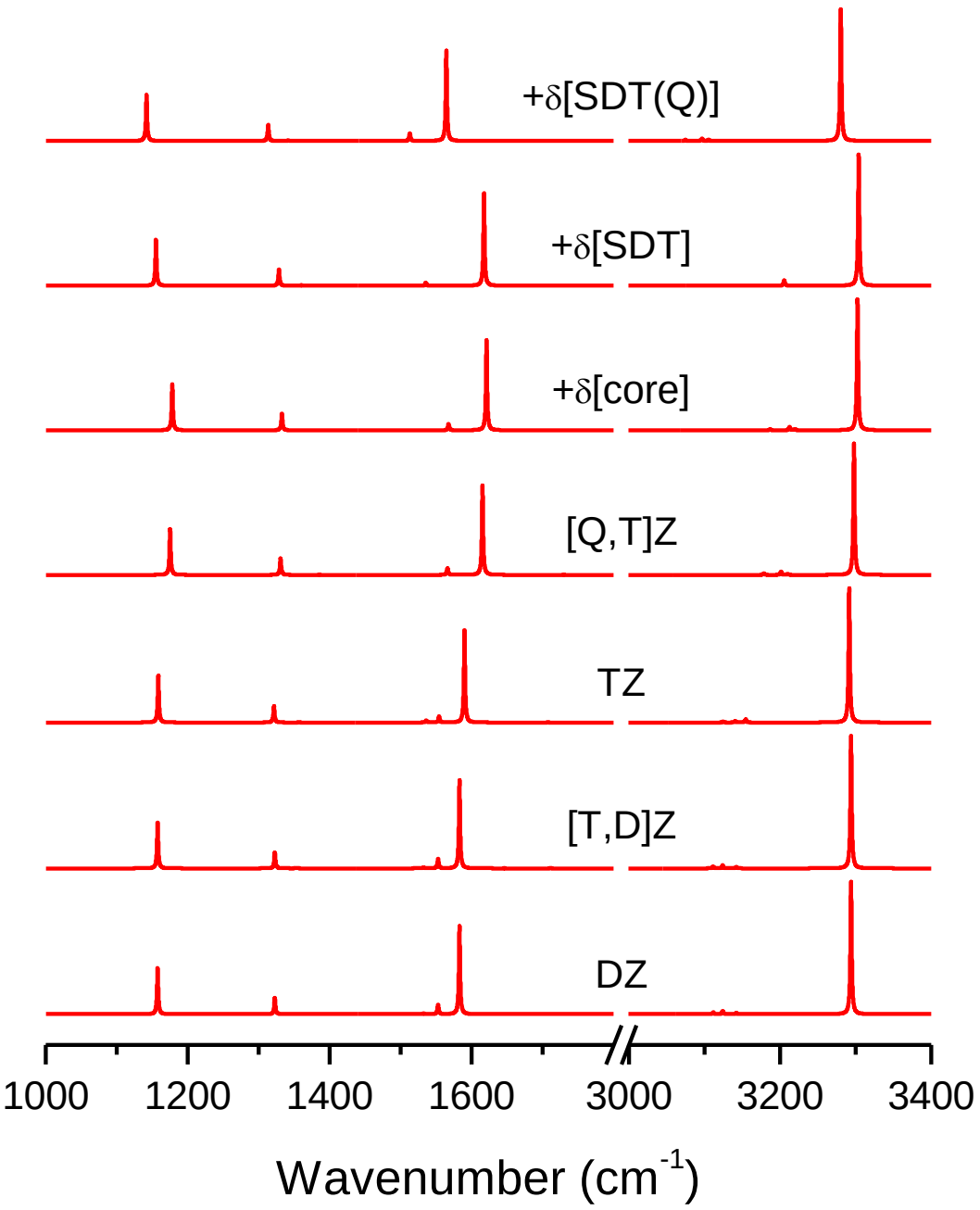

Figure 8.15. VPT2+K simulations of ^{3}tc HO_4^+ at various levels of theory. The simulations denoted by "+δ" are based on the [Q,T]Z force field, with additional corrections included in the determination of the harmonic frequencies. The corrections are successive, i.e. the +δ[SDT] simulation contains +δ[core], and the +δ[SDT(Q)] simulation contains +δ[SDT] and +δ[core].

predictions made with the hybrid [T,D]Z force field and a fully ANO-VT-TZ force field. For this system, the "TZ" simulation predicts 2890 cm^{-1}. This is yet closer to the experimental value, but the [T,D]Z and TZ difference is also non-negligible. We hypothesized that this breakdown of the hybrid approximation was due to changes in the normal coordinates between CCSD(T)/ANO-VT-DZ and CCSD(T)/ANO-VT-TZ, which we did not account for. To test this, we transformed the DZ cubic/quartic force constants into the TZ normal coordinates, using equations from Reference 73 and the procedure described in Reference 50.

The simulation with the resulting force field is given by "[T,D]Z $\{q_{TZ}\}$" in Figure 8.14. Curiously, the O-H stretch prediction is 2864 cm^{-1}, which is an equally inaccurate approximation to the TZ value as the substituted "[T,D]Z" simulation, although in the opposite direction. A numerical comparison of the force constants shows that 80% of them are brought into closer agreement with the TZ values by the coordinate transformation; however, it would seem that the most influential constants for the O-H stretch are either not accurate enough or are fortuitously more accurate in the [T,D]Z substituted force field.

The remaining simulations use the ANO-VT-TZ cubic/quartic force constants and the substituted hybrid approximation rather than transformation, as the transformation procedure requires the full quartic force field, which was intractable with ANO-VT-TZ. These force fields employ the harmonic scaling described in Section 8.2.3, avoiding expensive computations with the argon tag. They introduce a series of successive improvements to the harmonic frequencies. All refinements to the harmonic frequencies are carried through to the subsequent force fields, e.g. the "+QZ" force field improves the basis set, then the "+δ[core]" force field improves the basis set and also accounts for core correlation. It can be seen that the first three of these corrections have very little effect on the O-H stretch fundamental. Correcting for a larger basis set, then core-correlation, and then iterative triple excitations (CCSDT), the frequency prediction changes from 2890 cm^{-1} at CCSD(T)/ANO-VT-TZ to 2897, 2902, and then 2902 cm^{-1},

respectively. Although these corrections act in the wrong direction, they are quite small. When the final correction is introduced for perturbative quadruple excitations, the prediction for the O-H stretch fundamental becomes 2879 cm^{-1}. The agreement with experiment is improved by more than 30 cm^{-1} relative to the ROHF-CCSD(T)/ANO-VT-[T,D]Z simulations selected for the conformer comparisons (Fig. 8.8-8.9). It is not obvious what the force fields are "missing" that would explain the remaining ~ 40-60 cm^{-1} of disagreement. One possibility is that the argon-HO_4^+ interaction requires additional diffuse functions in the basis set for a good description; although, this has not been found to be important for other argon-tagged cations.[70] Related to this, some of the additive corrections to the harmonic frequencies may be sensitive to the argon tag, and it was not feasible for us to assess this. Finally, it should be noted that some of the uncertainty/inaccuracy derives from the lack of a single band center (2818 cm^{-1} and 2838 cm^{-1}) and the possibility that ^{3}*tc* may not be the specific conformer that is produced.

Most of the other transitions were already predicted accurately at [T,D]Z, yet the various corrections do also improve their agreement in a similar, non-monotonic fashion. The glaring exception is the far O-O stretch (experimentally 1585 cm^{-1}), where the final CCSDT(Q) correction reduces the harmonic frequency by 50 cm^{-1}, leading to a slightly worse agreement with experiment than the [T,D]Z simulations. This is mirrored by a nearly 0.01 Å lengthening of the corresponding ^{3}*tc* HO_4^+ bond length. Such a large quadruples correction is unexpected, even for a motion that involves the stretching of atoms with significant multiple-bond character. A typical single-configurational system would be expected to show thorough convergence to the full configuration interaction limit by CCSDT(Q). With respect to the basis set, it is also not apparent that the far O-O stretch is being given a converged description, as its CCSD(T) harmonic frequency increases by 5 cm^{-1} from DZ to TZ but then by 25 cm^{-1} from TZ to QZ. Furthermore, accurate predictions for the far O-O stretch are also complicated by the central O-O + near O-O stretch combination, which falls nearby in frequency and couples strongly. It is clearly seen in

Figure 8.14 that its position, as a weak feature, relative to the intense far O-O stretch is very sensitive to the level of theory.

8.4. Conclusions

The first infrared spectra were reported for HO_4^+ and DO_4^+. Assignment of these complex spectra motivated a computational study of the HO_4^+ potential energy surface in its various low-lying multiplicities. Several new, covalent-like conformers were identified on the singlet and triplet surfaces. These new conformers are two- and single-configurational, respectively, and structurally novel. They are the only reasonable match with the experimental infrared spectra. The $ArHO_4^+$ spectrum is consistent with the presence of one covalent-like isomer; whereas, the $ArDO_4^+$ spectrum is consistent with the presence of two different covalent-like isomers. The VPT2+K method successfully describes the covalent-like isomers. However, it is expected that accurate vibrational frequencies for the various PBD species, including the low-lying ^1cc and ^3cc isomers, will require full-dimensional (9D) variational calculations and very careful calibration of the electronic structure method. We expect that the majority of the error in our VPT2 predictions is due to error in the potential, and we have shown that much of this can be eliminated if higher levels of theory are applied. It would be valuable to benchmark composite single-reference/multi-reference electronic structure models on a wider variety of systems, as this study, to the best of our knowledge, represents their first application to the determination of equilibrium geometries and harmonic frequencies.

References

(1) Feng, W. Y.; Goldenberg, M.; Lifshitz, C. Reactions of Proton-Bound Dimers. *J. Am. Soc. Mass. Spectrom.* **1994**, *5*, 695-703.

(2) Guasco, T. L.; Johnson, M. A.; McCoy, A. B. Unraveling Anharmonic Effects in the Vibrational Predissociation Spectra of $H_5O_2^+$ and Its Deuterated Analogues. *J. Phys. Chem. A* **2011**, *115*, 5847-5858.

(3) Fournier, J. A.; Wolke, C. T.; Johnson, M. A.; Odbadrakh, T. T.; Jordan, K. D.; Kathmann, S. M.; Xantheas, S. S. Snapshots of Proton Accommodation at a Microscopic Water Surface: Understanding the Vibrational Spectral Signatures of the Charge Defect in Cryogenically Cooled $H^+(H_2O)_{n=2–28}$ Clusters. *J. Phys. Chem. A* **2015**, *119*, 9425-9440.

(4) Oka, T. Interstellar H_3^+. *Proc. Natl. Acad. Sci. U. S. A.* **2006**, *103*, 12235-12242.

(5) Geballe, T. R.; Oka, T. Detection of H_3^+ in Interstellar Space. *Nature* **1996**, *384*, 334-335.

(6) Klemperer, W. Astronomical Chemistry. *Annu. Rev. Phys. Chem.* **2011**, *62*, 173-184.

(7) Snow, T. P.; Bierbaum, V. M. Ion Chemistry in the Interstellar Medium. *Annu. Rev. Anal. Chem.* **2008**, *1*, 229-259.

(8) Petrie, S.; Bohme, D. K. Ions in Space. *Mass Spectrom. Rev.* **2007**, *26*, 258-280.

(9) Smith, D. The Ion Chemistry of Interstellar Clouds. *Chem. Rev.* **1992**, *92*, 1473-1485.

(10) Tielens, A. G. G. M. *The Physics and Chemistry of the Interstellar Medium*; Cambridge University Press, 2005, p 495.

(11) Hartquist, T. W. *The Molecular Astrophysics of Stars and Galaxies*; Clarendon Press: Oxford, 1998, p 539.

(12) Roscioli, J. R.; McCunn, L. R.; Johnson, M. A. Quantum Structure of the Intermolecular Proton Bond. *Science* **2007**, *316*, 249-254.

(13) Ault, B. S.; Steinback, E.; Pimentel, G. C. Matrix-Isolation Studies of Hydrogen-Bonding - Vibrational Correlation Diagram. *J. Phys. Chem.* **1975**, *79*, 615-620.

(14) Ricks, A. M.; Douberly, G. E.; Duncan, M. A. Infrared Spectroscopy of the Protonated Nitrogen Dimer: The Complexity of Shared Proton Vibrations. *J. Chem. Phys.* **2009**, *131*, 104312.

(15) Douberly, G. E.; Ricks, A. M.; Ticknor, B. W.; Duncan, M. A. Structure of Protonated Carbon Dioxide Clusters: Infrared Photodissociation Spectroscopy and Ab Initio Calculations. *J. Phys. Chem. A* **2008**, *112*, 950-959.

(16) Cheng, T. C.; Bandyopadyay, B.; Wang, Y.; Carter, S.; Braams, B. J.; Bowman, J. M.; Duncan, M. A. Shared-Proton Mode Lights up the Infrared Spectrum of Fluxional Cations H_5^+ and D_5^+. *J. Phys. Chem. Lett.* **2010**, *1*, 758-762.

(17) McDonald, D. C.; Wagner, J. P.; Duncan, M. A. Communication: Infrared Photodissociation Spectroscopy of the H_6^+ Cation in the Gas Phase. *J. Chem. Phys.* **2018**, *149*, 031105.

(18) Douberly, G. E.; Ricks, A. M.; Ticknor, B. W.; Duncan, M. A. The Structure of Protonated Acetone and Its Dimer: Infrared Photodissociation Spectroscopy from 800 to 4000 cm^{-1}. *Phys. Chem. Chem. Phys.* **2008**, *10*, 77-79.

(19) Wagner, J. P.; McDonald, D. C.; Duncan, M. A. Infrared Spectroscopy of the Astrochemically Relevant Protonated Formaldehyde Dimer. *J. Phys. Chem. A* **2018**, *122*, 192-198.

(20) Wagner, J. P.; McDonald, D. C.; Duncan, M. A. Spectroscopy of Proton Coordination with Ethylenediamine. *J. Phys. Chem. A* **2018**, *122*, 5168-5176.

(21) Solca, N.; Dopfer, O. IR Spectrum and Structure of Protonated Ethanol Dimer: Implications for the Mobility of Excess Protons in Solution. *J. Am. Chem. Soc.* **2004**, *126*, 9520-9521.

(22) Moore, D. T.; Oomens, J.; van der Meer, L.; von Helden, G.; Meijer, G.; Valle, J.; Marshall, A. G.; Eyler, J. R. Probing the Vibrations of Shared, OH^+O-Bound Protons in the Gas Phase. *Chemphyschem* **2004**, *5*, 740-743.

(23) Duong, C. H.; Gorlova, O.; Yang, N.; Kelleher, P. J.; Johnson, M. A.; McCoy, A. B.; Yu, Q.; Bowman, J. M. Disentangling the Complex Vibrational Spectrum of the Protonated Water Trimer, $H^+(H_2O)_3$, with Two-Color IR-IR Photodissociation of the Bare Ion and Anharmonic VSCF/VCI Theory. *J. Phys. Chem. Lett.* **2017**, *8*, 3782-3789.

(24) McDonald, D. C.; Mauney, D. T.; Leicht, D.; Marks, J. H.; Tan, J. A.; Kuo, J. L.; Duncan, M. A. Communication: Trapping a Proton in Argon: Spectroscopy and

Theory of the Proton-Bound Argon Dimer and Its Solvation. *J. Chem. Phys.* **2016**, *145*, 231101.

(25) Asvany, O.; Schlemmer, S.; Szidarovszky, T.; Császár, A. G. Infrared Signatures of the HHe_n^+ and DHe_n^+ (n = 3–6) Complexes. *J. Phys. Chem. Lett.* **2019**, *10*, 5325-5330.

(26) Tan, J. A.; Kuo, J. L. A Theoretical Study on the Infrared Signatures of Proton-Bound Rare Gas Dimers (Rg-H^+-Rg), Rg = {Ne, Ar, Kr, and Xe}. *J. Chem. Phys.* **2019**, *150*, 124305.

(27) Fortenberry, R. C. Rovibrational Characterization and Interstellar Implications of the Proton-Bound, Noble Gas Complexes: $ArHAr^+$, $NeHNe^+$, and $ArHNe^+$. *ACS Earth Space Chem.* **2017**, *1*, 60-69.

(28) Janssen, C. L.; Allen, W. D.; Schaefer, H. F.; Bowman, J. M. The Infrared-Spectrum of the Hydrogen Bifluoride Anion - Unprecedented Variation with Level of Theory. *Chem. Phys. Lett.* **1986**, *131*, 352-358.

(29) Xavier, G. D.; Bernal-Uruchurtu, M. I.; Hernández-Lamoneda, R. Communication: Ab Initio Study of O_4H^+: A Tracer Molecule in the Interstellar Medium? *J. Chem. Phys.* **2014**, *141*, 081101.

(30) Xavier, F. G. D.; Hernández-Lamoneda, R. Ab Initio Study of the O_4H^+ Novel Species: Spectroscopic Fingerprints to Aid Its Observation. *Phys. Chem. Chem. Phys.* **2015**, *17*, 16023-16032.

(31) Kohguchi, H.; Jusko, P.; Yamada, K. M. T.; Schlemmer, S.; Asvany, O. High-Resolution Infrared Spectroscopy of O_2H^+ in a Cryogenic Ion Trap. *J. Chem. Phys.* **2018**, *148*, 144303.

(32) Cunningham, A. J.; Payzant, J. D.; Kebarle, P. A Kinetic Study of the Proton Hydrate H^+ $(H_2O)_n$ Equilibria in the Gas Phase. *J. Am. Chem. Soc.* **1972**, *94*, 7627-7632.

(33) Widicus Weaver, S. L.; Woon, D. E.; Ruscic, B.; McCall, B. J. Is HO_2^+ a Detectable Interstellar Molecule? *Astrophys. J.* **2009**, *697*, 601-609.

(34) Kluge, L.; Gartner, S.; Brunken, S.; Asvany, O.; Gerlich, D.; Schlemmer, S. Transfer of a Proton Between H_2 and O_2. *Philos. Trans. R. Soc., A* **2012**, *370*, 5041-5054.

(35) Reid, G. R. *Adv. Atom. Mol. Phys.* **1976**, *12*, 375.

(36) Parise, B.; Bergman, P.; Du, F. Detection of the Hydroperoxyl Radical HO_2 Toward ρ Ophiuchi A. *Astron. Astrophys.* **2012**, *541*, L11.

(37) Phillips, T. G.; Knapp, G. R. Interstellar Ozone. *Bull. Am. Astron. Soc.* **1980**, *12*, 440.

(38) Wyrowski, F.; Menten, K. M.; Güsten, R.; Belloche, A. First Interstellar Detection of OH^+. *Astron. Astrophys.* **2010**, *518*, A26.

(39) Renzler, M.; Ralser, S.; Kranabetter, L.; Barwa, E.; Scheier, P.; Ellis, A. M. Observation of Stable HO_4^+ and DO_4^+ Ions from Ion-Molecule Reactions in Helium Nanodroplets. *Phys. Chem. Chem. Phys.* **2016**, *18*, 13169-13172.

(40) Hiraoka, K.; Saluja, P. P. S.; Kebarle, P. Stabilities of Complexes $(N_2)_nH^+$, $(CO)_nH^+$, and $(O_2)_nH^+$ for n = 1 to 7 Based on Gas-Phase Ion-Equilibria Measurements. *Can. J. Chem.* **1979**, *57*, 2159-2166.

(41) Szymczak, J. J.; Gora, R. W.; Roszak, S.; Majumdar, D.; Wang, J.; Grabowski, S. J.; Leszczynski, J. Proton Bound Open Shell Systems - Theoretical Studies on $O_2H^+(O_2)_n$ (n = 1-6) Complexes. *Mol. Phys.* **2006**, *104*, 2327-2336.

(42) Douberly, G. E.; Ricks, A. M.; Ticknor, B. W.; Mckee, W. C.; Schleyer, P. V. R.; Duncan, M. A. Infrared Photodissociation Spectroscopy of Protonated Acetylene and Its Clusters. *J. Phys. Chem. A* **2008**, *112*, 1897-1906.

(43) Duncan, M. A. Infrared Laser Spectroscopy of Mass-Selected Carbocations. *J. Phys. Chem. A* **2012**, *116*, 11477-11491.

(44) J. F. Stanton, J. Gauss, L. Cheng, M. E. Harding, D. A. Matthews, and P. G. Szalay, CFOUR, Coupled-cluster techniques for computational chemistry, a quantum-chemical program package, With contributions from A. A. Auer, R. J. Bartlett, U. Benedikt, C. Berger, D. E. Bernholdt, Y. J. Bomble, O. Christiansen, F. Engel, R. Faber, M. Heckert, O. Heun, M. Hilgenberg, C. Huber, T.-C. Jagau,

D. Jonsson, J. Jusélius, T. Kirsch, K. Klein, W. J. Lauderdale, F. Lipparini, T. Metzroth, L. A. Mück, D. P. O'Neill, D. R. Price, E. Prochnow, C. Puzzarini, K. Ruud, F. Schiffmann, W. Schwalbach, C. Simmons, S. Stopkowicz, A. Tajti, J. Vázquez, F. Wang, J. D. Watts and the integral packages MOLECULE (J. Almlöf and P. R. Taylor), PROPS (P. R. Taylor), ABACUS (T. Helgaker, H. J. Aa. Jensen, P. Jørgensen, and J. Olsen), and ECP routines by A. V. Mitin and C. van Wüllen, for the current version, see http://www.cfour.de.

(45) Neese, F. The ORCA Program System. *Wiley Interdiscip. Rev.: Comput. Mol. Sci.* **2012**, *2*, 73-78.

(46) Neese, F. Software Update: The ORCA Program System, Version 4.0. *Wiley Interdiscip. Rev.: Comput. Mol. Sci.* **2018**, *8*, e1327.

(47) Guo, Y.; Sivalingam, K.; Valeev, E. F.; Neese, F. Explicitly Correlated N-Electron Valence State Perturbation Theory (NEVPT2-F12). *J. Chem. Phys.* **2017**, *147*, 064110.

(48) Martin, J. M. L.; Kesharwani, M. K. Assessment of CCSD(T)-F12 Approximations and Basis Sets for Harmonic Vibrational Frequencies. *J. Chem. Theory Comput.* **2014**, *10*, 2085-2090.

(49) Adler, T. B.; Knizia, G.; Werner, H. J. A Simple and Efficient CCSD(T)-F12 Approximation. *J. Chem. Phys.* **2007**, *127*, 221106

(50) Franke, P. R.; Brice, J. T.; Moradi, C. P.; Schaefer, H. F.; Douberly, G. E. Ethyl + O_2 in Helium Nanodroplets: Infrared Spectroscopy of the Ethylperoxy Radical. *J. Phys. Chem. A* **2019**, *123*, 3558-3568.

(51) Moradi, C. P.; Morrison, A. M.; Klippenstein, S. J.; Goldsmith, C. F.; Douberly, G. E. Propargyl + O_2 Reaction in Helium Droplets: Entrance Channel Barrier or Not? *J. Phys. Chem. A* **2013**, *117*, 13626-13635.

(52) Davis, M. M.; Weidman, J. D.; Abbott, A. S.; Douberly, G. E.; Turney, J. M.; Schaefer, H. F. Characterization of the 2-Methylvinoxy Radical + O_2 Reaction: A Focal Point Analysis and Composite Multireference Study. *J. Chem. Phys.* **2019**, *151*, 124302.

(53) Weidman, J. D.; Allen, R. T.; Moore, K. B.; Schaefer, H. F. High Level Theoretical Characterization of the Vinoxy Radical ($\bullet CH_2CHO$) + O_2 Reaction. *J. Chem. Phys.* **2018**, *148*, 184308.

(54) Claudino, D.; Gargano, R.; Bartlett, R. J. Coupled-Cluster Based Basis Sets for Valence Correlation Calculations. *J. Chem. Phys.* **2016**, *144*, 104106.

(55) Stanton, J. F. Why CCSD(T) Works: A Different Perspective. *Chem. Phys. Lett.* **1997**, *281*, 130-134.

(56) Rosnik, A. M.; Polik, W. F. VPT2+K Spectroscopic Constants and Matrix Elements of the Transformed Vibrational Hamiltonian of a Polyatomic Molecule with Resonances Using Van Vleck Perturbation Theory. *Mol. Phys.* **2014**, *112*, 261-300.

(57) Franke, P. R.; Douberly, G. E. Rotamers of Isoprene: Infrared Spectroscopy in Helium Droplets and Ab Initio Thermochemistry. *J. Phys. Chem. A* **2018**, *122*, 148-158.

(58) Schneider, H.; Vogelhuber, K. M.; Schinle, F.; Stanton, J. F.; Weber, J. M. Vibrational Spectroscopy of Nitroalkane Chains Using Electron Autodetachment and Ar Predissociation. *J. Phys. Chem. A* **2008**, *112*, 7498-7506.

(59) Vazquez, J.; Stanton, J. F. Treatment of Fermi Resonance Effects on Transition Moments in Vibrational Perturbation Theory. *Mol. Phys.* **2007**, *105*, 101-109.

(60) Vazquez, J.; Stanton, J. F. Simple(r) Algebraic Equation for Transition Moments of Fundamental Transitions in Vibrational Second-Order Perturbation Theory. *Mol. Phys.* **2006**, *104*, 377-388.

(61) Bloino, J.; Barone, V. A Second-Order Perturbation Theory Route to Vibrational Averages and Transition Properties of Molecules: General Formulation and Application to Infrared and Vibrational Circular Dichroism Spectroscopies. *J. Chem. Phys.* **2012**, *136*, 124108.

(62) Feierabend, K. J.; Havey, D. K.; Varner, M. E.; Stanton, J. F.; Vaida, V. A Comparison of Experimental and Calculated Spectra of HNO_3 in the Near-Infrared Using Fourier Transform Infrared Spectroscopy and Vibrational Perturbation Theory. *J. Chem. Phys.* **2006**, *124*, 124323.

(63) Martin, J. M. L.; Lee, T. J.; Taylor, P. R.; Francois, J. P. The Anharmonic-Force Field of Ethylene, C_2H_4, by Means of Accurate Ab Initio Calculations. *J. Chem. Phys.* **1995**, *103*, 2589-2602.

(64) Misiewicz, J. P.; Moore, K. B.; Franke, P. R.; Morgan, W. J.; Turney, J. M.; Douberly, G. E.; Schaefer, H. F. Sulfurous and Sulfonic Acids: Predicting the Infrared Spectrum and Setting the Surface Straight. *J. Chem. Phys.* **2020**, *152*, 024302.

(65) Matthews, D. A.; Stanton, J. F. Quantitative Analysis of Fermi Resonances by Harmonic Derivatives of Perturbation Theory Corrections. *Mol. Phys.* **2009**, *107*, 213-222.

(66) MRCC, a quantum chemical program suite written by M. Kállay, Z. Rolik, J. Csontos, P. Nagy, G. Samu, D. Mester, I. Ladjánszki, L. Szegedy, B. Ladóczki, K. Petrov, M. Farkas, B. Hégely. See also. Z. Rolik, L. Szegedy, I. Ladjánszki, B. Ladóczki, and M. Kállay,. J. Chem. Phys. **139**, 094105 (2013), as well as: www.mrcc.hu.

(67) Peterson, K. A.; Dunning, T. H. Accurate Correlation Consistent Basis Sets for Molecular Core-Valence Correlation Effects: The Second Row Atoms Al-Ar, and the First Row Atoms B-Ne Revisited. *J. Chem. Phys.* **2002**, *117*, 10548-10560.

(68) McDonald, D. C.; Wagner, J. P.; McCoy, A. B.; Duncan, M. A. Near-Infrared Spectroscopy and Anharmonic Theory of Protonated Water Clusters: Higher Elevations in the Hydrogen Bonding Landscape. *J. Phys. Chem. Lett.* **2018**, *9*, 5664-5671.

(69) Wagner, J. P.; McDonald, D. C.; Duncan, M. A. Near-Infrared Spectroscopy and Anharmonic Theory of the $H_2O^+Ar_{1,2}$ Cation Complexes. *J. Chem. Phys.* **2017**, *147*, 104302.

(70) McDonald, D. C.; Wagner, J. P.; Duncan, M. A. Mid/Near Infrared Spectroscopy of the H_2Cl^+ Ar Cation Complex Compared to the Predictions of Anharmonic Theory. *Chem. Phys. Lett.* **2018**, *691*, 51-55.

(71) Crawford, T. D.; Stanton, J. F.; Allen, W. D.; Schaefer, H. F. Hartree-Fock Orbital Instability Envelopes in Highly Correlated Single-Reference Wave Functions. *J. Chem. Phys.* **1997**, *107*, 10626-10632.

(72) Wagner, J. P.; McDonald, D. C.; Duncan, M. A. An Argon-Oxygen Covalent Bond in the $ArOH^+$ Molecular Ion. *Angew. Chem., Int. Ed.* **2018**, *57*, 5081-5085.

(73) Hoy, A. R.; Mills, I. M.; Strey, G. Anharmonic Force Constant Calculations. *Mol. Phys.* **1972**, *24*, 1265-1290.

CHAPTER 9

CONCLUSIONS AND OUTLOOK

The HENDI methodology has made possible several detailed comparisons between experiment and theory of the CH stretching spectral region, for small-to-medium sized organic systems. The molecules discussed in Chapters 4, 5, and 6 exhibit densities of vibrational states, in the CH stretching region, that are sufficiently high to provide a challenge for anharmonic models but not so high that eigenstate-resolved spectra cannot be obtained. Truly, these systems occupy a "sweet spot." It can be seen that systems of larger size have HENDI spectra comprising numerous, overlapping bands, and it can be difficult to obtain much insight into the underlying anharmonic coupling. See, for instance, the spectra of the nitrite precursors of the ethyl and propyl radicals, respectively (Fig. 6.3, 4.2, and 4.4). Similarly, smaller systems often possess simpler CH stretching spectra that are either non-resonant or dominated by a very small number of anharmonic resonances (Sections 3.8.2 and 3.10).[1-2]

In modeling the CH stretch regions of hydrocarbons with large effective Hamiltonian simulations, the significance of Darling-Dennison couplings could be explored. In both of the propyl radicals and isoprene, their contribution was found to be minimal in the CH stretching region. Although a detailed benchmarking study has not been performed, it is expected that theoretical models which neglect Darling-Dennison coupling will still be very successful here. The intensities in these hydrocarbon systems were derived from linear harmonic oscillator transition moments. The agreement with experiment is sufficiently good to facilitate spectral assignment. Use of the far more complicated deperturbed VPT2 transition moments does not appear to be necessary for simulations of CH stretches.[2] It may even be the case that large

effective Hamiltonian simulations using harmonic oscillator transition moments provide superior predictions to small effective Hamiltonian simulations based on more rigorous transition moments, which appears to be more prevalent in the literature.

In small alkenes (isoprene and propene), strong Fermi couplings occur between the highest frequency CH stretches and combinations involving both C=C stretching and CH_2 bending.[3] In isoprene, this is found to be the dominant type of anharmonic coupling in the region above 3050 cm^{-1}. In propene, a Fermi resonance of this type causes the antisymmetric CH_2 stretch fundamental to split into two strong features.[3] This likely generalizes to larger alkenes. In both systems, VPT2+K also predicts that there is a moderate tendency for the CH stretches to mix amongst themselves. Most of this mixing is due to indirect coupling rather than to direct Darling-Dennison coupling. Such a thing is permitted by large effective Hamiltonians but is missed entirely in simulations that attempt to distill the anharmonic coupling problem down to a series of simple two- or three-state interactions.

The comparisons made in Chapter 4 between VPT2+K and Sibert's local mode Hamiltonian model suggest that the latter is a valuable tool for spectral assignment of alkyl radicals. It may be used as a complement to *ab initio* methods or rather successfully as a standalone model. Some of its advantages include its low cost, its avoidance of anharmonic couplings with low frequency modes, and the more intuitive interpretation of Fermi coupling allowed by localized coordinates. It suffers in that it requires careful parameterization in order to describe new types of couplings (e.g. those described in the previous paragraph). The local mode Hamiltonian "simple model" performs similarly to VPT2+K for *n*-propyl radical but significantly better for *i*-propyl radical.[4] The poor performance of VPT2+K for *i*-propyl is likely due to an inaccurate treatment of coupling to the large-amplitude radical CH wagging motion. An effective solution to the problem of strongly-coupled large-amplitude coordinates, in the framework of rectilinear vibrational perturbation theory, has not yet been developed.

Chapter 6 and the entirely theoretical work of Chapter 7 both support the previously acknowledged idea that O-O stretching fundamentals of alkyl peroxy radicals are difficult for electronic structure theory to describe.[5-7] Errors in harmonic frequencies can be in excess of 50 cm^{-1} when using CCSD(T) with polarized double-zeta basis sets. Moreover, the O-O stretch coordinate is sensitive to choice of reference wavefunction, appearing to be more accurate with ROHF. The reference dependence is exaggerated in the lowest electronically-excited state of *tert*-butylperoxy radical (Table 7.19). Errors tend to also manifest in anharmonic frequencies whenever hybrid approximations are made in computing the force field. These errors arise from differing amounts of localization of the O-O and C-O stretching normal coordinates at different levels of theory. For ethylperoxy radical, eliminating the normal coordinate mismatch error using a force field transformation does not lead to great improvements in the accuracy of O-O stretching anharmonic force constants, as they still suffer from large errors due to the basis set. It would be useful to determine the requirements for a level of theory to achieve a given level of accuracy for these transitions, considering that they are often strongly vibronically active and are useful in distinguishing different conformers of peroxy radicals.

In Chapter 8, in order to describe the HO_4^+ system, single-reference multi-reference (MR/SR) composite energy schemes were employed. Composite schemes of this type, which have been used previously to obtain accurate single point energies along potential energy surfaces, are used here to determine optimized geometries, harmonic frequencies, and relative energetics for several conformers in several spin multiplicities.[8] The energetics agree well with purely multi-reference methods, and the frequency predictions for select conformers are also in reasonable agreement with high-quality single-reference methods. Benchmarking studies would be helpful to establish the accuracy of MR/SR approaches and to assess their performance in different types of multi-configurational situations. The experimental spectra presented in this

chapter are interpreted as arising from novel, covalent-like conformers of HO_4^+ and DO_4^+, which were identified for the first time with the MR/SR scheme.

In Chapter 6, the reaction between ethyl radical and O_2 in a helium droplet appears to produce significant amounts of both the *trans* and *gauche* rotamers of ethylperoxy radical. This result is different from the similar, barrierless reactions forming the allylperoxy and propargylperoxy radicals in helium droplets, in which only a single conformer could be detected.[8-9] The dynamics of bimolecular reactions in helium droplets are not well understood. In addition to following a potential energy surface that is nearly the same as the gas-phase potential surface, the dynamics of a helium droplet reaction also depend on the rate of energy dissipation to the droplet. The dissipation rate varies with the type of internal coordinate; furthermore, it is plausible that it could be similar to the rate of intermolecular association. To assist those whom might attempt to model this, it would be of value to experimentally study further peroxy radical reactions, to add to the dataset. Good candidates include vinylperoxy and *i*-propylperoxy, which each can exist as two possible rotamers, and *n*-propylperoxy, which has five distinct rotamers.[7] Reactions between OH and alkenes, some of which are thought to be barrierless or to have submerged barriers, would also be worthwhile to study.[10] Their dynamics would be different, owing to the strong influence of their hydrogen-bonded pre-reactive complexes.

References

(1) Martin, J. M. L.; Lee, T. J.; Taylor, P. R.; Francois, J. P. The Anharmonic-Force Field of Ethylene, C_2H_4, by Means of Accurate Ab Initio Calculations. *J. Chem. Phys.* **1995**, *103*, 2589-2602.

(2) Vazquez, J.; Stanton, J. F. Treatment of Fermi Resonance Effects on Transition Moments in Vibrational Perturbation Theory. *Mol. Phys.* **2007**, *105*, 101-109.

(3) Pullen, G. T.; Franke, P. R.; Lee, Y. P.; Douberly, G. E. Infrared Spectroscopy of Propene in Solid *para*-Hydrogen and Helium Droplets: The Role of Matrix Shifts in the Analysis of Anharmonic Resonances. *J. Mol. Spectrosc.* **2018**, *354*, 7-14.

(4) Tabor, D. P.; Hewett, D. M.; Bocklitz, S.; Korn, J. A.; Tomaine, A. J.; Ghosh, A. K.; Zwier, T. S.; Sibert, E. L. Anharmonic Modeling of the Conformation-Specific IR Spectra of Ethyl, *n*-Propyl, and *n*-Butylbenzene. *J. Chem. Phys.* **2016**, *144*, 224310.

(5) Copan, A. V.; Schaefer, H. F.; Agarwal, J. Examining the Ground and First Excited States of Methyl Peroxy Radical with High-Level Coupled-Cluster Theory. *Mol. Phys.* **2015**, *113*, 2992-2998.

(6) Launder, A. M.; Turney, J. M.; Agarwal, J.; Schaefer, H. F. Ethylperoxy Radical: Approaching Spectroscopic Accuracy via Coupled-Cluster Theory. *Phys. Chem. Chem. Phys.* **2017**, *19*, 15715-15723.

(7) Hoobler, P. R.; Turney, J. M.; Schaefer, H. F. Investigating the Ground-State Rotamers of *n*-Propylperoxy Radical. *J. Chem. Phys.* **2016**, *145*, 174301.

(8) Moradi, C. P.; Morrison, A. M.; Klippenstein, S. J.; Goldsmith, C. F.; Douberly, G. E. Propargyl + O_2 Reaction in Helium Droplets: Entrance Channel Barrier or Not? *J. Phys. Chem. A* **2013**, *117*, 13626-13635.

(9) Leavitt, C. M.; Moradi, C. P.; Acrey, B. W.; Douberly, G. E. Infrared Laser Spectroscopy of the Helium-Solvated Allyl and Allyl Peroxy Radicals. *J. Chem. Phys.* **2013**, *139*, 234301.

(10) Allodi, M. A.; Kirschner, K. N.; Shields, G. C. Thermodynamics of the Hydroxyl Radical Addition to Isoprene. *J. Phys. Chem. A* **2008**, *112*, 7064-7071.